Numerical modeling of liquefaction-induced failure of geostructures subjected to earthquakes

Ioanna Rapti

NNT : 2016SACLC025

THÈSE DE DOCTORAT DE L'UNIVERSITÉ PARIS-SACLAY,

préparée à CentraleSupélec.

ÉCOLE DOCTORALE N°579

Sciences mécaniques et énergétiques, matériaux et géosciences.

Spécialité de doctorat: Génie Civil

Présentée par

Ioanna RAPTI

"Numerical modeling of liquefaction-induced failure of geostructures subjected to earthquakes"

Thèse soutenue àÂ Châtenay-Malabry, le 01/04/2016.

Composition du jury:

M. SEMBLAT Jean-François	Directeur de laboratoire, IFSTTAR	Président
M. KOTRONIS Panagiotis	Professeur, Ecole Centrale de Nantes	Rapporteur
M. LANZO Giuseppe	Professeur, Sapienza Università di Roma	Rapporteur
M. BONELLI Stéphane	Directeur de Recherche, Irstea	Examinateur
Mme. MODARESSI Arezou	Professeur, CentraleSupélec	Directrice de Thèse
M. LOPEZ-CABALLERO Fernando	Professeur Assistant, CentraleSupélec	Co-encadrant de Thèse
M. FOUCAULT Alexandre	Ingénieur Chercheur, EDF R&D	Encadrement industriel
M. VOLDOIRE François	Ingénieur Chercheur, EDF R&D	Encadrement industriel

Laboratoire de Mécanique des Sols, Structures et Matériaux
CNRS, CentraleSupélec.

Acknowledgements

I would like to express my gratitude to my professors and supervisors at CentraleSupélec , namely Arezou Modaressi and Fernando Lopez-Caballero, as well as, my supervisors at EDF R&D , Alexandre Foucault and François Voldoire. Each of them advised and helped me with his unique way to realise this thesis. I would like especially to thank Arezou and Fernando who taught me many things, but most importantly they inspired me how to become a good scientist. I would also like to express my appreciation to Fernando, who was the first one to believe and invest in me. Besides the academic guidance, he was always next to me as a friend.

Particularly I would like to thank the members of my committee, namely Jean-François Semblat, Panagiotis Kotronis, Giuseppe Lanzo, Stéphane Bonelli, for accepting participating in this thesis work and for their insightful comments and advice.

I would like to acknowledge the support of the other students at the MSSMat laboratory at CentraleSupélec , as well as, my coworkers at EDF R&D . Thank you for providing a great environment to work in. Several people, outside of civil engineering, also contributed making this experience unforgettable, notably my friends in Paris and Athens. Special thanks to my friend Martha for her support and contribution during her internship at EDF R&D .

Above all, I would not have been in this position right now had I not been supported by my parents, Margarita and Nikos: thank you so much for everything you have done for over 27 years. Last but not least, the most influencial person during many years in all aspects of life is Thymios, I thank him for supporting me and being always next to me in both good and difficult times.

To a person who inspired me to enter the research world,
to Frank,

université PARIS-SACLAY | ÉCOLE DOCTORALE Sciences mécaniques et énergétiques, matériaux et géosciences (SMEMAG)

Title: Numerical modeling of liquefaction-induced failure of geostructures subjected to earthquakes

Keywords: dynamic analysis, nonlinear coupled hydromechanical behavior, soil liquefaction, earthquake loading, FE modeling

Abstract: The increasing importance of performance-based earthquake engineering analysis points out the necessity to assess quantitatively the risk of liquefaction. In this extreme scenario of soil liquefaction, devastating consequences are observed, e.g. excessive settlements, lateral spreading and slope instability. The present PhD thesis discusses the global dynamic response and interaction of an earth structure-foundation system, so as to determine quantitatively the collapse mechanism due to foundation's soil liquefaction. As shear band generation is a potential earthquake-induced failure mode in such structures, the FE mesh dependency of results of dynamic analyses is thoroughly investigated and an existing regularization method is evaluated. The open-source FE software developed by EDF R&D , called Code_Aster , is used for the numerical simulations, while soil behavior is represented by the ECP constitutive model, developed at CentraleSupélec .

Starting from a simplified model of 1D SH wave propagation in a soil column with coupled hydromechanical nonlinear behavior, the effect of seismic hazard and soil's permeability on liquefaction is assessed. Input ground motion is a key component for soil liquefaction apparition, as long duration of mainshock can lead to important nonlinearity and extended soil liquefaction. Moreover, when a variation of permeability as function of liquefaction state is considered, changes in the dissipation phase of excess pore water pressure and material behavior are observed, which do not follow a single trend. The effect of a regularization method with enhanced kinematics approach, called first gradient of dilation model, on 1D SH wave propagation is studied through an analytical solution. Deficiencies of the use of this regularization method are observed and discussed, e.g. spurious waves apparition in the soil's seismic response.

Next, a 2D embankment-type model is simulated and its dynamic response is evaluated in dry, fully drained and coupled hydromechanical conditions. Two criteria are used to define the onset of the structure's collapse. The second order work is used to describe the local instability at specific instants of the ground motion, while the estimation of a local safety factor is proposed by calculating soil's residual strength. Concerning the failure mode, the effect of excess pore water pressure is of great importance, as an otherwise stable structure-foundation system in dry and fully drained conditions becomes unstable during coupled analysis.

Finally, a levee-foundation system is simulated and the influence of soil's permeability, depth of the liquefiable layer, as well as, characteristics of input ground motion on the liquefaction-induced failure is evaluated. For the current levee model, its induced damage level (i.e. settlements and deformations) is strongly related to both liquefaction apparition

and dissipation of excess pore water pressure on the foundation. A circular collapse surface is generated inside the liquefied region and extends towards the crest in both sides of the levee. Even so, when the liquefied layer is situated in depth, minor effect on the levee response is found.

This research work can be considered as a reference case study for seismic assessment of embankment-type structures subjected to earthquake and provides a high-performance computational framework accessible to engineers.

université PARIS-SACLAY | ÉCOLE DOCTORALE Sciences mécaniques et énergétiques, matériaux et géosciences (SMEMAG)

Titre: Modélisation numérique de la liquéfaction des sols : application à l'analyse sismique de la tenue des barrages

Mots-clés: analyse dynamique, comportement hydroméchanique couplé non linéaire, liquéfaction de sol, chargement sismique, modélisation par éléments finis

Résumé: L'importance croissante de l'évaluation de la performance des structures soumis au chargement sismique souligne la nécessité d'estimer le risque de liquéfaction. Dans ce scénario extrême de la liquéfaction du sol, des conséquences dévastatrices sont observées, par exemple des tassements excessifs et des instabilités de pentes. Dans le cadre de cette thèse, la réponse dynamique et l'interaction d'un système ouvrage en terre-fondation sont étudiées, afin de déterminer quantitativement le mécanisme de ruine dû à la liquéfaction du sol de la fondation. Par ailleurs, les chargements sismiques peuvent induire dans les ouvrages en terre un mode de rupture générant des bandes de cisaillement. Une étude de sensibilité aux maillages a donc été engagée dans le cadre de travail pour quantifier la dépendance des résultats de l'analyse dynamique. Par conséquent, l'utilisation d'une méthode de régularisation est évaluée au cours des analyses dynamiques. Le logiciel open-source Code_Aster , basé sur la méthode des Eléments Finis et développé par EDF R&D , est utilisé pour les simulations numériques, tandis que le comportement du sol est représenté par le modèle de comportement de l'ECP, développé à CentraleSupélec .

En premier lieu, un modèle simplifié de propagation 1D des ondes SH dans une colonne de sol avec comportement hydromécanique couplé non linéaire a été simulé. L'effet des caractéristiques du signal sismique et de la perméabilité du sol sur la liquéfaction du sol est évalué. Le signal sismique d'entrée est un élément important pour l'apparition de la liquéfaction, puisque la durée du choc principal peut conduire à de fortes non linéarités et à un état de liquéfaction étendu. En outre, quand une variation de perméabilité en fonction de l'état de liquéfaction est considérée, des changements significatifs sont observés pendant la phase de dissipation de la surpression interstitielle de l'eau et au comportement du matériau. En revanche, ces changements ne suivent pas une tendance unique. Puis, l'effet d'une méthode de régularisation avec cinématique enrichie, appelée premier gradient de dilatation, sur la propagation des ondes SH est étudié au travers d'une solution analytique. Des problèmes à la réponse dynamique du sol sont observés et discutés quand cette méthode de régularisation est appliquée (ex. apparition des ondes parasites).

Ensuite, un modèle 2D d'un déblai est simulé et sa réponse dynamique est évaluée en conditions sèches, complètement drainées et hydromécanique couplées. Deux critères sont utilisés pour définir le début de la rupture de la structure. Le travail du second ordre est utilisé pour décrire l'instabilité locale à des instants spécifiques du mouvement sismique, tandis que l'estimation d'un facteur de sécurité locale est proposée prenant en compte la résistance résiduelle du sol. En ce qui concerne le mode de ruine, l'effet de la surpression interstitielle de l'eau est de grande importance, puisqu'un déblai stable en conditions sèches et

complètement drainées, devient instable lors de l'analyse couplée à cause de la liquéfaction de la fondation.

Enfin, un système digue-fondation est simulé et l'influence de la perméabilité du sol, la profondeur de la couche liquéfiable, ainsi que, les caractéristiques du signal sismique sur la ruine induite par la liquéfaction du sol est évaluée. Pour ce modèle de digue, le niveau de dommages (c.-â-d. tassements et déformations) est fortement lié à la fois à l'apparition de la liquéfaction dans la fondation et la dissipation de la surpression d'eau. Une surface d'effondrement circulaire est générée à l'intérieur de la couche du sol liquéfié et se propage vers la crête dans les deux côtés de la digue. Pourtant, lorsque la couche liquéfiée est située en profondeur, la digue est moins affectée par la liquéfaction de la fondation pour ce cas particulier de chargement.

Ce travail de recherche se concentre sur une étude de cas de référence pour l'évaluation sismique des ouvrages en terre (ex. déblais routières, remblais, digues ou barrages) soumis à un séisme et fournit des méthodes et outils de calculs numériques performants accessible aux ingénieurs.

Contents

Notations and abbreviations

For the sake of brevity, the notations and abbreviations are described by its most common meaning in the present thesis. However, some symbols are not included in this list because they concern single cases.

Latin Alphabet

a_1	regularization parameter
a_h	horizontal acceleration
a_v	vertical acceleration
$a_{bed,max}$	maximum acceleration of ground motion at bedrock
$a_{out,max}$	maximum acceleration of ground motion at outcropping
a_1, a_2,	deviatoric hardening (ECP model parameters)
b	Biot's coefficient (Chapter 2)
c_m, c_c,	isotropic hardening (ECP model parameters)
d	distance between CSL and ICL (ECP model parameter)
D	soil damping
E	Young modulus
f_{ij}	micro deformation gradient (Chapter 4)
f_k, f_{iso}	deviatoric and isotropic yield surfaces (ECP model)
F_k	isotropic hardening function (ECP model)
g	gravity acceleration
G_{max}	maximum shear modulus
G_{ref}	shear modulus at reference pressure (ECP model parameter)
I_{Arias}	Arias intensity
k_s	soil permeability
K	bulk modulus of soil skeleton
K_0	coefficient of lateral earth pressure
K_w	bulk modulus of water phase
K_s	bulk modulus of soil grains
ℓ_c	characteristic length of regularization
m	cyclic loading path (ECP model parameter) or double micro traction force (Chapter 4)
M_w	moment magnitude
n	soil porosity
n_e	degree of nonlinearity (ECP model parameter)

N_{cycles}	number of cycles
p	mean stress
p_i	external forces per unit area (Chapter 4)
P_i	double external forces per unit area (Chapter 4)
p'_k	mean effective stress of the k plane (ECP model)
p_0	confinement pressure
p_{c0}	initial critical mean stress (ECP model parameter)
p_c	critical mean stress (ECP model parameter)
p_w	pore water pressure
p'_{ref}	mean effective reference stress (ECP model parameter)
q	deviatoric stress
q_k	deviatoric stress of the k plane (ECP model)
R	Joyner-Boore source-to-site distance
r_d^{ela}, r_{iso}^{ela}, r_d^{cyc}, r_{iso}^{cyc}, r^{hys}, r^{mob}	threshold domain (ECP model parameters)
r_k	friction mobilization degree (ECP model)
r_u	excess pore water pressure ratio
S_j	double stresses vector (Chapter 4)
t	time
t_i	boundary traction per unit area (Chapter 4)
T	period
t_5, t_{95}	time of I_{Arias} of 5% and 95%
T_{ij}	double surface traction tensor (Chapter 4)
T_m	mean period
T_p	predominant period
$T_{V/A}$	period of equivalent harmonic wave
u_i	displacement vector
$\dot{u}_i^w$	velocity vector of water phase
$\dot{u}_i$	velocity vector of solid phase
$\dot{u}_i^r$	relative velocity vector of the fluid phase to that of the solid phase
u_h	horizontal displacement
u_v	settlement (i.e. vertical displacement)
$V_{s,30}$	average shear wave velocity in the upper 30 meters
V_P	P-wave velocity
V_S	S-wave velocity

Greek Alphabet and other symbols

$\alpha(r_k)$	hardening evolution function (ECP model)
α_ψ	volumetric constant (ECP model parameter)
β	plastic compressibility modulus (ECP model parameter) or Newmark integration parameter
γ	shear strain or Newmark integration parameter
Δp_w	excess pore water pressure

δ_{ij}	Kronecker's delta
ε_{ij}	strain tensor
ε_d	deviatoric strain
ε_v	volumetric strain
ε^p	plastic strain
κ	scalar of micro dilation stress (Chapter 4)
$\dot{\lambda}^p$	plastic multiplier
ν	Poisson's ratio
ξ	damping
ρ	total density
ρ_w	water density
ρ_s	solid density
Σ_{ijk}	double stress tensor (Chapter 4)
σ_{ij}	total stress tensor
σ'_{ij}	effective stress tensor
σ'_h	effective horizontal stress vector
σ'_v	effective vertical stress vector
τ	shear stress
τ_{ij}	stress tensor associated to the microstructure (Chapter 4)
ϕ'_{apt}	apparent friction angle
ϕ'_{pp}	friction angle at critical state (ECP model parameter)
χ	micro volume change (Chapter 4)
ψ	characteristic angle (ECP model parameter)
ω	circular frequency

Abbreviations

BTF	Borehole Transfer Function (or TF: Transfer Function)
CSL	Critical State Line
ECP	Ecole Centrale Paris
EDP	Engineering Parameter Demand
FE	Finite Element
FF	Free Field
FFT	Fast Fourier Transform
FS	Factor of Safety
GEFDyn	Géomécanique Eléments Finis DYNamique
HM	HydroMechanical
ICL	Isotropic Consolidation Line
IM	Intensity Measure
LMS	Loose-to-Medium Sand
MDS	Medium-to-Dense Sand
NGA	Next Generation Attenuation
PBEE	Performance-Based Earthquake Engineering
PEER	Pacific Earthquake Engineering Research Center
PGA	Peak Ground Acceleration

PGV	Peak Ground Velocity
PSA	Pseudo-Spectra of Acceleration (or acceleration response spectra)
PSHA	Probabilistic Seismic Hazard Analysis
PSV	Pseudo-Spectra of Velocity
SED	Specific Energy Density

Chapter 1

Introduction

1.1 General Context

The seismic hazard of France was recently re-evaluated and new seismic maps were developed (Figure 1.1, http://www.planseisme.fr/). After the catastrophic Tohoku earthquake in 2011 in Japan, it was required that French nuclear and hydroelectric facilities implement complementary safety standards and new seismic safety margins were set. In this general context of seismic re-evaluation, EDF R&D develops numerical tools and methods to assess the stability and security of critical structures, such as nuclear and hydroelectric power plants, subjected to earthquake loading.

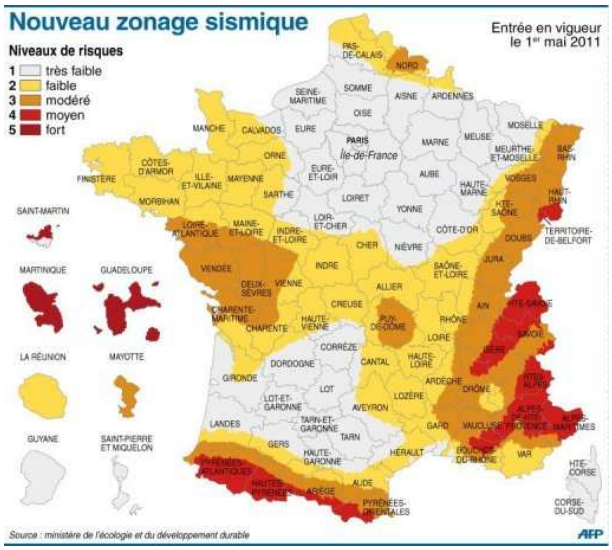

Figure 1.1: Seismic map of France (2010) (http://www.planseisme.fr/).

The program of EDF R&D in the hydraulic domain focuses on the simulation of the dynamic response of hydroelectric power plants. The purpose of the current research work is to assess the safety margins of dams or embankments by modeling their construction phases and the seismic excitation, in order to provide a general case study that could be used for a large variety of embankment-type geostructrures in the industrial sector. This includes assessing the safety margins against the risks of failure due to extreme scenarios, particularly soil liquefaction of structure's foundation.

Liquefaction of saturated sandy soils is a phenomenon that occurs under seismic loading. The passage of a seismic wave causes loss of strength and shear stiffness of the soil and leads to an increase of pore water pressure generated by the cyclic deformations. The sudden deconsolidation of the material results in soil decomposition and loss of stability of structures founded on that type of soil.

In the context of risk analysis, the seismic vulnerability of geostructures should be assessed by proposing robust criteria. Relevant criteria used by engineers to assess damage of structures caused by liquefaction are based mainly on the properties of materials (Idriss and Boulanger, 2015), the pore water pressure generation and also the medium's settlements that occur during and after the seismic event, most notably during the dissipation phase of excess pore water pressure.

However, recent studies highlight the need to determine the onset of soil liquefaction (Borja, 2006; Andrade et al., 2013), as well as the extent of the liquefiable layer by means of advanced simulation methods. Earthquake-induced liquefaction can lead to large settlements and localized failure modes (i.e. sliding surfaces) and cause instability problems to the structure. In order to take into account such a phenomenon, a very fine modeling of the hydraulic flow coupled to the soil's mechanical behavior is mandatory.

For the purposes of the advanced modeling needed for the project, the open-source Finite Element software developed by EDF R&D , called Code_Aster , is used. Code_Aster is a software created in 1989 for the needs of EDF group (http://www.code-aster.org/). It is coded in Fortran and Python and is capable to simulate and solve different types of mechanical, thermal, acoustic or seismic problems with the finite element method. The structural modeling operators are developed mainly by the department of Mechanical and Acoustic Analyses (AMA) of EDF R&D .

1.2 Objectives

The main objective of this PhD work, financed by the hydraulic program of EDF R&D , is the development of advanced numerical methods and tools, in order to simulate the dynamic response of earth structures, such as embankments (Figure 1.2a), levees and earth dams (Figure 1.2b) subjected to earthquakes, but also other steps of the life cycle of such structures. In particular the coupled hydromechanical (HM) modeling of such structures and their potential failure mode due to earthquake-induced soil liquefaction is extensively discussed.

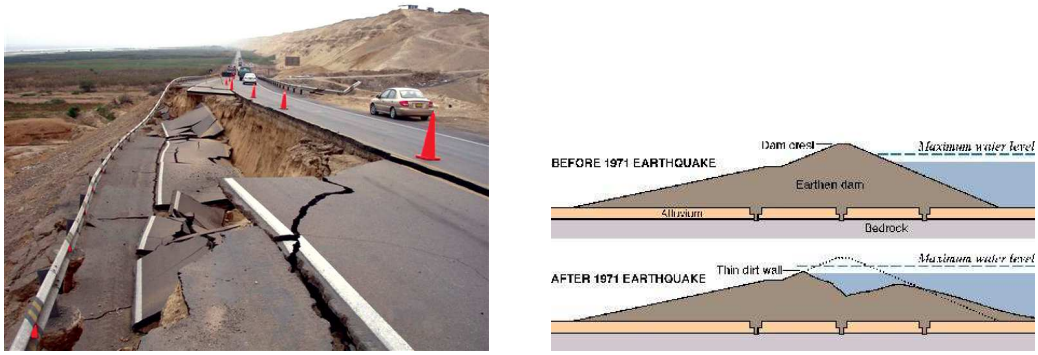

(a) (b)

Figure 1.2: Examples of earthquake-induced failure of geo-structures: a) Peru earthquake 2007 (M_w=8.0), b) San Fernando dam 1971 (M_w=6.6).

Several studies have analyzed earthquake triggered landslides and the effect of ground-shaking on foundation-structure systems founded near slope crests. Limit equilibrium analytical methods (Figure 1.3a) or numerical simulations (Figure 1.3b) have been used for structural security assessment and risk analysis, so as to estimate structural behavior during and after ground motions (Kourkoulis et al., 2010; Oka et al., 2012).

Localized failure patterns are observed in most geotechnical structural failures, such as slope failures, settlements of foundation structures, soil sliding masses and can cause great

damage. Shear band generation is identified as a potential earthquake-induced failure mode in dry foundation-structure systems (Kourkoulis et al., 2010; Park and Kutter, 2012; Hiraoka et al., 2013; Rapti et al., 2014a).

However, the presence of water dramatically alters soil behavior. From California's earthquake in 1971, where the Lower San Fernando Dam collapsed (Seed et al., 1975b), until recently during the 2010 Maule earthquake in Chile and 2011 Tohoku earthquake in Japan (Oka et al., 2012; Ishikawa et al., 2015), liquefaction-induced failures of earth structures have been reported (Ozutsumi et al., 2002; Verdugo et al., 2012; Okamura et al., 2013).

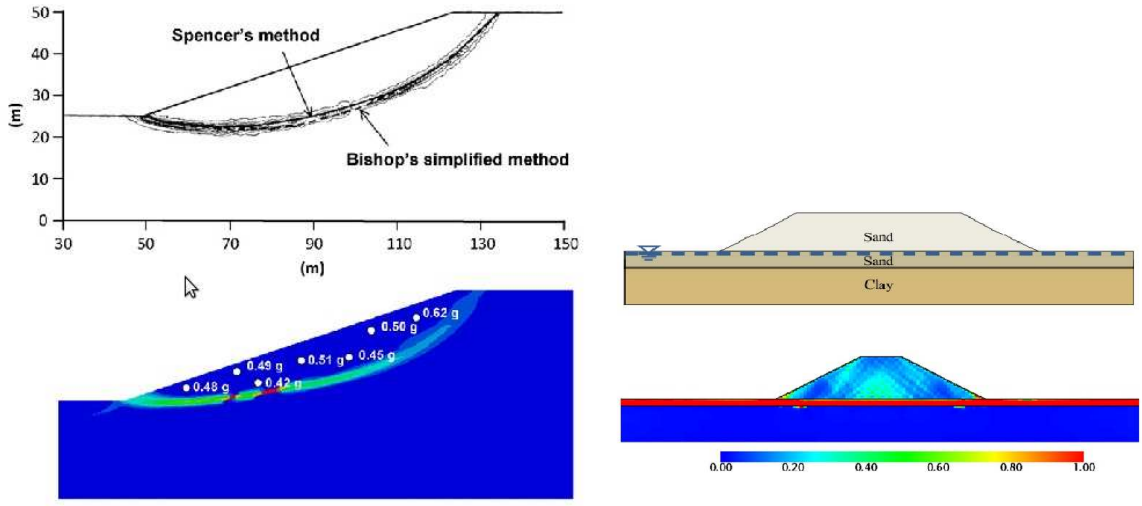

(a) (b)

Figure 1.3: Numerical modeling of slope stability: a) FE limit analysis failure surface compared with Bishop's and Spencer's limit equilibrium methods (Kourkoulis et al., 2010), b) Numerical model and distribution of accumulated plastic deviatoric strain (Oka et al., 2012).

The present research describes the global dynamic response of a structure-foundation system and their interaction. The main objectives are to identify the onset of the expected failure path for the structure-foundation system, to determine quantitatively for each particular case the collapse mechanism due to soil liquefaction and to evaluate the post-earthquake stability by proposing robust criteria suitable for dynamic analyses through FE simulation. Throughout this PhD work, earthquake-induced failure modes of earth structures are investigated by performing numerical simulations with the open-source FE software Code_Aster . The version 11.7 of Code_Aster is used for all numerical simulations presented. For the advanced representation of soil behavior, the fully coupled effective stress ECP constitutive model developed at CentraleSupélec (Hujeux, 1985) is used. The different steps of this PhD thesis, focused on the advanced numerical simulation of geotechnical structures under seismic loading, can be summarized as follows:

- **State-of-the-art of Code_Aster for nonlinear dynamic simulations.**

  Provide a complete study of SH wave propagation in dry and coupled HM nonlinear media for assessing software's response, as well as, numerical methods' performance.

- **Assessment of the seismic response of earth structures with advanced stability criteria.**
  - Study the response of embankment type-structures subjected to a large range of ground motions and propose robust stability criteria applicable to dynamic analyses.
  - Investigate localization phenomena, i.e. shear band generation due to material or geometry heterogeneity, as potential failure pattern.
  - Disseminate the use of advanced numerical simulation methods through comparison of results of FE analysis to simplified empirical methods used in common engineering practice.
- **Modeling of liquefaction-induced soil failure.**
  - Investigate the implications of earthquake-induced liquefaction and define the damage patterns of geostructures.
  - Indicate the onset of liquefaction and explore diffuse or localized failure zones.
  - Furthermore, study the effect of soil permeability and its evolution on the liquefaction-induced collapse of the structure.
- **Evaluation of mesh sensitivity of results.**

  As in case of FE simulations under static conditions, mesh sensitivity of results has been reported, the question that arises is whether the same mesh effect exists in dynamic conditions, too. Consequently the following objectives are set:
  - Explore the effect of the mesh on results of dynamic analyses and conclude whether there is need of using regularization methods for the FE simulation.
  - Simultaneously, evaluate the performance of an existing regularization method with enhanced kinematics approach, in case of SH wave propagation.

1.3 Organization and Outline

In order to reach the aforementioned objectives, several studies were performed, as presented in the general plan of the thesis in Figure 1.4. Starting from the verification of the FE software in case of 1D SH wave propagation in dry and coupled HM nonlinear media and passing through the evaluation of 1D SH wave propagation in dry regularized nonlinear media, a 2D embankment-type model is simulated and its dynamic response is evaluated in all cases, i.e. dry, dry regularized and coupled HM. The dynamic analysis of the 2D embankment model could be considered as the intermediate step so as to proceed to the final goal, i.e. the simulation of a levee resting on a liquefiable layer and subjected to earthquake loading.

As mentioned previously, the realized research work refers to the failure mode of embankment-type structures due to soil liquefaction. Consequently, in **Chapter 2** the theoretical background of porous media, with an emphasis on coupled HM soil behavior

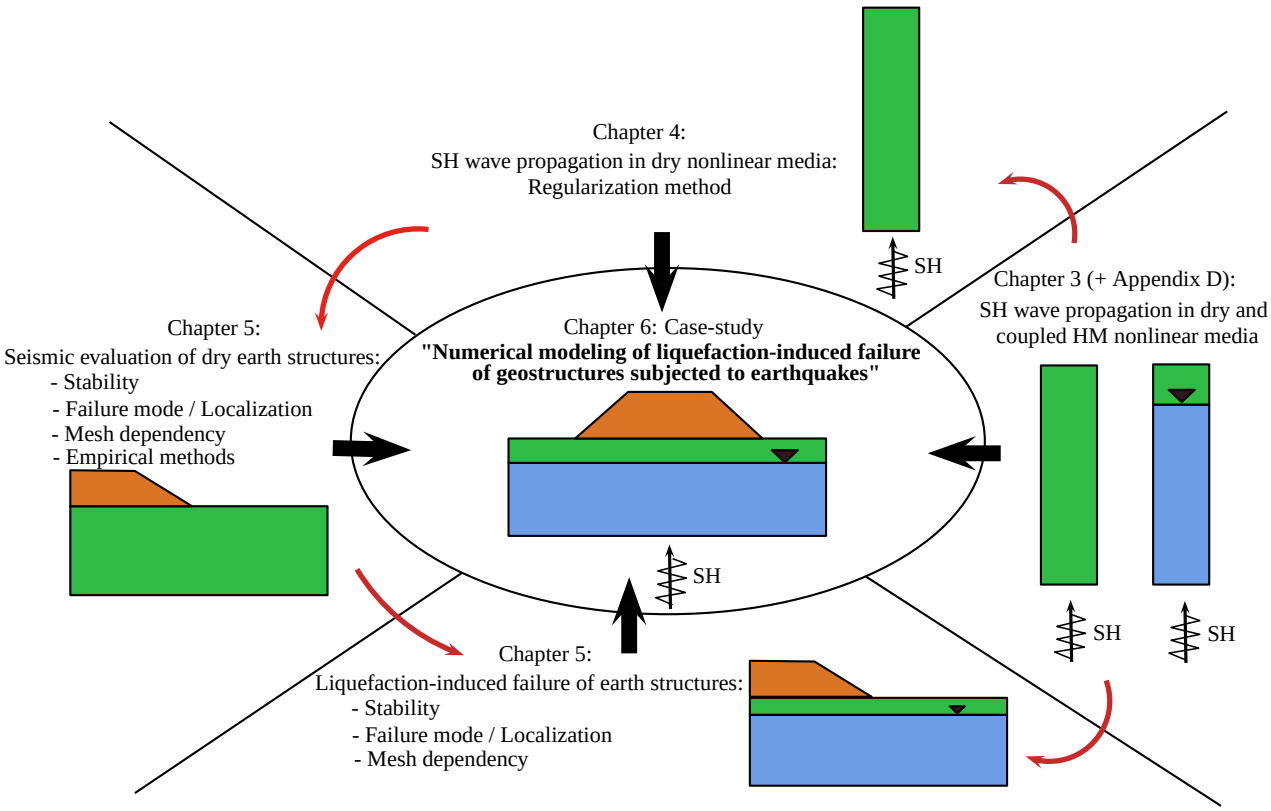

Figure 1.4: Thesis plan.

under dynamic conditions and soil liquefaction is provided. The theory of strain localization is also developed, as a localized failure mode is expected for the structure and will be extensively discussed in the following chapters.

Initially, the State-of-the-art of the FE software, Code_Aster , is provided for the case of dynamic analysis. Before proceeding to advanced modeling of structures, a verification procedure is performed in case of 1D SH wave propagation in dry and coupled HM nonlinear media. In this scope, a soil column subjected to earthquake loading is simulated in **Chapter 3** and a parametric study is performed. In case of coupled media the effect of the seismic hazard, as well as, of soil's permeability and its evolution on the column's dynamic response are discussed.

One of the main issues treated is the investigation of mesh sensitivity of results and the evaluation of the applicability of an existing regularization method in case of dynamic analysis. As previously, before applying this regularization method in complex FE models, a dry nonlinear soil column is simulated so as to evaluate the effect of this method on wave propagation. **Chapter 4** proposes an analytical solution of SH wave propagation in classical and regularized micromorphic media and discusses the applicability of the regularization method in cases of dynamic loading. Numerical examples follow the analytical approach.

After the software validation with simple models, **Chapter 5** presents the dynamic analysis of an initially dry embankment - foundation system and focuses on the earthquake-induced failure mode. Then, the same dry embankment is based on a liquefiable founda-

tion and the implications of liquefaction-induced soil failure are discussed using a coupled HM model. The mesh senvitivity issue is also considered in both models.

Finally, **Chapter 6** assembles the different aspects treated in the previous chapters and presents a case-study focused on the liquefaction-induced failure mode of a levee-type model. The influence of soil's permeability and depth of the liquefiable foundation on the collapse path is examined.

Chapter 7 summarizes the findings of this work and proposes topics for further study and research.

All chapters are written to be autonomous, as self-contained documents. Therefore, there is some repetition in the introductory concepts and model description presented in different chapters. Information regarding theoretical formulations of used constitutive models, material parameters and input ground motions have been placed in appendices to simplify the lecture of the document.

Chapter 2

Theoretical background

2.1 Introduction

The increasing importance of performance-based earthquake engineering points out the necessity to quantitatively assess the risk of liquefaction and its expected effects over a wide range of ground motion levels. Liquefaction is a decrease in shear strength and/or stiffness caused by the increase in pore water pressure in saturated cohesionless soils during a rapid ground movement. In such case, two phenomena are expected: flow liquefaction and cyclic mobility, which are both highly damaging with effects like excessive settlement, flow failures and lateral spreading, as shown in Figure 2.1. Earthquake-induced liquefaction can lead to large settlements and localized failure modes (i.e. sliding surfaces) and cause instability problems to the structure (Okamura et al., 2013; Sadeghi et al., 2014; Ishikawa et al., 2015).

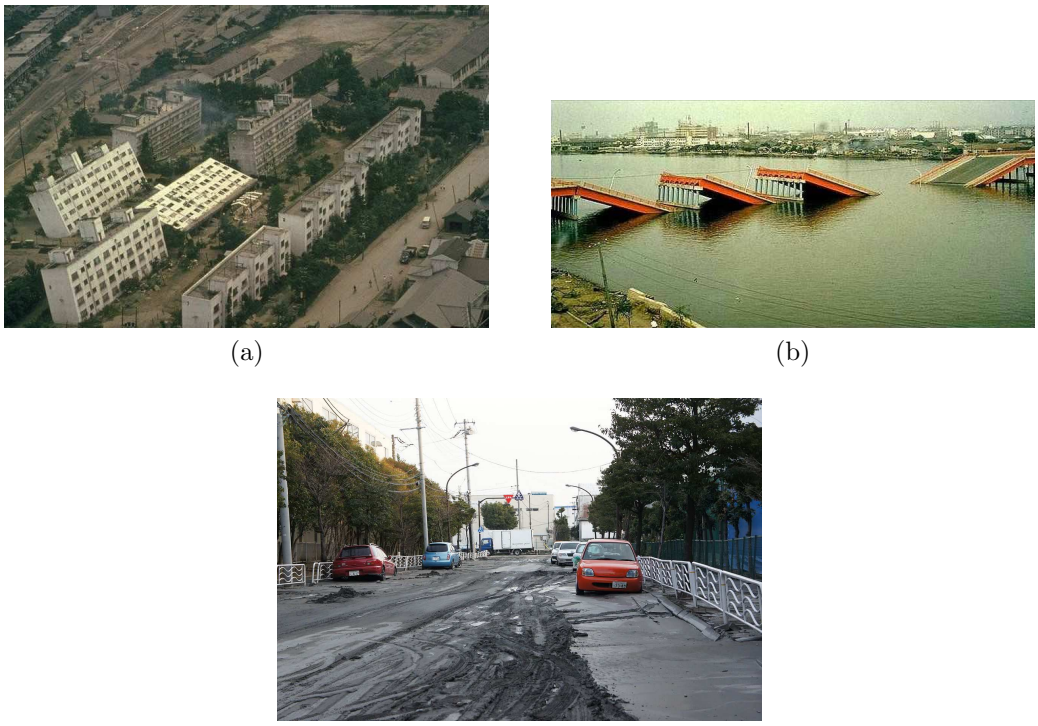

(a) (b)

(c)

Figure 2.1: Liquefaction-induced damages: a) Ground failure caused buildings to suffer bearing capacity failures and tilt severely after Niigata earthquake in 1964 (M_w=7.5), b) Lateral spreading caused the foundations of the bridge to move laterally and collapse after Niigata earthquake in 1964 (M_w=7.5), c) Ground failure caused damages to roads in Koto, Tokyo after the 2011 Tohoku earthquake in Japan (M_w=9.0).

The evaluation of liquefaction potential can be achieved by two types of approaches: empirically based simplified procedures and models based on the nonlinear soil behavior. Given the need of assessing numerically liquefaction hazard and its effects, both approaches are often assembled in a probabilistic framework (Koutsourelakis et al., 2002; Kramer and Mitchell, 2006; Lu et al., 2009; Taiebat et al., 2010; Jafarian et al., 2011).

In this chapter the theoretical background of wave propagation in porous media, their

dynamic behavior and subsequently soil liquefaction are presented through a bibliographical research. Firstly, the coupled HM soil behavior under dynamic loading is introduced and then, the phenomenon of liquefaction is explained in detail. Finally, as soil liquefaction can lead to localization phenomena, the theory of strain localization is discussed.

2.2 Coupled hydro-mechanical soil behavior

2.2.1 Overview

The mechanical behavior of saturated geomaterials and especially of soils, is governed largely by the interaction of their solid skeleton with the fluid, generally water, present in the pore structure. This interaction is particularly strong in problems involving dynamic loading and may lead to catastrophic softening of the material known as liquefaction which frequently occurs during earthquakes (Zienkiewicz et al., 1990).

According to Prevost (1980), when free drainage conditions prevail, the steady state pore-water pressures depend only on the hydraulic conditions and are independent of the soil skeleton response to external loads. Therefore, in that case, a single phase continuum description of soil behaviour is certainly adequate. Similarly, a single phase description of soil behaviour is also adequate when no drainage (i.e. no flow) conditions prevail. However, in intermediate cases in which some flow can take place, there is an interaction between the skeleton strains and the pore water phase. The solutions of these problems require that soil behaviour be analyzed by incorporating the effect of the transient flow of the pore water through the voids and therefore, require that a multiphase continuum formulation be available for porous media.

The mathematical theory governing the behavior of porous media saturated by a viscous fluid for linear elastic materials was first established by Biot (1941). Based on the work of von Terzaghi, Biot's theory was the starting point of the theory of poroelasticity. Afterwards, Biot extended his theory to anisotropic cases (Biot, 1955) and to poro-viscoelasticity (Biot, 1956a). A dynamic extension of this theory was also provided by Biot, in two papers, one refering to low frequency range Biot (1956b) and the other covering the high frequency range Biot (1956c). The general accepted opinion is that there are two dilatational body waves and two shear waves, according to the theory given by Biot (1956b). Biot's theory is based on the assumption of compressible constituents and some of his results have been taken as standard references and the basis for subsequent analyses in acoustics, geophysics and geomechanics. Nonetheless, because of the difficulty of coupled differential equations to be solved exactly, it appears that numerical approaches have to be adopted to attain solutions (De Boer et al., 1993).

Later, a different version of the porous media theory was based on the mixture theory developed by Truesdell and Toupin (1960). They presented a treatise on the classical field theories, where they developed in detail properties of motion and the fundamental physical principles of balance for single materials and mixtures (Arduino and Macari, 2001). The fluid-saturated porous material is modelled as a two-phase system composed of an incompressible solid phase and an incompressible fluid phase (De Boer et al., 1993). Biot's theory is a special case of linearised theory of mixtures with constant volume fractions, called "frozen volume fraction" (Schanz and Diebels, 2003). According to Schanz

and Diebels (2003), in case of incompressible constituents the governing equations are the same in both theories. Zienkiewicz (1982), Zienkiewicz and Shiomi (1984) and Prevost (1980) extended Biot's theory and the mixture theory in nonlinear material behavior and large strain effects.

$\underline{u} - p_w$ formulation for incompressible solid - compressible fluid

Zienkiewicz (1982) provided the zones of applicability of the various formulations existing for describing dynamic coupled HM problems, as illustrated in Figure 2.2, where Zone I corresponds to quasi-static slow phenomena, Zone II accounts for moderate phenomena and Zone III for fast phenomena. In the scope of this PhD thesis, the coupled HM soil behavior is represented by the $\underline{u} - p_w$ formulation, which accounts for the coupling of soil skeleton deformation ($\underline{u}$) with pore water pressure (p_w) and is valid in Zone II. In the current work, the range of frequencies of earthquakes is between 10^{-2}-20Hz, the fundamental soil frequencies are less than 10Hz and the permeability is between 10^{-6}-10^{-2}m/s and consequent to Figure 2.2, the dynamic problems treated are situated in Zone II, justifying the choice of $\underline{u} - p_w$ formulation. In such a case, the fluid's relative acceleration ($\ddot{\underline{u}}^r$) with respect to soil skeleton is much smaller than the acceleration of the solid phase ($\ddot{\underline{u}}$) and is considered negligible.

In this section the mathematical framework is introduced for studying the dynamic response of a coupled soil-pore water system, using $\underline{u} - p_w$ formulation, based on Biot's theory (Aubry and Modaressi, 1988; Modaressi, 1987; Aubry and Modaressi, 1990; Oka et al., 1994; Zienkiewicz et al., 1990; Coussy, 1991; Di and Sato, 2004; Tang et al., 2012). The following assumptions are made for this study:

1. The soil grains are incompressible.
2. The soil skeleton is filled with compressible water.
3. The infinitesimal strain tensor is used.
4. The relative acceleration of the fluid phase (water) to that of the solid phase (soil) is much smaller than the acceleration of the solid phase (soil).

Adopting the soil mechanics sign convention (compression positive), the total stress tensor σ_{ij} is defined as:

$$\sigma_{ij} = \sigma'_{ij} + b \cdot p_w \cdot \delta_{ij} \tag{2.1}$$

where σ'_{ij} is the Terzaghi's effective stress tensor used widely in soil mechanics (Bishop and Blight, 1963), p_w is the pore water pressure, δ_{ij} is Kronecker's delta and b is the material parameter of Biot's theory, known as Biot's coefficient:

$$b = 1 - \frac{K}{K_s} \tag{2.2}$$

where K_s and K stand for soil grains and soil skeleton bulk moduli. In soil mechanics the compressibility of grains is neglected, so in the following equations b=1.

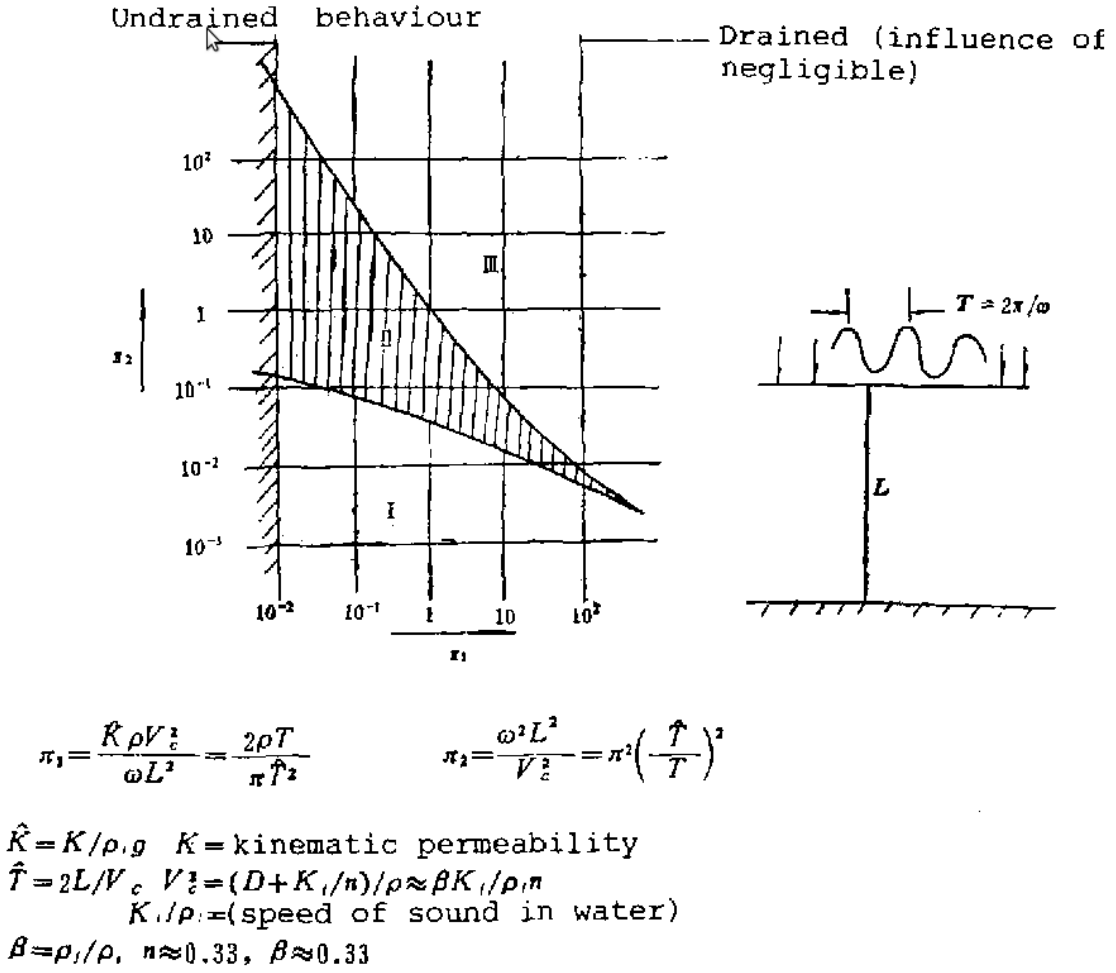

Figure 2.2: Zones of applicability of various assumptions (Zienkiewicz, 1982).

Mass balance

The local equations of balance of mass for soil and water phase are:

$$\frac{\partial((1-n)\cdot\rho_s)}{\partial t} + ((1-n)\cdot\rho_s\cdot\dot{u}_i)_{,i} = 0 \tag{2.3}$$

$$\frac{\partial(n\cdot\rho_w)}{\partial t} + (n\cdot\rho_w\cdot\dot{u}_i^w)_{,i} = 0 \tag{2.4}$$

where n stands for porosity, $\dot{u}_i^w$, $\dot{u}_i$ are the velocities of water and solid phase, respectively, and ρ_s= solid density, ρ_w= water density. From the mass balance equations of each phase and by taken into consideration the solid incompressibility, the general mass balance equation is obtained as:

$$\dot{u}_{i,i}^r + \dot{u}_{i,i} + \frac{n\cdot\dot{p}_w}{K_w} = 0 \tag{2.5}$$

where K_w stands for the water bulk modulus defined as K_w=$\dot{p}_w/\dot{u}^w_{i,i}$ and $\dot{u}^r_i$ is the relative velocity of the water phase to that of the solid phase defined as $\dot{u}^r_i$= $n \cdot (\dot{u}^w_i - \dot{u}_i)$.

Equilibrium equation

By taking into consideration the last assumption and neglecting the relative acceleration, the equilibrium of the mixture reads:

$$\sigma_{ij,j} + \rho \cdot F_i \quad = \quad \rho \cdot \ddot{u}_i \tag{2.6}$$

or in terms of effective stresses:

$$\sigma^{'}_{ij,j} + p_{w,i} + \rho \cdot F_i \quad = \quad \rho \cdot \ddot{u}_i \tag{2.7}$$

where $\ddot{u}_i$ is the acceleration of the solid phase (soil), ρ is the total density defined as ρ= (1-n) $\cdot\rho_s$ + n $\cdot\rho_w$ and F_i are the body massic forces.

Darcy's Law

The generalized Darcy's law for this case, where the relative acceleration of water is neglected, is given as:

$$\dot{u}^r_i \quad = \quad -\frac{k_{s_{ij}}}{\gamma_w} \cdot (p_{w,i} + \rho_w \cdot F_i - \rho_w \cdot \ddot{u}_i) \tag{2.8}$$

where γ_w is the specific weight of water (γ_w=ρ_w $\cdot$ g, with g standing for the gravity acceleration), $k_{s_{ij}}$ is the permeability tensor (in m/s, similar to a velocity).

By differentiation of Darcy's law equation (Equations 2.8) and by substituing it in the mass balance equation (Equation 2.5), it is possible to eliminate the term of relative velocity and describe the problem as function of $\underline{u}$ and p_w variables only. Consequently, the final mass balance equation is expressed as:

$$-\, p_{w,ii} - \rho_w \cdot F_{i,i} + \frac{n \cdot \gamma_w}{k_{s_{ij}} \cdot K_w} \cdot \dot{p}_w + \frac{\gamma_w}{k_{s_{ij}}} \cdot \dot{u}_{i,i} + \rho_w \cdot \ddot{u}_{i,i} \quad = \quad 0 \tag{2.9}$$

Governing equations in Code_Aster

To summarize, the $\underline{u}$-p_w formulation derived from Biot's theory for incompressible solid - compressible fluid is implemented into Code_Aster as presented above. However, in the description of Darcy's law the soil skeleton's acceleration ($\ddot{u}$) is neglected (Granet, 2015) and consequently the governing equations solved in the FE software are:

$$\sigma^{'}_{ij,j} + p_{w,i} + \rho \cdot F_i - \rho \cdot \ddot{u}_i \quad = \quad 0 \tag{2.10}$$

$$-p_{w,ii} - \rho_w \cdot F_{i,i} + \frac{n \cdot \gamma_w}{k_{s_{ij}} \cdot K_w} \cdot \dot{p}_w + \frac{\gamma_w}{k_{s_{ij}}} \cdot \dot{u}_{i,i} \quad = \quad 0 \tag{2.11}$$

The soil skeleton displacement $\underline{u}$ and pore water pressure p_w are the unknown variables and verify the above governing equations, the limit and initial conditions, as well as, the material's constitutive law which is described in Appendix B.

2.3 Soil liquefaction

2.3.1 Definition of liquefaction

Liquefaction is a phenomenon wherein a saturated soil, notably sand, subjected to monotonic or cyclic shear loads loses a large percentage of its shear resistance and flows in a manner resembling to a liquid (Castro and Poulos, 1977). In saturated soils, pore water pressure drainage may be prevented due to the presence of silty or clayey inclusions, or may not have time to occur due to rapid loading. Under these conditions, the tendency to compact is translated into an increase in pore-water pressure, a reduction in effective stress and a corresponding shear degradation. If the excess pore water pressure at a certain location in a purely frictional soil reaches the initial value of the effective vertical stress, then all shear strength is lost at this location and the soil liquefies, behaving like a viscous fluid. A simplified schematic representation of soil liquefaction is illustrated in Figure 2.3, while the response of very loose specimens of Hostun sand after laboratory undrained triaxial compression tests is shown in Figure 2.4 (Servant et al., 2005). In case of medium-to-dense and dense granular materials subjected to cyclic loading excess pore water pressure is also induced, but due to their tendency to dilate during shear, the softening is only temporary leading to increased cyclic shear strains, but not to major strength loss and large ground deformations.

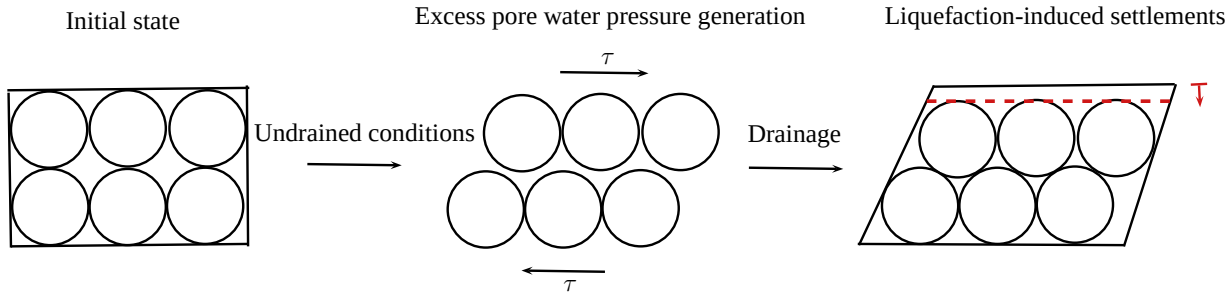

Figure 2.3: Soil liquefaction.

2.3.2 Liquefaction effects

Liquefaction is the underlying cause of many large scale soil failures including sliding in saturated natural slopes, and failures of geostructures such as river dams and road embankments (e.g. the lower San Fernando Dam during the 1971 San Fernando Earthquake, Mochikoshi dams during the 1978 Izu-Ohshim-Kinkai earthquake, Chang and Shivlaka dams during the 2001 Bhuj earthquake) (Andrianopoulos et al., 2014). Liquefaction's most important effects are the following:

- **Alteration of ground motion**

  Because of the softening given by excess pore pressure during an earthquake, high frequency components of a bedrock motion are not transmitted to the surface. Transient ground oscillations can decouple the liquefied soils from the superficial soils,

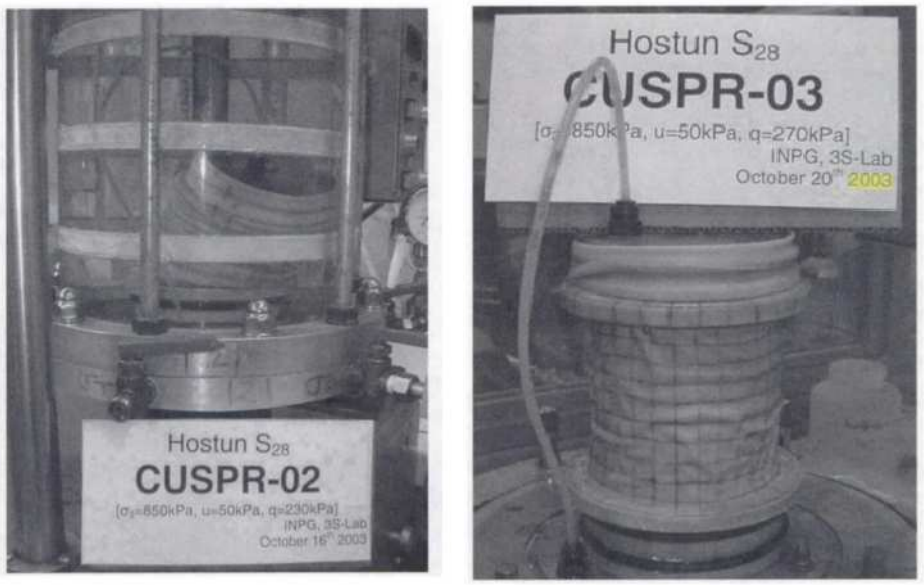

(a) (b)

Figure 2.4: Undrained triaxial compression tests on very loose specimens of Hostun sand: a) Total liquefaction, b) Partial liquefaction (Servant et al., 2005).

causing the latter to break into blocks separated by fissures that open and close during the earthquake (Kramer, 1996).

- **Sand boils development**

  The non uniformity of soil conditions drives the escaping pore water to flow through cracks or channels. Sand particles are carried through these channels to form sand boils in the surface (Figure 2.5a). The development of sand boils depends on many factors such as magnitude of excess pore pressure, the thickness, density, and depth of the liquefiable zone and of the layers on top of it. Sand boils are useful indicators of high excess pore pressure generation (Bhattacharya et al., 2011).

- **Settlement**

  Subsurface densification is manifested at the ground surface in form of settlement. Earthquake-induced settlement causes distress to shallow foundation structures, damage to utilities and damage in life-lines. The settlement of saturated sands is influenced by the properties of the sand, the forces induced by other soil layers and the earthquake-induced excess pore pressure. Tokimatsu and Seed (1987) produced a chart for estimation of volumetric strain from cyclic stress ratio and standard penetration resistance. The presence of sand boils produces irregular post-earthquake settlements that result in differential movement damaging structures, pavements and pipelines on or near the ground surface (Figure 2.5b) (Kramer, 1996).

(a) (b)

Figure 2.5: a) Sand boils and ground fissures appeared after the 1964 Niigata earthquake (M_w=7.5), b) Effects of lateral spreading on road following the 2011 Christchurch earthquake (M_w=6.3).

- **Instability**

  Liquefaction-induced instabilities are among the most damaging earthquake hazards. It can be observed in the form of flow slides, lateral spreads, retaining wall failures and foundation failures. Instability occurs when the shear stresses required to maintain equilibrium of a soil deposit exceed the shear strength of that deposit (Borja, 2006; Andrade et al., 2013). The evaluation of the residual strength of liquefied sand is a very difficult problem because of the stress path dependent strengths.

2.3.3 Liquefaction phenomena

There are two liquefaction phenomena: flow liquefaction and cyclic mobility. Flow liquefaction is known to be less frequent but far more severe than cyclic mobility. Cyclic mobility can occur in a much broader range of soils and its effects can occasionally be highly damaging. The evaluation of liquefaction hazard should consider both phenomena given the importance and likelihood of appearance.

- **Flow liquefaction**

The flow liquefaction phenomenon occurs when the static shear stress is greater than the shear strength of the liquefied soil, an unstable state at which soil strength drops sufficiently as to allow static stresses to produce failure. The large deformations are characterized by the sudden nature of their origin, the speed with which they develop and the large distance over which the liquefied materials often move.

The determination of flow liquefaction has been studied by several researchers (Kramer and Seed, 1988; Ishihara, 1993; Vaid and Chern, 1983). First Casagrande (1936) defined

the Critical Void Ratio (CVR) as the boundary between loose and dense states (contractive behavior i.e. increasing density, decreasing void ratio of loose sands and dilative behavior, i.e. decreasing density, increasing void ratio of dense sands).

Then, Castro and Poulos (1977) introduced the Steady State of Deformation as a state in which the mass is continuously deforming at constant volume, constant normal effective stress, constant shear stress and constant velocity. The Steady State Line (SSL) is the locus of points that describe the relationship of void ratio and effective confining pressure in the steady state of deformation (Figure 2.6) (Sladen et al., 1985).

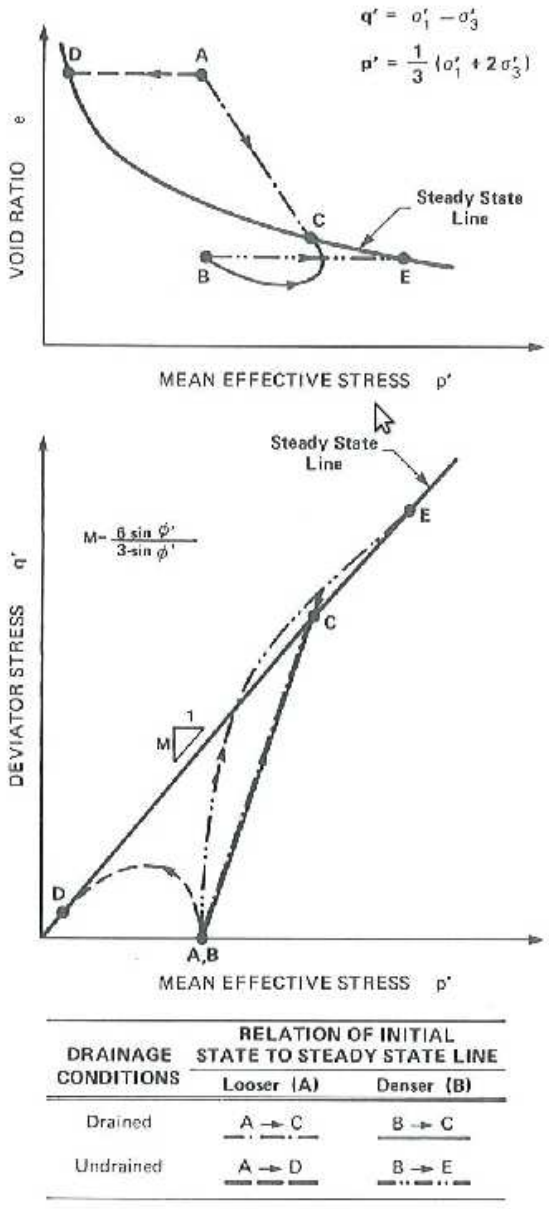

DRAINAGE CONDITIONS	RELATION OF INITIAL STATE TO STEADY STATE LINE	
	Looser (A)	Denser (B)
Drained	A → C	B → C
Undrained	A → D	B → E

Figure 2.6: Typical steady state line, showing the effect of soil behavior in triaxial compression, of soil state in relation to the steady state line (Sladen et al., 1985).

Been and Jefferies (1985) combined the influence of void ratio and stress level with reference to the steady state to describe sand behavior by introducing a physical parameter (ψ). It was defined as the void ratio difference between the initial sand state and the steady state conditions at the same mean effective stress. When the state parameter is positive, the soil exhibits contractive behavior and may be susceptible to flow liquefaction. When it is negative, dilative behavior will occur and the soil is not susceptible to flow liquefaction.

The Flow Liquefaction Surface (FLS) or Collapse surface is also defined as the locus of points describing the effective stress conditions at the initiation of flow liquefaction for same initial void ratio but different effective confining pressures (Vaid and Chern, 1983; Sladen et al., 1985).

Many studies have been performed concerning the evaluation of initiation of liquefaction. Starting from the determination of the Cyclic Stress Ratio (CSR) (Seed and Lee, 1966; Seed and Idriss, 1971; Seed et al., 1975a; Ambrasseys and Menu, 1988; Arango, 1996; Youd and Noble, 1997; Kramer and Mitchell, 2006) and Cyclic Resistance Ratio (CRR) (Pyke et al., 1975; Seed et al., 1975a), until more recently Borja (2006), Andrade (2009), Andrade et al. (2013), Mohammadnejad and Andrade (2014) explored the onset of flow liquefaction. Based on Hill's loss of uniqueness or stability criterion (Hill, 1958), they proposed criteria to predict the onset of flow liquefaction instability (Figure 2.7).

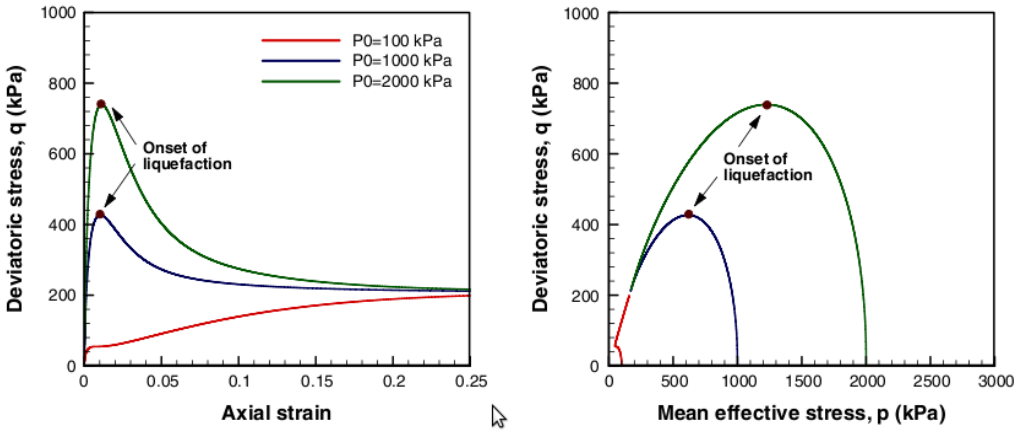

Figure 2.7: Numerical results of undrained triaxial compression test on samples of loose Toyoura sand (Mohammadnejad and Andrade, 2014).

- **Cyclic Mobility**

Cyclic mobility occurs when the static shear stress is less than the shear strength of the liquefied soil. The deformations develop incrementally during the earthquake and are driven by both cyclic and static shear stresses. According to the Steady State concept as defined by Poulos (1971), Castro and Poulos (1977), Sladen et al. (1985), cyclic mobility can occur in both loose and dense soils and can develop when the shear stress is smaller than the steady-state shear strength (Kramer, 1996). In clean medium-to-dense sands, the mechanism of liquefaction-induced shear deformation is illustrated in Figure 2.8, where a cycle-by-cycle degradation in shear strength occurs and then, a regain in shear stifness

and strength at large shear strain along with an increase in effective confinement happens (shear-induced dilative tendency) (Elgamal et al., 2002). This behavior of sands depicts the cyclic mobility with strains of great amplitude, but not flow liquefaction, i.e. flow-failure or unbounded shear deformation.

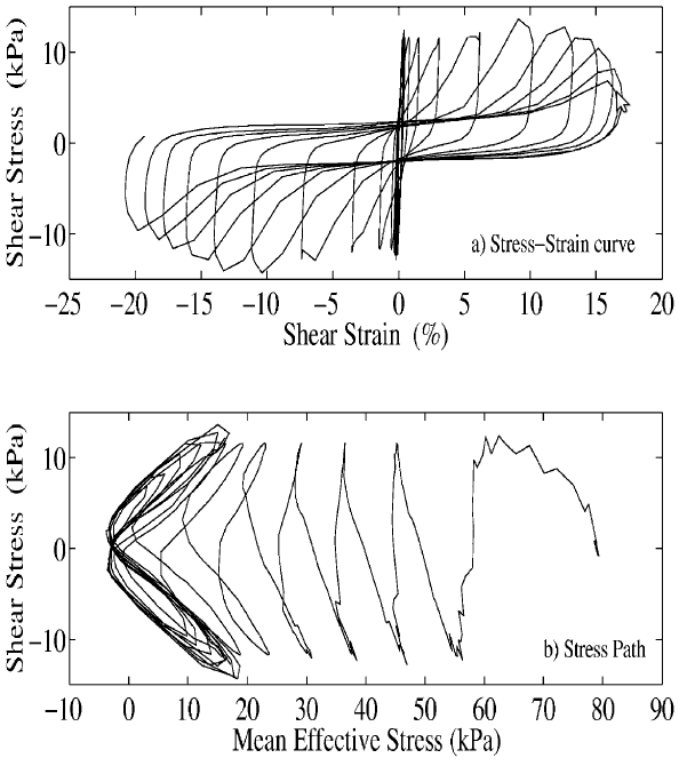

Figure 2.8: Stress-strain and stress path response for Nevada sand (DR=60%) in a stress-controlled, undrained cyclic simple shear test (Elgamal et al., 2002).

2.4 Strain localization

Localization phenomena are observed in most geotechnical structural failures and can cause great damage. In many cases of soil liquefaction, shear localization phenomena are initiated in the liquefied region combined with large settlements and eventual lateral spreading (Okamura et al., 2013; Sadeghi et al., 2014; Ishikawa et al., 2015). Shear band generation is also identified as a potential earthquake-induced failure mode in dry foundation-structure systems (Kourkoulis et al., 2010; Park and Kutter, 2012; Hiraoka et al., 2013; Rapti et al., 2014a).

Deformation and localization analysis is a crucial issue and has been intensively investigated in the last decades. On the one hand, many researchers have focused on the description of the strain localization in solid mechanical problems based on the classical theory of Rice (1976), including crack openings in concrete or shear bands in soils under static (Borja, 2002; Bazant and Jirasek, 2002) or dynamic conditions (Loret and Prevost,

1990; Loret et al., 1995). In contrast to solid mechanical problems, as geotechnical applications do not only concern a single solid material, the soil, but they also affect the pore-fluids, water and air, the coupling of the solid deformation with the pore-fluid flow should be considered. As a result, other studies have focused on the application of localization analysis to triphasic materials consisting of the soil skeleton, the pore-water and the pore-gas, known as unsaturated or partially saturated soil (Larsson and Larsson, 2000; Zhang et al., 2001; Ehlers et al., 2004) or fully saturated soils (Oka et al., 1995; Benallal and Comi, 2003; Benallal, 2005).

For the purpose of this work, strain localization is treated as an eventual failure mode, in the general context of earthquake-induced collapse of geostructures, so a brief review of the classical theory of localization is presented in the following section.

2.4.1 General theory

The behavior of granular materials, such as gravel, sands or soils, subjected to a high level of sollicitations is characterized by the localization of strain and damage in relatively narrow zones. Strain localization is manifested by large strains concentrated in a narrow band, with continuous transition to much smaller strains in the surrounding parts of the body. In physical terms, this corresponds to a damage process zone with a higher concentration of defects around its center.

In the context of localization analysis, an important question is under which conditions the inelastic strain increments can localize in one or more narrow bands separated from the remaining part of the body by weak discontinuity surfaces. Across such surfaces, the displacement field remains continuous but the strain field can have a jump (Jirasek, 2015).

Let us recall the theory of classical localization analysis as described by Rudnicky and Rice (1975), Rice (1976), Ottosen and Runesson (1991). Classical localization analysis is restricted to one point x_d of the discontinuity surface Γ_d at incipient loss of strain continuity. The discontinuity surface splits the body (at least locally) into subdomains Ω^+ and Ω^- (Figure 2.9).

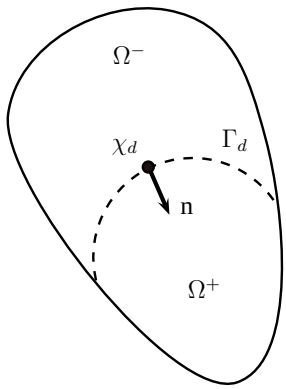

Figure 2.9: Body split by a potential discontiuity surface.

Let denote $\dot{\sigma}_{ij}^{+}$ and $\dot{\sigma}_{ij}^{-}$ the stress rates of the second-order tensors σ_{ij}, on one and the other side of the discontinuity surface just next to the point χ_d. Even though the

stress and strain rate can be discontinuous across Γ_d the corresponding jumps are not completely arbitrary. The stress jump rate jump is constrained by the traction continuity condition (Equation 2.12) and the strain rate jump by the displacement continuity condition (Equation 2.13) (Rice, 1976).

$$n \cdot \dot{\sigma}_{ij}^{+} = n \cdot \dot{\sigma}_{ij}^{-} \tag{2.12}$$

$$\left(\frac{\partial \dot{u}_i}{\partial x_i}\right)^{+} = \left(\frac{\partial \dot{u}_i}{\partial x_i}\right)^{-} + c_i \otimes n_j \tag{2.13}$$

where u_i is the diplacement field, n is the unit vector normal to Γ_d and c_i is an arbitrary mulitplier first-order tensor with components c_1, c_2, c_3.

The criterion developed by Rice (1976) which describes the shear band formation and eventually the localized failure mode, corresponds to the vanishing of determinant of the acoustic tensor $\underline{\underline{Q}}$:

$$det(Q_{ij}(n)) = det(n_i \cdot D_{ijkl}^{ep} \cdot n_l) = 0 \tag{2.14}$$

where D_{ijkl}^{ep} is the elasto-plastic tensor.

From the mathematical point of view, singularity of the acoustic tensor indicates the so-called *loss of ellipticity*. The acoustic tensor is in this context called the *localization tensor* (Jirasek, 2015).

2.4.2 Mesh dependency of shear bands

Localization problems are particularly challenging to model in conventional Finite Element simulations due to discontinuities and large strains inside the shear bands. Pathological sensitivity of the results of the FE simulations to the element size are reported in most cases due to the loss of ellipticity in the governing equations. In a finite element solution, the element size serves as a length scale and the solutions become very sensitive to the mesh size and orientation. The strain localizes into a single element, the energy dissipation continues to decrease and all of these non-physical properties are reflected in the mesh-sensitive load-displacement response (Bazant et al., 1985). To remedy the loss of ellipticity, a length scale must be incorporated, implicitly or explicitly, into the material description of the formulation of the boundary value problem.

Rate-dependent material models introduce length scales (Needleman, 1988) and consequently do not lose strong ellipticity when strain localization is caused by inhomogeneity. In strain gradient theories, the stress depends on strain derivatives, and these methods explicitly introduce material characteristic lengths (de Borst and Muhlhaus, 1992). For rate-independent materials in standard continuum theories, on the other hand, no length scale appears in the boundary value problem.

Several regularization technics are proposed to eliminate the mesh dependency of results, such as adaptive meshing where refinement of the mesh is applied in the localized regions (Deb et al., 1996), mesh-free simulations where non-locality is embedded in the

weight function (Chen et al., 2000; Li et al., 2000) or gradient-enriched models (Vardoulakis and Aifantis, 1991; Mindlin, 1965).

The gradient-enriched plasticity theories can be divided into two distinct groups:

- *Strain gradient models* which characterize the deformation at a material point not only by the conventional strain (related to the displacement gradient) but also by the strain gradient (related to the second gradient of displacement). These models can also take into account second or higher-order gradients of strains. The importance of such a model is that it can be adjusted to every constitutive model.

- *Models with gradients of internal variables*, some of which also incorporate the gradients of the dissipative forces conjugate to the internal variables.

The fundamental difference between these two groups of models is that strain gradients considered as additional observable state variables are conjugate to higher-order stresses that enter the equilibrium equations, while gradients of internal variables are conjugate to certain dissipative thermodynamic forces that can enter the evolution equations for internal variables but do not appear in the equilibrium equations (Jirasek, 2015).

In the scope of this research work, the strain-gradient theory proposed by Mindlin (1965) is the basis of the regularization method (Fernandes et al., 2008) used and will be discussed in detail in the corresponding chapter (Chapter 4).

Chapter 3

1D SH wave propagation in coupled HM nonlinear media

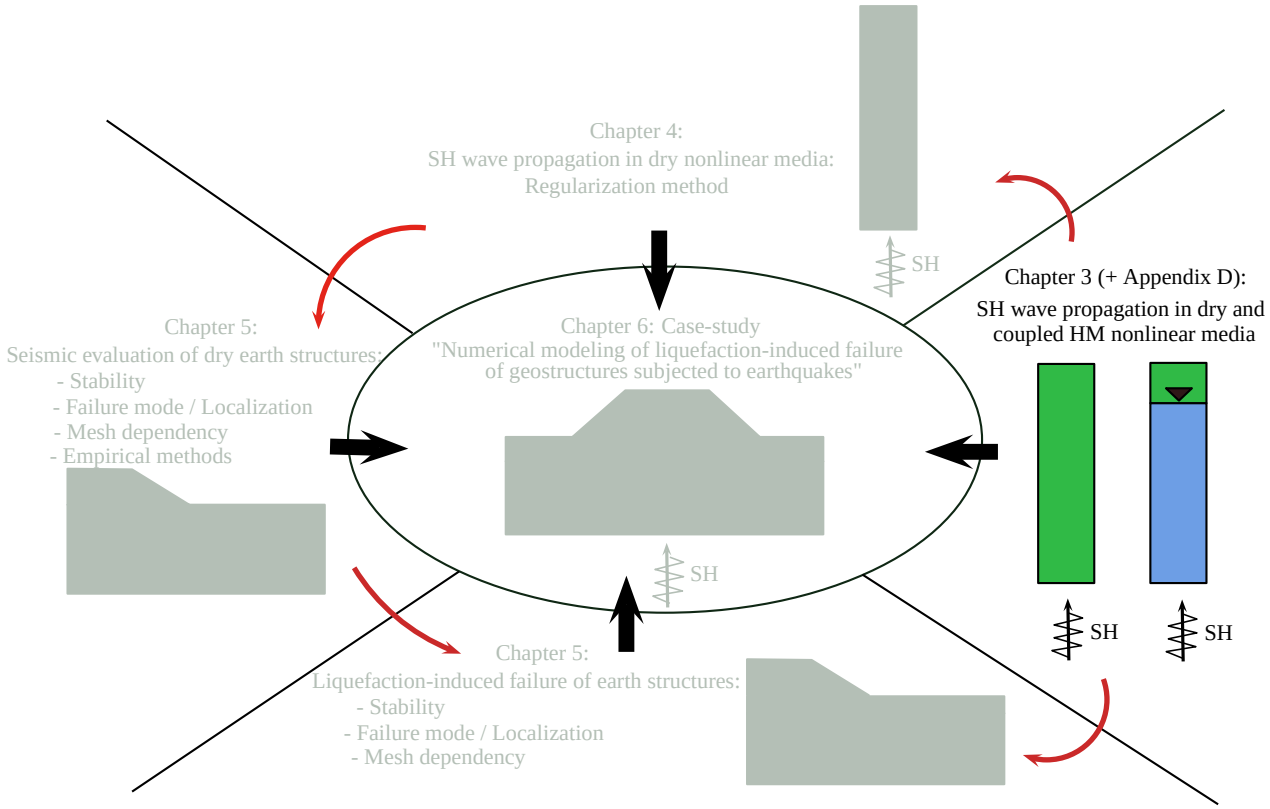

3.1 Introduction

This research is looking for insights about the global dynamic response of a structure-foundation system, focused on determining quantitatively the collapse mechanism in both dry and coupled HM conditions by means of FE simulations. In the latter case, in saturated soils, pore water pressure drainage may be prevented due to the presence of silty or clayey inclusions, or may not have time to occur due to rapid loading. Under these conditions, the tendency to compact is translated into an increase in pore water pressure, reduction in effective stress and corresponding shear degradation. Two phenomena are expected: flow liquefaction and cyclic mobility, both are highly damaging and lead to excessive settlements, flow failures or lateral spreading, as explained thoroughly in Section 2.3.

The increasing importance of performance-based earthquake engineering points out the necessity to quantitatively assess the risk of liquefaction and its effects over a wide range of ground motion levels. Several studies have analyzed the dynamic response of geostructures subjected to earthquakes and focus on the presence of water that can dramatically alter soil behavior (Oka et al., 2012; Verdugo and González, 2015).

However, before launching advanced FE simulations, it is important to evaluate the response of the FE software in several conditions. In this context, the State-of-the-art of Code_Aster (version 11.7) is provided for dynamic analyses, through simplified verifications procedures of 1D SH wave propagation. The reference software used, whose results are compared to those of Code_Aster , is a software developed at CentraleSupélec , called GEFDyn (Aubry et al., 1986). For the verification procedures two numerical models are simulated passing from a simpler one to a more complex: a) a dry elastic and nonlinear soil column and b) a coupled HM nonlinear soil column. For the sake of brevity, in this chapter only the verification of the coupled HM nonlinear model is presented. The verification in dry condition (i.e. case a) can be found in Appendix D.

Once the verification of the software is done, following the theory developed previously of coupled HM soil behavior and soil liquefaction, dynamic analyses of 1D SH wave propagation are performed in order to assess the effect of liquefaction on soil's response. On the one hand, the selection of accelerograms for geotechnical earthquake engineering is becoming increasingly important and strongly related to nonlinear dynamic analyses, as discussed by Cameron and Green (2004) for soil site amplification and Anastasopoulos et al. (2010), Liel and Raghunandan (2013), Causse et al. (2014a) for seismic assessment of structures. The input ground motion is considered as a key component and soil liquefaction can be related to the characteristics of the input motion, such as duration, amplitude or frequency. On the other hand, liquefaction is inextricably related to soil's permeability as permeable soils can dissipate rapidly the excess pore water and liquefaction phenomenon may be less extended or prevented (Di and Sato, 2003; Lakeland et al., 2014).

In this sense, two parametric studies are conducted for the coupled HM soil column referring to: a) the liquefaction vulnerability of soil on the characteristics of the input ground motion and b) the sensitivity of the liquefaction-induced failure on soil's permeability. The first analysis is used as a reference earthquake database for the choice of input motions in the following chapters, while the latter contains material presented and

published in the proceedings of the 9th French Conference on Earthquake Engineering (9ème Colloque National AFPS 2015) (Rapti et al., 2015a). Code_Aster (version 11.7) is used for all numerical simulations and the ECP constitutive model for soil's behavior representation.

3.2 Numerical model of coupled HM nonlinear soil column

3.2.1 Geometry - Boundary conditions

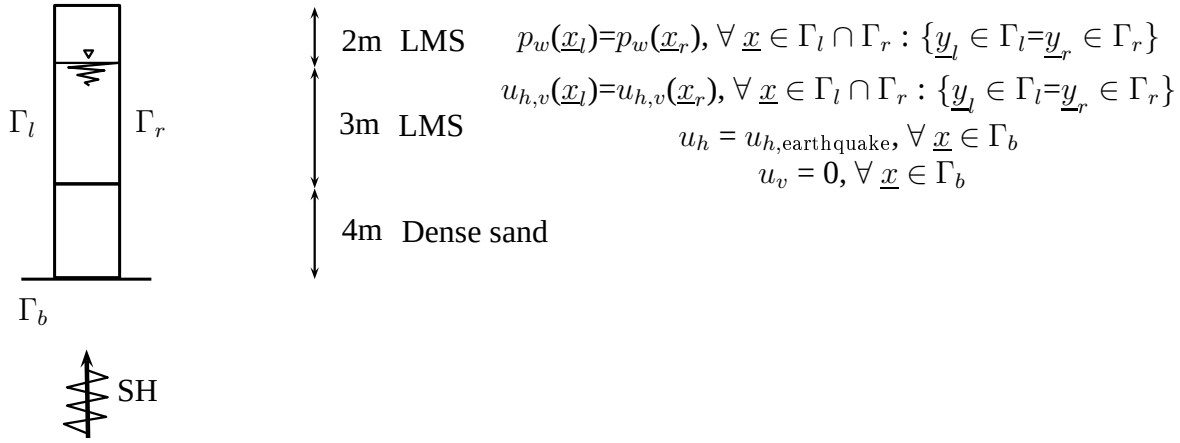

Figure 3.1: Numerical model: 9m high coupled HM nonlinear soil column.

The model consists of a nonlinear soil column of 9m, as presented in Figure 3.1. A mesh of 8-node quadrilateral elements of 0.25m length is used. Each node has 3 degrees of freedom (u_h, u_v and pore water pressure p_w). Note that the water table is situated 2m below the free surface. Periodicity condition is applied on the lateral boundaries, i.e. all nodes of a horizontal section have the same displacement and pore water pressure. The seismic signal is imposed at the base and no radiation is possible.

3.2.2 Soil behavior

The ECP constitutive model is used to represent soil behavior and a loose-to-medium sand (LMS) is used for the liquefiable layer and a dense sand (Dense sand 1) at the lower part of the soil column. For further information about the model refer to Appendix B and for material parameters to Table B.1 in Appendix B.6.

In order to understand the behavior of the chosen materials under dynamic loading and especially when liquefaction occurs, cyclic shear drained and cyclic triaxial undrained tests are conducted. Both tests were carried out at confining pressure corresponding to the average geostatic pressure of the soil column, i.e. 50kPa.

$G/G_{max} - \gamma$ and $D - \gamma$ curves are generated after the shear cyclic drained test simulation for the LMS material (Figure 3.2a and 3.2b) and are in good agreement with the

reference curves given by Seed and Idriss (1970). It can be remarked that according to Figure 3.2b there is no material damping in low strains, which implies a need of adding numerical damping, as will be discussed in Section 3.2.4. The liquefaction curve for the LMS is provided in Figure 3.2c after triaxial cyclic undrained test. The results match relatively good with the experimental ones provided by Byrne et al. (2004), which correspond to the liquefaction response of Nevada sand for a range of relative densities.

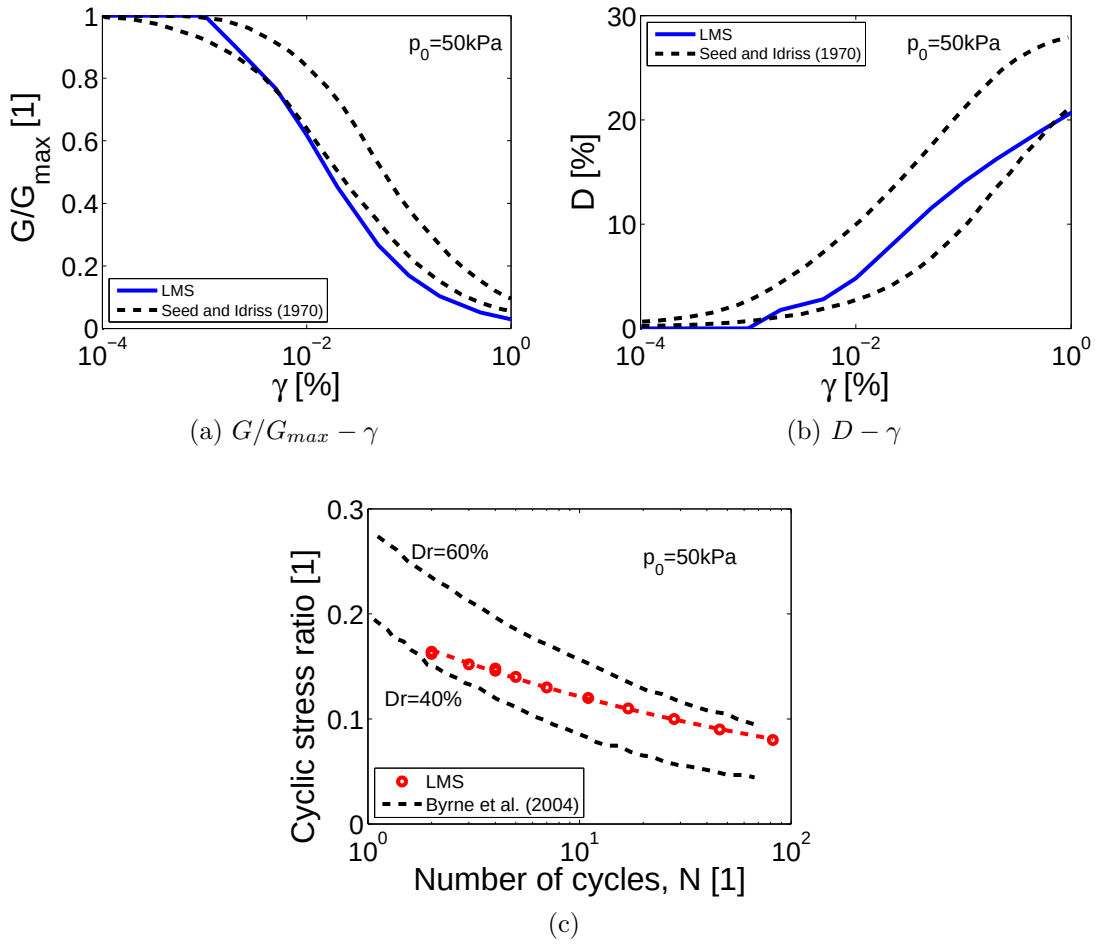

(a) $G/G_{max} - \gamma$ (b) $D - \gamma$

(c)

Figure 3.2: Soil response of one material point with the ECP constitutive model (p_0=50kPa, K_0=1.0): a), b) Shear cyclic drained test compared to Seed and Idriss (1970), c) Cyclic triaxial undrained test: Liquefaction curve compared to Byrne et al. (2004).

3.2.3 Hydraulic behavior

A fully coupled effective stress dynamic approach using the $\underline{u}$-p_w formulation derived from Biot's theory for incompressible solid - compressible fluid is used, as explained in Chapter 2.2 (Equations 2.10, 2.11).

For the verification procedure (Section 3.3) and the liquefaction vulnerability analysis (Section 3.4), the initial value of permeability of LMS layer is considered to be constant

and equal to k_s=1·10^{-4}m/s, corresponding to a typical clean sand of medium permeability. While in the study of variable permeability (Section 3.5) two values of initial permeability are used, i.e. k_s=1·10^{-4}m/s and 1·10^{-5}m/s, referring to a typical clean sand of medium permeability and a silty sand of low permeability, respectively (Bardet, 1997). In the lower part of the column the initial permeability of the dense sand layer is equal to k_s=1·10^{-5}m/s in all simulations. The provided soil characterization is based on the relation of permeability with particle size and void ratio established by NAVFAC (1982) and on the classification of soils after Terzaghi and Peck (1967).

For the needs of FE modeling, the value of fluid compressibility used, is higher than the real one of water. When the real value of water compressibility (4.5·10^{-10} Pa^{-1}) is used, it is possible that due to the rapid dynamic loading, an abrupt increase in pore water pressure happens and liquefaction occurs. A relevant study for the choice of the value of compressibility was performed and can be found in Appendix D. The hydraulic parameters of each material are presented in Table 3.1.

Table 3.1: Hydraulic parameters of the used soils.

Parameter	LMS	Dense sand 1
Water mass density, ρ_w [kg/m^3]	1000	1000
Porosity, n [1]	0.35	0.35
Initial permeability, k_s [m/s]	1·10^{-4}/1·10^{-5}	1·10^{-5}
Water compressibility, H_w [Pa^{-1}]	9.35·10^{-8}	9.35·10^{-8}

3.2.4 Numerical parameters

The FE analysis is performed in two steps: a) as the model is nonlinear, a static analysis was performed in order to calculate the initial stresses, b) the seismic signal is imposed and a dynamic analysis follows.

The implicit method of Newmark integration is used for the dynamic analysis with a time step equal to Δt=10^{-3}s. Since, the model is elastoplastic, no damping exists in the elastic domain (see Figure 3.2b) and numerical damping should be added. It is shown that a non-dissipative scheme ($\beta = 0.25$ and $\gamma = 0.5$) cannot be used, as an amplification of the seismic signal appears at the end of the ground motion and creates a noise in a wide range of frequencies. For further details about this study and the integration scheme used refer to Appendix A.1. According to the generalized α-method, the value of damping depends on the time step and frequency (i.e. spectral radius $\rho_\infty(\Delta t, f)$) (Kuhl and Crisfield, 1999; Hughes, 2000; Kontoe et al., 2008; Ruiz and Saragoni, 2009; Montoya-Noguera and Lopez-Caballero, 2015). In this case, it was calculated as function of the fundamental frequency in elastic conditions and is equal to $\xi = 0.2\%$, as the set of integration parameters used is $\beta = 0.31$ and $\gamma = 0.61$ (spectral radius ρ_∞=0.8).

The low-strain frequency analysis provides a fundamental elastic period for the soil column equal to T_p=0.15s (f_p=6.8Hz), as shown in Figure 3.3. It is obtained from the Borehole Transfer Function from the top to base (i.e. ratio of the frequency response at column's surface over the bedrock frequency response) for a sample seismic signal at very low amplitude (10^{-6}g) to ensure elastic soil behavior.

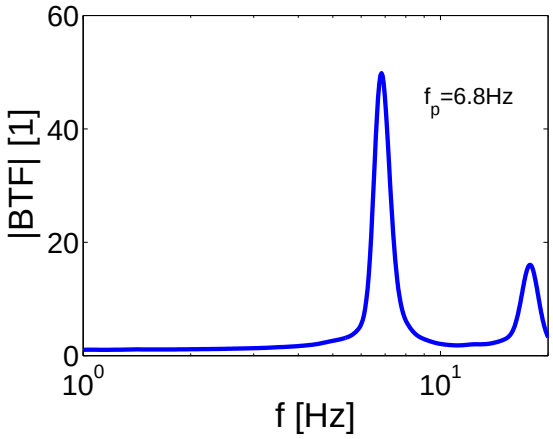

Figure 3.3: Borehole Transfer Function of coupled HM soil column in elasticity.

3.2.5 Input ground motions

Throughout this chapter, a wide range of ground motions - real and synthetic - are used (163 ground motions in total) and presented in detail in Appendix C. Their acceleration spectra are plotted in Figure 3.4 for 5% damping. Note that all input and outpout signals have a baseline correction and are filtered using a non-causal bandpass filter of order 4, between 0.1-20Hz. Then, in each section representative motions are selected and imposed to the soil column to assess the effect of seismic hazard on soil's dynamic response.

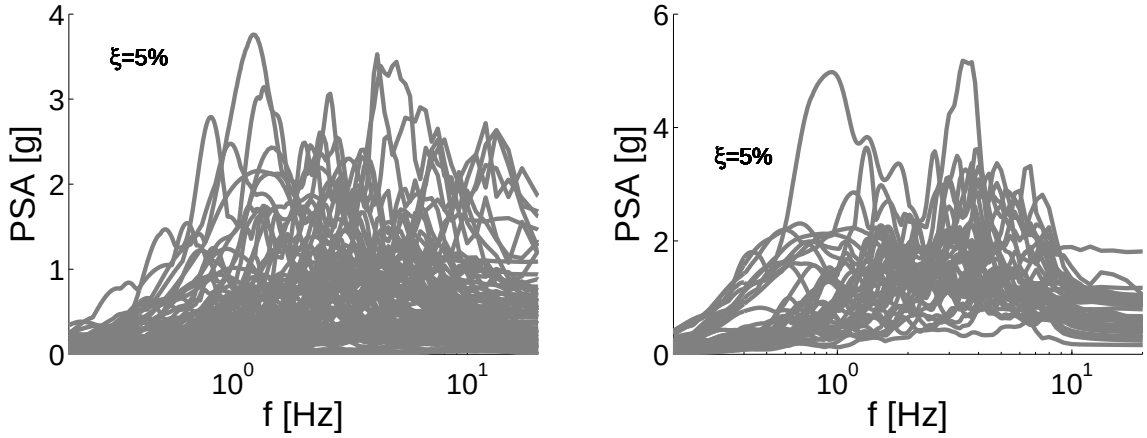

(a) (b)

Figure 3.4: Acceleration spectra of input motions (ξ=5%): a) Real, b) Synthetic.

3.3 Verification of Code_Aster : Dynamic response of coupled HM nonlinear soil column

This section refers to the verification of Code_Aster in case of SH wave propagation in coupled HM nonlinear media and more precisely of soil liquefaction. The soil column model presented previously is simulated and subjected to a wide range of input motions. The same dynamic analyses are performed using both Code_Aster and GEFDyn with the same numerical integration parameters and the results are compared for several responses, such as acceleration, settlement and pore water pressure evolution. Then, the dynamic response provided by Code_Aster is further investigated. For the sake of brevity, only results of Friuli earthquake, presented in Figure 3.5, are discussed, as the same conclusions are drawn for all input signals.

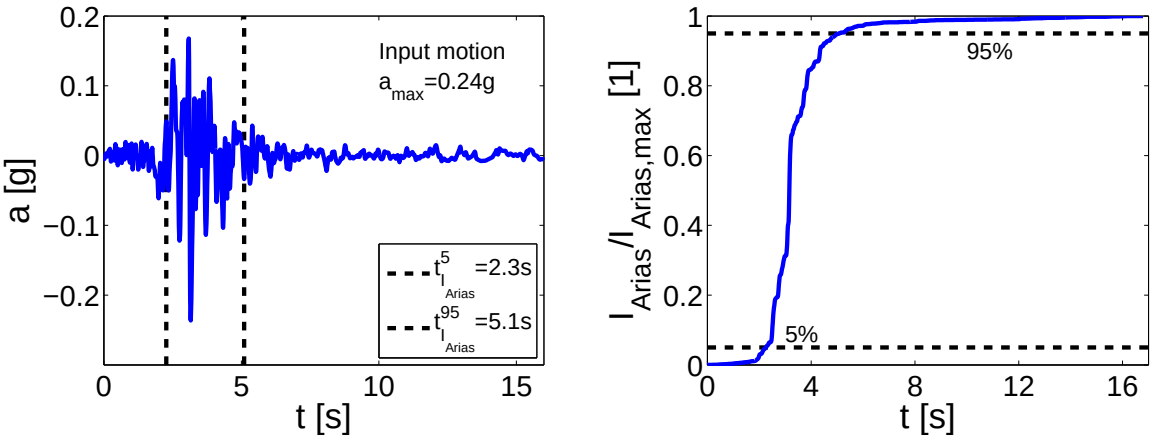

(a) (b)

Figure 3.5: Input ground motion (Friuli earthquake): a) Accelerogram, b) Arias intensity.

3.3.1 Excess pore water pressure generation

In order to assess soil liquefaction apparition, the excess pore water pressure ratio is used, defined as $r_u = \Delta p_w / \sigma'_{v,0}$. To take into account both "true liquefaction" (i.e. r_u=1.0) and cyclic mobility (i.e. 0.7< r_u <1.0 with development of large strains), it is assumed that liquefaction appears when r_u is greater than 0.8 (Lopez-Caballero and Modaressi-Farahmand-Razavi, 2013).

The contours of excess pore water pressure ratio r_u are plotted in Figure 3.6 from the results of Code_Aster and it is noticed that the ground motion leads the column to liquefy, as in the whole layer of LMS, r_u is greater than 0.8. The apparition of liquefaction is observed when Arias intensity reaches 5% (t^5_{Arias}=2.3s), while the dissipation of excess pore water pressure starts some seconds after the end of the mainshock (t^{95}_{Arias}=5.1s).

Subsequently, the comparison between the two software programs is carried out for the profiles of pore water pressure (p_w) along the lateral surface of the soil column at the beginning and at the end of the ground motion. It is important to note that the results

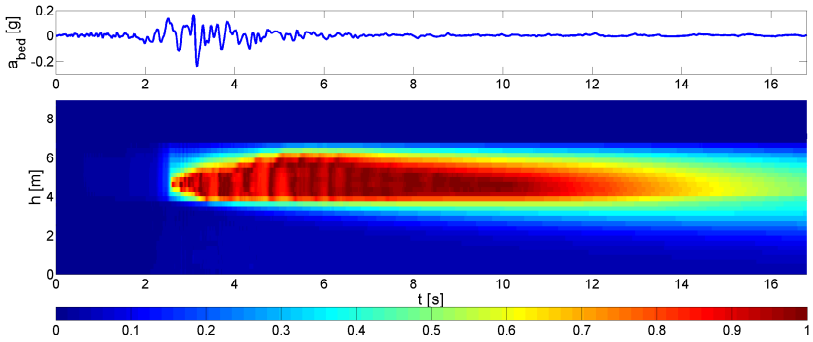

Figure 3.6: Excess pore water pressure ratio r_u during ground motion.

of pore water pressure are evaluated at the nodes for both software codes, as they are degrees of freedom of the FE formulation. In Figure 3.7, the results of both FE codes coincide in the layer of LMS (liquefiable soil), but it is remarked that in the lower part of the soil column (layer of dense sand), the dissipation is faster in GEFDyn .

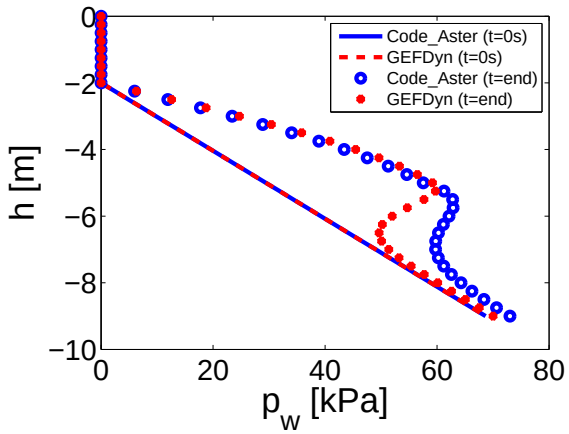

Figure 3.7: Comparison Code_Aster -GEFDyn: Profile of pore water pressure (p_w) along the column's lateral surface.

To further examine the build-up of pore water pressure in both FE codes, the evolution of excess pore water pressure (Δp_w) during the ground motion is calculated at 4m and 7m below the column's surface, i.e. at the middle of the liquefiable layer of LMS and the layer of dense sand, respectively. Concerning the response in the liquefiable layer in Figure 3.8a, there is good agreement between the software codes, as in both of them pore water pressure is generated simultaneously with the mainshock of the ground motion. Furthermore, the same level of Δp_w is reached and the dissipation phase also coincides. On the contrary, in Figure 3.8b, noticeable differences appear in the layer of dense sand, as Code_Aster generates more pore water pressure and the dissipation is slower, as already mentioned. In Code_Aster , the excess pore water pressure generated in the liquefiable layer tries to dissipate mostly towards the lower part of the soil column due to gravity

forces. As the dense soil at the bottom layer is less permeable, pore water pressure dissipates very slowly. This significant increase of pore water pressure in the lower part of the column would be further discussed in the following sections.

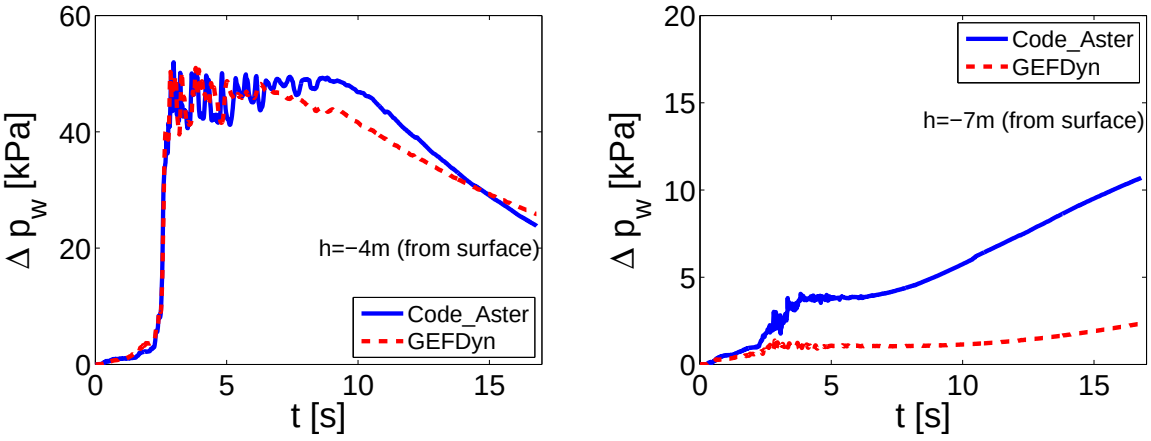

(a) h=-4m from surface.

(b) h=-7m from surface.

Figure 3.8: Comparison Code_Aster -GEFDyn: Excess pore water pressure (Δp_w) evolution during the ground motion.

3.3.2 Evolution of effective stresses

Next, in order to further examine the differences noticed previously, the profiles of horizontal and vertical effective stresses are calculated for various instants of the motion for both software programs, as calculated at the nodes of the lateral surface of the column. The instants chosen refer to the column's stress state before, during and after the mainshock, as indicated in the input accelerogram of Figure 3.5.

In Figure 3.9a the initial vertical effective stress ($\sigma'_{v,0}$) is always identical for both software codes. However, as it concerns the profile of initial horizontal effective stress ($\sigma'_{h,0}$), initially differences were found due to the fact that during the static analysis the soil column tries to find its own equilibrium and each software provides a different initial equilibrium state. More precisely, while in Code_Aster equilibrium is obtained with the initial stresses provided by the user, in GEFDyn the value of K_0 (i.e. coefficient of lateral earth pressure) changes intending to reach equilibrium. For this reason, the value of K_0 has been changed in Code_Aster in order to approach the response of GEFDyn and obtain the identical curves of Figure 3.9b. The profiles in Figures 3.9c, 3.9d are quite similar globally and the margins observed may be due to the slightly different initial equilibrium state. Also, it should be taken into account that the integration scheme of ECP elastoplastic model varies for each software, i.e. implicit integration in Code_Aster - explicit integration in GEFDyn (Foucault, 2010).

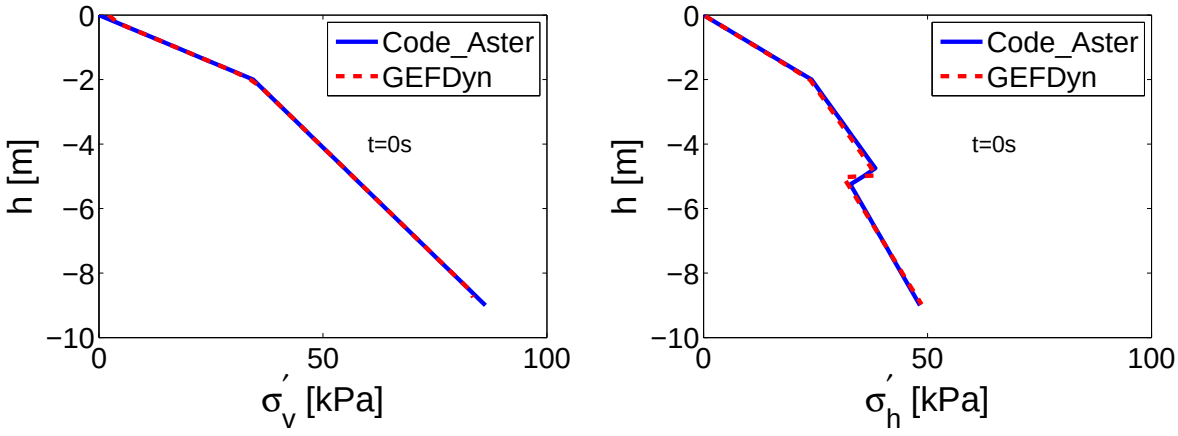

(a) σ'_v: Initial state (t=0s). (b) σ'_h: Initial state (t=0s).

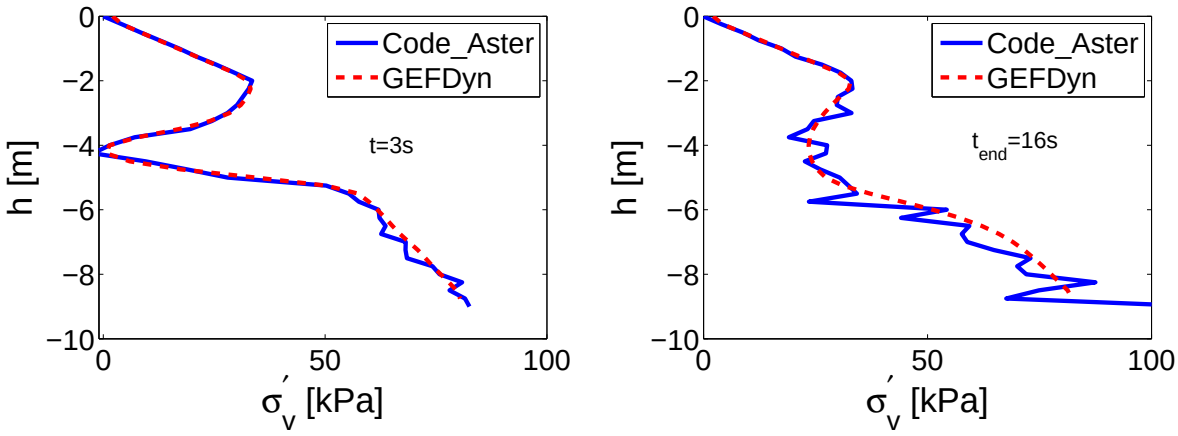

(c) σ'_v: Mainshock (t=3s). (d) σ'_v: End of earthquake (t=16s).

Figure 3.9: Comparison Code_Aster - GEFDyn : Profile of effective stresses at various instants of the ground motion.

3.3.3 Ground surface settlement

In Figure 3.10 the comparison of ground surface settlement is presented and contrary to the previous results, the gap between the two software programs is greater. The curves start to diverge at the same time with the mainshock and generation of excess pore water pressure. Settlements obtained by Code_Aster are lower than those by GEFDyn . Previous studies (unpublished work of A. Foucault and as commented in Figure D.1b in Appendix D) have shown differences in the generation of volumetric deformations - linked to vertical displacements (settlement) - between the two codes with the ECP elastoplastic model. As aforementioned, it is also supposed that this gap comes from the different integration schemes of the ECP elastoplastic model and due to the fact that the two codes handle in a different way soil liquefaction as Code_Aster accepts a small value of soil traction which is not the case in GEFDyn (Foucault, 2010).

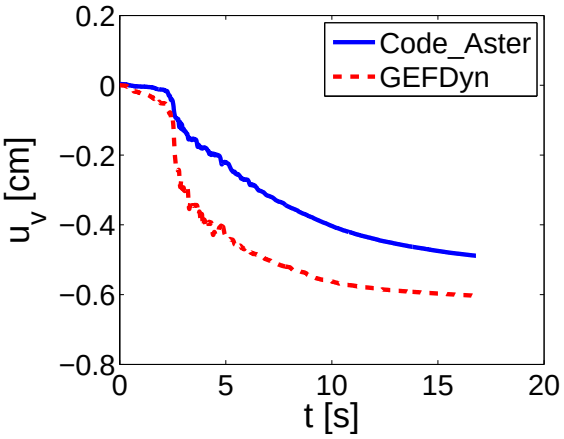

Figure 3.10: Comparison Code_Aster -GEFDyn: Evolution of ground surface settlement during ground motion.

3.3.4 Acceleration

Finally, a comparison in terms of FF horizontal acceleration and frequency is accomplished. As shown in Figure 3.11 the results of both FE codes are in good agreement.

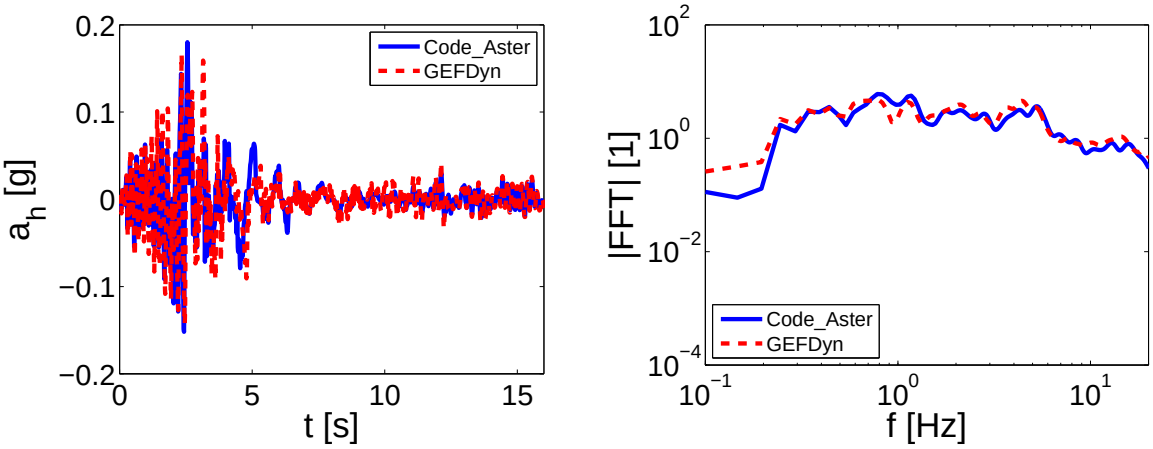

(a) (b)

Figure 3.11: Comparison Code_Aster - GEFDyn : a) FF horizontal acceleration, b) Fourier transform of FF horizontal acceleration.

As the results of both FE codes are globally in agreement, in the following sections, the dynamic response of the soil column is further investigated, as obtained by Code_Aster only.

3.3.5 Dissipation of pore water pressure

Intending to evaluate the column's behavior after the end of the ground motion - during the dissipation phase - two different simulations are perfomed using Code_Aster until 140s

after the mainshock. In both of them, the initial state of the soil column is considered to be the final state of the previous dynamic analysis, i.e. the end of the ground motion. In the first simulation, a second dynamic analysis with zero input acceleration follows the first one, while in the second one a static analysis is performed by taking into account only gravity loading:

1. *Dynamic:* Static(g) + Dynamic(earthquake: a_{bed}) + Dynamic(earthquake: a_{bed}=0)
2. *Static:* Static(g) + Dynamic(earthquake: a_{bed}) + Static(g)

In Figure 3.12, both analyses provide the same evolution of pore water pressure and settlement in different levels of the soil column. More precisely, in Figure 3.12a the dissipation of excess pore water pressure in the liquefiable layer has started after the main peak of the ground motion and is completed some seconds after the mainshock (about 30s). Simultaneously with the dissipation in the liquefiable layer, a slow increase of Δp_w is observed in the layer of dense sand (Figure 3.12b), which implies that the water tries to dissipate towards the lower part of the column.

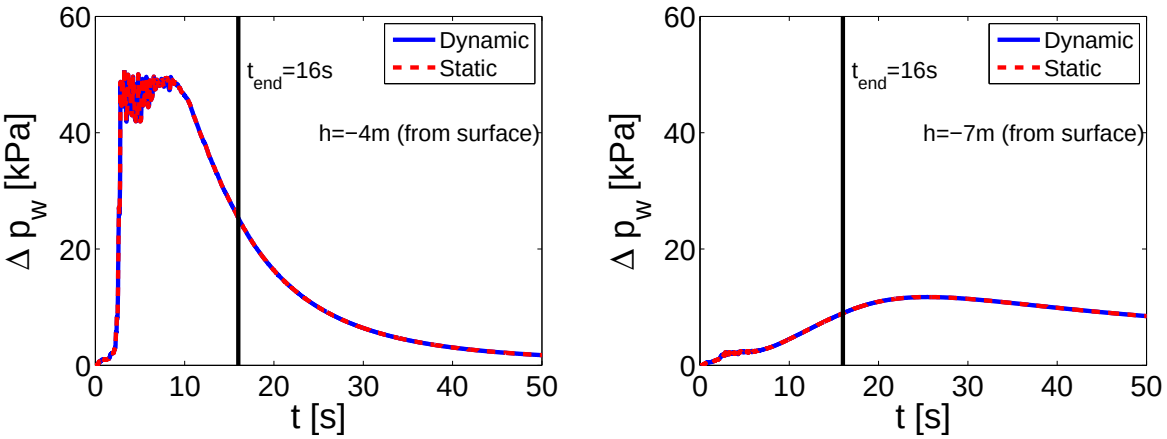

(a) h=-4m from surface.

(b) h=-7m from surface.

Figure 3.12: Excess pore water pressure evolution during and after the ground motion, as obtained by Code_Aster .

To determine the direction of water dissipation, the hydraulic head h_w is calculated, using the Bernouilli Equation 3.1, where water is supposed to move at velocity $\dot{u}^w$. However, as in most soil flow problems, the term $(\dot{u}^w)^2/2\cdot$ g is neglected, because $\dot{u}_i^w$ is much smaller compared to the pressure and elevation head (smaller than 1m/s).

$$h_w = \frac{(\dot{u}^w)^2}{2 \cdot \mathrm{g}} + \frac{p_w}{\gamma_w} + z \tag{3.1}$$

where p_w is the pore water pressure, $\gamma_w = \rho_w \cdot$ g is the water unit weight, g is the gravity acceleration and z the elevation above a given point.

In Figure 3.13, a great part of water dissipates towards the base of the column and then, travels to the upper part. The dissipation is slow as the lower part consists of a less

permeable sand and hydrostatic equilibrium (i.e. 7m) is reached 40-60s after the end of the ground motion.

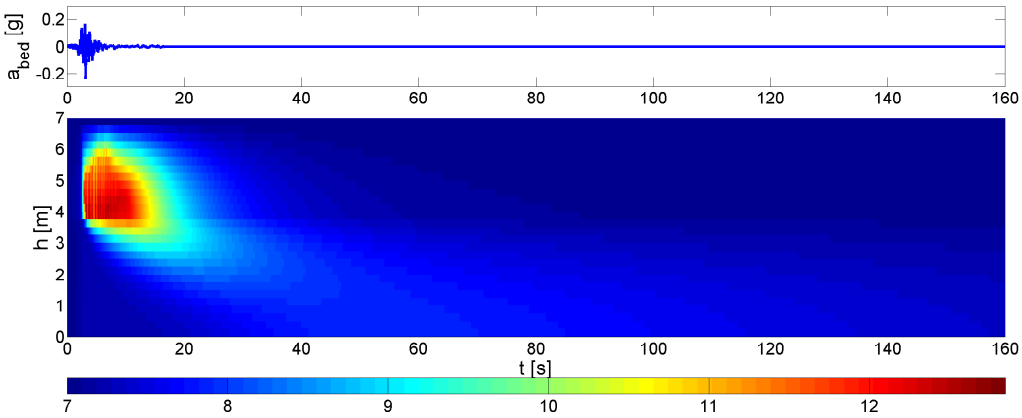

Figure 3.13: Contours of hydraulic head during and after ground motion, as obtained by Code_Aster .

Finally, in Figure 3.14 the evolution of ground surface settlement is plotted and no post-liquefaction settlements u_v are noticed during the dissipation phase. The settlements tend to stabilize after the end of the ground motion.

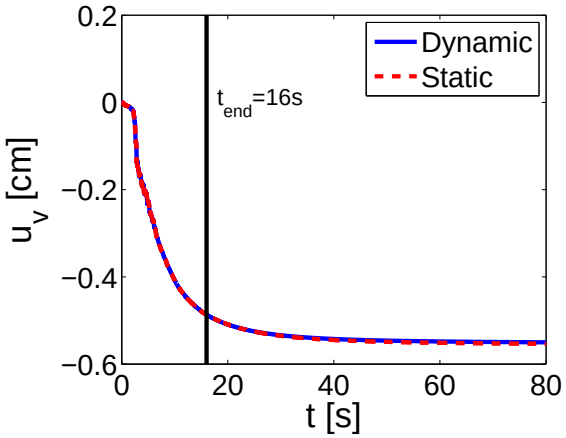

Figure 3.14: Ground surface settlement evolution during and after ground motion, as obtained by Code_Aster .

3.3.6 Mesh dependency

As discussed in Section 2.4, most of the times, the FE simulations under static loading are mesh dependent, especially when localization phenomena appear due to softening associated to constitutive behavior. This challenging topic of mesh dependency is introduced

in this section and a mesh sensitivity analysis of results is performed in Code_Aster . To explore the mesh effect on shear bands under dynamic loading for a coupled HM model, various meshes are used for the soil column: 0.10m, 0.20m, 0.50m, 1m element's length and the deviatoric strain ε_d is used as an index of strain localization (Equation 3.2).

$$\varepsilon_d = \sqrt{\frac{2}{3}\epsilon_{ij} : \epsilon_{ij}} \tag{3.2}$$

where $\epsilon_{ij} = \varepsilon_{ij} - \frac{1}{3}tr(\varepsilon)\delta_{ij}$.

In Figure 3.15a the profile of ε_d is plotted along the lateral surface of the soil column at the end of the ground motion. The soil column reaches 1% of deviatoric deformations and a shear localization zone appears in the liquefiable layer of LMS which is not mesh dependent, as all meshes used can detect this zone. No mesh dependency in terms of ground settlement and evolution of excess pore water pressure is observed according to the comparison of the results of different meshes in Figures 3.15b, 3.15c.

However, in all figures, slight differences appear for the coarser mesh (1m), which are attributed to the fact that a minimum number of elements is needed for wave propagation in nonlinear media. More in detail, the capability of the element length to represent a wide range of frequencies is established through the relation $\Delta z{=}\lambda/10$ between wavelength $\lambda{=}V_S/f$ (where V_S is the shear wave velocity), element's length Δz and frequency f (Kramer, 1996; Foerster and Modaressi, 2007). A mesh of 1m can provide an accurate response until a shear wave velocity of 300m/s for a signal's frequency of 30Hz (i.e. commonly maximum frequency of an input signal). So in this particular case of nonlinear soil behavior, this velocity could be reached due to soil degradation and such a mesh could not be able to represent properly the dynamic response. The issue of shear localization and mesh dependency will be further discussed in following chapters for larger scale models.

Synopsis

In this section the State-of-the-art of Code_Aster was established in case of SH wave propagation in coupled HM nonlinear media. The verification procedure provided a general agreement in the response of the two FE codes, namely Code_Aster and GEFDyn . The differences observed are considered insignificant for the global dynamic response. Next, the effect of seismic hazard and soil's permeability on the dynamic response of the soil column is evaluated, based on results of Code_Aster .

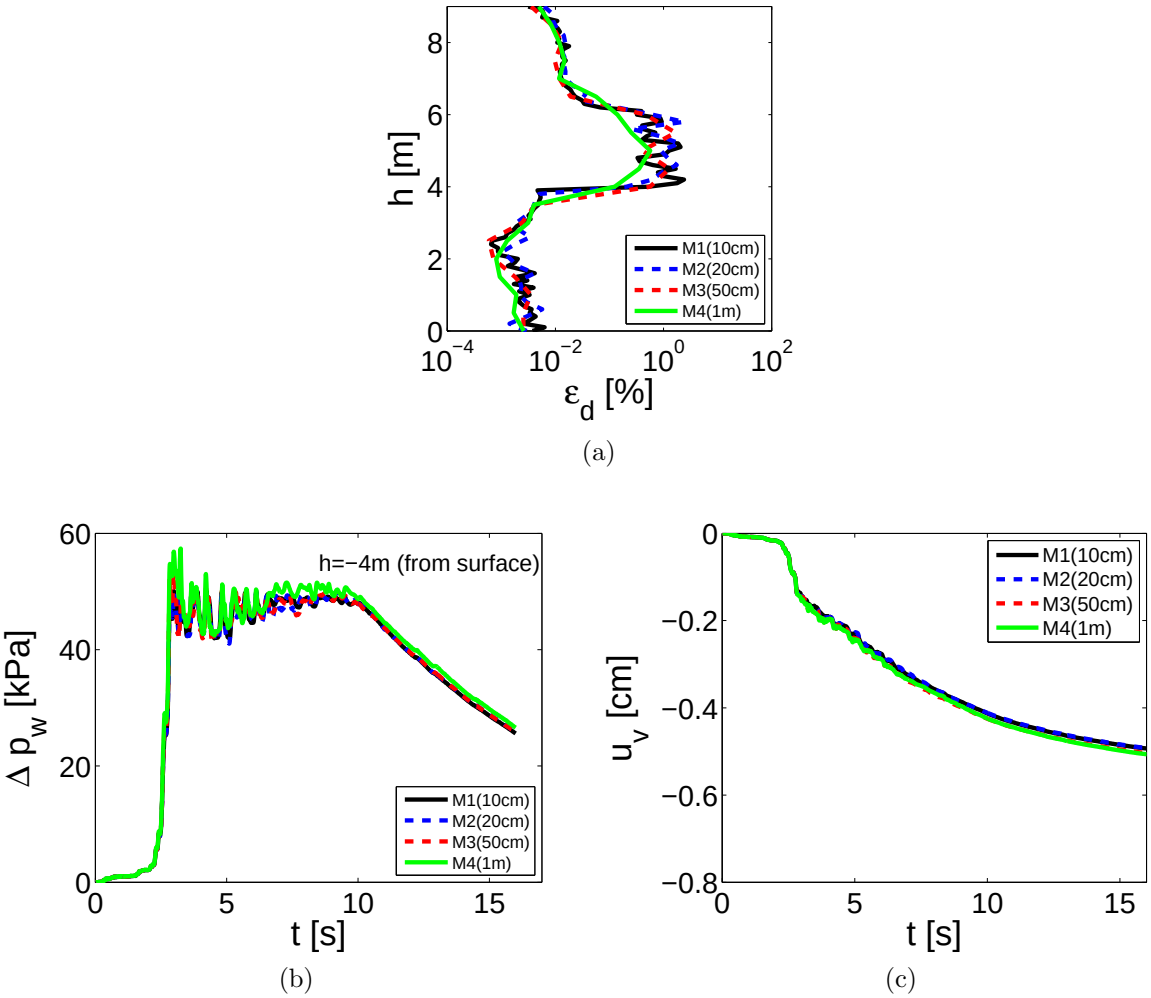

Figure 3.15: Mesh dependency evaluation of dynamic response with different meshes as obtained by Code_Aster : a) Profile of deviatoric strains (ε_d) at the end of the ground motion, b) Excess pore water pressure evolution, c) Ground surface settlement evolution.

3.4 Effect of earthquake's characteristics on the dynamic response

Several studies, e.g. Cameron and Green (2004), Anastasopoulos et al. (2010), Liel and Raghunandan (2013), underline the importance of the choice of the input motions in cases of nonlinear soil behavior and especially soil liquefaction apparition. For this reason, a liquefaction vulnerability analysis of the soil column subjected to all ground motions of Section 3.2.5 is performed, following PEER's approach for performance-based earthquake engineering.

3.4.1 Performance-Based Earthquake Engineering Methodology

Performance-Based Earthquake Engineering (PBEE) provides a framework under which many new and existing structures are analyzed for seismic adequacy and attempts to adress performances primarily at the system level in terms of risk of collapse, fatalities, repair costs and post-earthquake loss of function. PEER's PBEE approach involves four stages: hazard analysis, structural analysis, damage analysis, and loss analysis, as shown in Figure 3.16 (Porter, 2003). More in detail, the expression p[X|Y] refers to the probability density of X conditioned on knowledge of Y, and g[X|Y] refers to the occurrence frequency of X given Y given Y.

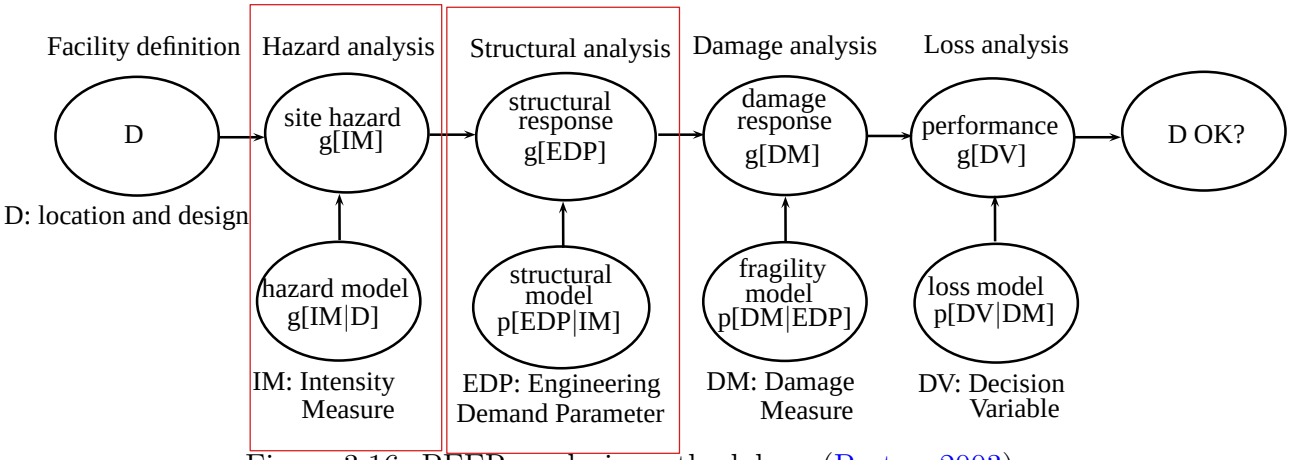

Figure 3.16: PEER analysis methodology (Porter, 2003).

According to Porter (2003), in the hazard analysis, one considers the seismic environment (e.g. nearby faults, mechanism, magnitude, site distance, site conditions etc.) and evaluates the seismic hazard at the facility of interest. The hazard curve describes the annual frequency with which seismic excitation is estimated to exceed various levels. For this analysis, seismic excitation can be parameterized via an intensity measure (IM), such as amplitude of motion, Arias intensity etc. In the next step, the engineers create a structural model of the facility of interest in order to estimate the uncertain structural response, measured in terms of a vector of engineering demand parameters (EDP), conditioned on seismic excitation. Thus, once an intensity measure is defined, the predicted structural response given an intensity measure level can be combined with Probabilistic Seismic Hazard Analysis (PSHA) to calculate the mean annual rate of exceeding a given structural response level. The proposed methodology is applicable to any EDP of interest and calculates the annual frequency of exceeding a given level of the EDP as follows (Baker and Cornell, 2005):

$$\begin{aligned} \lambda_{EDP}(z) &= \int_x p(EDP > z|IM = x) \cdot |d\lambda_{IM}(x)| \\ &= \sum_{all\ x_i} p(EDP > z|IM = x_i) \cdot \Delta\lambda_{IM}(x_i) \end{aligned} \tag{3.3}$$

where $\lambda_{EDP}(z)$ is the mean annual frequency of exceeding a given EDP value z, $\lambda_{IM}(x_i)$ is the mean annual frequency of exceeding a given IM value x_i (this is commonly referred to

as the ground motion hazard curve), and $\Delta\lambda_{IM}(x_i)$ is approximately the annual frequency of IM=x_i. The term p(EDP>z|IM=x_i) represents the probability of exceeding a specified EDP level, z, given IM=x_i, while the sum refers to the discrete summation approximation.

In the scope of this research, the liquefaction vulnerability analysis is limited to identifying the EDP of interest and IM for the seismic hazard analysis, which will be used as input data for the hazard and structural analyses, and not proceeding to a probabilistic analysis and fragility curves calculation. To assess the effect of seismic hazard on soil's dynamic response, comparisons in terms of identity (real or artificial), origin (conditions of source site) and type of signals (non pulse-like or pulse-like) are accomplished. For the particular soil column model, PGA (Peak Ground Acceleration), PGV (Peak Ground Velocity) and settlements are considered as EDP of interest, while maximum amplitude $a_{bed,max}$, Arias intensity (I_{Arias}), equivalent predominant period $T_{V/A}$, shear velocity $V_{s,30}$, duration of mainshock t_{595} (i.e. $t_{595} = t^{95}_{I_{Arias}}$ - $t^{5}_{I_{Arias}}$) and number of cycles N_{cycles} of the input signals are the given IMs. Next, the input ground motions are presented and then, the influence of the aforementioned IMs on the response of the soil column, through the EDPs chosen, is assessed.

3.4.2 Classification of input ground motions

The real ground motions used are classified according to the indications of NGA database (http://ngawest2.berkeley.edu) to: a) non pulse-like recorded on soil site with $V_{s,30}$ < 600m/s ("Real NPL soil") (Iervolino and Cornell, 2005; Sorrentino et al., 2008), b) non pulse-like recorded on rock site with $V_{s,30}$ >600m/s ("Real NPL rock") (Baker et al., 2011), c) pulse-like recorded on soil site with $V_{s,30}$ < 600m/s ("Real PL soil") (Shahi, 2013), d) pulse-like recorded on rock site with $V_{s,30}$ >600m/s ("Real PL rock") (Baker, 2007), e) near-fault of magnitude about 7 and distance about 5 km ("Real NF") (Cornell et al., 2002). A group of low amplitude real motions from a kik-Net station recorded on rock site is also used ("Real kik-Net"). Concerning the synthetic ground motions, the accelerograms are classified as generated by: a) real motions recorded on soil site ("Synthetic") (Dickinson and Gavin, 2011; Gavin and Dickinson, 2011), b) real near-fault motions ("Synthetic NF") (Cornell et al., 2002), c) the natural accelerogram of Friuli earthquake using the relevant options in Code_Aster ("Synthetic CA"). Further indications follow for the different categories of motions, while all their characteristics are presented in detail in Appendix C.

In the context of seismic hazard analysis, Cameron and Green (2004) found a close relation between the equivalent predominant period $T_{V/A}$ and the amplification of soft soil sites, while Kawase (2011) uses the inverse of $T_{V/A}$ (i.e. equivalent predomimant frequency) to examine the relationship between observed ground motions and structural damages. Consequently, $T_{V/A}$ (or $1/T_{V/A}$) is used as an IM and is an approximation of the predominant period of the motion taken as the intersection of the constant spectral acceleration and velocity. It is computed as:

$$T_{V/A} = 2 \cdot \pi \cdot \frac{\alpha_V(\xi = 5\%)}{\alpha_A(\xi = 5\%)} \cdot \frac{v_{bed,max}}{a_{bed,max}} \tag{3.4}$$

where $\alpha_V(\xi = 5\%)$=1.65, $\alpha_A(\xi = 5\%)$=2.12 and $v_{bed,max}$, $a_{bed,max}$ refer to the maximum

velocity and acceleration of the ground motion, respectively.

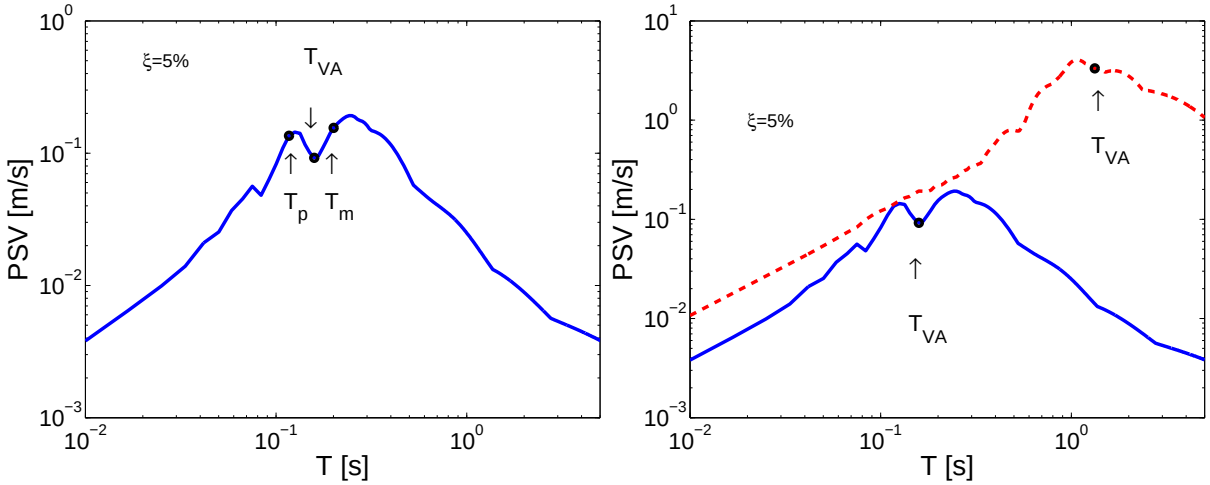

Figure 3.17: Pseudo-velocity spectrum of real ground motions (5% damping): a) Soil site motion, b) Comparison of soil site to near-fault motion.

In Figure 3.17a the equivalent predominant period $T_{V/A}$ of a real motion is marked and compared to the predominant (T_p) and mean period (T_m), while in Figure 3.17b the $T_{V/A}$ of two motions with different frequency content and origin is plotted. The predominant period T_p is defined as the period of vibration corresponding to the maximum value of the Fourier amplitude spectrum and the mean period T_m is given by the following equation established by Rathje et al. (1998):

$$T_m = \frac{\sum_i^n C_i^2 \cdot \frac{1}{f_i}}{\sum_i^n C_i^2} \text{ , for } 0.25\text{Hz} \leq f_i \leq 20\text{Hz} \tag{3.5}$$

where f_i, C_i are the *ith* frequency and Fourier amplitude, respectively.

In Figure 3.18 the diagram of $a_{bed,max}$ versus the equivalent predominant frequency is plotted for all input motions. In this diagram, equi-$v_{bed,max}$ lines will be a slope from left-down side to right-up side, indicating uniform velocity of 10, 50, 100 and 200cm/s. It is assumed that the intensity of the motion and consequently the severity of expected damages follow the direction of increasing velocity from the right-down corner towards the left-up one, as these motions will give high values of $a_{bed,max}$ and $v_{bed,max}$ at the same time. The red continuous line indicate an acceleration of 8m/s^2 and the dashed red line uniform velocity of 100 cm/s. These lines are considered to be danger lines based on observations in Kobe, above which major damages are caused (Kawase, 2011). Following these recommendations, among the selected ground motions, the near-fault earthquakes - "Real NF" and "Synthetic NF" - are classified as the most severe in Figure 3.18a. However, in Figure 3.18b, where the real earthquakes are classified according to the soil velocity $V_{s,30}$ of the site, a large dispersion is observed and no conclusion for the motion's intensity is drawn.

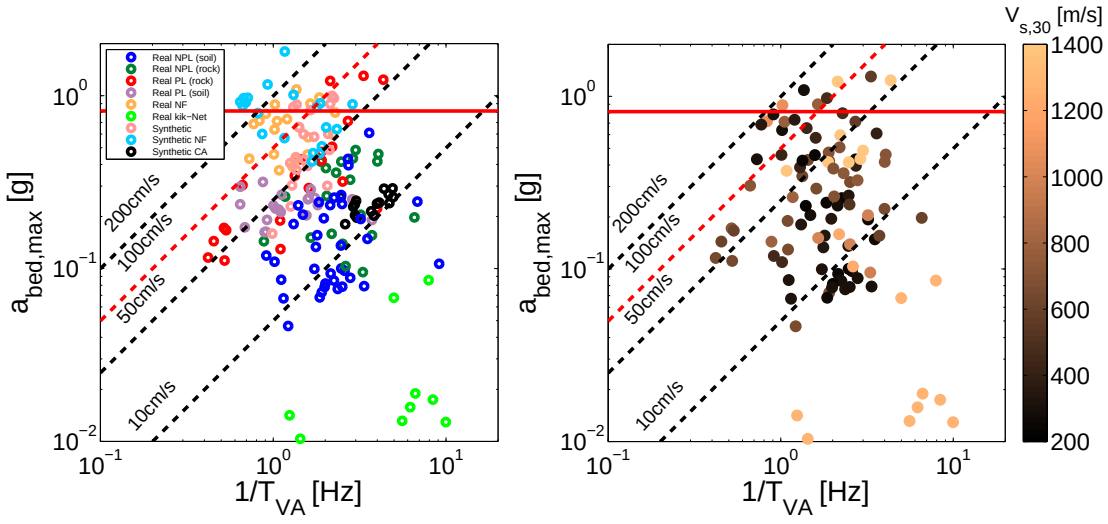

(a) (b)

Figure 3.18: Relation between input IM: $a_{bed,max}$ and $T_{V/A}$: a) Classification of all ground motions, b) Classification of real earthquakes according to $V_{s,30}$ of the site.

3.4.3 Dynamic response of soil column

In the context of structural analysis, the dynamic response of the soil column subjected to all aforementioned ground motions is presented. Firstly, the PGA obtained at free-field (FF) is calculated as function of the maximum amplitude of the input signal $a_{bed,max}$. In Figure 3.19a, important differences in the response of the soil column are observed as two separate branches are generated. Stronger nonlinearity (lower branch) appears for the real motions recorded on soil site and the relevant synthetic ones. This is also verified in Figure 3.19b, where the smaller values of $V_{s,30}$ are mostly observed in the lower branch for the real motions. Moreover, it seems that the soil site motions of the lower branch are globally longer in duration of mainshock (t_{595}) as it is shown in Figure 3.19c. Nevertheless, no influence of the number of cycles N_{cycles} of the input motion is remarked in Figure 3.19d, as there is a large dispersion of results. The relation between PGA-PGV is widely used as an index of soil nonlinearity (Idriss, 2013; Chandra et al., 2014). The response in terms of PGA-PGV at FF follows a homogeneous trend, as shown in Figure 3.20. The greater values with strong nonlinearity come from the near fault signals, validating the aforementioned classification of the severity of these motions.

Consequent to this statement, the near-fault motions provide mostly the greater values of settlements at the end of each ground motion (Figure 3.21a). This can be clearer in Figure 3.21b, where the increasing severity following the direction of increasing uniform velocity from the right-down corner towards the left-up one is validated. No close relation between settlements and $V_{s,30}$, t_{595} and N_{cycles} can be identified, as after a certain level of earthquake intensity where the soil liquefies, a limit level of settlements is reached independently of the value of IM. The corresponding figures are omitted.

In common engineering practice, the selection of pertinent input ground motions for dynamic structural analysis is a difficult task in the framework of PBEE. For this reason,

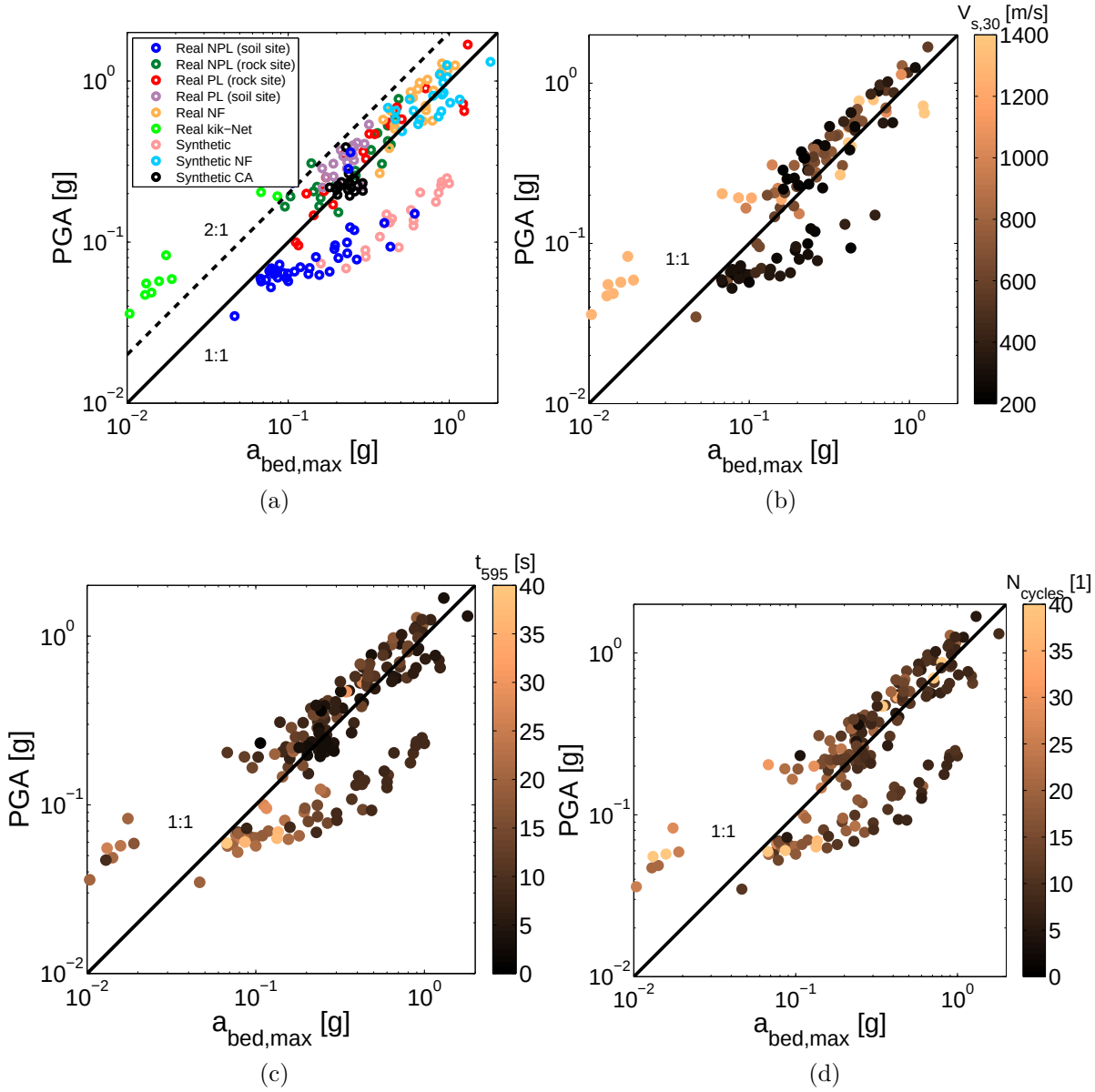

Figure 3.19: PGA at FF classified according to: a) input signal's type, b) shear velocity $V_{s,30}$ of real motions, c) duration of mainshock t_{595}, d) number of cycles N_{cycles} of input signal

it is usual to generate artificial accelerograms from target natural ones (Zentner, 2014). The question that arises from this approach is how close or different is the response of synthetic and natural accelerograms. In the light of this comparison, a comparison between the results of the synthetic motions generated by Code_Aster and those obtained from the natural accelerogram of Friuli follows. Next, to adress the effect of site conditions on the dynamic response, a comparison between real motions recorded on soil and rock site is performed. Finally, according to Baker (2007), pulse-like ground motions have been identified as imposing exteme demands on structures to an extent not predicted by typical

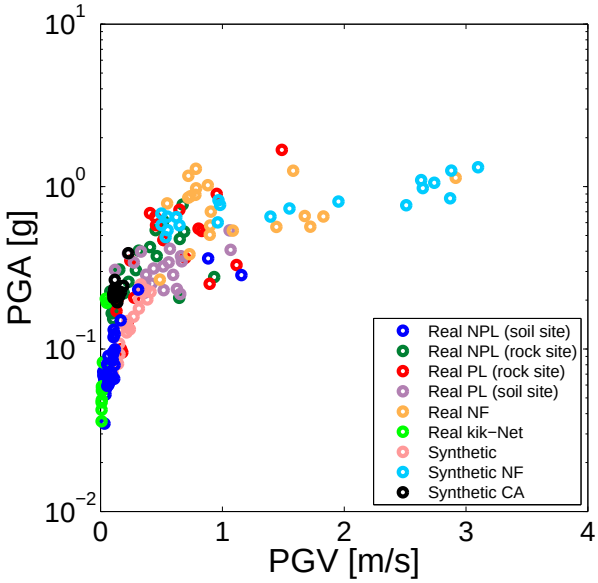

Figure 3.20: PGA classified according to input signal's type as function of PGV at FF.

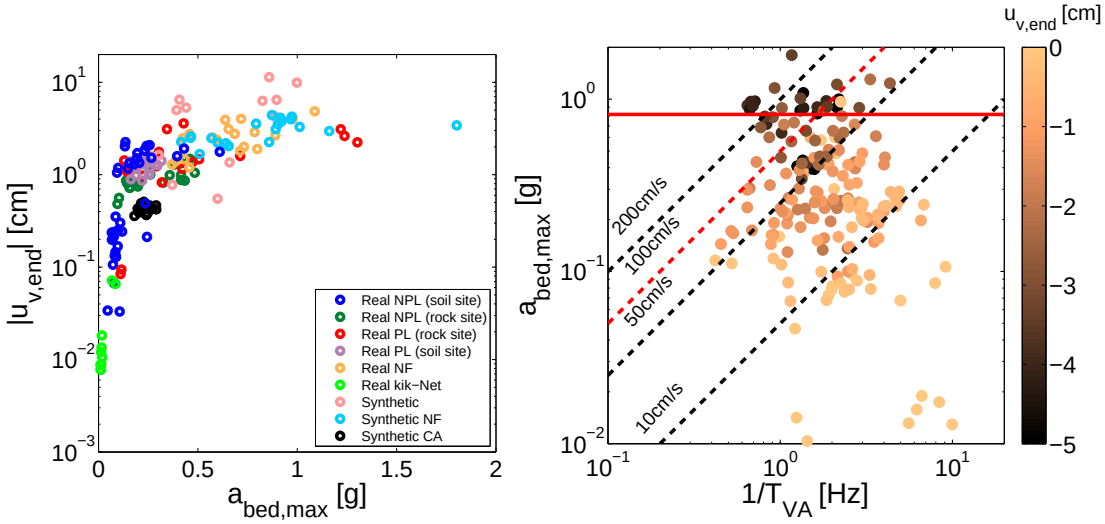

(a) (b)

Figure 3.21: Settlement u_v at free-field classified according to: a) input signal's type as function of $a_{bed,max}$, b) relation between input IM: $a_{bed,max}$ and $T_{V,A}$.

measures such as response spectra. Thus, the third comparison refers to non pulse-like and pulse-like motions and discusses their effect on earthquake-induced liquefaction.

Comparison of synthetic motions to Friuli earthquake

The synthetic motions generated by the option *GENE_ACCE_SEISME* of Code_Aster based on the natural accelerogram of Friuli, as well as the original motion, are shown in color in Figure 3.22. The synthetic motions are classified as slightly less severe than the

real one, according to the approach explained before.

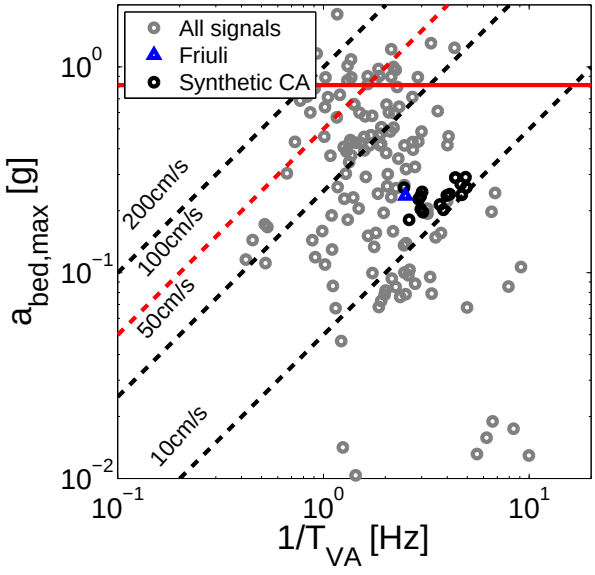

Figure 3.22: Relation between input IM: $a_{bed,max}$ and $T_{V,A}$ - Comparison of synthetic motions generated by Code_Aster and Friuli.

Good agreement in the results of the dynamic analyses are obtained in terms of PGA and settlements (Figure 3.23a, 3.23b). However, as mentioned before, the synthetic motions are less severe than the real one due to the lower values of the obtained PGV at FF in Figure 3.23c. The difference in terms of PGV is surprisingly important and may be linked to the peak in low frequencies of Friuli in the response spectra in Figure 3.24a, which is not observed in the synthetic motions apart from one case. Nevertheless, no further explanation can be provided. Furthermore, as it concerns the response spectra of PSA at FF, those of synthetic motions are quite dispersed compared to the natural one in Figure 3.24a. In terms of earthquake-induced liquefaction and settlements, the results match very well as the mean response of the synthetic motions is very close to this obtained from the real earthquake (Figure 3.24b, 3.24c, 3.24d).

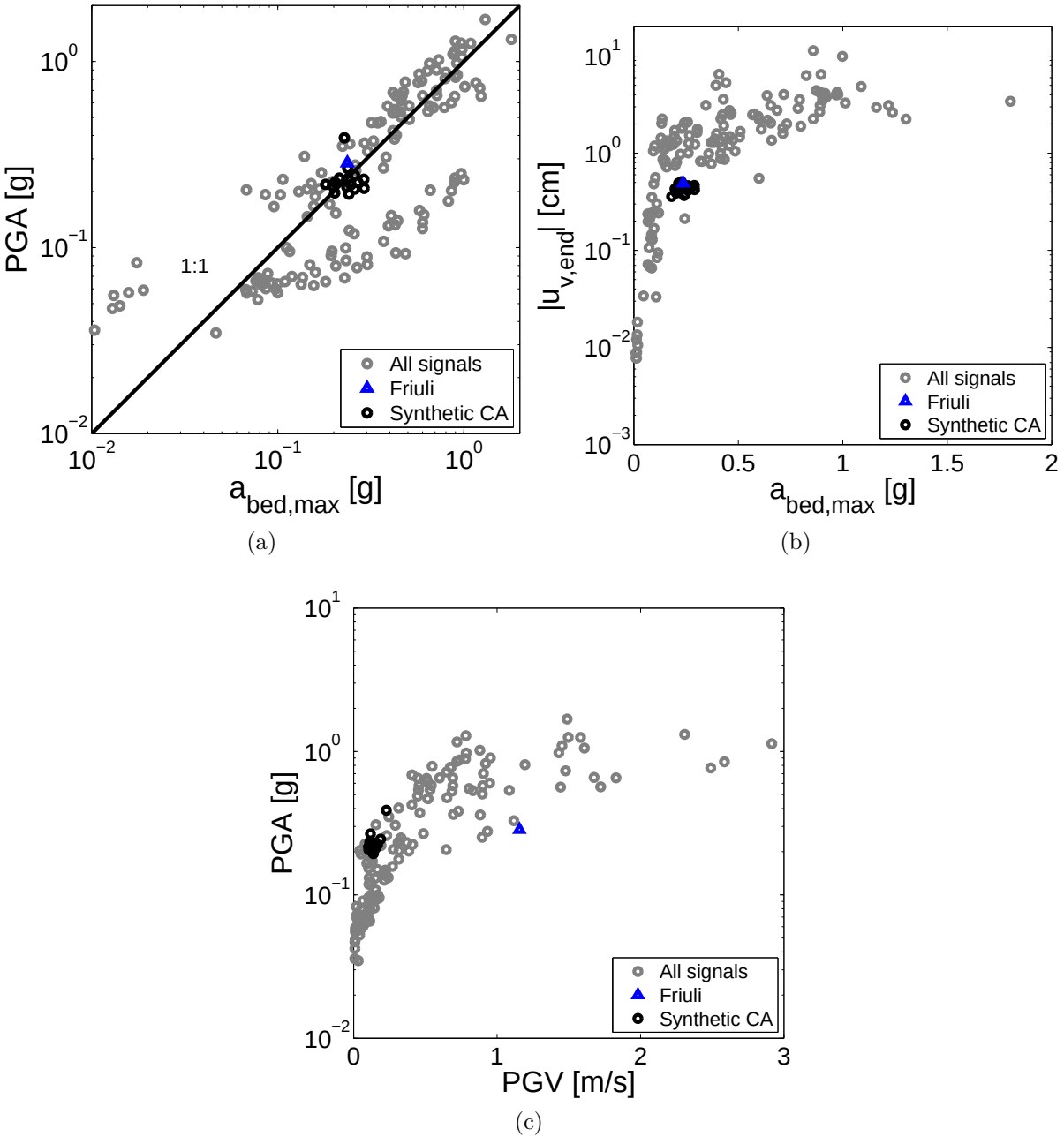

Figure 3.23: Comparison of synthetic motions and Friuli (in grey all other motions): Soil column's response in terms of: a) PGA as function of the input motion $a_{bed,max}$, b) Settlements at FF as function of the input motion $a_{bed,max}$, c) PGA-PGV at FF.

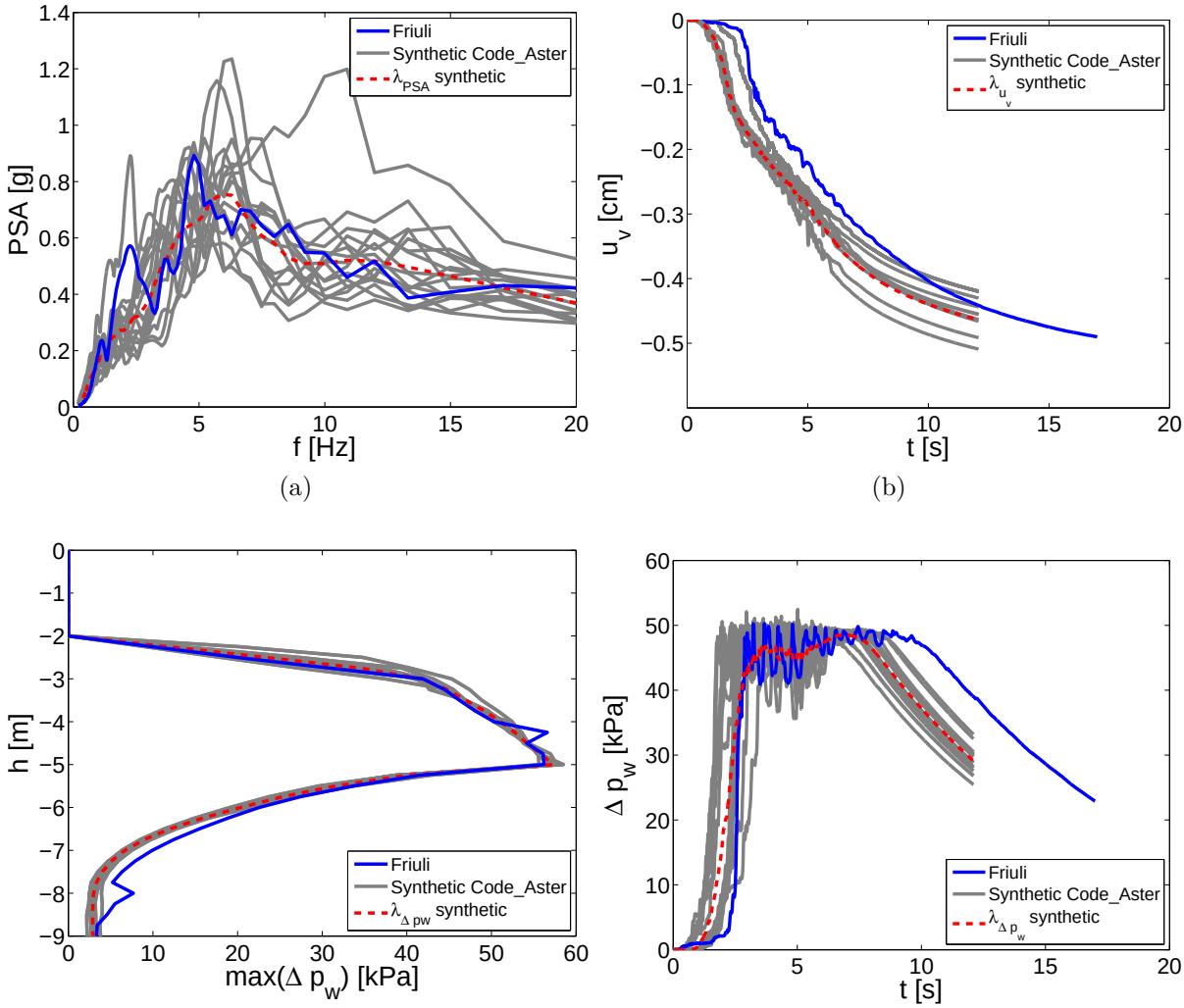

Figure 3.24: Comparison of synthetic motions and Friuli: Soil column's response in terms of: a) Response spectra PSA at FF as function of frequency, b) Settlements at FF, c) Maximum excess pore water pressure (Δp_w) along the soil column, d) Evolution of excess pore water pressure (Δp_w) at h=-4m from the surface.

Origin of input ground motion

This section is dedicated to the sensitivity study of soil and rock site motions on the dynamic response. The input motions compared are plotted in Figure 3.25, where non pulse-like motions recorded on soil site ($V_{s,30} < 600$m/s) are colored in blue and those on rock site ($V_{s,30} > 600$m/s) in green. Globally a soil site motion differs from a rock site motion in terms of frequency content and duration of mainshock. The first one is situated mostly in low frequencies and it is longer compared to a shorter in duration rock site motion found in higher frequencies. The two sets of motions compared are: T1a 5 / Rb 5 and T1a 3/ Rb 3 and indicated with the two arrows (for motions' characteristics refer to Tables C.2, C.3 in Appendix C). The choice is based on the same intensity of the motions but different origin.

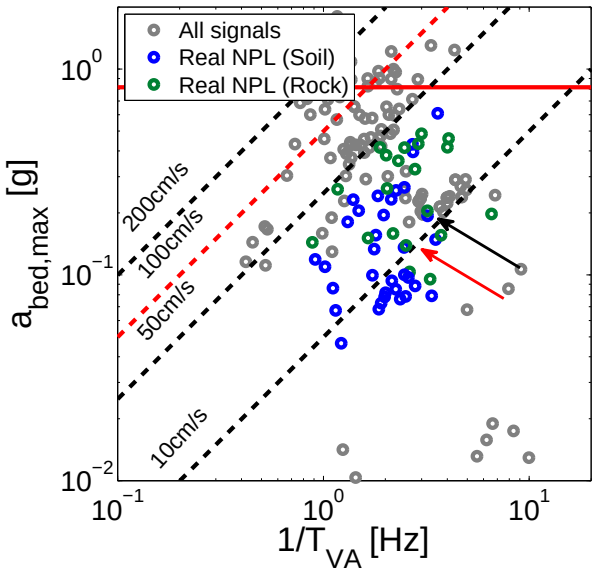

Figure 3.25: Relation between input IM: $a_{bed,max}$ and $T_{V,A}$ - Comparison of NPL soil site motion / NPL rock site motion

The motions indicated with the red arrow are the T1a 5 / Rb 5, whose accelerograms, Arias intensity and acceleration spectra are plotted in Figures 3.26a, 3.26b, 3.26e. Both motions are of same magnitude and source-to-site distance. The mainshock of soil site motion is longer, as calculated by the t_{595}, and contains the double number of cycles, as well as, double Arias intensity. While their response spectra are very close, the soil site motion is more apparent in low frequencies (T>1s), as shown in Figure 3.26e. Contrary, the motions indicated with the black arrow (T1a 3/Rb 3) are of same magnitude and resemble in the number of cycles and Arias intensity, but differ in duration of mainshock (Figures 3.26c, 3.26d). The source-to-site distance of the soil site motion (T1a 3) is smaller than this of rock site motion (Rb 3) and for this reason the soil site motion is not significantly apparent in low frequencies, as observed in Figure 3.26f.

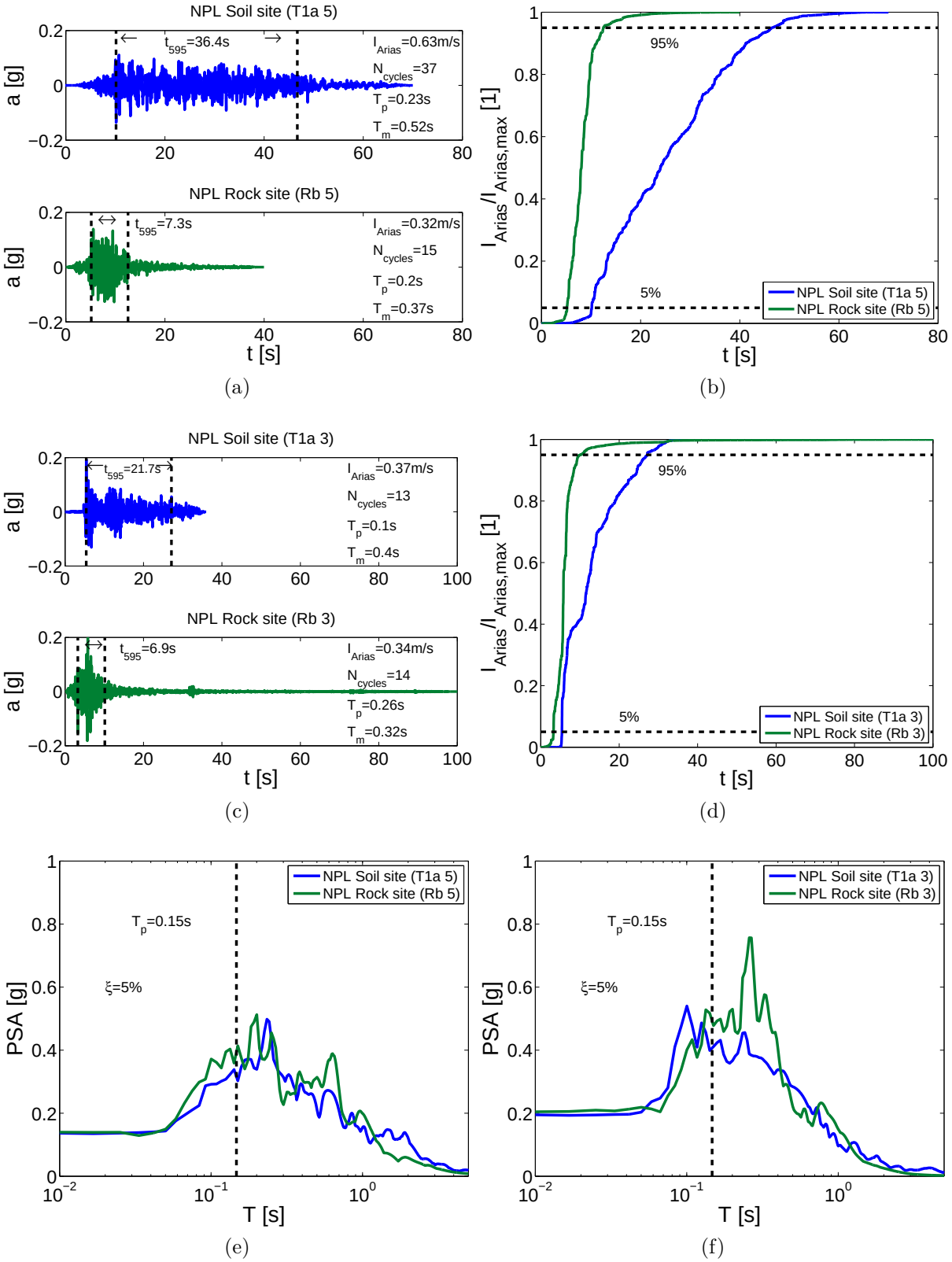

Figure 3.26: Input ground motions for comparison NPL soil site motion-NPL rock site motion: a) Accelerograms T1a 5/Rb 5, b) Arias intensity T1a 5/Rb 5, c) Accelerograms T1a 3/Rb 3, d) Arias intensity T1a 3/Rb 3, e), f) Acceleration response spectra (ξ=5%) T1a 5/Rb 5 and T1a 3/Rb 3, respectively (T_p of soil is indicated with the dashed line).

For comparison reasons, in the left part of Figure 3.27, the response of all ground motions is plotted in grey, while that of soil and rock site in blue and green, respectively. In the right part, in blue and green are the two sets of motions chosen for comparison and the rest of soil/rock site in grey. Observing Figures 3.27a, great differences are found as the soil site motions provide stronger nonlinearity, implying extended liquefaction state, as also commented by Chandra et al. (2014). Although the two sets of selected input motions are of same amplitude, significant deamplification of acceleration is remarked for the soil site motions compared to the rock site ones (Figure 3.27b). In Figures 3.27c, after a certain level of input motion's amplitude liquefaction occurs and settlements reach a limit value. However, differences appear between the soil and rock site motions in Figure 3.27d, as the first ones provide the double value of settlement.

Indeed, in Figure 3.28 the contours of r_u define extended liquefaction in time for the soil site motions. Especially, in the second comparison (T1a 3/Ra 3), with motions of same amplitude, intensity and number of cycles, the origin of the motion combined to the duration of mainshock are proven to be crucial for soil liquefaction analysis. This statement is in agreement with the research work of Verdugo and González (2015) after observations of liquefaction-induced ground damages during the 2010 Maule earthquake in Chile. The lower frequency soil site motions amplify the soil liquefaction and induced strong nonlinearity. The same conclusion is drawn observing Figure 3.29, where the evolution of excess pore water pressure is compared in both cases. The rock site motions with shorter duration of mainshock provide a limited liquefaction state.

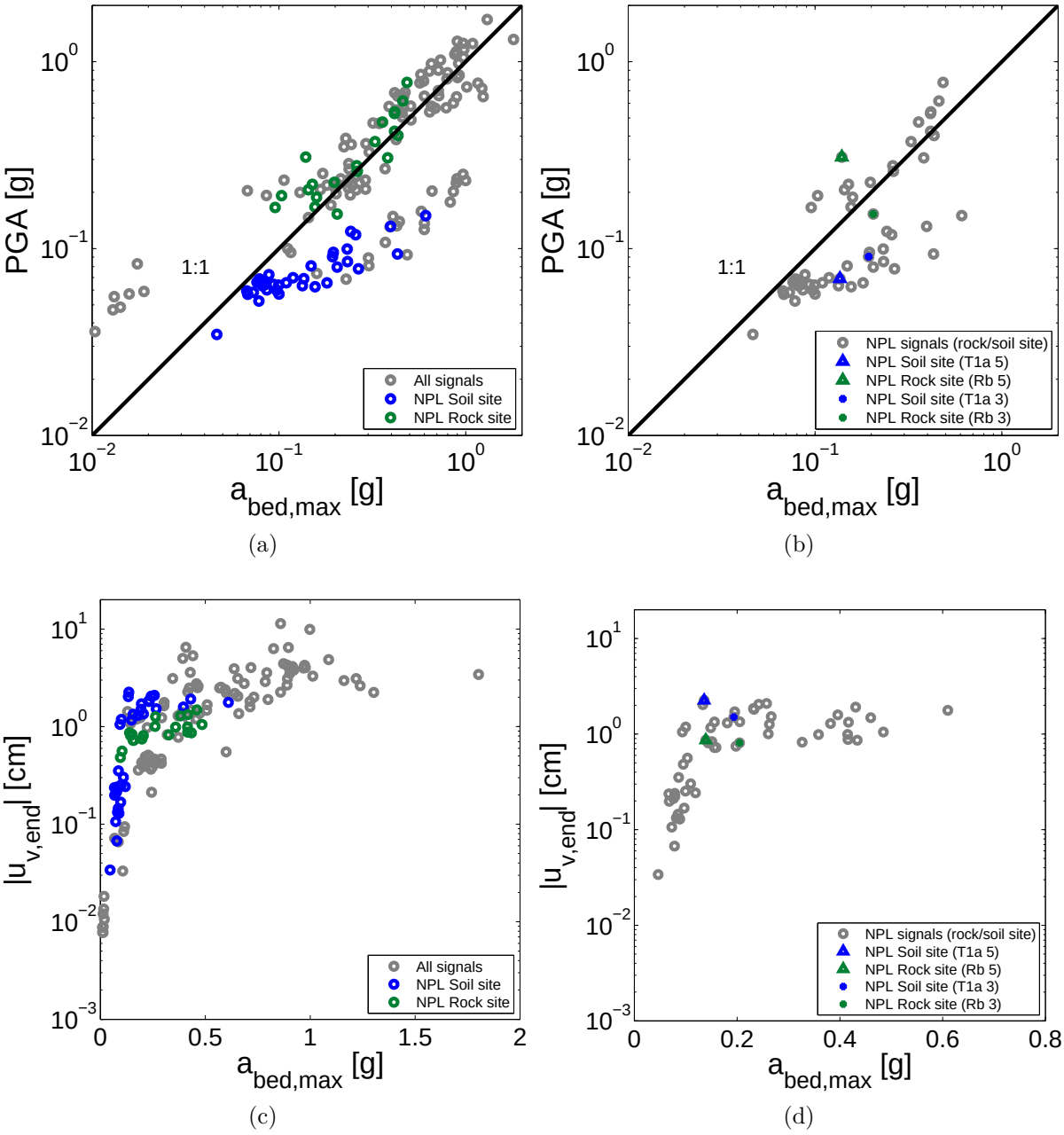

Figure 3.27: Soil column's responsein terms of PGA and settlements. Left figures: comparison of NPL soil - rock site (in grey all other motions), Right figures: comparison of selected motions T1a 5/Rb 5 and T1a 3/Rb 3 (in grey all other soil-rock site motions).

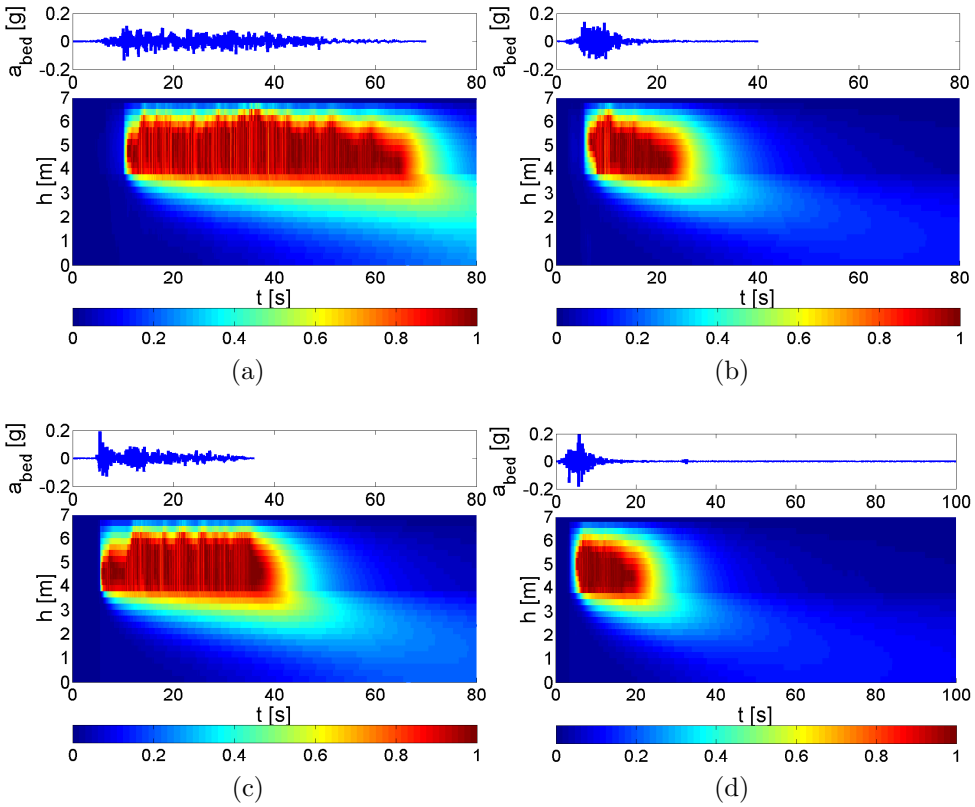

Figure 3.28: Excess pore water pressure ratio during ground motion: a) NPL soil site motion (T1a 5), b) NPL rock site motion (Rb 5), c) NPL soil site motion (T1a 3), d) NPL rock site motion (Rb 3).

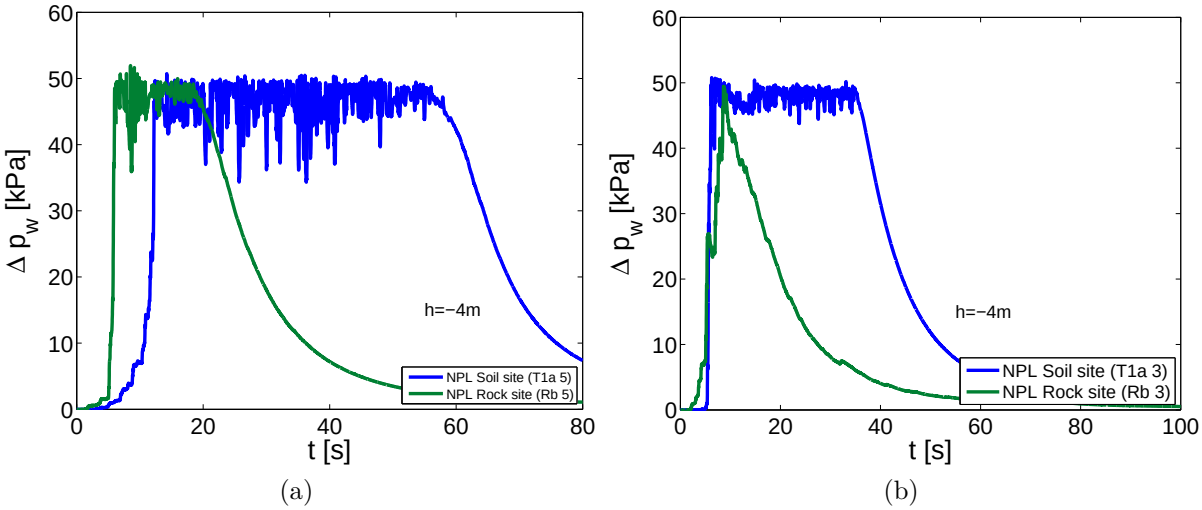

Figure 3.29: Evolution of pore water pressure (at h=-4m from the surface): a) Comparison NPL soil site motion (T1a 5) - NPL rock site motion (Rb 5), b) Comparison NPL soil site motion (T1a 3) - NPL rock site motion (Rb 3).

Type of input ground motion

Near-fault ground motions containing strong velocity pulses, called pulse-like, are of interest in the field of seismology and earthquake engineering, as they have been identified to impose extreme demands on structures, as discussed by Mavroeidis et al. (2004) and Baker (2007). Consequently, the influence of type of input motion on the dynamic response is realized by comparing motions classified as non pulse-like (in blue color) and pulse-like (in red color) in Figure 3.30. This classification is given by NGA database, based on the work of Baker (2007). According to this approach, a pulse-like ground motion is considered to be a record with a short-duration pulse that occurs early in the velocity time history and has large amplitude. The most important cause of these velocity pulse is forward-directivity effects in the near-fault region. Forward directivity results when the fault rupture propagates toward the site at a velocity nearly equal to the propagation velocity of shear waves and the direction of fault slip is aligned with the site (Baker, 2007).

As previously, the arrow in Figure 3.30 indicates the set of non pulse-like / pulse-like motions compared. The choice is based on the same intensity of the motions but different type. The chosen motions, both recorded on rock site, are the Ra 9/ Pa 3 and their accelerograms, Arias intensity and response spectra are plotted in Figure 3.31. The characteristics of the two motions are quite similar and they mostly differ in frequency content (higher frequency for the non pulse-like motion).

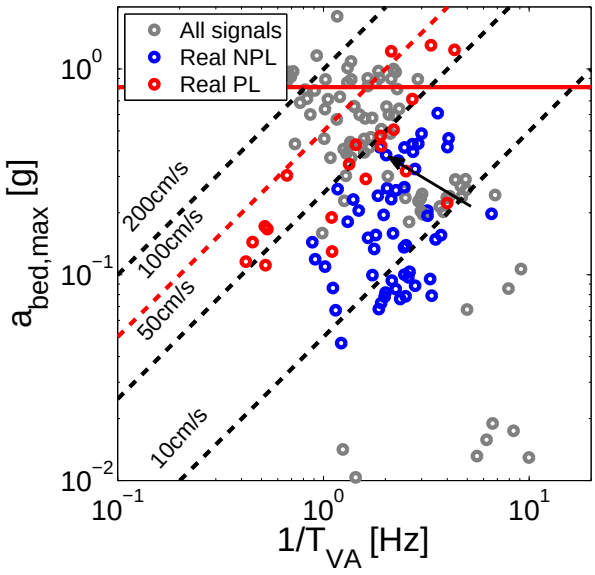

Figure 3.30: Relation between input IM: $a_{bed,max}$ and $T_{V,A}$ - Comparison of NPL / PL.

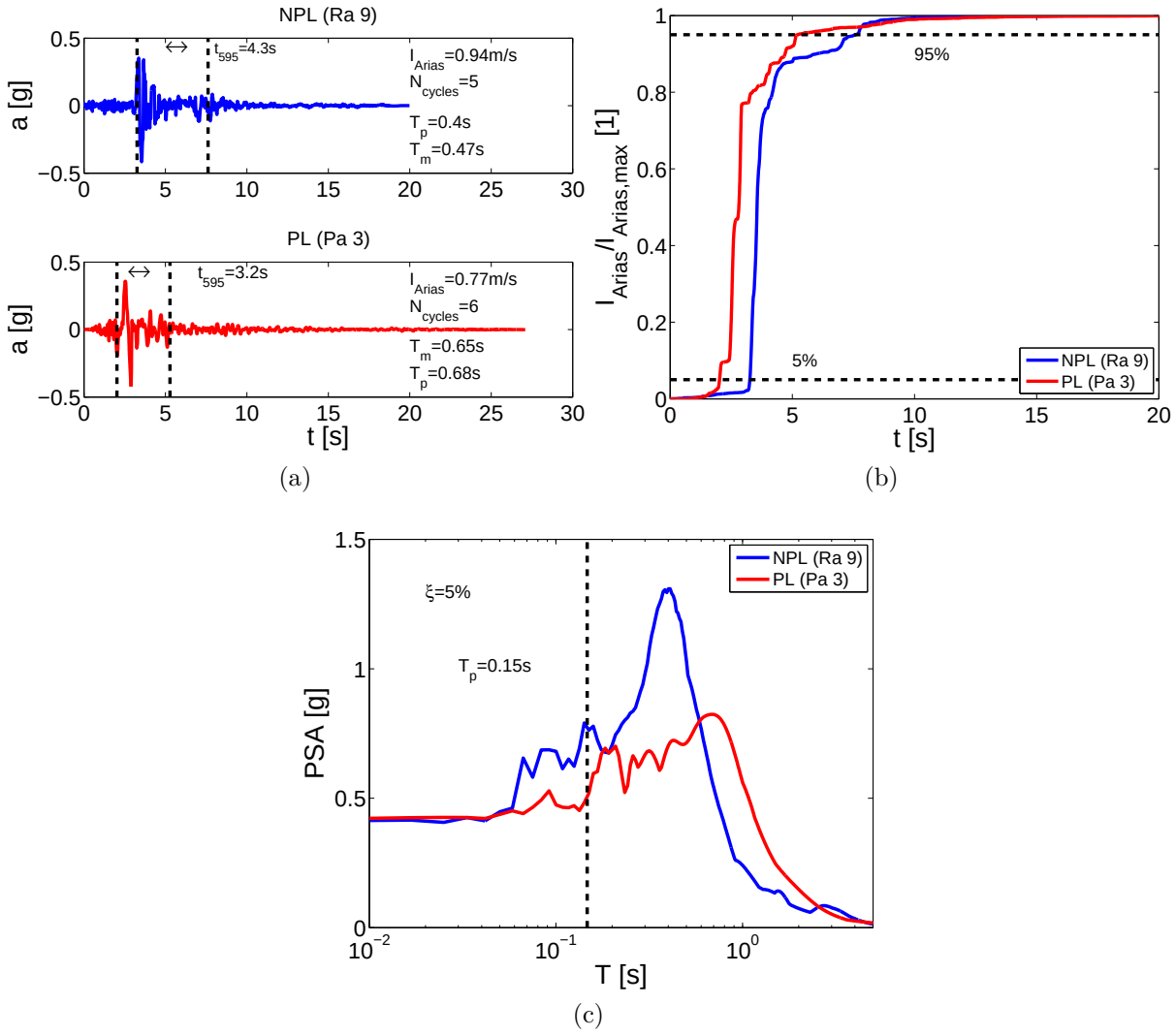

Figure 3.31: Input ground motions for comparison NPL motion - PL motion: a) Accelerograms Ra 9/Pa 3, b) Arias intensity Ra 9/Pa 3, c) Acceleration response spectra (ξ=5%) Ra 9/Pa 3.

As before, the left part of Figure 3.32 provides the response of all ground motions plotted in grey, while that of non pulse-like and pulse-like in blue and red, respectively. In the right part, in blue and red is the set of motions chosen for comparison and the rest of on pulse-like / pulse-like in grey. In Figure 3.32a, the margins in the response are not very significant and only the soil site non pulse-like motions diverge, forming the lower branch, as explained in the previous section. Similarly, in terms of settlements in Figure 3.32c, no noticeable differences appear. As it concers the two motions of same severity chosen, their responses are very close (Figures 3.32b, 3.32d).

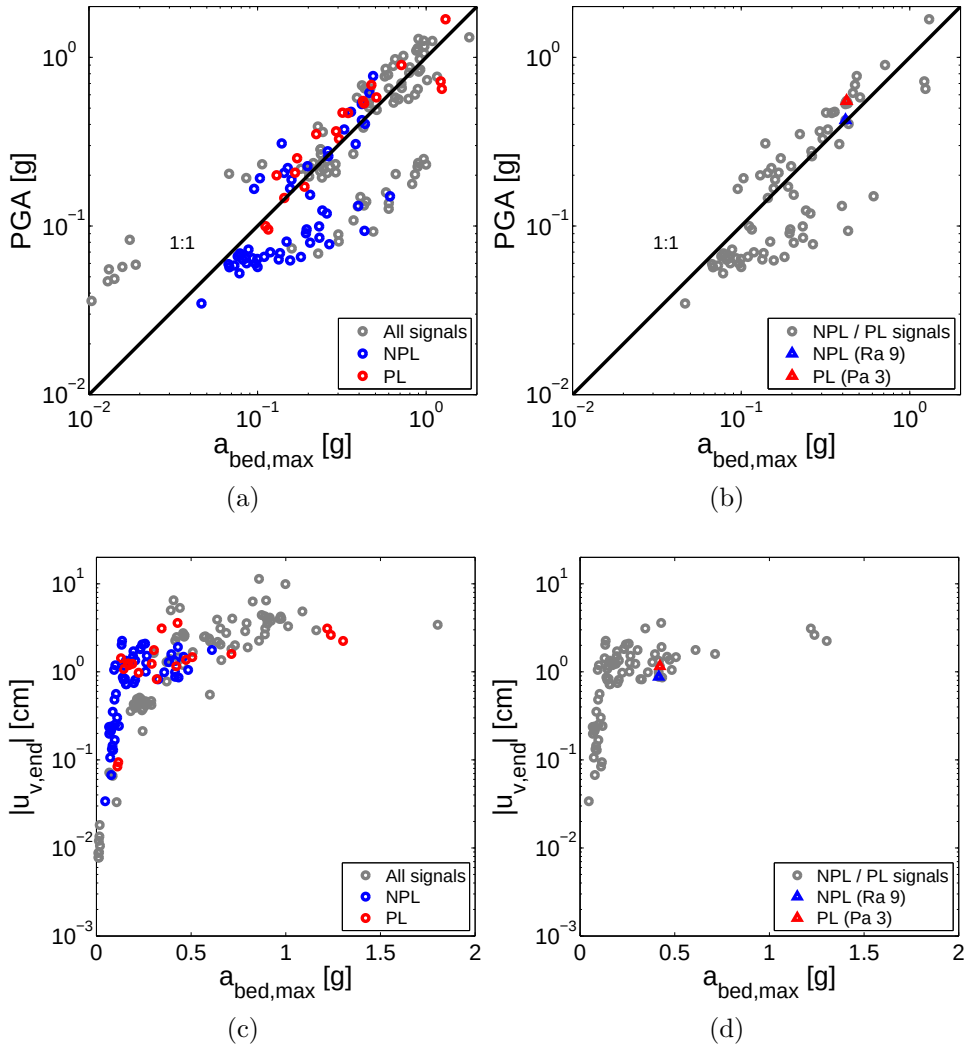

Figure 3.32: Soil column's response in terms of PGA and settlements. Left figures: comparison of NPL - PL (in grey all other motions), Right figures: comparison of selected motions Ra 9/Pa 3 (in grey all other NPL - PL motions).

Comparing the response of the two chosen motions in terms of liquefaction state (Figure 3.33), no remarkable differences are noticed. Especially, in Figure 3.34 the evolution of excess pore water pressure at the middle of the liquefied layer follows the same trend for both motions.

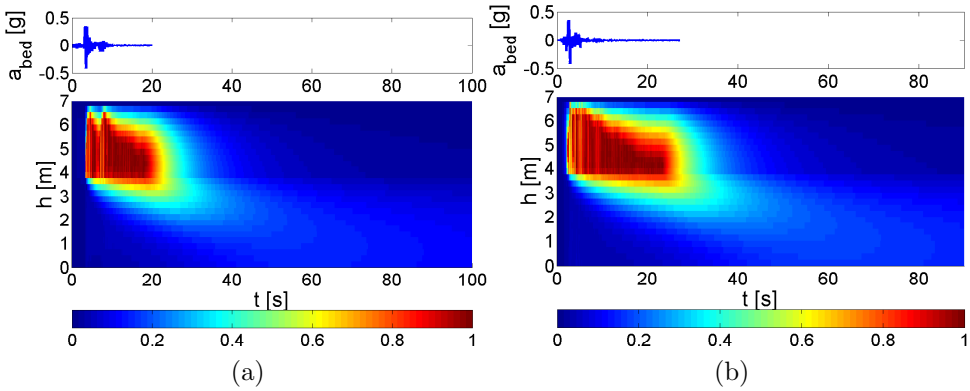

Figure 3.33: Excess pore water pressure ratio during ground motion:a) NPL (Ra 9), b) PL (Pa 3).

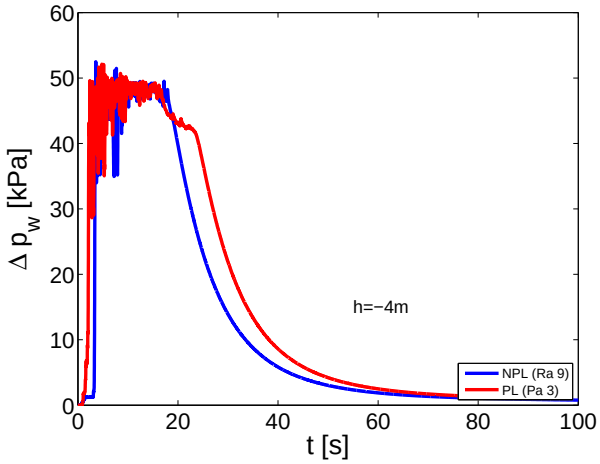

Figure 3.34: Evolution of pore water pressure (at h=-4m from the surface): Comparison NPL (Ra 9) - PL (Pa 3).

Synopsis

To summarize, the seismic hazard analysis of the soil column showed that the important IMs are a combination of the equivalent predominant frequency, the maximum acceleration and velocity of the input ground motion, which characterize the intensity of the motion. As a second step the duration of mainshock (t_{595}), which can depend on the origin of input motion (soil or rock site), should also be considered, since it can be very severe in case of soil liquefaction. PGA and liquefaction-induced settlements are identified as representative EDP, in the context of liquefaction analysis. Next, the effect of soil's permeability on liquefaction-induced failure is discussed and the soil site motions are imposed to the soil column, as they are proven to be crucial for liquefaction.

3.5 Effect of variation of permeability during soil liquefaction

Liquefaction is inextricably related to soil's permeability as permeable soils can dissipate rapidly the excess pore water and liquefaction phenomenon may be less extended or prevented. Researchers have explored the effect of soil's permeability and focus on the change of permeability during liquefaction as the soil grains tend to move away and the contact between them is lost. Noticeably within the context of the VELACS (verification of liquefaction analysis by centrifuge studies) project, different values of soil permeability were used for the build-up and dissipation phase for the centrifuge validation of a numerical model for soil liquefaction (Popescu and Prevost, 1993). Laboratory triaxial tests on sand specimens show that the behavior of soil in shear is highly dependent on its hydrological properties, which interact with the effective stress history of the material, as changes in permeability were observed during shear zone propagation (Bolton et al., 1998; Sulem and Ouffroukh, 2006). Moreover, Feia et al. (2016) observed changes of the permeability when shear banding occurs after triaxial tests of unconsolidated sands under shear and tried to correlate fine particles production with permeability changes. However, it was remarked that permeability is a complex material property, as it depends upon various factors as pore shape and size, tortuosity, connectivity, etc. Furthermore, Coelho et al. (2004) state that the permeability of sand increases significantly during the shaking, after observations of centrifuge tests.

Previous studies of modeling of soil liquefaction recommend to use a variable permeability during the ground motion, to better simulate the phenomenon of liquefaction and represent the change in the soil behavior (Taiebat et al., 2007; Shahir et al., 2012). Di and Sato (2003) and Menéndez et al. (2010) performed FE simulations by assuming a dependence of soil permeability on void ratio, when considerable values of deformations or settlements appear due to soil nonlinearity. On the other hand, variation of permeability as function of liquefaction state is discussed by Haigh et al. (2012), Shahir et al. (2014), after experimental results of laboratory tests. An increase of permeability during soil liquefaction is considered due to the greater voids between the grains which move away. The research done is concentrated mainly on observing the evolution of excess pore water pressure and trying to fit the experimental response to an empirical numerical model with variable permeability, by proposing functions which take into account this variation of permeability regarding to liquefaction state. While the aforementioned studies intend to propose a function for the variation of permeability, in the current study the objective is to evaluate the effect of taking into account such an assumption of variable permeability.

3.5.1 Problem statement

To study whether it is crucial or not to account for the change of soil permeability during liquefaction in the numerical simulations, three different simulations are performed, as follows:

1. Constant permeability equal to the initial values of k_s.
2. Increased and constant permeability equal to 5$\cdot$ $k_{s,initial}$, when r_u=1.

3. Variable permeability as function of r_u.

where $r_u = \Delta p_w \,/\, \sigma'_{v,0}$ is the excess pore water pressure ratio, which is used as liquefaction index.

The first simulation refers to the traditional approach used widely in FE simulations, where the soil permeability is supposed to be constant during an earthquake. Then, an increased and constant value of permeability is used once the value of excess pore water pressure r_u exceeds a certain level (simulation 2). Finally, a more accurate function for the variation of permeability which takes into account the progressive increase/decrease of permeability during the earthquake is considered. More precisely, in the third case the following function is used, based on the propositions of Shahir et al. (2012, 2014) after experimental results of centrifuge tests (Figure 3.35):

$$k_s = \begin{cases} k_{s,initial} \cdot (1 + 9 \cdot r_u^2) & \text{if } 0.1 < r_u < 1 \text{ , pore water pressure build-up phase} \\ 10 \cdot k_{s,initial} & \text{if } r_u = 1 \text{ , flow liquefaction phase} \\ k_{s,initial} \cdot (1 + 9 \cdot r_u^{10}) & \text{if } 0.1 < r_u < 1 \text{ , pore water dissipation phase} \end{cases} \tag{3.6}$$

where the constants used were calibrated such that results of numerical simulations match the experimental ones.

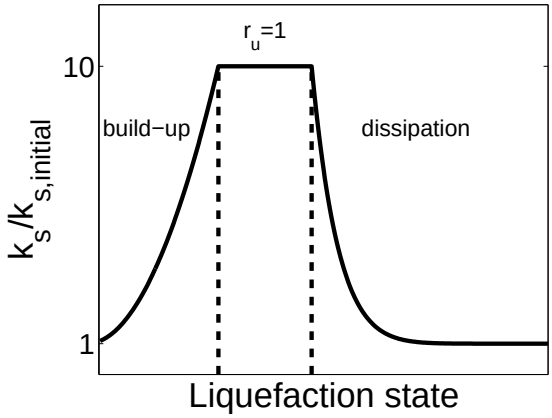

Figure 3.35: Variation of permeability as function of r_u (simulation 3).

The aforementioned functions of variable permeability (i.e. simulations 2 and 3) were implemented into the FE software Code_Aster. Note that as the value of r_u is evaluated in each Gauss point, non-convergence problems may appear during the simulation as slight differences in the generation of pore water pressure exist among the Gauss points, i.e. one gauss point may tend to generate pore water pressure, while in another one pore water pressure remains constant or decreases. For this reason and trying to eliminate non-convergence problems, it is chosen to change the permeability during the ground motion only if $r_u > 0.1$ and $\Delta r_u > 0.1\%$. As a result, slight differences in the value of r_u, which may perturbate the response, are not taken into account.

The variation of permeability is expected to affect signifactly the dissipation phase and liquefaction-induced settlements, since a large value of permeability is considered

during dissipation. For this reason it is necessary to compare the response of soils with different values of initial permeability. Two values for initial permeability are chosen for the LMS layer, a clean sand of medium permeability and a silty sand of low permeability, as explained in Section 3.2.3. In the current section, only results of the clean sand are discussed, as both studies led to the same outcome. For the study with the silty sand refer to Appendix E. It should be mentioned that globally the permeability of the dense layer remains unchanged or changes slightly throughout all simulations, as no significant excess pore water pressure is generated.

A parametric study is performed for the soil column subjected to real and synthetic ground motions for all three simulations and both values of initial permeability. Its dynamic response is compared for constant initial, constant increased and variable permeability in terms of PGA, settlement and excess pore water pressure. Based on the results of liquefaction vulnerability analysis in the previous section, the real motions recorded on soil site (ita, T1 motions) (Iervolino and Cornell, 2005; Sorrentino et al., 2008) and synthetic seismic motions (GV motions) (Dickinson and Gavin, 2011; Gavin and Dickinson, 2011) generated by motions recorded on soil site from PEER database are proven to be the most crucial, leading to strong soil nonlinearity and liquefaction. Consequently, in the study of variation of permeability, these motions are used (54 in total) and their spectra are presented in Figure 3.36. Their characteristics can be found in detail in Appendix C.

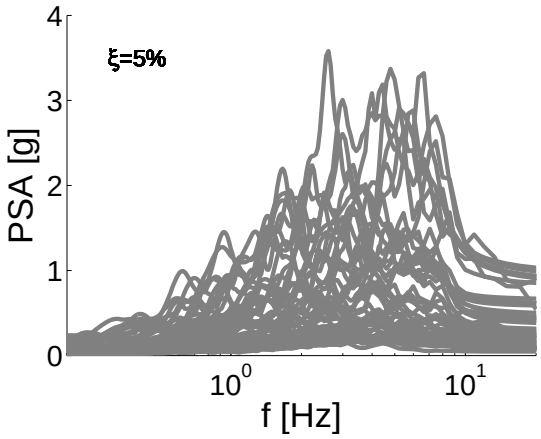

Figure 3.36: Acceleration spectra of input motions (ξ=5%).

3.5.2 Parametric study for clean sand of medium permeability

To better evaluate the effect of taking into account a permeability varying as function of the excess pore water pressure ratio r_u, 2 ground motions were chosen to discuss the dynamic response of the soil column. The ground motions chosen are the: ita La 7 and T1a 4 of amplitudes 0.1 and 0.4g, respectively, i.e. initially the lower ground motion does not lead to liquefaction and gradually liquefaction is reached for the stronger one.

The evolution of pore water pressure at 4m below the surface (in the middle of the liquefiable soil layer) is plotted for both ground motions and all simulations in Figure 3.37. In all simulations, the build-up phase is identical and the same value of Δp_w is

reached, which defines the liquefaction state at around 50kPa. The dissipation starts earlier in simulations 2 and 3 and is faster, as the soil behavior changes by increasing its permeability. This can be better explained by observing Figure 3.38 where the curves of shear stresses (τ) - shear strains (γ) are plotted for specific instants of the stronger motion. At the beginning of the motion (t=1-2s), the mechanical behavior inside the liquefiable layer (at h=-4m from the surface) is identical for all simulations. However, in Figure 3.38b at t=28-30s a different behavior is obtained. The familiar "banana-shaped" hysteresis loops of liquefaction observed in the laboratory appear for the simulation with constant permeability, while the simulations with increased and variable permeability have almost reverted to a linear response (especially the simulation 2 indicated with the red curve).

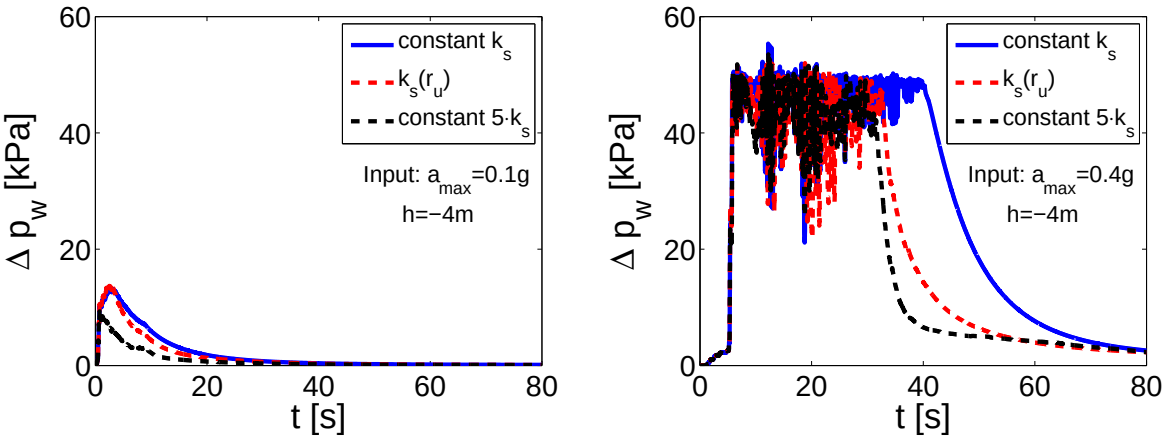

(a) Input ground motion: a_{max}=0.1g.

(b) Input ground motion: a_{max}=0.4g.

Figure 3.37: Comparison of three simulations: Evolution of pore water pressure during ground motion (at h=-4m from the surface).

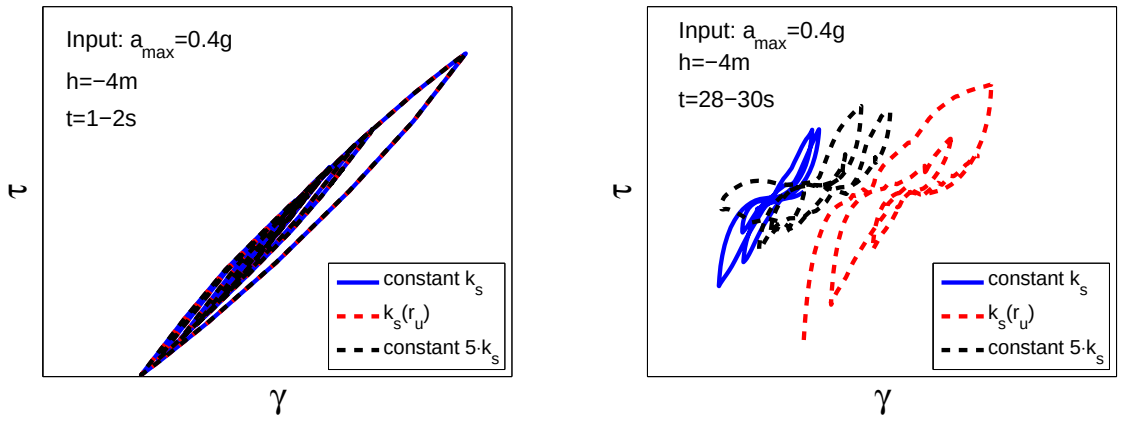

(a) (b)

Figure 3.38: Comparison of shear stresses (τ) - shear strains (γ) of three simulations at h=-4m from the surface for the strong input motion (a_{max}=0.4g): a) t=1-2s, b) t=28-30s.

The same conclusions are drawn by observing Figure 3.39, where the contours of r_u are plotted for the stronger motion ($a_{bed,max}$=0.4g). In simulations 2 and 3 with increased and variable permeability, the liquefaction state is more limited as the dissipation phase starts earlier during the coda phase of the earthquake (i.e. last seconds of the ground motion where its amplitude decreases significantly).

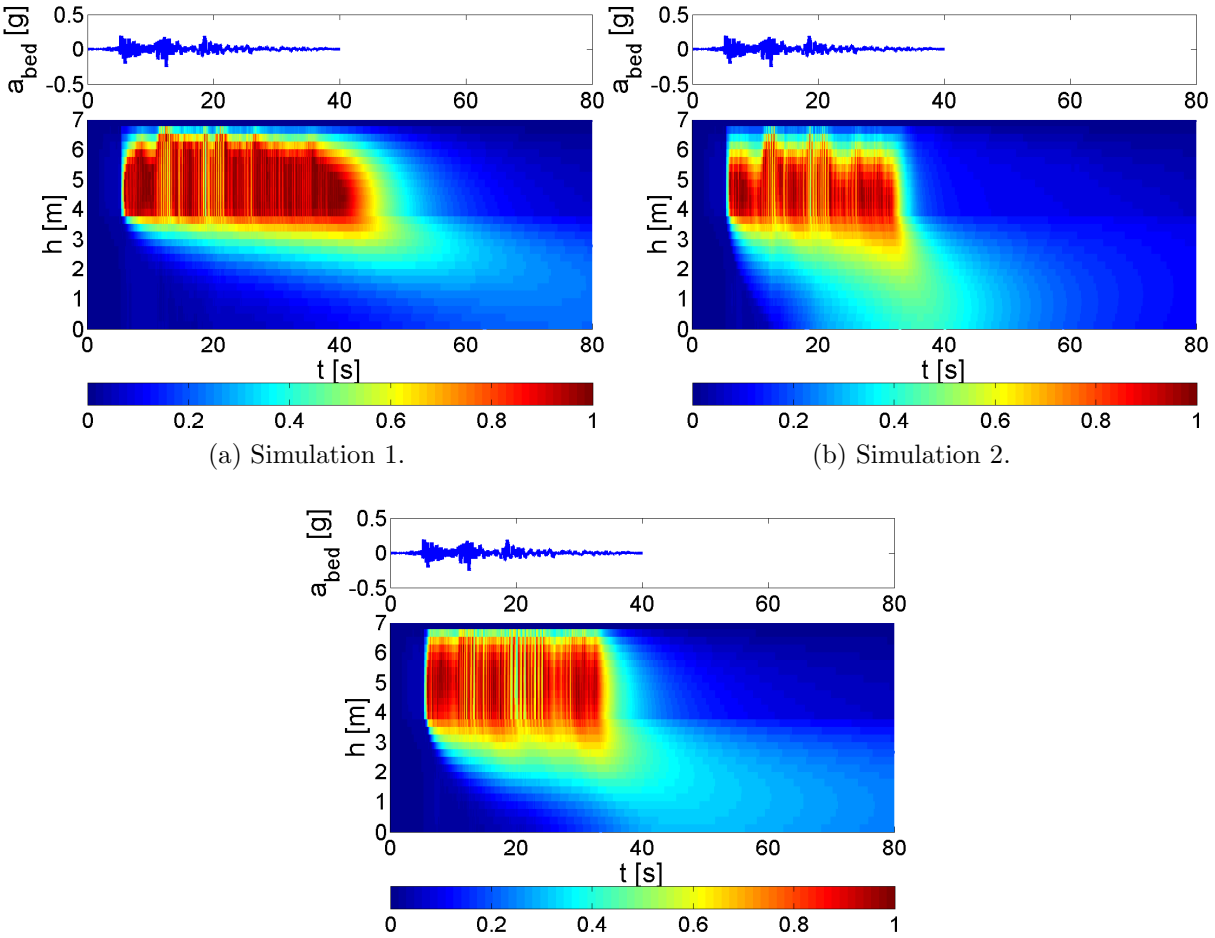

(a) Simulation 1.

(b) Simulation 2.

(c) Simulation 3.

Figure 3.39: Comparison of three simulations: Excess pore water pressure ratio during ground motion (a_{max}=0.4g).

A difference factor of Δp_w (Equation 3.7) is calculated in the whole column, i.e. results of all nodes (z=0-H) of the soil column and in each time step (t=0-N) are taken into account, as drawn in Figure 3.40. The results of the first simulation (with constant k_s) are considered as the reference values, so in Equation 3.7 $x(t,z)$ corresponds to simulation 1 and $y(t,z)$ to simulations 2 or 3.

$$\varepsilon = \frac{\sum_{z=0}^{H}\left(\sum_{t=0}^{N}\frac{|x(t,z)-y(t,z)|}{|x(t,z)|}\right)}{H \cdot N} \cdot 100\% \tag{3.7}$$

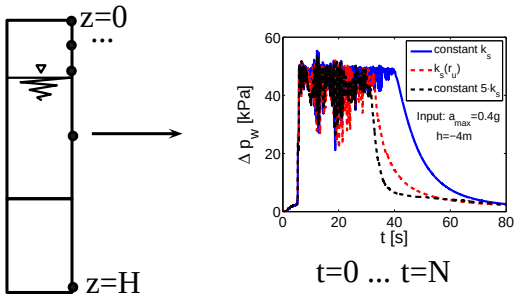

Figure 3.40: Calculation of difference factor ε.

In Figure 3.41 the maximum, mean and minimum difference factors of Δp_w are plotted for all input motions, as function of the maximum acceleration of the input signal. The difference in pore water pressure is observed especially for ground motions greater than 0.2g, as earthquake-induced liquefaction appears. Great divergence of around 60% is observed in case of constant increased permeability, as the permeability changes abruptly and remains constant during the ground motion (Figure 3.41a). While a difference of around 40% is remarked for moderate and strong motions between simulations with constant and variable permeability (simulations 1-3) in Figure 3.41b. All aforementioned differences result from the dissipation phase mostly, as it was already discussed.

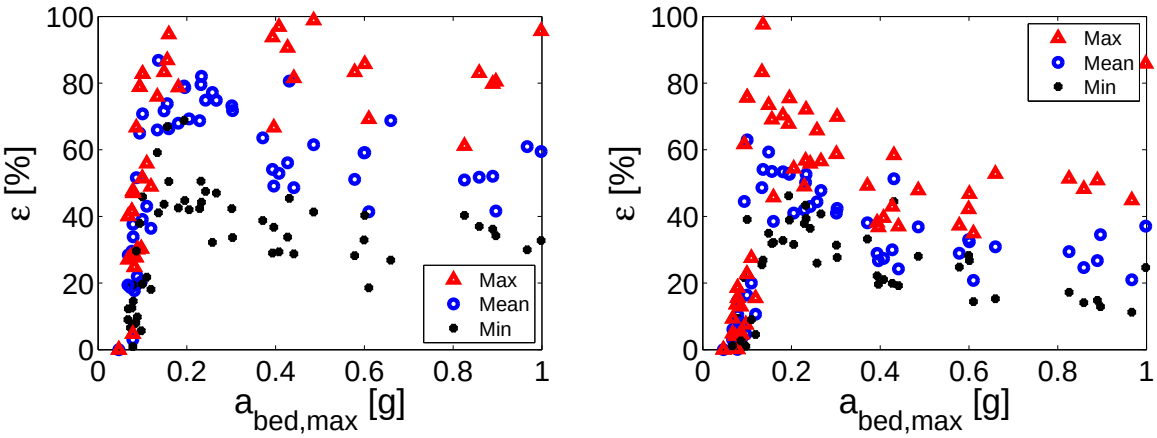

(a) Simulations 1-2.

(b) Simulations 1-3.

Figure 3.41: Difference estimation of Δp_w between the two permeability functions as function of maximum acceleration of input motion.

The horizontal acceleration measured at the top of the soil column (FF) and the Fourier transform are plotted for both ground motions and for all simulations in Figures 3.42, 3.43. In case of low motions where no liquefaction occurs, the change of permeability is negligible, so no changes in the acceleration and frequency are observed, as expected (Figures 3.42a, 3.43a). For the stronger motion an amplification of the acceleration is observed (Figure 3.42b) in case of variable permeability (simulation 3), as the soil has been densified due to faster dissipation. As it concerns the Fourier transform, slight

differences appear, referring mostly to low frequencies, i.e. during liquefaction phase (Figure 3.43b).

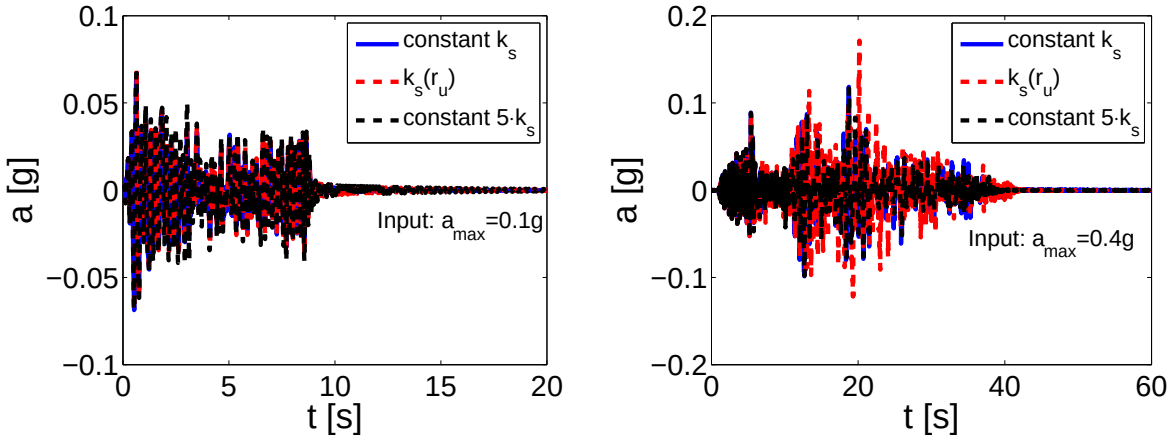

(a) Input ground motion: a_{max}=0.1g. (b) Input ground motion: a_{max}=0.4g.

Figure 3.42: Horizontal acceleration at FF.

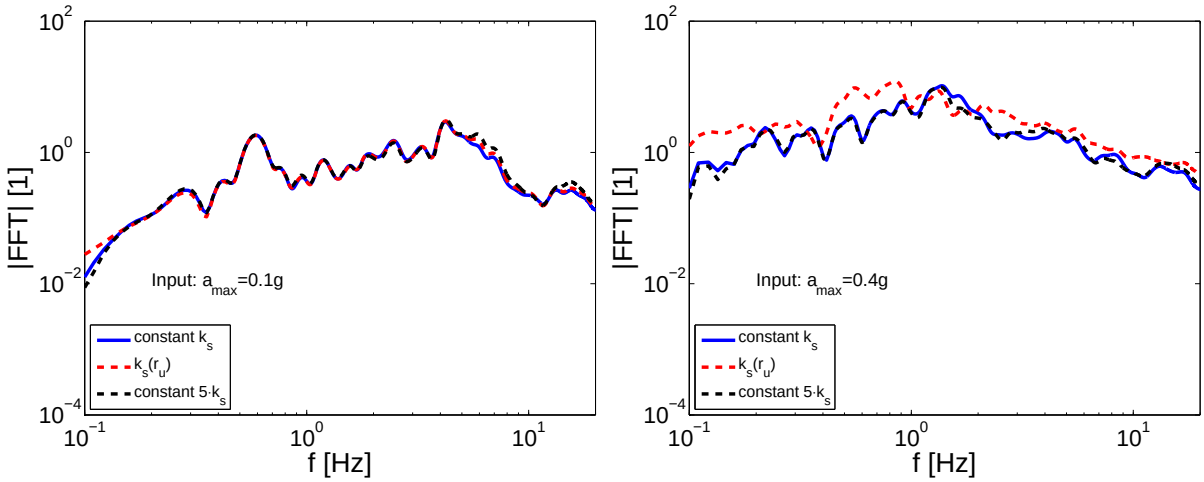

(a) Input ground motion: a_{max}=0.1g. (b) Input ground motion: a_{max}=0.4g.

Figure 3.43: Fourier transform of horizontal acceleration at FF.

The spectral coherency is also used to examine the relation between the signals in a wide range of frequencies. Spectral coherency is commonly used to estimate the causality between two signals (Equation 3.8). For the purpose of this study, it is used to assess the effect of the variable permeability in the frequency domain on the measured FF acceleration for all simulations.

$$\bar{\gamma}_{jk}(\omega) = \frac{\bar{S}_{jk}(\omega)}{\sqrt{\bar{S}_{jj}(\omega)\bar{S}_{kk}(\omega)}} \tag{3.8}$$

where $\bar{S}_{jk}(\omega)$: smoothed cross spectral density and $\bar{S}_{jj}(\omega)$: smoothed power spectral density.

In Figure 3.44a, the obtained signals of horizontal acceleration for simulations with constant and constant increased permeability are quite close (coherency close to 1). However, in case of variable permeability (Figure 3.44b), the signal of the strong motion completely diverges in low frequencies, as expected, due to liquefaction and soil nonlinearity. In higher frequencies it tends to reach greater values.

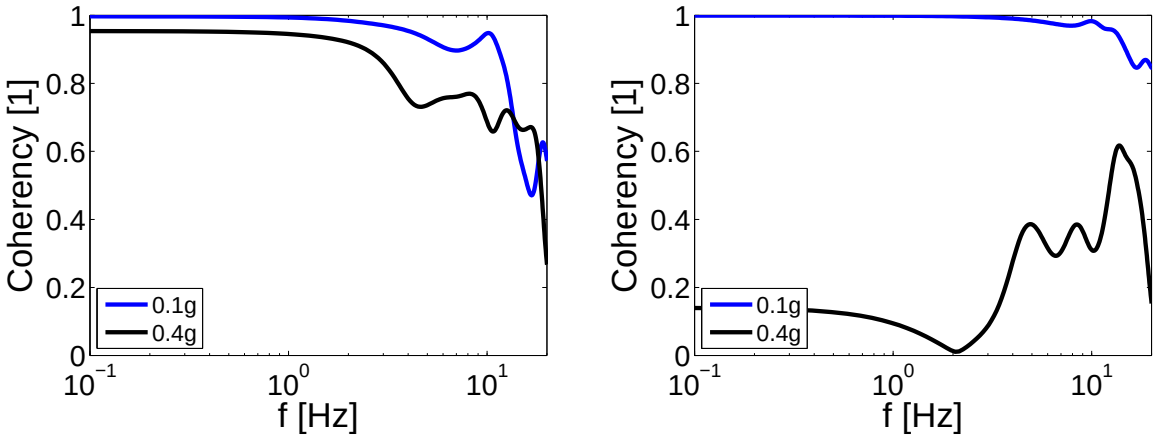

(a) Coherency between simulations 1-2.

(b) Coherency between simulations 1-3.

Figure 3.44: Coherency of measured acceleration for all simulations.

Next, following the recommendations of the previous liquefaction vulnerability analysis, the PGA and settlements are calculated as representative parameters for liquefaction analysis. In the simulation of increased and constant permeability the values of PGA coincide with those of constant permeability in Figure 3.45a. In case of variable permeability and input ground motions lower than 0.2-0.3g (where $r_u < 0.1$ and the permeability does not change or changes slightly) the response is almost identical, as expected. On the contrary, for the stronger ones, as the function of variable permeability controls the pore water pressure generation and accelerates dissipation, it leads to a more limited in time liquefaction state. Thus, greater values of PGA appear, as liquefaction lasts less and soil densification occurs. Moreover, in Figure 3.45b, in case of constant or constant increased permeability, stronger soil nonlinearity is observed, as indicated by the relation between PGA-PGV, due to liquefaction state duration.

Concerning the ground settlement at the end of each ground motion, slighter differences appear among the three simulations. More precisely, in Figures 3.46a, 3.46b all points are around the 1:1 line, i.e. the values of settlement almost coincide for all approaches. The three points in Figure 3.46b are chosen to observe the mechanical behavior of soil at the middle of the liquefied layer. The first point that provided identical settlements (yellow point), is always contractant and the responses coincide in both simulations according to Figure 3.47a. While both other points provided greater settlements in case of variable permeability and their response is completely different. The one closer to the line 1:1 (green point) is always contractant (Figure 3.47b), but in case of variable permeability

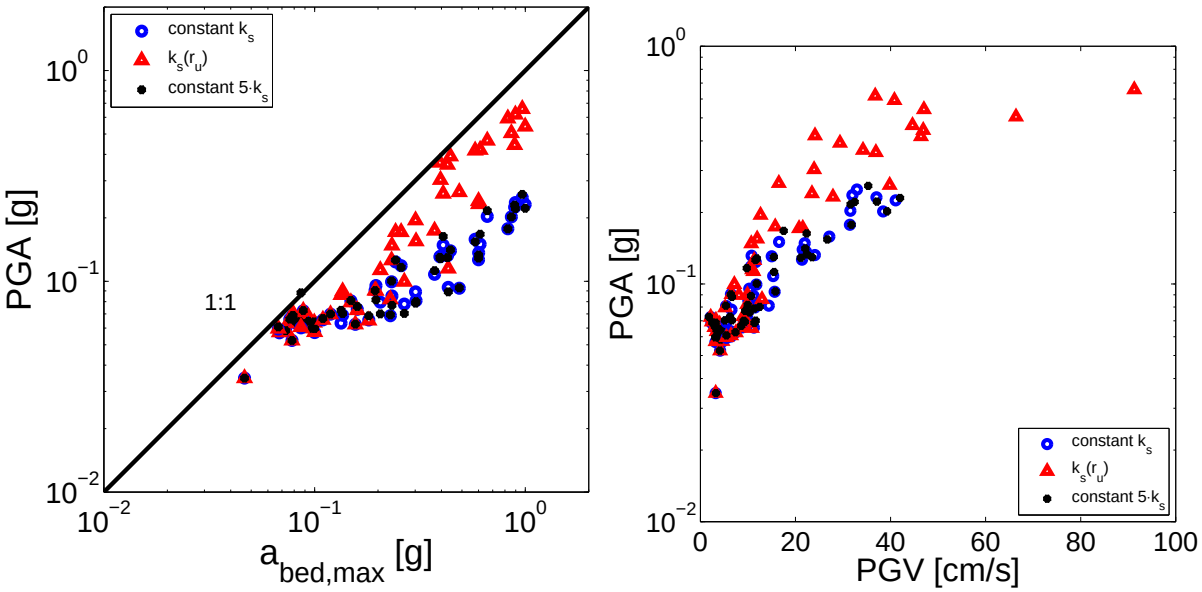

(a) All simulations. (b) All simulations.

Figure 3.45: Comparison of PGA at FF for all simulations as function of: a) $a_{bed,max}$, b) PGV at FF.

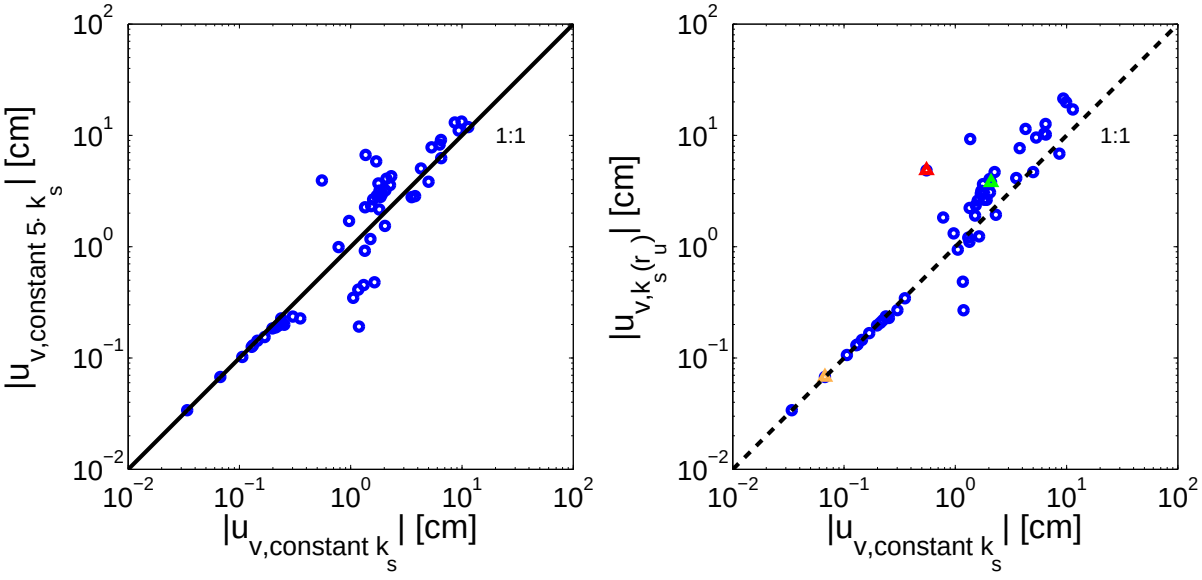

(a) Simulations 1-2. (b) Simulations 1-3.

Figure 3.46: Comparison of settlement at the end of the ground motion.

it tends to stabilize and then it contracts further. Contrary the more distant one (red point), in case of variable permeability, it contracts initially and then it dilates, probably due to the densification of soil during dissipation (Figure 3.47c). Consequently, it can be concluded that a variable permeability does not affect noticeably liquefaction-induced settlements, but changes the material behavior. The changes observed do not follow a

unique tendency and one single conclusion cannot be drawn.

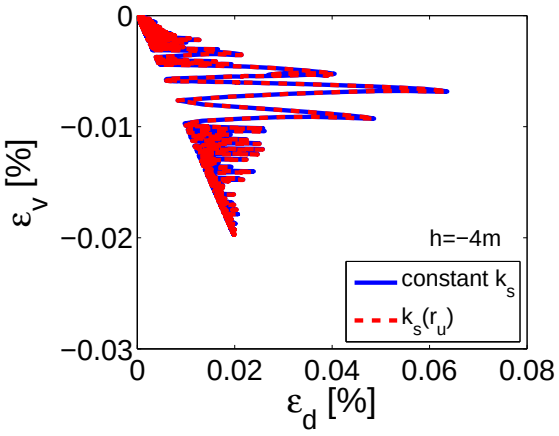

(a) Yellow point

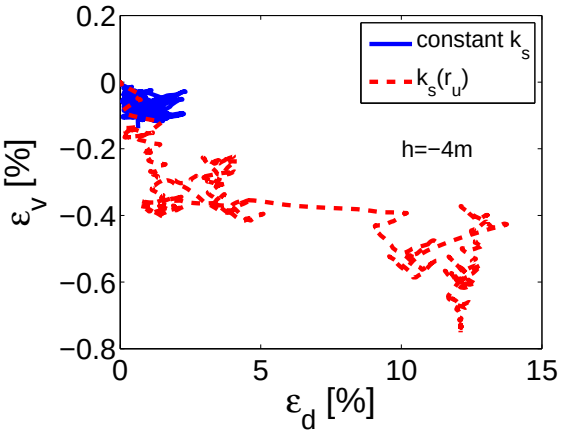

(b) Green point

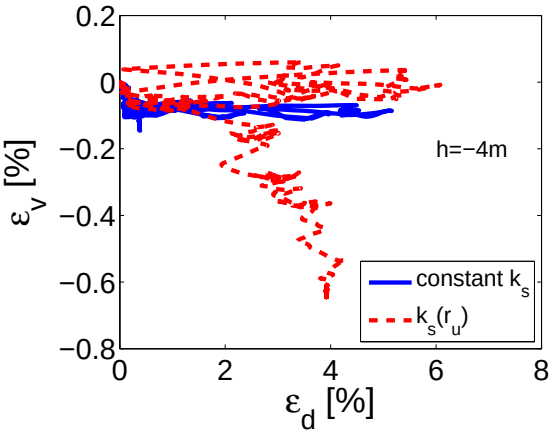

(c) Red point

Figure 3.47: Comparison of volumetric - deviatoric deformations at h=-4m from surface.

Synopsis

The latter observations conclude to the fact that soil liquefaction is a complex phenomenon, where numerous parameters interfere. Liquefaction problematic should be treated in a global scale and the entire dynamic response of soil must be considered so as to provide robust conclusions. However, it can be concluded that the second simulation with increased constant permeability is not very reliable. It provides an abrupt and very quick decrease of pore water pressure, although it gives almost the same response in terms of acceleration and settlement. This statement is in agreement with the conclusions presented by Shahir et al. (2012), as it underlines that this simulation cannot capture all features of the soil response in liquefaction modeling and may erroneously predict no liquefaction. In Appendix E the same parametric study is performed for the silty sand and only the results of the first and third simulation are discussed.

3.6 Partial Conclusions

The first part of this chapter is dedicated to the State-of-the-art of Code_Aster in case of SH wave propagation in coupled HM nonlinear media. The results of the dynamic analyses are compared to those obtained by GEFDyn , which is considered as reference software and a good agreement between the software programs is found. The following conclusions are stated:

- Both FE codes generate pore water pressure simultaneously with the main shock and they dissipate progressively during the coda phase of the signal.
- The profiles of effective stresses obtained are very close for both softwares. In some cases, the curves slightly diverge, which can be attributed to the different integration scheme of ECP elastoplastic model for each software.
- The most important difference is observed in the layer of dense sand. In Code_Aster the excess pore water pressure generated in the liquefiable layer dissipates initially towards the bottom very slowly as the dense sand is less permeable.
- A significant gap is noticed in the values of settlement for the two models, which can be explained due to differences in the generation of volumetric deformations when using the ECP elastoplastic model in each software, as well as, differences in the way that soil liquefaction is treated.
- In terms of measured acceleration at FF, the results are almost identical.
- Concerning the dynamic analysis using Code_Aster, it is deduced that the dissipation is completed some seconds after the end of the motion and no post-liquefaction settlement is detected.
- Moreover, it is pointed out that a shear band appears in the liquefiable layer which is not mesh dependent. No mesh sensitivity is remarked in the evolution of settlements and pore water pressure, as well.

Next, the effect of earthquake's characteristics on the dynamic response of the soil column was assessed. The important IMs are a combination of the equivalent predominant frequency, the maximum acceleration and velocity of the input ground motion, which characterize the intensity of the motion. Near-fault motions are classified as the most severe, as they lead to significant accelerations and velocities. Furthermore, the response of the column is strongly related to the origin of the input ground motion. Earthquakes recorded on soil site lead very quickly to important nonlinearity and extended soil liquefaction, due to long duration of mainshock (t_{595}). Consequently, t_{595} is also considered an important IM, while PGA and liquefaction-induced settlements are identified as representative EDP, in the context of liquefaction analysis. This study consists a reference earthquake database for all dynamic simulations in the current PhD work.

Finally, a parametric study of variable permeability during dynamic analysis was performed for three simulations: constant permeability equal to the initial value, increased

and constant permeability and variable permeability as function of r_u. The most significant differences appear in the dissipation phase of pore water pressure. When a variation of permeability is taken into account and as its value increases during liquefaction, the dissipation is always faster and starts earlier. Nevertheless, negligible gaps are obtained in terms of settlements, although the change in material behavior is significant. It is noticed that the simulation of increased and constant permeability is not very reliable, as it provides an abrupt and very quick decrease of pore water pressure, although it gives almost the same response in terms of acceleration and settlement. This statement is in agreement with the conclusions presented by Shahir et al. (2012) for the simulation of constant increased permeability, as it underlines that this simulation cannot capture all features of the soil response in liquefaction modeling and may erroneously predict no liquefaction. To sum up, it is concluded that soil liquefaction is a complex phenomenon, where numerous parameters interfere and a unique conclusion cannot be drawn, as also remarked by Feia et al. (2016). The response of soils in case of liquefaction should be treated in a global scale so as to provide robust conclusions. Series of laboratory tests should be performed in order to observe the evolution of permeability during shaking, define the soil parameters that interact and propose an evolution law for soil's permeability, as also discussed by Haigh et al. (2012).

The liquefaction analysis of this chapter is considered as a first step for the simulation of larger scale models in the following chapters (Chapters 5, 6). In the next chapter a regularization method will be applied to the nonlinear soil column in dry conditions, so as to assess the response of regularized media in case of SH wave propagation.

Chapter 4

Regularization method in dynamic conditions

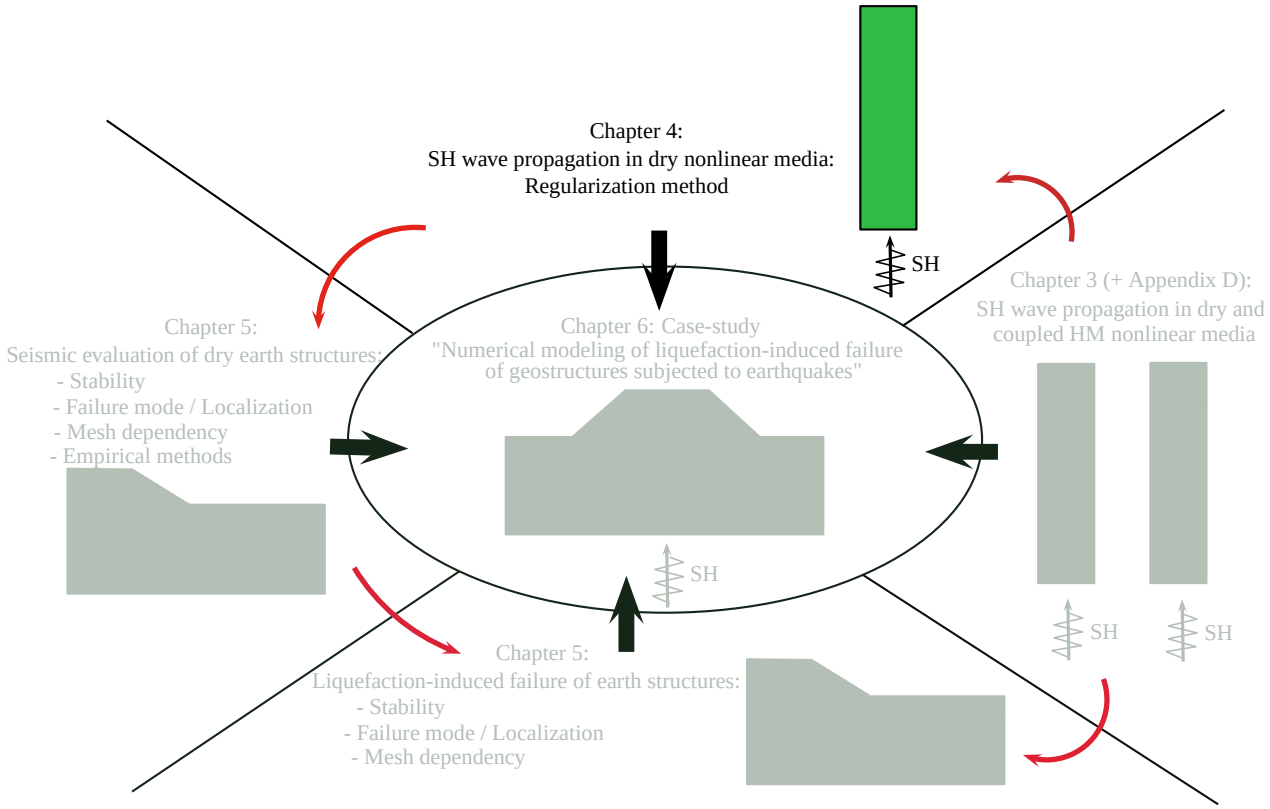

4.1 Introduction

Seismic wave propagation influences soil behavior, most notably the evolution of pore pressure in sands and shear strength in clays. These phenomena can lead to strain localization and consequently cause instability before ultimate failure, as developed in Section 2.4. Experimental studies have shown that for static monotonic loading, a shear band mechanism takes place suddenly before the peak of the load-displacement curve (Desrues and Chambon, 2002). Previous studies have focused mainly on mesh dependency problems of shear localization zones under monotonic loading, as well as on the capacity of regularization methods, such as the first gradient of dilation model, to mitigate mesh sensitivity (Fernandes et al., 2008; Foucault et al., 2011; Plassart et al., 2013). This particular method enhances the kinematics of the medium and expands the effects of microstructure to macro scale.

Consequent to the verification study of the previous chapter in case of SH wave propagation, the current chapter investigates the applicability of this regularization method in cases of dynamic loading. Initially, the mesh dependency problem and the theory of first gradient of dilation model are described. Next, an analytical solution for shear wave propagation in nonlinear classical and regularized media is developed, to evaluate the effect of regularization on wave propagation. Through a numerical simulation of a simplified model under dynamic loading, i.e. the dry nonlinear soil column used for the verification procedure of Appendix D.1, deficiencies of the regularization method in case of dynamic loading are observed and discussed. Code_Aster (version 11.7) is used for all numerical simulations and the ECP constitutive model for soil's behavior representation. This chapter contains material presented and published in the proceedings of the conference on Computer Methods and Recent Advances in Geomechanics (IACMAG 2014) (Rapti et al., 2014b) and accepted with corrections in the journal "Computers and Geotechnics".

4.2 Mesh dependency: Overview

In classical continuum theory, a strain-softening region of finite width cannot be obtained and the occurence of strain-softening leads immediately to localization of strain into a single finite element (Bazant et al., 1985). As the element size is reduced, the width of the strain-localization region and the energy consumed by strain-softening failure converge to zero and the response exhibits extreme noise due to instability (Bazant et al., 1985).

Classical theories of soil plasticity are not equipped with an internal length. Therefore they are not suited for addressing problems of strain localization. In particular, they break down in the post-bifurcation regime where ellipticity is lost and a critical dependence of the solution on the mesh size appears, accompanied by instability and convergence problems (Aifantis, 1984). The inclusion of strain gradients into the strain energy function of solids prevents loss of ellipticity in the governing equilibrium equations and allows for the description of localized deformations beyond the bifurcation point when the material is in the softening regime (Aifantis, 1984). The resulting governing equations are singular perturbations of the original ones with the internal length playing the role of the perturbation parameter (Vardoulakis and Aifantis, 1991).

Starting from the micromorphic medium approach (Germain, 1973) and combined with a gradient model (Mindlin, 1964, 1965), a regularization method, called first gradient of dilation model, is proposed by Fernandes et al. (2008), following the work of Chambon et al. (2001) and Matsushima et al. (2002). The micromorphic approach introduces an internal length by taking into account the micro-deformation gradient. Though, the simplified method of first gradient of dilation takes into account only the volumetric part of the micro-deformation gradient, which governs the mesh dependency of shear bands, for coupled volumetric-deviatoric constitutive models.

The theoretical background of this regularization method will be presented in detail and an analytical solution is proposed for micromorphic media under shear dynamic loading in the following sections.

4.3 Theory of regularization method

4.3.1 Classical media: The principle of virtual work

The spatial version of the principle of virtual work in the case of dynamic loading, states that the body B, which occupies an open region Ω with a regular boundary $\partial\Omega$ in each reference configuration, is in equilibrium if, and only if, its Cauchy stress field σ_{ij}, satisfies Equation 4.1. Note that body forces are neglected as it is assumed that the initial stresses calculated are in equilibrium with the body forces.

$$\int_{\Omega}[\sigma_{ij} : \nabla u_i^* + \rho\ddot{u}_i \cdot u_i^*]\,\mathrm{d}v - \int_{\partial\Omega} t_i \cdot u_i^*\,\mathrm{d}s = 0 \quad , \forall\ \mathrm{u}_i^*\ \epsilon\ \mathrm{V}^* \tag{4.1}$$

where t_i is the boundary traction per unit area and V^* is the space of admissible displacements of B.

By assuming that the field σ_{ij} is sufficiently regular and symmetric, the following identity is obtained:

$$\sigma_{ij} : \nabla u_i^* = \mathrm{div}(\sigma_{ij} \cdot u_i^*) - \mathrm{div}(\sigma_{ij}) \cdot u_i^* \tag{4.2}$$

Next, by substituting the above expression into Equation 4.1, it follows that:

$$\int_{\Omega}[\mathrm{div}(\sigma_{ij} \cdot u_i^*) + (\mathrm{div}(\sigma_{ij}) - \rho\ddot{u}_i) \cdot u_i^*]\,\mathrm{d}v - \int_{\partial\Omega} t_i \cdot u_i^*\,\mathrm{d}s = 0 \quad , \forall\ \mathrm{u}_i^*\ \epsilon\ \mathrm{V}^* \tag{4.3}$$

By applying the divergence theorem for a tensor-valued field for the first term of the above equation, the following identity is obtained:

$$\int_{\Omega} \mathrm{div}(\sigma_{ij} \cdot u_i^*)\,\mathrm{d}v = \int_{\partial\Omega} \sigma_{ij} \cdot u_i^* \cdot n_j\,\mathrm{d}s \tag{4.4}$$

Taking into account the symmetry of σ_{ij}, which implies $\sigma_{ij}u_i^* \cdot n_j = \sigma_{ij}n_j \cdot u_i^*$, together with the identity of equation 4.4, the weak form of equilibrium (Equation 4.3) can be rewritten in the equivalent form:

$$\int_{\Omega}[\mathrm{div}(\sigma_{ij}) - \rho\ddot{u}_i] \cdot u_i^*\,\mathrm{d}v + \int_{\partial\Omega}(t_i - \sigma_{ij} \cdot n_j) \cdot u_i^*\,\mathrm{d}s = 0 \quad , \forall\ \mathrm{u}_i^*\ \epsilon\ \mathrm{V}^* \tag{4.5}$$

The strong form of equilibrium in the volume Ω is obtained by considering $u_i^* = 0$ in the surface in Equation 4.5:

$$div(\sigma_{ij}) = \rho \cdot \ddot{u}_i \quad , \text{in } \Omega \tag{4.6}$$

$$t_i = \sigma_{ij} \cdot n_j \quad , \text{in } \partial\Omega \tag{4.7}$$

where n_j is the outward unit vector normal to the boundary $\partial\Omega$ of B and t_i is the applied boundary traction vector field on $\partial\Omega$.

4.3.2 Micromorphic model

According to the theory of media with microstructure, in addition to the classical displacement field u_i, a field of second order tensor which models the strains and the rotation of the grains themselves is considered. It is denoted f_{ij} and called micro deformation gradient (Mindlin, 1964; Chambon et al., 2001; Fernandes et al., 2008). Note that no micro-inertial terms are considered. The equilibrium equation for micromorphic media can be written as follows, for any kinematically admissible fields $(u_i^*,\ f_{ij}^*)$:

$$\int_\Omega \left(\sigma_{ij} \cdot \frac{\partial u_i^*}{\partial x_j} + \tau_{ij} \cdot \left(f_{ij}^* - \frac{\partial u_i^*}{\partial x_j} \right) + \Sigma_{ijk} \cdot \frac{\partial f_{ij}^*}{\partial x_k} + \rho \cdot \ddot{u}_i \cdot u_i^* \right) \mathrm{d}v = \int_{\partial\Omega} (t_i \cdot u_i^* + T_{ij} \cdot f_{ij}^*)\, \mathrm{d}s \tag{4.8}$$

where σ_{ij} is the macro stress, τ_{ij} is the relative additional stress associated to the microstructure, Σ_{ijk} is the double stress, and t_i and T_{ij} are the traction forces and double surface tractions acting on the boundary, respectively.

As shown before, by applying the divergence theorem to the weak equilibrium equation, the strong form of equilibrium (Equations 4.9, 4.10) and boundary conditions (Equations 4.11, 4.16) can also be obtained.

$$\frac{\partial(\sigma_{ij} - \tau_{ij})}{\partial x_j} = \rho \cdot \ddot{u}_i \quad , \text{in } \Omega \tag{4.9}$$

$$\frac{\partial \Sigma_{ijk}}{\partial x_k} - \tau_{ij} = 0 \quad , \text{in } \Omega \tag{4.10}$$

$$(\sigma_{ij} - \tau_{ij}) \cdot n_j = t_i \quad , \text{in } \partial\Omega \tag{4.11}$$

$$\Sigma_{ijk} \cdot n_k = T_{ij} \quad , \text{in } \partial\Omega \tag{4.12}$$

A second gradient of displacement model is a model where the microstrain is assumed to be equal to the macrostrain i.e. $f_{ij} = \partial u_i / \partial x_j$. This assumption is very useful in the framework of FE simulations, as it decreases the number of independent variable fields. The aforementioned kinematic condition is similar to the incompressibility condition (Chambon et al., 2001). Therefore, the principle of virtual work of Equation 4.8 for any kinematically admissible fields u_i^* can be rewritten as:

$$\int_\Omega \left(\sigma_{ij} \frac{\partial u_i^*}{\partial x_j} + \Sigma_{ijk} \cdot \frac{\partial^2 u_i^*}{\partial x_j \partial x_k} + \rho \cdot \ddot{u}_i \cdot u_i^* \right) \mathrm{d}v = \int_{\partial\Omega} \left(p_i \cdot u_i^* + P_i \cdot \frac{\partial u_i}{\partial x_j} \cdot n_j \right) \mathrm{d}s \tag{4.13}$$

where p_i and P_i are the external and double external forces per unit area.

As before, after applying the divergence theorem, the strong form of equilibrium reads:

$$\frac{\partial \sigma_{ij}}{\partial x_j} - \frac{\partial^2 \Sigma_{ijk}}{\partial x_j \partial x_k} = \rho \cdot \ddot{u}_i \quad \text{, in } \Omega \tag{4.14}$$

Let us denote D the normal derivative of any quantity q, such as $Dq = (\partial q/\partial x_k)n_k$, and D_j the tangential derivatives, such as $D_j q = \partial q/\partial x_j - (\partial q/\partial x_k)n_k n_j$. The boundary conditions defining the external and double external forces per unit area are:

$$\begin{aligned} p_i &= \sigma_{ij} \cdot n_j - n_k \cdot n_j \cdot D\Sigma_{ijk} - \frac{D\Sigma_{ijk}}{Dx_k} \cdot n_j - \frac{D\Sigma_{ijk}}{Dx_j} \cdot n_k + \dots \\ \dots &+ \frac{Dn_l}{Dx_l} \cdot \Sigma_{ijk} \cdot n_j \cdot n_k - \frac{Dn_j}{Dx_k} \cdot \Sigma_{ijk} \end{aligned} \tag{4.15}$$

$$P_i = \Sigma_{ijk} \cdot n_j \cdot n_k \tag{4.16}$$

4.3.2.1 Micromorphic dilation model

The micro deformation gradient introduces an internal length. This approach results in a FE computation with many additional degrees of freedom, as studied for nonlinear geotechnical applications. On the contrary, a dilation model based only on volumetric changes uses a scalar as an additional kinematic variable instead of a complete second order tensor. This approach decreases the number of degrees of freedom of the FE model and consequently, the computational time needed for the simulation (Fernandes et al., 2008; Foucault et al., 2011).

Let u_i be the usual displacement field, ε_v and χ the macro and micro volume change, respectively. In addition to classical stresses σ_{ij}, the relative micro dilation stress κ (scalar) and the double stresses S_j (vector) are introduced. For any kinematically admissible field (u_i^*, χ^*):

$$\int_\Omega \left(\sigma_{ij} \cdot \frac{\partial u_i^*}{\partial x_j} + \kappa \cdot (\chi^* - \varepsilon_v^*) + S_j \cdot \frac{\partial \chi^*}{\partial x_j} + \rho \cdot \ddot{u}_i \cdot u_i^* \right) \mathrm{d}v = \int_{\partial\Omega} (t_i \cdot u_i^* + m \cdot \chi^*) \, \mathrm{d}s \tag{4.17}$$

where t_i are the traction forces and m is the double micro traction force, both acting on the boundary.

By applying the divergence theorem, the following equation can be obtained:

$$\begin{aligned} &- \int_\Omega \left(\frac{\partial \sigma_{ij}}{\partial x_j} + \frac{\partial \kappa}{\partial x_i} + \rho \cdot \ddot{u}_i \right) \cdot u_i^* \, \mathrm{d}v - \int_\Omega \left(\kappa + \frac{\partial S_j}{\partial x_j} \right) \cdot \chi^* \, \mathrm{d}v + \dots \\ \dots &+ \int_{\partial\Omega} ((\sigma_{ij} + \kappa \cdot \delta_{ij}) \cdot n_j \cdot u_i^* + S_j \cdot n_j \cdot \chi^*) \, \mathrm{d}s = \int_{\partial\Omega} (t_i \cdot u_i^* + m \cdot \chi^*) \, \mathrm{d}s \end{aligned} \tag{4.18}$$

The balance equation and the boundary conditions read:

$$\frac{\partial \sigma_{ij}}{\partial x_j} + \frac{\partial \kappa}{\partial x_i} = \rho \cdot \ddot{u}_i \tag{4.19}$$

$$\kappa + \frac{\partial S_j}{\partial x_j} = 0 \tag{4.20}$$

$$t_i = (\sigma_{ij} + \kappa \cdot \delta_{ij}) \cdot n_j \tag{4.21}$$

$$m = S_j \cdot n_j \tag{4.22}$$

As explained before, so as to decrease the number of independent variable fields, the macro volumetric change ε_v is enforced to be equal to the micro dilation χ (ε_v=χ). Consequently, by applying $\chi = \partial u_i/\partial x_i$ in Equation 4.18, the principle of virtual work for a first gradient of dilation model is obtained:

$$\int_\Omega \left(\sigma_{ij} \cdot \frac{\partial u_i^*}{\partial x_j} + S_j \cdot \frac{\partial^2 u_i^*}{\partial x_j \partial x_i} + \rho \cdot \ddot{u}_i \cdot u_i^* \right) \mathrm{d}v = \int_{\partial\Omega} (t_i \cdot u_i^* + m \cdot \frac{\partial u_i^*}{\partial x_i}) \, \mathrm{d}s \tag{4.23}$$

By applying the identity of Equation 4.2 and the divergence theorem of Equation 4.4 to the first term of Equation 4.23 and supposing that σ_{ij} is symmetric, it is obtained:

$$\begin{aligned} \int_\Omega \sigma_{ij} \cdot \frac{\partial u_i^*}{\partial x_j} \mathrm{d}v &= \int_\Omega \left(\frac{\partial}{\partial x_j} \cdot (\sigma_{ij} \cdot u_i^*) - \frac{\partial \sigma_{ij}}{\partial x_j} \cdot u_i^* \right) \mathrm{d}v \\ &= \int_\Omega - \frac{\partial \sigma_{ij}}{\partial x_j} \cdot u_i^* \, \mathrm{d}v + \int_{\partial\Omega} \sigma_{ij} \cdot n_j \cdot u_i^* \, \mathrm{d}s \end{aligned} \tag{4.24}$$

Next, by applying the same identities two times (Equation 4.2 and Equation 4.4) to the second term of Equation 4.23, it is obtained:

$$\begin{aligned} \int_\Omega S_j \cdot \frac{\partial^2 u_i^*}{\partial x_j \partial x_i} \mathrm{d}v &= \int_\Omega \left(\frac{\partial}{\partial x_j} \left(S_j \cdot \frac{\partial u_i^*}{\partial x_i} \right) - \frac{\partial u_i^*}{\partial x_i} \cdot \frac{\partial S_j}{\partial x_j} \right) \mathrm{d}v \\ &= - \int_\Omega \left(\frac{\partial u_i^*}{\partial x_i} \cdot \frac{\partial S_j}{\partial x_j} \right) \mathrm{d}v + \int_{\partial\Omega} S_j \cdot n_j \cdot \frac{\partial u_i^*}{\partial x_i} \mathrm{d}s \\ &= - \int_\Omega \left(\frac{\partial}{\partial x_i} \left(\frac{\partial S_j}{\partial x_j} \cdot u_i^* \right) - \frac{\partial^2 S_j}{\partial x_i \partial x_j} \cdot u_i^* \right) \mathrm{d}v + \int_{\partial\Omega} S_j \cdot n_j \cdot \frac{\partial u_i^*}{\partial x_i} \mathrm{d}s \\ &= \int_\Omega \frac{\partial^2 S_j}{\partial x_i \partial x_j} \cdot u_i^* \, \mathrm{d}v + \int_{\partial\Omega} \left(- \frac{\partial S_j}{\partial x_j} \cdot n_i \cdot u_i^* + S_j \cdot n_j \cdot \frac{\partial u_i^*}{\partial x_i} \right) \mathrm{d}s \end{aligned} \tag{4.25}$$

Now if we remplace Equations 4.24 and 4.25 into Equation 4.23 the final equation of the principle of virtual power for the first gradient of dilation model is obtained:

$$\begin{aligned} &\int_\Omega \left(- \frac{\partial \sigma_{ij}}{\partial x_j} + \frac{\partial^2 S_j}{\partial x_i \partial x_j} + \rho \cdot \ddot{u}_i \right) \cdot u_i^* \, \mathrm{d}v + \\ &\int_{\partial\Omega} \left(\sigma_{ij} \cdot n_j \cdot u_i^* - \frac{\partial S_j}{\partial x_j} \cdot n_i \cdot u_i^* + S_j \cdot n_j \cdot \frac{\partial u_i^*}{\partial x_i} \right) \mathrm{d}s = \\ &\int_{\partial\Omega} \left(t_i \cdot u_i^* + m \cdot \frac{\partial u_i^*}{\partial x_j} \right) \mathrm{d}s \end{aligned} \tag{4.26}$$

The strong form of equilibrium in the volume Ω is obtained from Equation 4.26 by considering u_i^* =0 on the surface:

$$\frac{\partial \sigma_{ij}}{\partial x_j} - \frac{\partial^2 S_j}{\partial x_i \partial x_j} = \rho \cdot \ddot{u}_i \tag{4.27}$$

As u_i^* and ε_v^* are not independent, we have to rearrange the terms related to the boundaries, so finally the boundary conditions read:

$$p_i = \sigma_{ij} \cdot n_j - n_i \cdot n_j \cdot D\Sigma_j - \frac{D\Sigma_j}{Dx_j} \cdot n_i - \frac{D\Sigma_j}{Dx_i} \cdot n_j + \frac{Dn_p}{Dx_p} \cdot \Sigma_j \cdot n_j \cdot n_i \tag{4.28}$$

$$P_i = \Sigma_j \cdot n_j \cdot n_i \tag{4.29}$$

The classical and the second part of the constitutive equations are decoupled and the double stresses depend on the second derivatives of displacement in an isotropic linear elastic manner (Mindlin, 1965; Fernandes et al., 2008). The corresponding constitutive equation for the first gradient of dilation model can be defined using a new parameter a_1, which stands for the elastic rigidity modulus of the first gradient model as follows in the cartesian coordinate frame (Fernandes et al., 2008; Foucault et al., 2011; Raude et al., 2015):

$$[S_j] \quad = \quad (N+1) \cdot a_1 \cdot \delta_j^i \cdot [\frac{\partial \varepsilon_v}{\partial x_i}] \tag{4.30}$$

where N stands for the dimensions of the problem (N=2 for 2D simulation). This formulation is valid for FE simulations in Code_Aster .

4.4 Coupled S-P wave propagation in nonlinear media

Previous studies propose analytical solutions of wave propagation and dispersion in elastic and nonlinear microstructured media (Papargyri-Beskou et al., 2009; Dingreville et al., 2014; Madeo et al., 2015; Misra and Poorsolhjouy, 2016) and underline the fact that wave propagation is affected when micro-elastic terms are taken into account in material's behavior. In this section, an analytical solution of coupled S-P wave propagation in nonlinear micromorphic media is developed, in case of applying the regularization method of first gradient of dilation model. For simplicity reasons, let us consider 1D S wave propagation in a plane strain model of a nonlinear soil column, as presented in Figure 4.1. Periodicity condition is applied on the lateral boundaries, i.e. all nodes of a horizontal section have the same displacement. The seismic signal is imposed at the base and no radiation is possible.

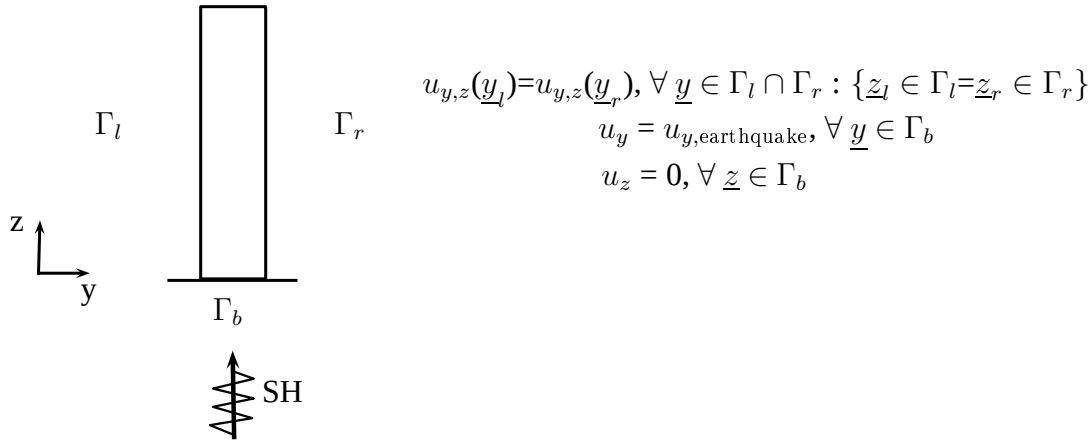

Figure 4.1: S wave propagation in a 9m high dry nonlinear soil column.

To calculate the dynamic equilibrium of this particular model, the plane strain (i.e. $\varepsilon_{xx} = \varepsilon_{xy} = \varepsilon_{xz} = 0$) and the periodicity condition of the soil column (i.e. $\partial u_y / \partial y = 0 \Rightarrow$

$\varepsilon_{yy} = 0$) are taken into account and it is supposed that $\sigma_{yz} = \sigma_{zy}$. Consequently, admitting that $\partial/\partial t(\partial A/\partial x_i) = \partial/\partial x_i(\partial A/\partial t)$ for any general field $A(x,t)$ with continuous partial derivatives, the dynamic equilibrium in nonlinear classical media under shear loading in the y-z plane of the current configuration and with zero body forces can be written in rate form as follows (Bigoni and Petryk, 2002; Meurer et al., 2002; Andrianov et al., 2013):

$$\operatorname{div}(\dot{\sigma}_{ij}) \;=\; \rho\ddot{u}_i \Rightarrow$$

$$\begin{bmatrix} \frac{\partial \dot{\sigma}_{zz}}{\partial z} \\ \\ \frac{\partial \dot{\sigma}_{yz}}{\partial z} \end{bmatrix} = \begin{bmatrix} D_{zzzz} & D_{zzyz} \\ \\ D_{yzzz} & D_{yzyz} \end{bmatrix} \cdot \begin{bmatrix} \frac{\partial^2 \dot{u}_z}{\partial z^2} \\ \\ \frac{\partial^2 \dot{u}_y}{\partial z^2} \end{bmatrix} = \begin{bmatrix} \rho\ddot{u}_z \\ \\ \rho\ddot{u}_y \end{bmatrix} \tag{4.31}$$

where D_{zzzz}, D_{zzyz}, D_{yzzz}, D_{yzyz} are the components of the 4th order elastoplastic tangent matrix $\mathbf{D}^{ep}$ in each time step, defined by the consistency condition $\dot{f}$=0 (where f refers to the yield function of soil's constitutive model). Notice that antisymmetric elastoplastic matrix $\mathbf{D}^{ep}$ can be included in case of non-associative plasticity.

However, in case of regularized micromorphic nonlinear media, the matrix of the first gradient of dilation model is taken into account (as introduced by Dingreville et al. (2014) for one-dimensional problem) and the dynamic equilibrium in rate form reads:

$$\operatorname{div}(\dot{\sigma}_{ij}) - \frac{\partial^2 \dot{S}_j}{\partial x_i \partial x_j} \;=\; \rho\ddot{u}_i \Rightarrow$$

$$\begin{bmatrix} \frac{\partial \dot{\sigma}_{zz}}{\partial z} - \frac{\partial^2 \dot{S}_z}{\partial z^2} \\ \\ \frac{\partial \dot{\sigma}_{yz}}{\partial z} \end{bmatrix} = \begin{bmatrix} D_{zzzz} & D_{zzyz} \\ \\ D_{yzzz} & D_{yzyz} \end{bmatrix} \cdot \begin{bmatrix} \frac{\partial^2 \dot{u}_z}{\partial z^2} \\ \\ \frac{\partial^2 \dot{u}_y}{\partial z^2} \end{bmatrix} - \begin{bmatrix} 3a_1 \cdot \frac{\partial^4 \dot{u}_z}{\partial z^4} \\ \\ 0 \end{bmatrix} = \begin{bmatrix} \rho\ddot{u}_z \\ \\ \rho\ddot{u}_y \end{bmatrix} \tag{4.32}$$

where $S_z = 3a_1 \cdot \frac{\partial^2 u_z}{\partial z^2}$ is the rigidity term of the micromorphic model.

The possible solutions of the differential Equations 4.31, 4.32 are a sum of two waves travelling in opposite directions, according to the standard form of a harmonic wave (Kramer, 1996):

$$\begin{aligned} \dot{u}_z(z,t) &= \dot{u}^+_{z,0} \cdot \exp[i(\omega t - k_P z)] + \dot{u}^-_{z,0} \cdot \exp[i(\omega t + k_P z)] \\ \dot{u}_y(z,t) &= \dot{u}^+_{y,0} \cdot \exp[i(\omega t - k_S z)] + \dot{u}^-_{y,0} \cdot \exp[i(\omega t + k_S z)] \end{aligned} \tag{4.33}$$

where ω = circular frequency of applied load, k_P = P wavenumber and k_S = S wavenumber.

Applying Equation 4.33 in Equations 4.31, 4.32 the following systems are obtained for classical and regularized media, respectively:

$$\mathbf{D}'_{NR} \cdot \dot{u}_i = \begin{bmatrix} D_{zzzz} \cdot k_P^2 - \rho\omega^2 & D_{zzyz} \cdot k_S^2 \\ D_{yzzz} \cdot k_P^2 & D_{yzyz} \cdot k_S^2 - \rho\omega^2 \end{bmatrix} \cdot \begin{bmatrix} \dot{u}_z \\ \dot{u}_y \end{bmatrix} = \begin{bmatrix} 0 \\ 0 \end{bmatrix} \tag{4.34}$$

$$\mathbf{D}'_{R} \cdot \dot{u}_i = \begin{bmatrix} D_{zzzz} \cdot k_P^2 + 3a_1 \cdot k_P^4 - \rho\omega^2 & D_{zzyz} \cdot k_S^2 \\ D_{yzzz} \cdot k_P^2 & D_{yzyz} \cdot k_S^2 - \rho\omega^2 \end{bmatrix} \cdot \begin{bmatrix} \dot{u}_z \\ \dot{u}_y \end{bmatrix} = \begin{bmatrix} 0 \\ 0 \end{bmatrix} \tag{4.35}$$

where "NR" stands for classical media ("No Regularization") and "R" for regularized ("Regularization").

The systems of Equations 4.34, 4.35 have non trivial solution, if and only if, the determinant of $\mathbf{D}'$ is zero i.e. $\det(\mathbf{D}'_{NR})=\det(\mathbf{D}'_{R})=0$, by providing the Equations 4.36 and 4.37 for the wavenumbers.

$$k_{S,NR} = \sqrt{\frac{D_{zzzz} \cdot k_P^2 \cdot \rho\omega^2 - \rho^2\omega^4}{D_{zzzz} \cdot D_{yzyz} \cdot k_P^2 - D_{yzyz} \cdot \rho\omega^2 - D_{yzzz} \cdot D_{zzyz} \cdot k_P^2}} \tag{4.36}$$

$$k_{S,R} = \sqrt{\frac{D_{zzzz} \cdot \rho\omega^2 \cdot k_P^2 - \rho^2\omega^4 + 3a_1 \cdot \rho\omega^2 \cdot k_P^4}{D_{zzzz} \cdot D_{yzyz} \cdot k_P^2 - D_{yzyz} \cdot \rho\omega^2 - D_{yzzz} \cdot D_{zzyz} \cdot k_P^2 + 3a_1 \cdot D_{yzyz} \cdot k_P^4}} \tag{4.37}$$

It is noticed that Equation 4.37 provides a different relation between $k_{S,R}$ and $k_{P,R}$ in regularized media, as two additional terms linked to the rigidity of the first gradient of dilation model appear in the solution of S-wavenumber. Although a regularization method should not affect the dynamic response of a medium, it is pointed out that wave propagation changes due to the gradient model used. Note that if there was no coupling between S and P wave propagation, in the case of S-wave propagation the P wavenumber is zero, so Equation 4.37 would be identical to the solution of classical media (Equation 4.36) and the gradient model would not affect S-wave propagation.

4.5 Numerical example

According to the analytical solution of Section 4.4, differences appear in the wave propagation in classical and regularized media. The applicability of the aforementioned regularization method is investigated through a numerical simulation of the 9m high nonlinear dry soil column of Figure 4.1 subjected to earthquake loading. For comparison reasons, two simulations are performed for the same model, one without regularization ("NR") and one with regularization ("R").

4.5.1 Soil constitutive model

The ECP elastoplastic multi-mechanism model (Hujeux, 1985) accounts for soil behavior representation under cyclic loading and is described for this particular case of S wave propagation in the soil column. More details about the model can be found in Appendix B.

Adopting the soil mechanics sign convention (compression positive), the deviatoric primary yield surface of the $y-z$ plane in this particular isotropic stress state case (K_0=1, i.e. $\sigma_{zz}=\sigma_{yy}$) of shear wave propagation is given by:

$$f_{yz}(\sigma_{yz}, \sigma_{zz}, \varepsilon^p_{zz}, r_{yz}) \quad = \quad |\sigma_{yz}| - \sin\phi \cdot \sigma_{zz} \cdot F_{yz}(\sigma_{zz}, \varepsilon^p_{zz}) \cdot r_{yz} \tag{4.38}$$

where σ_{zz} and σ_{yz} are the effective values of stress tensors, ϕ is the friction angle, whereas the internal variable r_{yz} accounts for the isotropic hardening generated by plastic shearing.

It represents progressive friction mobilization in the soil and their product reaches unity at perfect plasticity mode. The function F_{yz} introduces volumetric hardening or softening, through the plastic volumetric strain ε^p_{zz}:

$$F_{yz}(\sigma_{zz}, \varepsilon^p_{zz}) = 1 - b \cdot \ln \frac{\sigma_{zz}}{\sigma_c(\varepsilon^p_{zz})} \tag{4.39}$$

$$\sigma_c(\varepsilon^p_{zz}) = \sigma_{c0} \cdot \exp(-\beta \cdot \varepsilon^p_{zz}) \tag{4.40}$$

where the parameter b controls the form of the yield surface in the $y-z$ plane and varies from 0 (Coulomb type) to 1 (Cam-Clay one), σ_{c0} is the critical mean effective stress corresponding to the initial state, β is the plastic compressibility modulus.

The hardening evolution rule $\dot{r}_{yz}$ accounts for the degree of friction mobilization of the deviatoric mechanism $y-z$:

$$\dot{r}_{yz} = \dot{\lambda}^p \cdot \frac{(1 - r_{yz})^2}{a(r_{yz})} \tag{4.41}$$

where the function $a(r_{yz})$ controls the hardening evolution and $\dot{\lambda}^p$ is the plastic multiplier.

The evolution of plastic deviatoric strains follow an associated flow rule:

$$\dot{\varepsilon}^p_{yz} = \dot{\lambda}^p \cdot \frac{\sigma_{yz}}{|\sigma_{yz}|} \tag{4.42}$$

while the evolution of plastic volumetric strains is controlled by a Roscoe-type dilatancy flow rule (Schofield and Wroth, 1698):

$$\dot{\varepsilon}^p_{zz} = \dot{\lambda}^p \cdot \alpha_\psi \cdot \alpha(r_{yz}) \cdot \left(\sin\psi - \frac{\sigma_{yz}}{\sigma_{zz}} \right) \tag{4.43}$$

where ψ is the characteristic angle and α_ψ is a constant parameter. The parameter $\alpha(r_{yz})$ allows that for drained conditions, there is no volume variations until a certain level of shearing is achieved. The dilatancy flow rule provides a coupling between deviatoric and volumetric plastic strains. Consequently, even if in this particular case only S wave propagation is considered, P-induced waves would be generated through this coupling.

From the consistency condition $\dot{f}_{yz}$=0 (Equation 4.44), the components of the elasto-plastic tangent matrix $\mathbf{D}^{ep}$ of the ECP elastoplastic model are calculated.

$$\frac{\partial f_{yz}}{\partial \sigma_{yz}} \cdot \dot{\sigma}_{yz} + \frac{\partial f_{yz}}{\partial \sigma_{zz}} \cdot \dot{\sigma}_{zz} + \frac{\partial f_{yz}}{\partial \varepsilon^p_{zz}} \cdot \dot{\varepsilon}^p_{zz} + \frac{\partial f_{yz}}{\partial r_{yz}} \cdot \dot{r}_{yz} = 0 \tag{4.44}$$

where:

$$\frac{\partial f_{yz}}{\partial \sigma_{yz}} = \frac{\sigma_{yz}}{|\sigma_{yz}|} \tag{4.45}$$

$$\frac{\partial f_{yz}}{\partial \sigma_{zz}} = -\sin\phi + b \cdot r_{yz} \cdot \sin\phi \cdot \left(1 + \ln\frac{\sigma_{zz}}{\sigma_c}\right) \tag{4.46}$$

$$\frac{\partial f_{yz}}{\partial \varepsilon^p_{zz}} = \sigma_{zz} \cdot \sin\phi \cdot b \cdot \beta \cdot r_{yz} \tag{4.47}$$

$$\frac{\partial f_{yz}}{\partial r_{yz}} = -\sigma_{zz} \cdot \sin\phi \cdot \left(1 - \ln\frac{\sigma_{zz}}{\sigma_c}\right) \tag{4.48}$$

$$\dot{\sigma}_{yz} = 2 \cdot G \cdot (\dot{\varepsilon}_{yz} - \dot{\varepsilon}^p_{yz}) = 2 \cdot G \cdot \left(\dot{\varepsilon}_{yz} - \dot{\lambda}^p \cdot \frac{\sigma_{yz}}{|\sigma_{yz}|}\right) \tag{4.49}$$

$$\dot{\sigma}_{zz} = B \cdot (\dot{\varepsilon}_{zz} - \dot{\varepsilon}^p_{zz}) = B \cdot \left(\dot{\varepsilon}_{zz} - \dot{\lambda}^p \cdot \alpha_\psi \cdot \alpha(r_{yz}) \cdot \left(\sin\psi - \frac{\sigma_{yz}}{\sigma_{zz}}\right)\right) \tag{4.50}$$

where G and B stand for the shear and bulk moduli, respectively. By replacing Equations 4.45-4.50 in the consistency Equation 4.44, the plastic multiplier is obtained:

$$\dot{\lambda}^p = \frac{2 \cdot G \cdot \frac{\sigma_{yz}}{|\sigma_{yz}|} \cdot \dot{\varepsilon}_{yz} + \left(-\sin\phi + b \cdot r_{yz} \cdot \sin\phi \cdot \left(1 + \ln\frac{\sigma_{zz}}{\sigma_c}\right)\right) \cdot B \cdot \dot{\varepsilon}_{zz}}{H} \tag{4.51}$$

where H is the hardening modulus and is defined as:

$$\begin{aligned} H &= 2 \cdot G \cdot \left(-\sin\phi + b \cdot r_{yz} \cdot \sin\phi \cdot \left(1 + \ln\frac{\sigma_{zz}}{\sigma_c}\right)\right) \cdot B \cdot \alpha_\psi \cdot \alpha(r_{yz}) \cdot \left(\sin\psi - \frac{\sigma_{yz}}{\sigma_{zz}}\right) + \dots \\ \dots &+ \sigma_{zz} \cdot \sin\phi \cdot b \cdot \beta \cdot \alpha_\psi \cdot \alpha(r_{yz}) \cdot \left(\sin\psi - \frac{\sigma_{yz}}{\sigma_{zz}}\right) + \dots \\ \dots &+ \sigma_{zz} \cdot \sin\phi \cdot \left(1 - \ln\frac{\sigma_{zz}}{\sigma_c}\right) \cdot \frac{(1 - r_{yz})^2}{a(r_{yz})} \end{aligned} \tag{4.52}$$

Consequently, from Equations 4.49,4.50 and taking into account the plastic multiplier given by Equation 4.51, the terms of the elastoplastic matrix are calculated as follows:

$$\begin{aligned} D_{zzzz} &= B \cdot \left[1 - \frac{B}{H} \cdot \alpha_\psi \cdot \alpha(r_{yz}) \cdot \left(\sin\psi - \frac{\sigma_{yz}}{\sigma_{zz}}\right) \cdot \left(-\sin\phi + b \cdot r_{yz} \cdot \sin\phi \cdot \left(1 + \ln\frac{\sigma_{zz}}{\sigma_c}\right)\right)\right] \\ D_{zzyz} &= -\frac{B}{H} \cdot 2 \cdot G \cdot \frac{\sigma_{yz}}{|\sigma_{yz}|} \cdot \alpha(r_{yz}) \cdot \left(\sin\psi - \frac{\sigma_{yz}}{\sigma_{zz}}\right) \\ D_{yzzz} &= -2 \cdot G \cdot \frac{B}{H} \cdot \frac{\sigma_{yz}}{|\sigma_{yz}|} \cdot \left(-\sin\phi + b \cdot r_{yz} \cdot \sin\phi \cdot \left(1 + \ln\frac{\sigma_{zz}}{\sigma_c}\right)\right) \\ D_{yzyz} &= 2 \cdot G \cdot \left(1 - \frac{2 \cdot G}{H}\right) \end{aligned} \tag{4.53}$$

4.5.2 Mechanical characteristics

A medium-to-dense sand (MDS) is used for the soil column, with uniform shear wave velocity (V_S=200m/s). Figure 4.2 presents soil response, after simulation of triaxial and cyclic shear drained tests of one soil element at confining pressure corresponding to the average geostatic pressure of the column, i.e. 50kPa. The curves of shear drained tests $G/G_{max} - \gamma$ and $D - \gamma$ are in good agreement with the reference curves given by Seed and Idriss (1970). For further details about material parameters refer to Table B.1 in Appendix B.6.

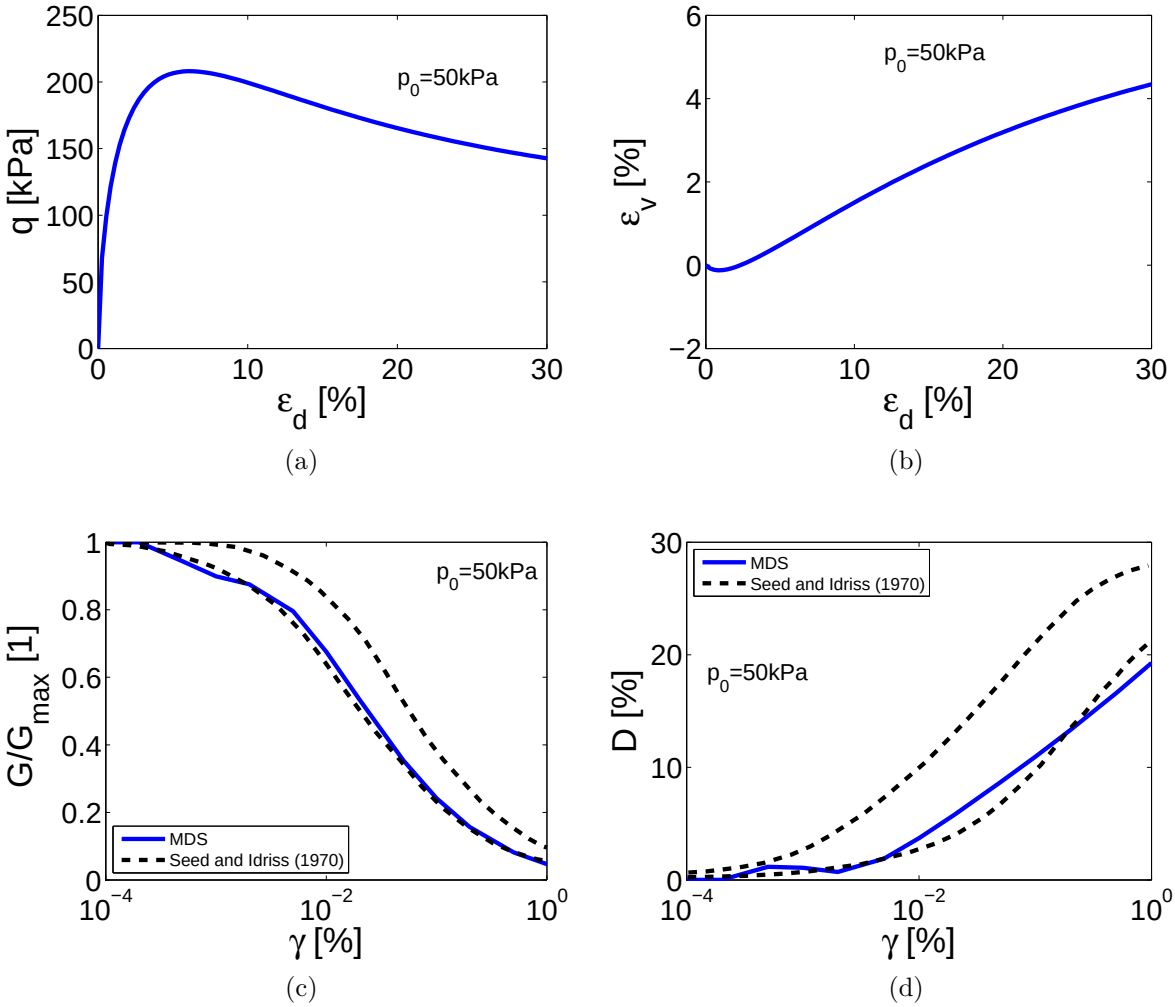

Figure 4.2: Soil response of one material point with the ECP constitutive model (p_0=50kPa, K_0=1.0): a,b) Monotonic triaxial drained test, c,d) Cyclic shear test compared to Seed and Idriss (1970) results.

4.5.3 Numerical parameters

The FE analysis is performed in two steps: a) as the model is nonlinear, a static analysis is performed in order to calculate the initial stresses, b) the seismic signal is imposed and a dynamic analysis follows. A mesh of 8-node quadrilateral elements of 0.20m length is used.

The implicit method of Newmark integration is used for the dynamic analysis with a time step equal to Δt=10^{-3}s and numerical damping equal to $\xi = 0.2\%$ is added, as explained previously in Section 3.2.4.

The low-strain frequency analysis provides a fundamental elastic period for the soil column equal to T_p=0.17s, i.e. f_p=5.8Hz (Figure 4.3a). It is obtained from the Borehole Tranfer Function from the top to base (i.e. ratio of the frequency response at column's surface over the bedrock frequency response) for a sample seismic signal at very low amplitude (10^{-6}g) to ensure elastic soil behavior.

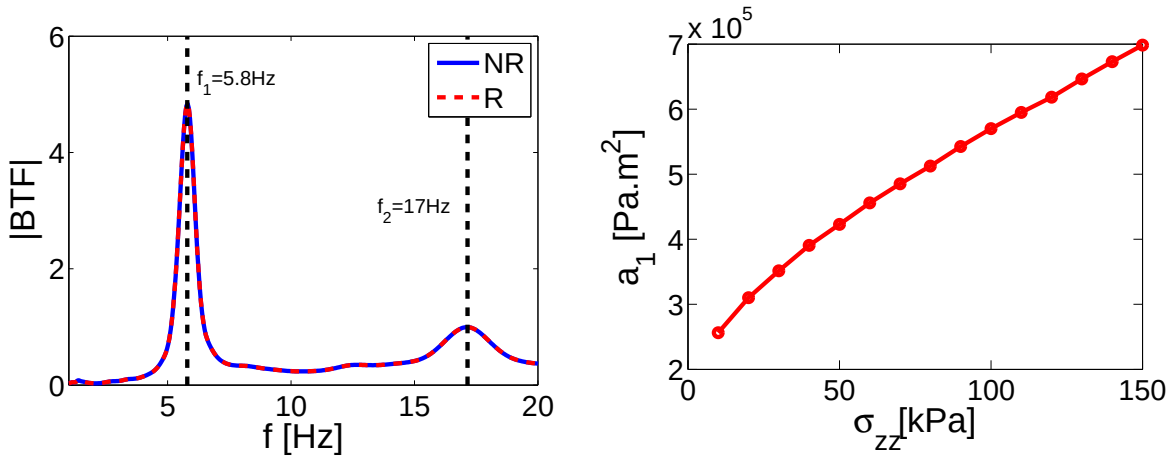

(a) (b)

Figure 4.3: a) Borehole Transfer Function of dry nolinear soil column in elasticity and b) Regularization parameter a_1 as function of σ_{zz} for ℓ_c=1m.

4.5.4 Regularization parameters

The theory of first gradient of dilation model is applied to the ECP elastoplastic model (Hujeux, 1985), as it is implemented into Code_Aster . According to analytical solution of a 1D soil element under shear loading, the characteristic length of regularization ℓ_c should be calibrated from the tangent rigidity operator $\mathbf{D}^{ep}$ (Equation 4.54) (Foucault et al. (2011), Raude et al. (2015) based on Chambon et al. (2001)). The purpose is to control the characteristic length by this partial distribution of localized bifurcation bands induced by uniqueness loss in the rate boundary value problem at the band scale.

$$\ell_c \quad = \quad F(\mathbf{D}^{ep}) \cdot \sqrt{(N+1) \cdot a_1} \tag{4.54}$$

Previous studies have shown that it is necessary to have 4-5 finite elements across the shear band to catch adequately the localised bifurcation mode (Foucault et al., 2011).

Therefore, for usual geotechnical structures, whose characteristic dimensions are about 10 or 100 m, a trade-off in terms of mesh element size has to be adopted to define a typical characteristic length of likely shear bands and it is proposed ℓ_c=1m following these suggestions. Then, the a_1 parameter is deduced by Equation 4.54. The same value of a_1 (a_1=40000$Pa \cdot m^2$) is used all along the column and is calculated as function of the mean value of σ_{zz} at the soil column (Figure 4.3b). The procedure followed to identify the regularization parameter used can be found in detail in Appendix F.

4.5.5 Input seismic motion

For the dynamic analysis of the model without and with regularization, Friuli earthquake with a scaling factor equal to 2 ($a_{bed,max}$=0.47g) is imposed as SH waves, as shown in Figure 4.4 (motion's characteristics in Appendix C.1.7). The motion's amplitude is doubled so as to accentuate its effect on the soil column. More in detail, as evoked previously, the solution of wave propagation changes when shear-induced plastic volumetric strain appear and coupling between S and P-induced waves is generated. So, in order to achieve that, a stronger motion is needed to lead to important values of deviatoric strains and generate plastic volumetric strains through the dilatancy flow rule.

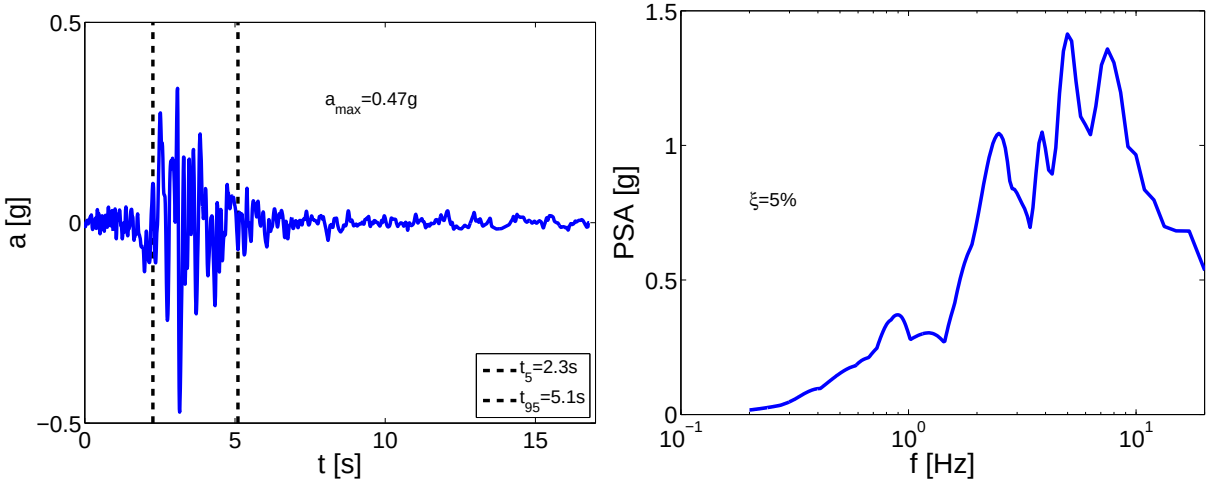

Figure 4.4: Input ground motion: a) Accelerogram, b) Response spectrum ($\xi = 5\%$).

4.5.6 Results of dynamic analysis

Recall that the main reason of using a regularization method is to mitigate mesh dependency when a shear band is detected. Consequently, if no localization phenomena appear, the response without and with regularization should be identical, while in case of localization a smoother response is expected for a regularized medium. Shear localization refers to the concentration of high values of strains in a certain region, called shear band. Thus, in order to observe such phenomena, the profile of the norm of deviatoric strain ε_d

is plotted and is used as an index of strain localization (Equation 4.55):

$$\varepsilon_d = \sqrt{\frac{2}{3}\epsilon_{ij} : \epsilon_{ij}} \tag{4.55}$$

where: $\epsilon_{ij} = \varepsilon_{ij} - \frac{1}{3}tr(\varepsilon)\delta_{ij}$.

As observed in Figure 4.5a, while no localization phenomena appear in the soil column (i.e. the response in terms of deviatoric strains follows a smooth evolution along the column), a perturbation in the response is clearly noticed when the regularization method is applied (red curve), namely oscillations appear between 6-8m and spurious values of ε_d are calculated.

So as to better observe the response of the soil, the evolution of shear and volumetric strains is illustrated in Figure 4.6. The strains are calculated at a point close to the column's free surface (h=8m), as the greatest differences at the profile of ε_d (Figure 4.5a) are observed in the upper part of the column. In Figure 4.6a, it is noticed that initially the two curves coincide, whereas after the onset of the mainshock (t=2.3s) and the apparition of greater values of strains, the response differs between the two simulations (NR and R). Although the soil column is subjected only to S waves, volumetric strains also appear in Figure 4.6b after the onset of the mainshock and the generation of shear strains, due to the coupling between shear and volumetric strains through the dilatancy flow rule (Equation 4.43), as explained previously. More precisely, in Figure 4.6b, where the evolution of volumetric strain is plotted, it is remarked that initially no volumetric strains appear, but after the beginning of the mainshock (t=2.3s), volumetric strains appear and their evolution differs between the two simulations (NR and R). It is noticed that the regularization restricts the generation of volumetric strains, as smaller values of ε_v are obtained.

Intending to verify the statement that the noise in the R simulation is generated due to the coupling of S and P wave propagation, a simulation with the dilatancy flow rule deactivated is also performed (i.e. no shear-induced plastic volumetric strains generation). In Figure 4.5b, it is noticed that the dynamic response is identical for both cases (NR and R), as expected. When the dilatancy flow rule is deactivated, the first gradient of dilation model does not affect the response.

So as to further investigate the dynamic response in case of regularization with dilatancy flow rule activated, the FF horizontal and vertical-induced acceleration are plotted in Figure 4.7. It is interesting to remark that though no P waves (corresponding to vertical acceleration) are directly introduced to the model, in Figure 4.7b important values of vertical acceleration start to appear at t$\simeq 2s$ due to the generation of shear-induced plastic volumetric strains (see also Figure 4.6b). This significant apparition of vertical acceleration can be directly linked to soil's behavior which is strongly dilative, as shown in Figure 4.2b. Furthermore, differences in the dynamic response are pointed out mainly in the plot of vertical-induced acceleration.

To further examine these differences in the dynamic response, the Borehole Transfer Function from top to base of the horizontal acceleration is calculated for both cases. Figure 4.8a shows that in the case without regularization (blue curve), there is a degradation of the fundamental frequency due to nonlinearity, as expected. The frequency of the first peak (f_1) is close to 3.5Hz and of the second peak (f_2) is close to 15Hz, instead of 5.8Hz and

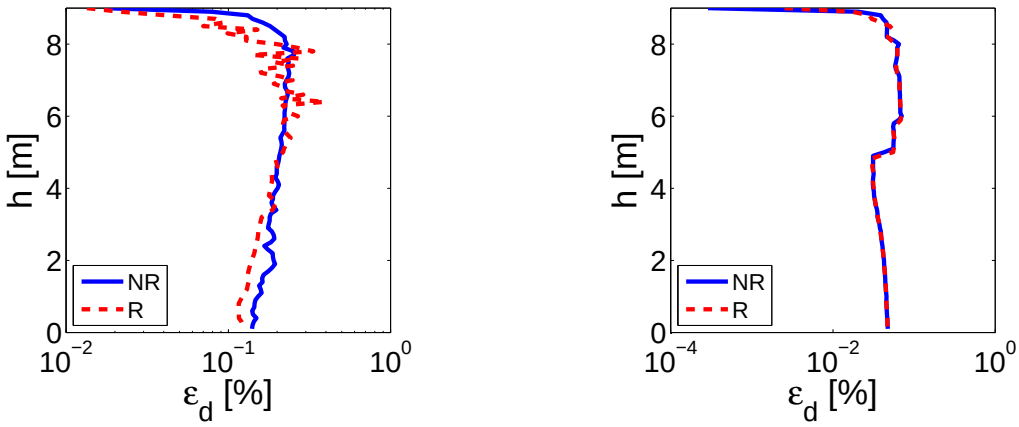

(a) (b)

Figure 4.5: Profile of deviatoric strains ε_d at the end of the ground motion: a) Dilatancy rule activated, b) Dilatancy rule deactivated: No shear-induced volumetric strains.

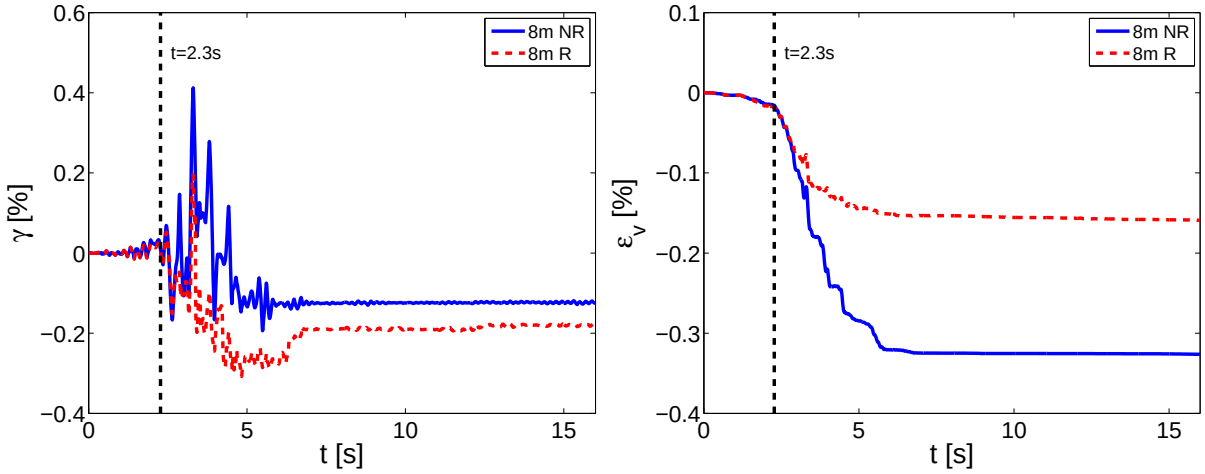

(a) Shear strains γ. (b) Volumetric strains ε_v.

Figure 4.6: Evolution of strains during the ground motion at h=8m (close to the free surface).

17Hz in the linear case, respectively. However, in the case of regularization (red curve), while the same degradation is noted for the first peak, the frequency of the second peak is around the value found in elasticity (17Hz). Moreover, the Borehole Transfer Function is calculated for the simulations of dilatancy flow rule deactivated and in Figure 4.8b, it is shown that both curves coincide, as expected.

Another way to observe the effect on the obtained acceleration in the time-frequency domain is to use the S-transform proposed by Stockwell et al. (1996) and Pinnegar and Mansinha (2003) is used. While the Fourier Transform provides an image of the dynamic response as function of frequency, the S-transform combines frequency with time and gives the evolution of frequencies and their amplitude during a motion. In Figure 4.9 the

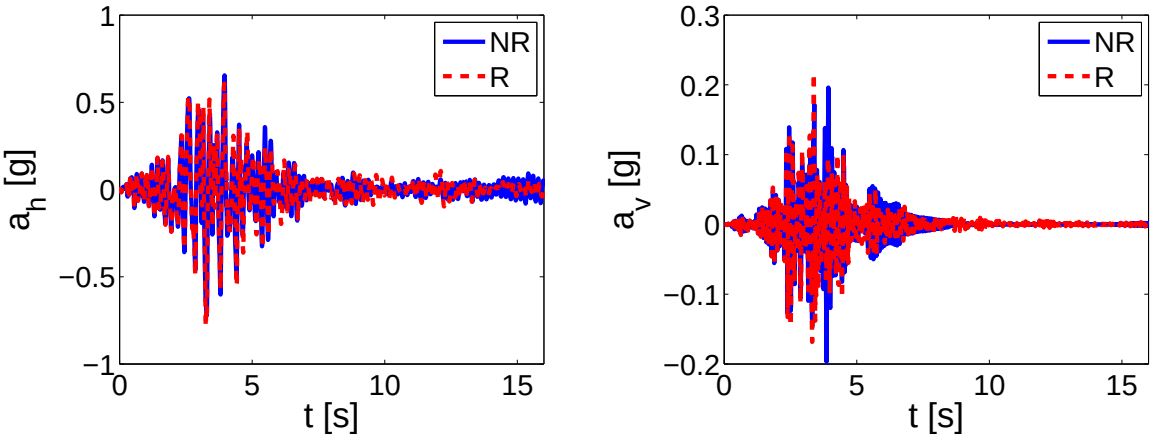

(a) (b)

Figure 4.7: FF acceleration without and with regularization: a) Horizontal, b) Vertical-induced.

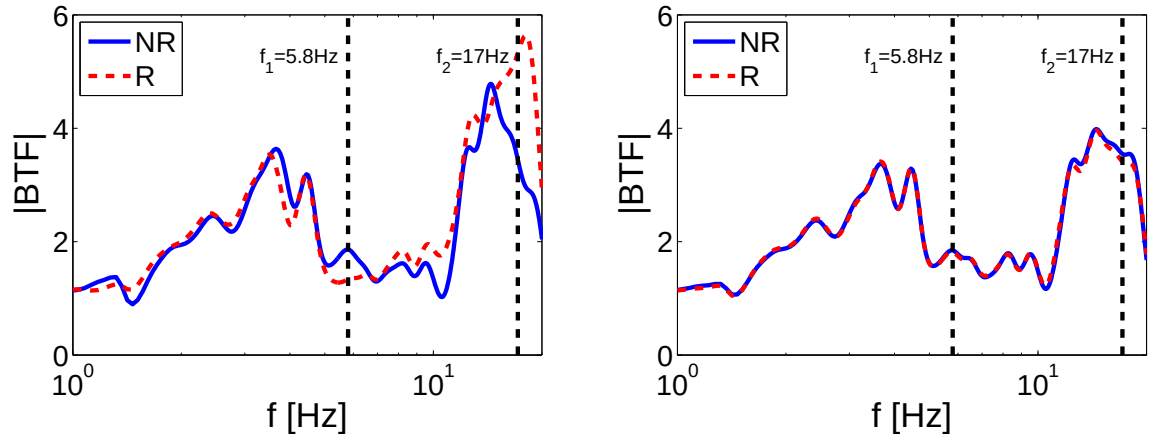

(a) (b)

Figure 4.8: Borehole Transfer Function of FF horizontal acceleration: a) Dilatancy rule activated, b) Dilatancy rule deactivated: No shear-induced volumetric strains.

S-transform for both simulations is plotted and it can be remarked that different response is obtained for frequencies greater than 10Hz for the case of regularization (Figure 4.9b). Nonetheless, it is not clear if these differences concern only high frequency noise.

Therefore, the spectral coherency is also used to examine the relation between two signals in a wide range of frequencies. Spectral coherency is commonly used to estimate the causality between two signals and calculated as follows:

$$\bar{\gamma}_{jk}(\omega) = \frac{\bar{S}_{jk}(\omega)}{\sqrt{\bar{S}_{jj}(\omega)\bar{S}_{kk}(\omega)}} \tag{4.56}$$

where $\bar{S}_{jk}(\omega)$: smoothed cross spectral density and $\bar{S}_{jj}(\omega)$: smoothed power spectral

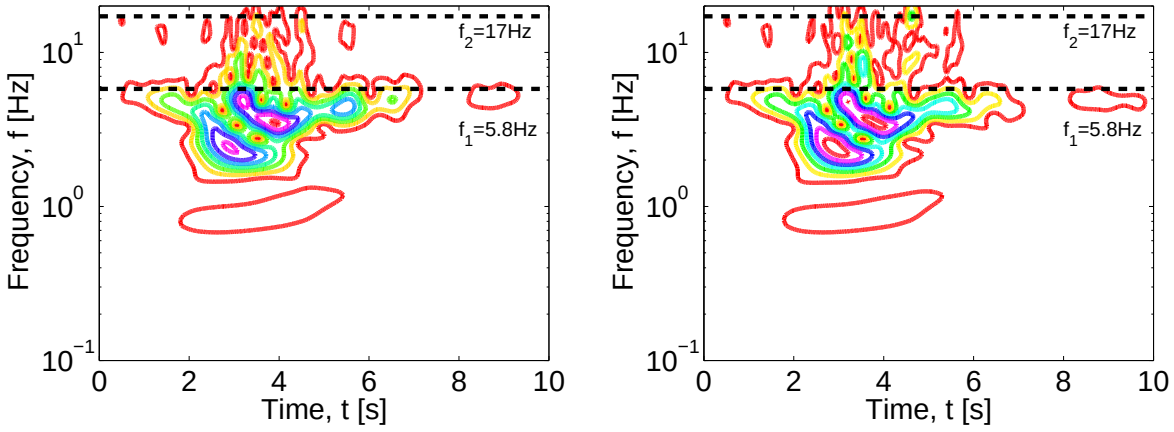

Figure 4.9: S-transform of FF horizontal acceleration: a) Without regularization, b) With regularization.

density. For the purpose of this study, it is used to assess the effect of the regularization method in the frequency domain on the FF acceleration without and with regularization. As it is observed in Figure 4.10a, the obtained signals of horizontal acceleration are identical until 3Hz (coherency equal to 1) and then, they diverge. This remark can be related to Figure 4.8a, where both curves coincide until the first peak (3.5Hz). However, in the case of vertical-induced acceleration, the coherency diverges from 1 in a wide range of frequencies, which means that the noise affects the whole signal. This result is in agreement with the analytical relation of $k_{S,R}$-$k_{P,R}$, as the rigidity matrix of the regularization is multiplied by ω, i.e. the whole frequency range of the input motion (see Equation 4.37).

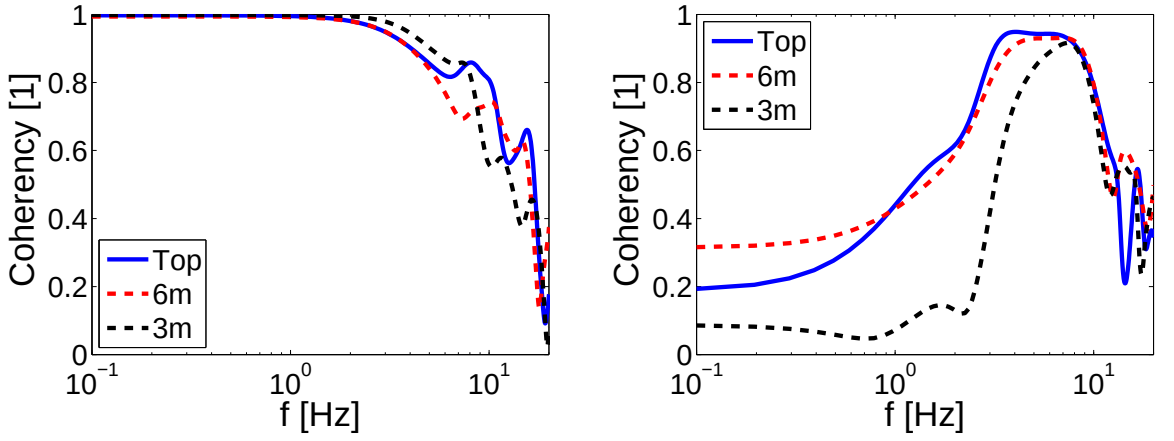

Figure 4.10: Coherency of FF acceleration without and with regularization: a) Horizontal, b) Vertical induced.

As mentioned before, the main problem appears in the vertical-induced acceleration resulting from the generation of plastic volumetric strains, as the regularization acts in the volumetric part. When the dilatancy rule is activated, plastic volumetric strains are generated through the coupling of volumetric-deviatoric strains and simultaneously the regularization is activated. Therefore, in the equation of S-wave propagation, the terms linked to k_P (Equation 4.37) and the rigidity of the first gradient model ($3a_1$) appear and noise is generated in the wave propagation (i.e. spurious waves). As the dilatancy rule links S and P-induced waves, this noise is spread in the medium during the ground motion.

After a sensitivity analysis for the parameter of regularization a_1, it is concluded that the perturbation appears always irrespective of the choice of the regularization parameter. For the sake of brevity, the results are omitted, as no further information is provided.

Intending to further examine the effect of the regularization method on wave propagation and mechanical soil behavior as well, analytical signals are imposed to the soil column and several aspects of the column's dynamic response are explored using technics of signal analysis. The results of this analysis can be found in Appendix G. Furthermore, the same analysis was performed in case of P wave propagation and similar conclusions were drawn. The corresponding results are omitted as P wave propagation is not in the scope of the current PhD work.

4.6 Partial Conclusions

Mesh sensitivity of results is indicated when performing FE simulations. In order to treat this deficiency, regularization methods are proposed so as to obtain an identical response irrespective of the mesh used. In this chapter, the applicability of a regularization method with enhanced kinematics, called first gradient of dilation model (Fernandes et al., 2008), was explored in case of dynamic analyses, through an analytical solution and a numerical example.

In case of coupled S-P wave propagation in regularized micromorphic media, additional terms linked to the rigidity matrix of the regularized part, appear in the equation of wave propagation. These terms affect the wave propagation and medium's dynamic response. In case of regularization smaller values of volumetric strains and vertical-induced acceleration appear, which imply that the wave propagation is restricted and the waves are trapped in the medium. Furthermore, the regularized induced response remains more in an elastic regime as the frequency peak of the second mode has not degraded. The noise appears in a wide range of frequencies, as the coefficient of regularization is multiplied by the frequencies of the input signal in the wavenumber equation.

More precisely, in case of S-wave propagation, when the permanent strains remain at a low level, the dynamic response is not affected, but when plastic volumetric strains are generated due to large deviatoric ones, the first gradient of dilation model is activated and has a detrimental effect on wave propagation in the soil. Further numerical examples demonstrating the abnormal dynamic response of the regularized medium can be found in Appendix G. Moreover, the current regularization method is also applied on a larger scale model to observe its influence on the S and P wave propagation for a real case-study.

Noise on the dynamic response is always apparent and results of the latter study can be found in Appendix H.

Even if the complete theory of micromorphic media is applied, i.e. the whole tensor of a gradient model which regularizes both deviatoric and volumetric deformations, additional terms corresponding to the regularization would still appear in the wave propagation equation. It should be examined whether a nonlinear model could be used for the regularization part instead of an elastic rigidity matrix, so both regularization and classical part follow the same behavior. Furthermore, to better adjust this method in dynamic problems, the work proposed by Polizzotto (2012, 2013) could be also tested, as higher order inertia effects are taken into account. Finally, the use of another method of regularization suitable for dynamic loading could be investigated.

Consequent to these conclusions, the first gradient of dilation model can not be used in its current state in case of dynamic analysis. As it will be discussed in the following chapter, where the earthquake-induced failure of a larger scale model is assessed, results of dynamic analyses do not exhibit mesh sensitivity for the particular cases studied. For this reason, further research for the applicability of this particular regularization method or the inquiry of another regularization method do not interfere in the scope of this PhD work.

Chapter 5

Earthquake-induced failure of earth structures

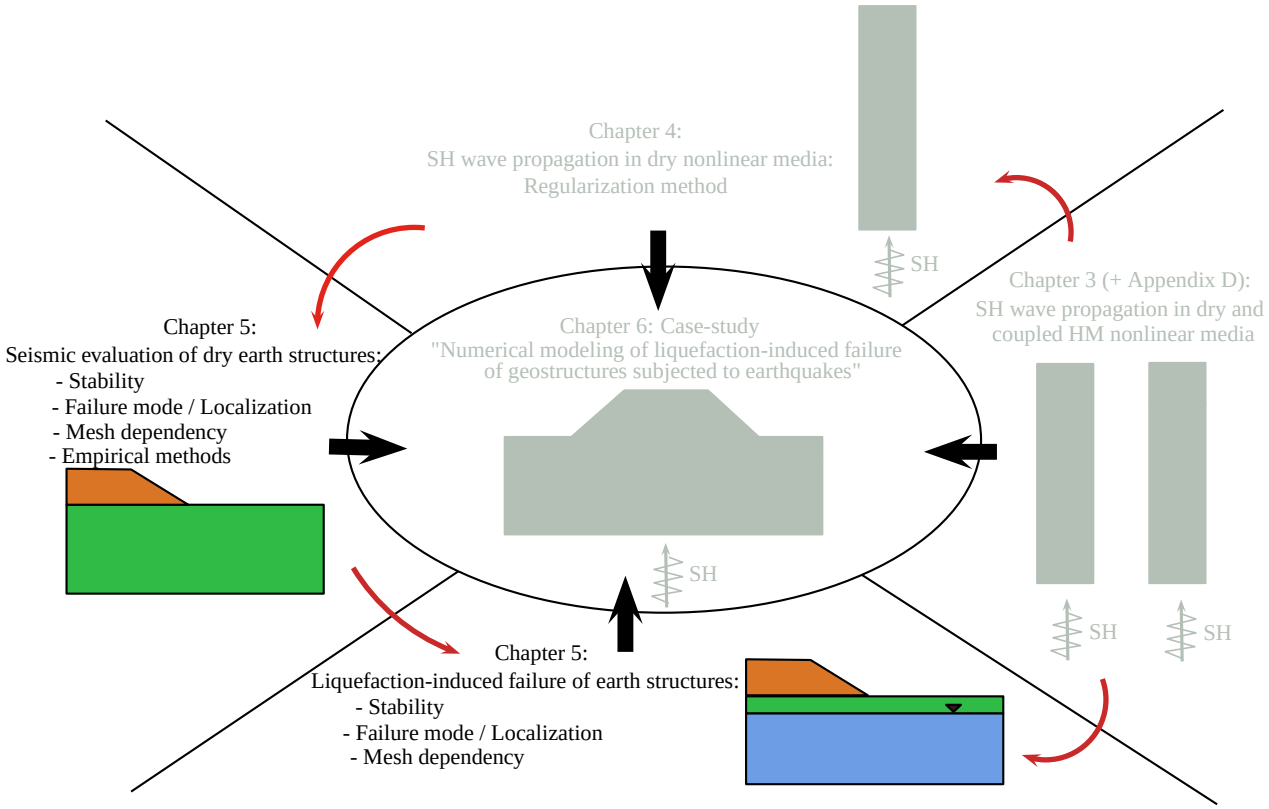

5.1 Introduction

Failure mechanisms of geotechnical structures during or after seismic events involve strain concentrations and large displacements in materials with highly inelastic behavior: soil masses sliding along weak planes, slope failures, soil liquefaction and liquefaction-induced settlements of foundations, etc. The prediction of these failure modes is a topic of great interest in earthquake geotechnical engineering, particularly for structural security assessment and risk analysis, which requires estimation of structural behavior during and after collapse (Zabala et al., 2007). Limit equilibrium analytical methods or numerical simulations have been used to estimate structural behavior during and after ground motions (Kourkoulis et al., 2010; Oka et al., 2012).

Following the study of 1D SH wave propagation on a soil column model, the current chapter describes the global dynamic response and interaction of a structure - foundation system. The main objective is to determine quantitatively the collapse mechanism and evaluate the post-earthquake stability. It is divided into two main parts: firstly a dry embankment - foundation model is simulated so as to define the collapse mechanism, and then, the same dry embankment is founded on a liquefiable foundation in order to evaluate the implications of earthquake-induced soil liquefaction on the structure's response. For this reason, a plane-strain FE model of an embankment-foundation system is built to analyze the failure modes and earthquake-induced deformations. In all simulations, the advanced soil behavior is represented using the fully coupled effective stress ECP constitutive model developed at CentraleSupélec (Hujeux, 1985). Numerical simulations are performed using the open-source FE software Code_Aster (version 11.7).

The first study was partially presented and published in the proceedings of the 9th International Conference on Structural Dynamics (EURODYN 2014) (Rapti et al., 2014a). While the latter contains material presented and published in the proceedings of the 5th ECCOMAS Thematic Conference on Computational Methods in Structural Dynamics and Earthquake Engineering (COMPDYN 2015) (Rapti et al., 2015b) and submitted for review in the journal "Soil Dynamics and Earthquake Engineering".

5.2 Dynamic response of dry embankment-foundation system

Questions regarding the seismic safety of existing dams that have not been designed to withstand earthquakes or have been designed using methods of analysis that are now considered outdated have been raised (Andrianopoulos et al., 2014). Bouckovalas and Papadimitriou (2005) pointed out the alteration/amplification of peak horizontal seismic ground accelerations in front and behind an embankment's crest and the production of parasitic vertical accelerations due to slope topography.

Shear band generation is identified as a potential earthquake-induced failure mode in dry foundation-structure systems (Oldecop et al., 2004; Kourkoulis et al., 2010; Park and Kutter, 2012; Hiraoka et al., 2013; Rapti et al., 2014a). Static failure is mentioned to be different from dynamic in terms of the spreading of shear band and depth of slip surface. Static failure tends to be distinct within a thin localized shear band, while during dynamic

loading the safety factor may be below one for multiple slip surfaces, which produces wider shear bands (Park and Kutter, 2012). According to Kourkoulis et al. (2010) and Park and Kutter (2012), in case of embankment-type structures subjected to seismic excitation, all possible shear bands extend from toe to crest. The possible failure zone initiates at the toe of the slope and propagates towards its crest.

However, localization problems are particularly challenging to model in conventional FE simulations due to discontinuities and large strains inside the shear bands (Zabala et al., 2007). Previous studies have focused mainly on the simulation and representation of structure's failure surface due to shear band generation using adaptive FE meshes and particle methods. The reason of using these methods is to capture localized deformation zones and large displacements without mesh distortion (Zabala et al., 2007; Hiraoka et al., 2013). Furthermore, when localization phenomena appear, strain softening models may introduce mesh sensitivity of results due to the loss of ellipticity in the governing equations (Bazant et al., 1985). Mesh dependency has already been introduced in cases of static loading, when a shear band mechanism is initiated just before the peak in the load-displacement curve (Desrues and Chambon, 2002; Foucault et al., 2011).

In the general context of seismic assessment of dry earth structures, the dynamic response of a dry embankment-foundation system subjected to several ground motions is evaluated and the onset and path of the collapse mechanism is determined. As mesh dependency of results is often remarked in FE simulations, a sensitivity analysis concerning the finite element's length is performed. Firstly, the numerical model and the dynamic loading are presented. Thereafter, the dynamic response of the model is explored in terms of acceleration, displacement, stability and shear deformations. The effect of the FE mesh refinement on the failure mode and shear band generation is thoroughly investigated. A local safety factor is estimated through soil's residual strength and the results of FE simulation are compared with the simplified methods for predicting earthquake - induced slope displacements.

5.2.1 Numerical model of dry embankment-foundation system

A rigid box model is chosen for the numerical simulation of the embankment-foundation system, so as to amplify the effect of the ground motion and better compare the results of the sensitivity studies. In such a model, the seismic waves remain trapped and the earthquake-induced phenomena are accentuated. The FE analysis is performed in three steps: a) as the model is nonlinear, a static analysis is performed in order to calculate the initial stresses, b) an excavation takes place at the right upper part to create the embankment and c) the final step is the application of the seismic signal.

5.2.1.1 Geometry - Boundary conditions

The model consists of a 2m high dry embankment composed of a loose-to-medium sand (LMS) and placed over a dry soil substratum. The first 2m of the foundation consist of the same loose-to-medium sand (LMS), while the rest 6m of the foundation are composed of a medium-to-dense dry sand (MDS). The embankment's slope inclination is equal to 1:2 (vertical:horizontal). The seismic signal is introduced as horizontal displacement at

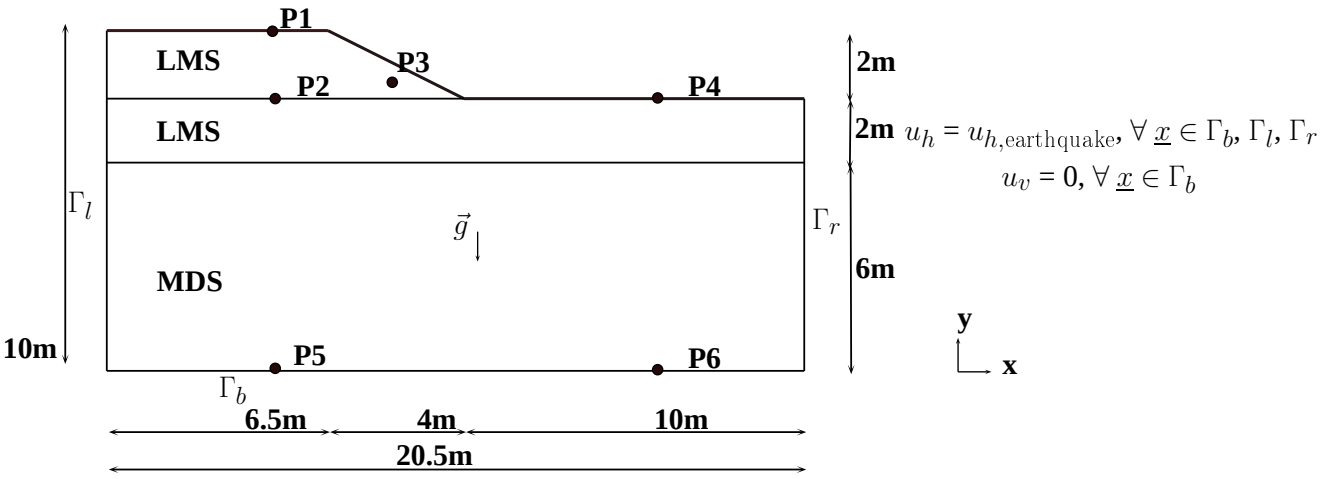

Figure 5.1: Numerical model of dry embankment resting on dense dry substratum.

the boundaries and vertical displacements are fixed only at the base. The dimensions and geometry of the model, as well as, some representative points chosen for the analysis of results are presented in Figure 5.1.

5.2.1.2 Soil behavior

The ECP constitutive model represents soil behavior of the loose-to-medium sand (LMS) and medium-to-dense sand (MDS). For further information about the model refer to Appendix B and for material parameters to Table B.1 in Appendix B.6.

In order to understand the behavior of the chosen materials under dynamic loading, triaxial and cyclic shear drained tests are conducted at confining pressures corresponding to the average geostatic pressure of the embankment (p_0=17kPa) for the LMS and the foundation (p_0=120kPa) for the MDS. Figures 5.2a and 5.2b represent deviatoric stress - strain and volumetric - deviatoric strain curves for both materials used in the model under the drained triaxial test simulation. It can be noticed that the MDS is a strongly dilative material, while the LMS is a contractive one. $G/G_{max} - \gamma$ and $D - \gamma$ curves are also generated after the shear cyclic drained test simulations (Figure 5.2c and 5.2d). The curves are close to the reference ones given by Seed and Idriss (1970).

5.2.1.3 Numerical parameters

The implicit method of Newmark integration is used for the dynamic analysis with a time step equal to Δt=10^{-3}s and numerical damping equal to $\xi = 0.2\%$ is added, as explained previously in Section 3.2.4.

The low-strain frequency analysis provides a fundamental elastic period for the embankment - foundation system equal to $T_p \simeq 0.1$s (f_p=9.6Hz), as shown in Figure 5.3. It is obtained from the Borehole Tranfer Function from the crest to base (i.e. Fourier spectral ratios between the response at embankment's surface over the bedrock) for a sample seismic signal at very low amplitude (10^{-6}g) to ensure elastic soil behavior. In this particular model the response Crest-Bedrock is obtained from the transfer function between points

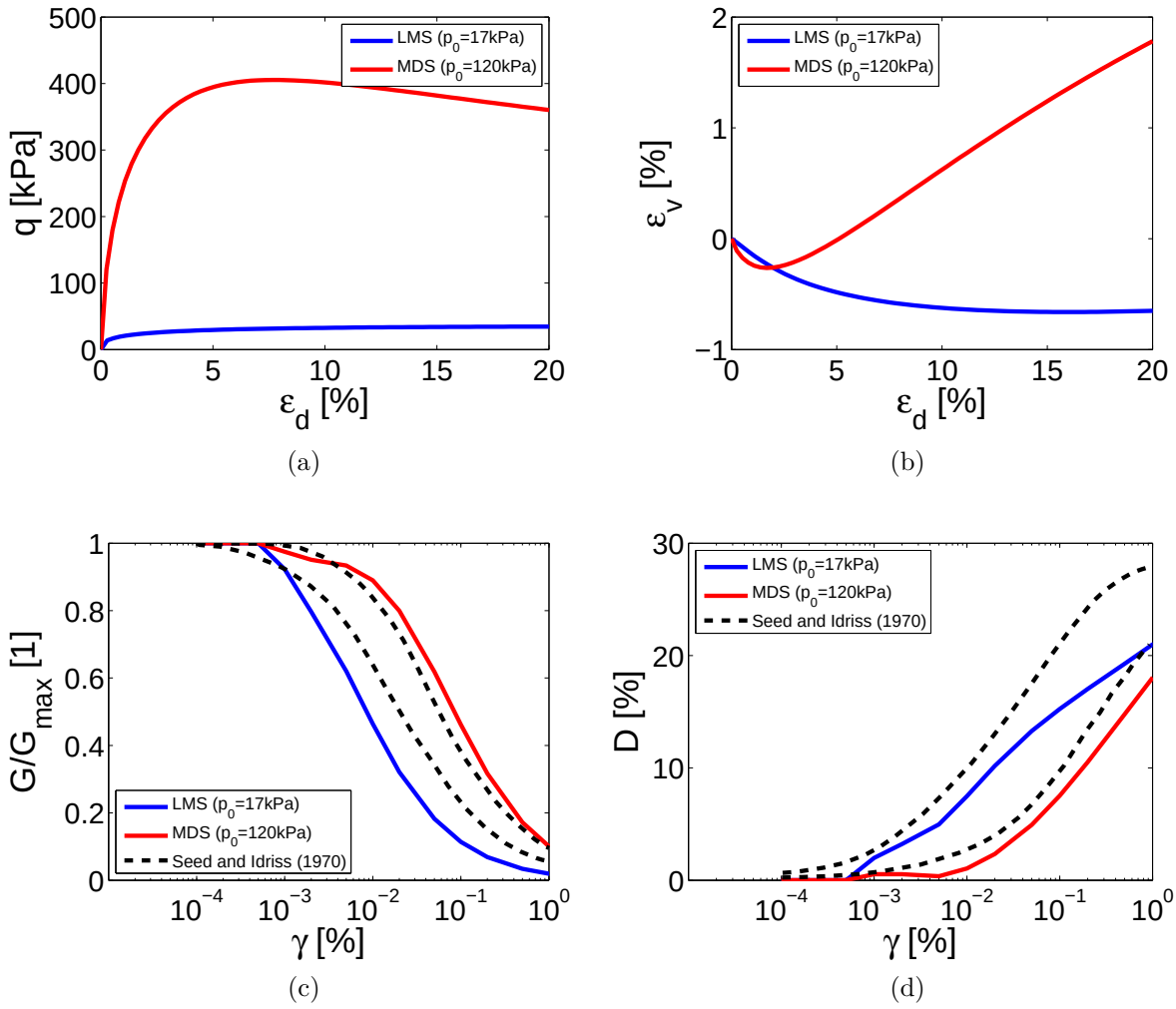

Figure 5.2: Soil response of one material point under: a,b) triaxial drained test and c,d) shear cyclic drained test compared to Seed and Idriss (1970).

P1-P5 of Figure 5.1, while Base-Bedrock and FF-Bedrock FF refer to points P2-P5 and P4-P6, respectively.

5.2.1.4 Finite element mesh

To evaluate the sensitivity of results to the FE mesh, 5 different meshes were created using 6-node triangular elements. The meshes generated from finer to coarser depending on the element's length are: Mesh 1 (5cm, 26618 nodes/14160 elements), Mesh 2 (10cm, 11409 nodes/6314 elements), Mesh 3 (15cm, 10690 nodes/5651 elements), Mesh 4 (25cm, 4040 nodes/2368 elements), Mesh 5 (50cm, 5803 nodes/3128 elements). The refinement of the mesh corresponds to the layer of the LMS inside the embankment body and the upper part of the foundation (Figure 5.4), while for the rest a mean element size of 50cm is used. Although mesh 4 is finer in the layer of LMS, in the lower part is slightly coarser than mesh 5, due to automatic refinement provided by the software. This fact explains

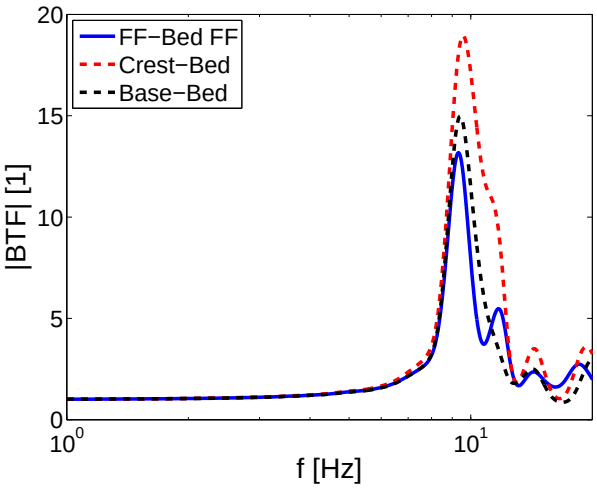

Figure 5.3: Borehole Transfer Function of dry embankment - foundation system.

the greater number of nodes and elements found in mesh 5.

5.2.1.5 Input ground motions

For the mesh sensitivity study, Friuli earthquake (Italy, 1976) is used as reference case. The accelerogram and the normalized Arias intensity of the input motion are plotted in Figure 5.5.

Next a parametric study is conducted and the following ground motions from PEER database are imposed to the embankment - foundation model:

- 6 real ground motions non pulse-like ground motions recorded on soil site: ita Lb 7 ($a_{bed,max}$=0.09g), T1a 1 ($a_{bed,max}$=0.15g), Friuli ($a_{bed,max}$=0.24g), T1a 10 ($a_{bed,max}$=0.26g), T1a 8 ($a_{bed,max}$=0.4g), T1b 8 ($a_{bed,max}$=0.6g) (Iervolino and Cornell, 2005; Sorrentino et al., 2008)

- 2 strong synthetic ground motions generated by natural accelerogram recorded on soil site: GVa 7 ($a_{bed,max}$=0.89g), GVb 5 ($a_{bed,max}$=1g) (Dickinson and Gavin, 2011; Gavin and Dickinson, 2011)

The selection of these motions is based on their amplitude. The characteristics and the accelerograms of the ground motions can be found in Appendix C. The response spectra of all motions are plotted in Figure 5.6, where the spectrum of Friuli earthquake is colored in blue. Note that all input and outpout signals have a baseline correction and are filtered using a non-causal bandpass filter of order 4, between 0.1-20Hz.

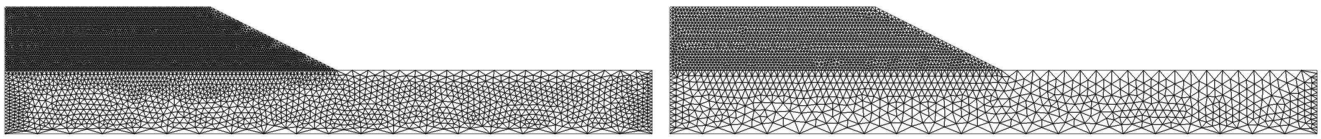

(a) Mesh 1 (5cm)

(b) Mesh 2 (10cm)

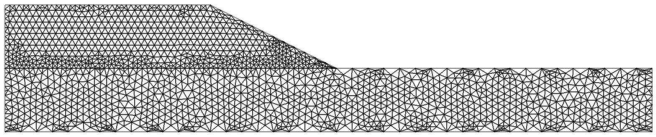

(c) Mesh 3 (15cm)

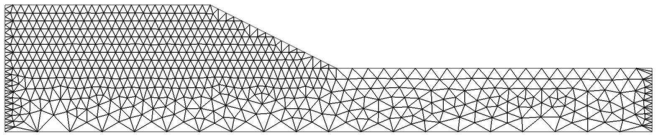

(d) Mesh 4 (25cm)

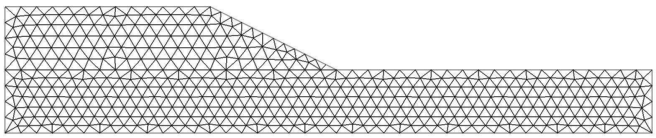

(e) Mesh 5 (50cm)

Figure 5.4: FE meshes for the dry embankment - foundation system.

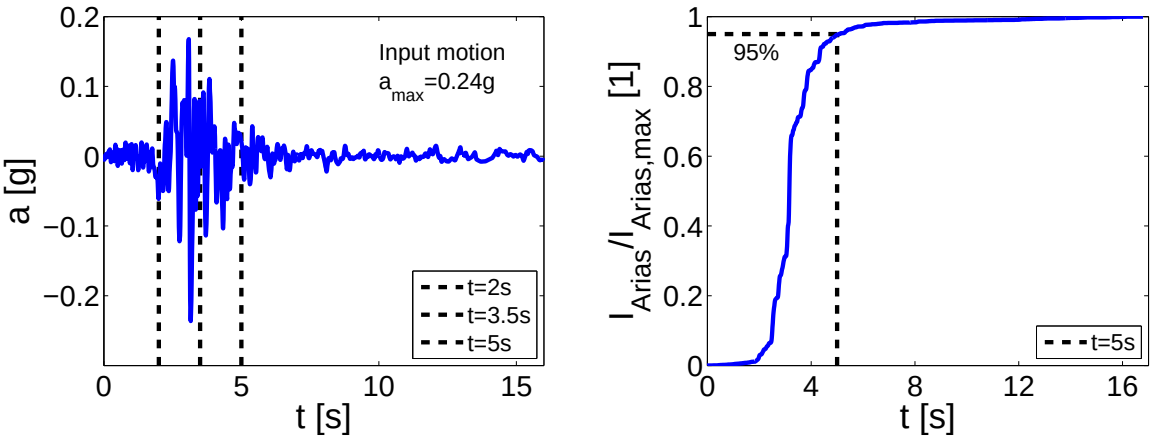

(a) (b)

Figure 5.5: Input seismic signal of Friuli earthquake: a) Accelerogram, b) Normalized Arias intensity.

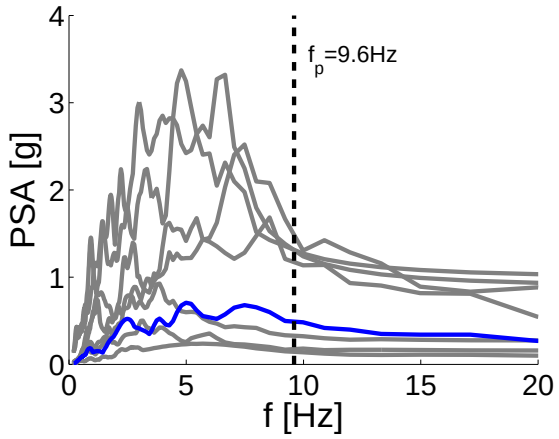

Figure 5.6: Response spectra of input ground motions (ξ=5%) and Friuli spectrum in blue color (the system's fundamental frequency is illustrated with the dashed line).

5.2.2 Typical dynamic response and mesh sensitivity assessment

As aforementioned, in order to define the expected failure path and the onset of collapse of the dry structure-foundation system, the dynamic analysis with Friuli earthquake is examined in the following sections, unless otherwise mentioned. The earthquake-induced accelerations, displacements and deformations, as well as, the embankment's stability, are assessed during the ground motion simultaneously with an extended mesh sensitivity evaluation.

5.2.2.1 Displacement

The typical dynamic response of the model is shown in Figure 5.7, where the horizontal and vertical displacements are presented at the end of the ground motion. The right part of the embankment and the upper part of the foundation close to the slope tend to move horizontally, while almost the whole embankment settles down. This movement implies a circular failure mode for the embankment extended inside the upper layer of the foundation (LMS layer). Comparing the response of meshes 2 (10cm) and 4 (25cm), no mesh sensivity is observed and consequently, the results of the other meshes are omitted.

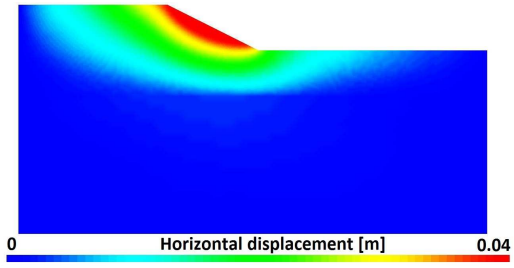

(a) Horizontal displacements.

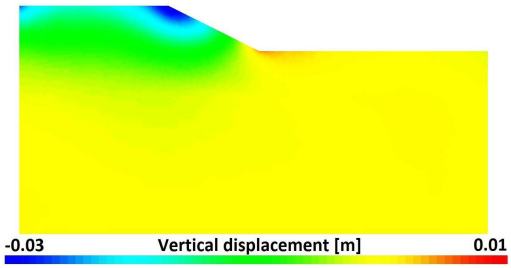

(b) Vertical displacements.

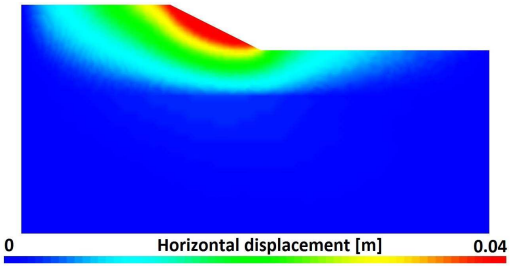

(c) Horizontal displacements.

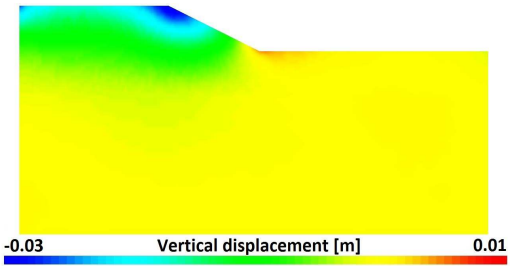

(d) Vertical displacements.

Figure 5.7: Deformed shape at the end of the ground motion (Friuli earthquake): a,b) Mesh 2 (10cm), c,d) Mesh 4 (25cm).

The evolution of relative horizontal and vertical displacements of the crest (P1) and slope (P3) to that at FF (P4) is plotted in Figure 5.8 and compared for all meshes. At the beginning of the main shock (t=2-3s, see accelerogram of Friuli earthquake in Figure 5.5a) a sudden increase of horizontal displacement and settlement happens. Then, at the end of the main shock and during the coda phase (i.e. last seconds of the ground motion where the amplitude decreases) the displacements stabilize. The slight differences among

the response of the meshes should not be considered as a result of mesh effect. They are attributed to the fact that we could not obtain exactly the same point in all meshes, as in the coarser ones, less nodes are generated in the FE mesh, so it is recommended to take into consideration the global response of Figure 5.7.

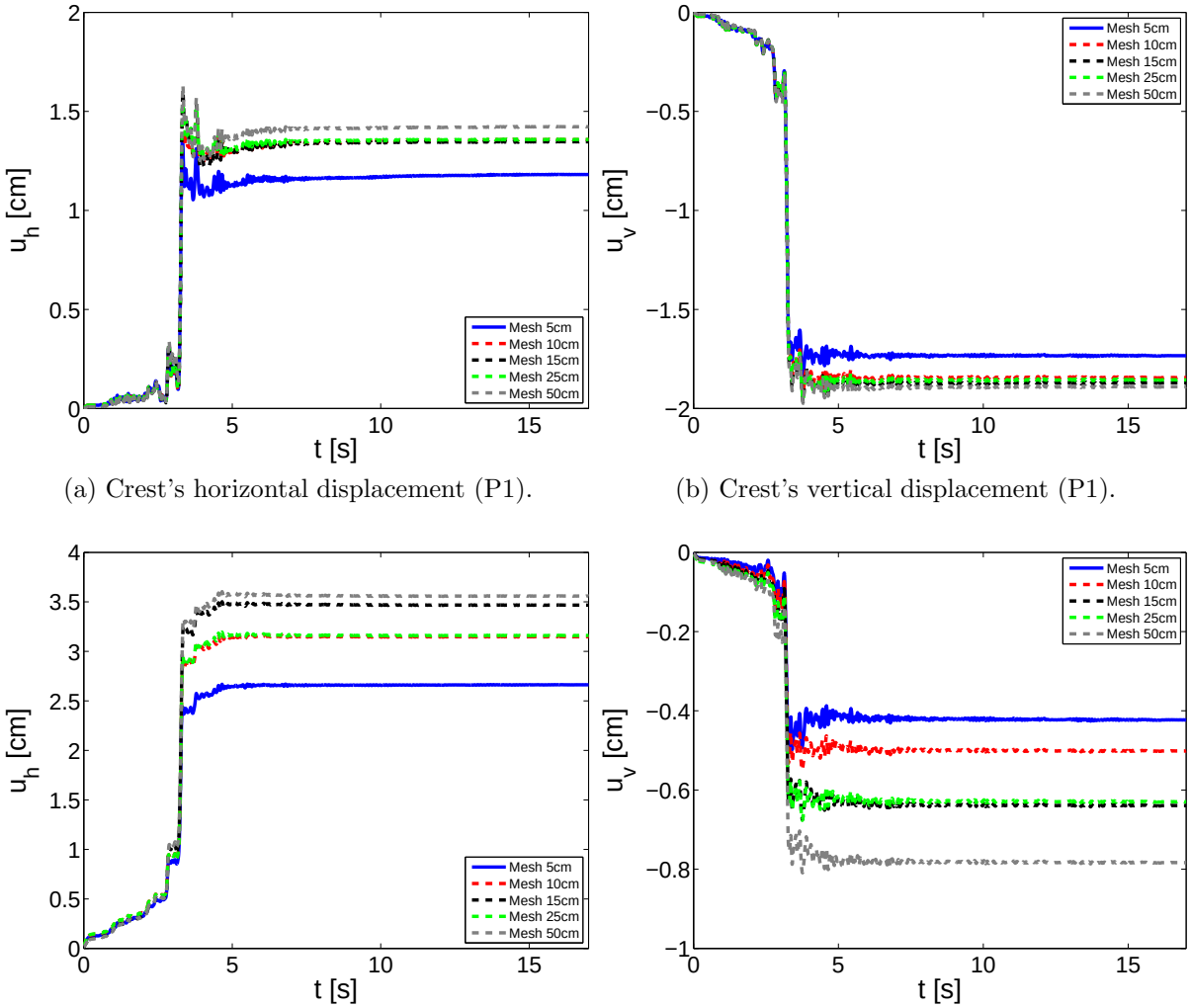

(a) Crest's horizontal displacement (P1).

(b) Crest's vertical displacement (P1).

(c) Slope's horizontal displacement (P3).

(d) Slope's vertical displacement (P3).

Figure 5.8: Comparison of relative displacements to FF for all meshes (Friuli earthquake).

5.2.2.2 Acceleration

The horizontal accelerations during the earthquake are measured at the crest (P1), base (P2), inside the slope (P3) of the embankment, as well as, at FF (P4) (see points in Figure 5.1). The response of these representative points is compared for all meshes in Figure 5.9 and is almost identical. As previously explained, the negligible differences are due to the different nodes selected in each mesh. The same conclusion is drawn from the response in terms of frequency, as presented in Figure 5.10 where the Fourier transform of the horizontal acceleration is calculated.

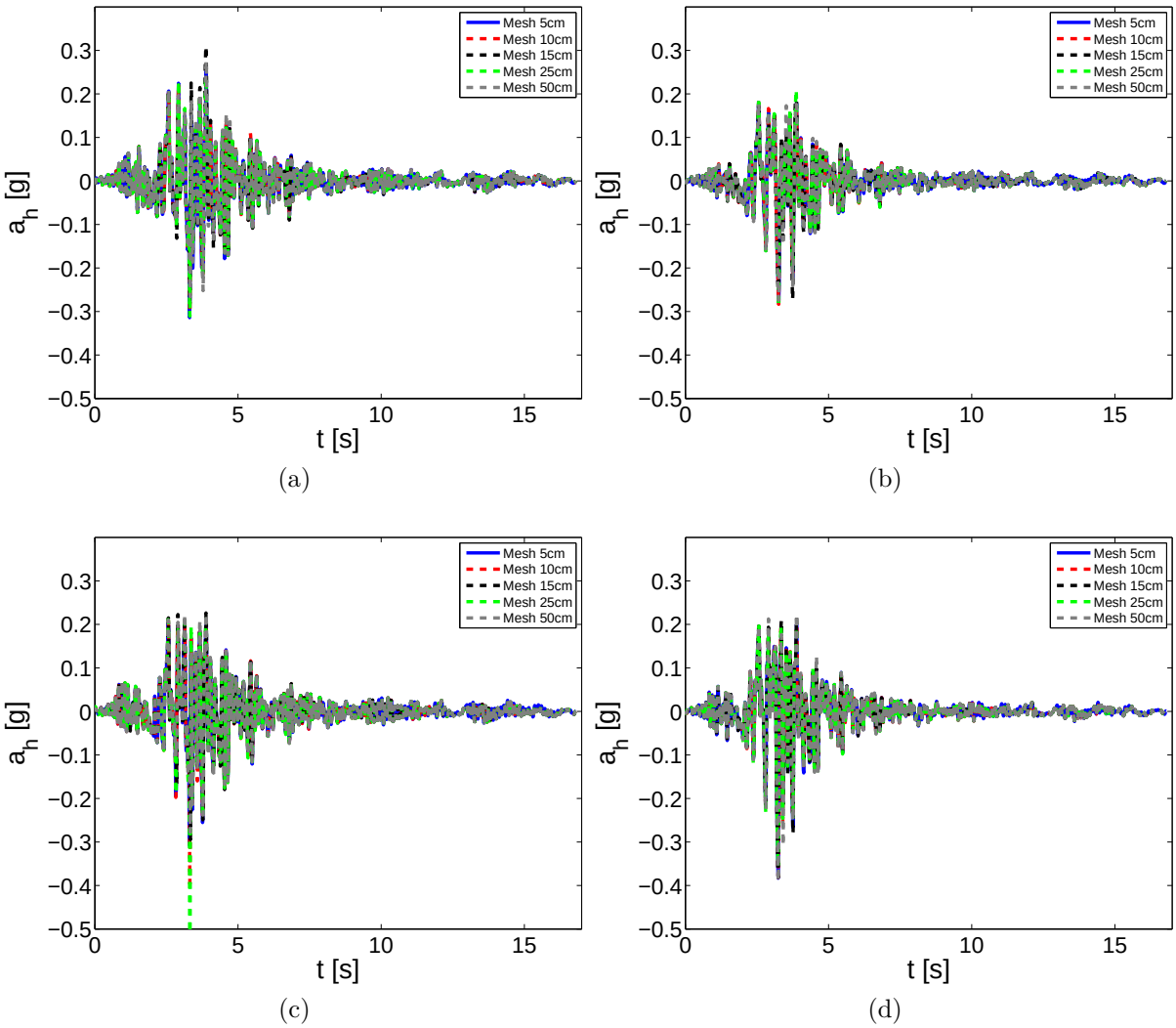

Figure 5.9: Comparison of absolute horizontal acceleration for all meshes (Friuli earthquake): a) Crest (P1), b) Base (P2), c) Slope (P3), d) FF (P4).

Finally, the response of the structure - foundation system for different levels of input motions is evaluated through the parametric dynamic analysis with the 8 ground motions (Section 5.2.1.5). The analysis is carried out only for mesh 4 (25cm). This choice of mesh is based on two criteria: a) the capability of the element length to represent a wide range of frequencies and b) CPU time of simulation. The relation $\Delta z{=}\lambda/10$ established between the wavelength $\lambda{=}V_S/f$ (where V_S is the shear wave velocity), element's length Δz and frequency f (Kramer, 1996; Foerster and Modaressi, 2007) provides an accurate response of the LMS with a mesh of 25cm until a shear wave velocity of 75m/s (i.e. 20% of deformation) for a signal's frequency of 30Hz (i.e. commonly maximum frequency of an input signal). Based on the CPU time of the dynamic analysis with Friuli earthquake for all meshes, mesh 4 (25cm) requires the least computational time (refer to Figure I.1 in Appendix I).

For these reasons, the mesh 4 (25cm) is used for the parametric study and the PGA

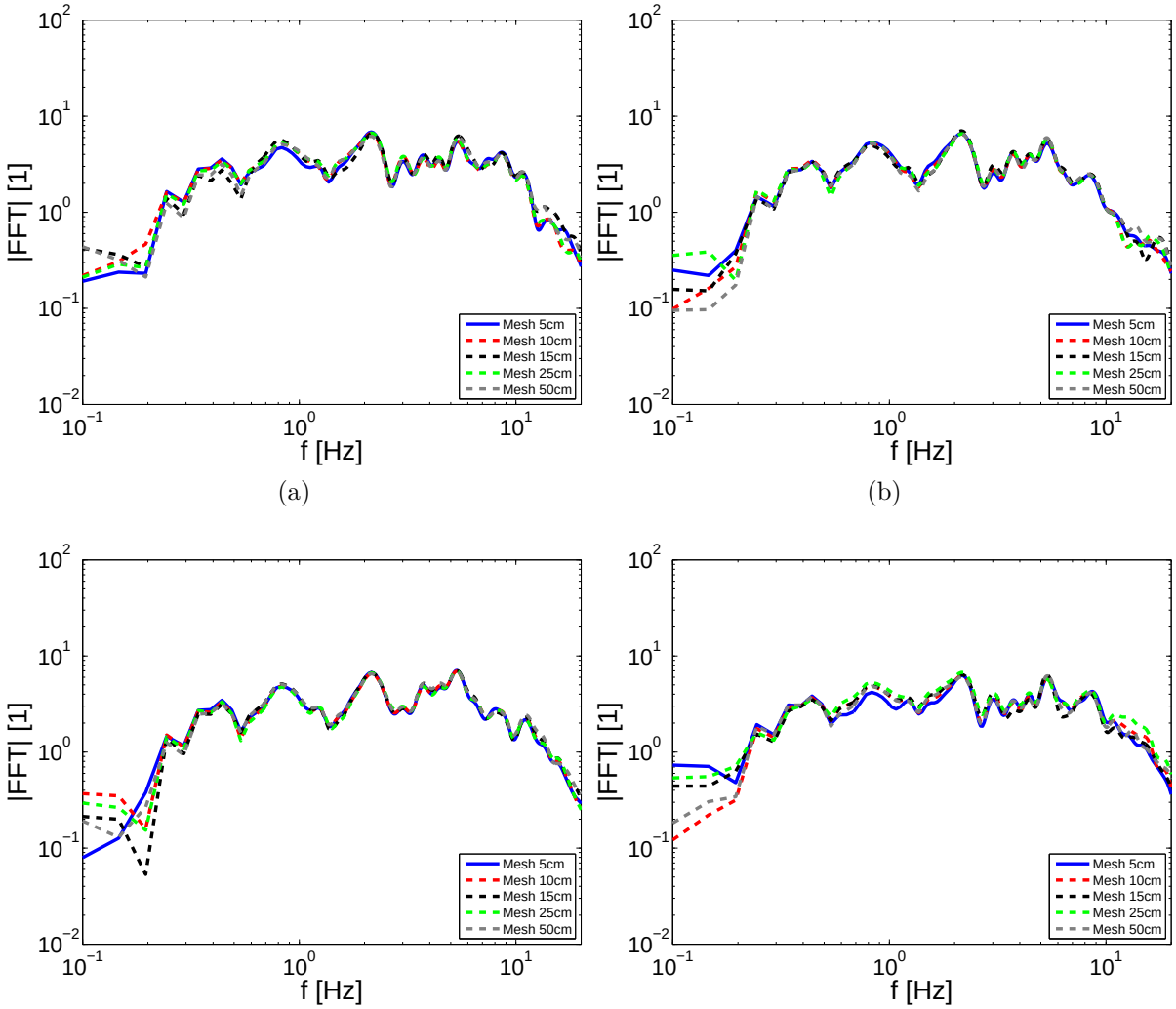

Figure 5.10: Comparison of fourier transform of horizontal acceleration for all meshes (Friuli earthquake): a) Crest (P1), b) Base (P2), c) Slope (P3), d) FF (P4).

is calculated at the crest, base of the embankment and FF for all input ground motions in Figure 5.11. The results of the two synthetic strong motions ($a_{bed,max}$=0.89g and $a_{bed,max}$=1g) are not illustrated in the figure, as excessive displacements led to the model's collapse and the simulations stopped due to convergence problems.

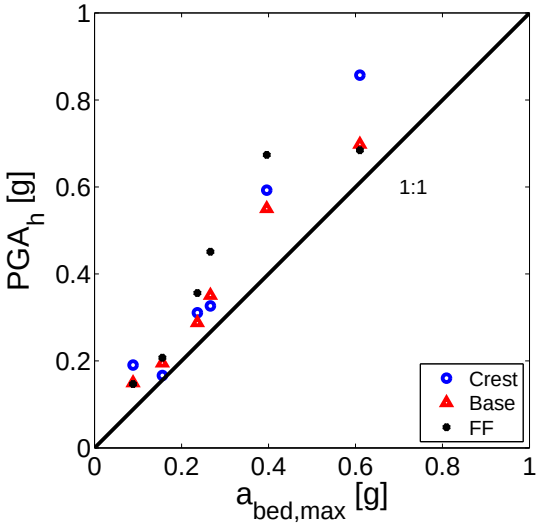

Figure 5.11: Horizontal PGA as function of $a_{bed,max}$ for mesh 4 (25cm).

5.2.2.3 Stability

Based on Hill's instability criterion (Hill, 1958), the stability of the embankment is tested by calculating the second order work density ($d^2W=\dot{\sigma}'_{ij}:\dot{\varepsilon}_{ij}/|\dot{\sigma}'_{ij}||\dot{\varepsilon}_{ij}|$) (Hamadi et al., 2008; Buscarnera and di Prisco, 2012). This criterion is not cumulative and gives only an image of instability at specific instants of the ground motion and specific locations, as shown in Figure 5.12 where the contours are plotted at the beginning of the main shock (t=2s) and at the end of the groung motion (t=17s) for mesh 4 (25cm).

Instability (blue color) is remarked close to the embankment's slope during the main shock (Figure 5.12a), while at the end of the motion it remains stable (Figure 5.12b). The results of other meshes are omitted, as no further information is provided.

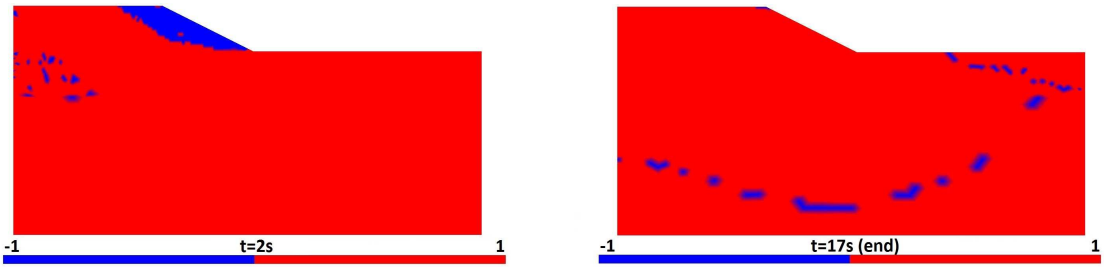

(a) t=2s. (b) t=17s (end)

Figure 5.12: Contours of second order work sign (Friuli earthquake with mesh 4).

5.2.2.4 Shear deformations

In order to represent the shear deformations, the contours of deviatoric deformations ε_d are plotted at the end of the motion for all meshes in Figure 5.13. Due to geometry heterogeneity at the toe of the embankment, a shear band initiates and is diffused towards

the crest. The shear band mechanism is not mesh dependent concerning the failure path generated, although insignificant variance can be detected in terms of amplitude of the shear deformations. A similar collapse mechanism, which is mesh insensitive, is also identified according to the work of Kourkoulis et al. (2010).

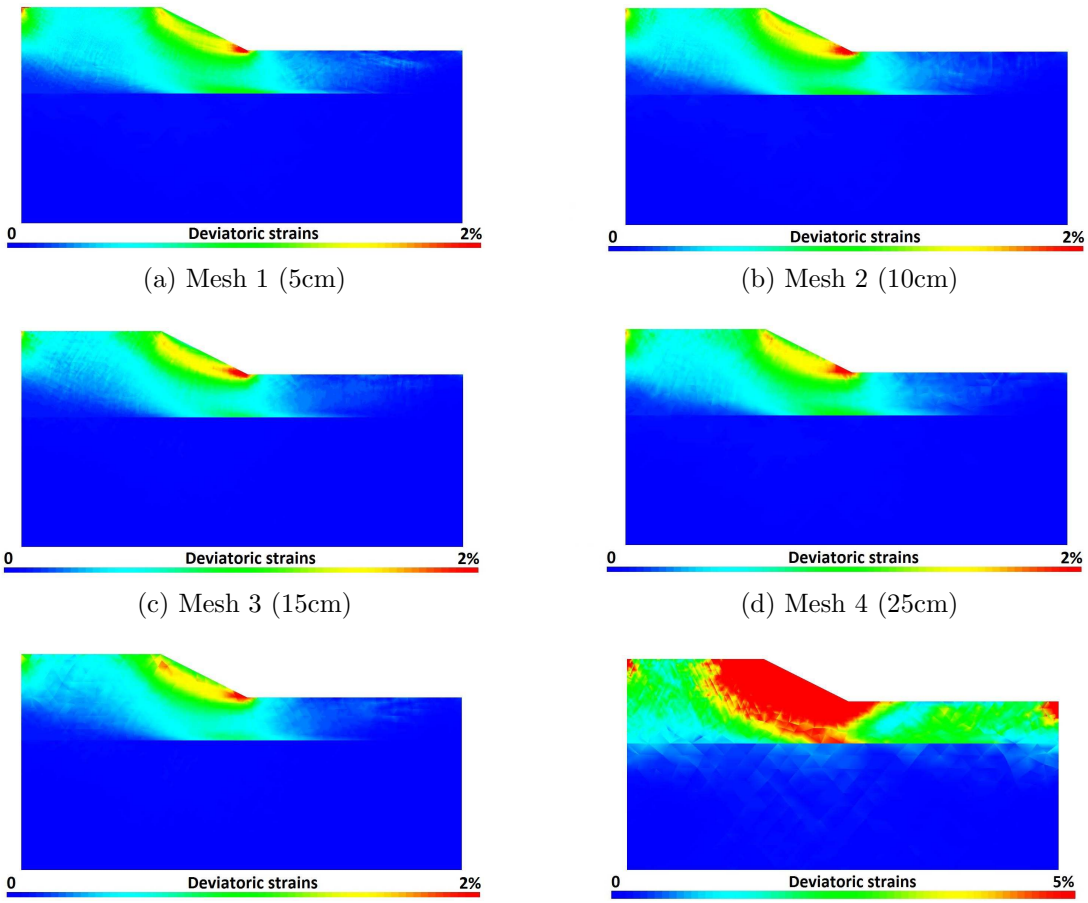

(a) Mesh 1 (5cm) (b) Mesh 2 (10cm)

(c) Mesh 3 (15cm) (d) Mesh 4 (25cm)

(e) Mesh 5 (50cm) (f) Mesh 4 (25cm)

Figure 5.13: Deviatoric strains ε_d at the end of the ground motion: a-e) Friuli earthquake, f) T1a 8 earthquake.

For stronger ground motions more important values of shear deformations (around 25%) are remarked and can lead to local collapse of the embankment, as shown in Figure 5.13f for the ground motion T1a 8 ($a_{bed,max}$=0.4g). However, the simulations performed use the hypothesis of small deformations, thus, values of deformations greater than 5% are approximate. The results of shear strains in Figure 5.13f should be treated qualitatively and are used only to define the progressive failure mechanism of the system.

5.2.3 Safety factor estimation through soil's residual strength

In common engineering practice, the assessment of the seismic stability of embankments and dams is performed through pseudo-static analysis (or limit equilibrium methods) (Akhlaghi and Nikkar, 2014), displacement-based (Newmark or sliding block) methods

(Elgamal et al., 1990) and dynamic stress-deformation numerical analysis (Seed et al., 1973). The first two methods constitute the basis of the engineering practices and thus, are consistently evaluated by researchers who try to establish new design criteria.

Traditionally, homogeneous slopes are analyzed for determining the safety factor by simplified methods, such as the ordinary method of slices (Fellenius, 1927) or Bishop's modified method (Bishop, 1955), which assume circular failure surfaces. Later, methods such as Janbu's generalized procedure of slices (Janbu, 1957) or Spencer's method (Spencer, 1967) take into account heterogeneities in the determination of the safety factor.

The prediction of earthquake-induced displacements is based on the assumption of the sliding rigid block defined by the failure surface and firstly introduced by Newmark (1965). Since then, many empirical methods are proposed, e.g. Sarma (1975); Makdisi and Seed (1978); Whitman and Liao (1985); Ambrasseys and Menu (1988); Jibson (1994); Bray and Travasarou (2007); Jibson (2007), for obtaining more accurate preliminary estimates of permanent earthquake-induced displacements of earth dams and embankments from the results of limit equilibrium pseudo-static slope stability assessment.

However, all these limit equilibrium and simplified displacement-based methods are susceptible to numerical errors resulting from inherent inaccuracies in the analyses (Duncan and Wright, 1980; Kramer, 1996). In most cases the uncertainties are related to the definition of geometry and soil properties, as well as on the approximations involved in the analytical technics, i.e. definition of failure surface or soil shear strength (Duncan and Wright, 1980). Non-linear FE methods are proven to be more efficient in re-producing the shape and location of slip surfaces, capturing progressive failure phenomena, handling irregular slope geometries in 2 and 3 dimensions and complex soil stratigraphy (Kourkoulis et al., 2010), apart from the numerical errors such as mesh sensitivity. Nevertheless, the crucial question concerning the determination of a safety factor in the context of seismic vulnerability analysis still remains in case of advanced FE simulations.

In the light of this problematic, a local safety factor is proposed in this section, so as to determine the soil's residual strength after a ground motion. Firstly, the definition of this criterion is discussed through a shear test of a laterally infinite soil element and then, the local safety factor of the dry embankment - foundation system is calculated. Finally, a critical failure surface is estimated using the proposed local safety factor and the results of the FE analysis are compared to some simplified methods for predicting the earthquake-induced displacements of the rigid block.

5.2.3.1 Definition of local safety factor

The local safety factor proposed is based on the used ECP elastoplastic model and provides for any state a direct measure of "distance to reach the critical state". Following the work of Lopez-Caballero and Modaressi-Farahmand-Razavi (2013), through the parameter r_k of the elastoplastic model, it is possible to define an apparent friction angle (ϕ'_{apt}) as follows:

$$\sin \phi'_{apt} = \frac{q_k}{p'_k \cdot F_k} \tag{5.1}$$

$$r_k = \frac{\sin \phi'_{apt}}{\sin \phi'_{pp}} \tag{5.2}$$

where p'_k and q_k are the effective mean and deviatoric values of stress tensor projected on the k plane, ϕ'_{pp} is the friction angle at critical state and the function F_k controls the isotropic hardening associated with the plastic volumetric strain. For furher details about these parameters refer to the constitutive model's description in Appendix B. The parameter r_k varies between 0 and 1 where perfect plasticity is reached and is defined as the inverse of a local safety factor (r_k=1/FS, i.e. near collapse when r_k=FS=1.0).

In order to explain the function of this safety index, shear tests of a laterally infinite case are performed. The soil element (1m×1m), composed of the LMS material, is initially confined at the average geostatic pressure of the embankment (p_0=17kPa) and then it is subjected to three different loadings, shown in Figure 5.14. The first loading is a monotonic one and a horizontal displacement of 20cm is imposed progressively to the soil element. The next two loadings refer to a cyclic loading of 10 cycles with imposed horizontal displacement of ±1cm and ±0.5cm and then a monotonic loading until a value of 20cm.

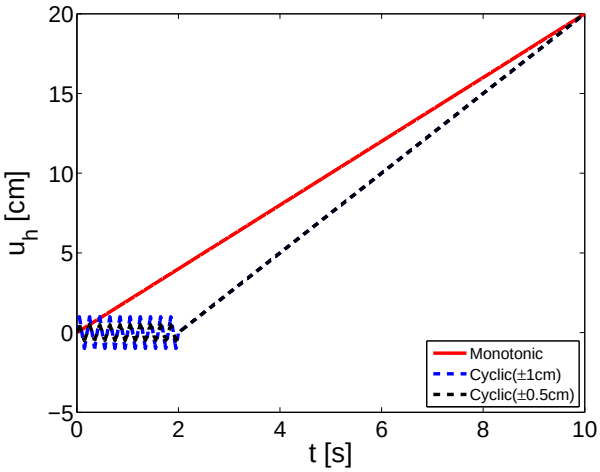

Figure 5.14: Monotonic and cyclic loading for the biaxial drained shear test of one soil element: Imposed horizontal displacement.

The response of the soil element after the 3 shear tests is presented in Figure 5.15. In Figure 5.15a, where the volumetric and deviatoric deformations are plotted, a peak is noticed when the cyclic loading finishes and the monotonic one starts (noted with a circle in the blue and black curves). This peak indicates the sharp change of soil's contractive behavior to a dilative one, while in case of monotonic loading (red curve) this change in soil's behavior happens more gradually. The same behavior can be noticed in Figure 5.15b where the volumetric deformations are plotted over the effective mean stress.

According to Figures 5.15c and 5.15d the soil regains strength inside the shear loops compared to the monotonic loading path. Subsequently, the maximum shear stress (τ, q) reached in cases of cyclic loading is greater than this of the monotonic one. So as to compare the monotonic loading with the cyclic ones, the factor Δr_k is calculated in Figures 5.15e, 5.15f. More in detail, in the curve of monotonic loading (red curve) the last points before the first unloading of the cyclic paths are noted with the circles (blue corresponds to the cyclic loading of ±1cm and black to the loading of ±0.5cm). The

starting points of the monotonic loading after the cyclic ones are also indicated in the curves of cyclic loadings (blue and black). So, it can be remarked that if the soil element is loaded with a cyclic path before the monotonic one, it has a gain in strength as the value of Δr_k is negative. For instance, the cyclic loading of $\pm$1cm provides a gain of approximately 0.2 in the value of r_k. From a value of $r_k \simeq 0.8$ following the monotonic path, a decrease is noticed when a cyclic preloading is performed and the new starting point is at a value of $r_k \simeq 0.6$. Nonetheless, the r_k parameter reaches the same level (close to 1) at perfect plasticity irrespective of the loading path, as shown in Figures 5.15e, 5.15f.

The ratio of apparent to critical friction angle provides a reliable measure of soil's strength, which is independent of the loading path and can be used as a criterion for estimating the local state of soil and eventually the local safety factor of geostructures. The parameter r_k will be next calculated and used as a safety factor indicator for the embankment - foundation model.

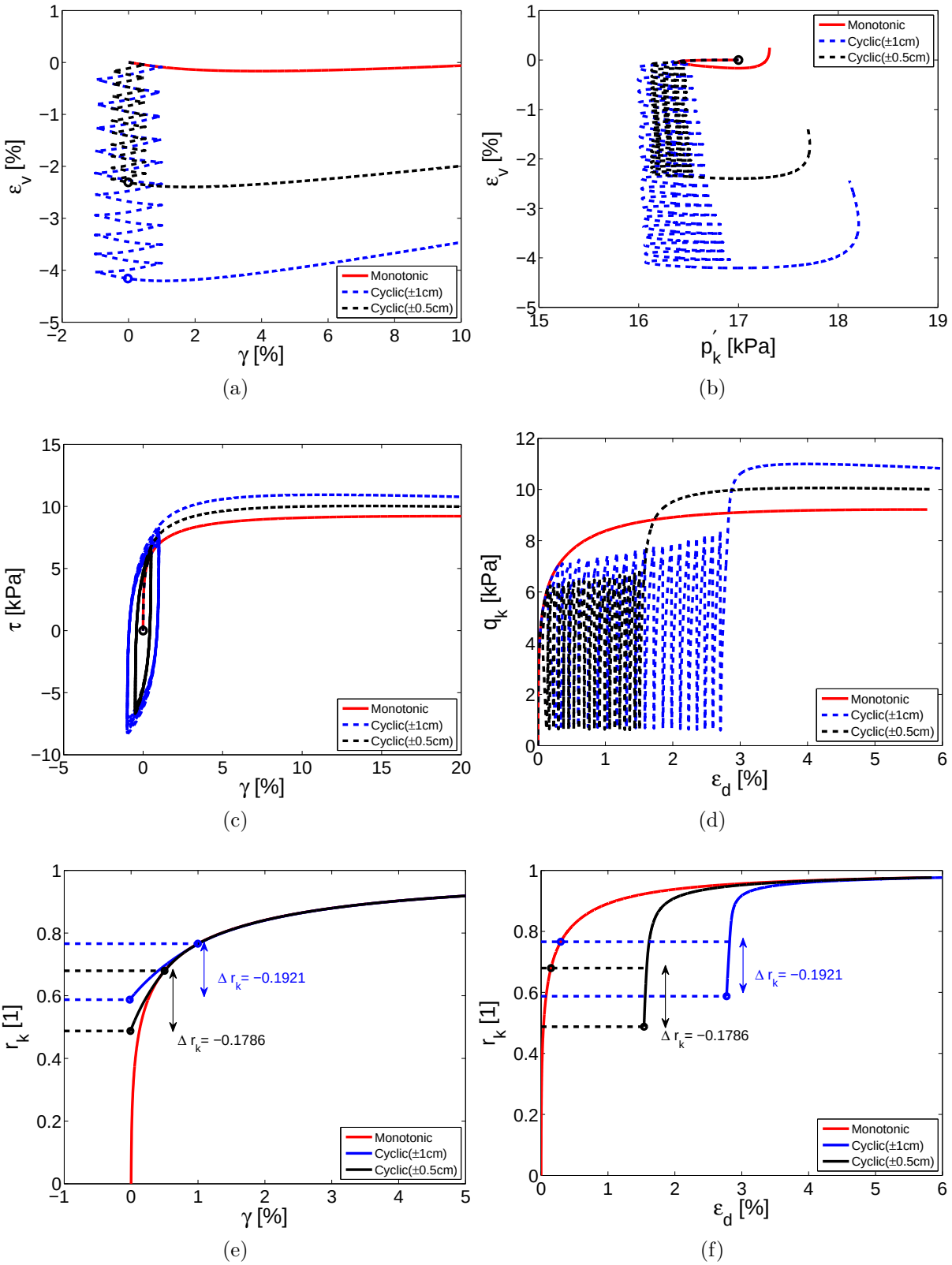

Figure 5.15: Response of one soil element under shear test: a) ε_v-γ, b) ε_v-p'_k, c) τ-γ, d) q_k-ε_d, e) evolution of r_k as function of shear strains, f) evolution of r_k as function of deviatoric strains.

5.2.3.2 Safety factor of embankment - foundation model

In this section the parameter r_k is calculated for the embankment - foundation model and for the sake of brevity, only results of the mesh 4 (25cm) are presented, as the response of all meshes is identical. During the mainshock (t=3.5s), the same circular surface of collapse is remarked close to the embankment's slope in Figure 5.16b. Compared to the initial state (Figure 5.16a), the r_k increases from 0.5 (green color) to 0.8 (yellow color) inside the slope, i.e. the local safety factor (FS=$1/r_k$) decreases from 2 to 1.25. At the end of the ground motion (Figure 5.16c), the soil has regained its strength ($r_k \simeq 0.5$) and only close to the slope of the embankment greater values of r_k appear (with yellow color $r_k \simeq 0.8$, i.e. FS$\simeq$1.25).

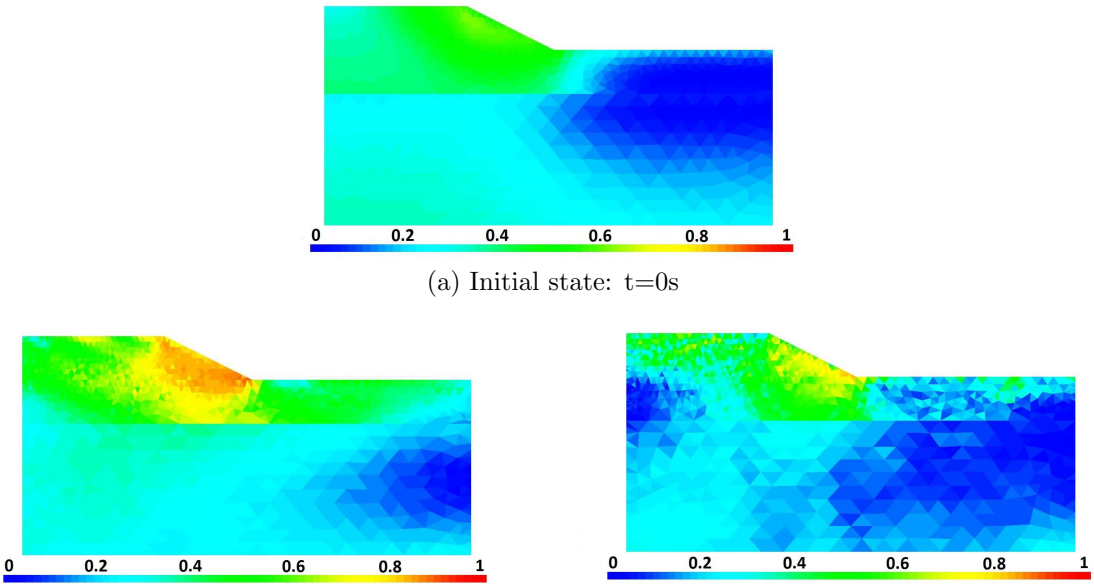

(a) Initial state: t=0s

(b) Mainshock: t=3.5s

(c) End of earthquake: t=17s

Figure 5.16: Contours of residual strength, r_k, for mesh 4 (25cm) during Friuli earthquake.

Contrary to the instability criterion of second order work (Section 5.2.2.3), r_k represents the cumulated response of the soil, as it takes into account soil degradation due to earthquake. Consequently $\Delta r_k = r_k(t)$-$r_k(t_0)$ provides an index of co-seismic soil's residual strength and refers only to earthquake-induced soil degradation, i.e. difference between initial state before the ground motion (Figure 5.16a) and during the ground motion (Figure 5.16b, 5.16c).

The contours of Δr_k are plotted in Figure 5.17 during the mainshock and at the end of the motion. During the mainshock, the right part of the embankment and the upper part of the foundation have significantly lost strength (red color in Figure 5.17a), forming the circular surface of eventual collapse. At the end of the motion in Figure 5.17b, the soil has regained partially its strength at the surface of the embankment (negative values of Δr_k in blue color), but still at the toe and at the left part of the embankment, as well as at FF, the soil remains degraded (positive values of Δr_k in yellow and red color).

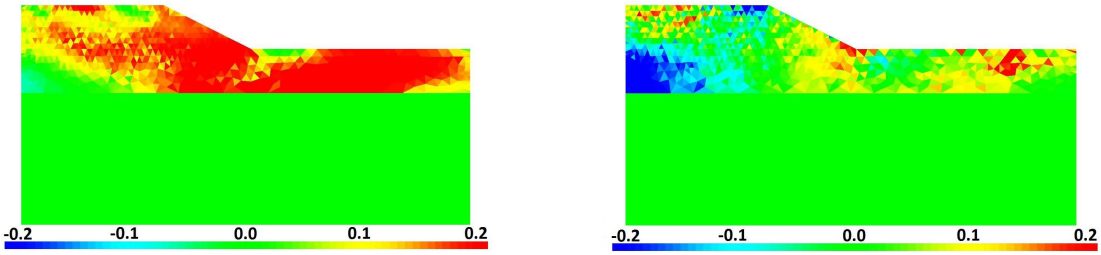

(a) t=3.5s (b) t=17s (end)

Figure 5.17: Contours of co-seismic residual strength, Δr_k, for mesh 4 (25cm) during Friuli earthquake.

5.2.3.3 Comparison of FE results with simplified methods

In this section, the predicted displacements using some of the aforementioned simplified methods are compared to the results of the FE simulation with mesh 4 (25cm) for all the input motions of the parametric analysis. The simplified methods considered are the following:

- The chart-based method developed by Makdisi and Seed (1978), which provides a range of the value of displacement:

$$\frac{u}{k_{max} \cdot g \cdot T_p} = f\left(\frac{k_c}{k_{max}}\right) \tag{5.3}$$

  where u is in m, k_c and k_{max} are the critical and peak seismic coefficients, respectively, and T_p the fundamental period of the structure.

- The relation developed by Ambrasseys and Menu (1988), which provides the median value of displacement:

$$\log u = 0.9 + \log\left[\left(1 - \frac{k_c}{k_{max}}\right)^{2.53} \cdot \left(\frac{k_c}{k_{max}}\right)^{-1.09}\right] \tag{5.4}$$

  where u is in m, k_c and k_{max} are the critical and peak seismic coefficients, respectively.

- The relation developed by Jibson (1994) providing the median value of displacement:

$$\log u = 1.460 \cdot \log I_{Arias} - 6.642 \cdot k_c + 1.546 \tag{5.5}$$

  where u is in cm, I_{Arias} is the arias intensity of the input signal and the critical seismic coefficient k_c.

For this particular model, a critical failure surface is estimated according to the values of the apparent friction angle ϕ'_{apt} calculated in the previous section, as shown in Figure 5.18. The critical coefficient k_c is the unitless equivalent of the yield acceleration a_c ($k_c =$

a_c/g), while the peak seismic coefficient k_{max} is the uniteless equivalent of the maximum acceleration and is defined as k_{max}=PGA/g.

According to the research work of Andrianopoulos et al. (2014) and the proposals of Makdisi and Seed (1978), to better estimate the peak seismic coefficient k_{max}, the wave propagation inside the slope should be taken into account. Thus, an acceleration close to the failure surface, instead of the crest's PGA, should be considered. In the current study, the maximum acceleration measured at the base of the embankment is used (PGA_{base}).

For the critical seismic coefficient k_c, two different values are considered. Firstly, k_c is supposed to be equal to 0.5·PGA/g, according to the value provided by EC8 and American regulations NCHRP 12-70 (Anderson et al., 2008) / FHWA 2011 (Kavazanjian et al., 2011) for ductile materials. Next, following the British standards (Charles et al., 1991; Gosschalk et al., 1994) a value of k_c=0.67·PGA/g is applied. Concerning the value of PGA chosen for the critical seismic coefficient, following the recommendations of the American regulations NCHRP 12-70 (Anderson et al., 2008) / FHWA 2011 (Kavazanjian et al., 2011), the maximum average acceleration (MHA) of the estimated failure surface is considered. Both values of k_c (0.5 or 0.67) provide a good estimation of the yield acceleration, as demonstrated by Andrianopoulos et al. (2014) through a parametric study.

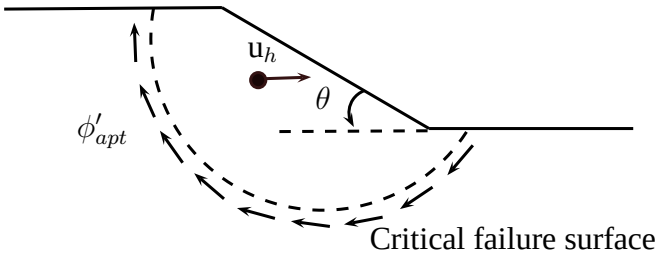

Figure 5.18: Estimation of critical failure surface of the embankment - foundation model.

As shown in Figure 5.18, a point at the center of the sliding block is chosen and its relative displacement to a reference point at FF (P4 of Figure 5.1) at the end of the ground motion is compared to the predicted one. In Figure 5.19 the diplacements obtained by the FE simulation are compared to those calculated by the above three equations for both values of seismic coefficients proposed by the different codes.

Concerning the choice of the critical seismic coefficient, globally the proposals of EC8 and American regulations standards are more coherent by providing a good estimation of displacements (Figure 5.19a), as also commented by Andrianopoulos et al. (2014). Comparing the different methods for displacement prediction in Figure 5.19a, the one of Makdisi and Seed (1978), which accounts for the characteristics of the ground motion and structure, predict displacements closer to those of the FE model, as underlined by Andrianopoulos et al. (2014), too. While the equation of Jibson (1994) mostly overestimates the displacement of the rigid block, the one of Ambrasseys and Menu (1988) overestimates the displacement in case of low or moderate motions and gradually as the input acceleration increases it slightly underestimates the response. The differences between the results obtained by the simplified methods and FE simulation are due to the uncertainties on the critical surface prediction and the empirical determination of the equations, as already discussed by Duncan and Wright (1980), Kramer (1996), Kourkoulis et al. (2010).

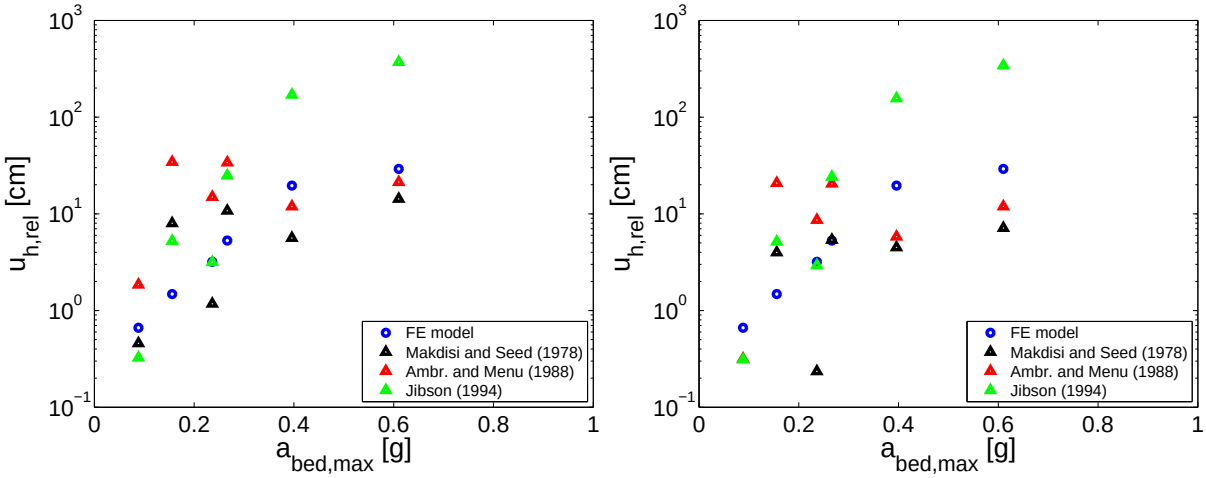

(a) (b)

Figure 5.19: Comparison of FE results with the predicted permanent diplacements from empirical simplified methods according to: a) EC8 / American regulations, b) British standards.

5.3 Liquefaction-induced failure of embankment - foundation system

Several studies have analyzed earthquake triggered landslides and the effect of ground-shaking on foundation-structure systems founded near slope crests. However, the presence of water dramatically alters soil behavior. Liquefaction is commonly observed in saturated cohesionless soils during earthquakes, where the strength and stiffness are significantly reduced by the generation of excess pore water pressure. In loose sands, the tendency of densification causes the excess pore water pressure to increase and the effective stresses to decrease. As the soil stiffness decreases, so does the effective shear-wave velocity and the predominant frequency shifts to lower values. Similarly, as the strains increase, the energy dissipation increases and the soil amplification will be reduced causing a "strong-motion deamplification effect" (Beresnev and Wen, 1996; Montoya-Noguera and Lopez-Caballero, 2015). Excessive vertical settlement, lateral spreading and even soil failure are considered as the most important consequences of liquefaction.

From California's earthquake in 1971, where the Lower San Fernando Dam collapsed (Seed et al., 1975b), until recently during the 2010 Maule earthquake in Chile and 2011 Tohoku earthquake in Japan (Oka et al., 2012; Ishikawa et al., 2015), liquefaction-induced failures of earth structures have been reported (Ozutsumi et al., 2002; Verdugo et al., 2012; Okamura et al., 2013). More than 170 sites, mainly associated with natural ground and covering an extension of 1000km, were affected by soil liquefaction after the 2010 Maule earthquake in Chile (Verdugo and González, 2015). While during Tohoku earthquake, wide-spread occurrence of liquefaction in an area more than 350km distant from the epicentre was observed, especially in man-made fill associated with reclaimed land (Ishihara, 2012; Verdugo and González, 2015).

In most cases of foundation's liquefaction, shear localization phenomena are initiated in the liquefied region, as well as within geostructures combined with large settlements and eventual lateral spreading (Okamura et al., 2013; Sadeghi et al., 2014; Ishikawa et al., 2015). The influence of foundation's soil type and earthquake's amplitude have proven to be critical (Ozutsumi et al., 2002; Adalier and Sharp, 2004; Xia et al., 2010; Maharjan and Takahashi, 2014).

In common practice, coupled HM effective stress analysis is used to evaluate the liquefaction-induced soil failure. In this work two types of analyses are conducted, a coupled analysis where excess pore water pressure generation is taken into account and a fully drained one with no pore water pressure generation. In the light of this comparison, the importance of a coupled analysis is highlighted, as it can capture the mechanism of progressive slope failure and the influence of the liquefiable foundation on the path of the generated failure zone.

In order to determine the collapse mechanism due to soil liquefaction, the same plane-strain FE model of the embankment-foundation system is built, but in this case the foundation consists of a liquefiable soil layer. Two different materials are used for the embankment to assess the influence of structure's soil quality in the response of the system. Both fully drained and undrained saturated conditions are analyzed. The first section is dedicated to the description of the numerical model. Next, the parametric dynamic analysis of the embankment is presented for both materials and simulations. By contrast to the fully drained analysis where the pore pressure generation is neglected, in the coupled effective stress analysis, the liquefaction-induced failure is predominant. Finally, a mesh sensitivity study is conducted and the effect of the input motion's characteristics is also discussed based on findings of Section 3.4.

5.3.1 Problem statement

The earthquake-induced failure path of earth structures is investigated through a parametric study of an embankment resting on a soil foundation and subjected to several earthquake motions. The effect of excess pore water pressure generation and earthquake-induced liquefaction on the dynamic response of the structure-foundation system are discussed.

Four parametric studies are conducted simultaneously to clarify the influence of the following parameters on the failure mode of the model:

- Embankment's soil type: a rigid and a soft embankment are simulated (refer to Section 5.3.2.2).
- Mesh sensitivity of results: 3 meshes with different refinement (refer to Section 5.3.2.3).
- Pore water pressure generation: fully drained and coupled effective stress analyses (refer to Section 5.3.2.4).
- Input earthquake motions: several ground motions are used in all aforementioned simulations (refer to Section 5.3.2.5).

5.3.2 Numerical model of dry embankment resting on liquefiable foundation

5.3.2.1 Geometry - Boundary conditions

The same dry embankment presented in section 5.2.1.1 is now placed over a loose-to-medium contractive saturated sand (LMS) layer and the water table is situated 1m below the embankment. A dense saturated substratum exists at the bottom part of the foundation. The dimensions of the model and its geometry are presented in Figure 5.20. As previously, the rigid box model is used where no water flux is possible at the lateral surfaces and the base. Note that the embankment remains always dry.

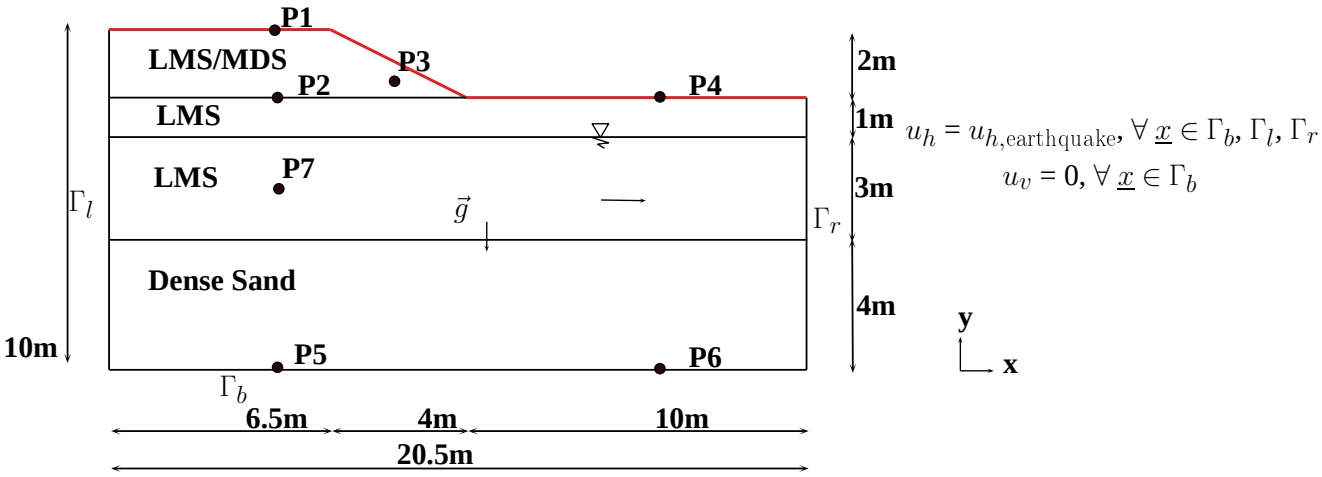

Figure 5.20: Illustration of numerical model.

5.3.2.2 Soil characteristics

Concerning the parametric analysis for the embankment's soil type, in the first model the dry embankment is composed of a dilative medium-to-dense sand (MDS), while in the second one, the contractive loose-to-medium sand (LMS) is used. The soil parameters can be found in Table B.1 in Appendix B.6.

Several tests are conducted in order to observe soil behavior at confining pressures corresponding to the average geostatic pressure of each layer, i.e. 17kPa and 45kPa for the dry MDS and LMS, and 60kPa for the saturated LMS. Figures 5.21a and 5.21b show deviatoric stress - strain and volumetric - deviatoric strain curves for both materials used in the embankment under drained triaxial test simulations. $G/G_{max} - \gamma$ and $D - \gamma$ curves are also generated after shear cyclic drained test simulation for the LMS (Figure 5.21c and 5.21d) to observe soil behavior under cyclic loading. The curves are in good agreement with the reference curves given by Seed and Idriss (1970). Finally, the liquefaction curve for the LMS is provided in Figure 5.22 after triaxial cyclic undrained test. The results match relatively good with the experimental ones provided by Byrne et al. (2004), which correspond to the liquefaction response of Nevada sand for a range of relative densities. The response of the dense sand (Dense sand 1 of Table B.1) of the substratum is omitted

as it is not affected by the dynamic analysis. However, the curves of one soil element tests and its parameters can be found in Appendix B.6.

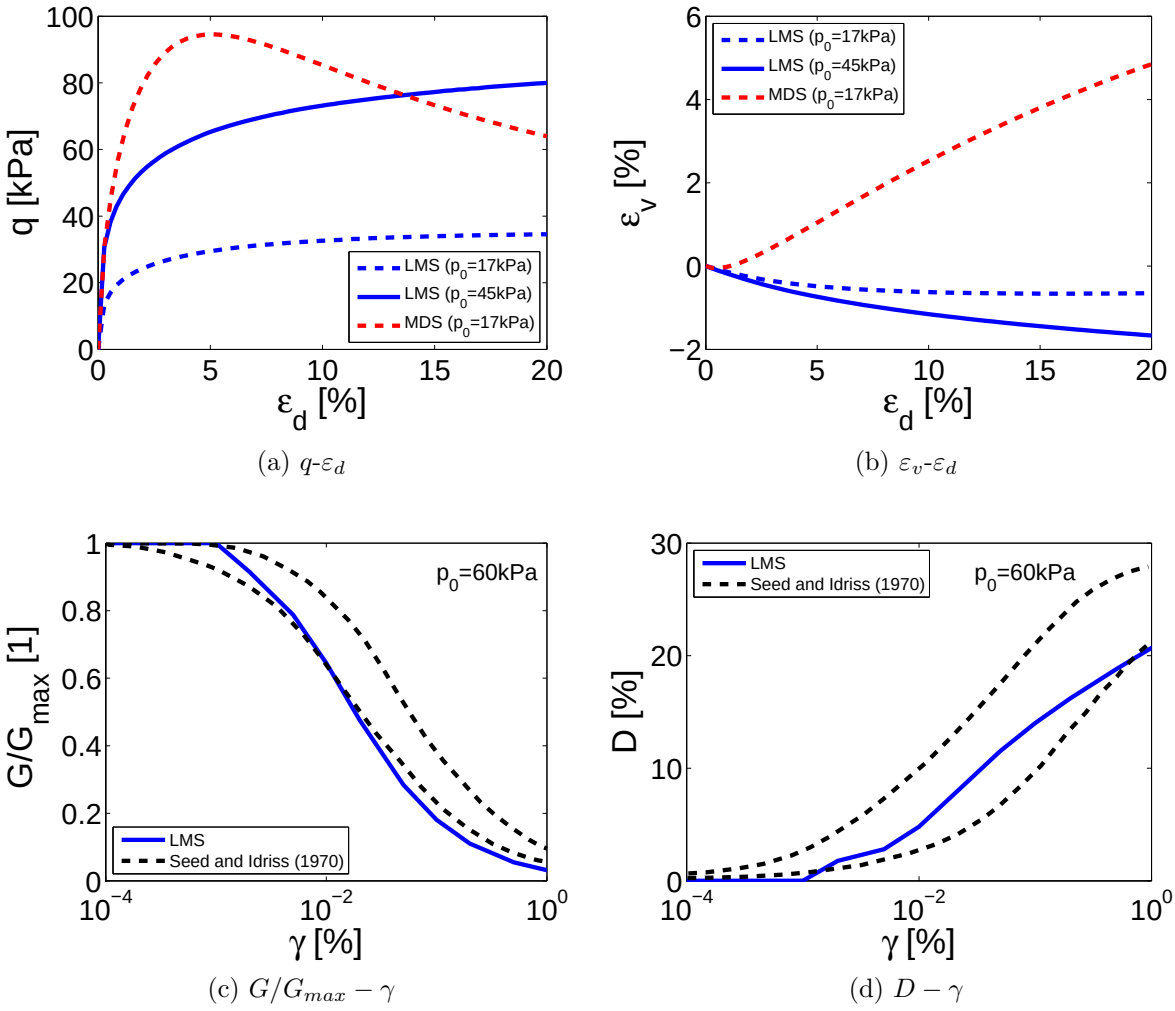

(a) q-ε_d (b) ε_v-ε_d

(c) $G/G_{max} - \gamma$ (d) $D - \gamma$

Figure 5.21: Soil response of one material point under: a,b) triaxial drained test and c,d) shear cyclic drained test compared to Seed and Idriss (1970).

5.3.2.3 Numerical parameters

The mesh 4 (25cm), which consists of 6-node triangular elements of 0.25m length on average (Figure 5.4d) is considered as the reference case. Only in the section of the mesh sensitivity analysis (Section 5.3.4) the other two meshes will be used (mesh 2 (10cm) of Figure 5.4b and mesh 5 (50cm) of Figure 5.4e).

As before, the implicit Newmark integration method is used for the dynamic analysis with a time step equal to Δt=10^{-3}s and numerical damping equal to $\xi = 0.2\%$ is added. The low-strain frequency analysis provides a fundamental elastic period for the structure-foundation system equal to T_p=0.1s (i.e. f_p=10Hz for the LMS model) (Figure 5.23). In this particular model the response Crest-Bedrock is obtained from the Borehole Transfer

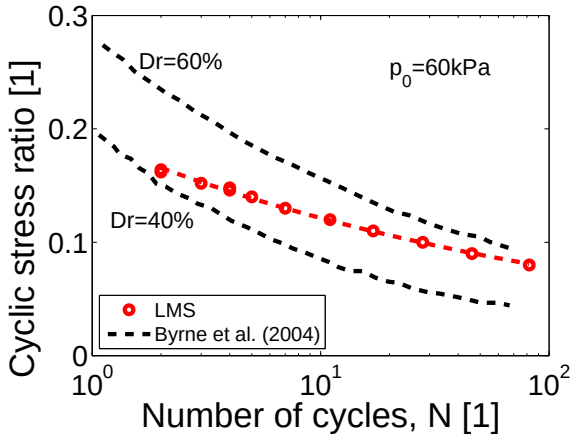

Figure 5.22: Soil response of one material point under triaxial cyclic undrained test: Liquefaction curve compared to Byrne et al. (2004).

Function between points P1-P5 of Figure 5.1, while Base-Bedrock and FF-Bedrock FF refer to points P2-P5 and P4-P6, respectively. Note that both fully drained and coupled simulations have the same fundamental frequency, as expected.

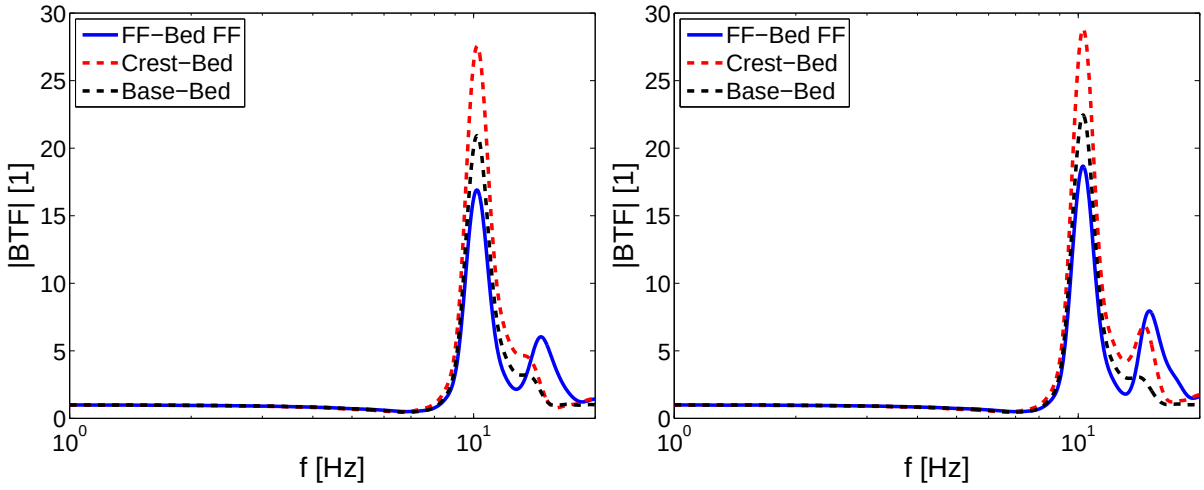

Figure 5.23: Transfer function of embankment - foundation system: a) Fully drained, b) Coupled simulation.

5.3.2.4 Hydraulic behavior

A fully coupled effective stress dynamic approach using the $\underline{u}$-p_w formulation derived from Biot's theory for incompressible solid - compressible fluid is used, as explained in Chapter 2.2 (Equations 2.10, 2.11). Two different simulations are performed, one fully drained, where no pore water pressure is generated, and one coupled effective stress analysis to evaluate the effect of liquefaction, as proposed by Montoya-Noguera and Lopez-Caballero

(2015). Note that the fully drained simulation is completely different from a dry one, as the existence of the water and its mass is taken into account for the inertial terms and using the effective stresses. However, as the permeability of the material is supposed to reach infinity ($k_s \rightarrow \infty$), the corresponding terms of equation 2.11 are zero and consequently the equation vanishes. The hydraulic parameters of each material are presented in Table 5.1. To simulate the fully drained analysis, a very large value of k_s is used for both materials (k_s=1m/s). For the coupled approach a permeability equal to k_s=1·10^{-4}m/s is used for the LMS material and corresponds to a typical clean sand of medium permeability (Bardet, 1997). This characterization is based on the relation of permeablity with particle size and void ratio established by NAVFAC (1982) and on the classification of soils after Terzaghi and Peck (1967). For the needs of FE modeling, the value of fluid compressibility used, is higher than the real one of water, as explained in Section 3.2 and Appendix D.

Table 5.1: Hydraulic parameters for the soil.

Parameter	Foundation (LMS)	Foundation (Dense sand)
Fluid mass density, ρ_w [kg/m^3]	1000	1000
Porosity, n [1]	0.35	0.35
Permeability, k_s [m/s]	1·10^{-4}	1·10^{-5}
Fluid compressibility, H_w [Pa^{-1}]	9.35·10^{-8}	9.35·10^{-8}

5.3.2.5 Input earthquake motions

In order to evaluate the dynamic response of the embankment due to the liquefiable foundation and following the liquefaction vulnerability analysis of the soil column (Section 3.4), input ground motions of various amplitude, frequencies, origin (soil or rock site) and type (pulse-like or non pulse-like) is performed. Due to excessive evolution of CPU time with the duration of the input signal for the dynamic analysis of the embankment-foundation model (refer to Appendix I.2), the ground motions used are limited to the 24 following ones:

- 2 ground motions recorded on soil site from the italian database *itaca* (irsn60, irsn168)
- Friuli earthquake (Italy, 1976) from PEER database
- 10 real non pulse-like moderate ground motions recorded on soil site (T1a 1-10) from PEER database (Iervolino and Cornell, 2005)
- 10 real pulse-like ground motions (Pa/b 1, Pa/b 2, Pa/b 3, Pa/b 4, Pa/b 5) recorded mostly on rock site from PEER database (Baker, 2007)
- 1 synthetic strong ground motion generated by real motion recorded on soil site (GVb 1) (Dickinson and Gavin, 2011; Gavin and Dickinson, 2011)

The characteristics of the motions used can be found in details in Appendix C. Note that all input and outpout signals have a baseline correction and are filtered using a non-causal bandpass filter of order 4, between 0.1-20Hz.

In Figure 5.24 the response spectra of all input motions are plotted with damping ξ=5% and the fundamental frequency f_p of the structure-foundation system is indicated. For the sake of brevity, the results of Friuli earthquake in 1976 in Italy are discussed in detail in the next section, as previously (Figure 5.5) and its response spectrum is colored in blue in Figure 5.24.

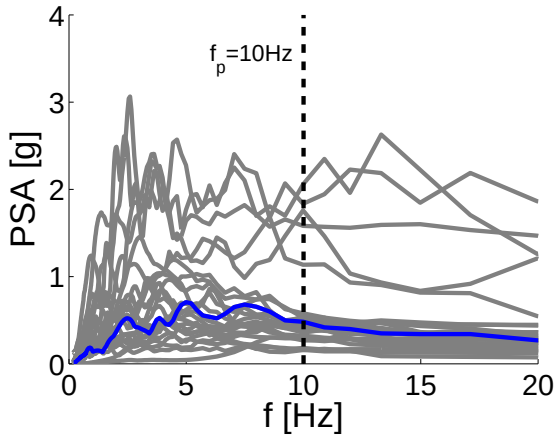

Figure 5.24: Response spectra of input ground motions (ξ=5%) and Friuli spectrum in blue color (the system's fundamental frequency is illustrated with the dashed line).

5.3.3 Typical dynamic response of fully drained and coupled HM model

In the following sections and in order to assess the collapse surface and the onset of failure of the global structure-foundation system, the model with the soft embankment (LMS) is considered as reference case in both simulations, because it is strongly affected by a wide range of ground motions. As aforementioned, the results of Friuli earthquake for the LMS model are discussed, unless otherwise mentioned. Then, its response is compared with the rigid embankment (MDS) to report the significant influence of structure's soil quality.

In the fully drained analysis, the foundation is not severely influenced by the earthquake and mostly the dynamic response of the embankment is evaluated. However in the case of coupled effective stress approach, the excess pore water pressure generation in the foundation has noticeable implications for both the foundation and the superstructure. The liquefied soil at the foundation creates an extended failure zone. The LMS model is led to failure for a certain level of input ground motion. Soil liquefaction was observed for moderate and strong input ground motions with $a_{bed,max}$ >0.2g, while for motions of $a_{bed,max}$ >0.4g, the whole system collapses (i.e. excessive displacements are observed and the simulation stops due to convergence issues). As it concerns the lower motions, where the pore water pressure generation is negligible, the dynamic response of both models is similar to that of the fully drained analysis, as discussed by Montoya-Noguera and Lopez-Caballero (2015).

The MDS embankment is very rigid and remains almost unaffected by all ground motions, so no failure path can be determined. Nevertheless, in case of coupled analysis

the embankment-foundation system collapses due to liquefaction for moderate and strong ground motions.

In both simulations the soil behavior is the same initially, as the initial stress state is identical. In the fully drained approach the initial stresses under the water level are computed according to the submerged weight of the material. The model has a total average unit mass equal to the coupled model, so the weight of the water contributes to the dynamic soil response. No excess pore water pressure is generated, contrary to the coupled simulation, where pore water pressure generation is taken into account (for further details refer to Montoya-Noguera and Lopez-Caballero (2015) where a complete study of fully drained and coupled approaches is presented). Thus, both dynamic simulations start from the same effective stress state, as shown in Figure 5.25.

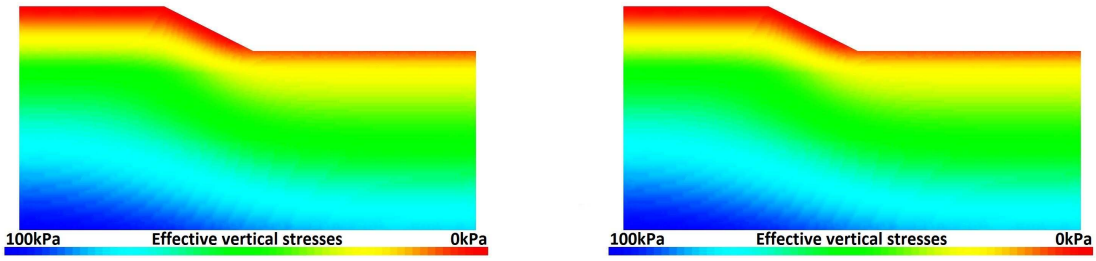

(a) (b)

Figure 5.25: Initial vertical effective stresses $\sigma'_{v,0}$ (in kPa) for LMS model: a) Fully drained effective stress simulation, b) Coupled effective stress simulation.

Both simulations provide the same material state initially, before the beginning of the ground motion, as evaluated through the parameter r_k in Figure 5.26 (for further details of this parameter refer to Section 5.2.3). Due to the excavation in the right upper part, noticeable values of r_k appear close to the embankment's slope (i.e. $r_k \simeq$0.4-0.6 and FS$\simeq$2.5-1.6).

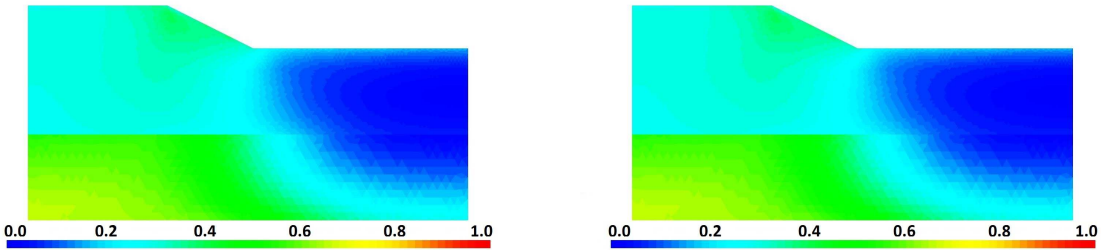

(a) (b)

Figure 5.26: Contours of residual strength, r_k, before the ground motion (LMS model): a) Fully drained effective stress simulation, b) Coupled effective stress simulation.

5.3.3.1 Excess pore water generation

In order to define soil liquefaction in the coupled effective stress simulation, the excess pore water pressure ratio is used, defined as r_u=$\Delta p_w/\sigma'_{v,0}$. To take into account both "true liquefaction" (i.e. r_u=1.0) and cyclic mobility (i.e. 0.7< r_u <1.0 with development of large strains), it is assumed that liquefaction appears when r_u is greater than 0.8 (Lopez-Caballero and Modaressi-Farahmand-Razavi, 2013).

During the main shock of each motion excess pore water pressure (Δp_w) is generated in the liquefiable layer of the foundation. The contours of r_u, plotted in Figure 5.27, show that the foundation liquefied (i.e. $r_u > 0.8$) during the mainshock (t=2-5s). The evolution of Δp_w can be related to Arias intensity (Figure 5.5b), as between t=2-5s almost the total intensity of the motion has been accumulated (95% of I_{Arias}). Progressively, the dissipation of pore water pressure starts, as the amplitude of the ground motion decreases (coda phase, i.e. last seconds of the ground motion where the amplitude decreases) and it has almost completely dissipated at the end of the ground motion (Figure 5.27b). Note that the fast pore water dissipation may be attributed to the value of permeability chosen (k_s=1·10^{-4}m/s, i.e. permeable soil).

For lower motions, liquefaction is not reached ($r_u < 0.3$), while for stronger ones the whole foundation was liquefied and reached r_u=1.0. In all cases, the dissipation of pore water pressure was completed during coda phase or some seconds after the end of the ground motion. The same response was obtained for the MDS model, but the zone of liquefied soil was sligthly thinner.

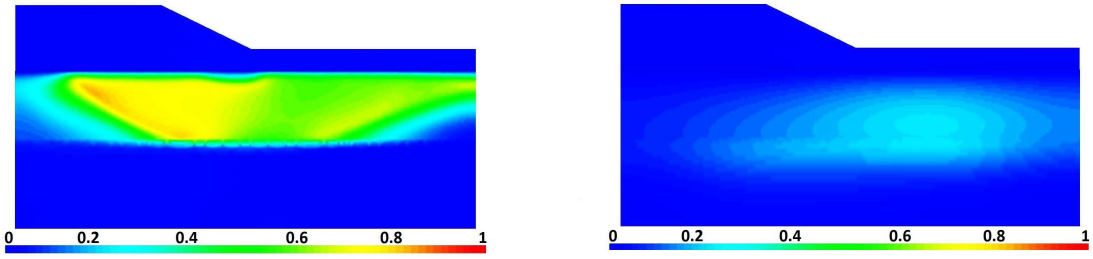

(a) t=3.5s (b) t=17s (end)

Figure 5.27: Excess pore water pressure ratio (r_u) during Friuli earthquake (LMS model).

5.3.3.2 Displacement

In the fully drained simulation, horizontal displacement is detected superficially at the slope and settlement occurs at the upper part of the embankment, as shown in the deformed shape of Figures 5.28a and 5.28b at the end of the motion. As the embankment is assymetric and constrained at the left boundary, it tends always to move to the right.

Nevertheless, in the case of coupled effective stress simulation, in both models (LMS / MDS) almost the whole embankment settles and moves to the right, while a large part of the foundation moves to the right and swells due to the excess pore water pressure (see deformed shape of Figures 5.28c and 5.28d). Contrary to the fully drained analysis, horizontal displacement is observed in the foundation part also due to liquefaction and a

circular failure mode is implied. This circular sliding surface is defined as lateral spreading, one of the most important consequences of soil liquefaction. Especially in the LMS model during the stronger motions, excessive displacements and settlements are remarked and the embankment-foundation system completely collapses.

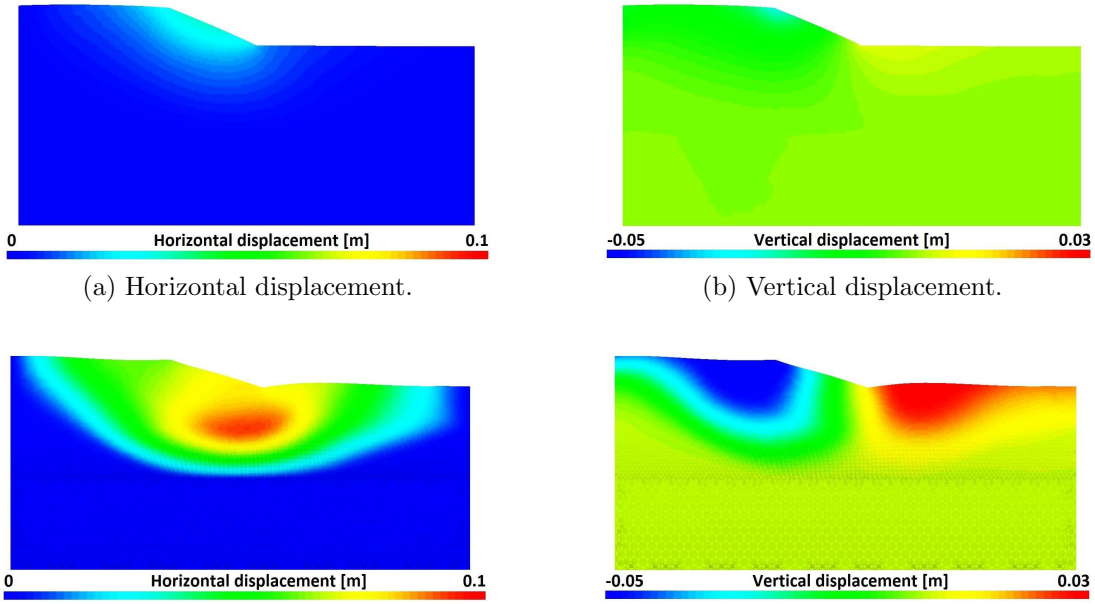

(a) Horizontal displacement.

(b) Vertical displacement.

(c) Horizontal displacement.

(d) Vertical displacement.

Figure 5.28: Deformed shape at the end of Friuli earthquake (LMS model): a,b) Fully drained effective stress simulation, c,d) Coupled effective stress simulation.

5.3.3.3 Acceleration

In Figure 5.29, the horizontal and vertical PGA along the top surface (red line in Figure 5.20) are plotted for Friuli earthquake and compared for both simulations. In the fully drained analysis an amplification of vertical acceleration is observed in Figure 5.29b. Even if vertical waves are not imposed to the model, due to both geometry and degradation of material important values of vertical acceleration appear, notably in case of fully drained approach. The important values of vertical PGA in the coupled approach in Figure 5.29b that appear close to the lateral boundaries may be due to the condition of zero flux at the boundaries.

The evolution of horizontal acceleration at the selected point at the crest (P1) is plotted in Figure 5.30a. While at the beginning of the ground motion the accelerograms coincide, during and after the mainshock in the coupled simulation smaller values of acceleration appear due to soil liquefaction, as already explained. Furthermore, observing the Fourier Transfrom of the horizontal acceleration for both simulations in Figure 5.30b, it is remarked that differences appear in the low frequencies, i.e. liquefaction state.

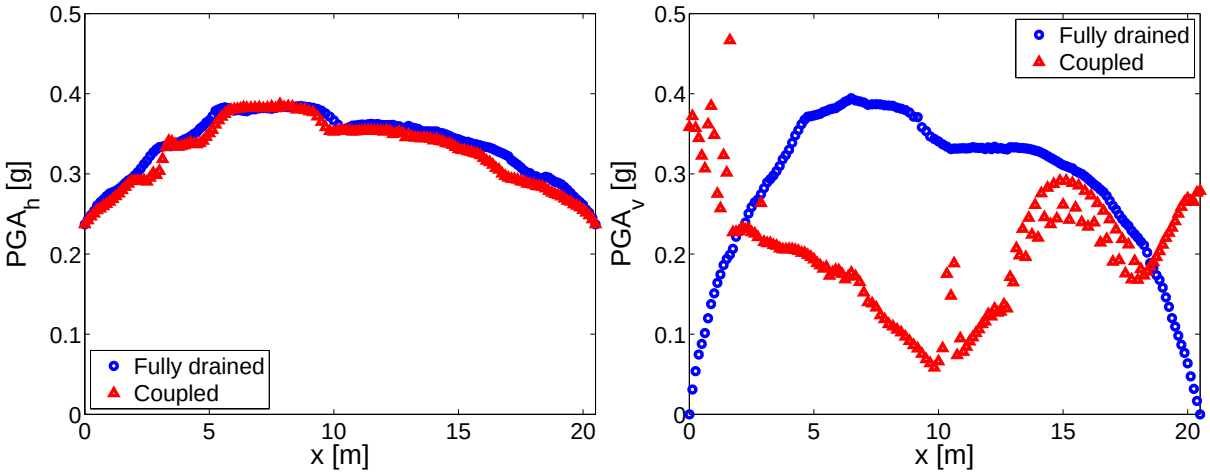

(a) (b)

Figure 5.29: PGA along the top surface after Friuli earthquake (LMS model): a)Horizontal, b)Vertical.

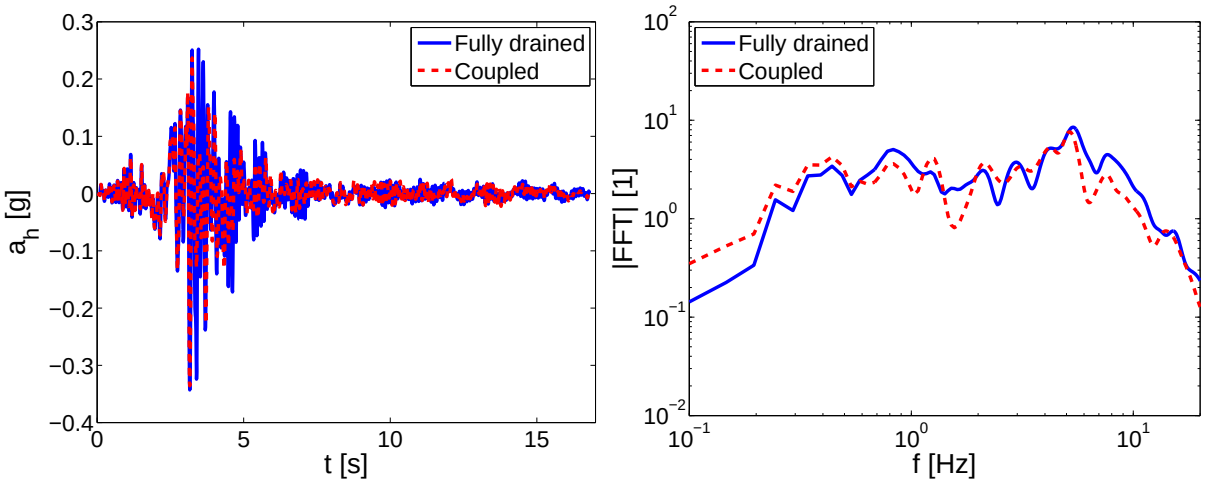

(a) (b)

Figure 5.30: Dynamic response measured at the crest (P1) after Friuli earthquake (LMS model): a) Horizontal acceleration, b) Fourier Transform of horizontal acceleration.

5.3.3.4 Stability

It is widely accepted that liquefaction is an instability and it can occur under static or dynamic conditions. Several researchers have shown the unstable behavior of the material and proposed instability criteria for defining the onset of soil liquefaction (Lade, 1994; Borja, 2006; Andrade et al., 2013; Mohammadnejad and Andrade, 2014). As evoked in Section 5.2.2.3, the stability of the embankment is tested by calculating the second order work density ($d^2W=\dot{\sigma}'_{ij}:\dot{\varepsilon}_{ij}/|\dot{\sigma}'_{ij}||\dot{\varepsilon}_{ij}|$) (Hill, 1958; Hamadi et al., 2008; Buscarnera and di Prisco, 2012).

In the fully drained approach, instabilities appear for the LMS model close to the slope instantaneously, only in case of stronger motions. For the sake of brevity, the figures are omitted as no important information is provided. On the other hand, in case of coupled approach, during the liquefaction phase (t=2-5s), both the embankment and foundation become unstable ($d^2W < 0$, blue color in Figure 5.31a). A circular surface of instability appears in both models (LMS/MDS) which implies the identified failure mode of the structure-foundation system due to liquefaction. At the end of the motion the system becomes stable ($d^2W > 0$, red color in Figure 5.31b). As the criterion is not cumulative, the stability at the end is instantaneous and does not mean that the structure-foundation system is not susceptible to deform again with another loading. Note that the instability is more significant in the LMS model during the ground motion, as almost the whole embankment is unstable for both moderate and strong input motions, even if at the end of all earthquakes it becomes stable.

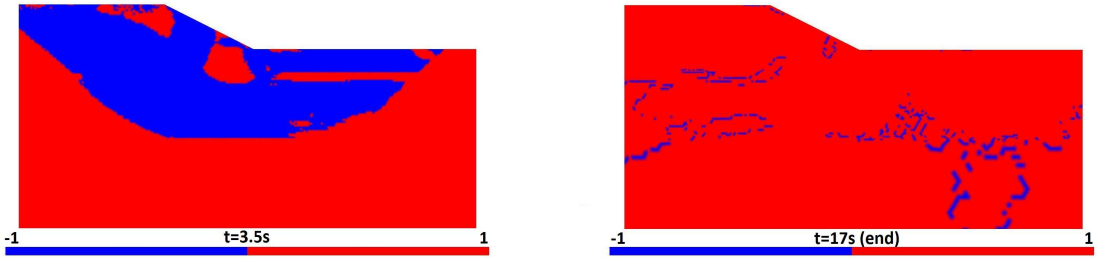

(a) Mainshock: t=3.5s (b) End of earthquake: t=17s

Figure 5.31: Contours of second order work sign during Friuli earthquake (LMS - Coupled effective stress simulation).

5.3.3.5 Shear deformations

The crucial difference between the soft and rigid model (LMS/MDS) is remarked in terms of shear strains generation for moderate and strong ground motions. In the fully drained approach, as expected, a shear band initiates at the toe of the LMS embankment and extends to the crest due to geometry heterogeneity at the base of the slope for all ground motions (Figure 5.32a, zoom of the shear band in Figure 5.32b). For the stronger motions, the level of shear strains increases significantly and the shear band generation is considered as an index of embankment's local collapse.

However, in the coupled approach of the LMS model, two different zones of shear deformations are noticed (Figure 5.32c). Due to the liquefaction at the upper foundation part, an extended zone of shear strains appears. Moreover, a shear band is clearly observed inside the embankment body extending from toe to crest, as detected previously in the fully drained approach. Even for lower motions, where no liquefaction-induced deformations are generated, the shear band in the embankment body is always obvious. Moreover, noticeable influence of the fixed boundary condition hypothesis is identified in the left part of the embankment, as alreary mentioned due to the important values of vertical PGA in Figure 5.29b. For stronger motions, instead of the shear band inside

the embankment, the whole part of the liquefied layer in the foundation reaches values of deviatoric strains close to 25%.

Concerning the rigid MDS embankment, in the fully drained simulation no noticeable deformations appear and no shear band generation is observed, consequently the corresponding figure is omitted. Contrary to the fully drained case, in the coupled simulation a concentration of shear strains is observed in the upper foundation part due to liquefaction (Figure 5.32d). This thick shear zone extends through the liquefied soil and leads to the aforementioned circular failure mode of the structure-foundation system. Note that the MDS embankment remains almost unaffected, as previously, and the collapse is driven by the liquefied foundation.

It should be mentioned that as the simulations performed use the hypothesis of small deformations, values of deformations greater than 5% are approximate. The results of shear strains in Figure 5.32 should be treated as qualitative and are used to evaluate the progressive failure mechanism of the system.

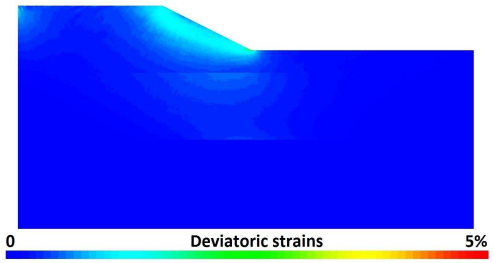

(a) LMS

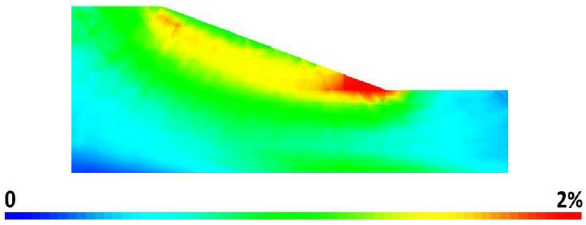

(b) LMS - Zoom of shear band.

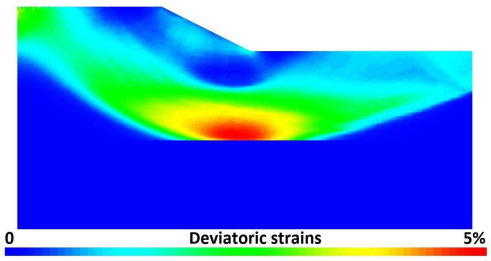

(c) LMS

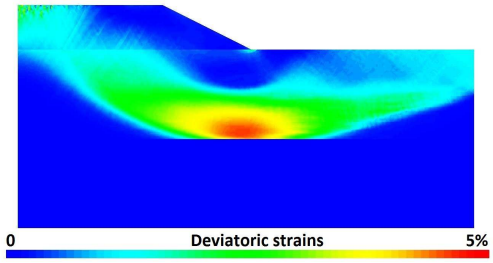

(d) MDS

Figure 5.32: Deviatoric strains ε_d at the end of Friuli earthquake: a,b) Fully drained effective stress simulation, c,d) Coupled effective stress simulation.

To sum up, in case of coupled simulation with a loose embankment and for a certain level of ground motion, the failure comes from both the structure and the foundation. First, a shear band is generated inside the embankment due to the geometry heterogeneity and then, a diffuse zone in the liquefied foundation leads to the circular failure mode.

5.3.3.6 Residual strength

Concerning soil's residual strength, the parameter r_k is used, as explained in depth in Section 5.2.3.1. For the sake of brevity, only results of the coupled approach are discussed,

as soil liquefaction led to noticeable displacements and instabilities of the structure-foundation system and affected material's behavior.

In Figure 5.33a during the mainshock (t=3.5s) and while liquefaction is reached (r_u=0.8), the same circular surface of collapse is remarked (Figure 5.31a), as r_k is close to 0.8 (i.e. FS=1.25). The two different failure paths defined according to the generated shear bands in Figure 5.32c, one inside the liquefied foundation and a second one close to the slope, are also observed in the contours of r_k. At the end of the ground motion (Figure 5.33b), the soil has regained partially its strength, as $r_k \simeq$0.6, i.e. FS$\simeq$1.6.

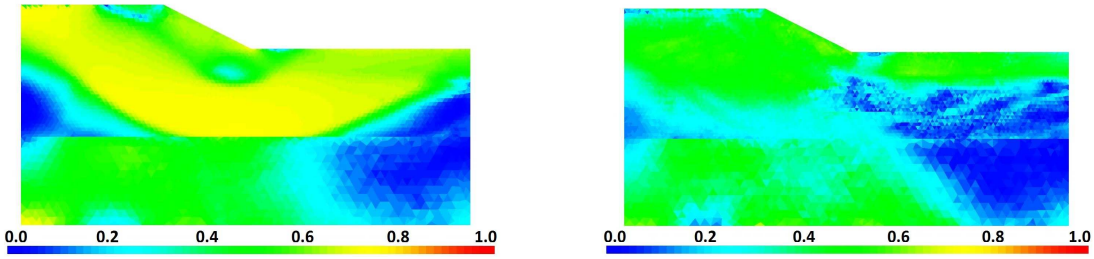

(a) Mainshock: t=3.5s (b) End of earthquake: t=17s

Figure 5.33: Contours of residual strength, r_k, during Friuli earthquake (LMS - Coupled effective stress simulation).

The contours of $\Delta r_k = r_k(t)$-$r_k(t_0)$ are plotted in Figure 5.34 during the mainshock and at the end of the motion. In Figure 5.34a the same circular surface of eventual collapse is noticed. However, at the end of the motion in Figure 5.34b, the soil has regained partially its strength. More in detail, the yellow part of Figure 5.34a has become green in Figure 5.34b which means that the value of r_k has decreased and as a result the safety factor has increased. Moreover, negative values of Δr_k, in blue color appear in Figure 5.34b, i.e. the soil has regained from its initial state. Finally, the detected zones of small values of safety factor that remain after the end of the motion are more limited. It is clearly indicated that the soil has lost significantly its resistance at FF due to liquefaction (i.e. red color in Figure 5.34b), compared to its initial state before the ground motion. The residual strength reaches values greater than 0.5 (around 0.6-0.7) and consequently the safety factor calculated is around $1/r_k$=1.6.

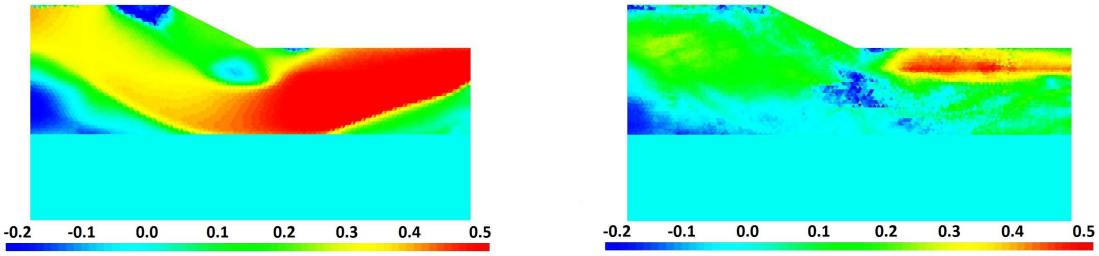

(a) Mainshock: t=3.5s (b) End of earthquake: t=17s

Figure 5.34: Contours of co-seismic residual strength, Δr_k, during Friuli earthquake (LMS - Coupled effective stress simulation).

5.3.4 Mesh sensitivity analysis of the coupled HM model

A mesh sensitivity analysis is performed for the coupled HM model and Friuli earthquake. The response of meshes 2 (10cm) and 5 (50cm) are compared to the reference one (mesh 4 of 25cm) in terms of shear deformations, acceleration and frequency.

In Figure 5.35 the contours of deviatoric strains at the end of Friuli earthquake are plotted and compared to Figure 5.32c. No mesh sensitivity of the diffuse shear zone in the foundation is remarked. The shear band inside the embankment is also mesh insensitive.

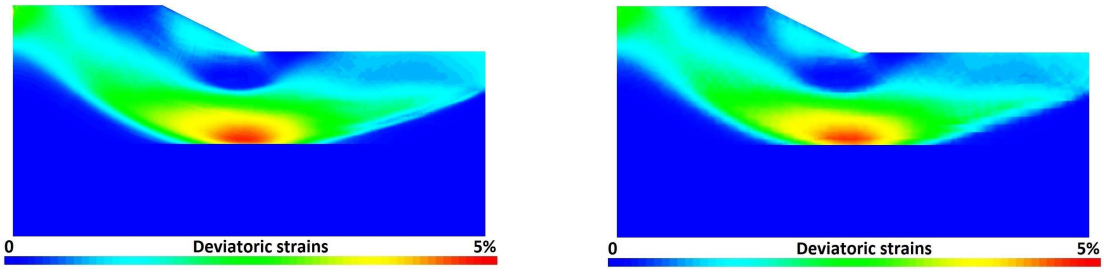

(a) (b)

Figure 5.35: Deviatoric strains ε_d at the end of Friuli earthquake (LMS model): a) Mesh 2 (10cm), b) Mesh 5 (50cm).

The same conclusion is drawn by comparing the obtained horizontal acceleration and its fourier transform at several points (crest, base, FF, liquefied zone, embankment's slope). The comparion of acceleration and fourier transform at the crest is plotted in Figure 5.36. The response of the other points is omitted, as no further information is provided.

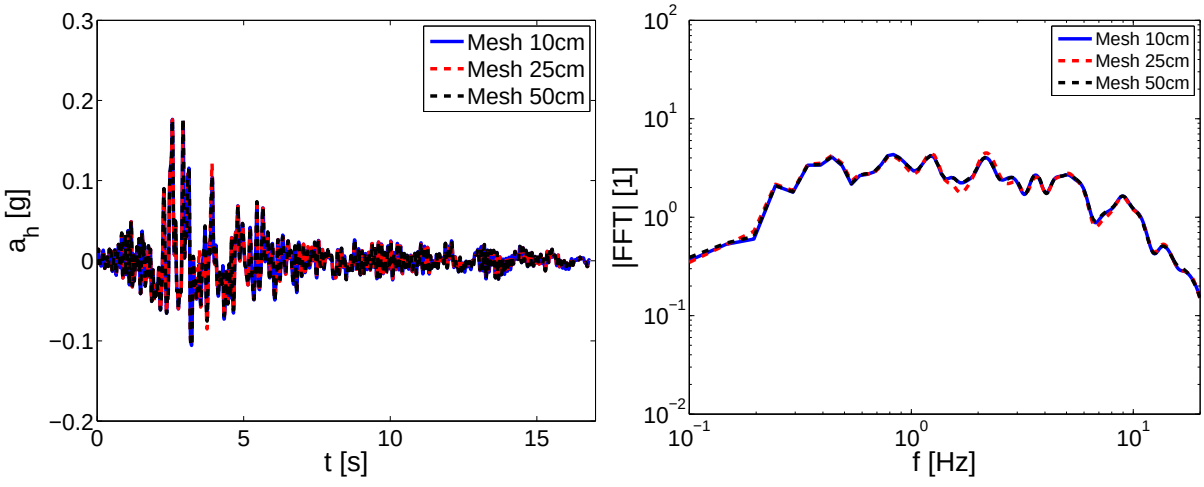

(a) (b)

Figure 5.36: Comparison of response at crest for all meshes (Friuli earthquake-Coupled simulation-LMS model): a) Horizontal acceleration, b) Fourier transform.

5.3.5 Parametric analysis of fully drained and coupled HM model

Finally, the parametric dynamic analysis with the 24 input motions shown in Figure 5.24 is presented for both fully drained and coupled effective stress analyses and for the LMS model with mesh 4 (25cm). The results of 4 ground motions with amplitudes much greater than 0.4g (input signals: Pa/b 1 and Pa/b 4) are eliminated in the following figures, as the simulations did not converge due to excessive displacements and total collapse.

The values of horizontal PGA (Peak Ground Acceleration) measured at the embankment's crest (point P1 in Figure 5.20) are plotted for both simulations and all ground motions in Figure 5.37 as function of the maximum input signal ($a_{bed,max}$). In case of fully drained analysis, greater values of PGA are obtained for almost all points, as there is an amplification of the seismic signal through its propagation in the soil. In the coupled analysis, the foundation's soil liquefaction leads to a deamplification of the seismic signal.

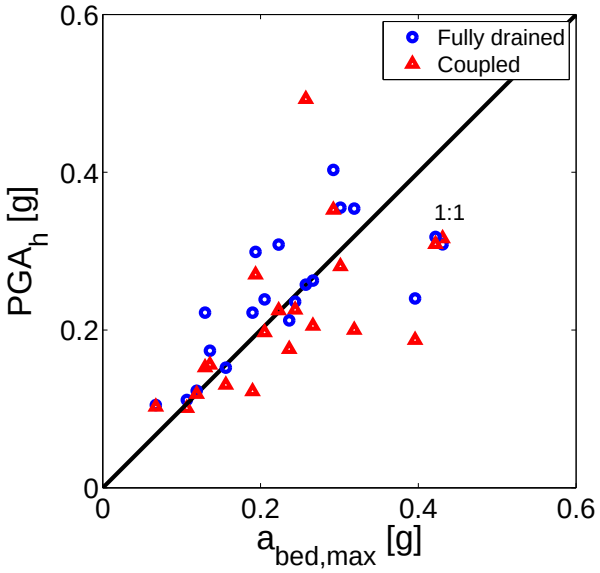

Figure 5.37: PGA at the crest as fuction of input signal's maximum acceleration $a_{bed,max}$ (LMS model).

Next, the values of horizontal and vertical PGA at the crest (P1), base (P2) of the embankment and FF (P4) are compared for the coupled effective stress simulation and all ground motions in Figure 5.38. Most of times, the crest provides the larger values of horizontal and vertical acceleration. However, for some stronger motions the acceleration at FF is greater, which is more obvious in the vertical component of Figure 5.38b. No safe conclusion can be drawn as there is an important dispersion of results.

The horizontal PGA obtained at FF is compared to that obtained at the surface of the soil column of Chapter 3 following the results of the liquefaction vulnerability analysis (Section 3.4). A noticeable contrast is observed in the column's response in Figure 5.39 relative to the embankment's one. Half of the column's PGA values are greater than the embankment's, while the rest ones are lower. Consequent to the conclusions drawn in the liquefaction vulnerability analysis of the soil column (Section 3.4), the signals recorded on soil site lead faster to strong nonlinearity of the soil column (refer to Section 3.4.3),

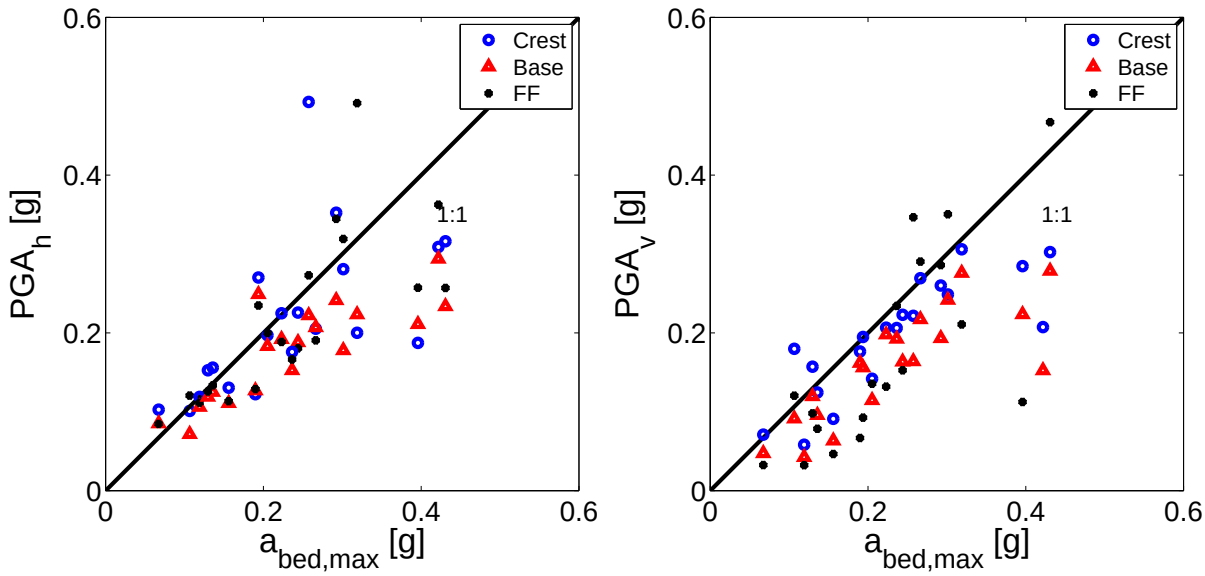

(a) (b)

Figure 5.38: PGA as fuction of $a_{bed,max}$ (Coupled simulation-LMS model): a) Horizontal, b) Vertical.

forming these two branches in the response of the column. This is not the case in the response of the embankment model, as its dynamic behavior follows a more homogeneous trend, since there is no significant dispersion of PGA and the points form a parabolic curve.

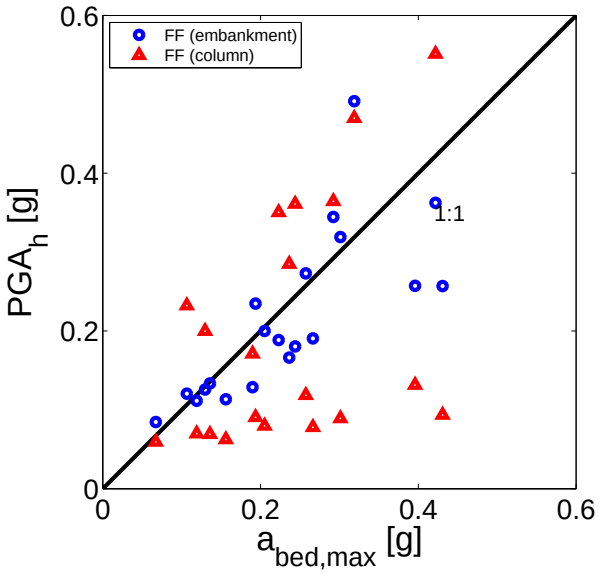

Figure 5.39: PGA at FF compared to PGA of a soil column as function of $a_{bed,max}$ (Coupled simulation-LMS model).

Finally, the absolute horizontal and settlements of the crest of the embankment (P1)

at the end of each ground motion are plotted for both simulations in Figure 5.40. The liquefaction in the foundation led to significantly greater horizontal displacements and settlements compared to the fully drained analysis.

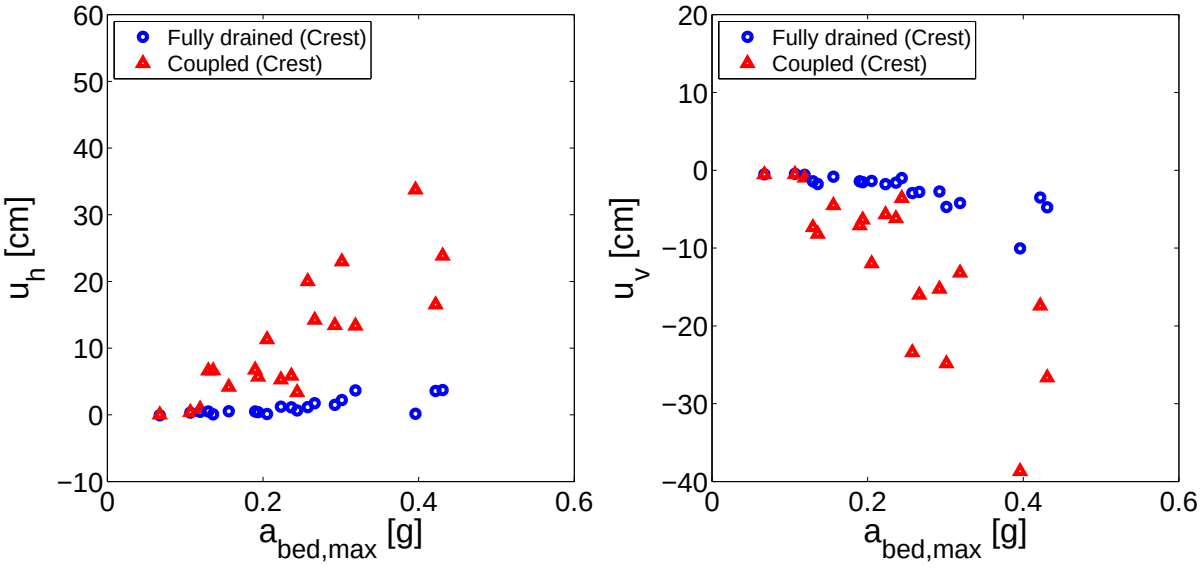

Figure 5.40: Displacement of crest at the end of each ground motion as function of $a_{bed,max}$ (LMS model): a) Horizontal, b) Vertical.

5.4 Partial Conclusions

This work provides an analysis of the dynamic response of an embankment - foundation system for both dry and coupled HM simulations. In the first part of the study, the analysis of a dry model composed of a loose embankment shows that the embankment cannot afford an earthquake stronger than 0.65-0.7g and it collapses. The potential local collapse of the embankment is driven by a mesh insensitive shear band which is generated at the toe due to geometry heterogeneity.

Robust criteria are used to define the onset of the structure's collapse. The second order work describes the local instability at specific instants of the ground motion, while the residual strength calculated provides an image of the evolution of safety factor of the structure. As demonstrated through a shear test of one soil element, the ratio of apparent to critical friction angle provides a reliable measure of soil's strength, which is independent of the loading path and can be used as a criterion for estimating the local state of soil and finally the local safety factor of geostructures. Applying both criteria in the case of the embankment model, slope instability was detected and a low value of safety factor was observed after the ground motion due to soil's degradation.

The results in terms of displacement were compared to the predicted earthquake-induced displacements using the empirical simplified methods used in common engineering practice and proposed by Makdisi and Seed (1978), Ambrasseys and Menu (1988),

Jibson (1994). A critical surface was estimated for the sliding block and a seismic coefficient related to the block's yield acceleration was calculated according to the research work of Andrianopoulos et al. (2014) and following the recommendations of EC8, British Standards (Charles et al., 1991; Gosschalk et al., 1994) and American regulations NCHRP 12-70 (Anderson et al., 2008) / FHWA 2011 (Kavazanjian et al., 2011). The predicted earthquake-induced displacements calculated by these empirical simplified methods mostly overestimated the embankment's displacements obtained by the FE numerical simulations. Through this comparison, the importance of using advanced numerical simulation methods is underlined.

Subsequently, a fully drained effective stress approach shows that a stiff embankment is generally unaffected by a ground motion. Nevertheless, a loose embankment can collapse for a certain level of ground motion, due to slope instability. As in the case of the dry model, a shear band generates inside the embankment's body and extends from the toe to crest.

Irrespective of the embankment's soil type, in case of liquefaction of the foundation (coupled effective stress analysis), the global structure-foundation system completely collapses as a circular failure zone is produced in depth. The foundation's liquefaction leads to large deformations of the structure, as also discussed by other researchers (Maharjan and Takahashi, 2014; Ishikawa et al., 2015). Settlements appear during the liquefaction phase of the model and they tend to stabilize during the dissipation phase some seconds after the end of the ground shaking. A circular sliding mass is developed which leads to lateral spreading. No post-liquefaction effects are detected.

In summary, the effect of excess pore water pressure is of great importance, as an otherwise stable structure-foundation system becomes unstable during coupled analysis and could fail due to a liquefiable zone in the foundation. It should also be noted that in case of loose embankments two distinct shear bands emerge and lead to extended failure.

This work demonstrates the capability of an elastoplastic constitutive model to represent cyclic behavior, i.e. the dynamic response and earthquake-induced deformations of a structure, due to the coupling of volumetric and deviatoric strains. The onset of local or general liquefaction-induced collapse of earth structures is defined and can be considered as a first step for dynamic analysis of large scale structures, such as seismic response of earth dams or levees, as follows in the next chapter. All the different elements treated in the current and previous chapters are used next in order to simulate a real case-study of a levee resting on liquefiable foundation.

Chapter 6

Case-study: Liquefaction-induced failure of a levee

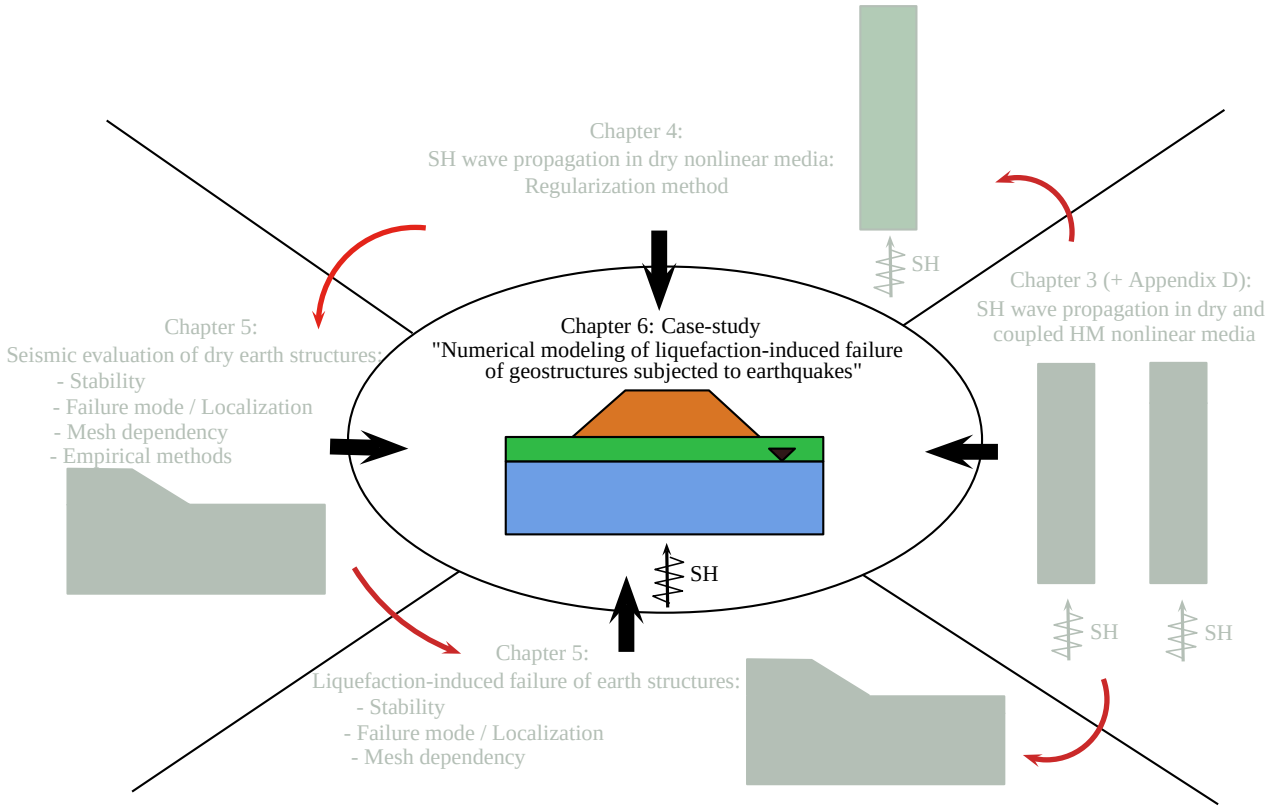

6.1 Introduction

Liquefaction-induced failure of earth structures, such as river dikes, levees, road embankments and earth dams, is identified as one of the most devastating consequencies of earthquakes. Previous numerical or experimental studies (e.g. centrifuge tests) have shown that the widespread damage to such embankments occurred mainly due to the liquefaction of foundation soil, resulting in excessive settlements, lateral spreading and slope instability (Aydingun and Adalier, 2003; Stamatopoulos and Aneroussis, 2004; Singh et al., 2005; Oka et al., 2012; Maharjan and Takahashi, 2014; Ishikawa et al., 2015; Lopez-Caballero et al., 2016). In most cases of foundation's liquefaction, important shear deformations are generated in the liquefied region and extended inside the geostructures. The shear zones, combined with large settlements and eventual lateral spreading, may lead to local or complete collapse of the earthen structures (Sasaki and Tamura, 2007; Okamura et al., 2013; Sadeghi et al., 2014; Ishikawa et al., 2015). The influence of foundation soil type and earthquake's characteristics have proven to be critical (Ozutsumi et al., 2002; Adalier and Sharp, 2004; Xia et al., 2010; Lanzo and Pagliaroli, 2012; Maharjan and Takahashi, 2014).

Sasaki and Tamura (2007) discussed the failure path of river dikes subjected to earthquakes following the classification of damage modes provided by the "Manual for repair methods of the civil engineering structures damaged by earthquakes" (Technical Note of PWRI, Vol. 45, 1986). Accoridng to this manual, embankment failure due to earthquakes is classified into 4 fundamental modes as shown in Figure 6.1. Type 1 and 2 refer to the failure in the embankment, type 3 is intense deformation of embankment due to soil liquefaction in the foundation, and type 4 is crest settlement without apparent deformation of the whole embankment.

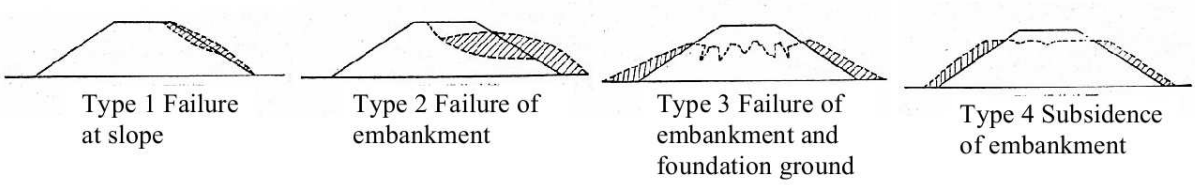

Figure 6.1: Classification of damage modes of failed dikes (Sasaki and Tamura, 2007).

Consequently, following the study of the embankment-foundation system under dynamic loading in case of dry, fully drained and coupled HM conditions of Chapter 5, in the current chapter a larger-scale model is developed and its dynamic response is evaluated so as to define the failure path. This analysis describes the dynamic response of a levee - foundation system and focuses on the liquefaction-induced failure. It can be considered as a reference case-study for seismic assessment of embankment-type structures subjected to earthquake loading. As in the previous chapters, parametric studies are conducted to explore the influence of the characteristics of the input motion, soil's permeability and depth of the liquefiable layer on the collapse mechanism.

For this reason, a plane-strain FE model of a levee - foundation system is built to analyze the liquefaction-induced failure modes. The onset of the expected failure path and stability of the structure-foundation system are discussed. Next, the effect of the depth of the liquefiable layer and soil's permeability on the liquefaction-induced failure is developed. Finally, as a first effort of liquefaction vulnerability analysis, the global response of the system subjected to different types of seismic excitation is provided, so as to assess the effect of the input motion. The advanced soil behavior is represented using the fully coupled effective stress ECP constitutive model developed at CentraleSupélec (Hujeux, 1985). Numerical simulations are performed using the open-source FE software Code_Aster (version 11.7).

6.2 Problem statement

A plane-strain model of a levee resting on liquefiable foundation is simulated, so as to investigate its dynamic response and the earthquake-induced failure mode due to foundation's liquefaction. Three studies are conducted simultaneously to clarify the liquefaction vulnerability on several parameters:

- Depth of liquefiable layer: two levee-type models are simulated, one with a liquefiable layer close to the free surface (below the levee) and a second one with the liquefiable layer situated in depth (refer to Section 6.3.1).
- Soil permeability: starting from a very permeable and continuing to a moderately permeable foundation, the slightly permeable foundation model is considered as the most crucial on the levee's collapse (refer to Section 6.3.4).
- Type of input ground motion: several ground motions are used in the case of less permeable model with a liquefiable foundation close to the free surface and an analysis similar to that of Section 3.4 for the soil column is conducted (refer to Section 6.3.5).

6.3 Numerical model of levee resting on liquefiable foundation

The FE analysis is performed in three steps: a) as the model is nonlinear, a static analysis is performed in order to calculate the initial stresses, b) the levee is constructed by layers (50cm/2days: total 36days), c) a model initialization is realized by imposing zero displacements, so as to account for the co-seismic displacements only, d) a dynamic analysis with zero input acceleration (a_{bed}=0) is performed to verify equilibrium and e) the final step is the application of the seismic signal.

6.3.1 Geometry - Boundary conditions

The 9m high levee is composed of a dry dense sand, placed over a loose-to-medium contractive saturated sand (LMS) layer. The levee remains always dry and the water

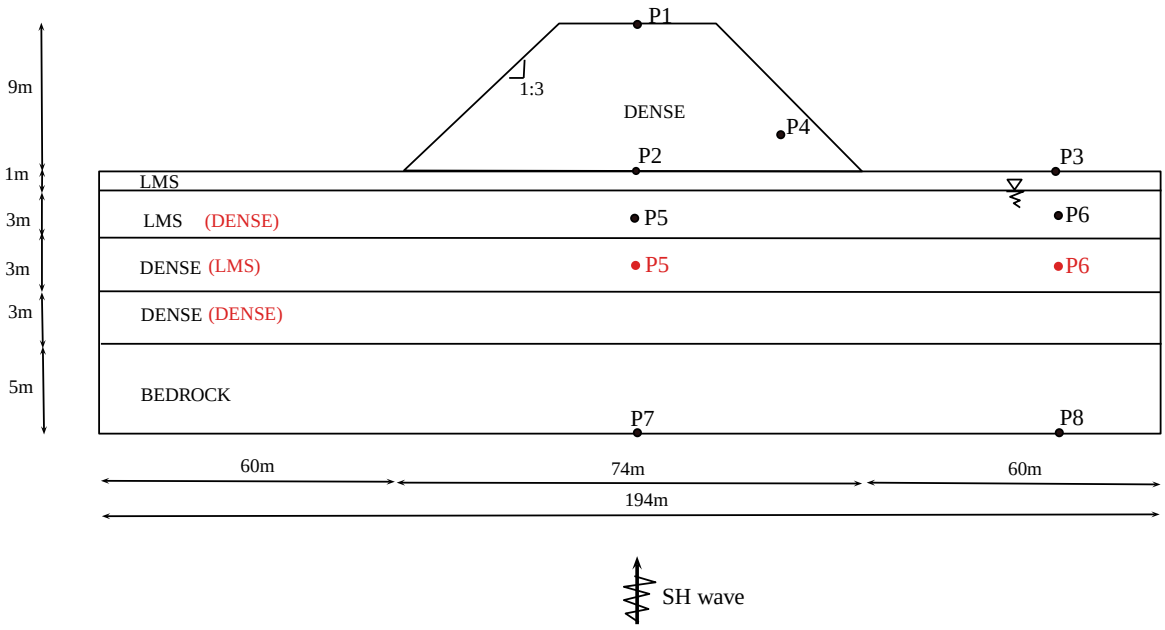

Figure 6.2: Illustration of numerical model.

table is situated 1m below the levee. The levee's slope inclination is equal to 1:3 (vertical:horizontal).

Firstly, the liquefiable layer (LMS layer) is supposed to be close to the free surface, as shown in Figure 6.2 with black color, and a dense saturated substratum exists at the bottom part of the foundation. Then, in order to assess the effect of the depth of the liquefied region on levee's response, the liquefiable layer is situated deeper, between two layers of dense sand, as presented in Figure 6.2 with red color. In both cases, an elastic rigid bedrock (V_s=1000m/s) is simulated below the dense substratum. The first model (black color in Figure 6.2) is considered as reference case for all simulations, unless otherwise mentioned. The second one (red color in Figure 6.2) will be only used in Section 6.5 to study the influence of the depth of liquefied layer. Representative points used for the dynamic analysis are presented in the figures.

For the construction phase, horizontal displacements are fixed at the lateral boundaries, as well as vertical displacements at the bedrock. However, for the dynamic analysis, vertically incident shear waves are introduced into the domain and as the response of an infinite semi-space is modelled, equivalent boundaries have been imposed on the nodes of lateral boundaries (i.e. the normal stress on these boundaries remains constant and the displacements of nodes at the same depth in two opposite lateral boundaries are the same in all directions). The model length ensures that the effect of the boundaries can be neglected and it satisfies the free field condition at the lateral boundaries. For the half-space bedrock's boundary condition, paraxial elements simulating "deformable unbounded elastic bedrock" have been used (Modaressi, 1987). The incident waves, defined at the outcropping bedrock are introduced into the base of the model after deconvolution. Thus, the obtained movement at the bedrock is composed of the incident waves and the reflected signal.

6.3.2 Soil characteristics

The dry levee is composed of a dilative dense sand (noted as Dense sand 2 in Table B.1 in Appendix B.6, where the soil parameters are presented). The foundation is composed of the same contractive loose-to-medium sand and dense sand, as in the embankment model of Section 5.3.2. Their parameters can be found in Table B.1 in Appendix B.6, noted as LMS and Dense sand 1.

In order to understand the behavior of the chosen materials under dynamic loading, cyclic shear drained and triaxial drained and cyclic undrained tests are conducted. For the sake of brevity, only the response of the dense sand used in the levee is presented, as the response of the other materials has already been shown in Section 5.3.2. Thus, Figure 6.3 shows deviatoric stress - strain and volumetric - deviatoric strain curves, as well as, $G/G_{max} - \gamma$ and $D - \gamma$ curves for the dense sand of the levee under drained triaxial and cyclic shear tests at confining pressure corresponding to the average geostatic pressure of the levee, i.e. 50kPa.

6.3.3 Numerical parameters

The FE mesh consists of 6-node triangular elements of 0.50m length on average (30054 nodes/17538 elements). The implicit method of Newmark integration is used for the dynamic analysis with a time step equal to Δt=10^{-3}s and numerical damping equal to ξ = 0.2% is added, as explained previously in Section 3.2.4.

The low-strain frequency analysis provides a fundamental elastic period for the structure-foundation system equal to T_p=0.22s (i.e. f_p=4.5Hz) (Figure 6.4). In this particular model the response Crest-Bedrock is obtained from the Borehole Transfer Function between points P1-P7 of Figure 6.2, while Base-Bedrock and FF-Bedrock FF refer to points P2-P7 and P3-P8, respectively.

6.3.4 Hydraulic behavior

A fully coupled effective stress dynamic approach using the $\underline{u}$-p_w formulation derived from Biot's theory for incompressible solid - compressible fluid is used, as explained in Chapter 2.2 (Equations 2.10, 2.11). The hydraulic parameters of each material are presented in Table 6.1. Initially, a permeability equal to k_s=1·10^{-4}m/s is used for the liquefiable layer corresponding to a typical clean sand of medium permeability. Then, in order to provide a sensitivity analysis of the liquefaction-induced collapse on the permeability of the liquefiable layer, two other values of permeability are used, i.e. k_s=1·10^{-3}m/s and k_s=1·10^{-5}m/s. The first one corresponds to a typical clean sand of high permeability, while the latter refers to a silty sand of low permeability (Bardet, 1997). This characterization is based on the relation of permeablity with particle size and void ratio established by NAVFAC (1982) and on the classification of soils after Terzaghi and Peck (1967). The permeability of the dense substratum is always considered 10 times lower than this of the liquefiable layer (k_s=1·10^{-4}m/s, 1·10^{-5}m/s, 1·10^{-6}m/s, respectively). For the needs of FE modeling, the value of fluid compressibility used, is higher than the real one of water, as explained in Section 3.2 and Appendix D.

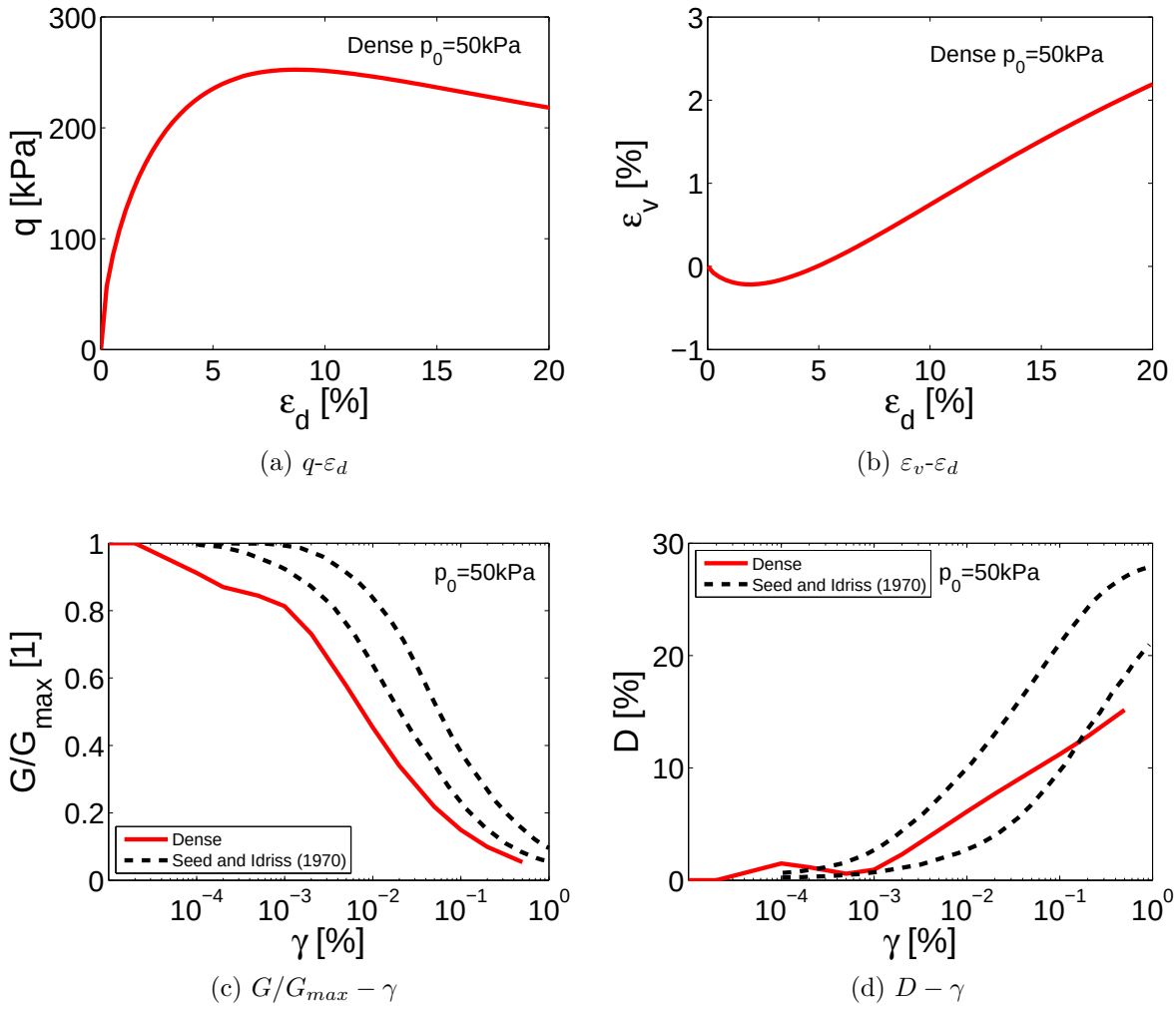

(a) q-ε_d (b) ε_v-ε_d

(c) $G/G_{max} - \gamma$ (d) $D - \gamma$

Figure 6.3: Soil response of one material point under: a,b) triaxial drained test and c,d) shear cyclic drained test compared to Seed and Idriss (1970).

Table 6.1: Hydraulic parameters for the soil.

Parameter	Foundation (LMS)	Foundation (Dense sand)
Fluid mass density, ρ_w [kg/m^3]	1000	1000
Porosity, n [1]	0.35	0.35
Permeability, k_s [m/s]	$1{\cdot}10^{-3}$ / $1{\cdot}10^{-4}$ / $1{\cdot}10^{-5}$	$1{\cdot}10^{-4}$ / $1{\cdot}10^{-5}$ / $1{\cdot}10^{-6}$
Fluid compressibility, H_w [Pa^{-1}]	$9.35{\cdot}10^{-8}$	$9.35{\cdot}10^{-8}$

6.3.5 Input ground motions

As developed in Section 3.4, the choice of input motion is a key component in the context of PBEE. Consequently, the effect of the characteristics of earthquake on liquefaction-induced failure is assessed, as previously. For this reason and based on the findings of the liquefaction vulnerability analysis of the soil column, representative ground motions are chosen to evaluate the dynamic response of the levee. Due to excessive evolution of CPU

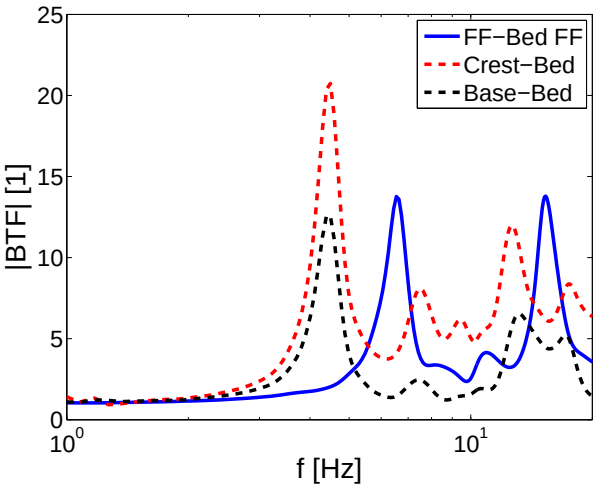

Figure 6.4: Borehole Transfer Function of levee - foundation system.

time with the duration of the input signal for the dynamic analysis of the levee-foundation model (refer to Appendix I), the ground motions used are limited to the 23 following ones:

- 2 ground motions from the italian database *itaca* (irsn60, irsn168)
- Friuli earthquake (Italy, 1976) from PEER database
- 3 real non pulse-like motions recorded on soil site (T1a 3,5,8) from PEER database (Iervolino and Cornell, 2005)
- 5 real non pulse-like recorded on rock site (Ra 1, Ra 2, Ra 9, Rb 5, Rb 5) from PEER database (Baker et al., 2011)
- 4 real pulse-like recorded on rock site (Pa 2, Pa 3, Pa 4, Pa 5) from PEER database (Baker, 2007)
- 8 synthetic ground motions generated by the option $GENE\_ACCE\_SEISME$ of Code_Aster and based on the natural accelerogram of Friuli earthquake

In Figure 6.5 the response spectra of all input motions are plotted with damping ξ=5% and the fundamental frequency f_p of the structure-foundation system is indicated. Note that all input and outpout signals have a baseline correction and are filtered using a non-causal bandpass filter of order 4, between 0.1-20Hz. The characteristics of all motions used can be found in details in Appendix C.

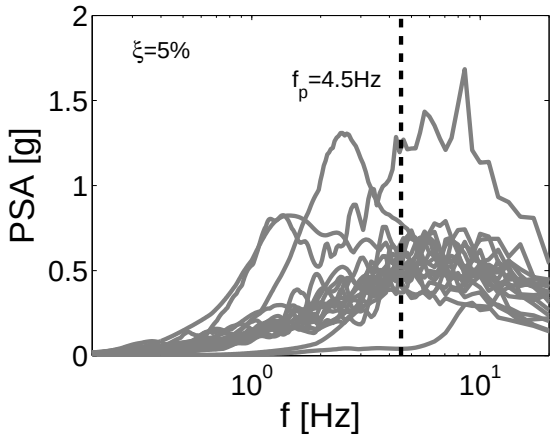

Figure 6.5: Response spectra of input ground motions (ξ=5%) (the system's fundamental frequency is illustrated with the dashed line).

6.4 Typical dynamic response of levee resting on liquefiable foundation

Before analyzing the influence of the aforementioned parameters on the dynamic response of the levee-foundation system, its typical response is presented in case of earthquake loading. The moderately permeable model (k_s=1·10^{-4}m/s) with the liquefiable layer situated close to the surface is used as reference case study. Due to important CPU time needed for the dynamic analysis, a moderate signal ($a_{out,max}$=0.24g) recorded on soil site with short duration of mainshock (t_{595}=0.91s) is chosen for the current analysis, i.e. "irsn168" motion from the italian database *itaca*. Its accelerogram and Arias intensity are plotted in Figure 6.6.

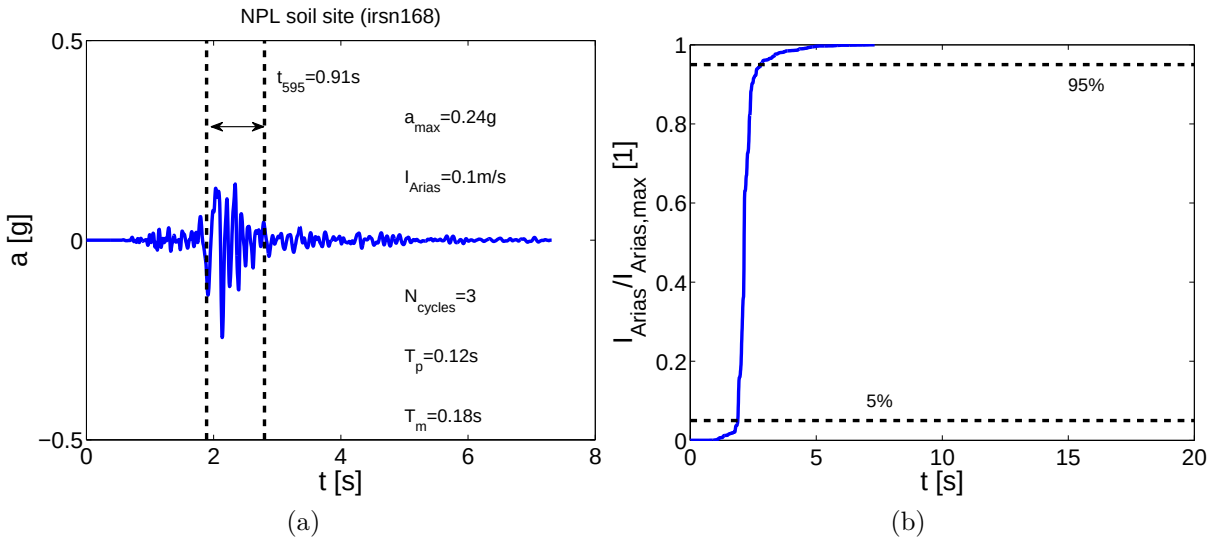

(a) (b)

Figure 6.6: Input seismic signal (irsn168): a) Accelerogram, b) Normalized Arias intensity.

As reported in the previous chapters (Sections 3.3.1, 5.3.3.1), to assess soil liquefaction apparition, the contours of excess pore water pressure ratio (i.e. r_u=$\Delta p_w/\sigma'_{v,0}$) are plotted in Figure 6.7. It is noticed that excess pore water pressure is generated in the liquefiable layer of the foundation and lead to liquefaction (i.e. r_u=1.0) below the FF during the mainshock (t=2-3s). Consequent to the results of the embankment model, the evolution of Δp_w is related to the mainshock and Arias intensity (Figure 6.6b), as between t=2-3s the total intensity of the motion has been accumulated (95% of I_{Arias}). The liquefaction extended from each toe of the levee to the FF part. However, low values of r_u are observed below the levee due to higher values of stresses and soil's consolidation. After the mainshock, the excess pore water pressure progressively dissipates, as the amplitude of the ground motion decreases (coda phase, i.e. last seconds of the ground motion where the amplitude decreases) and the dissipation is completed some seconds after the ground motion.

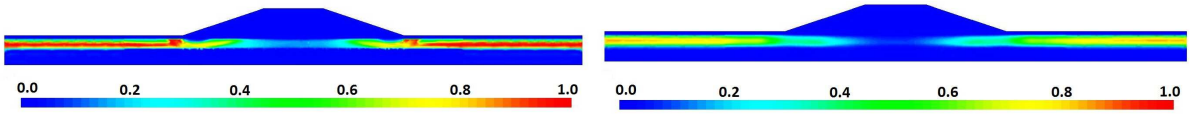

(a) Mainshock (t=2.4s). (b) End of earthquake (t=7.4s).

Figure 6.7: Typical dynamic response (irsn168 motion): Excess of pore water pressure ratio r_u.

Due to foundation's liquefaction, a circular slip surface is observed in both sides of the levee (Figure 6.8). The right and left part of the levee settle down superficially (Figure 6.8a) and move towards the FF part (Figure 6.8b). This failure path is also reported by Sasaki and Tamura (2007), Maharjan and Takahashi (2014) and Ishikawa et al. (2015), as lateral spreading combined with settlements. More precisely, as shown in Figure 6.1, this damage mode can be classified as Type 1, i.e. failure at slope. This type of sliding results from the liquefaction of the foundation and is produced during the mainshock due to the increase of excess pore water pressure. Consequently, no further post-liquefaction effects are detected, which is coherent to the results of Coelho et al. (2004) after observations in centrifuge tests of saturated sand deposits, where the most significant part of settlement occured simultaneously with the shaking.

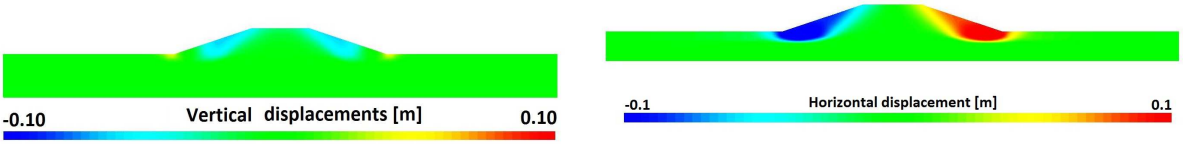

(a) Settlements. (b) Horizontal displacements.

Figure 6.8: Typical dynamic response (irsn168 motion): Deformed shape at the end of the ground motion.

Concerning the levee's stability, the second order work density ($d^2W=\dot{\sigma}'_{ij}:\dot{\varepsilon}_{ij}/|\dot{\sigma}'_{ij}||\dot{\varepsilon}_{ij}|$) is used as it represents the instability at specific instants of the ground motion and specific locations (for further details refer to Section 5.2.2.3). The contours of d^2W are presented at t=2.4s (during the mainshock of the ground motion) in Figure 6.9. The model underwent instability at both sides of the levee and inside the liquefied layer, implying the eventual circular slip surface which can lead to the system's collapse. At the end of the ground motion and although excess pore water pressures still appear, a stable state is reached. The corresponding figure is omitted as no further information is provided.

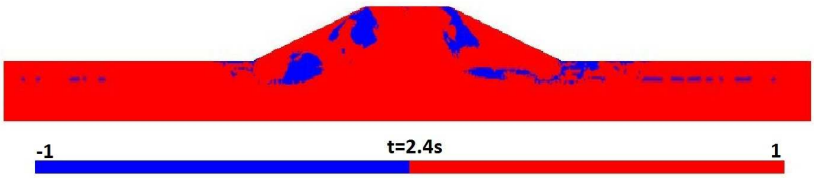

Figure 6.9: Typical dynamic response (irsn168 motion): Contours of second order work at t=2.4s (mainshock).

Furthermore, due to foundation's liquefaction, two different shear zones are generated in the liquefied layer below the toes of the levee, as shown in Figure 6.10. These shear zones propagate inside the levee body and verify the circular collapse surface identified previously. The generation of shear zones in the foundation is also reported in the research work of Oka et al. (2012) focused on the liquefaction-induced failures of river embankments during the Tohoku earthquake in 2011.

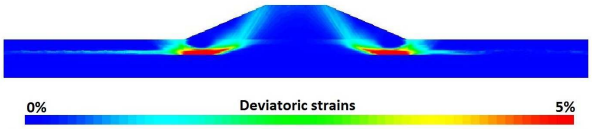

Figure 6.10: Typical dynamic response (irsn168 motion): Deviatoric strains ε_d at the end of the ground motion.

In order to verify the soil's behavior in the liquefied region and inside the shear band, one point in each region was selected and the evolution of volumetric - shear strains during the loading is examined. According to Figure 6.11a, it is noted that two types of responses appear following the onset of liquefaction (Figure 6.11b). As expected, before the pore water pressure build-up (t<2s) no generation of volumetric strains is obtained. Then, once the liquefaction has started (t=2.2s), the soil's behavior is purely contractive (blue curve, ε_v <0) in the liquefied region of the foundation, meaning that settlement appear. On the other hand, inside the shear band generated in the levee (red curve) the soil becomes dilative (ε_v >0) after the onset of mainshock (t=2.4s), meaning that the shear band is generated and extends towards the levee and crack opening occurs.

Finally, the soil's residual strength is calculated by using the parameter r_k, as explained in Section 5.2.3.1. Recall that it varies between 0 and 1 where perfect plasticity is reached and is defined as the inverse of a local safety factor (r_k=1/FS, i.e. near collapse when

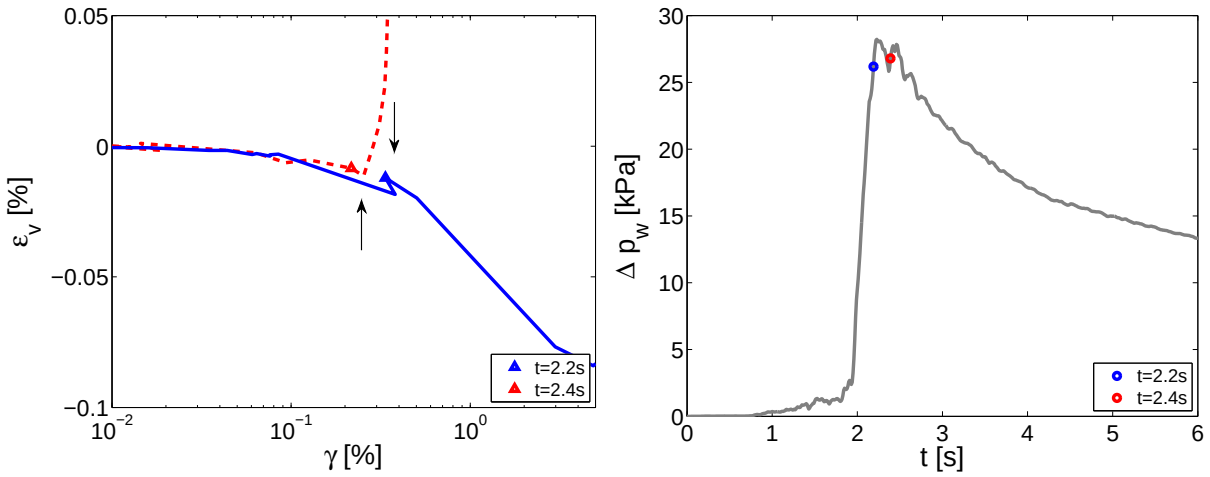

(a) (b)

Figure 6.11: Typical dynamic response (irsn168 motion): a) Mechanical behavior inside the liquefied part and the shear band, b) Evolution of Δp_w inside the liquefied region.

r_k=FS=1.0). In Figure 6.12a, the contours of r_k are plotted at the beginning of the ground motion and it can be noticed that before the ground motion and due to the construction of the levee, noticeable values of r_k appear in the liquefiable layer below the levee (i.e. r_k ≃0.6-0.8 and FS≃1.6-1.25). In Figure 6.12b during the mainshock (t=2.4s) and while liquefaction is reached (r_u=1.0), the same circular surface of collapse is remarked and r_k reaches unity (i.e. FS=1.0). Even at the end of the motion in Figure 6.12c important values of r_k appear inside the zone of shear strains in the foundation, providing a low safety factor of 1.2.

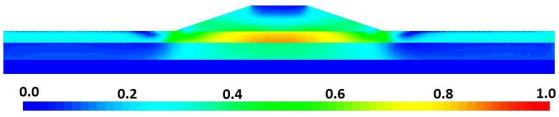

(a) Initial material state (t=0s).

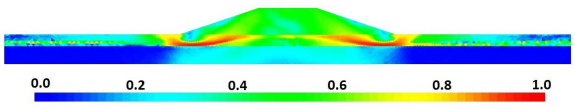

(b) Mainshock (t=2.4s).

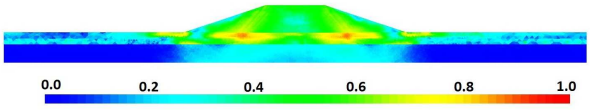

(c) End of earthquake (t=7.4s).

Figure 6.12: Typical dynamic response (irsn168 motion): Contours of residual strength, r_k.

In the following sections, in order to assess the influence of different factors on this typical dynamic response of the levee-foundation system, the results of the parametric studies are presented and compared to the typical dynamic response. Firstly, the effect of the depth of the liquefied layer and soil's permeability is evaluated and then, the influence of the characteristics of the input signal is discussed.

6.5 Effect of liquefiable layer's depth on the dynamic response

In this section, the influence of the depth of the liquefiable layer is assessed through dynamic analyses of the two models presented in Section 6.3.1. The moderately permeable model, whose typical response was presented previously, is chosen as reference case for this study and two input motions are imposed to the model. The first one is the short duration motion of moderate amplitude, "irsn168" (Figure 6.6), while the second one is a strong motion ($a_{out,max}$=0.42g) recorded on rock site with longer mainshock (t_{595}=0.91s), presented in Figure 6.13.

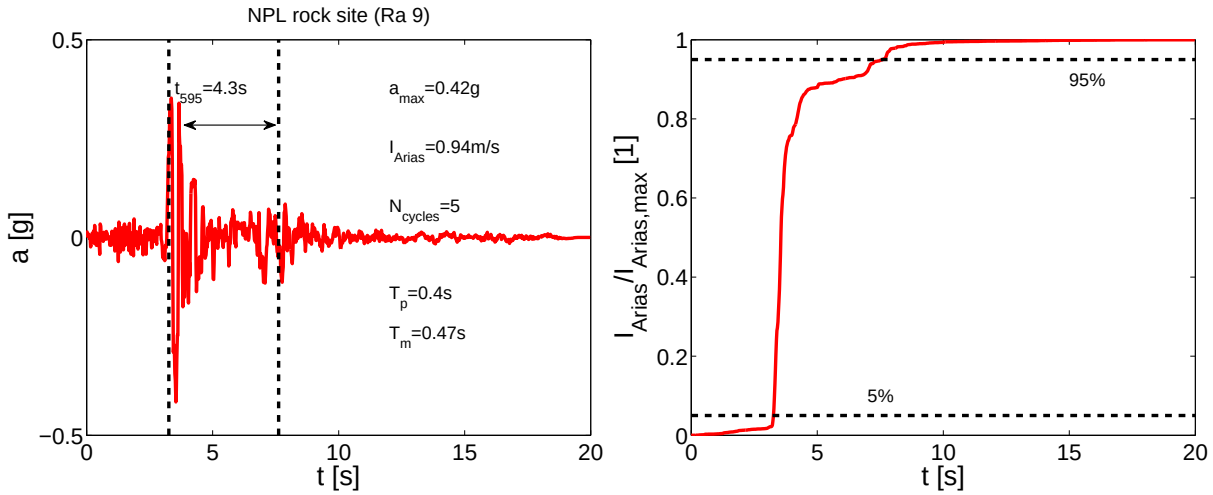

(a) (b)

Figure 6.13: Input seismic signal (Ra9): a) Accelerogram, b) Normalized Arias intensity.

Firstly, the contours of r_u are plotted in Figure 6.14 for both motions during their mainshock and at the end. It is observed that in both cases, excess pore water pressure (Δp_w) is generated in the liquefiable layer situated in depth in the foundation during the mainshocks (Figures 6.14a, 6.14c). In case of the lower motion, liquefaction (r_u >0.8) is apparent only below the FF area, while lower values of r_u are observed below the levee, as indicated previously (see corresponding Figure 6.7a). Nevertheless, in case of stronger motion in Figure 6.14c, liquefaction appears in the whole layer of LMS material. More in detail, the part below the FF is firstly liquefied with the main peak of the motion and then, excess pore pressure is generated below the levee as the water tries to dissipate. During both earthquakes, the excess pore water pressure progressively dissipates towards the upper part of the foundation, as increase of r_u appears at the end of the mainshocks at the denser upper layer (r_u=0.6 in Figures 6.14b, 6.14d). Compared to the previous model of Figure 6.7b, the dissipation is much slower in the current model with the lower motion and the excess pore water pressure has not dissipated at the end of the earthquake due to the less permeable layers of dense soil at the upper and lower part of the liquefied layer. As it concerns the strong motion, the layer of LMS remains liquefied (r_u=1) at the end of the earthquake (Figure 6.14d).

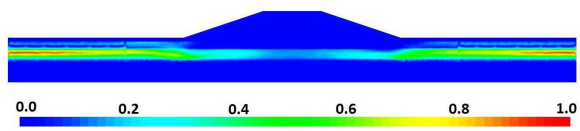

(a) Mainshock of irsn168 (t=2.4s).

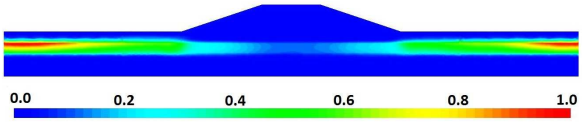

(b) End of irsn168 (t=7.4s).

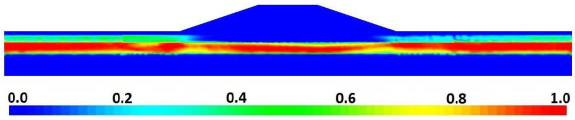

(c) Mainshock of Ra9 (t=5s).

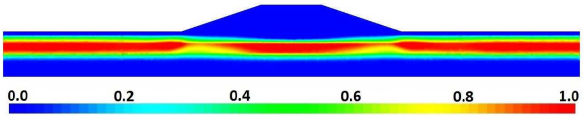

(d) End of Ra9 (t=20s).

Figure 6.14: Liquefiable layer in depth: Excess pore water pressure ratio (r_u) during the motions.

In case of the lower motion, although a part of the foundation liquefied, negligeable displacements are found, as the maximum values observed at the levee's slopes and crest are 1cm of horizontal displacements and 1cm of settlement, respectively. These values are significantly smaller compared to those obtained in the previous model in Figure 6.8. Consequent to the negligeable displacements, the levee remains stable and only instaneously local instability appears at the liquefied part of the foundation. For the sake of brevity, the corresponding figures are omitted.

However, when the stronger earthquake is imposed to the model, more important values of settlements appear all along the levee's crest, as shown in Figure 6.15a. This damage mode can be classified as Type 4 (Figure 6.1), i.e. crest settlement without apparent deformation of the whole levee. Furthermore, the foundation moves horizontally towards the FF part at the level of the liquefied layer (Figure 6.15b) and the displacements are not symmetric, i.e. the left part at the toe of the levee is more affected, probably due to the input signal's assymetry. It is also important to note that apart from the local instabilities at the liquefied foundation during the motion (as it was observed for the lower motion), at the end of the earthquake instabilities appear inside the levee too, as shown in Figure 6.16. This can be explained as the foundation remains completely liquefied at the end of the motion and the dissipation of water pressure is towards the upper soil layers.

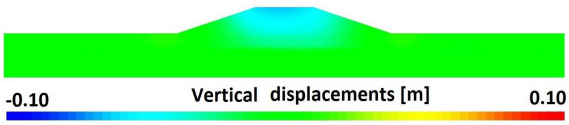

(a) Settlements.

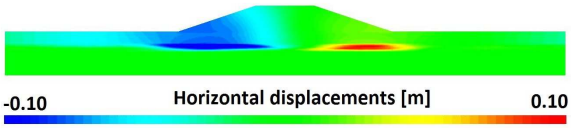

(b) Horizontal displacements.

Figure 6.15: Liquefiable layer in depth (Ra9 motion): Deformed shape at the end of the ground motion.

Next, concerning the shear strains at the end of the low motion, while in the previous model shear zones are generated in the liquefied region and propagate inside the levee

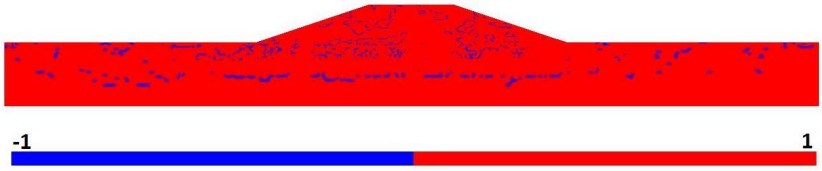

Figure 6.16: Liquefiable layer in depth (Ra9 motion): Contours of second order work at the end of earthquake.

body (Figure 6.10), in the current model the deformations are insignificant, as shown in Figure 6.17. As the liquefaction was situated in depth and mostly below the FF part, the levee is not affected in terms of shear strains. Even in the case of the stronger motion, where a zone of diffused shear strains is observed inside the liquefied layer in Figure 6.17b, no shear bands are propagated to the upper layers. Note that this statement is inextricably related to the characteristics of the ground motion and should not be used as a general conclusion. It is possible that in case of a longer duration of mainshock, more important deformations may appear inside the levee, too.

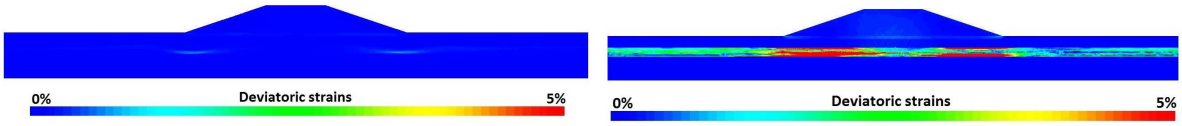

(a) End of irsn168. (b) End of Ra9.

Figure 6.17: Liquefiable layer in depth: Deviatoric strains ε_d at the end of the ground motions.

In Figure 6.18a, the contours of r_k are plotted at the beginning of the ground motion and as before, noticeable values of r_k appear in the liquefiable layer due to the construction of the levee (i.e. $r_k \simeq 0.8$ and FS$\simeq$1.25). During the lower ground motion the safety factor remains at acceptable levels and at the end of motion the soil has regained its strength, providing a safety factor of 1.6 (r_k=0.6), as shown in Figure 6.18c. Low values of residual strength are obtained inside the levee ($r_k \simeq 0.3$), i.e. soil densification, and as expected, it is almost unaffected by the earthquake-induced liquefaction.

Consequent to the aforementioned results, the model with the liquefiable layer situated in depth is less affected and for this reason, in the following section the model with the liquefiable layer close to the surface will be used.

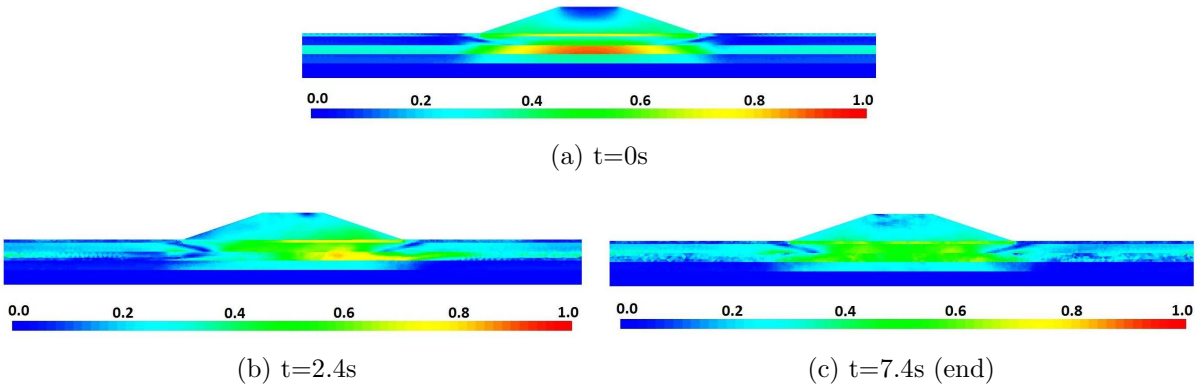

(a) t=0s

(b) t=2.4s

(c) t=7.4s (end)

Figure 6.18: Liquefiable layer in depth (irsn168): Contours of residual strength, r_k.

6.6 Effect of soil's permeability on the dynamic response

As discussed in Section 5.3.3 and presented previously, the collapse mechanism of earth structures in case of coupled HM modeling is driven mostly by the earthquake-induced liquefaction of the foundation. Consequent to these findings, the influence of soil's permeability on the liquefaction-induced failure mode of the levee-foundation system is assessed through the following parametric study. In the light of this study, three models of different soil permeability are used, as explained in Section 6.3.4. Next, the model of high permeability is noted as "very permeable" ($k_{s,\text{LMS}}$=1·10^{-3}m/s - $k_{s,\text{Dense}}$=1·10^{-4}m/s), "permeable" stands for the moderately permeable ($k_{s,\text{LMS}}$=1·10^{-4}m/s - $k_{s,\text{Dense}}$=1·10^{-5}m/s) whose response was presented in the previous sections, while the one of low permeablity is referred as "slightly permeable" ($k_{s,\text{LMS}}$=1·10^{-5}m/s - $k_{s,\text{Dense}}$=1·10^{-6}m/s). For the purposes of this study, the model with the liquefiable layer close to the surface is considered as reference case (Figure 6.2), as it was more affected by the earthquake. Moreover, due to important CPU time needed for the dynamic analyses, only the "irsn168" motion is used (Figure 6.6). Note that the results of the very and slightly permeable models are illustrated next and compared to those of the permeable model presented in Section 6.4.

Excess pore water pressure generation

Initially, the contours of r_u are plotted in Figure 6.19 for the very and slightly permeable model. Both models liquefied during the mainshock (Figure 6.19a, 6.19c) at the same area, irrespective of soil's permeability. However, differences appear in the dissipation phase. In the very permeable model the dissipation of pore water pressure happens immediately after the main peak of the motion, while in the slightly permeable model the liquefaction is more extended in time and important values of excess pore water pressure (r_u=1.0) remain even after the motion (Figure 6.19d). This difference in the dissipation can be observed clearly in Figure 6.20, where the evolution in time of excess pore water pressure is plotted for the two points of the liquefied layer, below the levee (P5) and at FF (P6) and for all models, i.e. very permeable, permeable, slightly permeable.

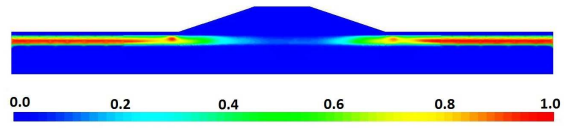

(a) Very permeable: Mainshock (t=2.4s)

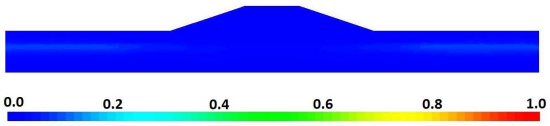

(b) Very permeable: End of earthquake (t=7.4s)

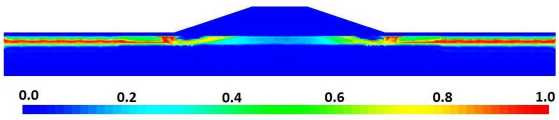

(c) Slightly permeable: Mainshock (t=2.4s)

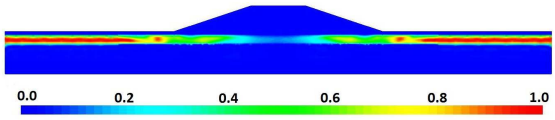

(d) Slightly permeable: End of earthquake (t=7.4s)

Figure 6.19: Influence of soil's permeability (irsn168): Excess pore water pressure ratio (r_u).

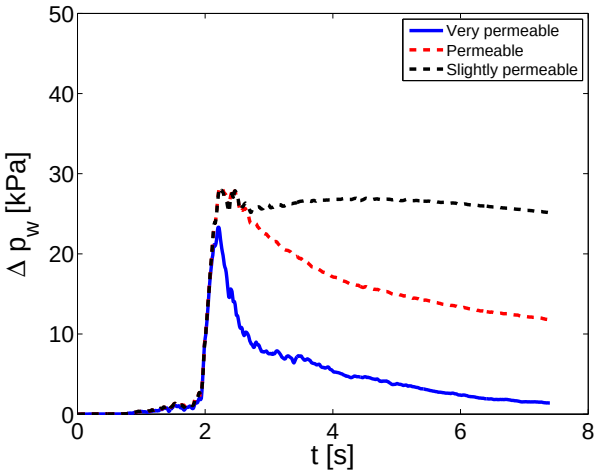

(a) LMS layer below the levee (P5)

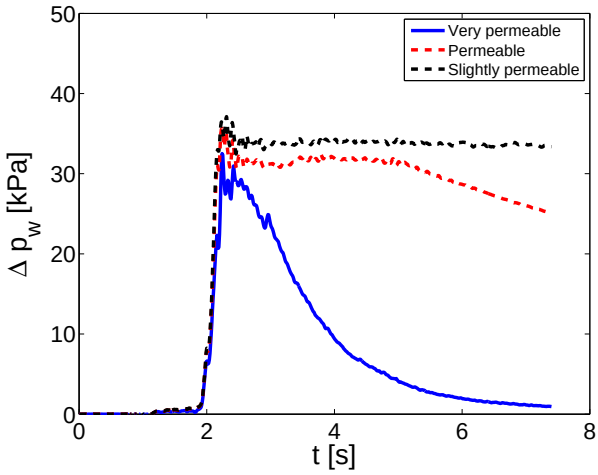

(b) LMS layer below FF (P6)

Figure 6.20: Influence of soil's permeability (irsn168): Excess pore water pressure (Δp_w) evolution during the ground motion.

Displacements

The liquefaction-induced settlements and horizontal displacements are also noticeably related to soil's permeability. This can be observed in Figure 6.21 where the evolution of relative to FF settlements and horizontal displacements inside the slope (P4) are plotted. For all values of permeability the displacements increase abruptly during the mainshock and reach a certain limit value in the coda phase. Moreover, in Figure 6.22 the final levee's settlement relative to FF is calculated along the middle cross-section, i.e. from top (P1) to base (P2). The main body of the levee is not strongly affected by the liquefaction-induced sliding as lower values of settlements are obtained, compared to the displacements of the sliding blocks close to the slope.

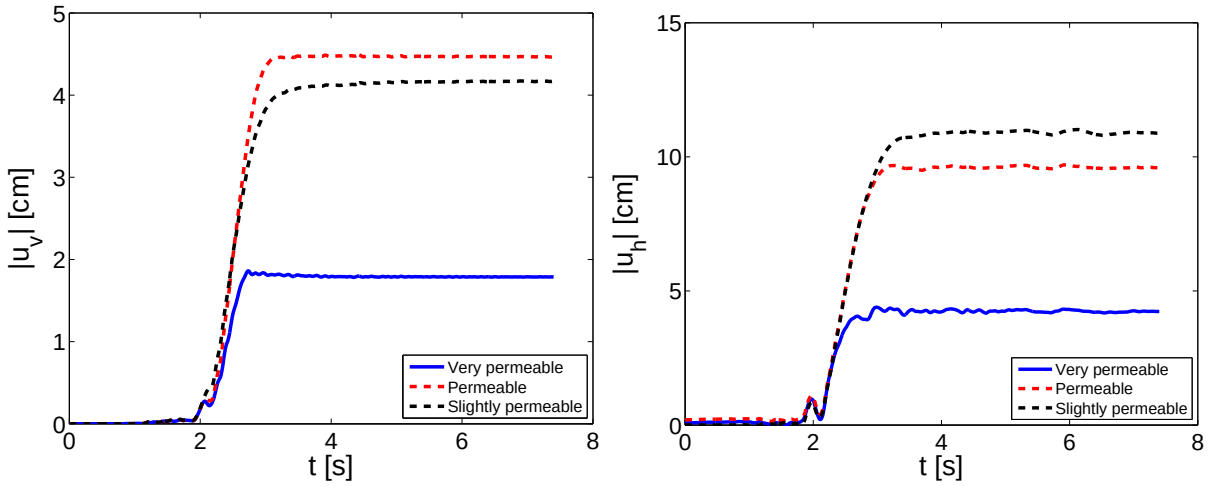

(a) Settlements. (b) Horizontal displacements.

Figure 6.21: Influence of soil's permeability (irsn168): Evolution of co-seismic displacements relative to FF during the ground motion inside the levee's slope (P4).

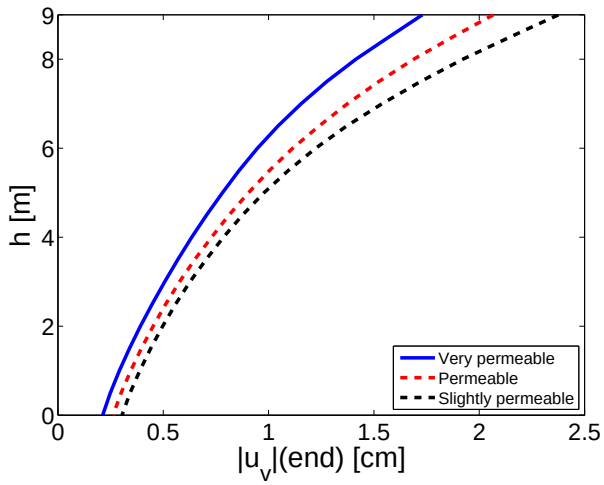

Figure 6.22: Influence of soil's permeability (irsn168): Co-seismic settlements at the middle cross-section of the levee relative to FF at the end of the motion.

Acceleration

The evolution of horizontal acceleration at the crest (P1) and FF (P3) are plotted in Figure 6.23. The response at the crest is almost identical for all models, while at FF the acceleration is deamplified during the coda phase for the permeable model and slightly permeable as liquefaction still remains and the excess pore water pressure has not dissipated. It is also noticed that in case of very permeable soil (blue curve), oscillations appear in the acceleration after the mainshock, as pore water pressure has been already dissipated and soil densification occured. Furthermore, observing the Fourier Transfrom of the horizontal acceleration for all models in Figure 6.24a, it is remarked that differences appear in the low frequencies at crest, i.e. liquefaction state. However, in Figure 6.24b

the response at FF is different in a wide range of frequencies between the very permeable and permeable or slightly permeable model, due to the aforementioned soil densification.

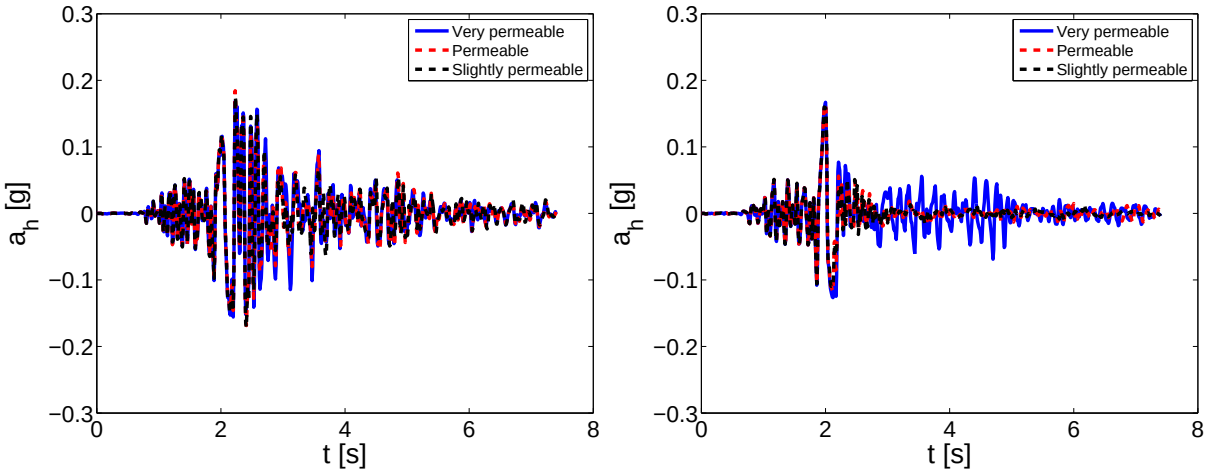

(a) Crest (P1). (b) FF (P3)

Figure 6.23: Influence of soil's permeability (irsn168): Horizontal acceleration.

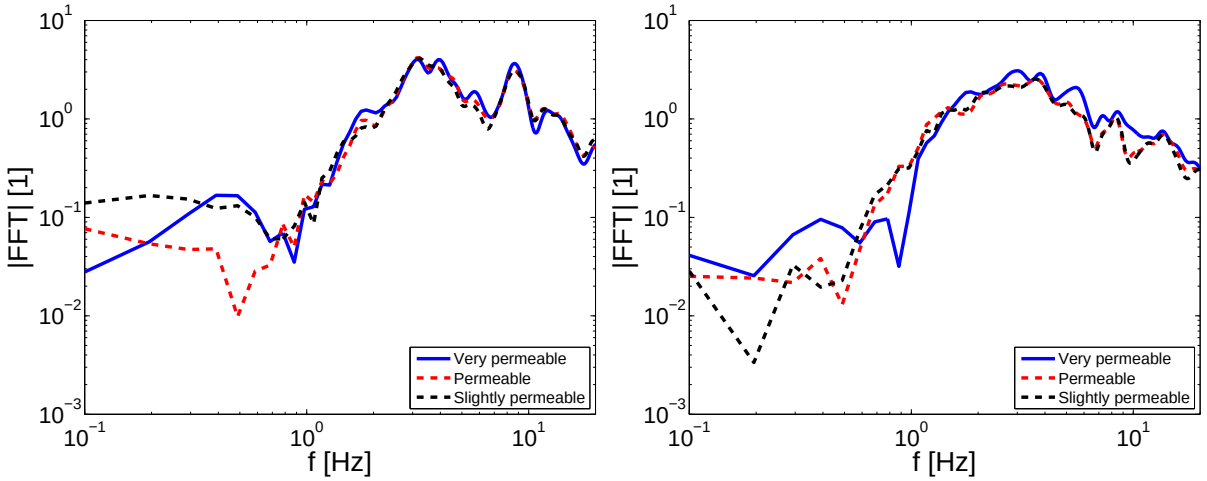

(a) Crest (P1) (b) FF (P3)

Figure 6.24: Influence of soil's permeability (irsn168): Fourier Transform of horizontal acceleration.

Stability

As observed in Figure 6.25, all models undergo instability at both sides of the levee and inside the liquefied layer, implying the eventual circular slip surface which can lead to the system's collapse. At the end of the ground motion and although in some cases excess

pore water pressures still appear, all models reach a stable state and the corresponding figures are omitted as no further information is provided.

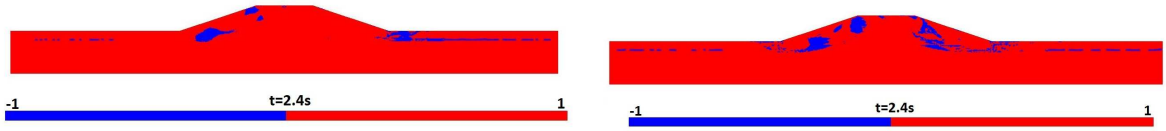

(a) Very permeable. (b) Slightly permeable.

Figure 6.25: Influence of soil's permeability (irsn168): Contours of second order work during the mainshock (t=2.4s).

Shear strains

Observing the deviatoric strains at the end of the ground motion in Figure 6.26, the two shear zones identified previously are generated in the liquefiable layer below the toes of the levee. Only in case of the slightly permeable model, these shear zones propagate inside the levee body (Figure 6.26b), as in the case of permeable model of Figure 6.10, and verify the circular collapse surface identified previously.

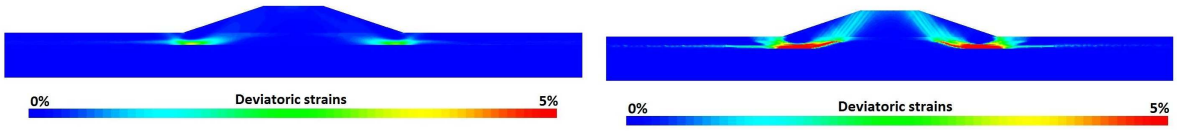

(a) Very permeable. (b) Slightly permeable.

Figure 6.26: Influence of soil's permeability (irsn168): Deviatoric strains ε_d at the end of the ground motion.

Safety factor through soil's residual strength

In Figures 6.27a, 6.27c during the mainshock (t=2.4s) and while liquefaction is reached (r_u >0.8), the same circular surface of collapse is remarked and r_k reaches unity (i.e. FS=1.0) in both models. Irrespective of soil's permeability, the safety factor is equal to 1 when the foundation is liquefied. However, in case of high permeability, at the end of the ground motion the soil has regained its strength as it reaches its initial state with $r_k \simeq 0.8$ (Figure 6.27b). While in slightly permeable model important values of r_k appear inside the zone of shear strains in the foundation, providing a low safety factor of 1.0 (Figure 6.27d).

As the slightly permeable model with the liquefiable layer situated close to the surface is the most affected one by the earthquake, it will be used in the following section for the liquefaction vulnerability analysis on the characteristics of the input motion.

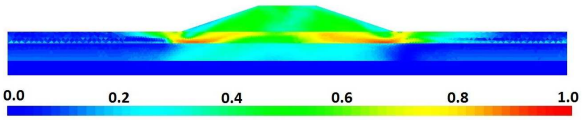

(a) Very permeable: Mainshock (t=2.4s)

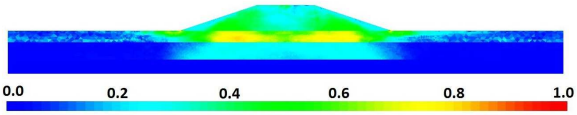

(b) Very permeable: End of earthquake (t=7.4s)

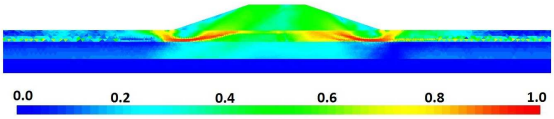

(c) Slightly permeable: Mainshock (t=2.4s)

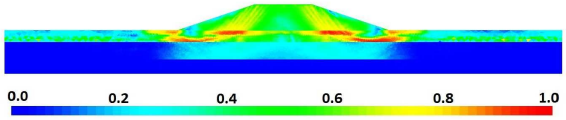

(d) Slightly permeable: End of earthquake (t=7.4s)

Figure 6.27: Influence of soil's permeability (irsn168): Contours of residual strength, r_k. a) Initial material state identical for all models, b,c) Very permeable, d,e) Permeable, f,g) Slightly permeable.

Synopsis

To sum up, after the results of the two parametric studies, the following conclusions can be drawn. On the one hand, in case that the liquefied soil layer is situated in depth in the foundation, the levee is not significantly affected. On the other hand, when the liquefied layer is situated close to the surface, it was shown when the dissipation of excess pore water pressure happens very quickly in case of permeable soils, the effect of liquefaction on the earth structure is negligible. Consequently, drainage technics (i.e. very permeable case) should be implemented in order to avoid liquefaction-induced failure of the earth structure, as also discussed by Brennan and Madabhushi (2002).

6.7 Effect of earthquake's characteristics on the dynamic response of slightly permeable model

As explained in Section 3.4 in the context of PBEE, the choice of the input ground motion is crucial for liquefaction vulnerability analysis. Following the parametric study of the soil column, where the effect of the seismic hazard was discussed, in this section the ground motions presented in Section 6.3.5 are imposed to the levee-foundation system and its dynamic response is studied. Recall that for the purposes of this analysis, the slightly permeable model with the liquefiable layer close to the surface is used (Figure 6.2), as it is the most affected one by the earthquake-induced liquefaction, unless otherwise mentioned.

In Figure 6.28, the values of horizontal and vertical PGA measured at the levee's crest, base and at FF (points P1, P2, P3 in Figure 6.2) are plotted for all ground motions as function of the maximum acceleration at outcropping ($a_{out,max}$). Concerning the horizontal PGA, it is not clear whether the crest or the base of the levee accelerate more (Figure 6.28a), whereas the vertical acceleration is obviously amplified at the crest due to soil degradation combined to the geometry effect (Figure 6.28b). Observing Figures 6.28a, 6.28b, it is noticed that the response at FF is more nonlinear for input motion's amplitude until 0.4g, while for the stronger motions the PGA at crest, base and FF mostly coincide

and is close to the line 1:1 (close to elastic behavior). In order to further examine this statement, the specific energy density (SED) is used which is the total kinetic energy over the full motion duration. It represents a measure to control the seismic wave energy of the accelerograms (Jafarian et al., 2011) and is calculated as:

$$SED = \int_0^t \dot{u}(t)^2 dt \tag{6.1}$$

In Figure 6.29, the SED is plotted and differences appear among the response of the different points for the stronger motions.

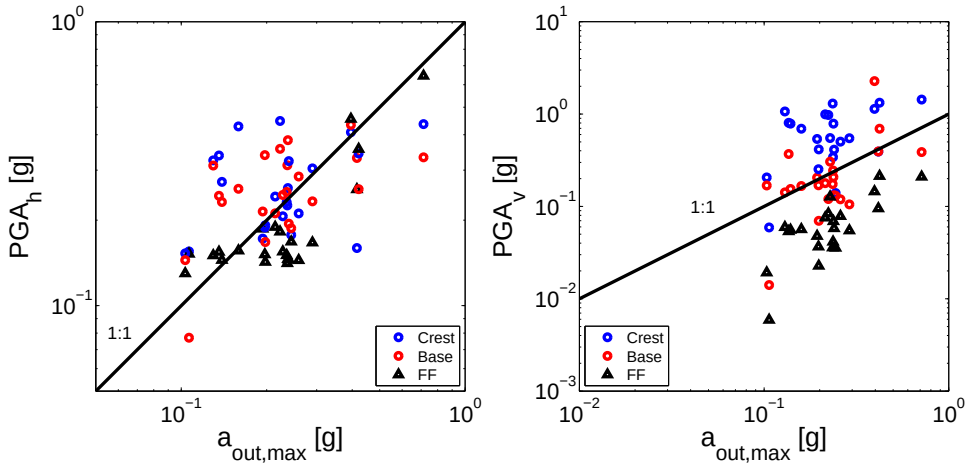

(a) Horizontal PGA. (b) Vertical PGA.

Figure 6.28: PGA as fuction of input signal's maximum acceleration $a_{out,max}$.

Moreover, two motions were selected, one with $a_{out,max}$=0.14g, where the acceleration is deamplified, and a second one with $a_{out,max}$=0.42g, whose response in terms of PGA is almost identical for all points (crest, base, FF). The motions chosen are plotted in Figure 6.30. In Figure 6.31, the acceleration time histories obtained at the crest (P1) and base (P2) of the levee are plotted for both motions and compared to the evolution of excess pore water pressure ratio below the levee (P5). For the low motion, in Figures 6.31a, 6.31b the maximum accelerations at crest and base are observed after the progressive generation of pore water pressure below the levee and as a result they are noticeably deamplified. However, in case of the stronger motion in Figures 6.31c, 6.31d, due to the peak of the seismic signal, the maximum acceleration values are noticed just before the generation of pore water pressure. Simultaneously with this peak, the value of r_u reaches unity and the layer below the levee is liquefied. For this reason the PGA found at the crest, base and FF is almost identical, as the signal instantaneously has travelled from the bedrock to the crest.

Damage level

Following the work of Kawase (2011), as explained in Section 3.4, to observe the damage level of the levee, the relative to FF crest settlements (P1) and horizontal displacements

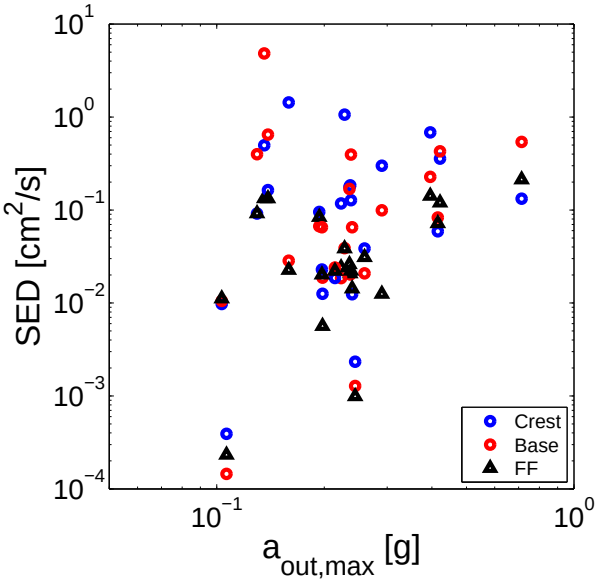

Figure 6.29: Specific Energy Density as fuction of input signal's maximum acceleration $a_{out,max}$.

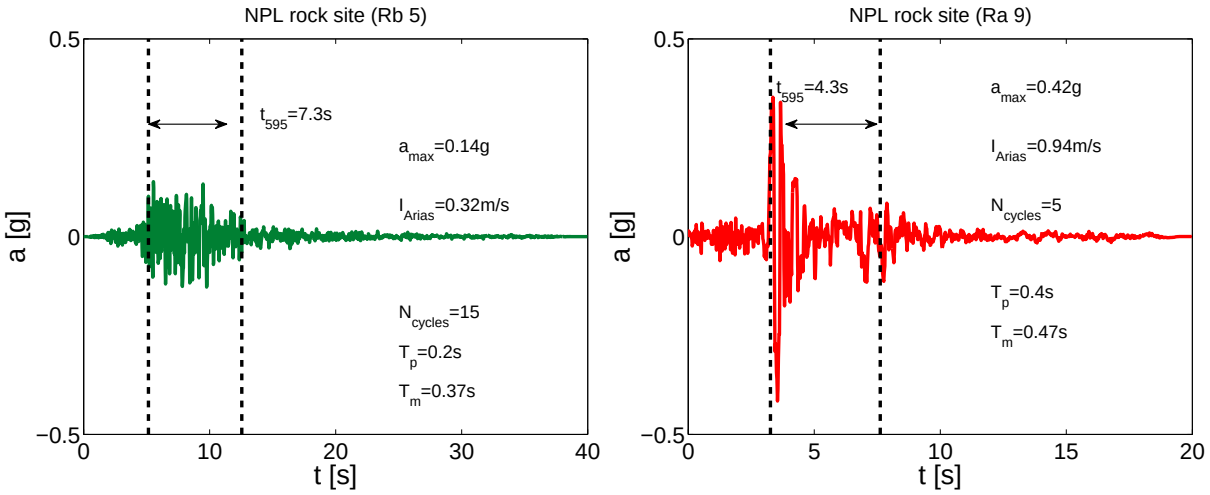

(a) (b)

Figure 6.30: Input ground motions: a) Low (Rb 5), b) Strong (Ra 9).

inside the slope of the levee (P4) as function of the maximum amplitude of the signal $a_{out,max}$ and equivalent predominant frequency $T_{V|A}$ are calculated in Figure 6.32. The circular failure path driven by the foundation's liquefaction led to significant settlements of the levee's crest (Figure 6.32a) followed by horizontal displacements of the slope (Figure 6.32b), moving as a rigid sliding block. Furthermore it is noticed that generally the increase of displacements follows the direction of increasing uniform velocity from the right-down corner towards the left-up one. Consequently, it can be concluded that for the liquefaction vulnerability analysis the IM is a vector depending on the equivalent pre-

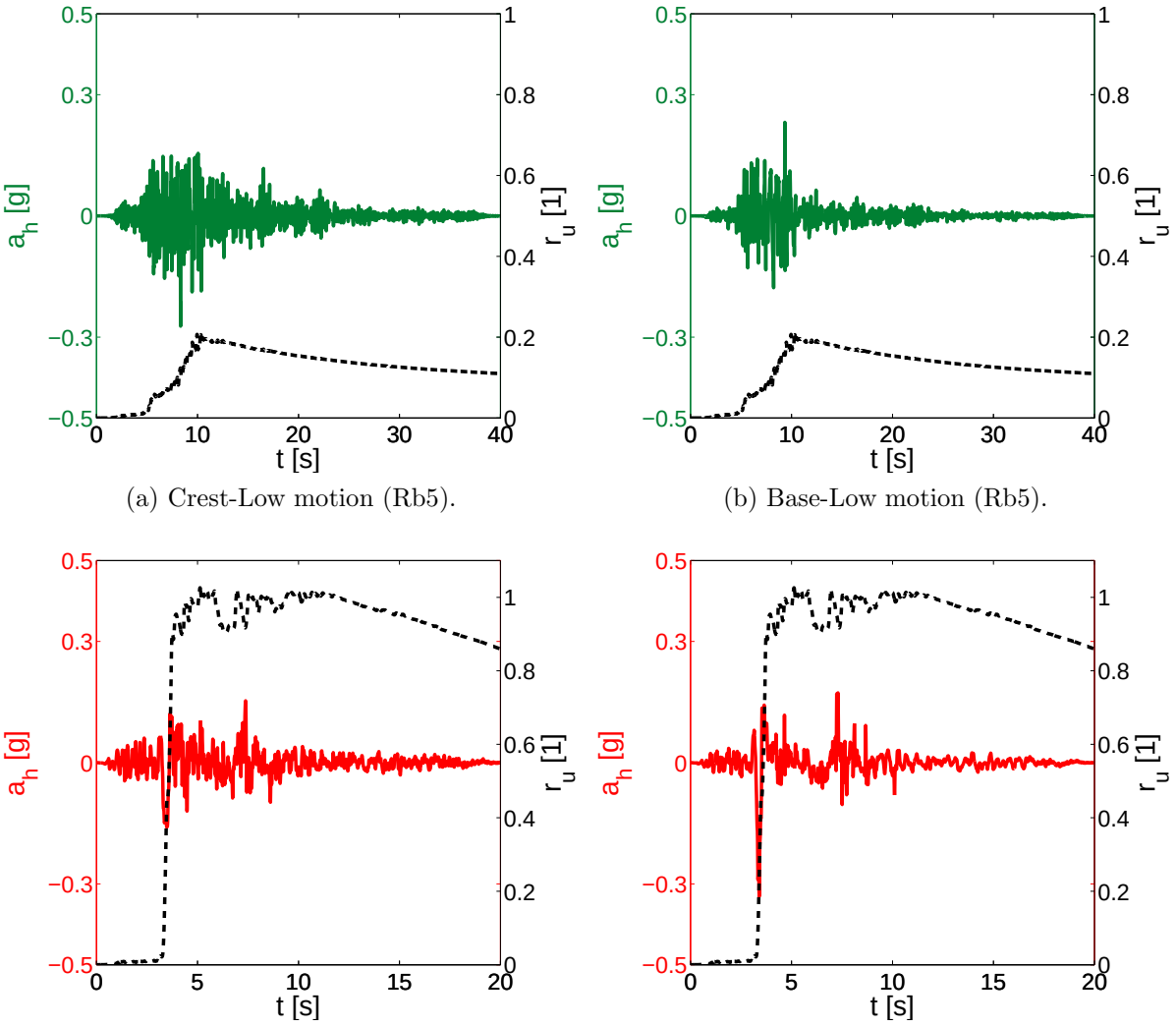

(a) Crest-Low motion (Rb5).

(b) Base-Low motion (Rb5).

(c) Crest-Strong motion (Ra9).

(d) Base-Strong motion (Ra9).

Figure 6.31: Horizontal acceleration and excess pore water pressure ratio r_u. of low motion (Ra 9): a) Crest, b) Base).

dominant frequency, the maximum acceleration and velocity of the input ground motion.

From an engineering point of view, Swaisgood (2003) investigated several dam cases that experienced an earthquake (e.g. dams in Philippines, California, Chile, Peru) and analyzed the database using statistical regression technics in order to identify the factors that have a major influence on the deformation and damage of embankment dams during earthquakes. Different types of dams were considered, but for the purposes of this study only the Hydraulic Fill (HF) and Earthfill (E) dams are taken into account. According to this work, crest settlement was selected as the parameter to represent earthquake related deformation because it was the most often mentioned quantified measurement of damage presented in the case histories. It appears to be directly related to the severity of deformation and cracking, i.e. as the percent of crest settlement increases, the extent of deformation and cracking that occurs also increases. Moreover, the PGA experienced by

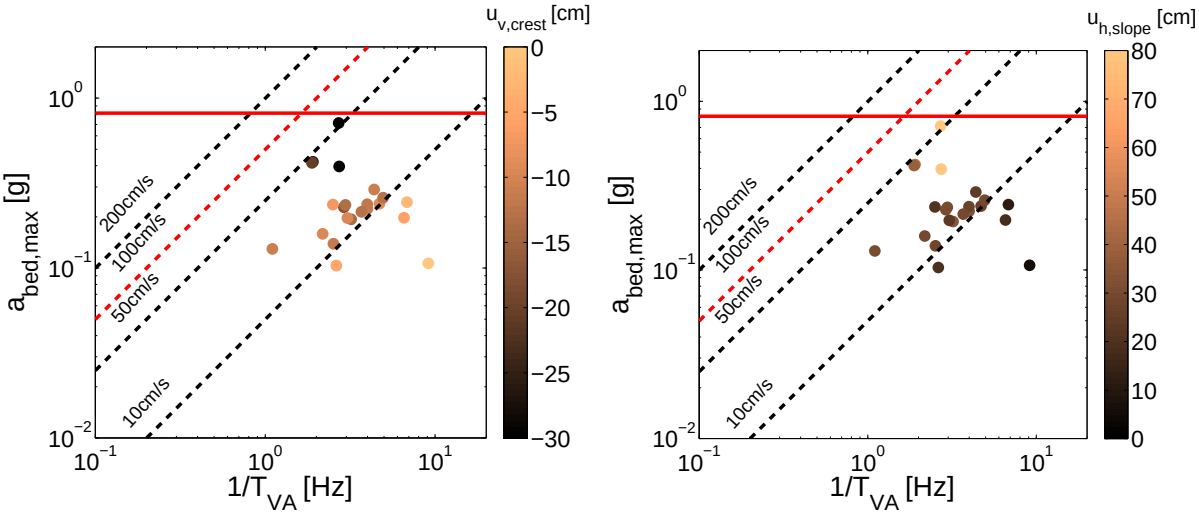

(a) Crest settlement (P1). (b) Slope's horizontal displacement (P4).

Figure 6.32: Relative to FF displacements classified according to the relation between input IM: $a_{bed,max}$ and $T_{V,A}$.

an embankment, as well as the magnitude (M) of the earthquake, had a major influence on the amount of crest settlement. It was found that the greater the PGA and M, the greater the deformations and damages. After these observations and statistical studies based on real case histories, ranges of the relative levels of damage were proposed and an empirical relation between crest settlement and PGA and magnitude was established as follows:

$$\frac{\delta u_{v,crest}}{H} = \exp(6.07 \cdot PGA + 0.57 \cdot M - 8) \text{ in } \% \tag{6.2}$$

where $\delta u_{v,crest}$/H is the percentage of crest settlement of the dam (in m) divided by the height H of the dam plus the thickness of the alluvium (in m), PGA is the peak ground acceleration of the foundation rock (in g) and M is the earthquake magnitude (in surface-wave scale, i.e. M_s). Following the work of Swaisgood (2003), Kim et al. (2011) performed centrifuge tests of typical types of Korean dams and the results obtained in terms of recorded settlements matched quite well to the values of field data of Swaisgood (2003) and the proposed damage levels, as the centrifuge results followed a similar trend.

Consequent to the aforementioned work and observations, the damage levels and relation proposed by Swaisgood (2003) are used and the results of the FE model are compared to the database of case histories. In order to calculate the settlement ratio of the levee, two approaches are used. First, the crest settlement is divided by the height of the levee plus the foundation (i.e. $\delta u_{v,crest}/(h_L+h_F)$, as shown in Figure 6.33) and the results are plotted as function of the maximum acceleration of the foundation bedrock ($a_{bed,max}$). This consideration calculates the ratio of crest settlement compared to whole height of soil layers. On the other hand, in order to account only for the levee's deformations, the relative to the base crest settlement is divided by the levee's height (i.e. $(\delta u_{v,crest}$-$\delta u_{v,base})/h_L$, as shown in Figure 6.33) and plotted as function of PGA at the levee's base

(PGA_{base}). Note that for both approaches the absolute measured settlements are used. The results of the FE model with both approaches are presented in Figure 6.34 and compared to the database of case histories. It is remarked that the response of the FE model follows the trend only for the cases where no liquefaction was observed and minor level of damage is obtained. However, in case of soil liquefaction, the levee experienced great settlement and its response is classified in the serious damage level.

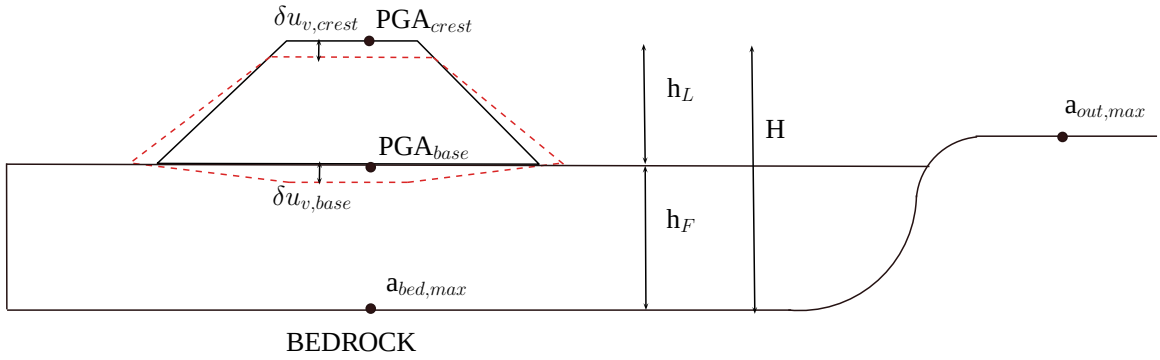

Figure 6.33: Schematic representation of calculation of levee's settlements.

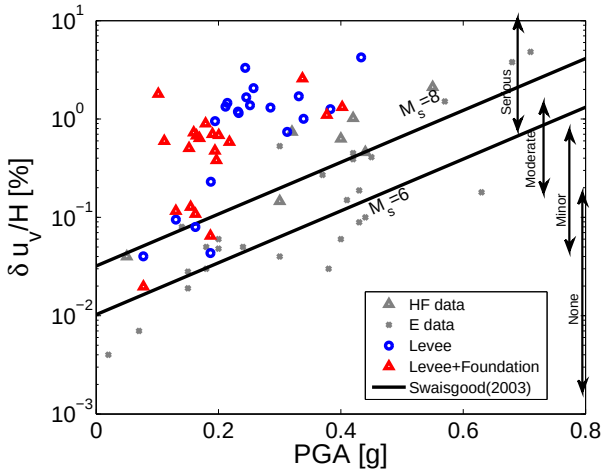

Figure 6.34: Comparison of the crest settlement ratio of the FE model to the case history database.

Comparing the two approaches, in terms of damage level, their response is quite close, but a shift to higher values of PGA is observed when only the response of the levee is taken into consideration (blue points). This is due to the fact that the signal is amplified travelling from the bedrock towards the base of the levee. In order to better observe this amplification, in Figure 6.35 the PGA obtained at the base is compared to that at the bedrock. The amplification is clear as mostly all points are over the line 1:1. The two points that are situated below the line are obtained from strong signals that liquefied the soil layer below the levee and consequently the signal that arrived at the base is deamplified. Consequently, it is underlined the importance of correctly choosing the acceleration needed for the calculations.

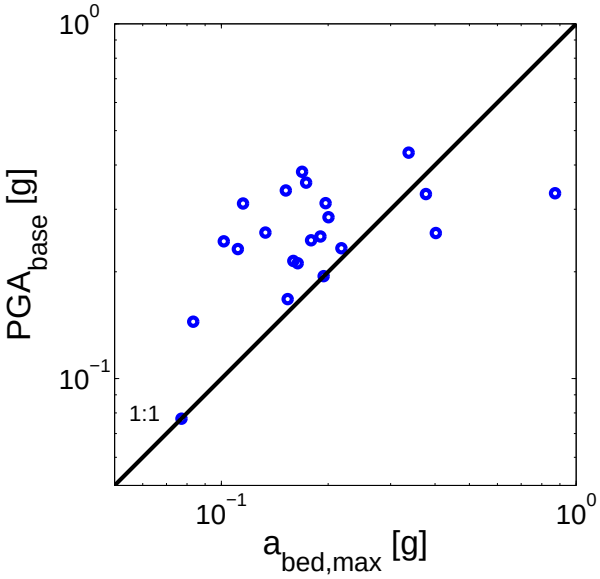

Figure 6.35: Comparison of the bedrock's to base's PGA.

In order to further observe the influence of soil liquefaction on the damage level, the same crest settlement ratio is calculated accounting for the whole height of soil layers for both models, i.e. liquefiable layer close to the surface and liquefiable layer in depth. As explained previously, in Figure 6.36 it is remarked that the response of the FE model follows the trend of the case histories only when no liquefaction or liquefaction in depth was observed (i.e. green points for the model with the liquefiable layer in depth) and moderate or minor level of damage is obtained. However, in case of soil liquefaction (red points for model with liquefiable layer close to surface), the levee experienced large settlements and its response is classified in the serious damage level.

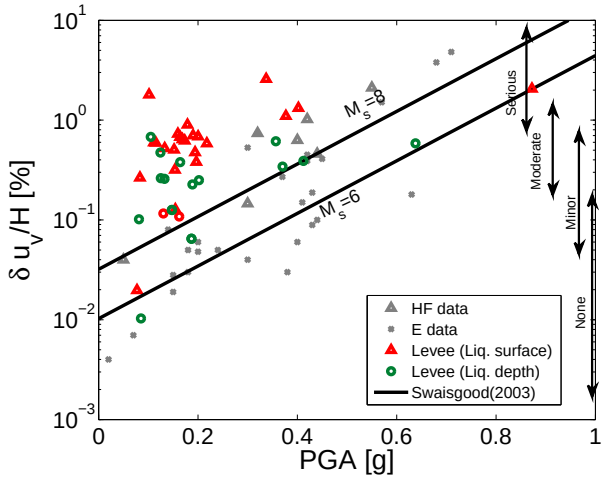

Figure 6.36: Comparison of the crest settlement ratio of the FE model to the case history database: Comparison between the two models (Liquefiable layer close to the surface and liquefiable layer in depth).

Moreover, it was found that serious levels of damage were reported in instances where the PGA exceeded 0.2g and as it can be seen in Figure 6.34 when PGA is greater than 0.2g, the results of the FE model are mostly classified in the serious damage range. However, it is noticed that a motion of 0.2g provided the same crest settlement ratio (i.e. damage level) with a motion of 0.6g, which implies that not only the amplitude of a motion is an important IM. As a result, the previous conclusion that the IM is a vector is verified. The effect of the earthquake's amplitude on the levee's damage is further investigated in the next section. Following the liquefaction vulnerability analysis of the soil column in Section 3.4, the effect of the origin (soil or rock site) and type (non pulse-like or pulse-like) of input motion, as well as, the comparison of the response obtained by Friuli earthquake and the relevant synthetic motions are also presented.

Amplitude of input motion

In order to evaluate the effect of the amplitude of input ground motion, three earthquakes are chosen of amplitudes $a_{bed,max}$=0.14, 0.24, 0.42g. In Figure 6.37 the crest settlement ratio of the levee obtained by the FE model is plotted for all input ground motions in grey and in color the response of the selected motions is illustrated. Furthemore, in Figure 6.38 the input accelerograms and response spectra of the chosen motions are presented.

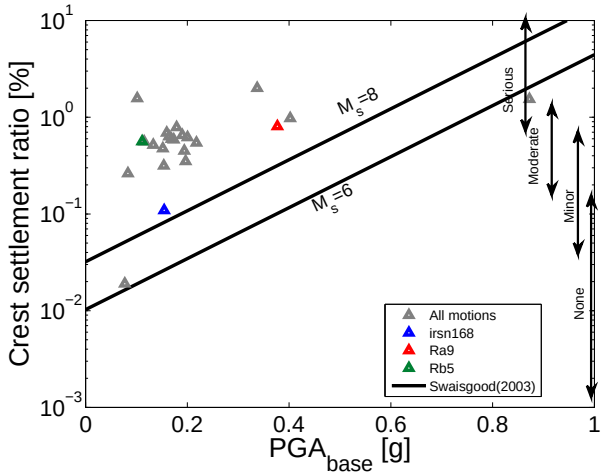

Figure 6.37: Comparison of the crest settlement ratio of the FE model: in grey all motions and in color the selected motions.

In Figures 6.39, 6.40 the deformed shape at the end of each ground motion is presented. As it concerns the horizontal displacements, in all cases both sides of the levee move towards the FF part. It is important to note that the low amplitude motions provides greater displcaments than the moderate, due to the longer duration of mainshock (t_{595}=7.3s for the low and t_{595}=0.91s for the moderate one) and cosequently extended in time liquefaction of the foundation. The same observation is made for the response in terms of settlements, as the low motion lead to greater settlements at the crest and sides of the levee (Figure 6.40a). However different failure mode is observed as the moderate motion imply a circular superficial failure mode in both sides of the levee, while the low

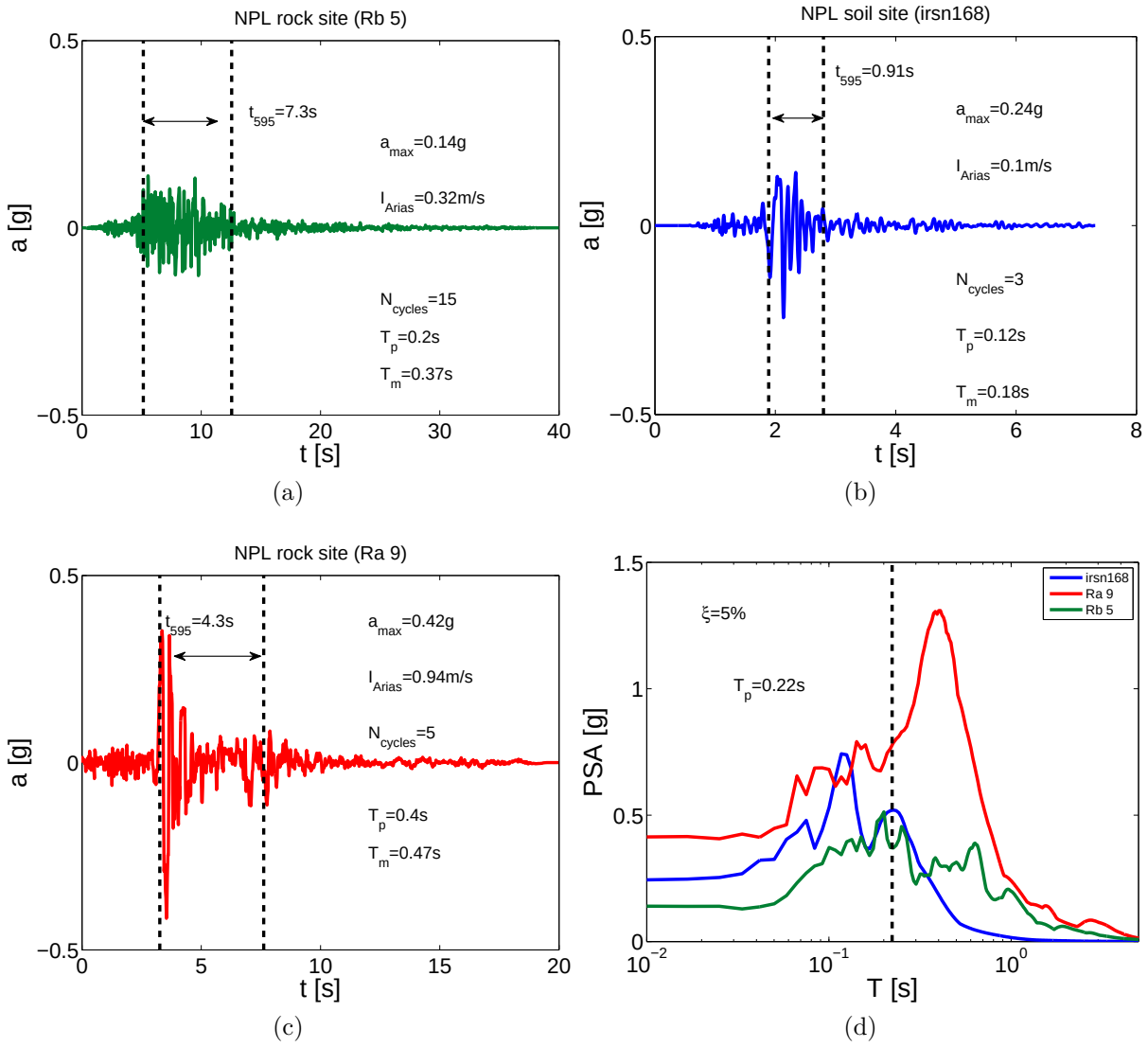

Figure 6.38: Input ground motions: a) Low (Rb 5), b) Moderate (irsn168), c) Strong (Ra 9), d) Acceleration response spectra (ξ=5%).

provides more extended settlements. The failure mode of the low motion can be classified as Type 2, while that of the moderate as Type 1 and both of them refer to failure in the levee, according to Figure6.1. Finally, in case of the strong motion, the whole foundation was liquefied, as shown in Figure 6.41, and as a consequence the whole levee settles down (Figure 6.40c) and is driven to complete collapse, i.e. failure Type 3 as indicated in Figure 6.1.

To further observe the failure path, the deviatoric deformations are illustrated at the end of the motion for all cases in Figure 6.42. In the case of low (Figure 6.42a), two shear bands are generated in the liquefied region and merge inside the levee providing a diffuse zone of shear deformations. While the moderate motion provided two thinner shear bands that propagate towards the crest. Nevertheless in the case of strong motion,

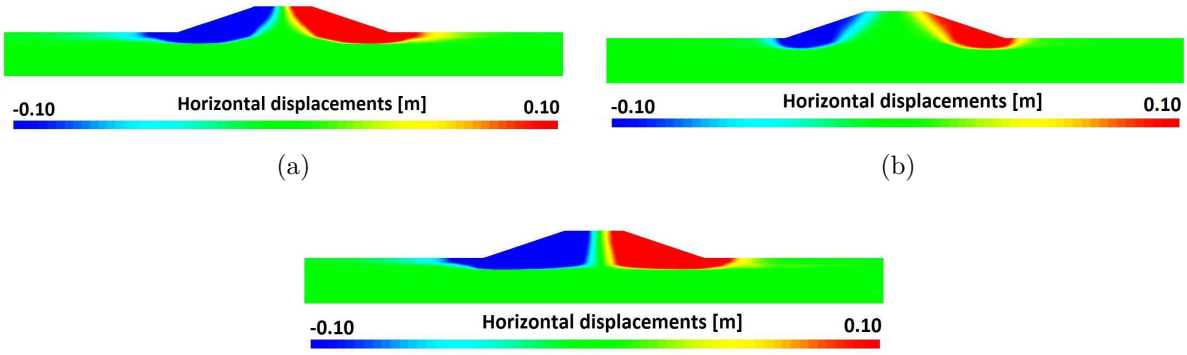

Figure 6.39: Horizontal displacements at the end of the ground motion: a) Low (Rb 5), b) Moderate (irsn168), c) Strong (Ra 9).

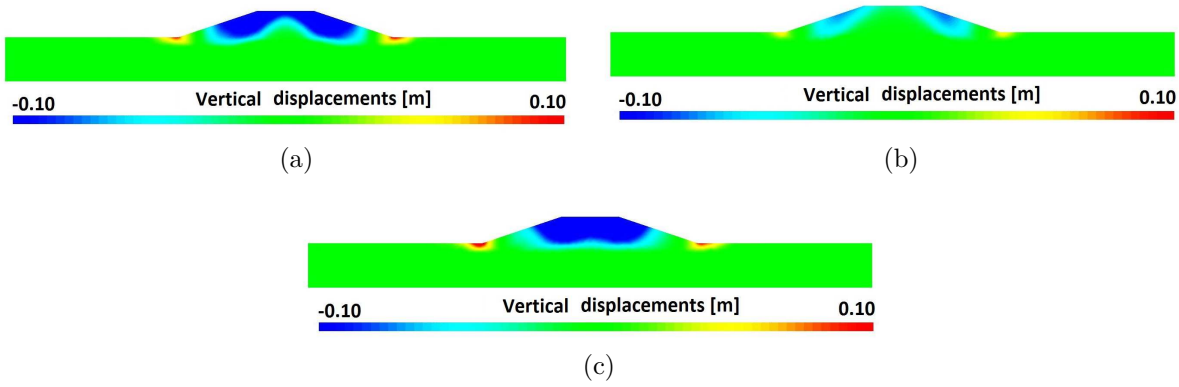

Figure 6.40: Settlements at the end of the ground motion: a) Low (Rb 5), b) Moderate (irsn168), c) Strong (Ra 9).

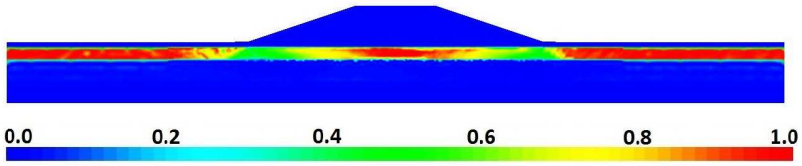

Figure 6.41: Excess pore water pressure ratio (r_u) during the mainshock (t=5s) of the strong motion (Ra9).

the shear deformations are more significant in the liquefied soil layer and a diffuse failure is observed. It is worth noting that in terms of soil's residual strength, at the end of the strong motion the soil in the liquefied layer has completely degraded and a local safety factor equal to 1 is obtained in some region (Figure 6.43).

According to the current results, it can be concluded that not only the amplitude of the ground motion is crucial for the response of such earth structures, but also the

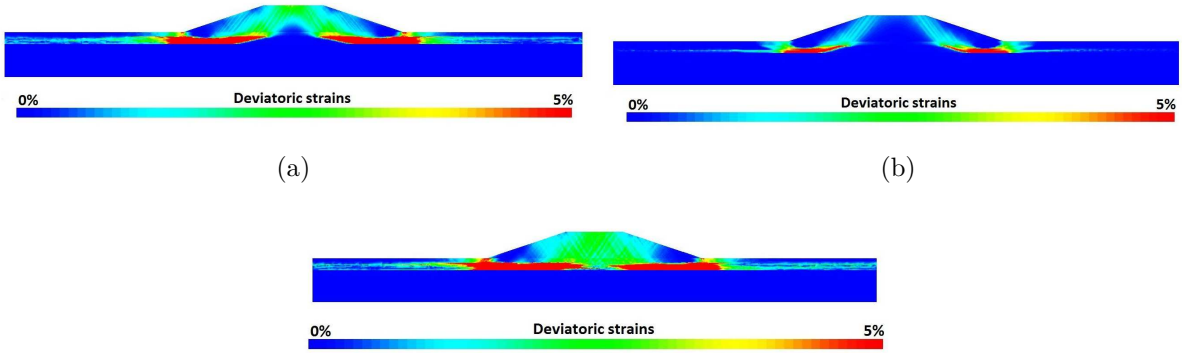

(a) (b)

(c)

Figure 6.42: Deviatoric strains ε_d at the end of the ground motion: a) Low (Rb 5), b) Moderate (irsn168), c) Strong (Ra 9).

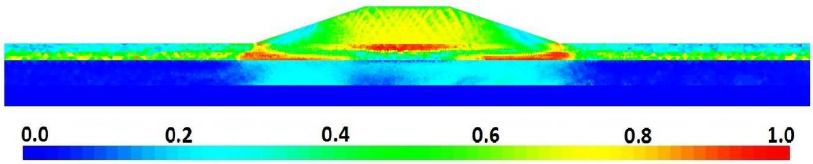

Figure 6.43: Contours of residual strength, r_k at the end of the strong motion (Ra9).

duration of mainshock should be considered.

Origin of input ground motion

Next, in order to assess the effect of the origin of input motion (recorded on soil or rock site), the same motions used in Section 3.4 are subjected to the levee-foundation system and their response is compared. Recall that both motions are of same magnitude and source-to-site distance (refer to Tables C.2, C.3 in Appendix C). The mainshock of soil site motion is longer, as calculated by the t_{595}, and contains the double number of cycles, as well as, double Arias intensity. While their response spectra are very close, the soil site motion is more apparent in low frequencies (T>1s), as shown in Figure 6.44b

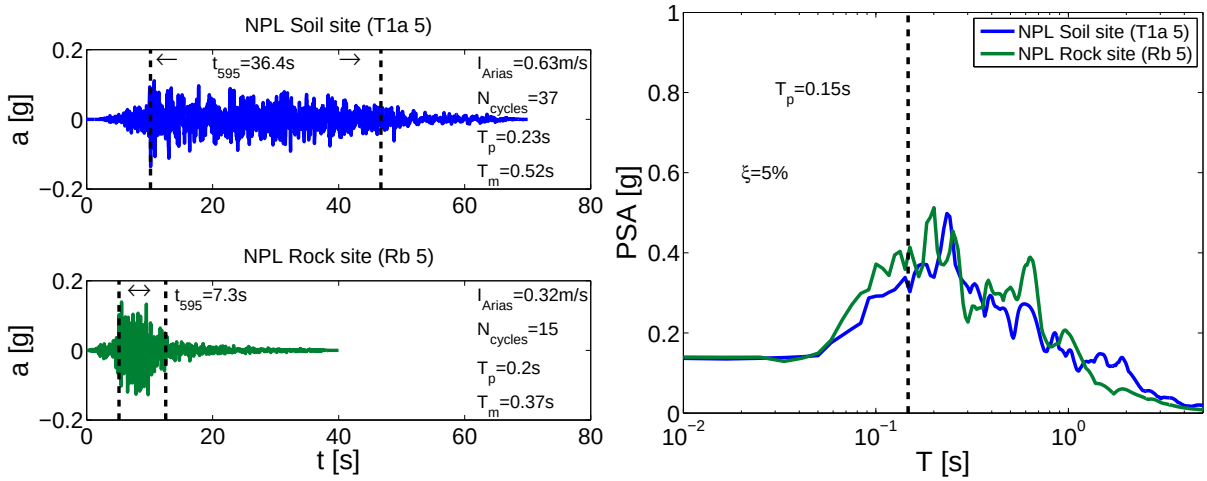

(a) (b)

Figure 6.44: Input ground motions for comparison NPL soil site motion-NPL rock site motion: a) Accelerograms T1a 5/Rb 5, b) Acceleration response spectra (ξ=5%) T1a 5/Rb 5 and T1a 3/Rb 3 (T_p of levee is indicated with the dashed line).

In Figure 6.45 the excess pore water pressure ratio r_u is plotted for both motions in two points inside the liquefied layer: below the levee (P5) in Figure 6.45a and below the FF (P6) in Figure 6.45b. As evoked in Section 3.4 also, the soil site motion leads to extended liquefaction in the whole LMS layer, while the rock site motion liquefies only the FF part. It is interesting to note also that according to Figure 6.45a in case of soil site motion, the foundation part below the levee is not initially liquefied (t<40s). However, after the liquefaction below the FF part, the water tries to dissipate towards the center of the foundation and soil liquefaction appears after the mainshock (t>40s) below the levee.

Due to the extended liquefaction in case of soil site motion, significant differences are obtained in terms of settlements of the crest (P1) relative to FF, as shown in Figure 6.46. Moreover, it is noticed that the levee settles progressively during the long mainshock of the soil site motion. This result verifies the statement that the soil site motions due to long duration of mainshock are more severe in terms of earthquake-induced liquefaction and liquefaction-induced settlements.

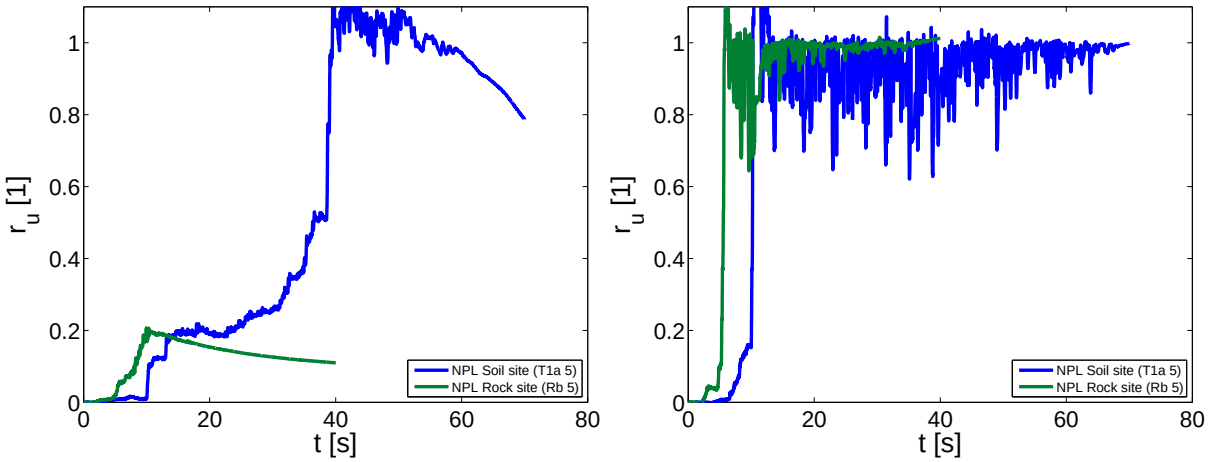

Figure 6.45: Comparison of evolution of r_u NPL soil site motion (T1a 5) - NPL rock site motion (Rb 5): a) below the levee (P5), b) below the FF (P6).

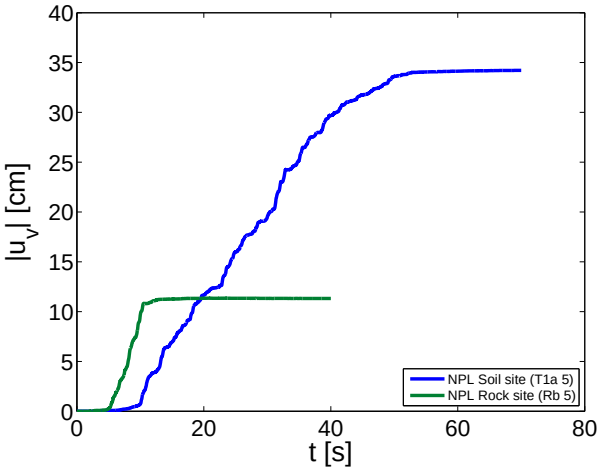

Figure 6.46: Comparison of crest's settlements: NPL soil site motion (T1a 5) - NPL rock site motion (Rb 5).

Comparison of synthetic motions to Friuli earthquake

As presented in Section 3.4, the response of Friuli earthquake is compared to this obtained by the synthetic motions generated by Code_Aster based on the natural accelerogram of Friuli. It was stated that the synthetic motions are slightly less severe than the real one, according to the classification provided in Figure 3.22 and their response was quite similar to that of Friuli for a simple, as that of the soil column (Section 3.4. Nevertheless, in the case of dynamic analysis of the levee, the reponse obtained varies a lot between the synthetic motions and Friuli signal. As observed in Figure 6.47a, the crest settlement ratio obtained by the synthetic motions is always greater than the one of Friuli earthquake. This can be further observed in Figure 6.47b, where the evolution in time of crest settlement relative to FF is represented for each ground motion.

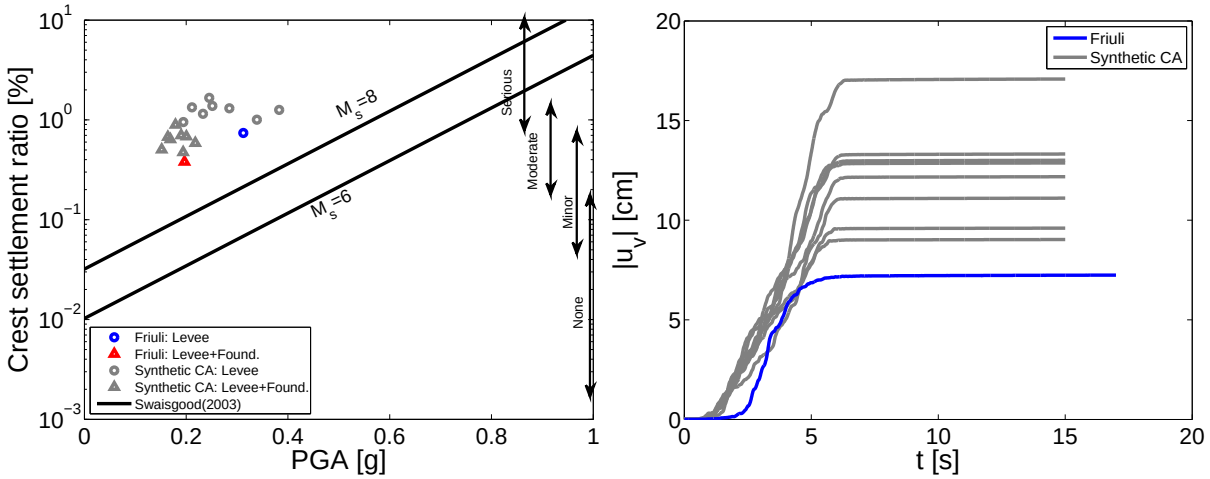

(a) (b)

Figure 6.47: Comparison of results obtained by synthetic motions and Friuli: a) Crest settlement ratio, b) Evolution of crest settlement during earthquake.

Noticeable differences are also obtained in terms of acceleration. More in detail, the response spectra at the crest, plotted in Figure 6.48a, diverge significantly with the increase of frequency. Furthermore, the profile of normalized PGA relative to the PGA at the base is plotted in the middle cross-section of the levee in Figure 6.48b. It can be seen that Friuli earthquake provides a deamplification of the PGA towards the crest, while the response of the synthetic motions do not follow the same trend. Finally, in Figures 6.48c, 6.48d the evolution of excess pore water pressure ratio r_u is illustrated below the levee (P5) and below the FF (P6). Although at FF the response of synthetic motions is close to that of Friuli as all motions led to liquefaction, below the levee remarkable differences appear. Friuli provides low values of r_u, while the synthetic motions provide increased values of r_u. It is worth noticing that even if comparing only the results of synthetic motions, the curves of generation of excess pore water pressure do not follow a unique tendency.

The aforementioned differences in soil liquefaction could be attributed to the margins in the characteristics of the input signals as shown in Table 6.2. More precisely, it is

noticed that the number of cycles, as well as the duration and Arias intensity change dramatically in case of generated synthetic motions. The same observations are discussed by Youd et al. (2001), Unjohn et al. (2012) too. So, it is important to be careful when synthetic motions are generated by natural accelerograms.

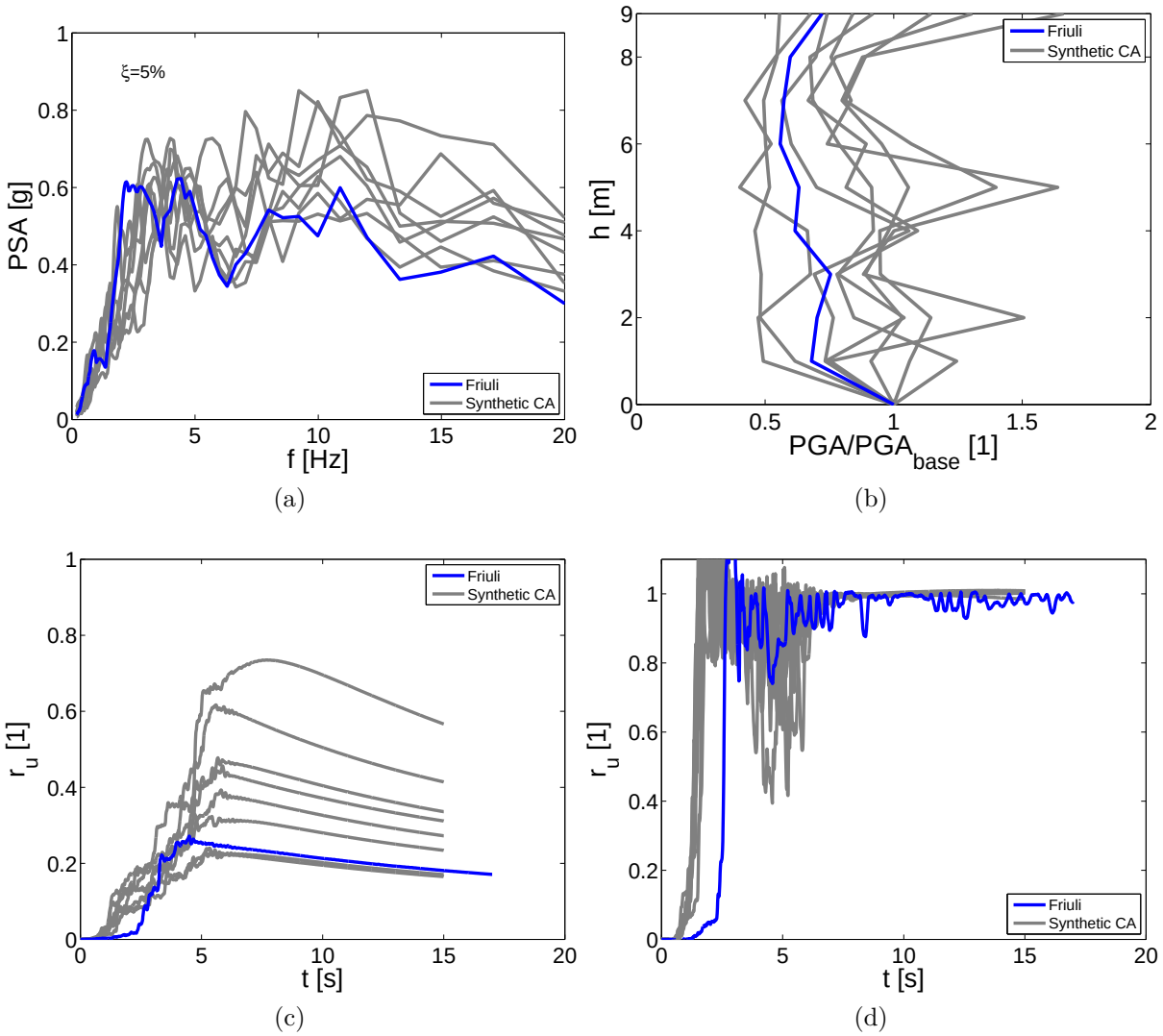

Figure 6.48: Comparison of results obtained by synthetic motions and Friuli: a) Response spectrum PSA at crest as function of frequency, b) Profile of normalized PGA at the levee's middle cross-section, c) Evolution of excess pore water pressure ratio (r_u) below the levee (P5), d) Evolution of excess pore water pressure ratio (r_u) below FF (P6).

Type of input ground motion

Lastly, the influence of type of input motion on the dynamic response is realized by comparing motions classified as non pulse-like (in blue color) and pulse-like (in red color). The same motions used in Section 3.4 are compared as they are both recorded on rock

Table 6.2: Properties of synthetic motions and Friuli earthquake.

Input motion	$\mathbf{a}_{out,max}$ **[g]** [min max]	$\mathbf{N}_{cycles}$ **[1]** [min max]	$\mathbf{t}_{595}$ **[s]** [min max]	$\mathbf{I}_{Arias}$ **[m/s]** [min max]
Synthetic motions	0.19 - 0.28	11 - 14	3.9 - 4.1	0.30 - 0.43
Friuli	0.24	4	2.8	0.22

site and have the same intensity. As it can be seen in Figure 6.49, the characteristics of the two motions are quite similar and they mostly differ in frequency content (higher frequency for the non pulse-like motion).

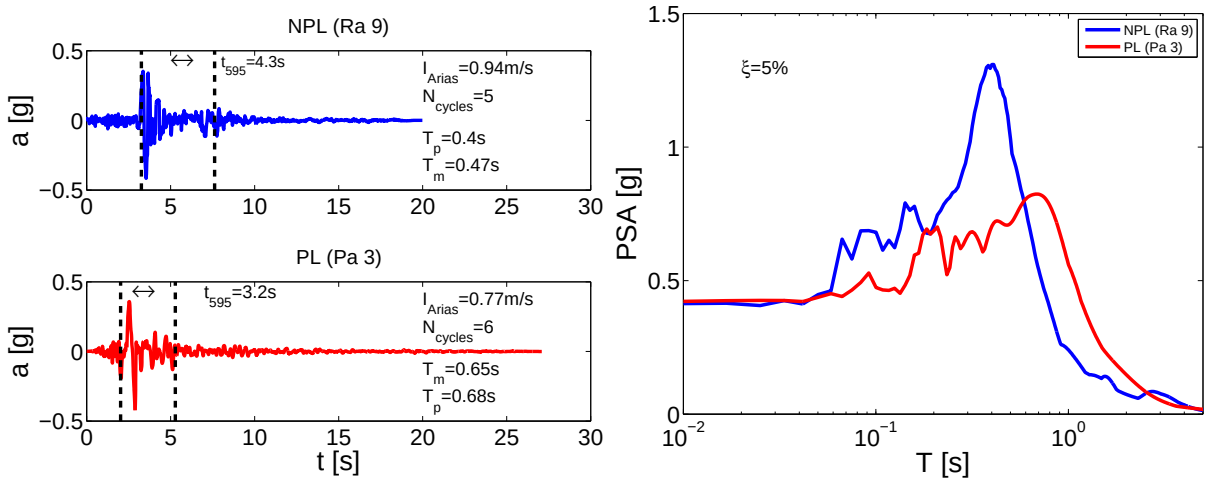

(a) (b)

Figure 6.49: Input ground motions for comparison Non Pulse-Like motion-Pulse-Like motion: a) Accelerograms Ra 9/Pa 3, b) Acceleration response spectra (ξ=5%) Ra 9/Pa 3.

As concluded in Section 3.4, the differences between the response of the non pulse-like and pulse-like motions chosen are not significant. Both of them lead to noticeable settlements during their mainshock (Figure 6.50a) and liquefied the LMS layer below the embankment as shown in Figure 6.50b. The margins obtained in terms of crest settlement in Figure 6.50a may be due to the difference in frequencies as the pulse-like motions is mostly situated in low frequencies.

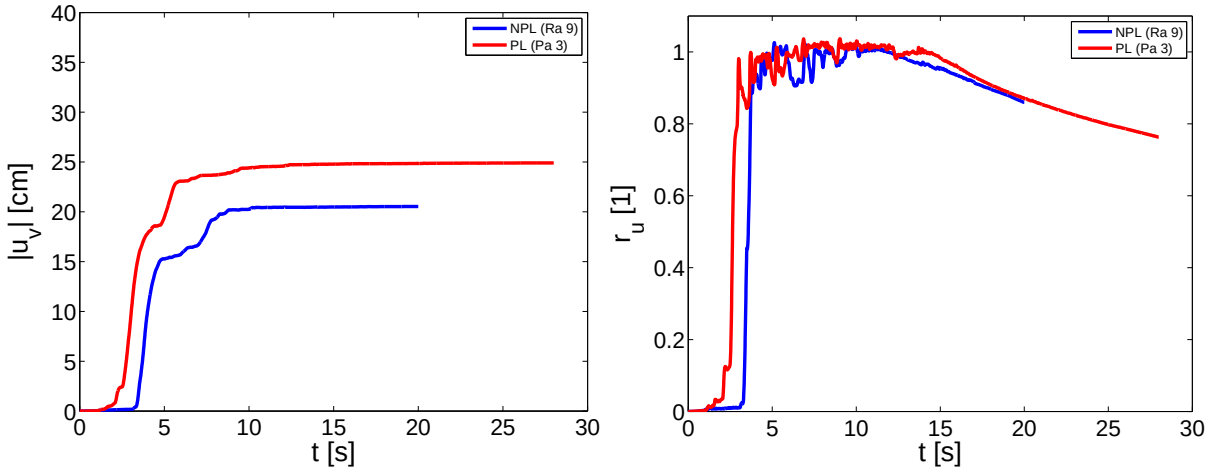

(a) (b)

Figure 6.50: Comparison of results obtained by NPL-PL motions: a) Evolution of crest settlement during earthquake, b) Evolution of excess pore water pressure ratio (r_u) below the levee (P5).

6.8 Partial Conclusions

Through a dynamic analysis of a levee founded on liquefiable soil substratum several aspects of the earthquake-induced failure mode of the structure were investigated. Firstly, the importance of soil permeability on the liquefaction-induced eventual collapse of the system was evaluated. Then, the influence of the depth of the liquefiable layer on the dynamic response of the system was evoked. The less permeable model with the liquefied layer situated close to the free surface was identified as the most critical one and a vulnerability analysis with several ground motions was performed.

In both models of varying depth of liquefiable foundation, liquefaction appears in the loose-to-medium sandy layer below the toes of the levee and expanding to the free-field area. Due to higher values of stresses and soil's consolidation below the levee, no significant excess pore water pressure is observed. These results come to an agreement with the results obtained after centrifuge tests performed by Sharp and Adalier (2006). Even so, when the liquefied layer is situated in depth, the levee is not affected by the ground motion for this particular model and earthquake loading. The liquefied layer is surrounded by two less permeable dense layer and consequently, the dissipation of excess pore water pressure happens very slowly towards the upper layer. There is no influence of foundation's liquefaction inside the levee, i.e. low values of displacements and no deformations are observed. The whole levee-foundation system remains almost stable during the ground motion (apart from instantaneous instabilities in the liquefied part) and an acceptable value of safety factor is finally calculated.

The dynamic behavior of the levee is strongly related to the liquefaction of the foundation. In case of a very permeable soil, although liquefaction appears, the dissipation of excess pore water pressure is very fast and the liquefaction-induced settlements and deformations are insignificant. These results are in agreement to the conclusions drawn

by Maharjan and Takahashi (2014) after centrifuge tests of earthen embankments founded on liquefiable foundations. Contrary, a permeable or slightly permeable layer dissipates slower and the influence of liquefaction on the structure is noticeable. A circular collapse surface is generated inside the liquefied region and extends towards the crest in both sides of the levee. A thick shear band driven by the liquefied foundation leads to the circular sliding accompanied by settlements and horizontal displacements.

It is worth noting that a circular local instability at both sides of the levee is detected in all models during the mainshock. However, all models reach a stable state at the end of the ground motion, irrespective of the excess pore water pressure that still appears in the slightly permeable foundation. This result discloses the deficiency of the second order work to take into account the accumulated co-seismic instability. For this reason, by calculating the soil's residual strength after the ground motion, low values of local safety factor (1.0-1.25) are found inside the liquefied layer in all models, denoting the significant degradation of the soil due to liquefaction. The earthquake-induced liquefaction led to soil degradation irrespective of its duration. Certainly, the slightly permeable model is more affected as the safety factor is close to 1.0 and the soil degradation is significantly apparent inside the levee, too.

However, through the liquefaction vulnerability analysis with several input ground motions, it is shown that the dynamic response of such structures is strongly related to the characteristics of the earthquake and the importance of the seismic hazard in order to define the expected failure path is discussed. Different failure paths are obtained which depend on the interaction among the levee, foundation's liquefaction and characteristics of earthquake. It is noticed that the important IMs are a combination of the equivalent predominant frequency, the maximum acceleration and velocity of the input ground motion. As a second step the duration of mainshock should also be considered, since it can be very severe in terms of structural damages. For instance a strong motion led to the extended liquefaction in the foundation part and the whole levee collapsed. Furthermore, even if the work concerning the synthetic motions was not deeply studied, the importance of chosing carefully synthetic motions generated by real ones is underlined.

To sum up, a collapse mechanism is identified for a levee-foundation system subjected to earthquake loading. Its crucial dependency on soil's permeability, depth of the liquefiable layer, as well as, characteristics of the ground motion is demonstrated through parametric studies. It should be highlighted that the aforementioned conclusions are strictly limited to the current model subjected to the particular ground motions chosen.

The influence of the characteristics of the input motions on the response of the structure should be further examined. Also, further research can be established on the influence of soil layer with anisotropic permeability to observe the direction and duration of pore water pressure dissipation and to explore the effect of earthquake loading history (role of the aftershocks). Moreover, a water filled levee or dam is expected to provide a different dynamic response, as water flow will appear inside the structure. Finally, it is imporant to provide solutions to reduce the CPU time needed for this type of dynamic analyses in order to proceed to probabilistic and fragility analyses.

Chapter 7

Conclusions and further research

In the general context of seismic assessment of earth structures, numerical methods and tools of high-performance should be developed to simulate the dynamic response of such structures subjected to earthquakes. Earthquake triggered landslides and the effect of ground-shaking on foundation-structure systems founded near slope crests is proven to be highly important in the domain of geotechnical earthquake engineering. Localized failure patterns are observed in most geotechnical structural failures, such as slope failures, settlements of foundation structures, soil sliding masses and can cause great damage. Especially in the extreme scenario of soil liquefaction, devastating consequences are observed, e.g. excessive settlements, lateral spreading and slope instability.

Findings presented in this work have illustrated the importance of advanced soil representation in order to account for eventual collapse of both dry and coupled hydromechanical structure - foundation systems. Even if partial conclusions were already given throught the dissertation, the main obtained results are highlighted in this chapter and discussed in the light of their contribution to the initial objectives. Further research work is proposed in each part of this study.

- The State-of-the-art of Code_Aster in case of SH wave propagation in dry and coupled HM nonlinear media was provided, by proposing a coherent methodology from 1D elastic models to 2D fully nonlinear coupled models, representing real case-studies. All results of the dynamic analyses were compared to those obtained by the reference software GEFDyn and a good agreement between the softwares was found.

- The effect of characteristics of input motions on the dynamic response of the soil column was assessed. In this study near-fault motions were classified as the most severe, as they led to significant accelerations and velocities. The response of a soil column was strongly related to the origin of the input ground motion. Earthquakes recorded on soil site led very quickly to important nonlinearity and extended soil liquefaction, due to long duration of mainshock (t_{595}). Consequently, in the context of liquefaction vulnerability analysis, for the chosen EDPs of interest, i.e. PGA and liquefaction-induced settlements, t_{595} is considered an important IM. This study was considered as a reference earthquake database for all dynamic simulations in the current PhD work, but further analyses could be performed in order to assess

the effect of other parameters of input motions. Moreover, probabilistic analyses could be conducted to evaluate the effect of seismic hazard on different types of structures.

- Moreover, researchers have explored the effect of soil's permeability and its evolution during the dynamic loading in the liquefaction case. Consequently, a variation of permeability as a function of liquefaction state (i.e. excess pore water pressure) was implemented and used in the numerical simulations. It was observed that such a consideration provides changes in the dissipation phase of excess pore water pressure and material behavior, which do not follow a single trend. Thus, it was concluded that soil liquefaction is a complex phenomenon, where numerous parameters interfere and the response of liquefied soils should be treated in a global scale so as to provide robust conclusions. Further research should be done and series of laboratory tests should be performed in order to observe the evolution of permeability during shaking, define the soil parameters that interact and propose an evolution law for soil's permeability.

- Next, the effect of a regularization method with enhanced kinematics approach, called first gradient of dilation model, on wave propagation was studied. Thus, an analytical solution for nonlinear classical and regularized media was developed in case of coupled S-P wave propagation on a soil column model. Through a numerical simulation, deficiencies of the use of this regularization method were observed and discussed, e.g. noise in the soil's seismic response. It was concluded that the first gradient of dilation model can not be used in its current state in case of dynamic analysis and it is proposed to examine whether a nonlinear model could be used for the regularization part instead of an elastic rigidity matrix, so both regularization and classical part follow the same behavior. Furthermore the inclusion of higher order inertial terms should be examined.

- A 2D embankment-type model was simulated and its dynamic response was evaluated in both dry and coupled hydromechanical conditions. Two criteria were used to define the onset of the structure's collapse. The second order work was used to describe the local instability at specific instants of the ground motion, while the estimation of a local safety factor was proposed by calculating the residual strength. This latter criterion provides a reliable measure of soil's strength by including material's state and estimates the safety factor of geostructures. Furthermore, the predicted earthquake-induced displacements calculated by the empirical simplified methods used in common engineering practice mostly overestimated the embankment's displacements obtained by the FE numerical simulations. Through this comparison, the importance of using advanced numerical simulation methods was underlined.

- Concerning the failure mode in dry conditions, local collapse of the embankment (i.e. shallow slope failure) was driven by a mesh insensitive shear band, which was generated at the toe due to geometry singularity. However, in case of coupled hydromechanical modeling liquefaction of the foundation led the global structure-foundation system to complete collapse (i.e. embankment and foundation collapse).

For the latter study and in order to better assess the implications of soil liquefaction, two hydromechanical approaches were considered: a fully drained and a coupled effective stress analysis. In the first one, local collapse of the embankment was observed as in the dry simulation, while in the second one, the foundation's liquefaction produced an extended circular collapse zone. Thus, it was concluded that the effect of excess pore water pressure is of great importance, as an otherwise stable structure-foundation system becomes unstable during coupled analysis. Moreover, this work demonstrated the capability of the used elastoplastic constitutive model to represent cyclic behavior, i.e. the dynamic response and earthquake-induced deformations of a structure, due to the coupling of volumetric and deviatoric strains.

- Finally, a levee - foundation system was simulated and the influence of soil's permeability and depth of the liquefiable layer on the liquefaction-induced failure was evaluated. For the current levee model, its induced damage level (i.e. settlements and deformations) was strongly related to both liquefaction apparition and dissipation of excess pore water pressure on the foundation. It was noted that the lower the permeability value, the higher the induced damage. A circular collapse surface was generated inside the liquefied region and extends towards the crest in both sides of the levee for low and moderate motions. While total collapse is expected for stronger motions, as the whole levee settled down. Even so, when the liquefied layer was situated in depth, minor effect on the levee response is found. Through the liquefaction vulnerability analysis with several input ground motions, it was shown that the dynamic response of such structures is strongly related to the characteristics of the earthquake. Different failure paths were obtained which depend on the interaction among the levee, foundation's liquefaction and characteristics of earthquake. It was noticed that signals with great amplitude or long duration of mainshock can be very severe in terms of structural damages. The influence of the characteristics of the input motions on the response of the structure should be further examined. Also, further research can be established on the influence of soil layer with anisotropic permeability to observe the direction and duration of pore water pressure dissipation and to explore the effect of earthquake loading history (role of the aftershocks). Moreover, a water filled levee or dam is expected to provide a different dynamic response, as water flow will appear inside the structure.

This research work can be considered as a reference case study for seismic assessment of embankment-type structures subjected to earthquake loading by means of FE simulations and notably, it provides an advanced computational framework accessible to engineers. Further research can be established on the influence of the seismic hazard on the liquefaction-induced failure risk of geostructures by conducting probabilistic analyses.

Appendices

Appendix A

Newmark time integration scheme

Dynamic Finite Element analyses of engineering structures employ step-by-step integration methods to obtain a time domain solution of the equation of motion. A basic requirement for an integration scheme is an unconditional stability for linear problems (Kontoe et al., 2008). An integration method is described as unconditionally stable if the numerical solution for any initial value problem does not grow without bound for any time step Δt, especially if the time step is large (Ebeling, 1992).

Throughout this PhD work the Newmark time integration method is used for the dynamic finite element analyses. Before applying this integration method, the theoretical background of the method is presented and a parametric analysis of a nonlinear soil column was performed, in order to better understand the effect of Newmark integration parameters on the damping estimation.

According to Kontoe et al. (2008), the Newmark integration parameters introduce a numerical damping, whose role is to eliminate spurious high-frequency oscillations without affecting low to medium frequency modes that are of earthquake engineering interest in soil mechanics.

The general governing finite element equation at time $t = t_{k+1}$, commonly known as the equation of motion, is:

$$[M] \cdot \{\ddot{u}(t_{k+1})\} + [C] \cdot \{\dot{u}(t_{k+1})\} + [K] \cdot \{u(t_{k+1})\} = \{R(t_{k+1})\} \tag{A.1}$$

where $[M]$, $[C]$, and $[K]$ are the global mass, damping and stiffness matrices, respectively, $\{R\}$ is the vector of the global applied loads, $\{u\}$ is the displacement vector and the superimposed dots indicate time differentiation. In the current study the term of damping is neglected.

The displacement and velocity are calculated with Newmark method as shown in Equations A.2 and A.3:

$$u(t_{k+1}) = u(t_k) + \dot{u}(t_k) \cdot \Delta t + (\frac{1}{2} - \beta)\ddot{u}(t_k) \cdot \Delta t^2 + \beta \cdot \ddot{u}(t_{k+1}) \cdot \Delta t^2 \tag{A.2}$$

$$\dot{u}(t_{k+1}) = \dot{u}(t_k) + (1 - \gamma) \cdot \ddot{u}(t_k) \cdot \Delta t + \gamma \cdot \ddot{u}(t_{k+1}) \cdot \Delta t \tag{A.3}$$

According to Kontoe et al. (2008), solving these implicit equations leads to the set of Equations A.4:

$$\begin{aligned} u_{k+1} &= [A] \cdot u_k \\ \dot{u}_{k+1} &= [A] \cdot \dot{u}_k \\ \ddot{u}_{k+1} &= [A] \cdot \ddot{u}_k \end{aligned} \tag{A.4}$$

where A is the amplification matrix that determines algorithmic characteristics such as stability, accuracy and numerical dissipation. The amplification matrix A is obtained by eliminating $\ddot{u}_k$ and $\ddot{u}_{k+1}$ from the Equations A.2 and A.3 (Hughes, 2000). The spectral radius (ρ_∞) is the maximum eigenvalue of the amplification matrix. The algorithm is stable when $\rho_\infty \leq 1$. For ρ_∞ equal to 1, the dissipation is equal to zero, but as ρ_∞ decreases, the algorithmic dissipation increases (Kontoe et al., 2008).

The Newmark integration parameters β and γ (Equations A.5 and A.6) used for the following parametric analysis are presented in Table A.1 (Kuhl and Crisfield, 1999).

$$\gamma = \frac{(3 - \rho_\infty)}{(2\rho_\infty + 2)} \tag{A.5}$$

$$\beta = \frac{1}{(\rho_\infty + 1)^2} \tag{A.6}$$

$$\tag{A.7}$$

The Newmark method is uncoditionally stable when the Equation A.8 is satisfied (Hughes, 2000).

$$2\beta \geq \gamma \geq \frac{1}{2} \tag{A.8}$$

Table A.1: Newmark integration parameters

ρ_∞	γ	β
1.0	0.50	0.25
0.9	0.55	0.28
0.8	0.61	0.31
0.7	0.68	0.35
0.6	0.75	0.39
0.5	0.83	0.44
0.4	0.93	0.51
0.3	1.04	0.59
0.2	1.17	0.69
0.1	1.32	0.83
0.0	1.50	1.00

A.1 Damping estimation

A 9m high nonlinear dry soil column is used for the study of damping estimation and is subjected to a sample seismic signal at very low amplitude to ensure elastic soil behavior. A parametric analysis is performed using all sets of Newmark parameters, as presented in Table A.1.

In Figure A.1a dissipation of energy is noticed as numerical damping increases, starting from a non dissipative scheme (ρ_∞=1.0) to the maximum value of numerical damping added (ρ_∞=0.0).

As aforementioned, Newmark parameters introduce a numerical damping ξ which can be determined as follows, according to (Ruiz and Saragoni, 2009):

$$\frac{u_{top}}{u_{max}} = B \cdot \exp(-\xi\omega_0 t) \cdot \cos(\omega \cdot t) \tag{A.9}$$

where u_{top} is the top displacement and u_{max} is the maximum displacement measured, B is a fluctuating function that depends on time (t), ω is the angular frequency equal to $2\pi \cdot f_p$ and f_p stands for the fundamental frequency.

The curve of u_{top}/u_{max} - $\omega \cdot t$ is plotted in Figure A.1c in order to calculate damping for each curve. In Figure A.1d, the relation of damping ξ and spectral radius ρ_∞ is demonstrated as it has been calculated according to Equation A.9. When spectral radius is equal to 1, damping is equal to 0 and there is no dissipation of energy, but when spectral radius decreases, the dissipation and damping increase. The relation between spectral radius and damping is almost linear.

It is recommended to add numerical damping to the model, so as to provide a damping in the elastic domain. More in detail, it is remarked a noise in the dynamic response in case of a non-dissipative scheme (β=0.25, γ=0.50). As shown in Figure A.2, where the horizontal acceleration measured at the top of the soil column relative to the base is plotted for a real earthquake ("ita Lb 1" input ground motion, refer to Appendix C), an amplification of the seismic signal at the last seconds of ground motion is produced for a non-dissipative scheme (blue curve). However, when damping is added (green curve) the noise dissapears.

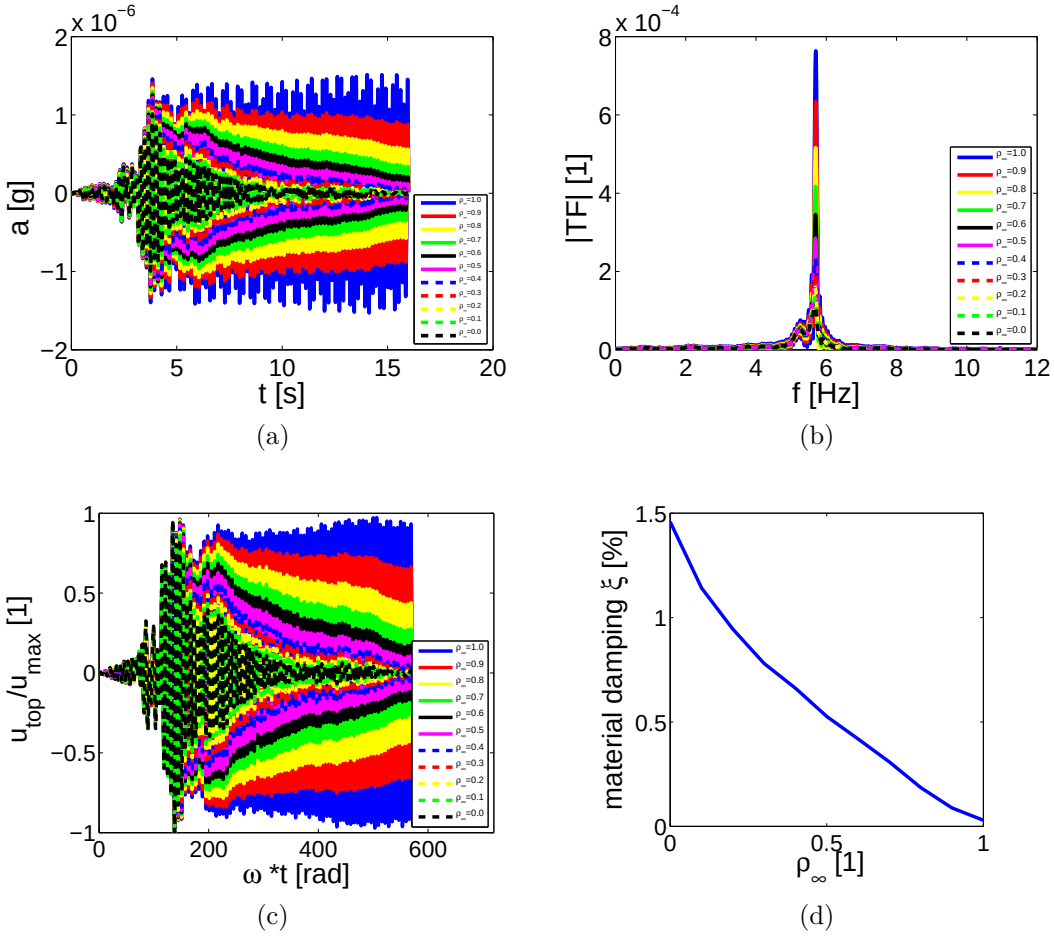

Figure A.1: Parametric analysis for different sets of Newmark parameters: a) Horizontal acceleration at the top of the column relative to the base, b) Transfer function, c) u_{top}/u_{max} - $\omega \cdot t$, d) Evolution of material damping as function of ρ_∞.

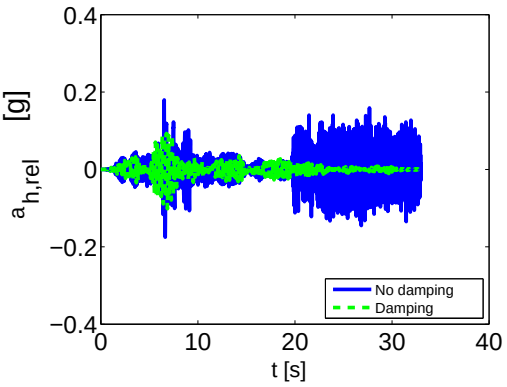

Figure A.2: Comparison of results with and without numerical damping: Horizontal relative acceleration at column's surface.

Appendix B

ECP multimechanism model

B.1 General hypotheses and characteristics of the model

The ECP elastoplastic multi-mechanism model (Hujeux, 1985) is used to represent soil behavior under cyclic loading, as it can take into account soil behavior in a large range of loading paths. Its principal characteristics are the following:

- The representation of all irreversible phenomena is idealized by four coupled elementary plastic mechanisms: three plane-strain deviatoric plastic deformation mechanisms in three orthogonal planes and an isotropic one.
- The model is written in terms of Terzaghi effective stresses and it uses a Coulomb-type failure criterion and the critical state concept.
- The evolution of hardening is based on plastic strain (deviatoric and volumetric strain for the deviatoric mechanisms and volumetric strain for the isotropic one).
- The model takes into account non-linear elasticity and to account for cyclic behavior both isotropic and kinematical hardenings are used.

Soil behavior is divided in four sub-domains:

1. Elastic domain: no energy dissipation and reversible deformations.
2. Hysteretic or pseudo-elastic domain: energy dissipation when plastic deformations appear, but the volumetric plastic strain variation is neglected.
3. Intermediate domain: the volumetric plastic strain variation is no longer neglected.
4. Mobilized domain: the shear stress mobilizes completely the shear resistance of the solid phase.

An implicit integration scheme is used for the equations of the model into Code_Aster (Foucault, 2009).

B.2 Elasticity

The elasticity domain is isotropic and nonlinear, where the bulk (K) and shear (G) moduli are functions of the mean effective stress (p'), as following:

$$K = K_{ref}\left(\frac{p'}{p'_{ref}}\right)^{n_e} \quad \text{and} \quad G = G_{ref}\left(\frac{p'}{p'_{ref}}\right)^{n_e} \tag{B.1}$$

with K_{ref} and G_{ref} being the bulk and shear moduli at the reference stress path (p'_{ref}) and n_e the degree of nonlinearity.

B.3 Yield surface and hardening laws for the deviatoric mechanisms

Adopting the soil mechanics sign convention (compression positive), the deviatoric primary yield surface of the k plane is given by:

$$f_k(p'_k, \varepsilon^p_v, r_k) \;=\; q_k - sin\phi'_{pp} \cdot p'_k \cdot F_k \cdot r_k \tag{B.2}$$

where p'_k and q_k are the mean and deviatoric values of stress tensors, ϕ'_{pp} is the friction angle at critical state, the function F_k controls isotropic hardening associated with the plastic volumetric strain, whereas r_k accounts for the isotropic hardening generated by plastic shearing. They represent progressive friction mobilization in the soil and their product reaches unity at perfect plasticity.

The function F_k, through the plastic volumetric stain ε^p_v, introduces volumetric hardening or softening:

$$F_k(p', \varepsilon^p_v) = 1 - b \cdot \ln\frac{p'}{p_c} \tag{B.3}$$

$$p_c = p_{c,0} \cdot \exp(\beta \cdot \varepsilon^p_v) \tag{B.4}$$

where b is a parameter that controls the form of the yield surface in the p'_k - q_k plane and varies from 0 to 1 passing from a Coulomb type surface to a Cam-Clay type one (Figure B.1), $p_{c,0}$ is the critical mean effective stress that corresponds to the initial state and β is the plastic compressibility modulus that introduces the influence of the densification of the material in the final resistance.

The hardening variable r_k can be interpreted as the degree of mobilization of the deviatoric mechanism k, i.e. the degree of friction mobilization. It corresponds to progressive plasticity evolution due to plastic shear distortion γ^p_k of the k mechanism. Thus, it accounts for the isotropic hardening generated by plastic deviatoric strains ε^p_d or γ^p_k. This variable varies from r^{el}_k (elastic domain) to its limit unit value in the perfect plasticity, as follows:

$$r_k = r^{el}_k + \left(\frac{\varepsilon^p_{d,k}}{a + \varepsilon^p_{d,k}}\right) \tag{B.5}$$

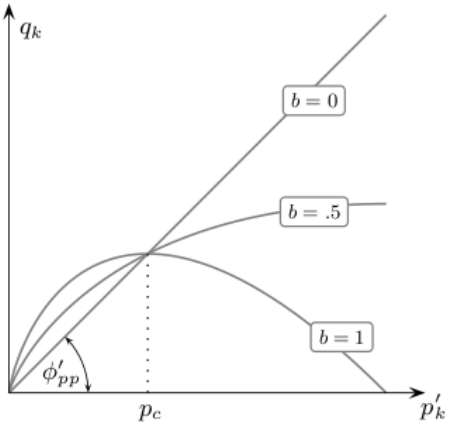

Figure B.1: Influence of parameter b on the yield surface shape.

The parameter a, in Equation B.5, controls the hardening evolution, by controlling r_k. It is an important parameter of the model because it controls the rigidity when the soil is in the plastic domain and is defined through the following relation:

$$a = a_1 + (a_2 - a_1) \cdot \alpha(r_k) \tag{B.6}$$

where $\alpha(r_k)$ is defied through the behavior domains described below:

$$\alpha(r_k) = \begin{cases} 0 & \text{if } r_k < r_k^{hys} \quad \text{pseudo-elastic domain} \\ \left(\frac{r_k - r_k^{mob}}{r_k^{mob} - r_k^{hys}}\right)^m & \text{if } r_k^{hys} < r_k < r_k^{mob} \quad \text{hysteretic domain} \\ 1 & \text{if } r_k^{mob} < r_k < 1 \quad \text{mobilized domain} \end{cases} \tag{B.7}$$

in which r_k^{hys} and r_k^{mob} are the thresholds friction mobilization sub-domains associated to mechanism k. Consequently, the parameter $\alpha(r_k)$ allows that for drained conditions, there is no volume variations until a certain level of shearing is achieved. In addition, for undrained conditions, it allows that the evolution of the pore water pressure will depend on the level of deformations. The evolution into the hysteretic domain is controlled by the value of m (Figure B.2).

In case of cyclic loading, the kinematic hardening can be expressed in terms of the position of the current stress state with respect to the position of the last load reversal, through the harderning variable r_k^c:

$$r_k^c = r_k^{el} + \left(\frac{|\varepsilon_{d,k}^p - \varepsilon_{d,k}^{p,h}|}{a + |\varepsilon_{d,k}^p - \varepsilon_{d,k}^{p,h}|} \right) \tag{B.8}$$

where $\varepsilon_{d,k}^{p,h}$ is the plastic deviatoric deformation of the mechanism k at the last load reversal h. The variable a obeys the same relations as in monotonic loading (Eq.B.6).

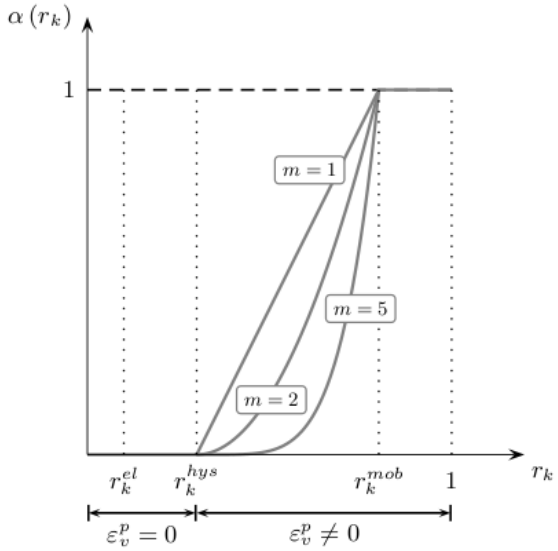

Figure B.2: Graphic representation of $\alpha(r_k)$ controlling the evolution of deviatoric mechanism k.

B.4 Plastic potential and flow rule for the deviatoric mechanisms

The evolution of the plastic deviatoric deformations follows an associated flow rule:

$$\dot{\varepsilon}_{d,k}^p = \dot{\lambda}_k^p \cdot \frac{\partial f_k}{\partial q_k} \tag{B.9}$$

where $\dot{\lambda}_k^p$ is the plastic multiplier for the mechanism k and can be obtained by the consistency condition $\dot{f}_k = 0$ over all active mechanisms.

The evolution of the volumetric plastic strains is controlled by a Roscoe-type dilatancy flow rule (Schofield and Wroth, 1698):

$$\dot{\varepsilon}_{v,k}^p = \dot{\lambda}_k^p \cdot \psi_k \tag{B.10}$$

$$\psi_k = \alpha_\psi \cdot \alpha(r_k) \cdot \left(\sin\psi - \frac{q_k}{p'_k}\right) \tag{B.11}$$

where ψ is the characteristic angle defining the limit between dilatancy ($\dot{\varepsilon}_v^p$ <0) and contractancy ($\dot{\varepsilon}_v^p$ >0) of the material (Figure B.3), α_ψ is a constant parameter.

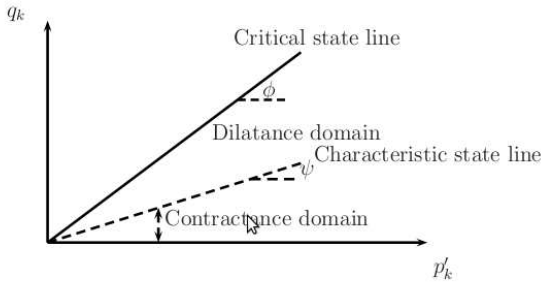

Figure B.3: Critical state and characteristic state lines.

B.5 Isotropic mechanism

The multimechanism model is able to correctly model the isotropic stress path, thanks to the fourth mechanism: the isotropic mechanism. This one, is only activated under isotropic part of the loading and it produces just volume changes. The yield function is described below:

$$f_{iso} = |p'| - d \cdot p_c \cdot r_{iso} \tag{B.12}$$

with r_{iso} the degree of mobilization of the mechanism, varying from the limit of elastic domain r_{iso}^{ela} to the unity according to:

$$r_{iso} = r_{iso}^{ela} + \frac{\varepsilon_{v,iso}^{p}}{c \cdot \frac{p_c}{p_{ref}} + \varepsilon_{v,iso}^{p}} \tag{B.13}$$

where the volumetric plastic strain associated to isotropic mechanism can be computed as $\varepsilon_{v,iso}^{p}$:

$$\varepsilon_{v,iso}^{p} = \int_0^t \dot{\varepsilon}_{v,iso}^{p} dt \tag{B.14}$$

The parameter d defines the distance of the isotropic consolidation line to the critical state line in the plane $(e - \ln p')$ or $(\varepsilon_{v,iso}^{p} - \ln p'\ )$. The parameter c controls the isotropic hardening.

Finally the four mechanisms are coupled through the hardening variable $\varepsilon_{v,iso}^{p}$:

$$\varepsilon_{v}^{p} = \sum_{k=1}^{3} (\varepsilon_{v,k}^{p}) + (\varepsilon_{v,iso}^{p}) \tag{B.15}$$

Concerning the isotropic mechanism under cyclic loading, the yield function is written as follows:

$$f_{iso}^{c} = |p^{c'}| - d \cdot p_c \cdot r_{iso}^{c} \tag{B.16}$$

The evolution of the degree of mobilization of the mechanism (r_{iso}) is the same as that for the monotonic case but is affected by the cyclic parameter:

$$r_{iso} = r_{iso}^{ela} + \frac{\varepsilon_{v,iso}^{p}}{c^{c} \cdot \frac{p_c}{p_{ref}} + \varepsilon_{v,iso}^{p}} \tag{B.17}$$

B.6 ECP model's soil parameters

The ECP model's parameters for all soil types used are summarized in the following table. The soil parameters were determined with the procedure defined by Lopez-Caballero et al. (2007), for their calibration and validation refer to Costa D'Aguiar et al. (2011) and Saez (2009). The soil parameters of the Dense sand 2 are given by Nguyen (2006).

Table B.1: ECP model's parameters for the soil.

Parameter	MDS	LMS	Dense sand 1	Dense sand 2
ρ [kg/m^3]: Soil density	1755	1755	1755	1755
ν [1]: Poisson's ratio	0.3	0.3	0.4	0.15
K_0 [1]: Coefficient of lateral earth pressure	0.5	0.7	0.7	0.7
Elasticity				
E [MPa]: Young's modulus	571.65	754	1850	1457
n_e [1]: Nonlinear degree	0.4	0.5	0.47	0.6
p'_{ref} [MPa]: Reference mean stress	1.0	1.0	1.0	1.0
V_S [m/s]: Shear wave velocity	354	406	613	598
Critical State and Plasticity				
β [1]: Plastic compressibility modulus	43	33	44	43
b [1]: Yield surface shape	0.2	0.12	0.8	0.23
d [1]: Isotropic consolidation distance	3.5	2.0	5.0	10.0
ϕ'_{pp} [^{o}]: Friction angle	31	30	37	36
p_{c0} [MPa]: Initial critical stress	1.8	$40{\cdot}10^{-3}$	0.4	1.2
Flow Rule and Hardening				
a_1 [1]: Primary plastic stiffness	0.0001	0.0001	0.0002	0.0001
a_2 [1]: Secondary plastic stiffness	0.004	0.005	0.0004	0.01
c^m [1]: Monotonic isotropic hardening	0.06	0.004	0.01	0.2
c^c [1]: Cyclic isotropic hardening	0.03	0.002	0.005	0.1
ψ [^{o}]: Characteristic angle	31	30	37	36
α_ψ [1]: Volumetric parameter	1.0	1.0	1.0	1.0
m [1]: Cyclic loading exponential	1.0	1.5	1.0	1.0
Threshold Domains				
r_d^{ela} [1]: Deviatoric elastic	0.005	0.03	0.005	0.001
r_{iso}^{ela} [1]: Isotropic elastic	0.001	0.001	0.0001	0.0001
r_d^{cyc} [1]: Cyclic deviatoric	0.005	0.03	0.005	0.001
r_{iso}^{cyc} [1]: Cyclic isotropic	0.001	0.001	0.0001	0.0001
r^{hys} [1]: Hysteretic	0.03	0.04	0.04	0.01
r^{mob} [1]: Mobilized	0.8	0.8	0.9	0.9

The evolution of shear modulus and shear wave velocity as function of the mean effective stress is presented in Figure B.4 for all materials used.

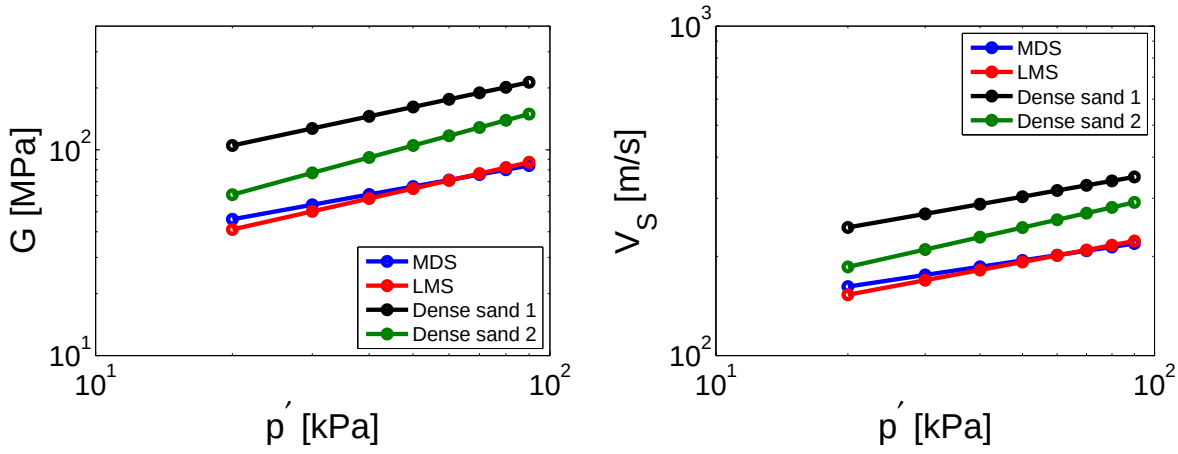

(a) (b)

Figure B.4: Evolution as function of mean effective stress of the: a) shear modulus, b) shear wave velocity V_S.

Figure B.5 shows deviatoric stress - strain and volumetric - deviatoric strain curves for all materials under drained triaxial test simulations. $G/G_{max} - \gamma$ and $D - \gamma$ curves are also generated by model simulations after shear cyclic drained test (Figure B.6). For comparison reasons, all tests were carried out at the same confining pressure equal to 50kPa.

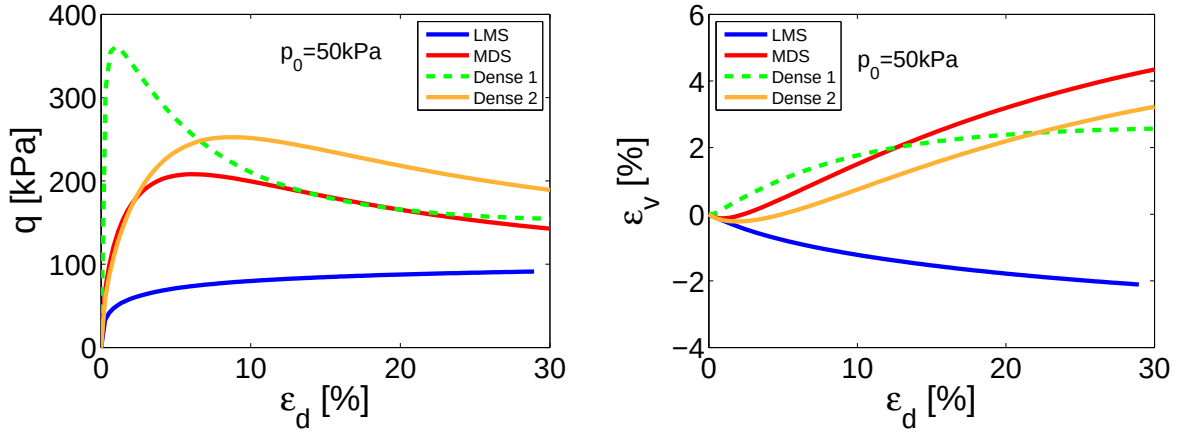

(a) (b)

Figure B.5: Soil response of one material point under triaxial drained test with the ECP constitutive model.

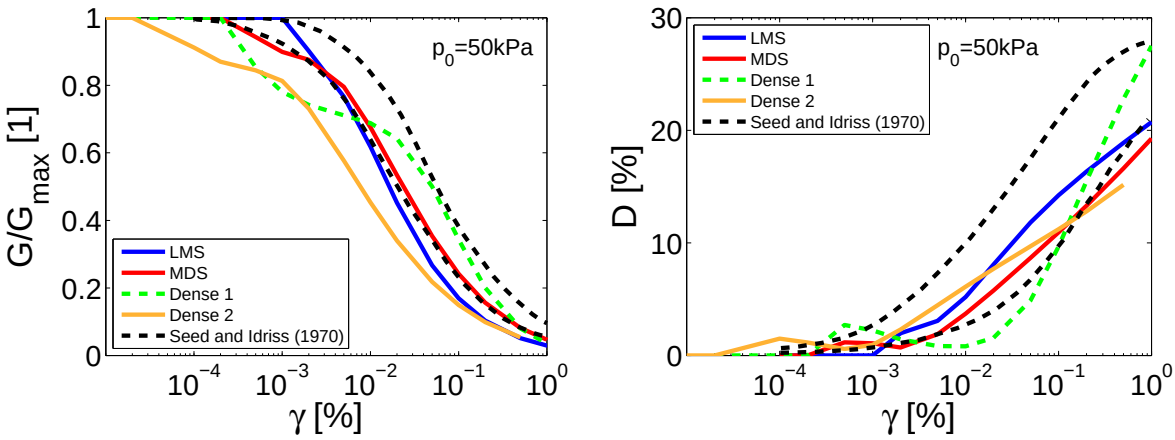

(a) (b)

Figure B.6: Soil response of one material point under shear cyclic drained test with the ECP constitutive model.

Appendix C

Input ground motions

The selection of accelerograms for geotechnical earthquake engineering is crucial as it is strongly related to nonlinear dynamic analyses. More than one engineering ground-motion parameter significantly influences the response of structures simultaneously. The selected ground-motion parameters should be capable of capturing all intensity, frequency content and duration information that significantly affects the elastic and inelastic response of structures.

Sets of accelerograms can be obtained/generated in various ways, including purely natural accelerograms to purely artificial. As the input ground motion should be compatible with the assumed earthquake scenario, research studies attempt to define criteria to select sets of accelerograms suitable for dynamic analyses (Causse et al., 2014b). However, natural records are not always available and simulation techniques are used to generate artificial accelerograms. Stochastic simulations are widely used for this reason.

In the scope of the current research work and following the PhD thesis of S. Montoya-Noguera and the research work at CentraleSupélec , various sets of real and synthetic (artificial) accelerograms are used to assess model's dynamic response for different earthquake scenarios. The density of input ground motions is presented in Figure C.1 and more details can be found in the following sections. All ground motions have a baseline correction and all output accelerograms obtained from the dynamic analyses are filtered using a non-causal bandpass filter of order 4, between 0.1-20Hz.

The groups of input ground motions used throughout this research work are:

- **Real recorded earthquakes**

    1. Non pulse-like low/moderate seismic motions recorded on soil site from PEER database ("NPL soil") (Iervolino and Cornell, 2005; Sorrentino et al., 2008)
    2. Non pulse-like seismic motions recorded on rock site from PEER database ("NPL rock") (Baker et al., 2011)
    3. Pulse-like seismic recorded on rock site motions from PEER database ("PL") (Baker, 2007)
    4. Pulse-like seismic recorded on soil site motions from PEER database ("PLS") (Shahi, 2013)
    5. Near-Fault seismic motions from PEER database ("NF") (Cornell et al., 2002)

6. Low seismic motions from kik-Net network in Japan ("kik-Net")
7. 3 individually selected earthquakes (Friuli, Hawaii, Emilia Romagna)

- **Synthetic earthquakes**

1. Strong seismic motions generated by real non pulse-like recorded on soil site ("Synthetic") (Dickinson and Gavin, 2011; Gavin and Dickinson, 2011)
2. Seismic motions generated by real near-fault seismic motions ("Synthetic NF") (Cornell et al., 2002)
3. Seismic motions generated by Code_Aster using Friuli earthquake as target motion ("Synthetic CA")

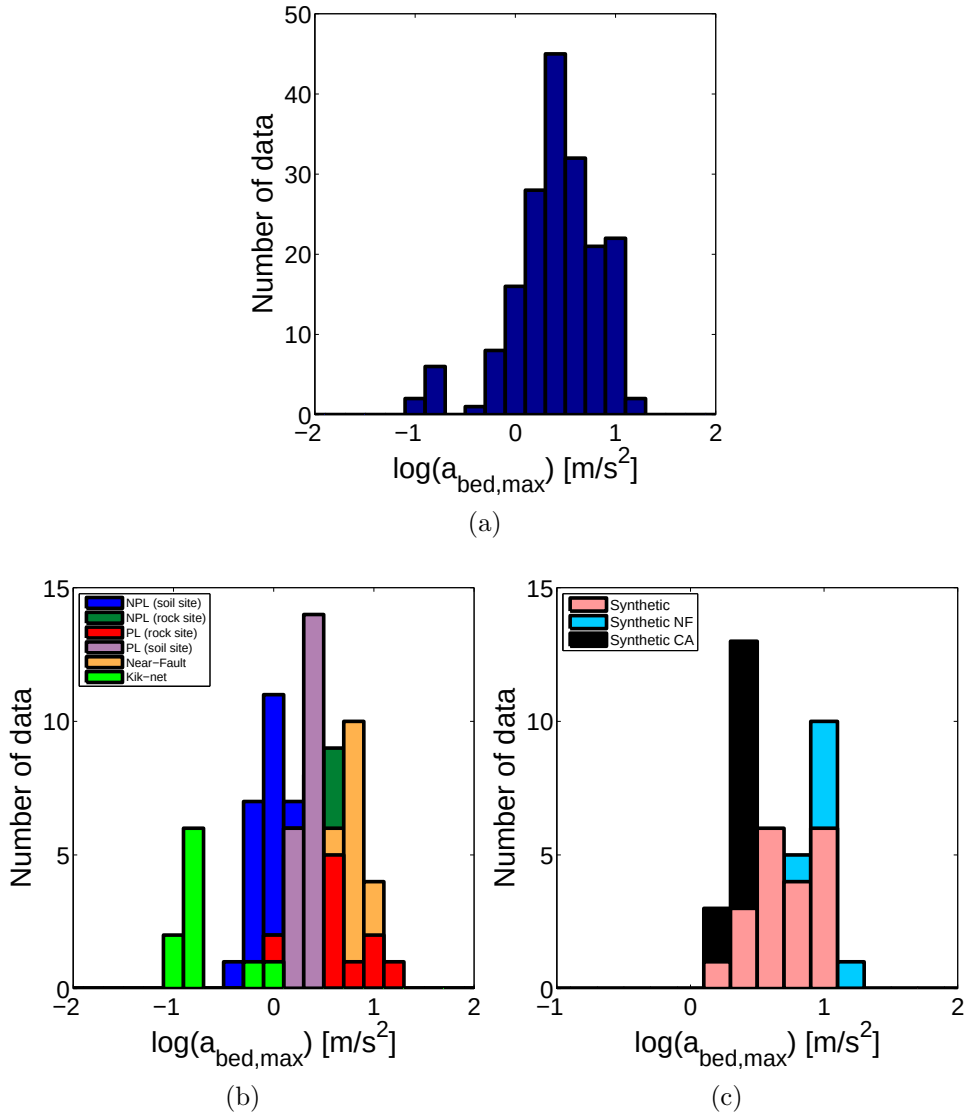

(a)

(b)

(c)

Figure C.1: Density of input ground motions: a) All motions, b) Real motions, c) Synthetic motions.

C.1 Real earthquakes

C.1.1 Non pulse-like seismic motions recorded on soil site from PEER database ("NPL soil")

Low seismic motions (ita L) (Sorrentino et al., 2008)

Unscaled ground motions in Table C.1 were selected based on distance R>15km and magnitude M_w <7.1, 0.07<PGA<0.1g, 7.4<PGV<8cm/s from PEER database. Only using the horizontal component in "a". They are recorded mostly on soil site ($V_{s,30}$ <600m/s). Their acceleration spectra can be found in Figure C.9a.

Table C.1: Properties of low non pulse-like seismic motions recorded on soil site.

Set*	Event	Year	Station	Record/Component	ID**	M_w	R*** [km]	$V_{s,30}$ [m/s]
ita La 1	Livermore 01-24 19:00	1980	Tracy-Sewage Treatm Plant	LIVERMOR_A-STP183	216	5.80	53.35	650
ita Lb 1	Livermore 01-24 19:00	1980	Tracy-Sewage Treatm Plant	LIVERMOR_A-STP093	216	5.80	53.35	650
ita La 2	Northridge 01-17 12:31	1994	Bell Gardens-Jaboneria	NORTHR_JAB220	951	6.69	41.27	267
ita Lb 2	Northridge 01-17 12:31	1994	Bell Gardens-Jaboneria	NORTHR_JAB310	951	6.69	41.27	267
ita La 3	Northridge 01-17 12:31	1994	Carson-Catskill Ave	NORTHR_CAT090	961	6.69	46.05	305
ita Lb 3	Northridge 01-17 12:31	1994	Carson-Catskill Ave	NORTHR_CAT180	961	6.69	46.05	305
ita La 4	Northridge 01-17 12:31	1994	Inglewood-Union Oil	NORTHR_ING000	981	6.69	37.18	316
ita Lb 4	Northridge 01-17 12:31	1994	Inglewood-Union Oil	NORTHR_ING090	981	6.69	37.18	316
ita La 5	Northridge 01-17 12:31	1994	Port Hueneme-Naval Lab.	NORTHR_PTH180	1059	6.69	47.58	249
ita Lb 5	Northridge 01-17 12:31	1994	Port Hueneme-Naval Lab.	NORTHR_PTH090	1059	6.69	47.58	249
ita La 6	Northridge 01-17 12:31	1994	San Jacinto-CDF Fire Station	NORTHR_CDF090	1071	6.69	147.47	307
ita Lb 6	Northridge 01-17 12:31	1994	San Jacinto-CDF Fire Station	NORTHR_CDF000	1071	6.69	147.47	307
ita La 7	San Fernando 02-09 14:00	1971	Gormon-Oso Pump Plant	SFERN_OPP000	65	6.61	43.95	308
ita Lb 7	San Fernando 02-09 14:00	1971	Gormon-Oso Pump Plant	SFERN_OPP270	65	6.61	43.95	308

* The "a" and "b" refer to the fact that one horizontal component is used in "a" and the other in "b".

** ID as given on the NGA database (http://ngawest2.berkeley.edu)

*** Joyner-Boore source-to-site distance.

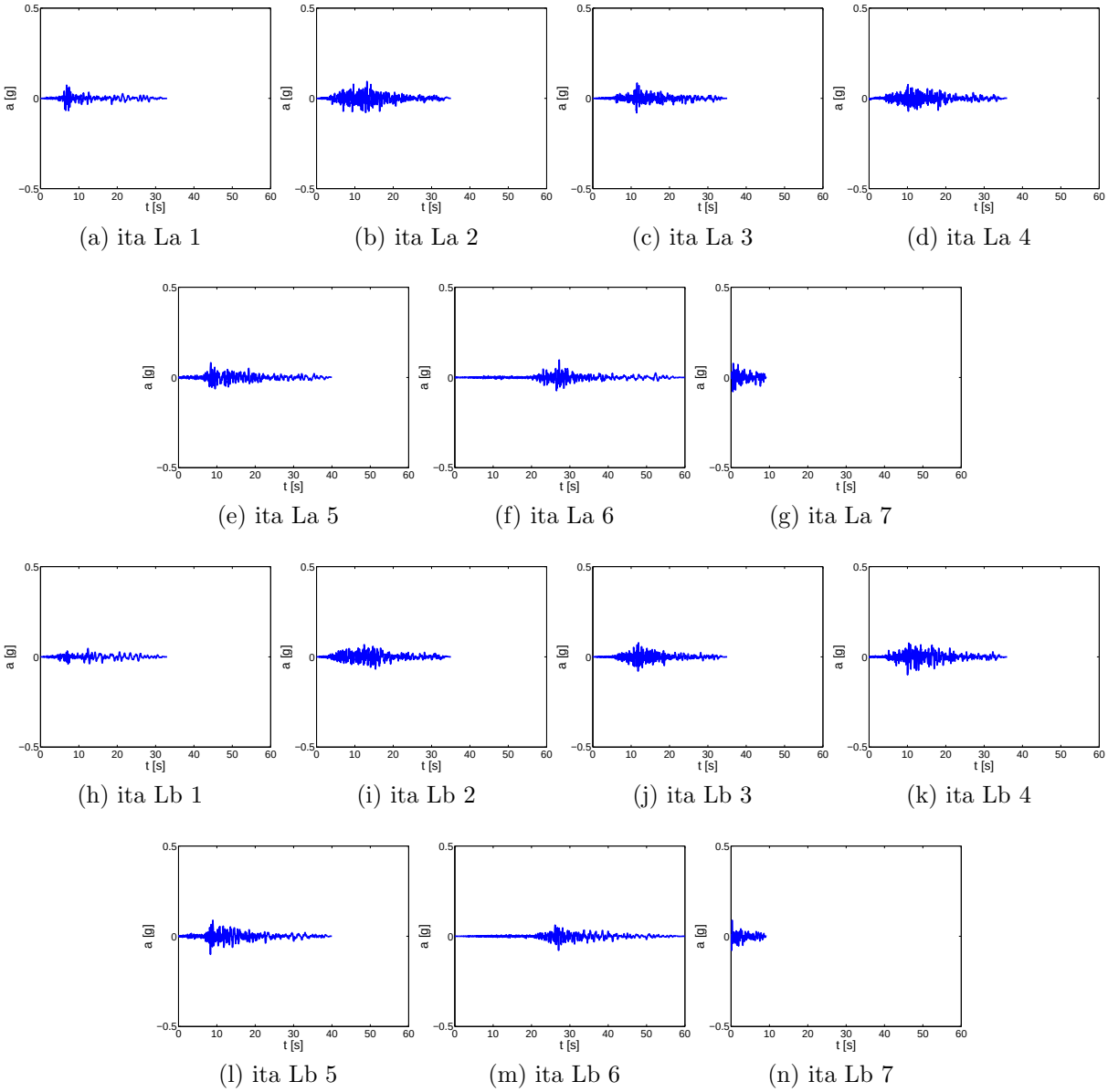

(a) ita La 1 (b) ita La 2 (c) ita La 3 (d) ita La 4

(e) ita La 5 (f) ita La 6 (g) ita La 7

(h) ita Lb 1 (i) ita Lb 2 (j) ita Lb 3 (k) ita Lb 4

(l) ita Lb 5 (m) ita Lb 6 (n) ita Lb 7

Figure C.2: Accelerograms of low non pulse-like real earthquakes recorded on soil site.

Moderate seismic motions (T1) (Iervolino and Cornell, 2005)

Unscaled ground motions in Table C.1 were selected based on "short distance-high magnitude" from PEER database. In particular, only California events have been considered, recorded on NEHRP C-D soil class and coming from free-field or one-story building instrument housing. The target sets for the record selection study are designed to be representative of a specific scenario event M_w and R that might be the realistic threat at a particular site, here a moment magnitude 7 at 20km. It led to events with magnitude range 6.7 to 7.4 and distance range 20 ± 5km. They propose several sets of 10 records each. They are recorded on soil site ($V_{s,30}$ <600m/s). Their acceleration spectra can be found in Figure C.9b.

Table C.2: Properties of moderate non pulse-like seismic motions recorded on soil site.

Set*	Event	Year	Station	Record/Component	ID**	M_w	R*** [km]	$V_{s,30}$ [m/s]
T1a 1	Cape Mendocino 04-25 18:06	1992	Eureka-Myrtle and West	CAPEMEND_EUR000	826	7.01	40.23	338
T1b 1	Cape Mendocino 04-25 18:06	1992	Eureka-Myrtle and West	CAPEMEND_EUR090	826	7.01	40.23	338
T1a 2	Cape Mendocino 04-25 18:06	1992	Fortuna-Fortuna Blvd	CAPEMEND_FOR000	827	7.01	15.97	457
T1b 2	Cape Mendocino 04-25 18:06	1992	Fortuna-Fortuna Blvd	CAPEMEND_FOR090	827	7.01	15.97	457
T1a 3	Imperial Valley 10-15 23:16	1979	Compuertas	IMPVALL_H-CMP015	167	6.53	13.52	260
T1b 3	Imperial Valley 10-15 23:16	1979	Compuertas	IMPVALL_H-CMP285	167	6.53	13.52	260
T1a 4	Imperial Valley 10-15 23:16	1979	Chihuahua	IMPVALL_H-CHI012	165	6.53	7.29	242
T1b 4	Imperial Valley 10-15 23:16	1979	Chihuahua	IMPVALL_H-CHI282	165	6.53	7.29	242
T1a 5	Landers 06-28 11:58	1992	North Palm Springs	LANDERS_NPS000	882	7.28	26.84	345
T1b 5	Landers 06-28 11:58	1992	North Palm Springs	LANDERS_NPS090	882	7.28	26.84	345
T1a 6	Landers 06-28 11:58	1992	Palm Springs Airport	LANDERS_PSA000	884	7.28	36.15	313
T1b 6	Landers 06-28 11:58	1992	Palm Springs Airport	LANDERS_PSA090	884	7.28	36.15	313
T1a 7	Loma Prieta 10-18 00:05	1989	Gilroy Array # 4	LOMAP_G04000	768	6.93	13.81	222
T1b 7	Loma Prieta 10-18 00:05	1989	Gilroy Array # 4	LOMAP_G04090	768	6.93	13.81	222
T1a 8	Loma Prieta 10-18 00:05	1989	WAHO	LOMAP_WAH000	811	6.93	11.03	388
T1b 8	Loma Prieta 10-18 00:05	1989	WAHO	LOMAP_WAH090	811	6.93	11.03	388
T1a 9	Northridge 01-17 12:31	1994	LA-Century City CC North	NORTHR_CCN360	988	6.69	15.53	278
T1b 9	Northridge 01-17 12:31	1994	LA-Century City CC North	NORTHR_CCN090	988	6.69	15.53	278
T1a 10	Northridge 01-17 12:31	1994	Moorpark-Fire Sta	NORTHR_MRP180	1039	6.69	16.92	342
T1b 10	Northridge 01-17 12:31	1994	Moorpark-Fire Sta	NORTHR_MRP090	1039	6.69	16.92	342

* The "a" and "b" refer to the fact that one horizontal component is used in "a" and the other in "b".

** ID as given on the NGA database (http://ngawest2.berkeley.edu)

*** Joyner-Boore source-to-site distance.

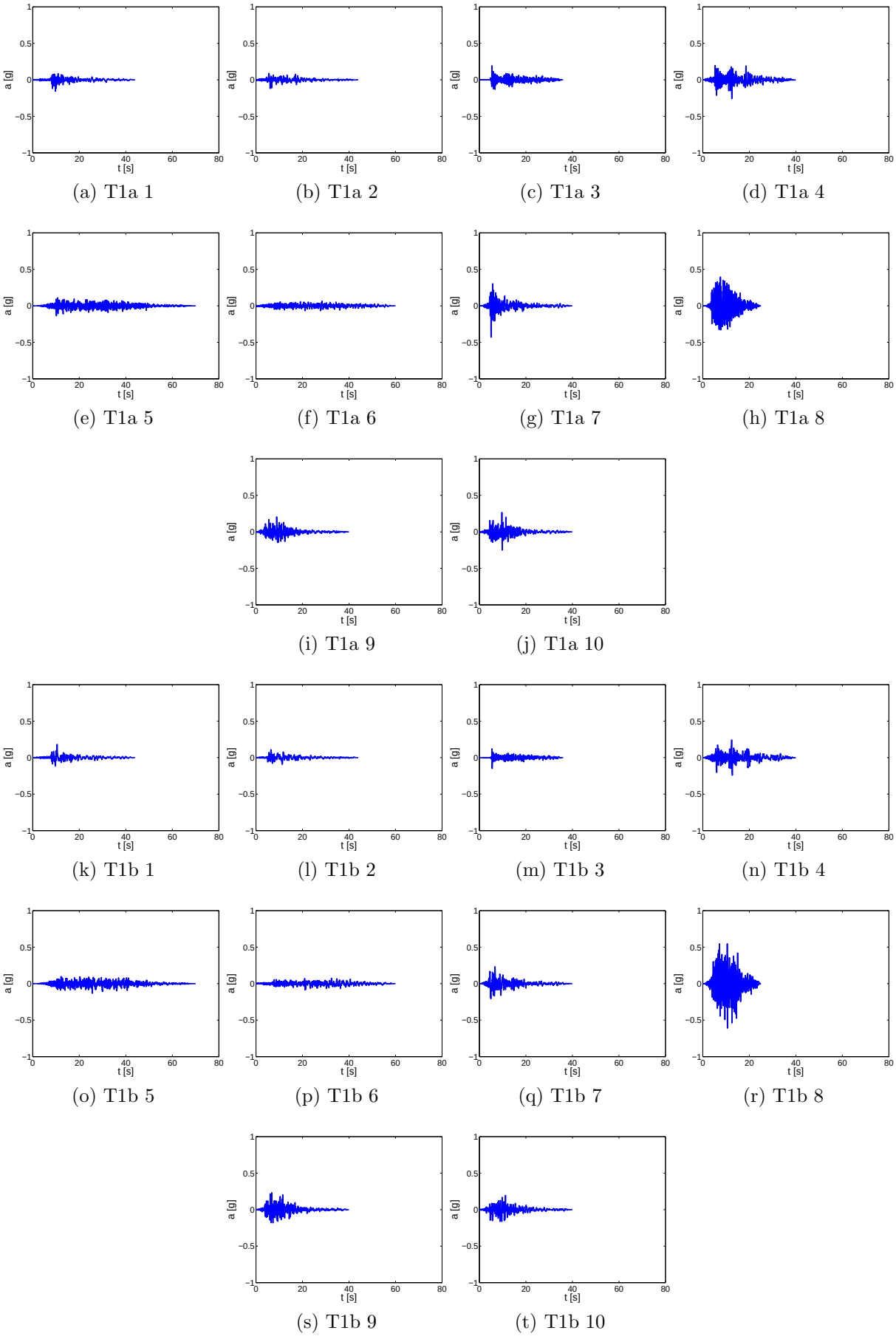

(a) T1a 1 (b) T1a 2 (c) T1a 3 (d) T1a 4

(e) T1a 5 (f) T1a 6 (g) T1a 7 (h) T1a 8

(i) T1a 9 (j) T1a 10

(k) T1b 1 (l) T1b 2 (m) T1b 3 (n) T1b 4

(o) T1b 5 (p) T1b 6 (q) T1b 7 (r) T1b 8

(s) T1b 9 (t) T1b 10

Figure C.3: Accelerograms of moderate non pulse-like real earthquakes recorded on soil site.

C.1.2 Non pulse-like seismic motions recorded on rock site from PEER database ("NPL rock") (Baker et al., 2011)

Unscaled ground motions in Table C.3 were selected based on "rock site records" seismic motions from PEER database. The response spectra of this ground motion set match the median and log standard deviations predicted for a magnitude 7 strike slip earthquake at a distance of 10 km (Figure C.9b). The site $V_{s,30}$ was assumed to be 760 m/s. This value was chosen because ground motions are intended to be representative of those observed at rock sites, or to be used as bedrock level ground motions for site response analyses. So, ground motions with shear wave velocity $V_{s,30}$ greater than 600m/s are included in the set (this was the narrowest range for which there were sufficient ground motions to ensure a good match to the target response spectrum distribution).

Table C.3: Properties of non pulse-like seismic motions recorded on rock site.

Set*	Event	Year	Station	Record/Component	ID**	M_w	R*** [km]	$V_{s,30}$ [m/s]
Ra 1	San Fernando 02-09	1971	Lake Hughes #4	SFERN_L04111	72	6.61	19.45	600
Rb 1	San Fernando 02-09	1971	Lake Hughes #4	SFERN_L04201	72	6.61	19.45	600
Ra 2	Northridge-01 01-17	1994	LA-Wonderland Ave	NORTHR_WON095	1011	6.69	15.11	1222
Rb 2	Northridge-01 01-17	1994	LA-Wonderland Ave	NORTHR_WON185	1011	6.69	15.11	1222
Ra 3	San Fernando 02-09	1979	Pasadena-Old Seismo Lab	SFERN_PSL180	80	6.61	21.5	969
Rb 3	San Fernando 02-09	1979	Pasadena-Old Seismo Lab	SFERN_PSL270	80	6.61	21.5	969
Ra 4	Kocaeli, Turkey 08-17	1999	Gebze	KOCAELI_GBZ000	1161	7.51	7.57	792
Rb 4	Kocaeli, Turkey 08-17	1999	Gebze	KOCAELI_GBZ270	1161	7.51	7.57	792
Ra 5	Northridge-01 01-17	1994	Vasquez Rocks Park	NORTHR_VAS000	1091	6.69	23.1	996
Rb 5	Northridge-01 01-17	1994	Vasquez Rocks Park	NORTHR_VAS090	1091	6.69	23.1	966
Ra 6	Loma Prieta 10-18	1989	Gilroy-Gavilan Coll.	LOMAP_GIL067	763	6.93	9.19	730
Rb 6	Loma Prieta 10-18	1989	Gilroy-Gavilan Coll.	LOMAP_GIL337	763	6.93	9.19	730
Ra 7	Loma Prieta 10-18	1989	Gilroy Array #1	LOMAP_G01000	765	6.93	8.84	1428
Rb 7	Loma Prieta 10-18	1989	Gilroy Array #1	LOMAP_G01090	765	6.93	8.84	1428
Ra 8	Loma Prieta 10-18	1989	UCSC Lick Observatory	LOMAP_LOB000	765	6.93	12.04	714
Rb 8	Loma Prieta 10-18	1989	UCSC Lick Observatory	LOMAP_LOB090	765	6.93	12.04	714
Ra 9	Northridge-01 01-17	1994	Pacoima Dam (downstr)	NORTHR_PAC175	1050	6.69	4.92	2016
Rb 9	Northridge-01 01-17	1994	Pacoima Dam (downstr)	NORTHR_PAC265	1050	6.69	4.92	2016
Ra 10	Northridge-01 01-17	1994	LA 00	NORTHR_LA0180	1012	6.69	9.87	706
Rb 10	Northridge-01 01-17	1994	LA 00	NORTHR_LA0270	1012	6.69	9.87	706

* The "a" and "b" refer to the fact that one horizontal component is used in "a" and the other in "b".

** ID as given on the NGA database (http://ngawest2.berkeley.edu)

*** Joyner-Boore source-to-site distance.

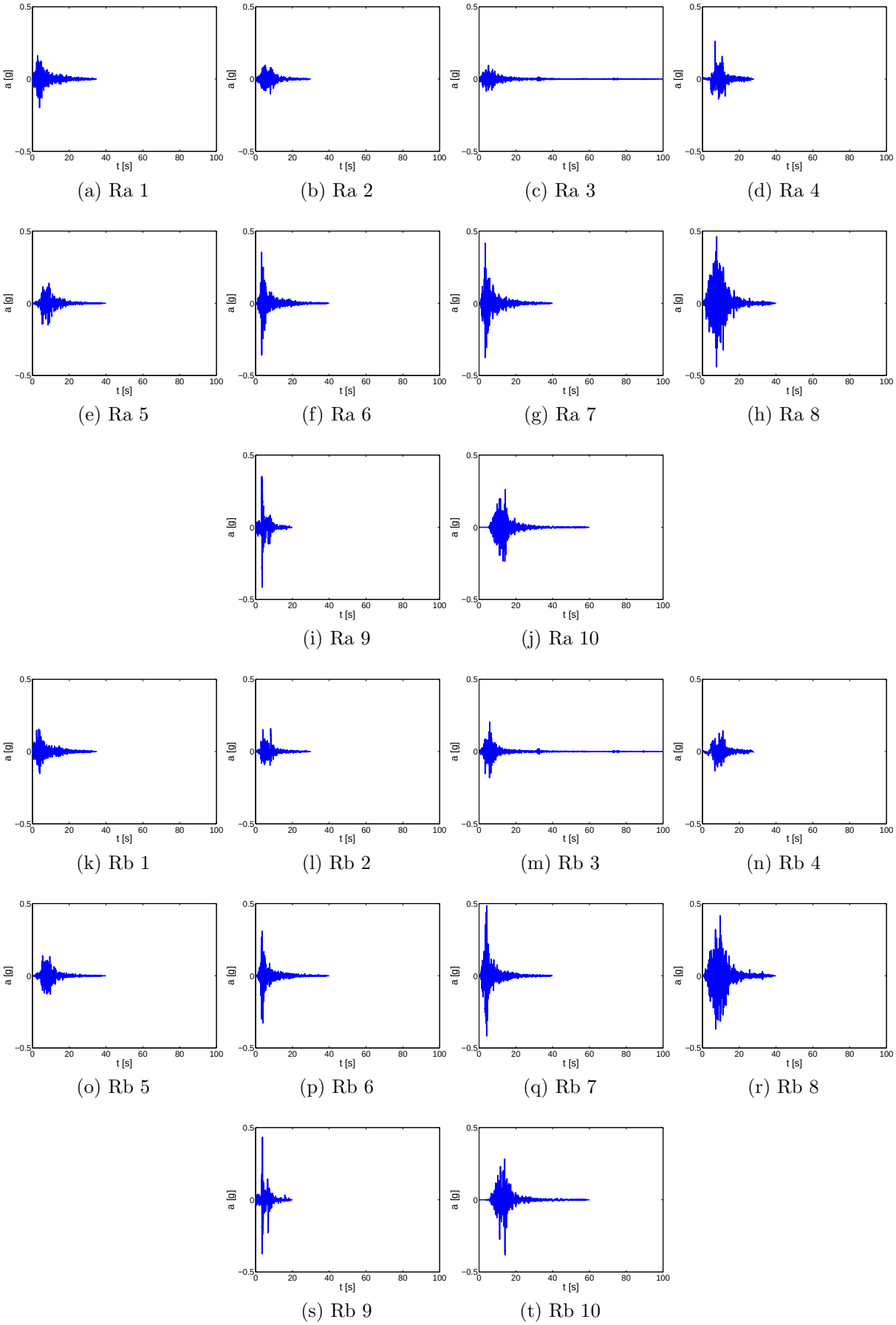

(a) Ra 1 (b) Ra 2 (c) Ra 3 (d) Ra 4

(e) Ra 5 (f) Ra 6 (g) Ra 7 (h) Ra 8

(i) Ra 9 (j) Ra 10

(k) Rb 1 (l) Rb 2 (m) Rb 3 (n) Rb 4

(o) Rb 5 (p) Rb 6 (q) Rb 7 (r) Rb 8

(s) Rb 9 (t) Rb 10

Figure C.4: Accelerograms of non pulse-like real earthquakes recorded on rock site.

C.1.3 Pulse-like seismic motions recorded on rock site from PEER database ("PL") (Baker, 2007)

Near-fault ground motions containing strong velocity pulses, called pulse-like, are of interest in the field of seismology and earthquake engineering, as they have been identified to impose extreme demands on structures. This type of ground motions contains strong velocity pulses of varying periods in their strike normal components. These velocity pulses are expected to occur in some ground motions observed near fault ruptures, due to directivity effects.

The classification as "pulse-like" given from PEER database is based on the method of Baker (2007). The procedure proposed by Baker (2007) uses wavelet-based signal processing to identify and extract the largest velocity pulse from a ground motion. If the extracted pulse is large realtive to the remaining features in the ground motion, the ground motion is classified as pulse-like.

Unscaled ground motions in Table C.4 were selected based on "pulse-like" criterion from PEER database. Their accleration spectra are plotted in Figure C.9d.

Table C.4: Properties of pulse-like seismic motions.

Set*	Event	Year	Station	Record/Component	ID**	M_w	R*** [km]	$V_{s,30}$ [m/s]
Pa 1	San Fernando 02-09	1971	Pacoima Dam (upper left abut)	SFERN_PUL254	77	6.61	0.0	2016
Pb 1	San Fernando 02-09	1971	Pacoima Dam (upper left abut)	SFERN_PUL164	77	6.61	0.0	2016
Pa 2	Irpinia, Italy-01 11-23	1980	Bagnoli Irpinio	ITALY_A-BAG000	285	6.9	8.14	650
Pb 2	Irpinia, Italy-01 11-23	1980	Bagnoli Irpinio	ITALY_A-BAG270	285	6.9	8.14	650
Pa 3	Coyote Lake 08-06	1979	Gilroy Array # 6	COYOTELK_G06230	150	5.74	0.42	663
Pb 3	Coyote Lake 08-06	1979	Gilroy Array # 6	COYOTELK_G06320	150	5.74	0.42	663
Pa 4	Morgan Hill 04-24	1984	Coyote Lake Dam - Southwest Abutment	MORGAN_CYC195	451	6.19	0.18	561
Pb 4	Morgan Hill 04-24	1984	Coyote Lake Dam - Southwest Abutment	MORGAN_CYC285	451	6.19	0.18	561
Pa 5	Morgan Hill 04-24	1984	Gilroy Array # 6	MORGAN_G06000	459	6.19	9.85	663
Pb 5	Morgan Hill 04-24	1984	Gilroy Array # 6	MORGAN_G06090	459	6.19	9.85	663
Pa 6	Chi-Chi Taiwan 09-20	1999	TCU045	CHICHI_TCU045-E	1485	7.62	26.0	705
Pb 6	Chi-Chi Taiwan 09-20	1999	TCU045	CHICHI_TCU045-N	1485	7.62	26.0	705
Pa 7	Chi-Chi Taiwan 09-20	1999	TCU064	CHICHI_TCU064-E	1502	7.62	16.59	646
Pb 7	Chi-Chi Taiwan 09-20	1999	TCU064	CHICHI_TCU064-N	1502	7.62	16.59	646
Pa 8	Chi-Chi Taiwan 09-20	1999	TCU076	CHICHI_TCU076-E	1511	7.62	2.74	615
Pb 8	Chi-Chi Taiwan 09-20	1999	TCU076	CHICHI_TCU076-N	1511	7.62	2.74	615
Pa 9	Chi-Chi Taiwan 09-20	1999	TCU102	CHICHI_TCU102-E	1529	7.62	1.49	714
Pb 9	Chi-Chi Taiwan 09-20	1999	TCU102	CHICHI_TCU102-N	1529	7.62	1.49	714
Pa 10	Chi-Chi Taiwan 09-20	1999	TCU128	CHICHI_TCU128-E	1548	7.62	13.13	600
Pb 10	Chi-Chi Taiwan 09-20	1999	TCU128	CHICHI_TCU128-N	1548	7.62	13.13	600

* The "a" and "b" refer to the fact that one horizontal component is used in "a" and the other in "b".

** ID as given on the NGA database (http://ngawest2.berkeley.edu)

*** Joyner-Boore source-to-site distance.

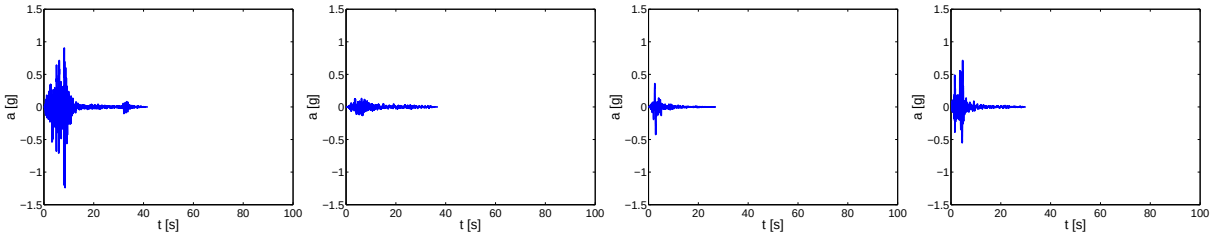

(a) Pa 1 (b) Pa 2 (c) Pa 3 (d) Pa 4

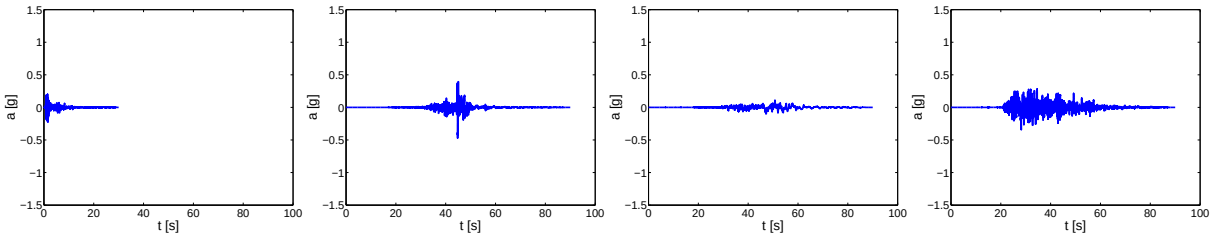

(e) Pa 5 (f) Pa 6 (g) Pa 7 (h) Pa 8

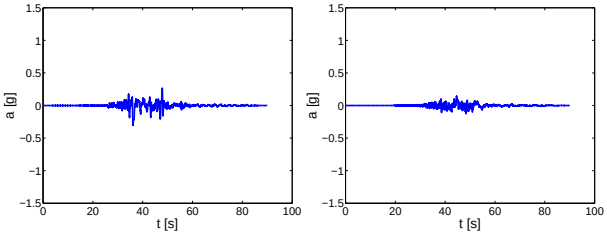

(i) Pa 9 (j) Pa 10

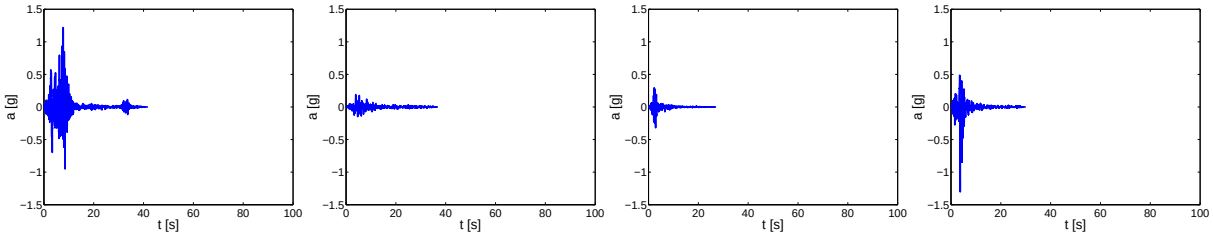

(k) Pb 1 (l) Pb 2 (m) Pb 3 (n) Pb 4

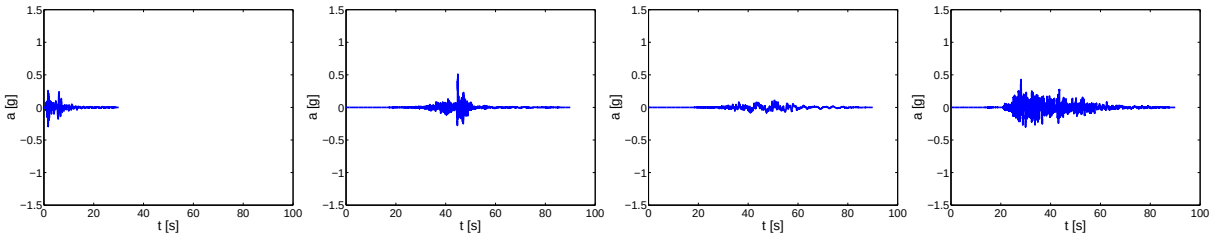

(o) Pb 5 (p) Pb 6 (q) Pb 7 (r) Pb 8

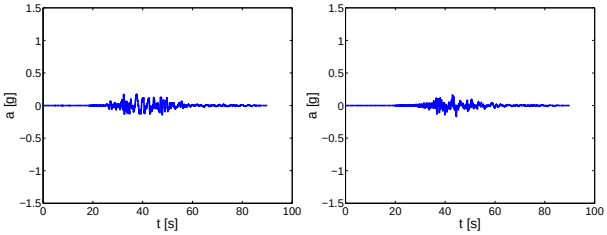

(s) Pb 9 (t) Pb 10

Figure C.5: Accelerograms of pulse-like real earthquakes recorded on rock site.

C.1.4 Pulse-like seismic motions recorded on soil site from PEER database ("PLS") (Shahi, 2013)

As previously, unscaled ground motions in Table C.4 were selected based on "pulse-like" criterion from PEER database and recorded on soil site. Their accleration spectra are plotted in Figure C.9d.

Table C.5: Properties of pulse-like seismic motions recorded on soil site.

Set*	Event	Year	Station	Record/Component	ID**	M_w	R*** [km]	$V_{s,30}$ [m/s]
PSa 1	Northern Calif-03 12-21	1954	Ferndale City Hall	NCALIF.FH_H-FRN044	20	6.5	26.7	219
PSb 1	Northern Calif-03 12-21	1954	Ferndale City Hall	NCALIF.FH_H-FRN314	20	6.5	26.7	219
PSa 2	Coyote Lake 08-06	1979	Gilroy Array #2	COYOTELK_G02050	147	5.74	1.8	767
PSb 2	Coyote Lake 08-06	1979	Gilroy Array #2	COYOTELK_G02140	147	5.74	1.8	767
PSa 3	Coyote Lake 08-06	1979	Gilroy Array #3 # 6	COYOTELK_G03050	148	5.74	0.42	663
PSb 3	Coyote Lake 08-06	1979	Gilroy Array #3 # 6	COYOTELK_G03140	148	5.74	0.42	663
PSa 4	Coyote Lake 08-06	1979	Gilroy Array #4	COYOTELK_G04270	149	5.74	0.18	561
PSb 4	Coyote Lake 08-06	1979	Gilroy Array #4	COYOTELK_G04360	149	5.74	0.18	561
PSa 5	Imperial Valley-06 10-15	1979	Agrarias	IMPVALL.H_H-AGR003	159	6.53	0.0	242
PSb 5	Imperial Valley-06 10-15	1979	Agrarias	IMPVALL.H_H-AGR173	159	6.53	0.0	242
PSa 6	Imperial Valley-06 10-15	1979	Brawley Airport	IMPVALL.H_H-BRA225	161	6.53	8.5	209
PSb 6	Imperial Valley-06 10-15	1979	Brawley Airport	IMPVALL.H_H-BRA315	161	6.53	8.5	209
PSa 7	Imperial Valley-06 10-15	1979	EC County Center FF	IMPVALL.H_H-ECC002	170	6.53	7.3	192
PSb 7	Imperial Valley-06 10-15	1979	EC County Center FF	IMPVALL.H_H-ECC092	170	6.53	7.3	192
PSa 8	Imperial Valley-06 10-15	1979	El Centro-Meloland Geot. Array	IMPVALL.H_H-EMO000	171	6.53	0.07	265
PSb 8	Imperial Valley-06 10-15	1979	El Centro-Meloland Geot. Array	IMPVALL.H_H-EMO270	171	6.53	0.07	265
PSa 9	Imperial Valley-06 10-15	1979	El Centro Array #10	IMPVALL.H_H-E10050	173	6.53	8.6	203
PSb 9	Imperial Valley-06 10-15	1979	El Centro Array #10	IMPVALL.H_H-E10320	173	6.53	8.6	203
PSa 10	Imperial Valley-06 10-15	1979	El Centro Array #3	IMPVALL.H_H-E03140	178	6.53	10.8	163
PSb 10	Imperial Valley-06 10-15	1979	El Centro Array #3	IMPVALL.H_H-E03230	178	6.53	10.8	163

* The "a" and "b" refer to the fact that one horizontal component is used in "a" and the other in "b".

** ID as given on the NGA database (http://ngawest2.berkeley.edu)

*** Joyner-Boore source-to-site distance.

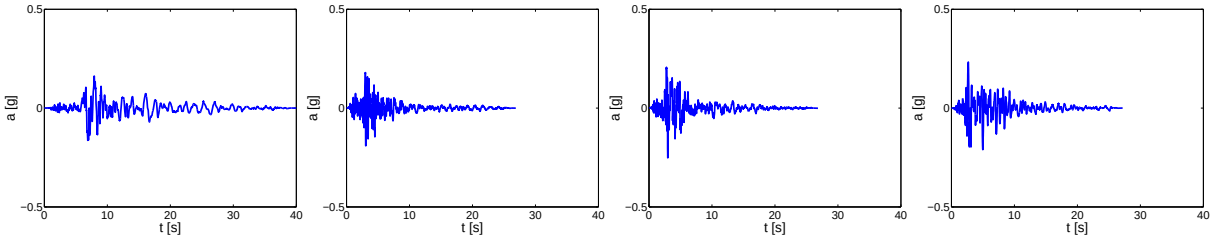

(a) PSa 1 (b) PSa 2 (c) PSa 3 (d) PSa 4

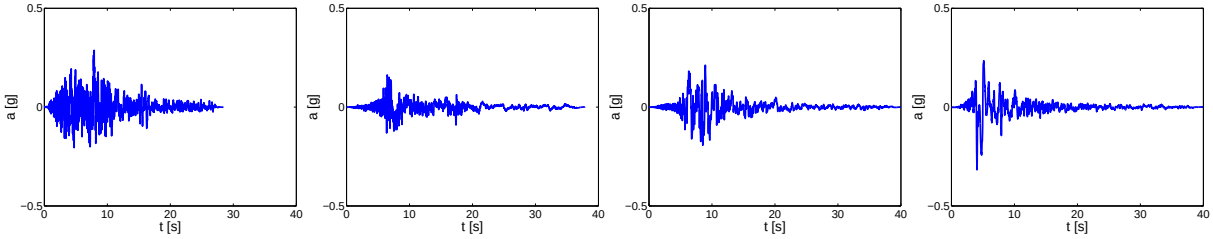

(e) PSa 5 (f) PSa 6 (g) PSa 7 (h) PSa 8

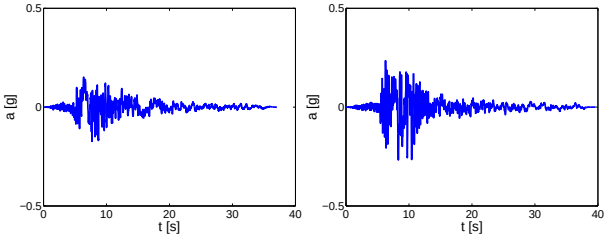

(i) PSa 9 (j) PSa 10

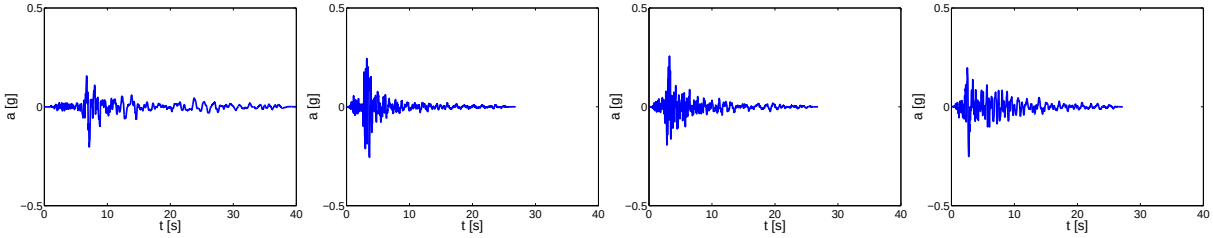

(k) PSb 1 (l) PSb 2 (m) PSb 3 (n) PSb 4

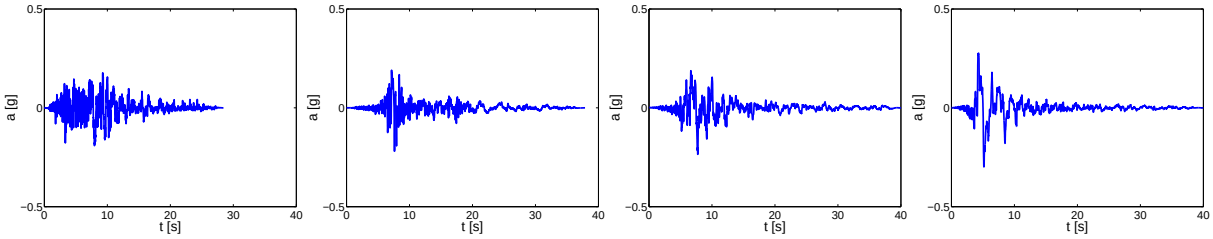

(o) PSb 5 (p) PSb 6 (q) PSb 7 (r) PSb 8

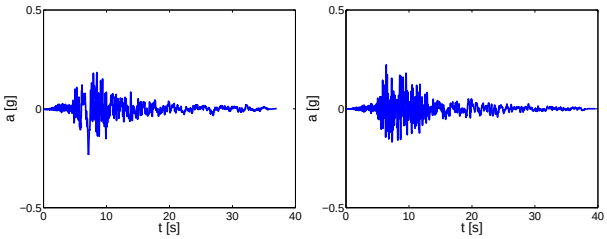

(s) PSb 9 (t) PSb 10

Figure C.6: Accelerograms of pulse-like real earthquakes recorded on soil site.

C.1.5 Near-fault (nf) (Somerville et al., 1997; Cornell et al., 2002)

For the purposes of SAC Phase 2 Steel Project a set of ground motion time histories corresponding to near-source motion on firm ground was developed for seismic zone 4 in United States (http://nisee.berkeley.edu/data/strong_motion/sacsteel/ground_motions.html). The ground motions were selected from earthquakes having a variety of faulting mechanisms (strike-slip, oblique, and thrust) in the magnitude range of 6 3/4 to 7 1/2. The closest distances for shallow crustal faults lie in the range of 0 to 10 km, and the closest distances for blind thrust faults lie in the distance range of 6 to 18 km. These magnitudes and distance ranges dominate the seismic hazard in Zone 4 for return periods of 10% in 50 years. The individual components of each ground motion have been rotated 45 degrees away from the fault-normal and fault-parallel orientations.

Based on "near-fault" demands, unscaled ground motions were selected from PEER database. The characteristics of the motions are presented in Table C.6 and their acceleration spectra are plotted in Figure C.9e.

Table C.6: Properties of near-fault seismic motions.

Set	Event	Year	Station	Record/Component	ID**	M_w	R*** [km]	$V_{s,30}$ [m/s]
nf 01	Tabas, Iran 09-16	1978	Tabas station	TABAS_TAB-L1	143	7.35	1.79	767
nf 02	Tabas, Iran 09-16	1978	Tabas station	TABAS_TAB-T1	143	7.35	1.79	767
nf 03	Loma Prieta 10-18	1989	BRAN	LOMAP_BRN000	741	6.93	3.85	477
nf 04	Loma Prieta 10-18	1989	BRAN	LOMAP_BRN090	741	6.93	3.85	477
nf 05	Loma Prieta 10-18	1989	Los gatos-Lexington Dam	LOMAP_LEX000	3548	6.93	3.22	1070
nf 06	Loma Prieta 10-18	1989	Los gatos-Lexington Dam	LOMAP_LEX090	3548	6.93	3.22	1070
nf 07	Cape Mendocino 04-25	1992	Petrolia	CAPEMEND_PET000	828	7.01	0.0	422
nf 08	Cape Mendocino 04-25	1992	Petrolia	CAPEMEND_PET090	828	7.01	0.0	422
nf 09	Erzican, Turkey 03-13	1992	Erzincan	ERZINCAN_ERZ-NS	828	6.69	0.0	352
nf 10	Erzican, Turkey 03-13	1992	Erzincan	ERZINCAN_ERZ-EW	828	6.69	0.0	352
nf 11	Landers 06-28	1992	Lucerne	LANDERS_LCN260	879	7.28	2.19	1369
nf 12	Landers 06-28	1992	Lucerne	LANDERS_LCN345	879	7.28	2.19	1369
nf 13	Northridge 01-17	1994	Rinaldi Receiving Sta	NORTHR_RRS228	1063	6.69	0.0	282
nf 14	Northridge 01-17	1994	Rinaldi Receiving Sta	NORTHR_RRS318	1063	6.69	0.0	282
nf 15	Northridge 01-17	1994	Sylmar-Olive View Med FF	NORTHR_SYL090	1086	6.69	1.74	441
nf 16	Northridge 01-17	1994	Sylmar-Olive View Med FF	NORTHR_SYL360	1086	6.69	1.74	441
nf 19	Kobe 01-16	1995	KJMA	KOBE_KJM000	1106	6.9	0.94	312
nf 20	Kobe 01-16	1995	KJMA	KOBE_KJM090	1106	6.9	0.94	312
nf 19	Kobe 01-16	1995	Takatori	KOBE_TAK000	1120	6.9	1.46	256
nf 20	Kobe 01-16	1995	Takatori	KOBE_TAK090	1120	6.9	1.46	256

** ID as given on the NGA database (http://ngawest2.berkeley.edu)
*** Joyner-Boore source-to-site distance.

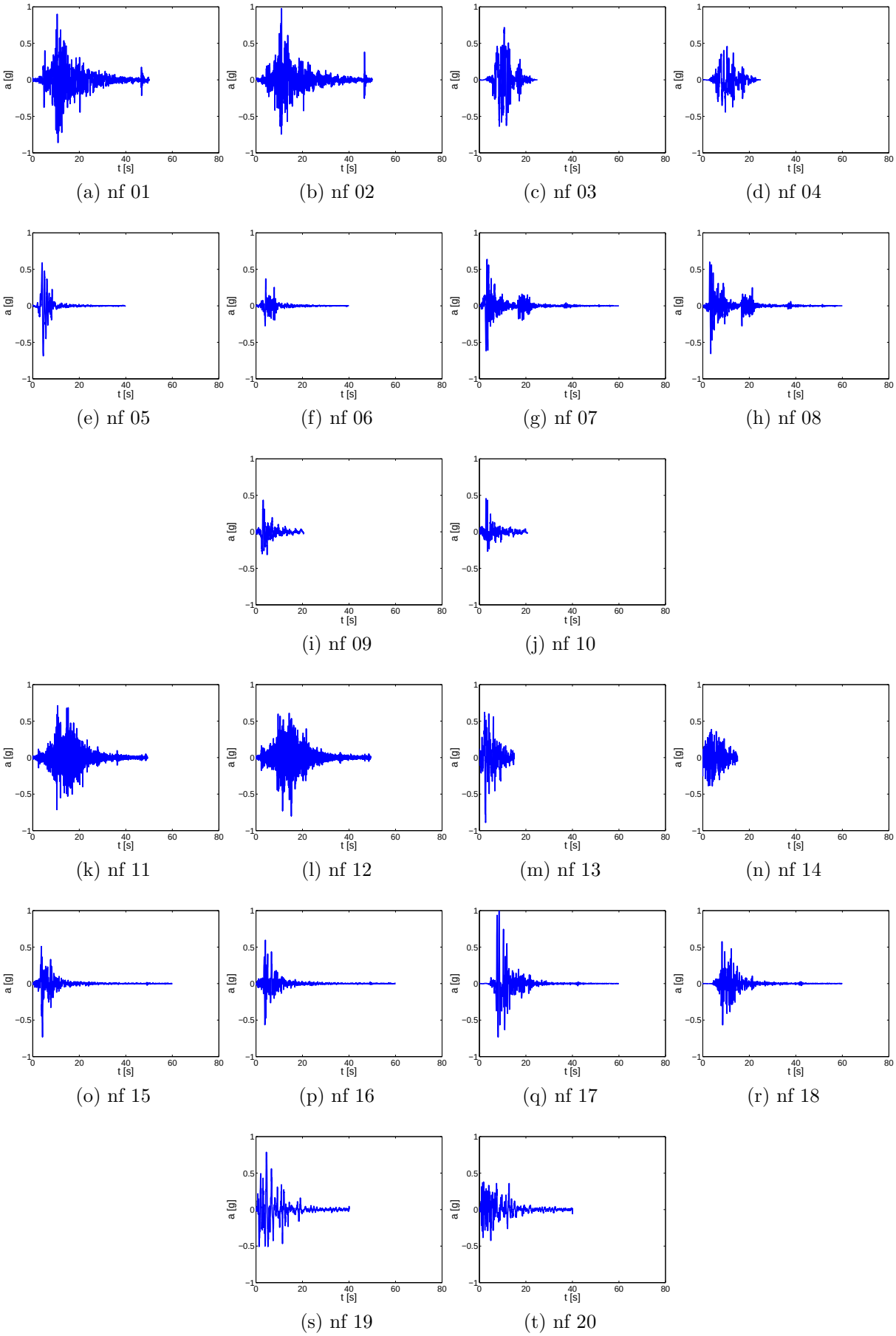

(a) nf 01 (b) nf 02 (c) nf 03 (d) nf 04

(e) nf 05 (f) nf 06 (g) nf 07 (h) nf 08

(i) nf 09 (j) nf 10

(k) nf 11 (l) nf 12 (m) nf 13 (n) nf 14

(o) nf 15 (p) nf 16 (q) nf 17 (r) nf 18

(s) nf 19 (t) nf 20

Figure C.7: Accelerograms of near-fault real earthquakes.

C.1.6 Low amplitude motions from Kik-net network - Station IWTH17

Low amplitude unscaled ground motions were selected from Kik-net network, Station IWTH17 ($V_{s,30}$=1270m/s). Their acceleration spectra are presented in Figure C.9f and their characteristics can be found in Table C.7.

Table C.7: Properties low amplitude motions from IWTH17 Station.

Set*	**Event**	$\mathbf{M_w}$	$\mathbf{D_{epicenter}}$ [km]	**Depth** [km]	**Longitude** [E]	**Latitude** [N]
iwth17 Ca,b 1	08-06-14 08:43	7.2	92.3	8	140.9	39.0
iwth17 Ca,b 2	11-03-12 23:43	6.1	95.5	30	142.7	39.5
iwth17 Ca,b 3	11-03-17 13:14	5.8	92.1	20	142.5	40.1
iwth17 Ca,b 4	02-05-12 10:29	5.1	66.9	96	141.2	39.2
iwth17 Ca,b 5	11-03-09 11:45	7.2	209.4	10	143.3	38.3

* The "a" and "b" refer to the fact that one horizontal component is used in "a" and the other in "b".

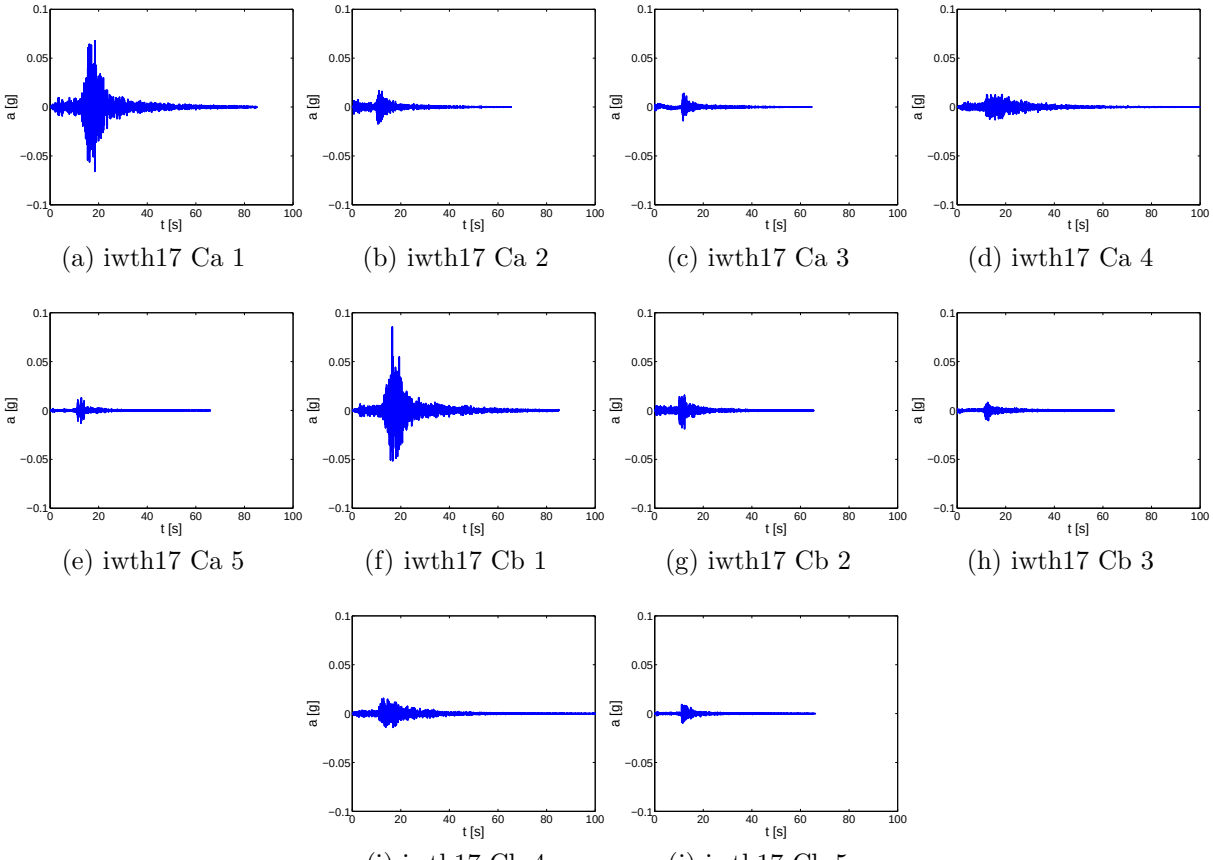

(a) iwth17 Ca 1 (b) iwth17 Ca 2 (c) iwth17 Ca 3 (d) iwth17 Ca 4

(e) iwth17 Ca 5 (f) iwth17 Cb 1 (g) iwth17 Cb 2 (h) iwth17 Cb 3

(i) iwth17 Cb 4 (j) iwth17 Cb 5

Figure C.8: Accelerograms of low amplitude real earthquakes from Kik-net network in Japan.

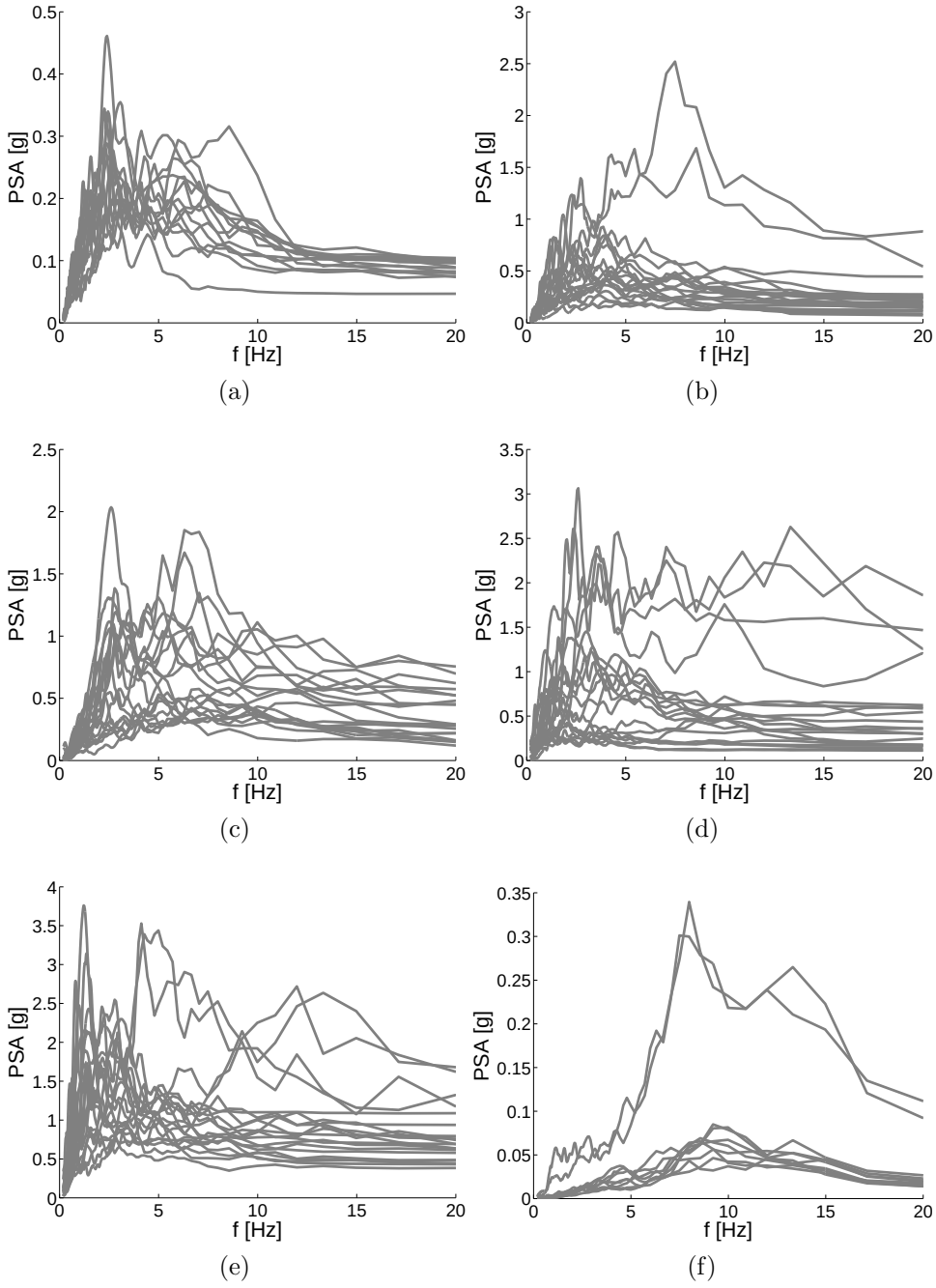

Figure C.9: Acceleration spectrum of real input seismic motions (ξ=5%): a) Low non pulse-like recorded on soil site, b) Moderate non pulse-like recorded on soil site, c) Non pulse-like recorded on rock site, d) Pulse-like, e) Near-Fault, f) Low from kik-Net network.

C.1.7 Friuli earthquake

Friuli earthquake is also used (FigureC.10) and found on PEER database. The characteristics of the ground motion are presented in table C.8 .

** ID as given on the NGA database (http://ngawest2.berkeley.edu)

Table C.8: Properties of Friuli earthquake

Set	Event	Year	Station	Record/Component	ID**	M_w	R*** [km]	$V_{s,30}$ [m/s]
Friuli	Friuli, Italy-01 05-06 20:00	1976	Tolmezzo	FRIULI.A_A-TMZ000	125	6.5	14.97	505

*** Joyner-Boore source-to-site distance.

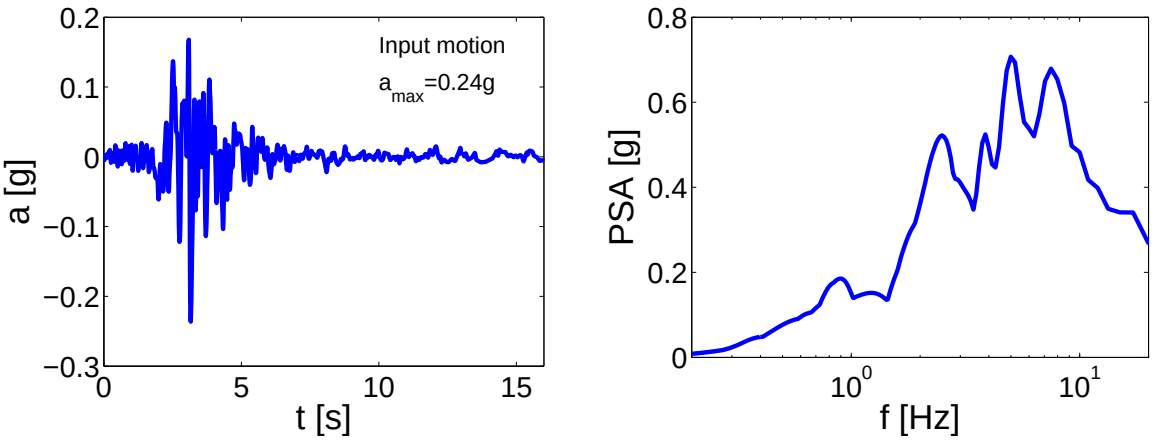

(a) (b)

Figure C.10: Friuli earthquake: a) Accelerogram, b) Spectrum (ξ=5%).

C.1.8 Earthquakes from italian database

Two earthquakes from the italian earthquake database (*itaca*) are also used. The first ground motion (irsn60) was recorded in Haiti in 2010 (01-18 12:17) with M_w=6.9. While the second one (irsn168) was recorded in Modena region (Italy) in 2012 (05-29 07:00) with M_w=6.0 (Table C.9).

Table C.9: Properties of italian seismic motions

Set	Event	Year	Station	Record/Component	ID**	M_w	R [km]	$V_{s,30}$ [m/s]
irsn60	Hawaii 01-18 12:17	2010	Chan00	EW	-	4.3	-	-
irsn168	Emilia-Romagna 05-29 7:00	2012	SAN0	HNE	IT-2012-0011	6.0	10.2	EC8 C* (inside building)

** ID as given on the italian database (http://itaca.mi.ingv.it)

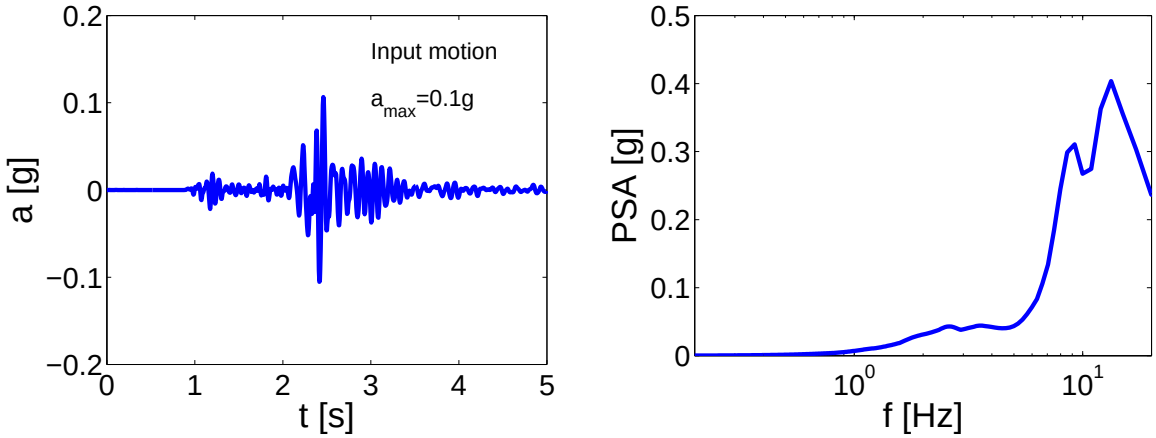

(a) (b)

Figure C.11: irsn60: a) Accelerogram, b) Spectrum (ξ=5%).

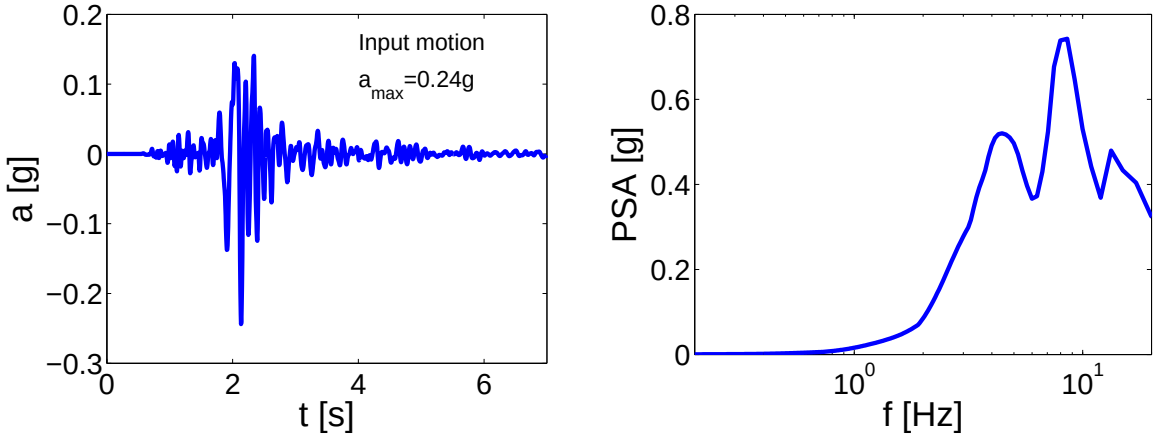

(a) (b)

Figure C.12: irsn168: a) Accelerogram, b) Spectrum (ξ=5%).

C.2 Synthetic earthquakes

C.2.1 Strong seismic motions (GV) (Dickinson and Gavin, 2011; Gavin and Dickinson, 2011)

Based on the data sets of the SAC Steel Project, Dickinson and Gavin (2011); Gavin and Dickinson (2011) generated synthetic strong ground motions from model parameters, as follows. A stochastic acceleration record is generated from power spectral density parameters over a specified frequency range by the method of spectral representation. The stochastic acceleration is then time modulated with an envelope function and integrated (in the frequency-domain) to give a stochastic velocity record. The stochastic velocity record is scaled to the specified amplitude. A velocity pulse is generated and added to the stochastic velocity. The combined velocity is then differentiated to give the final synthetic ground motion acceleration (Gavin and Dickinson, 2011).

The following set of synthetic strong motions is randomly generated by the following paramaters: peak pulse velocity V_p, period of the pulse T_p, number of cycles in the pulse N_c, location of the pulse T_{pk} and the phase of pulse ϕ. The values used for the generation of these particular seismic signals are presented in Table C.10 and the acceleration spectra of the artificial signals are plotted in Figure C.16a.

Table C.10: Input parameters for generation of strong synthetic ground motions.

Parameter	$\mathbf{V}_p$ [cm/s]	$\mathbf{T}_p$ [s]	$\mathbf{N}_c$ [1]	$\mathbf{T}_{pk}$ [s]	ϕ [rad]
Expected value E(X)	100	1.1	0.9	5.0	6.28
Variance Var(X)	40	1.2	0	0	0

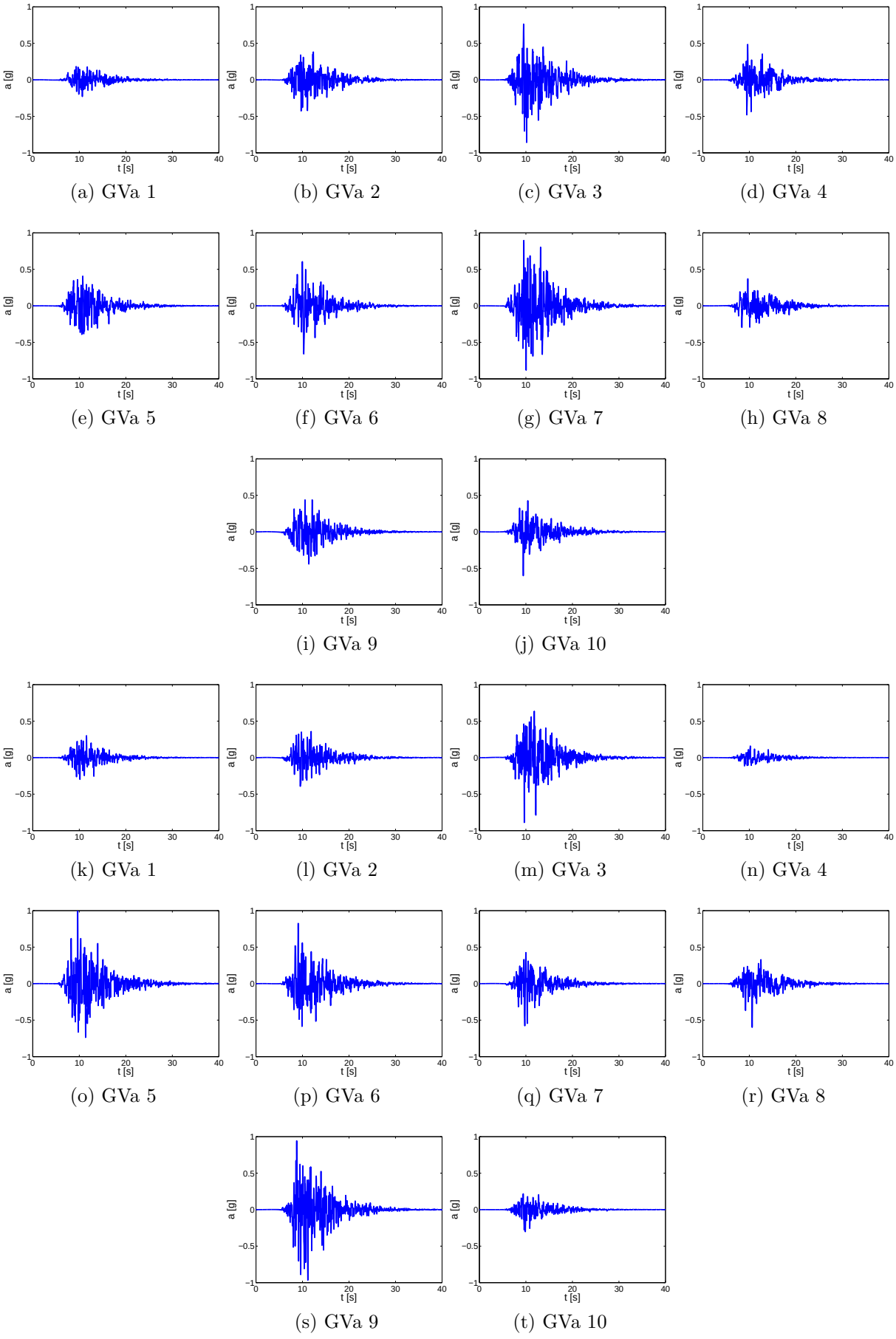

(a) GVa 1 (b) GVa 2 (c) GVa 3 (d) GVa 4

(e) GVa 5 (f) GVa 6 (g) GVa 7 (h) GVa 8

(i) GVa 9 (j) GVa 10

(k) GVa 1 (l) GVa 2 (m) GVa 3 (n) GVa 4

(o) GVa 5 (p) GVa 6 (q) GVa 7 (r) GVa 8

(s) GVa 9 (t) GVa 10

Figure C.13: Accelerograms of strong synthetic earthquakes.

C.2.2 Near-fault earthquakes (nfs) (Somerville et al., 1997; Cornell et al., 2002; Dickinson and Gavin, 2011)

For the purposes of SAC Phase 2 Steel Project, apart from the real recorded near-fault earthquakes of Section C.1.5, synthetic ground motions were generated from target spectra of real near-fault earthquakes.

The synthetic near-fault ground motions are generated through the superposition of a stohastic ground velocity record with a single, coherent, long-period velocity pulse. The stochastic ground motion velocity record is generated by the first simulating an enveloped and unscaled stochastic ground acceleration record, as explained in the previous section. For further details about the procedure followed for the generation of artificial signals refer to Dickinson and Gavin (2011).

The simulated time histories are for magnitude 7.1 earthquakes on the Palos Verdes fault (a strike-slip fault), and on the Elysian Park fault (a blind thrust fault whose shallowest depth is 10 km). The acceleration spectra of the synthetic ground motions are presented in Figure C.16b.

Table C.11: Properties of synthetic motions generated from real near-fault seismic motions

Set	**Event**	$\mathbf{M}_w$	$\mathbf{R}^{***}$ [km]
nfs 01	Elysian Park 1	7.1	17.5
nfs 02	Elysian Park 1	7.1	17.5
nfs 03	Elysian Park 2	7.1	10.7
nfs 04	Elysian Park 2	7.1	10.7
nfs 05	Elysian Park 3	7.1	11.2
nfs 06	Elysian Park 3	7.1	11.2
nfs 07	Elysian Park 4	7.1	13.2
nfs 08	Elysian Park 4	7.1	13.2
nfs 09	Elysian Park 5	7.1	13.7
nfs 10	Elysian Park 5	7.1	13.7
nfs 11	Palos Verdes 1	7.1	1.5
nfs 12	Palos Verdes 1	7.1	1.5
nfs 13	Palos Verdes 2	7.1	1.5
nfs 14	Palos Verdes 2	7.1	1.5
nfs 15	Palos Verdes 3	7.1	1.5
nfs 16	Palos Verdes 3	7.1	1.5
nfs 19	Palos Verdes 4	7.1	1.5
nfs 20	Palos Verdes 4	7.1	1.5
nfs 19	Palos Verdes 5	7.1	1.5
nfs 20	Palos Verdes 5	7.1	1.5

*** Joyner-Boore source-to-site distance.

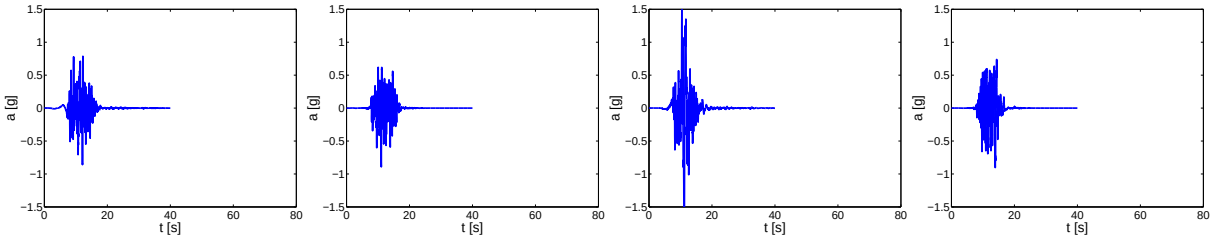

(a) nfs 01 (b) nfs 02 (c) nfs 03 (d) nfs 04

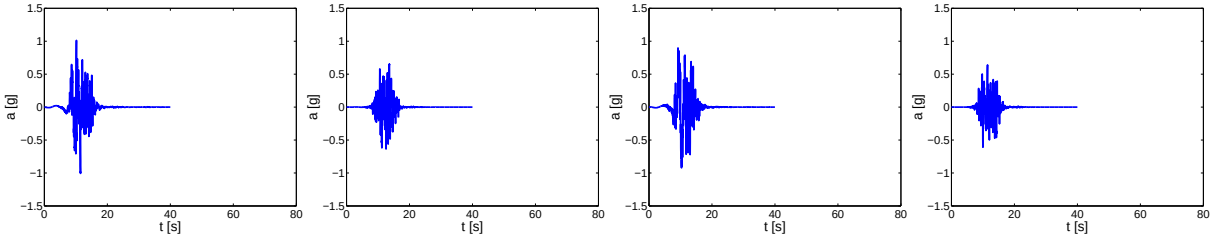

(e) nfs 05 (f) nfs 06 (g) nfs 07 (h) nfs 08

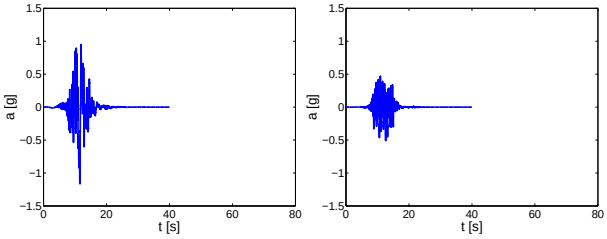

(i) nfs 09 (j) nfs 10

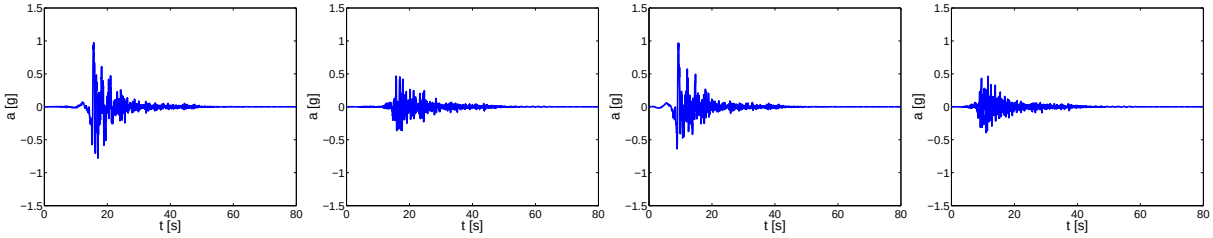

(k) nfs 11 (l) nfs 12 (m) nfs 13 (n) nfs 14

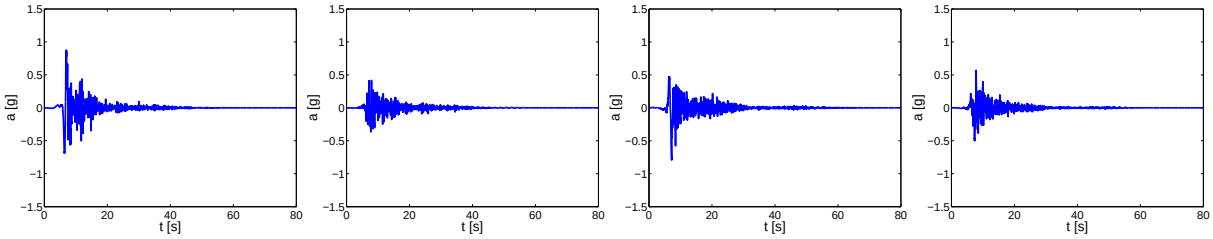

(o) nfs 15 (p) nfs 16 (q) nfs 17 (r) nfs 18

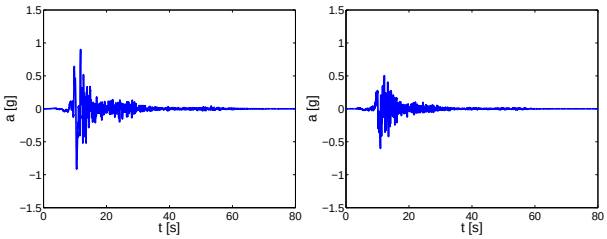

(s) nfs 19 (t) nfs 20

Figure C.14: Accelerograms of synthetic motions generated from real near-fault earthquakes.

C.2.3 Seismic motions generated by Code_Aster

In Code_Aster , the option $GENE\_ACCE\_SEISME$ generates artificial seismic motions using a stochastic process characterized by a power spectral density (PSD). In order to comply with a target response spectrum, a response-spectrum compatible PSD is identified, based on the classical Kanai-Tajimi model. Time dependency of the central requency is introduced by considering the central frequency as a function of time, yielding an evolutionary PSD model. The amplitude variation is generally introduced by a deterministic modulating function. Both the Jenning & Housner and the Gamma modulating function have been implemented in Code_Aster . These functions are parametrised by the strong motion duration TSM. For further details for the generator of synthetic motions refer to Zentner et al. (2014); Zentner (2015).

In this particular case, Friuli earthquake (Section C.1.7) is considered the target earthquake and the maximum amplitude $a_{bed,max}$ $\simeq$0.24g, fundamental frequency f_p $\simeq$5Hz and duration of the mainshock t$\simeq$4s are introduced to the generator, so as to produce 16 synthetic motions. The spectra of the generated motions are plotted in Figure C.16c.

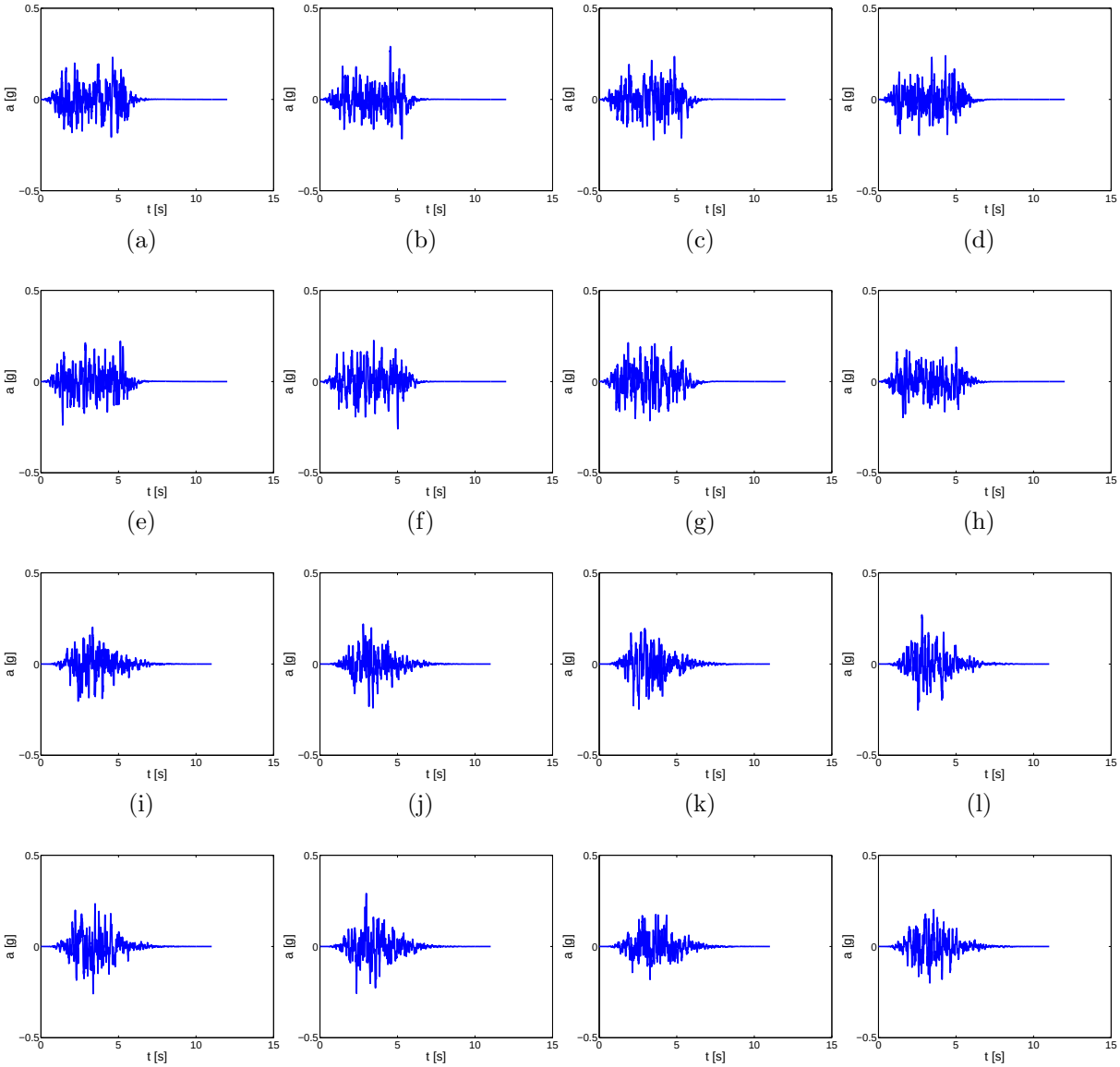

Figure C.15: Accelerograms of synthetic earthquakes generated in Code_Aster .

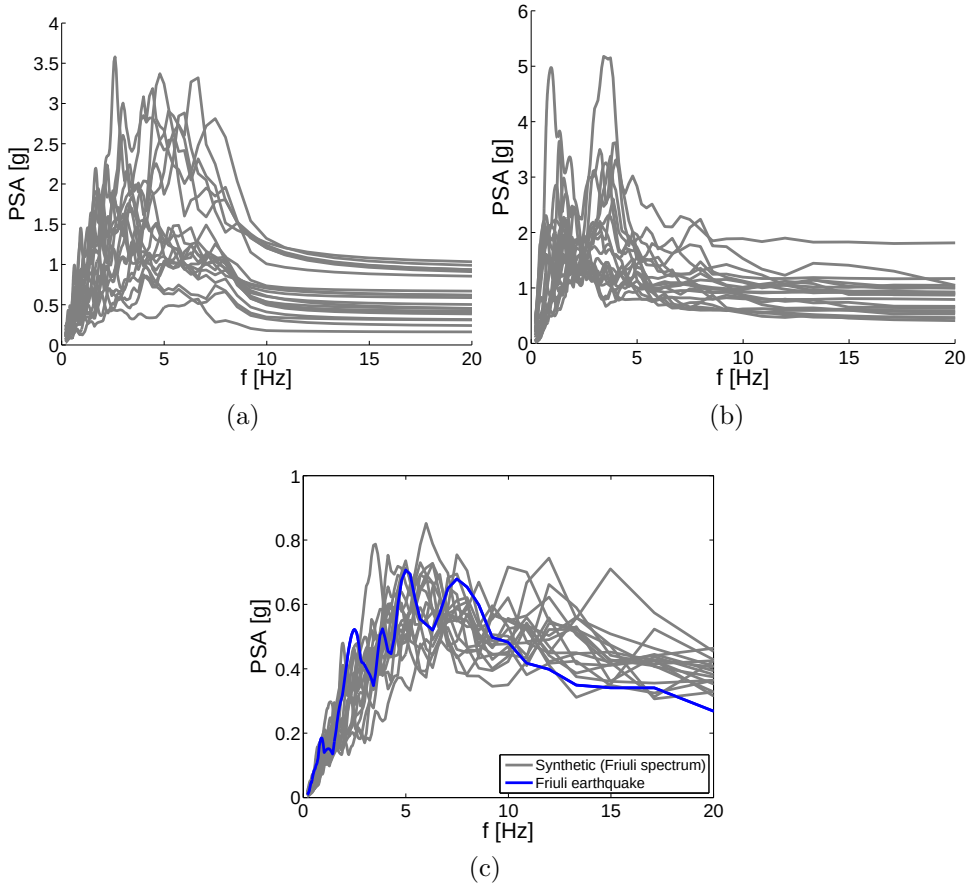

Figure C.16: Acceleration spectrum of synthetic input seismic motions (ξ=5%): a) Strong seismic motions (GV), b) Synthetic near-fault (nfs), c) Generated from Code_Aster based on the characteristics of Friuli earthquake.

Appendix D

Verification of Code_Aster : 1D SH wave propagation in soil column

D.1 Dry nonlinear media

Firstly, before the comparison of 1D SH wave propagation, a biaxial drained test was performed in one soil element with the LMS material (see Table B.1). While in Figure D.1a the response of both codes is in good agreement in terms of q - ε_d, differences are observed in the generation of volumetric deformations, as shown in Figure D.1b.

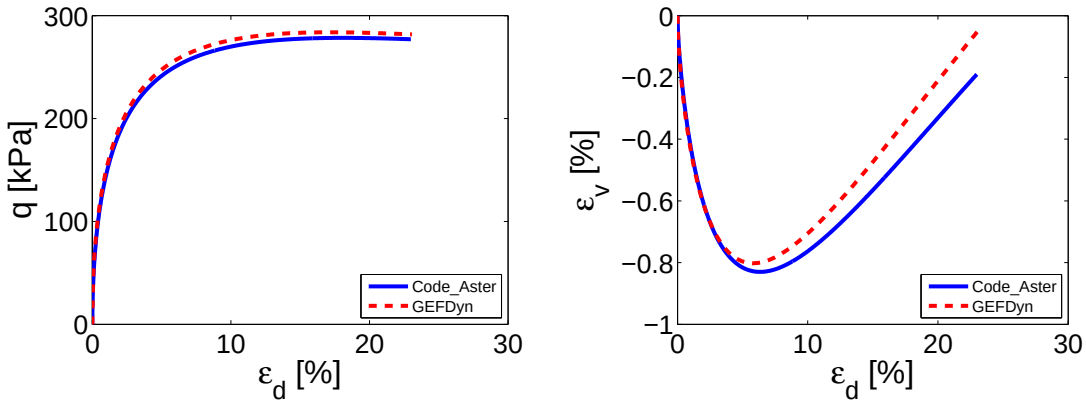

(a) (b)

Figure D.1: Comparison of soil response of one material point with the ECP constitutive model (p_0=100kPa, K_0=1.0) under biaxial drained test: a) q - ε_d, b) ε_d - ε_v.

Next, the verification analysis of Code_Aster in case of 1D SH wave propagation in a dry nonlinear soil column subjected to a wide range of ground motions is developed. The same model and analyses are performed in GEFDyn for comparison reasons.

D.1.1 Numerical model

Geometry - Boundary conditions

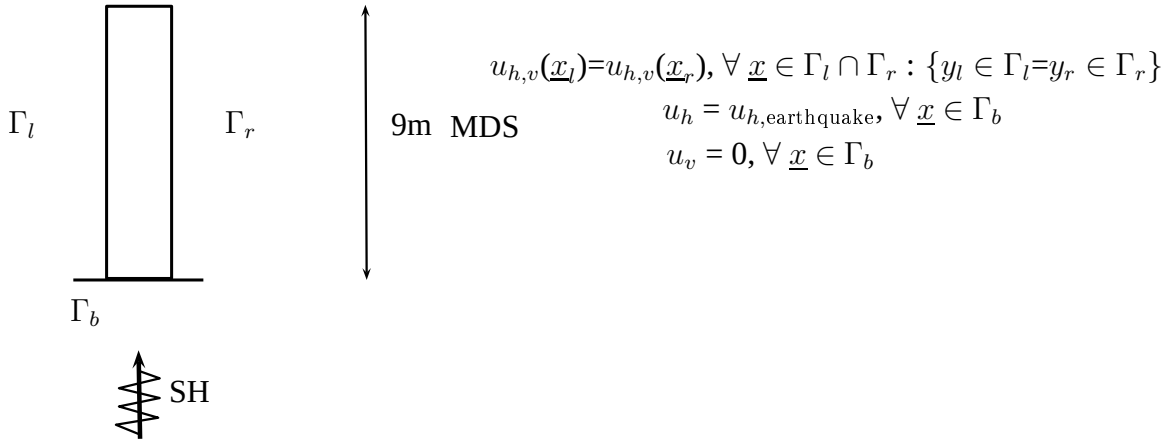

Figure D.2: Numerical model: 9m high dry nonlinear soil column founded on rigid base.

The model consists of a nonlinear soil column of 9m, as presented in Figure D.2. A mesh of 8-node quadrilateral elements of 0.25m length is used. Periodicity condition is applied on the lateral boundaries, i.e. all nodes of a horizontal section have the same displacement and pore water pressure. The seismic signal is imposed at the base and no radiation is possible.

Soil behavior

The ECP constitutive model represents soil behavior and a medium-to-dense sand (MDS) is used for the soil column. For further information about the model refer to Appendix B and for material parameters to Table B.1 in Appendix B.6.

Numerical parameters

The FE analysis is performed in two steps: a) as the model is nonlinear, a static analysis was performed in order to calculate the initial stresses, b) the seismic signal is imposed and a dynamic analysis is performed. The implicit method of Newmark integration is used for the dynamic analysis with a time step equal to Δt=10^{-3}s with a numerical damping equal to $\xi = 0.2\%$, as explained in Section 3.2.4. The low-strain frequency analysis provides a fundamental elastic period for the soil column equal to T_p=0.17s (f_p=5.8Hz), as obtained from the Borehole Transfer Function from the top to base (Figure D.3a).

Input ground motions

Real non pulse-like soil site motions (ita, T1 motions) (Iervolino and Cornell, 2005; Sorrentino et al., 2008) and synthetic seismic motions generated by real non pulse-like recorded on soil site (GV motions) (Dickinson and Gavin, 2011; Gavin and Dickinson,

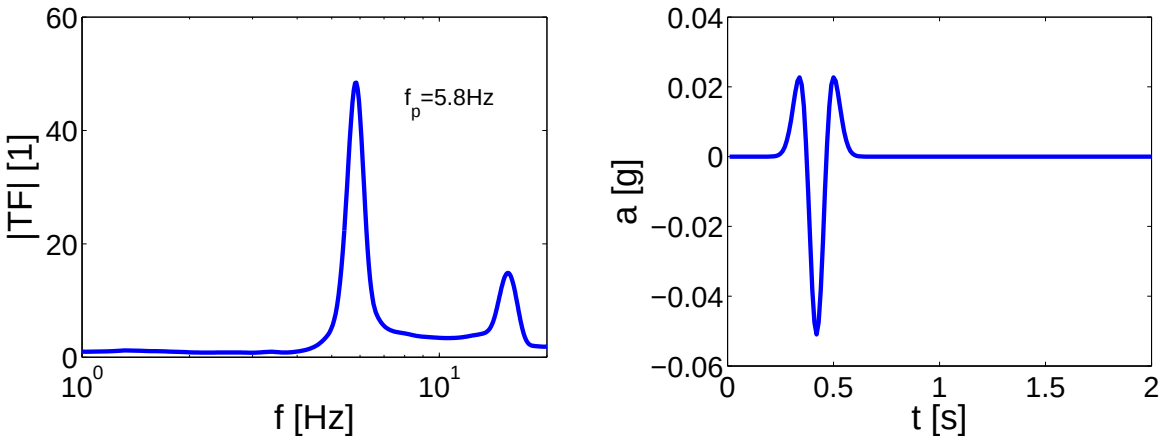

(a) (b)

Figure D.3: a) Borehole Transfer Function of dry nonlinear soil column in elasticity, b) Accelerogram of Ricker signal.

2011) were imposed to the soil column, selected from the PEER database (54 ground motions in total). Their characteristics can be found in Appendix C.

D.1.2 Results of dynamic analysis

The PGA and PGV measured at FF are calculated in Figure D.4. The points of PGA form a parabolic curve which implies the nonlinear soil behavior obtained with the stronger ground motions and the results of both software programs are in good agreement (Figure D.4a). The same conclusion is drawn by comparing PGV in Figure D.4b, as the points of the two software programs almost coincide.

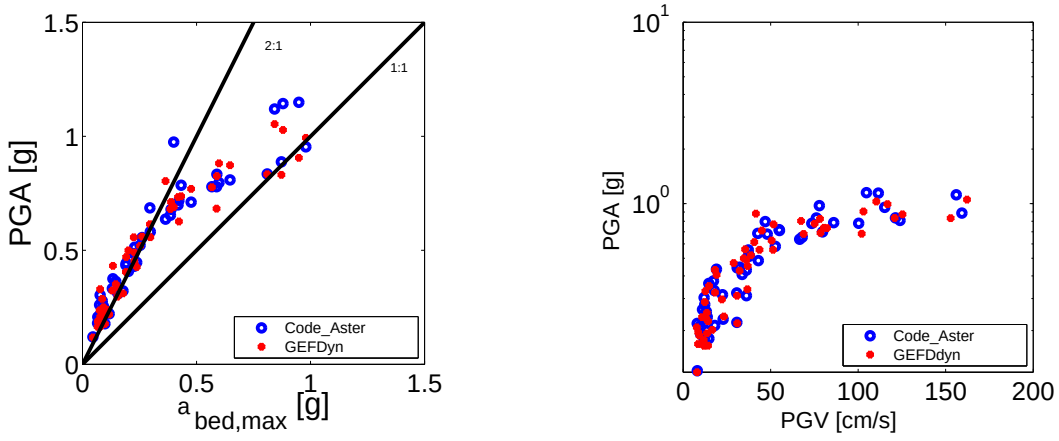

(a) (b)

Figure D.4: Comparison Code_Aster - GEFDyn : a) PGA as function of $a_{bed,max}$, b) PGA as function of PGV.

D.2 Coupled HM elastic media

Parametric consolidation tests were performed using an elastic soil column model, so as to investigate the sensitivity of results to various parameters.

Geometry - Boundary conditions

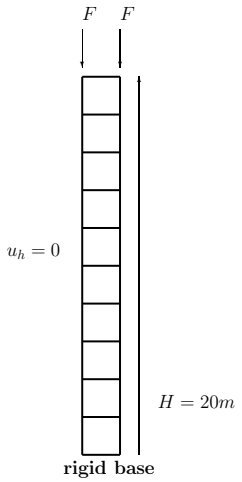

Figure D.5: Numerical model: 20m high coupled HM elastic soil column founded on rigid base.

The model consists of an elastic soil column of 20m. A mesh of 8-node quadrilateral elements of 1m length is used, as shown in Figure D.5. The lateral horizontal displacement is fixed ($u_h = 0$) and the column is founded on rigid base. The water table is supposed to be at the level of the column's surface ($h = 20m$) (drainage condition).

Mechanical characteristics

The material parameters used for the elastic soil column for the parametric analysis are presented in the Table D.1.

Table D.1: Soil properties.

Parameter	Soil
Young's modulus, E [MPa]	10
Poisson ratio, ν [·]	0.3
Coefficient of earth pressure at rest, K_0 [1]	1.0
Effective mass density, ρ [kg/m^3]	1700
Total mass density, ρ [kg/m^3]	2700
Fluid mass density, ρ_w [kg/m^3]	1000
Porosity, n [1]	0.35
Permeability, k_s [m/s]	$1{\cdot}10^{-8}$ / $1{\cdot}10^{-5}$
Fluid compressibility, H_w [Pa^{-1}]	$4.5{\cdot}10^{-10}$ / $9.35{\cdot}10^{-8}$

Loading

Constant load, equal to 500N, is imposed to the nodes at the top of the column, as presented in Figure D.6. The load is applied to the column at t_0=1s.

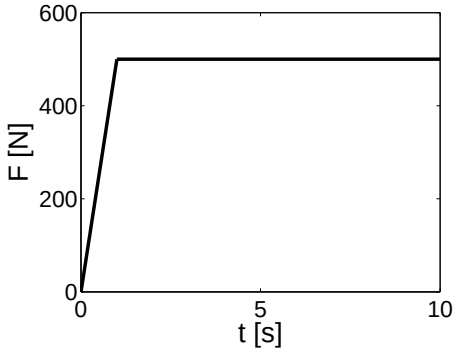

Figure D.6: Loading.

D.2.1 Results of parametric analysis of consolidation test

The influence of various parameters, such as time step, permeability, fluid compressibility and Newmark parameters, on the distribution and evolution of pore water pressure (p_w) is examined and presented in the following sections.

Influence of time step

In order to study the influence of time step on distribution of pore water pressure, three values of dt are used, 1s, 0.1s and 0.001s. The distribution of pore water pressure as function of depth is presented in Figure D.7 at t=10s. In this test, fluid compressibility is equal to $H_w = 4.5{\cdot}10^{-10}\text{Pa}^{-1}$ and permeability equal to $k_s = 1{\cdot}10^{-8}$m/s. As observed, there is no dependency of results on time step.

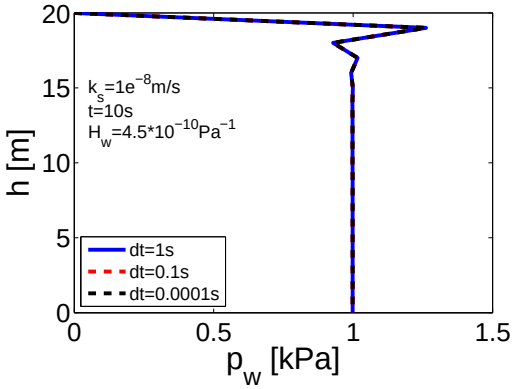

Figure D.7: Influence of time step (dt) on distribution of pore water pressure as function of depth.

Influence of permeability

Concerning permeability, two different values are used, k_s equal to $1{\cdot}10^{-8}$ and $1{\cdot}10^{-5}$m/s. As shown in Figure D.8a, when using a greater value of permeability, the oscillations which appeared at the surface, tend to disappear. Moreover, in Figure D.8 the time evolution of pore water pressure is presented for the two different values of permeability at two depths, -3m from the column surface and -10m from the column surface. Pore water pressure dissipation is produced more rapidly when material permeability is greater.

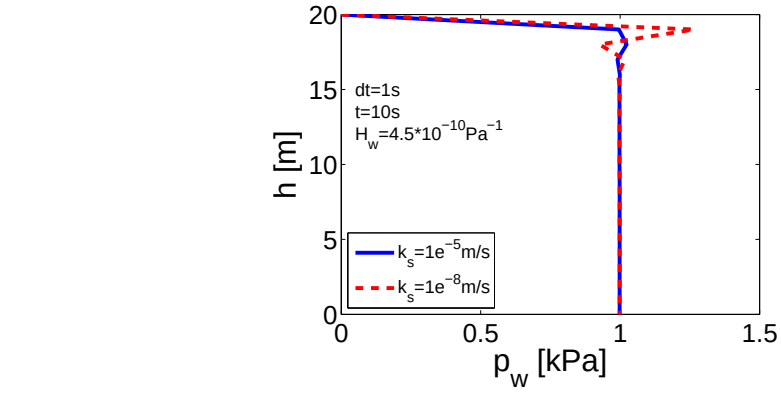

(a)

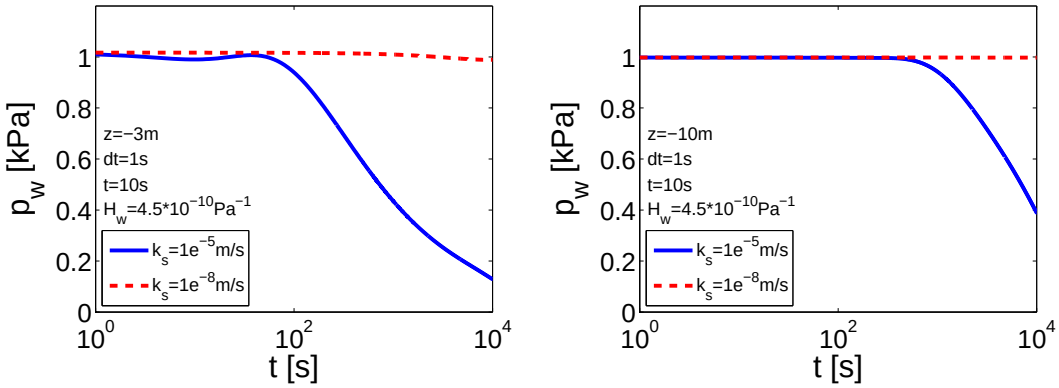

(b) Depth z=-3m (from surface) (c) Depth z=-10m (from surface)

Figure D.8: Influence of permeability on: a) distribution of pore water pressure as function of depth, b), c) evolution of pore water pressure as function of time.

Influence of fluid compressibility

Two values of fluid compressibility are used for the parametric analysis, H_w equal to $4.5{\cdot}10^{-10}\text{Pa}^{-1}$ (natural value of water compressibility) and $9.35{\cdot}10^{-8}\text{Pa}^{-1}$. Figures D.9a, D.9b demonstrates pore water pressure distribution as function of depth and it can be noticed that when using the natural value of water compressibility the pore water pressure slightly exceeds 1 due to rapid loading. Furthermore, the increase of compressibility leads to decrease of pore water pressure values, which means that the fluid is no more

incompressible. Comparing time evolution of pore water pressure, it can be remarked that with a greater value of compressibility, slight oscillations appear at the beggining of the loading (Figures D.9c, D.9d).

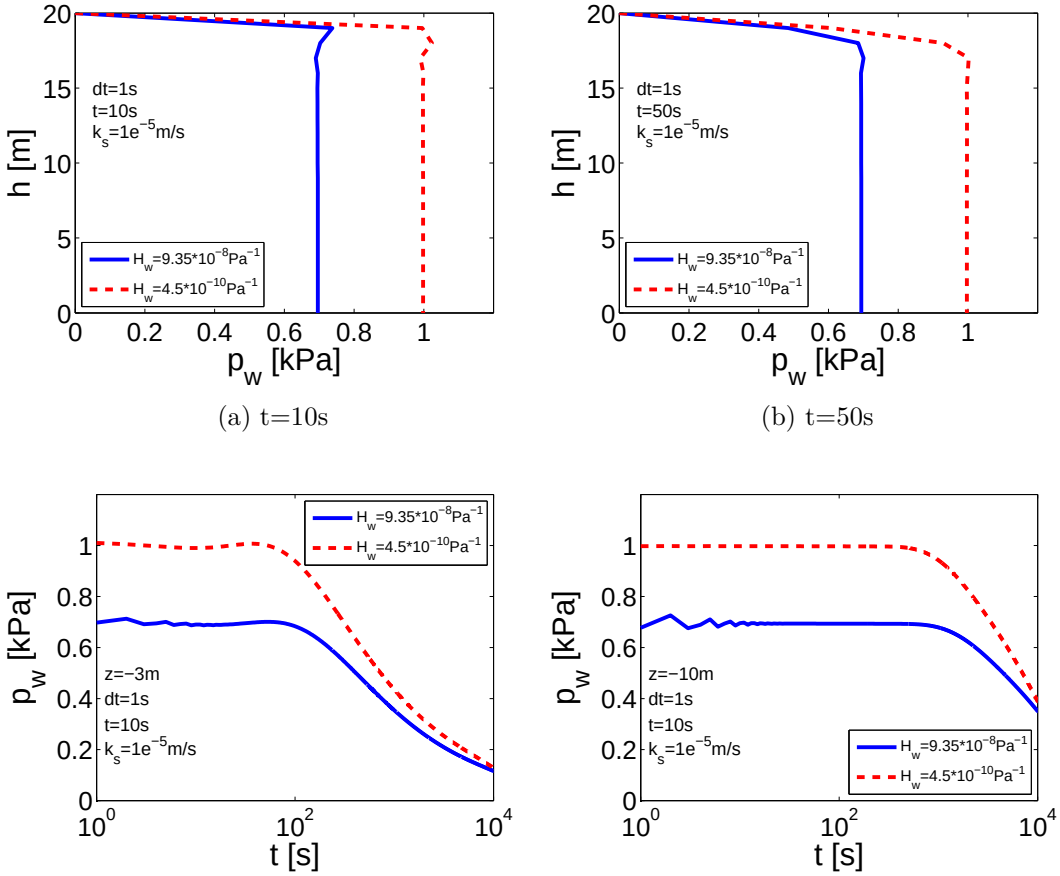

(a) t=10s (b) t=50s

(c) Depth z=-3m (from surface) (d) Depth z=-10m (from surface)

Figure D.9: Influence of compressibility on: a), b) distribution of pore water pressure as function of depth, c), d) evolution of pore water pressure as function of time.

Influence of Newmark parameters

The set of Newmark parameters used (β=0.31 - γ=0.61) adds numerical damping to the model. So as to estimate the influence of this numerical damping on model's response, a non-dissipative set of Newmark parameters is also used, with β=0.25 and γ=0.5. In Figure D.10a, no difference in distribution of pore water pressure as function of depth is remarked for the different Newmark parameters and for time step 0.1s. While, Figure D.10b shows the dissipation of pore water pressure when numerical damping (β=0.31 - γ=0.61) is added, as the oscillations disappear.

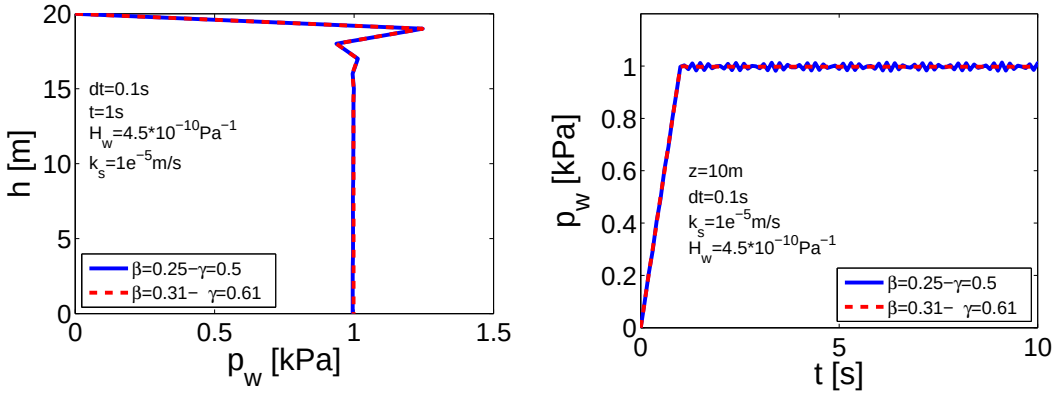

(a) (b)

Figure D.10: Influence of Newmark parameters on distribution of pore water pressure as function of: a) depth, b) time.

Influence of onset of loading

Finally, the effect of the onset of loading is tested for a time step 0.1s and Newmark parameters β=0.25 and γ=0.5. First, the load is imposed at t_0 = 1s and afterwards, at t_0 = 0.001s. From Figure D.11, it can be noticed that the decrease of t_0, ie loading velocity, increases the level of oscillations.

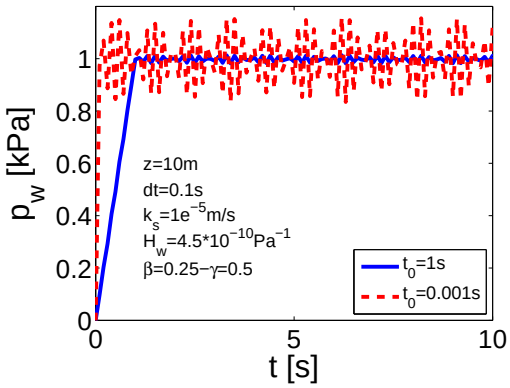

Figure D.11: Influence of onset of loading on evolution of pore water pressure as function of time.

D.3 Coupled HM nonlinear media

The soil column model of Section 3.2 is subjected to Friuli earthquake, in order to study the influence of water compressibility. As observed previously, when the real value of water compressibility ($4.5{\cdot}10^{-10}$ Pa^{-1}) is used, it is possible that due to the rapid dynamic loading, an abrupt increase in pore water pressure happens and liquefaction occurs. Furthermore, in case of low permeability, oscillations appeared in Figure D.8a. In order

to examine the effect of water compressible in case of liquefaction, the same parametric study with two values of water compressibility is performed. In Figure D.12 the evolution of excess pore water pressure is plotted at 4m from the column's free surface during the earthquake. On the one hand, the evolution of Δp_w is quite similar for both values of water compressibility. However, observing the red curve (natural value of water compressibility), an increase of pore water pressure appears at the beginning of the motion due to water's incompressibility. This fact implies that in case of an abrupt loading (i.e. earthquake with a peak during the first seconds of the motion), numerical problems may appear due to sudden increase of pore water pressure. For this reason, the water is supposed to be slightly compressible and water compressibility is equal to $9.35{\cdot}10^{-8}\text{Pa}^{-1}$ throughout this PhD work.

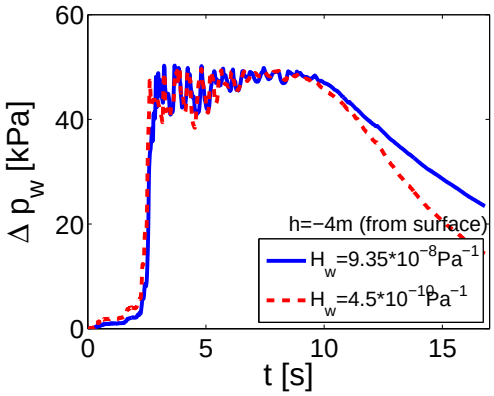

Figure D.12: Influence of water compressibility on soil liquefaction.

Appendix E

Effect of variation of permeability during soil liquefaction of a silty sand

Following the study of variation of permeability in Section 3.5.2, the silty sand of low permeability is used for the LMS layer and the same parametric study is performed. As already explained, only results of the first and third approach are compared and discussed.

The evolution of pore water pressure at 4m below the surface (in the middle of the liquefiable soil layer) is plotted for the 2 chosen ground motions in Figure E.1. As previously, for the stronger motion which lead to liquefaction, the build-up phase is identical and the same value of Δp_w is reached, by indicating the liquefaction state at around 50kPa. The dissipation is faster for the simulation with variation of permeability. Note that in case of low motion (Figure E.1a), in both simulations the values of excess pore water pressure with the silty sand are greater than with the clean sand (Figure 3.37a), as the less permeable soil is more susceptible to liquefy.

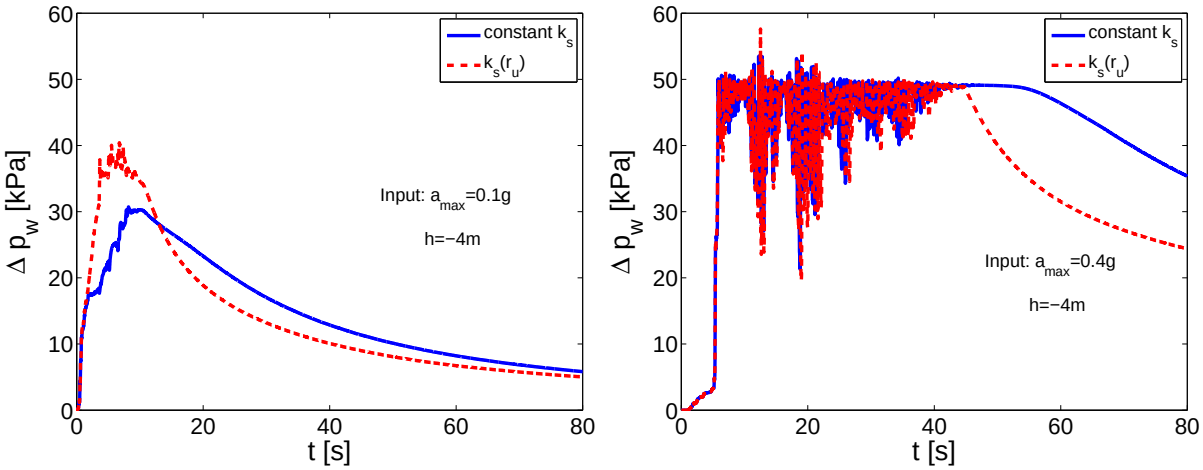

(a) Input ground motion: a_{max}=0.1g. (b) Input ground motion: a_{max}=0.4g.

Figure E.1: Comparison of two simulations in case of silty sand: Evolution of pore water pressure during ground motion (at h=-4m from the surface).

In Figure E.2 the controus of excess pore water pressure ratio are plotted for both

simulations. By comparing Figure E.2 to Figure 3.39 it can be remarked that when the silty sand of low permeability is used, the liquefaction is more extended and lasts some seconds after the end of the ground motion. Furthermore, as both layers, LMS and dense sand, have the same permeability, the dissipation is significantly slower. As it concers the comparison between the two simulations, the same conclusion can be drawn, i.e. the dissipation starts earlier and is more rapid in case of variable permeability.

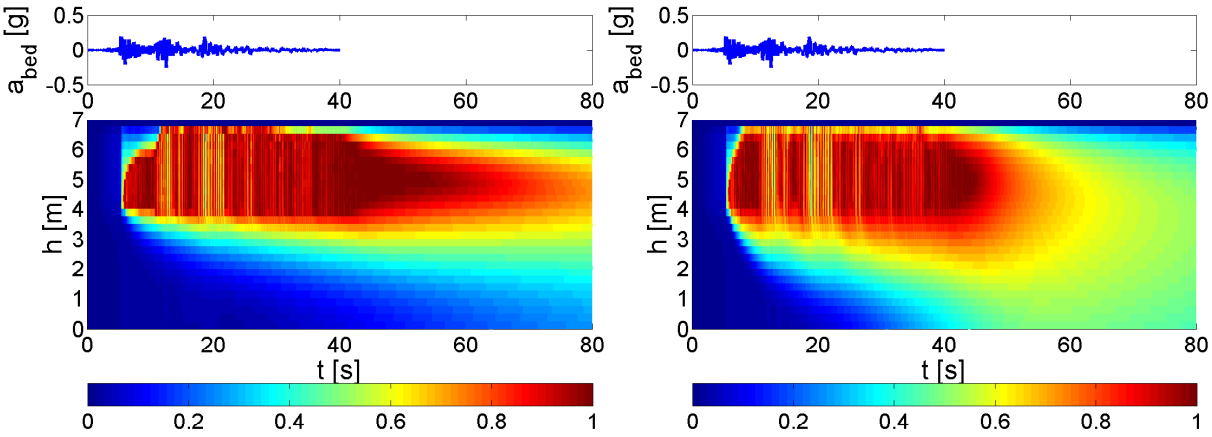

(a) Simulation 1. (b) Simulation 3.

Figure E.2: Comparison of two simulation in case of silty sand: Excess pore water pressure ratio during ground motion (a_{max}=0.4g).

As in the case of clean sand, the same mean values of 40% difference between the two simulations are found, as presented in Figure E.3.

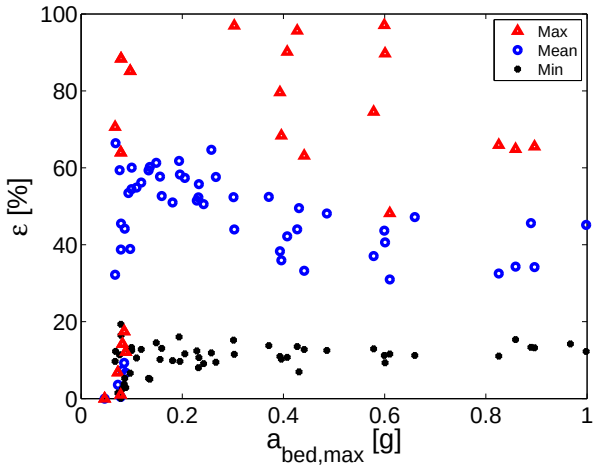

Figure E.3: Difference estimation of Δp_w between the two permeability functions as function of maximum acceleration of input motion in case of silty sand.

Concerning the response in terms of acceleration and frequency, the same differences were noticed for the moderate and stronger motions and for the sake of brevity the figures are omitted. In Figure E.4 it can be observed that for the motions of amplitude greater

than 0.4g, noticeable differences appear. Once again in the case of variable permeability the liquefaction state is more limited and grater values of PGA are obtained. In Figure E.4b the column's settlement is very close in both simulations. It can be concluded that even in case of silty sand of low permeability, where the liquefaction is more extended, the use of variable permeability does not change remarkably the ground settlement.

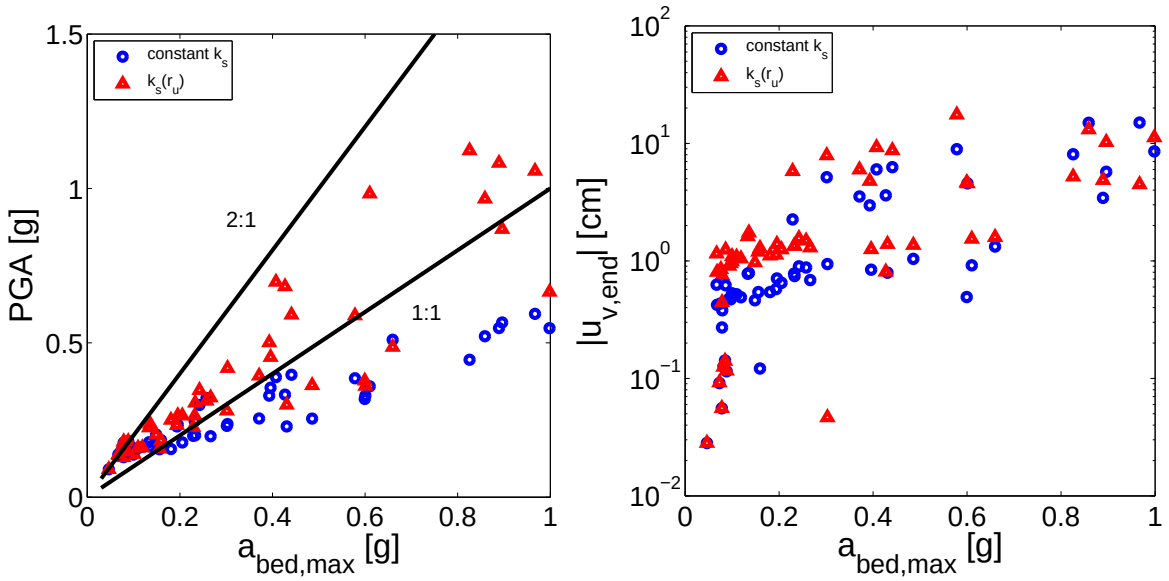

(a) (b)

Figure E.4: Comparison in case of silty sand: a) PGA, b) Ground settlement at the end of the ground motion.

Appendix F

Identification of regularization parameter a_1

Numerical results demonstrate mesh dependency under monotonic loading and the regularization method, called first gradient of dilation model is used to mitigate mesh sensitivity, as proposed by Fernandes et al. (2008) and Foucault et al. (2011). The method of first gradient of dilation model can enhance the kinematic of the medium and expand the effects of microstructure to global scale. The method is presented in detail in Section 4.3.

As it was demonstrated by Foucault (2010), the regularization parameter calculated directly by the theory of the first gradient of dilation model does not fit to the ECP constitutive model (Hujeux, 1985). The purpose of this study is to estimate the suitable parameter of regularization when using the ECP constitutive model for the soil, according to the PhD work of Foucault (2010). The procedure of identification of the regularization parameter needed is presented and two soil types have been tested in dry conditions using the ECP elastoplastic model.

F.1 Identification procedure

In Code_Aster , in order to apply the regularization method of first gradient of dilation model, the user should employ a material, called $ELAS\_2NDG$. In this material the regularization parameter a_1 should be determined. The option $PDIL\_ELGA$ of Code_Aster provides the corresponding value of the regularization parameter a_1 ($A1\_LC2$) for a requested characteristic length of the shear band ℓ_c and a given initial stress state (test case of Code_Aster : SSNV208A). Note that the option $PDIL\_ELGA$ is coded for a 2D problem, as the coeffient (n+1)=3, which corresponds to a 2D simulation, is already included (refer to equation 4.54).

However, according to the PhD work of Foucault (2010), when the ECP constitutive model is used, the obtained value of a_1 does not always correspond to an adequate value, capable to regularize the given problem. A procedure to better fit the regularization parameter to each material and to obtain the requested shear band is proposed in this section. By performing biaxial drained tests in a specimen with a given material and confining pressure, the regularization parameter can be adjusted. The procedure for

the identification of the regularization parameter is described (Figure F.1) and next a numerical example is presented.

1. **Estimation of the initial value of a_1 for a requested characteristic length, according to the test case SSNV208A:**

   Biaxial drained test is performed in one soil element. From the option $PDIL\_ELGA$, the regularization parameter is calculated (value of $A1\_LC2$), which corresponds to the requested characteristic length of the shear band. Note that this value of a_1 obtained depends on the material's confining pressure. The value of a_1 is the initial regularization parameter applied to the first gradient of dilation model, so as to proceed to a simulation with regularization.

2. **Biaxial drained test for the specimen with regularization, using the obtained initial value of a_1:**

   From the biaxial drained test with regularization, we calculate geometrically the thickness of the shear band in the specimen. The plasticity index (variable $V26$ of ECP model in Code_Aster) should also be examined to verify that the specimen has reached the softening regime.

3. **Calculation of reduction coefficient for the parameter a_1:**

   In case of different thickness of the shear band from the requested one (characteristic length ℓ_c), a coefficent should be applied to the initial value of a_1, so as to obtain the desired shear band. A biaxial drained test with the new value of a_1 should be performed to verify that the measured geometrically thickness of the shear band corresponds to the requested one (ℓ_c).

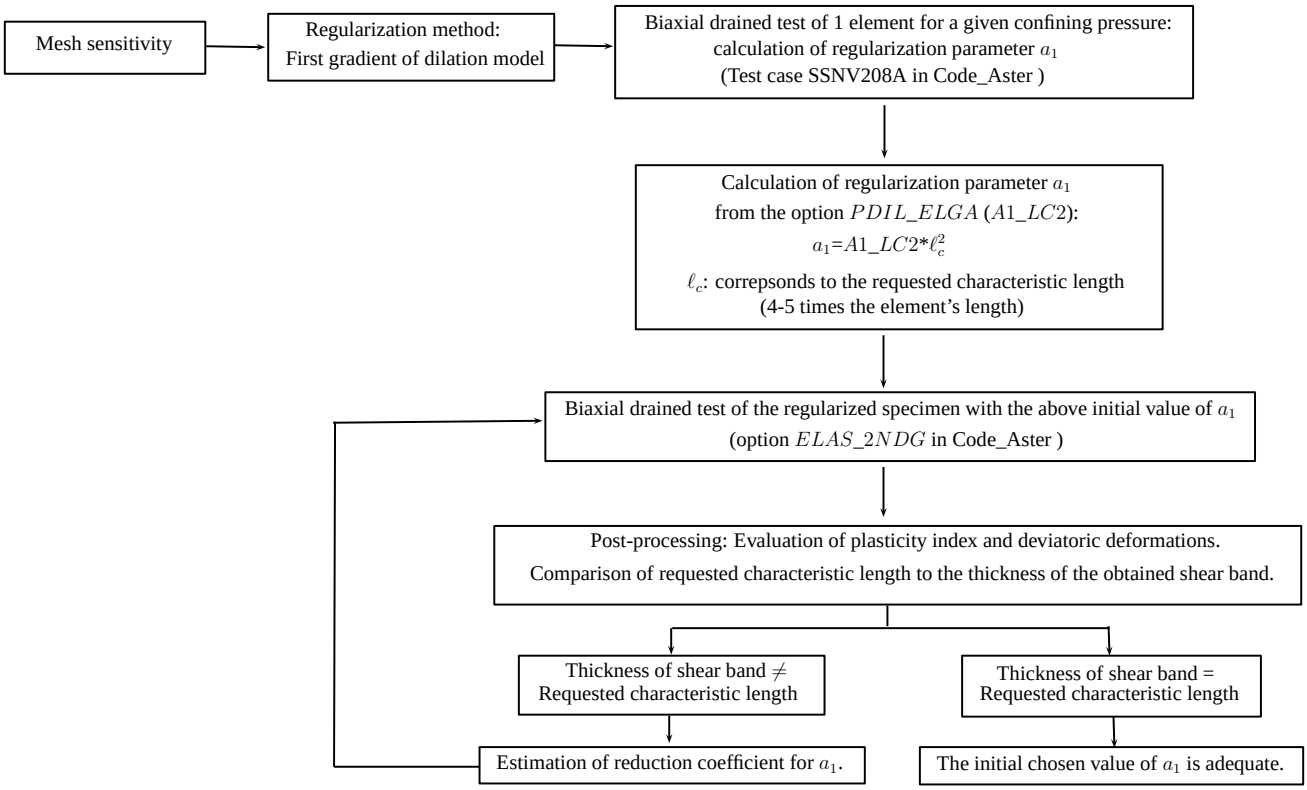

Figure F.1: Schematic illustration of identification procedure for the regularization parameter a_1.

F.2 Numerical model

Geometry - Boundary conditions

The model consists of a nonlinear soil specimen in dry conditions. The dimensions of the specimen are 0.2m of height and 0.1m of width, as shown in Figure F.2. Constant pressure is applied at both lateral surfaces (p_0) and displacement (u_v) at the top of the specimen. Concerning the boundary conditions, vertical displacements at the bottom of the specimen are vanishing (u_v=0) and the horizontal displacement of the rigth corner at the bottom of the specimen is also equal to zero. A finite element mesh of 512 elements was created using 8-node quadrilateral elements. The element's length is 0.00625×0.00625m.

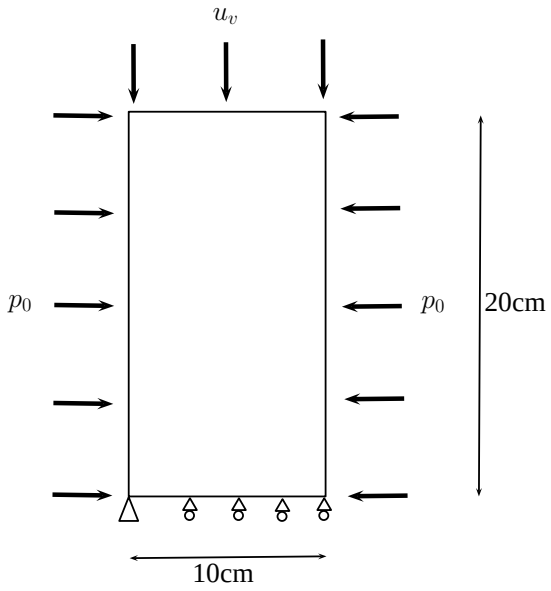

Figure F.2: Illustration of numerical model for the nonlinear soil specimen.

Mechanical characteristics

Hostun sand with relative density DR=88% is used for the drained biaxial tests under monotonic loading, as used in the PhD work of Foucault (2010). The ECP soil's parameters can be found in Table F.1 and material's response under drained triaxial tests for the confining pressures used is presented in Figure F.3.

Loading

Monotonic vertical displacement equal to u_v=0.32m/0.08m (depending on the confining pressure) is imposed gradually at the top of the specimen with a time discretization of 8000 time steps (δu_v=0.00004m/0.00001m). The total loading time is 2s.

Table F.1: ECP model's parameters for the soil.

Parameter	Hostun sand (DR=88%)
ρ_s [kg/m^3]: Solid density	2700
ν [1]: Poisson's ratio	0.3
K_0 [1]: Coefficient of lateral earth pressure	1.0
Elasticity	
E [MPa]: Young's modulus	478
n_e [1]: Nonlinear degree	0.0
p'_{ref} [MPa]: Reference mean stress	1.0
V_S [m/s]: Shear wave velocity	324
Critical State and Plasticity	
β [1]: Plastic compressibility modulus	17
b [1]: Yield surface shape	0.2
d [1]: Isotropic consolidation distance	2.5
ϕ'_{pp} [^{o}]: Friction angle	33
p_{c0} [MPa]: Initial critical stress	8.0
Flow Rule and Hardening	
a_1 [1]: Primary plastic stiffness	0.0002
a_2 [1]: Secondary plastic stiffness	0.018
c^m [1]: Monotonic isotropic hardening	0.0001
c^c [1]: Cyclic isotropic hardening	0.00005
ψ [^{o}]: Characteristic angle	33
α_ψ [1]: Volumetric parameter	1.0
m [1]: Cyclic loading exponential	1.0
Threshold Domains	
r_d^{ela} [1]: Deviatoric elastic	0.005
r_{iso}^{ela} [1]: Isotropic elastic	0.0001
r_d^{cyc} [1]: Cyclic deviatoric	0.005
r_{iso}^{cyc} [1]: Cyclic isotropic	0.0001
r^{hys} [1]: Hysteretic	0.25
r^{mob} [1]: Mobilized	0.9

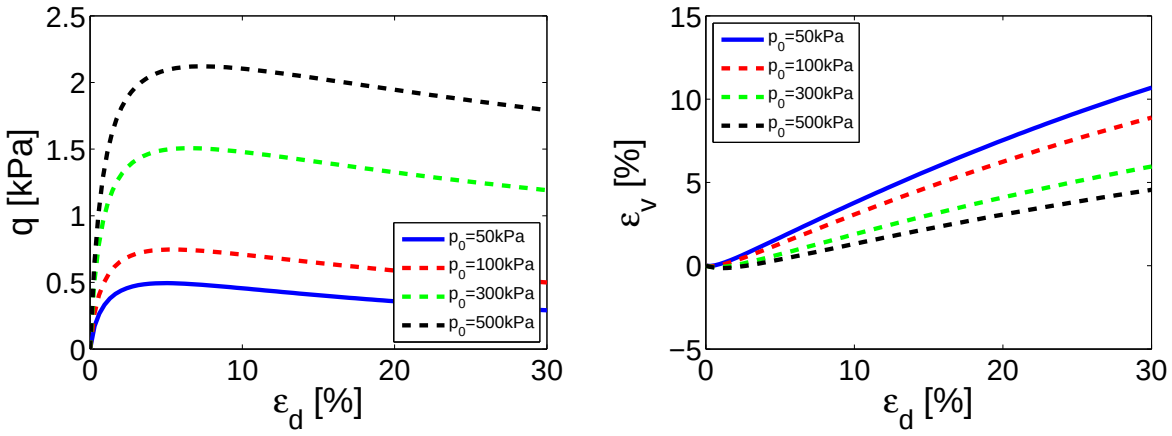

(a) (b)

Figure F.3: Soil response of one material point with the ECP constitutive model (K_0=1.0) of the Hostun sand under drained triaxial test: a) Hostun sand DR=88%

Regularization parameters

According to the thesis work of Foucault (2010), in order to obtain the proper value of the regularization parameter, we have to perform biaxial tests so as to test whether the value of a_1 found by equation 4.54 (Section 4.5.4) corresponds to the requested characteristic length. It has been proven that in some cases the value calculated by equation 4.54 does not correspond to a shear band with a width equal to the characteristic length. If the regularization parameter is large enough, we may eliminate the shear band mechanism and apply a strong regularization which will perturbate the results. So, in the thesis of Foucault (2010), two materials were tested and it was found that most of the times we have to divide the parameter a_1 by a coefficient in order to obtain a zone of localization of deformations and to avoid distinguishing the shear band mechanism due to a strong regularization.

As the main purpose of the biaxial tests is to identify the parameter that best fits to our material, various regularization parameters were examined consequent to the confining pressure. Previous studies have shown that it is necessary to have 4-5 finite elements across the shear band to catch adequately the localised bifurcation mode (Foucault et al., 2011). Therefore, a characteristic length ℓ_c=0.04m is used following these suggestions. In Figure F.4 the initial values of a_1 are plotted as function of σ_v for the material used and for the given characteristic length (ℓ_c=0.04m), as they have been calculated by equation 4.54.

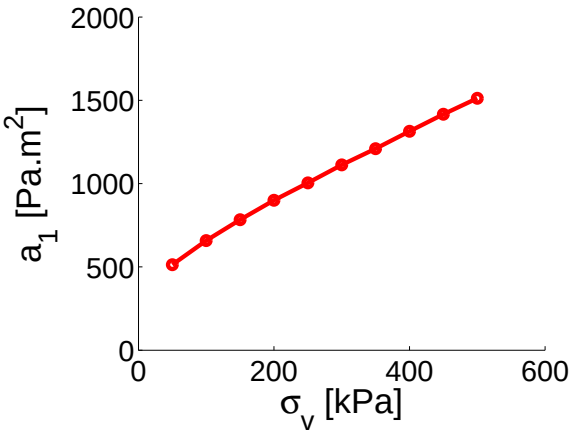

(a) Hostun sand (DR=88%) (K_0=1.0).

Figure F.4: Initial regularization parameter a_1 as function of σ_v for ℓ_c=0.04m.

F.3 Biaxial test of Hostun sand (DR=88%)

As aforementioned, in the case of Hostun sand (DR=88%) a characteristic length of 4cm is requested (ℓ_c=0.04m) and two confining pressures are applied to the specimen (p_0 = -500kPa, -100kPa). For both confining pressures, two biaxial tests were performed, one with the regularization parameter found by equation 4.54 and plotted in Figure F.4a and a second-one with this parameter divided by 25 (coefficient proposed by Foucault (2010) for this soil type).

F.3.1 p_0=-500kPa and u_v=-0.32m

The force - displacement curve (F_v-u_v) is plotted to observe the specimen's behavior for both values of a_1 (a_1=1500$Pa \cdot m^2$ and $a_1/25$=60$Pa \cdot m^2$) and it can be noticed that the specimen exceeds the peak and reaches the softening regime (Figure F.5).

When a shear band mechanism appears in the specimen, the deviatoric strains are concentrated on a zone of localization where the plasticity index is equal to 1 (plasticity). In order to study the response of the specimen, the plasticity index and the contours of deviatoric strain are plotted. In Figure F.6, the plasticity index and the deviatoric strains of the specimen are plotted at t=0.15s (u_v=0.024m) and t=2s (t_{end}, u_v=0.32cm) for the initial value of a_1=1500$Pa \cdot m^2$. The results are plotted at t=0.15s for comparison reasons, as the biaxial test with $a_1/25$=60$Pa \cdot m^2$ stopped at t=0.15s due to non convergence. Observing Figure F.6a, it can be pointed out that the applied regularization is strong enough and no shear band appears. While the material is in the softening regime (see also material behavior in Figure F.5), no localization phenomena are noticed. Even at the end of the test (Figure F.6b), while we have the occurence of a shear band at the bottom of the specimen, the plasticity index demonstrates that the whole lower part of the specimen is plastic. The regularization applied has eliminated the shear band mechanism as it is very strong.

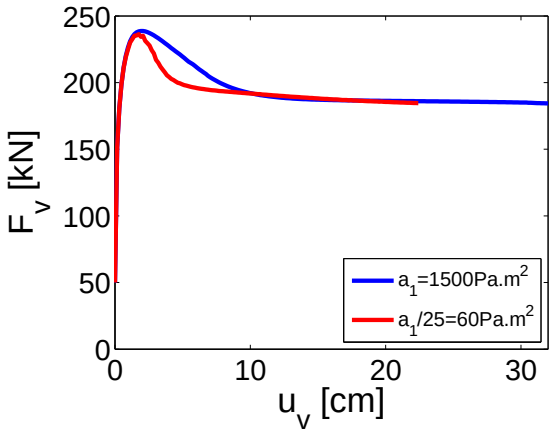

Figure F.5: $F_v - u_v$ curve of Hostun sand (DR=88%) at confining pressure p_0=-500kPa.

As a second approach, in Figure F.7 the response of the specimen is presented with a lower value of regularization parameter ($a_1/25$=60$Pa \cdot m^2$) at t=0.15s (the end of the test). It is clear that a shear band mechanism has appeared (3-4 elements in the plasticity zone), starting from the left upper corner of the specimen and going down diagonally. Moreover, the plasticity index indicates a zone of plasticity of 4cm width, approximately, at the same location where the shear band emerges. Consequently, for this material and with confining pressure of -500kPa, it is verified the statement that the initial regularization parameter calculated by equation 4.54 should be divided by 25, in order to obtain the shear band with a width equal to the characteristic length requested.

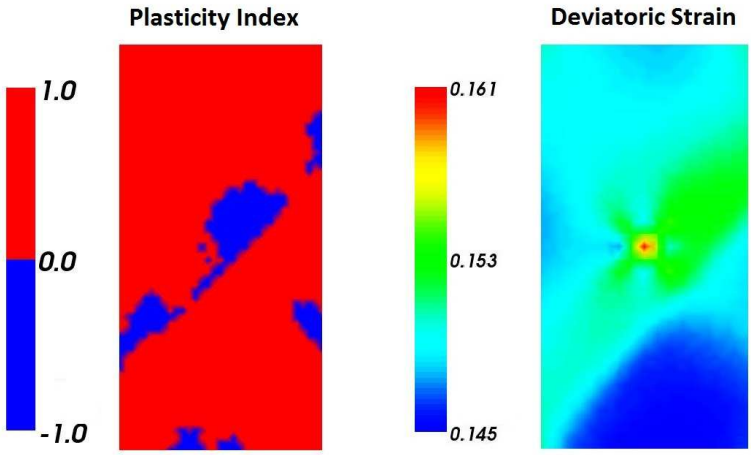

(a)

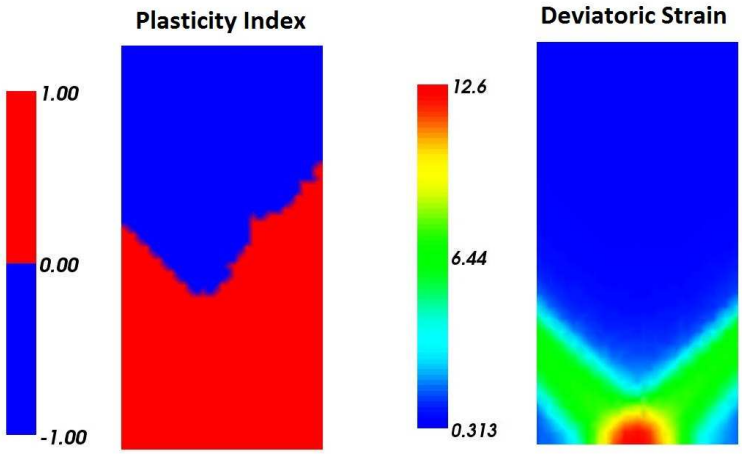

(b)

Figure F.6: Biaxial test of Hostun sand (DR=88%) - p_0=-500kPa, a_1=1500$Pa \cdot m^2$: a) t=0.15s (u_v=0.024m), b) t=2s (t_{end}, u_v=0.32cm).

F.3.2 p_0=-100kPa and u_v=-0.08m

Intending to evaluate the sensitivity of the aforementioned coefficient, the same biaxial test is perfomed with confining pressure equal to p_0=-100kPa. For this confining pressure, three values of a_1 are tested: initial a_1=660$Pa \cdot m^2$, $a_1/25$=26$Pa \cdot m^2$ and $a_1/50$=13$Pa \cdot m^2$. For all values of a_1 the specimen reaches the softening regime (Figure F.8).

For the sake of brevity, the results with the initial value a_1=660$Pa \cdot m^2$ are omitted, as no shear band was observed in the specimen. From Figure F.9a, it is clear that the coefficient equal to 25 does not fit to a biaxial test with confining pressure of -100kPa. These results demonstrate a sensitivity of this coefficient to the confining pressure of the specimen, i.e. the coefficient applied is not a characteristic of the material used, but it also depends on the confining pressure. Consequently, it is proposed to take into account an

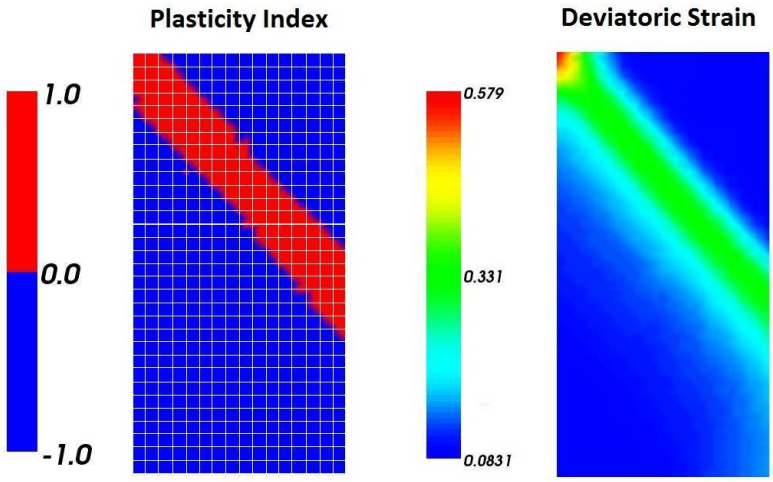

Figure F.7: Biaxial test of Hostun sand (DR=88%): p_0=-500kPa, $a_1/25$=60$Pa \cdot m^2$, t=0.15s (t_{end}, u_v=0.024m).

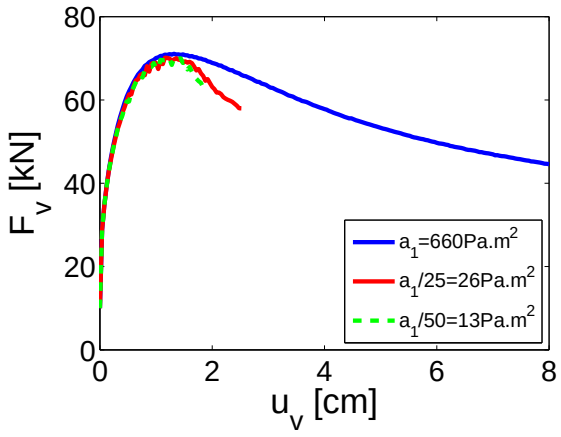

Figure F.8: $F_v - u_v$ curve of Hostun sand (DR=88%) at confining pressure p_0=-100kPa.

evolution of the multiplier coefficient with respect to the initial conditions of the specimen (i.e. confining pressure).

A new decreased value of the coefficient is tested and a_1 is divided by 50 ($a_1/50$=13$Pa \cdot m^2$). In Figure F.9b, it is clear that a band of plasticity almost equal to 0.04m (ℓ_c requested) appears and at the same time there is a shear band mechanism created at the specimen. Thus, the proper coefficient for the Hostun sand (DR=88%) and a confining pressure of -100kPa is 50.

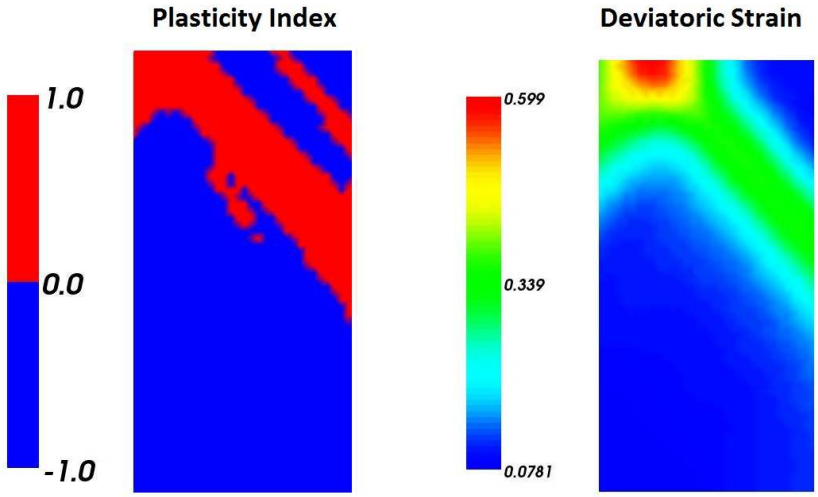

(a)

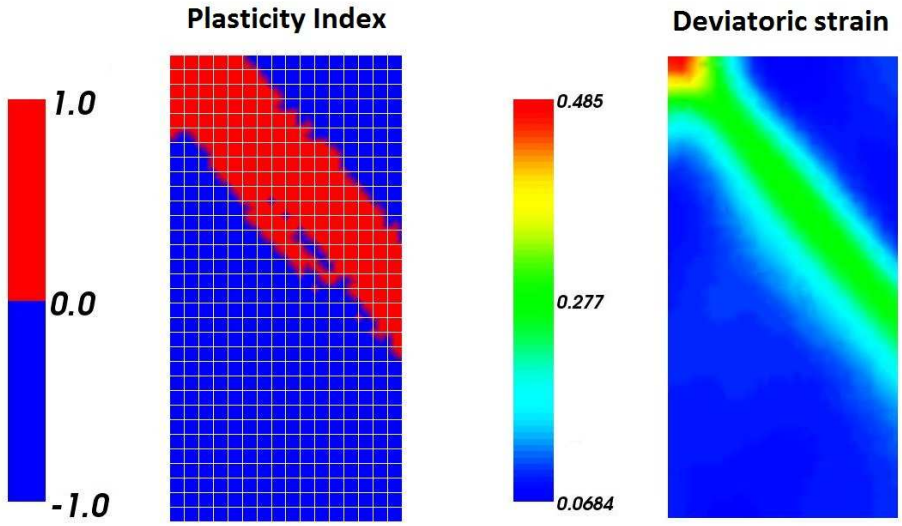

(b)

Figure F.9: Biaxial test of Hostun sand (DR=88%) with p_0=-100kPa: a) $a_1/25$=$26Pa{\cdot}m^2$, t=0.63s (t_{end}, u_v=0.025m), b) $a_1/50$=$13Pa \cdot m^2$, t=0.48s (t_{end}, u_v=0.02m).

Synopsis

To sum up, each time the regularization method of the first gradient of dilation model is used with the ECP constitutive model, biaxial tests should be performed to estimate the adequate value of regularization parameter that corresponds to the requested characteristic length. It is likely that when the initial value of a_1 (Equation 4.54) is used, the applied regularization is very strong and the shear band mechanism disappears. So, the value of a_1 should be divided by a coefficient estimated from a series of biaxial tests performed.

Appendix G

1D SH wave propagation in nonlinear regularized media

As discussed in Chapter 4, deficiencies are observed when applying the regularization method of first gradient of dilation model in case of dynamic analysis. The additional terms of the first gradient of dilation model interfere on the equations of wave propagation and the dynamic response of the medium is perturbated (e.g. oscillations in the response in terms of deviatoric deformations). In the light of further investigating this abnormal response, analytical signals are imposed to the soil column model (Figure 4.1) as S waves horizontally propagating in order to examine in which frequencies the perturbation appears. Each signal concentrates all its energy in one frequency, as shown in Figure G.1a. The number in the name of the signal stands for its fundamental frequency. The maximum acceleration of the signals ($a_{bed,max}$) varies between 0.032-0.037g. For each input motion two simulations are performed: a) without regularization ("NR") and b) with regularization ("R") using the parameters indicated in Section 4.5.4 for a requested characteristic length equal to ℓ_c=1m.

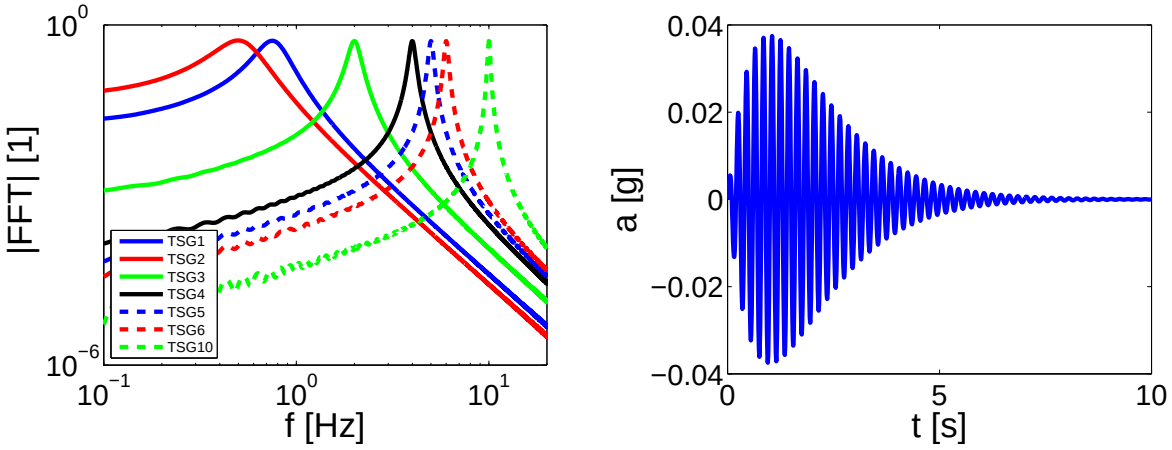

(a) (b)

Figure G.1: Input analytical signals: a) Fourier transform, b) Accelerogram of TSG5.

Recall that a regularization method is used to eliminate the mesh effect of results and especially of shear bands. If no localization phenomena appear, the response without and with regularization should be identical, while in case of localization a smoother response is expected for the regularized medium. In order to observe the shear deformations in the soil column, the profile of deviatoric strain ε_d is computed (Equation 4.55).

Initially, in Figure G.2 the profile of ε_d is plotted without and with regularization at the end of the dynamic analysis for all signals. A perturbation close to the column's surface is clearly detected, especially for signal TSG5 (Figure G.2e), although no localization phenomena appear. Generally, it is observed that the analytical signals with a fundamental frequency close to soil column's fundamental frequency (f_p=5.8Hz) led to more significant deformations due to resonance, i.e. permanent deviatoric deformations exceed 10^{-2}% for signals TSG4, TSG5, TSG6 and consequently the effect of the regularization is strongly apparent (Figure G.2d, G.2e, G.2f). For this reason and for the sake of brevity, only results of signal TSG5 with a fundamental frequency of 5Hz (see accelerogram in Figure G.1b) are discussed in the following sections.

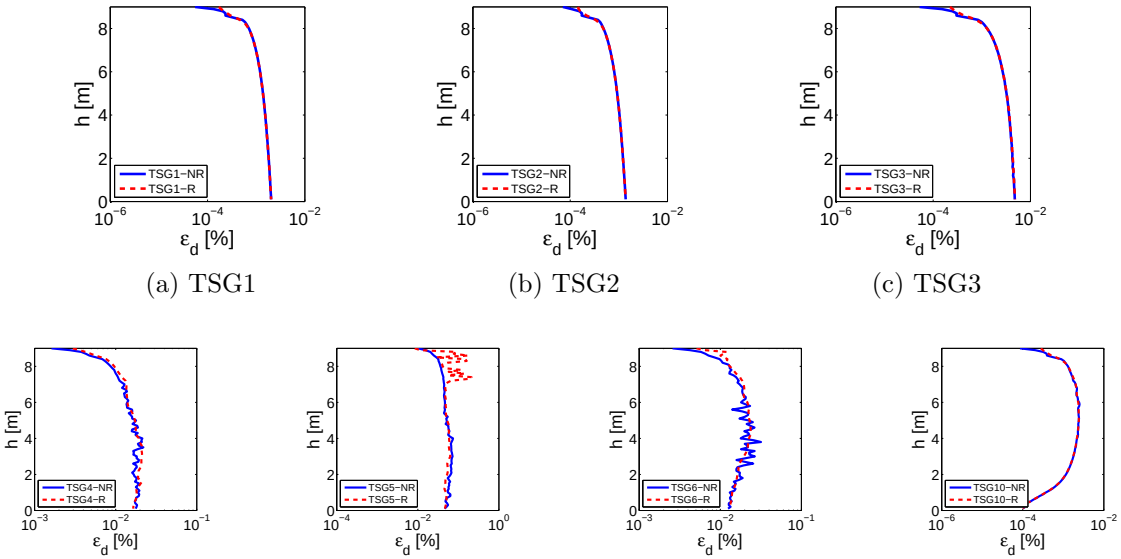

(a) TSG1 (b) TSG2 (c) TSG3

(d) TSG4 (e) TSG5 (f) TSG6 (g) TSG10

Figure G.2: Profile of deviatoric strains ε_d at the end of the input motion.

G.1 Dynamic response of soil column

As aforementioned, the dynamic response of the soil column subjected to the TSG5 analytical signal will be discussed, as the perturbation is more apparent in this case. Although the regularization refers only to the elimination of the mesh effect and should not affect the dynamic response of the model, in Figure G.3 noticeable differences appear in the accelerograms without and with regularization. Furthermore, in terms of frequency in Figure G.4, where the S-transform is calculated, noise appears during the mainsock (t=2-3s) when the regularization method is applied.

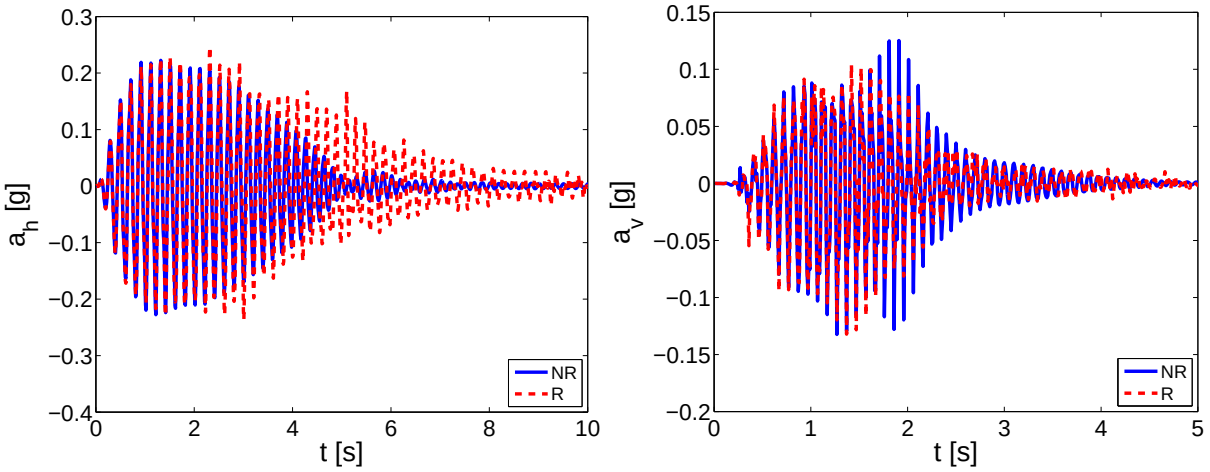

(a) (b)

Figure G.3: FF acceleration without and with regularization: a) Horizontal acceleration, b) Induced vertical acceleration.

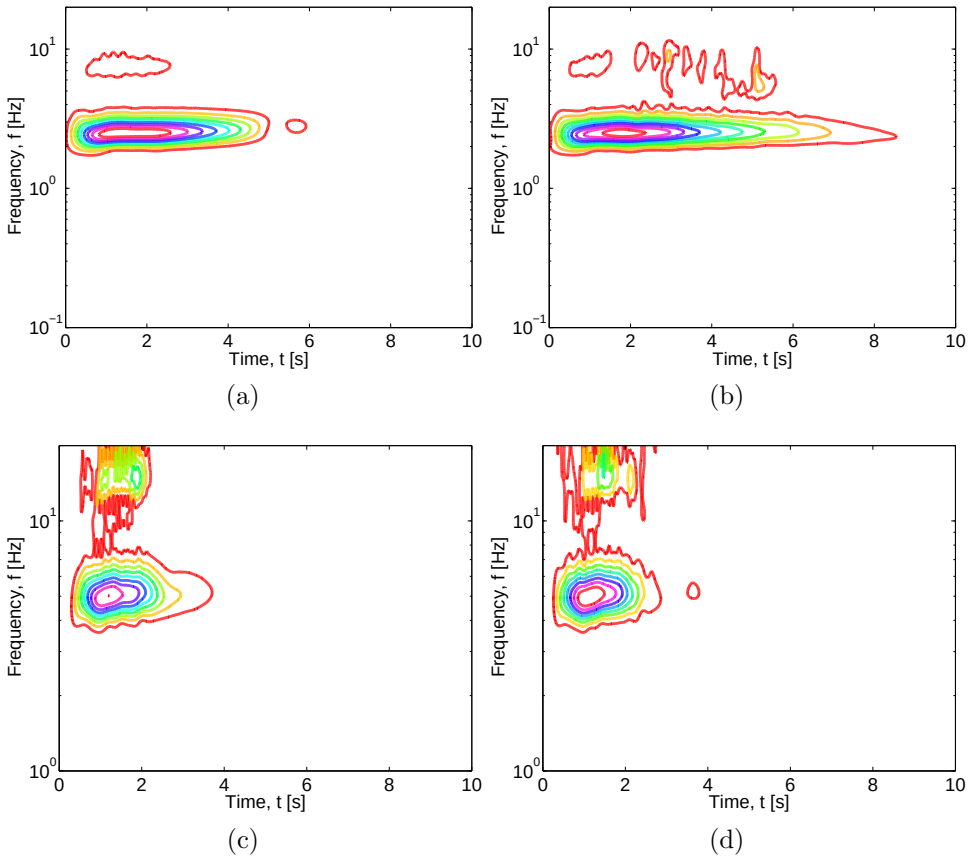

(a) (b)

(c) (d)

Figure G.4: Comparison of S-transform without and with regularization: a) FF horizontal acceleration-Without regularization, b) FF horizontal acceleration-With regularization, c) Induced vertical acceleration-Without regularization, d) Induced vertical acceleration-With regularization.

The coherency is calculated for the obtained horizontal acceleration without and with regularization in different levels of the soil column, as shown in Figure G.5. It can be verified that the noise appears in a wide range of frequencies and as result a filter of low or high frequencies can not be used to eliminate the perturbation. The perturbation is apparent all along the soil column and not only concentrated close to the surface, as it was stated before.

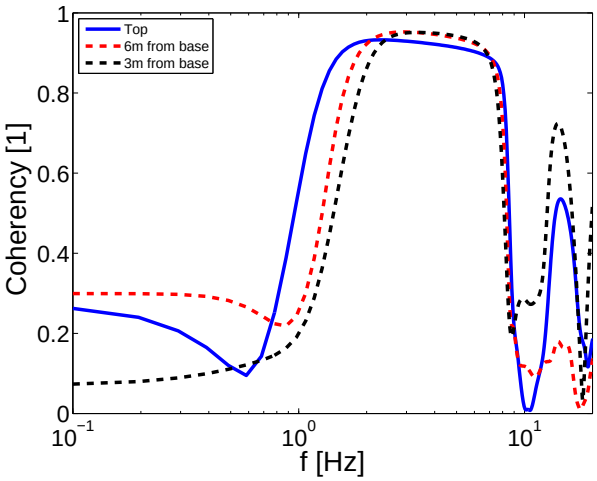

Figure G.5: Coherency of horizontal acceleration without and with regularization.

To sum up, the noise generated by the regularization applied, appears all along the soil column and in a wide range of frequencies when permanent deformations exceed a certain level. In the following section the mechanical behavior of the soil column is examined for both cases, regularized and non regularized, to better identify the origin of the perturbation.

G.2 Study of mechanical behavior

When the column is close to resonance and significant deviatoric deformations appear ($\varepsilon_d > 10^{-2}\%$), the perturbation in the soil column appears due to the regularization method applied. With respect to this remark, cyclic shear tests in one material point for a wide range of shear strains γ (γ=2$\cdot$ ε_d) and confining pressures are performed. The shear strain γ varies between $10^{-3}\%$-$10^{0}\%$, while three confining pressures were chosen corresponding to the geostatic pressure at 3m, 6m and 8m from the base of the column (100kPa, 50kPa and 20kPa, respectively).

Observing Figure G.6, it is noticed that when γ reaches the value of $2{\cdot}10^{-2}\%$ (i.e. ε_d=$10^{-2}\%$), volumetric deformations are generated. This value of γ corresponds to the volumetric cyclic threshold shear strain γ^{tv}, as defined by Vucetic (1994). As the terms of rigidity added through the regularization method are related to the gradient of volumetric deformations, when volumetric deformations appear, the regularization method is activated and it generates the perturbation identified previously.

In Figure G.7, the evolution of volumetric deformations during the input ground motion all along the soil column is plotted in relation to the vertical acceleration obtained

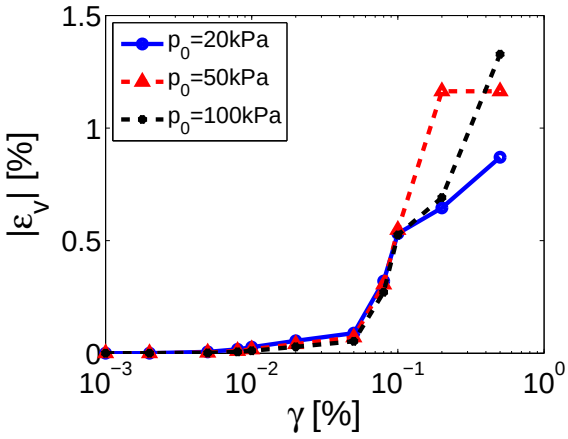

Figure G.6: Soil response after cyclic shear tests in one material point.

at the surface of the soil column. The evolution of vertical acceleration coincides with the generation of volumetric deformations and when the volumetric deformations reach a constant level, the vertical acceleration tends to zero progressively. The application of the regularization leads to greater values of volumetric deformations in the upper part of the column during the mainshock (t=2-3s) (Figure G.7b), which can be related to the perturbation close to the surface (Figure G.2e). Though, in the lower part of the column, greater volumetric deformations appear in the case without regularization (Figure G.7a). The different response between the upper and the lower part of the column is related to the choice of the regularization parameter a_1 as function of the mean vertical stress σ_v. In the upper part of the column the vertical stress σ_v is lower than the mean value used to calculate the regularization parameter a_1, so the regularization applied is stronger than this needed. Consequently, it results to stronger perturbation at the upper part.

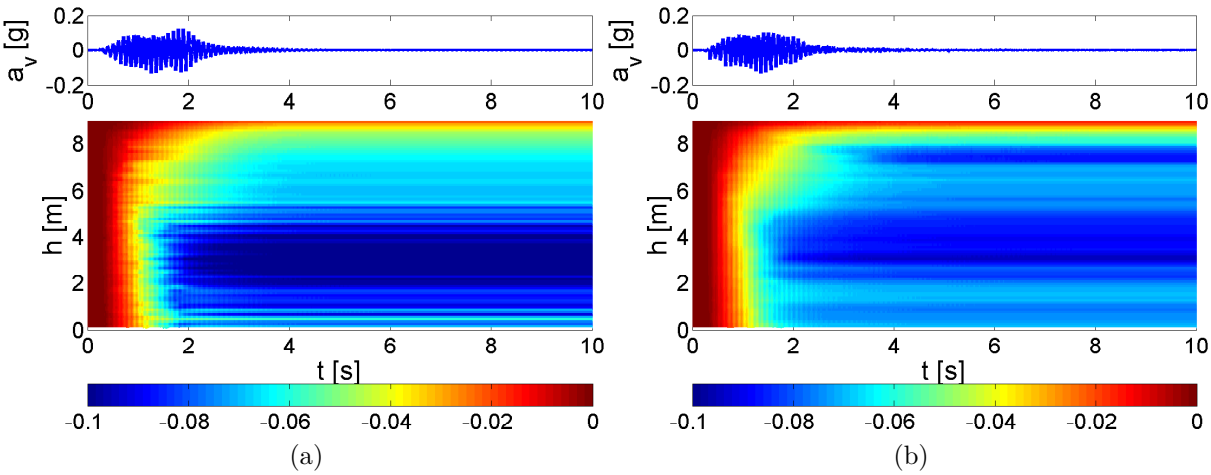

Figure G.7: Contours of volumetric deformation(%) related to the generation of vertical acceleration: a) Without regularization, b) With regularization.

This statement can also be verified observing the curves ε_v-ε_d, p_k-ε_v at different levels

of the soil column (3, 6 and 8m from the base). Close to the surface (Figure G.8c, G.8d) the value of ε_v with regularization is greater, while progressively it decreases (Figure G.9c, G.9d) and close to the base of the column (Figure G.10c, G.10d) the value of ε_v with regularization is smaller compared to this without regularization.

In all curves p_k-q_k, q_k-ε_d, ε_v-ε_d, p_k-ε_v, τ-γ (Figure G.8, G.9, G.10 and G.11), it is clear that the regularization method applied provides a different mechanical behavior. More precisely, in Figures G.8b, G.9b and G.10b the curves coincide initially, but when deviatoric deformations become greater of $10^{-2}\%$ the curves completely diverge as the regularization is activated. In Figures G.8c and G.9c it is demonstrated that the first gradient of dilation model enforces the soil column to remain more in elasticity, as the relation between ε_v-p_k is linear for greater values of p_k. Last, in Figure G.11a the slope is steeper in the case with regularization due to the additional elastic matrix of rigidity of the regularized model.

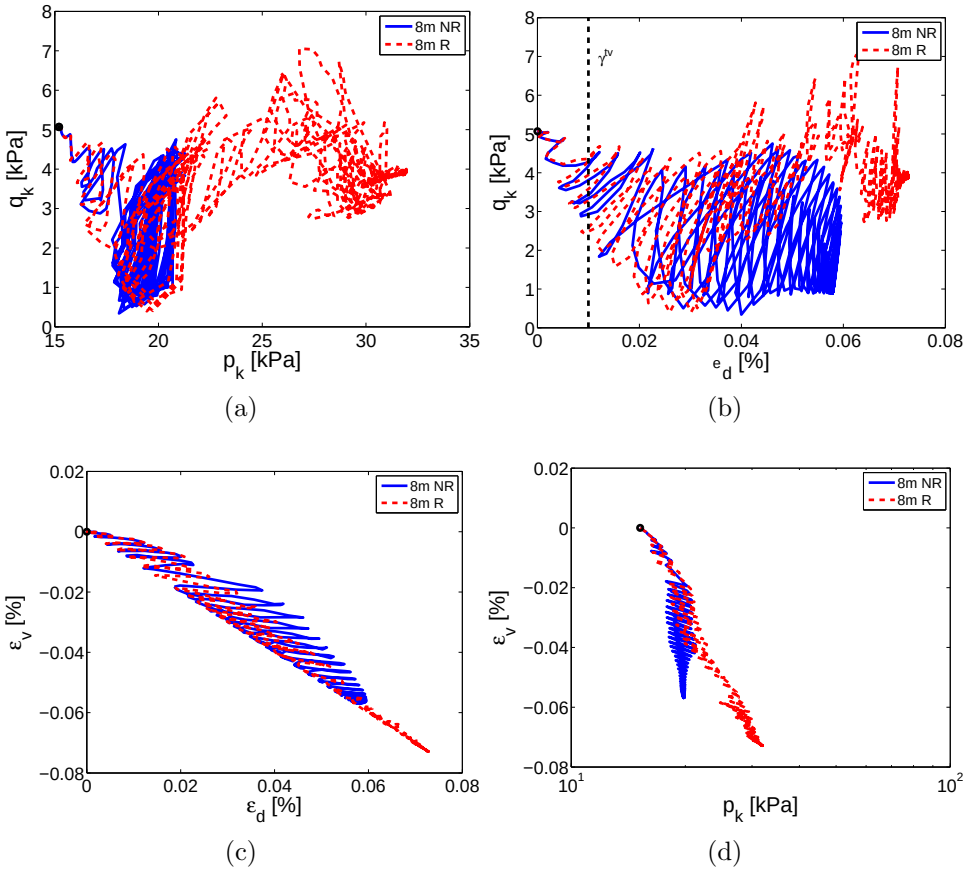

Figure G.8: Mechanical behavior (8m from base): a) p_k-q_k, b) q_k-ε_d, c) ε_v-ε_d, d) p_k-ε_v.

To sum up, the problem with the regularization starts when volumetric deformations are generated and the first gradient of dilation model is activated. The elastic matrix of rigidity added does not respond properly to the dynamic response of the column and it leads the material to stay more in elasticity providing an abnormal mechanical behavior. In the following sections, the contribution of shear-induced volumetric deformations and of

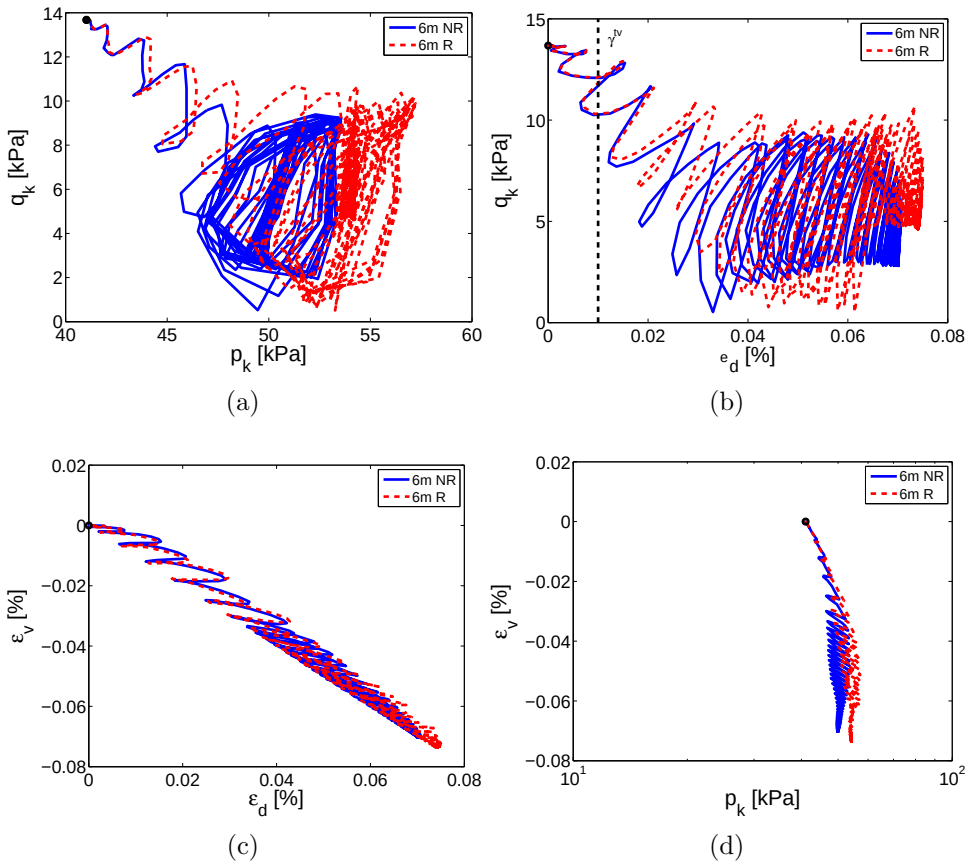

Figure G.9: Mechanical behavior (6m from base): a) p_k-q_k, b) q_k-ε_d, c) ε_v-ε_d, d) p_k-ε_v.

those generated by the isotropic mechanism is evaluated. For this reason, three simulations are performed:

1. Isotropic mechanism deactivated: no generation of volumetric deformations due to the shear-induced P-wave propagation.

2. Zero shear-induced volumetric deformations: no generation of volumetric deformations due to the coupling of volumetric and deviatoric strains.

3. A combination of the previous two simulations.

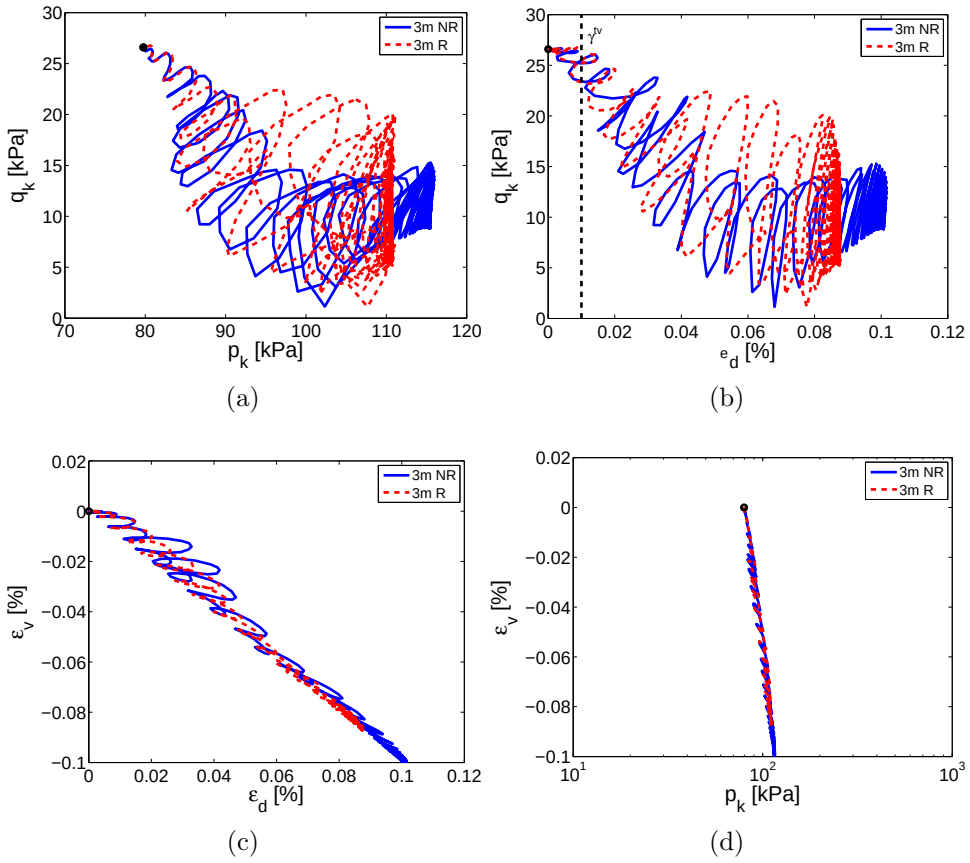

Figure G.10: Mechanical behavior (3m from base): a) p_k-q_k, b) q_k-ε_d, c) ε_v-ε_d, d) p_k-ε_v.

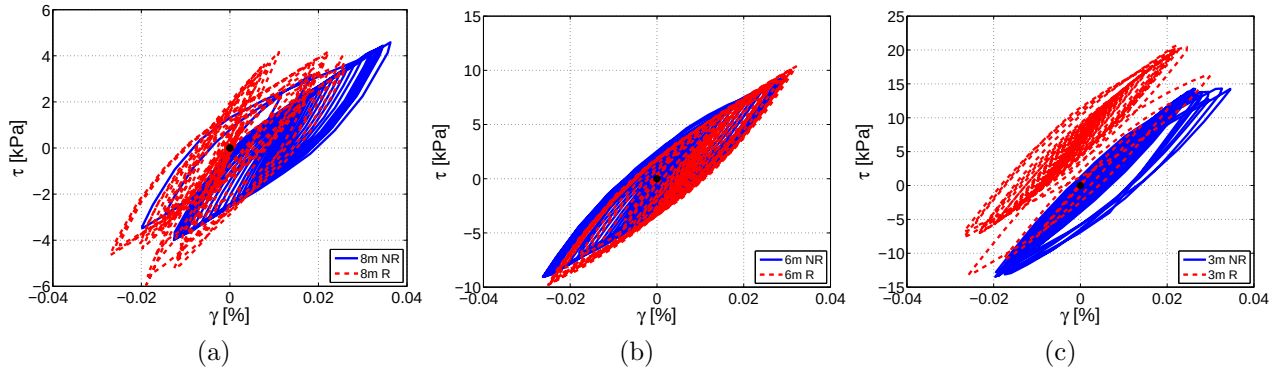

Figure G.11: Mechanical behavior τ-γ at: a) 8m, b) 6m, c) 3m from base.

G.2.1 Isotropic mechanism deactivated

In order to deactivate the isotropic mechanism and eliminate volumetric deformation from shear-induced P waves, the parameters r_{iso}^{ela}, r_{iso}^{cyc} of the ECP model should be equal to 1. Thus, the volumetric deformations that may appear come from the shear wave propagation (shear-induced volumetric deformations). In Figure G.12 the response of one element of the medium-to-dense sand (MDS) is plotted after drained triaxial test simulation and cyclic shear drained test with a confining pressure of -50kPa. Both curves of the initial material and with r_{iso}=1 are plotted.

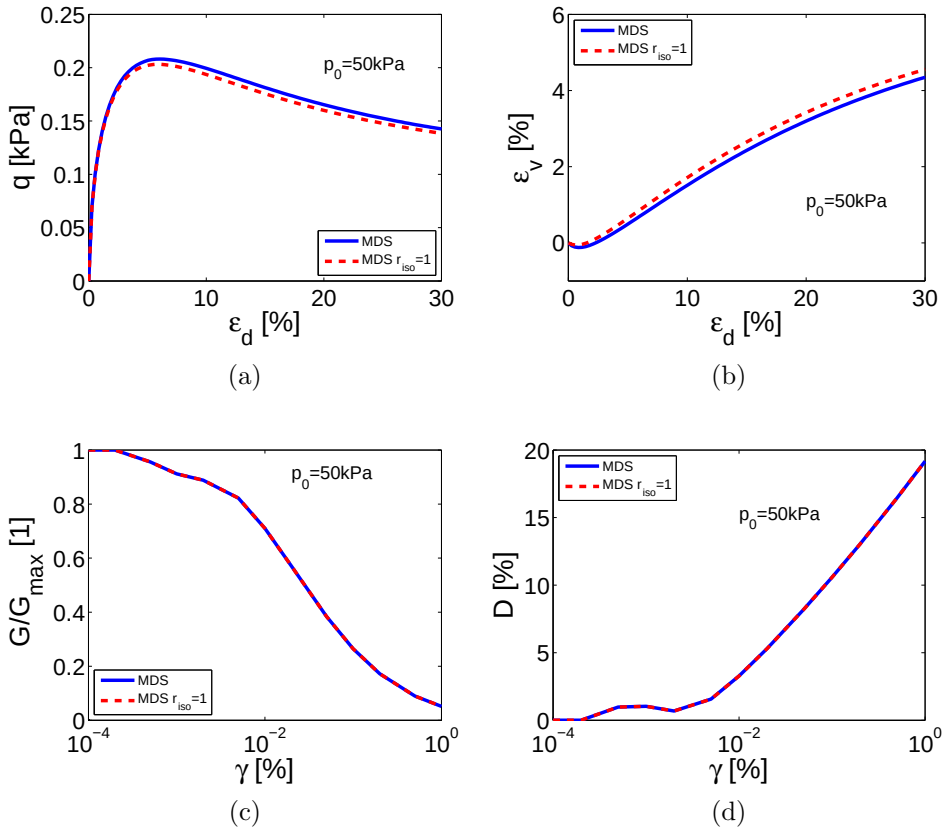

Figure G.12: Soil response of one element with isotropic mechanism deactivated: a,b) Drained triaxial test, c,d) Cyclic shear drained test.

In order to test the effect of the regularization when the isotropic mechanism is deactivated, the analytical signal of 5Hz is imposed to the column, as previously. In Figure G.13a, the profile of deviatoric strains is plotted at the end of the input motion and it is noticed that the perturbation of the signal still exists. So, the contribution of volumetric deformations of the isotropic mechanism in the response of the regularized column is of minor importance.

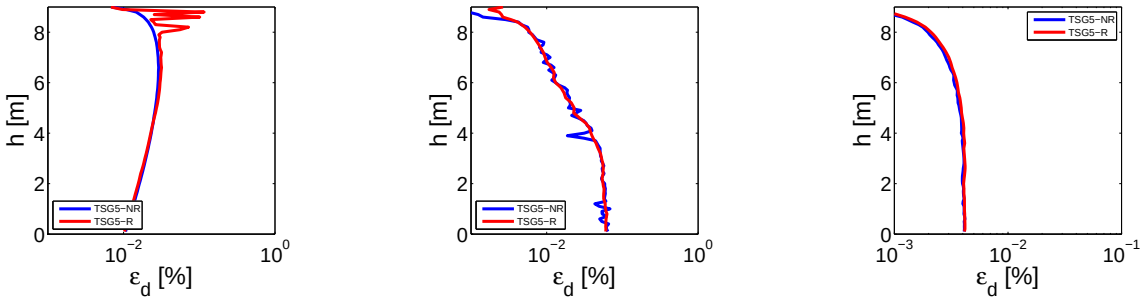

Figure G.13: Profile of deviatoric strains ε_d: a) Isotropic mechanism deactivated, b) Zero shear-induced volumetric deformations, c) Isotropic mechanism deactivated and zero shear-induced volumetric deformations.

G.2.2 Zero shear-induced volumetric deformations

As a second approach, the shear-induced volumetric deformations are neglected, i.e. the parameter α_ψ of the ECP model, which controls the coupling of volumetric-deviatoric strains, is set to be 0. More precisely, through the dilatancy rule, the plastic shear-induced volumetric deformations are linked to the plastic deviatoric strains. If the dilatancy rule is deactivated, no plastic volumetric deformations will be generated due to plastic shear strains. As before, drained triaxial test simulation and cyclic shear drained test with a confining pressure of -50kPa were performed in one element of the medium-to-dense sand (Figure G.14). Note that in Figure G.14b, while the initial material is contractive at the beginning and then dilative, in case of α_ψ=0 the material becomes purely contractive.

Subsequently, the profile of deviatoric strains is plotted for the same analytical signal TSG5. No perturbation appears all along the soil column, even though the volumetric cyclic threshold shear strain (i.e. ε_d=10^{-2}%) has been exceeded. Although great perturbation appeared at the S-transform (Figure G.4b) for the initial material, in the case of $\alpha_\psi = 0$ no difference appears between the S-transform without and with regularization (Figure G.15).

However, the coherency plotted in Figure G.16a still demonstrates a perturbation at low frequencies. As the signal is concentrated only in one frequency (5Hz) and there is no signal in the low frequencies (<1Hz), the response of the column in these frequencies is only due to the waves that reflect and propagate in the medium like a form of noise. Consequently, this perturbation observed should not be attributed to the regularization.

For the sake of brevity, only the curves p_k-q_k, q_k-ε_d, ε_v-ε_d, p_k-ε_v at 8m from the base (close to the free surface) are presented in Figure G.17. Generally, there is an agreement between the response of the column without and with regularization in all four plans when $\alpha_\psi = 0$, in contrast with the results obtained in the previous section with the initial model (Figure G.8). Note that although the shear-induced volumetric deformations are prevented and the isotropic mechanism is almost deactive as no compression waves exist, volumetric deformations still appear (see Figure G.17c, G.18). It can be supposed that these volumetric deformations may result from the deformations developped in the other

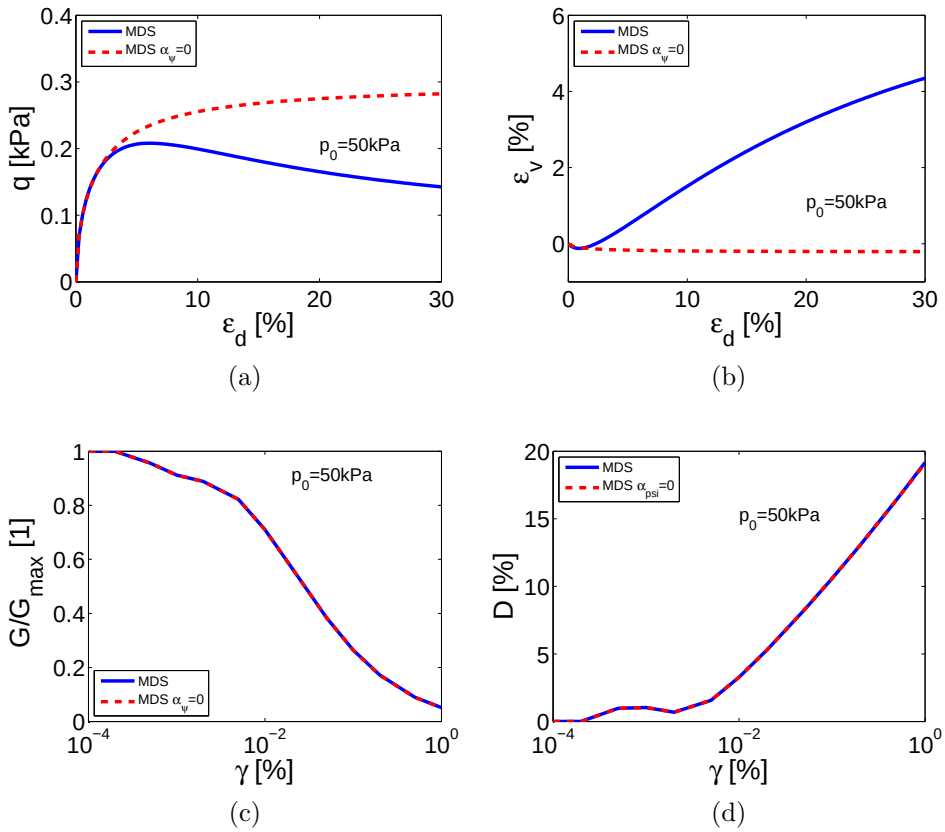

Figure G.14: Soil response of one element with zero shear-induced volumetric deformations: a,b) Drained triaxial test, c,d) Cyclic shear drained test.

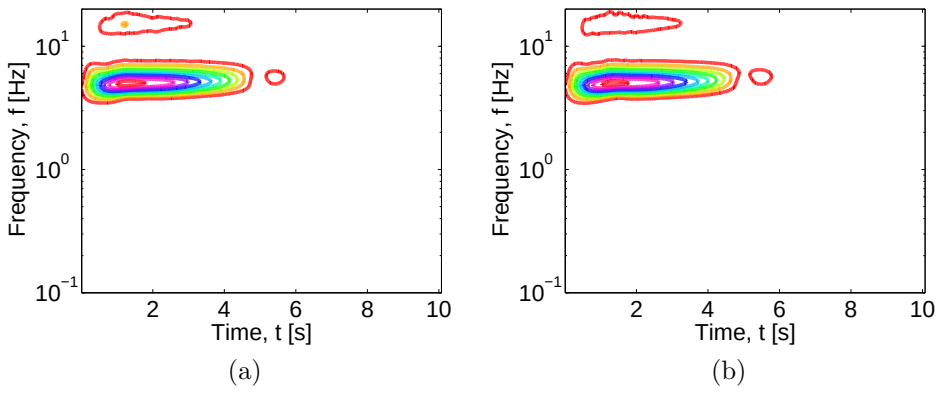

Figure G.15: S-transform for the FF horizontal acceleration with zero shear-induced volumetric deformations: a) Without regularization, b) With regularization.

plans, perpendicular to the plan y-z of the column.

In Figure G.19, there is an agreement between the contours of volumetric deformation plotted without and with regularization and when the regularization is applied the

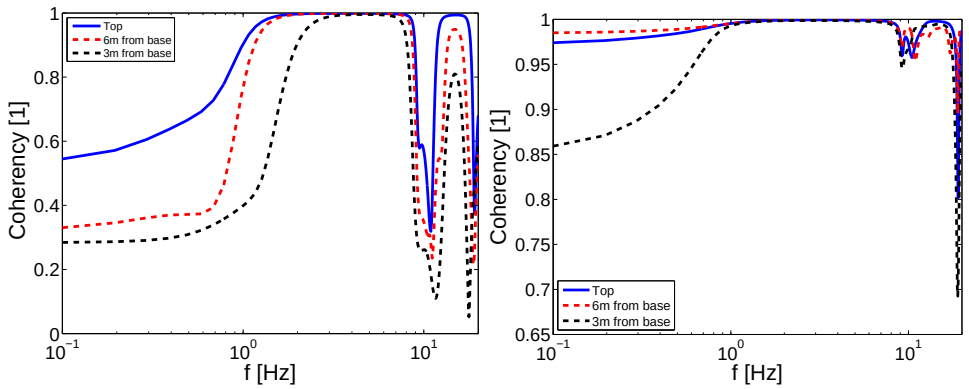

Figure G.16: Coherency of horizontal acceleration without and with regularization: a) Zero shear-induced volumetric deformations, b) Isotropic mechanism deactivated and zero shear-induced volumetric deformations.

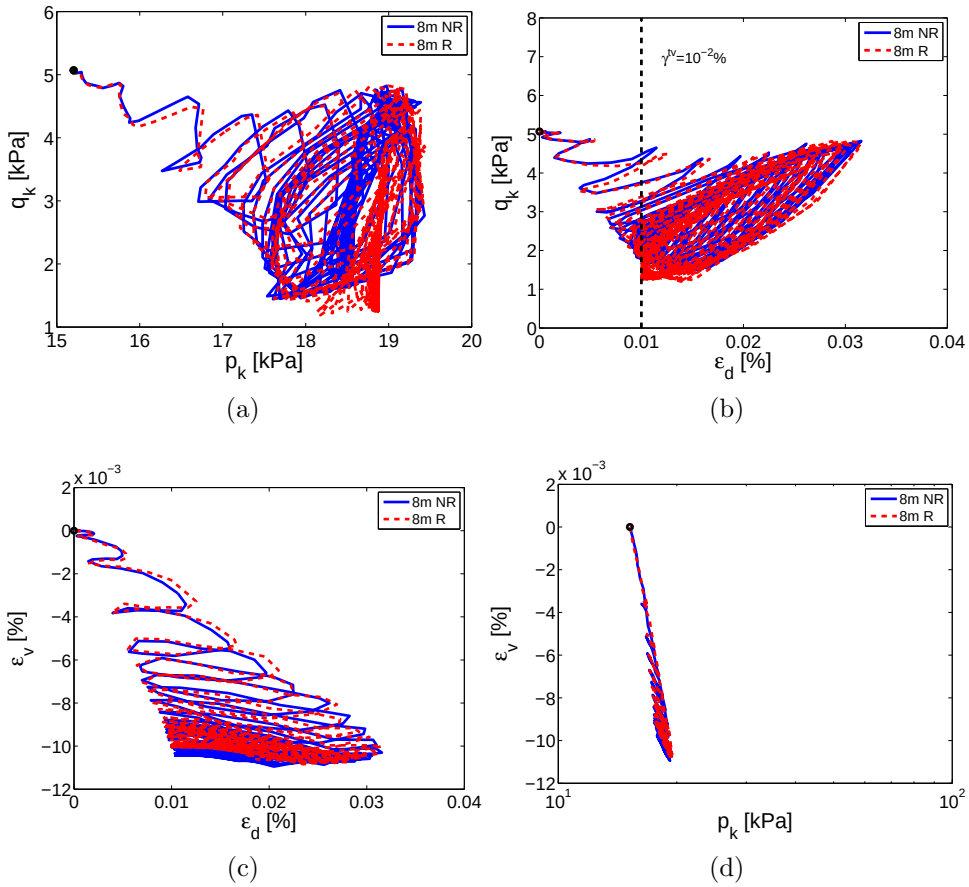

Figure G.17: Mechanical behavior with zero shear-induced volumetric deformations (8m from base): a) p_k- q_k, b) q_k-ε_d, c) ε_v-ε_d, d) p_k-ε_v.

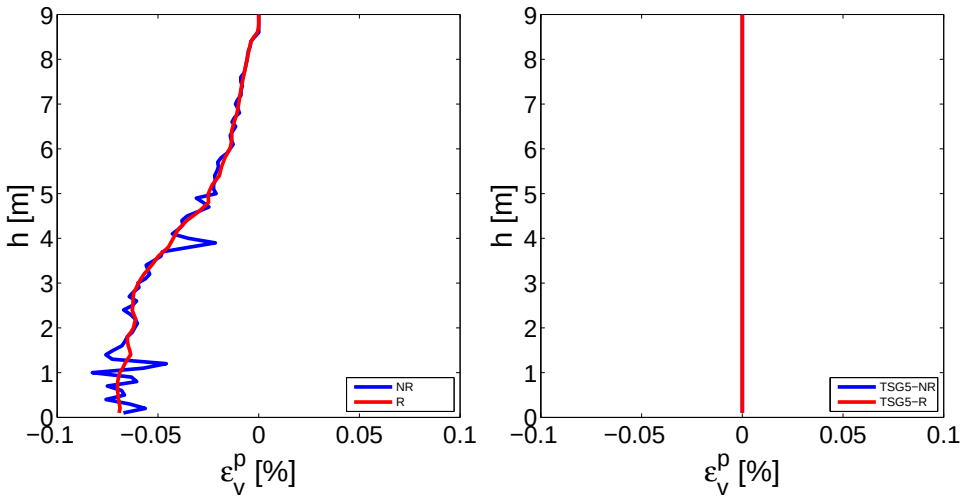

(a) (b)

Figure G.18: Profile of plastic volumetric deformations at the end of the input ground motion: a) Zero shear-induced volumetric deformations, b) Isotropic mechanism deactivated and zero shear-induced volumetric deformations.

response is smoother, as expected.

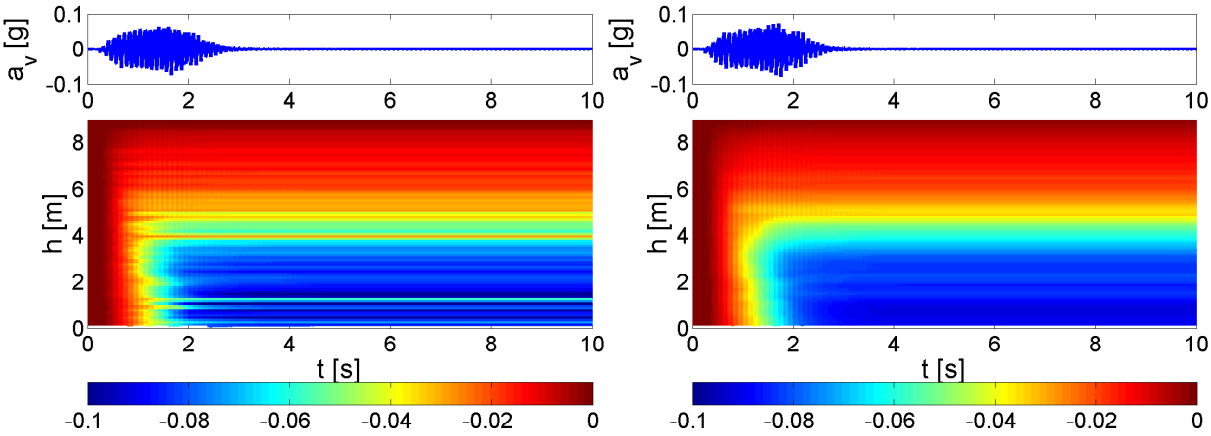

(a) (b)

Figure G.19: Contours of volumetric deformation(%) related to the generation of vertical acceleration with zero shear-induced volumetric deformations: a) Without regularization, b) With regularization.

In the following section, both the isotropic mechanism is deactivated and the shear-induced volumetric deformations are prevented, in order to observe the evolution of volumetric deformations.

G.2.3 Isotropic mechanism deactivated and no plastic volumetric deformations

In order to observe the origin of generation of volumetric deformations, the isotropic mechanism is deactivated ($r_{iso} = 1$) and the shear-induced volumetric deformations are blocked ($\alpha_\psi = 0$). In Figure G.13c, the profile of deviatoric strains is presented and no perturbation seems to appear. This assumption is also verified by calculating the S-transform (Figure G.20) and the coherency (Figure G.16b), as well.

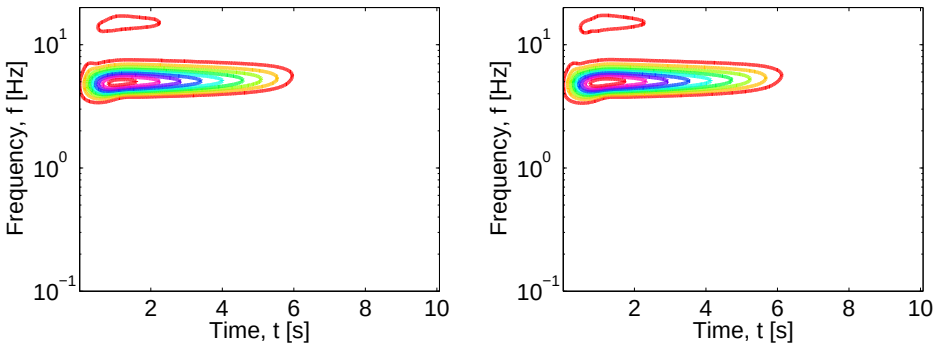

Figure G.20: S-transform for the FF horizontal acceleration with isotropic mechanism deactivated and zero shear-induced volumetric deformations: a) Without regularization, b) With regularization.

As previously for the sake of brevity, only the curves p_k-q_k, q_k-ε_d, ε_v-ε_d and p_k-ε_v at 8m from the base are illustrated in Figure G.21. There is an agreement between the response of the column, in case of α_ψ=0 and r_{iso}=1, without and with regularization and the volumetric deformations remain at a low level. So, it is concluded that the low volumetric deformations correspond to the deformations developped in the other plans, but their contribution to the response of the column is not important. This can be verified by plotting the contours of ε_v along the soil column in Figure G.22, where the value of ε_v is almost zero without and with regularization. No plastic volumetric deformations are generated, as it can be noticed in Figure G.18b.

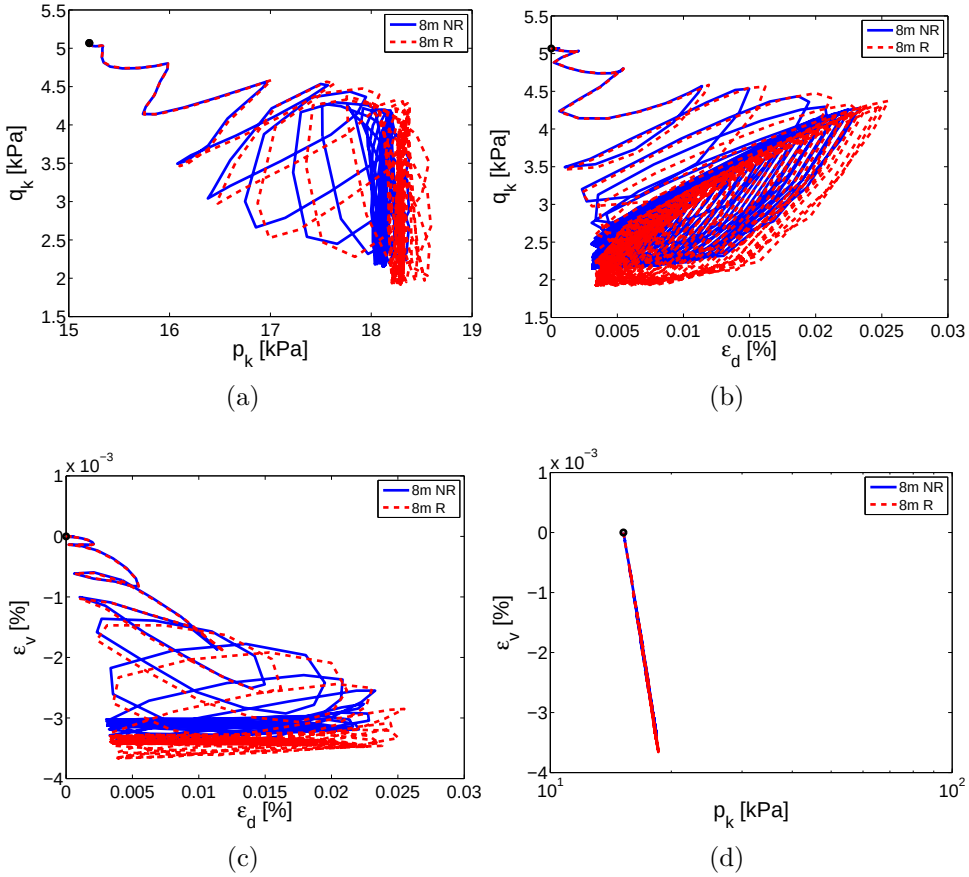

Figure G.21: Mechanical behavior with isotropic mechanism deactivated and zero shear-induced volumetric deformations (8m from base): a) p_k-q_k, b) q_k-ε_d, c) ε_v-ε_d, d) p_k-ε_v.

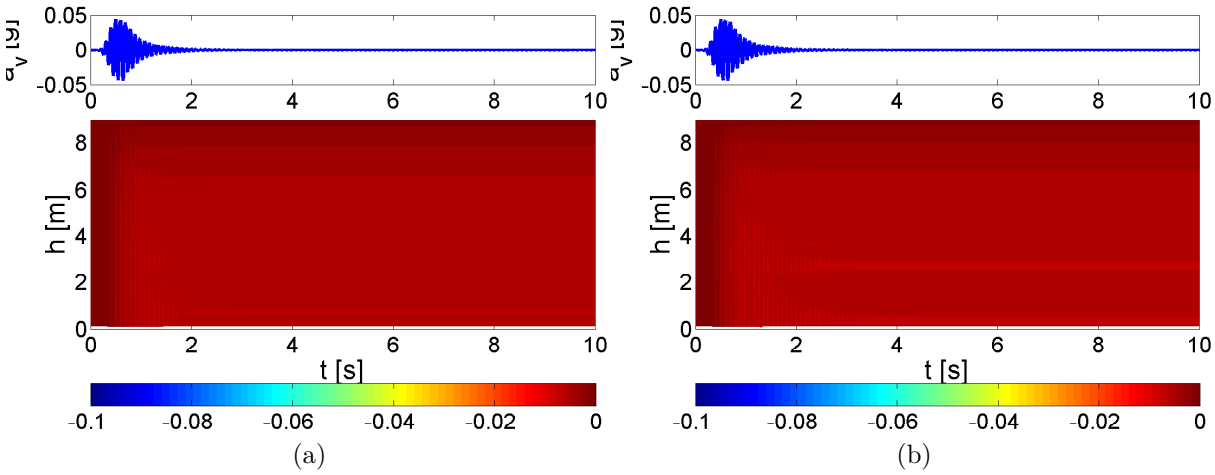

Figure G.22: Contours of volumetric deformation (%) related to the generation of vertical acceleration with isotropic mechanism deactivated and zero shear-induced volumetric deformations: a) Without regularization, b) With regularization.

Synopsis

To sum up, the perturbation caused when the regularization is applied comes from the coupling of volumetric-deviatoric strains. As already mentioned in the concluding remarks of Chapter 4 in case of S-wave propagation, when the permanent strains remain at a low level, there is no noise in the dynamic response, but when plastic volumetric strains are generated due to large deviatoric ones, the first gradient of dilation model is activated and has a detrimental perturbation effect on wave propagation in the soil (e.g. oscillations in the profile of deviatoric strains and noise in the acceleration's signal).

Appendix H

Dynamic analysis of regularized dry embankment-foundation system

As extensively discussed in Section 5.2.2, there is no mesh effect on the results of the dynamic analyses of the dry embankment - foundation system. However, in order to examine the effect of the regularization method (presented in Chapter 4) on wave propagation, the first gradient of dilation model is applied to the embankment - foundation system. Friuli earthquake is imposed to the model and mesh 4 (25cm) is used for CPU time reasons.

In Figure H.1 the contours of deviatoric deformations ε_d are plotted at the end of the motion. It is important to highlight that the regularization should not change the dynamic response of the model if no localization phenomena appear. Nonetheless, in Figure H.1 the response of the whole embankment and of the upper part of the foundation is extremely perturbated compared to the results obtained without regularization (Figure 5.13d). The lower part of the foundation, composed of the dense sand, is not affected from the ground motion and no deviatoric and shear-induced volumetric deformations appear. Consequently, there is no effect on its dynamic response, as the regularization is not activated in this part of the model.

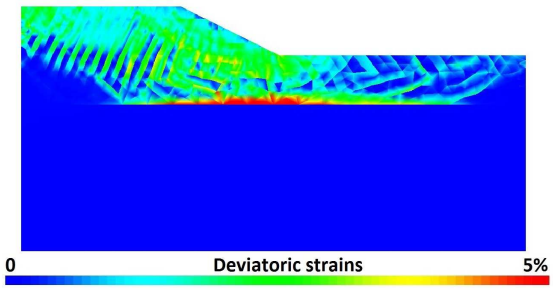

Figure H.1: Deviatoric strains ε_d at the end of the ground motion (Friuli earthquake) for the regularized mesh 4 (25cm).

The spectral coherency (Equation 4.56 in Section 4.5) of the horizontal and vertical acceleration without and with regularization obtained at the top (P1), base (P2), inside the slope (P3) and free-field (P4) is calculated in Figure H.2. The obtained signals, and especially those of vertical acceleration, diverge in a wide range of frequencies. While

the free-field and base response should be identical for both analyses as no localization phenomena, the coherency calculated diverges from 1. It can be concluded that the regularization generated spurious waves in the areas of shear deformations and they are diffused in the whole embankment and upper layer of the foundation.

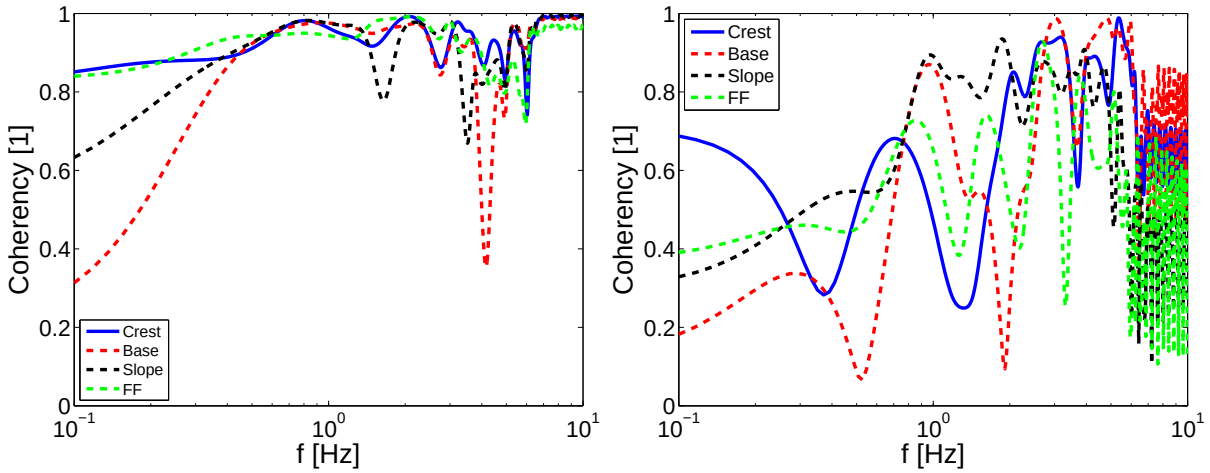

Figure H.2: Coherency of absolute acceleration for mesh 4 (25cm) and Friuli earthquake without and with regularization: a) Horizontal acceleration, b) Vertical acceleration.

Appendix I

CPU time of FE simulations

The users of FE softwares are concerned of CPU time of advanced numerical simulations and for this reason the CPU time of all simulations of Chapters 5, 6 are provided in the current appendix.

I.1 Dry embankment-foundation system

Based on the CPU time of the dynamic analysis with Friuli earthquake for all meshes (presented in Section 5.2.2), mesh 4 (25cm) requires the least computational time, as shown in Figure I.1.

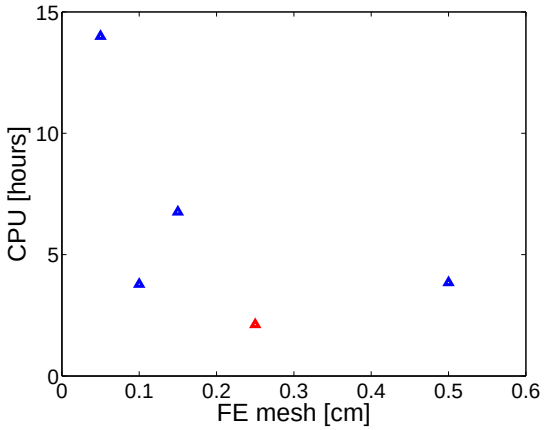

Figure I.1: CPU time in relation to the FE mesh.

I.2 Dry embankment resting on liquefiable foundation

The CPU time of both simulations (fully drained - coupled) are provided for all dynamic analyses in Figure I.2. All simulations had a duration between 1-4 days approximately and the CPU time is always greater for coupled model. The duration of the simulation

increases importantly in this case due to the strong soil's nonlinearity and difficulties in convergence.

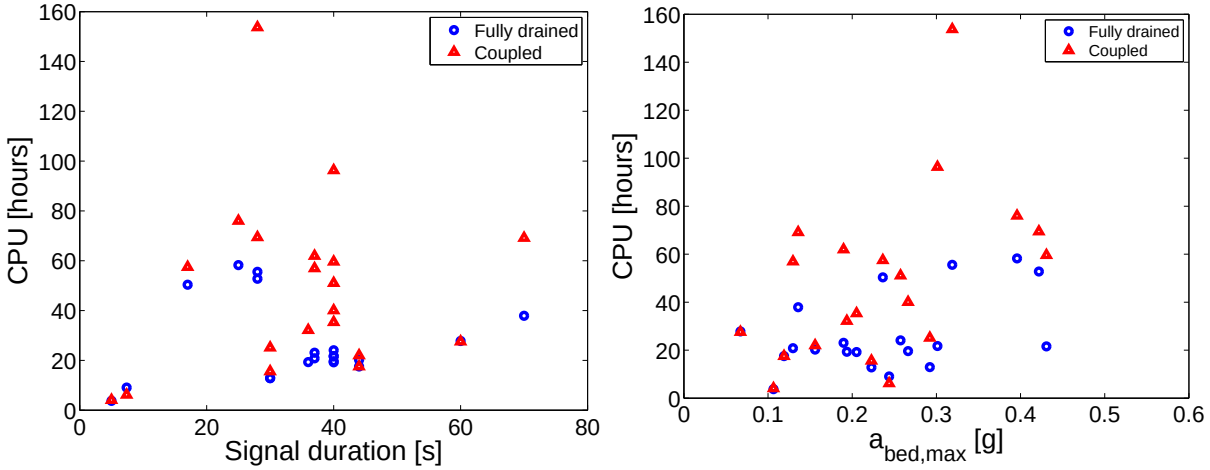

(a) (b)

Figure I.2: Comparison of CPU time for both simulations: a) CPU as function of signal's duration, b) CPU as function of signal's $a_{bed,max}$.

I.3 Levee resting on liquefiable foundation

In Figure I.3 the CPU time of the FE simulation of the levee-foundation system is plotted as function of the duration of the mainshock of all input ground motions. An important growth of the CPU time is remarked as the duration of the mainshock increases.

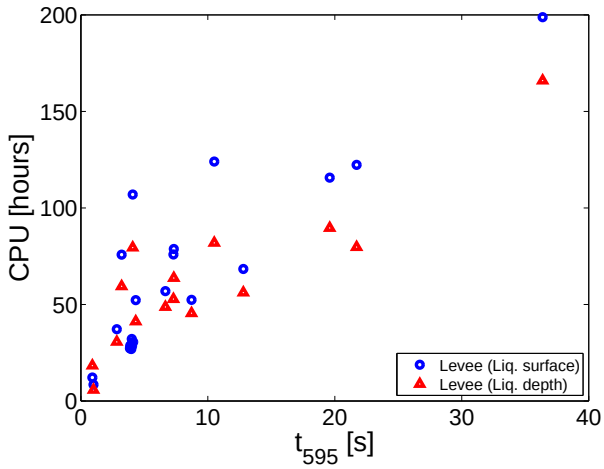

Figure I.3: Comparison of CPU time for all dynamic analyses as function of the duration of earthquake's mainshock.

Bibliography

Adalier, K. and Sharp, M. K. (2004). Dynamic behavior of embankment dam on liquefiable foundation subject to moderate earthquake loading. In *13th World Conference on Earthquake Engineering*, number 1025, Vancouver, B.C., Canada.

Aifantis, E. C. (1984). On the Microstructural Origin of Certain Inelastic Models. *Journal of Engineering Materials and Technology*, 106:326–330.

Akhlaghi, T. and Nikkar, A. (2014). Evaluation of the Pseudostatic Analyses of Earth Dams Using FE Simulation and Observed Earthquake-Induced Deformations: Case Studies of Upper San Fernando and Kitayama Dams. *The Scientific World Journal*, 2014.

Ambrasseys, N. N. and Menu, J. (1988). Earthquake-induced ground displacements. *Earthquake Engineering and Structural Dynamics*, 16(7):985–1006.

Anastasopoulos, I., Gazetas, G., Loli, M., Apostolou, M., and Gerolymos, N. (2010). Soil failure can be used for seismic protection of structures. *Bulletin of Earthquake Engineering*, 8:309–326.

Anderson, D., Martin, G., Lam, I., and Wang, J. (2008). Seismic Analysis and Design of Retaining Walls, Buried Structures, Slopes, and Embankments (NCHRP Report 611). Technical report, National Cooperative Highway Research Program. Transportation Research Board, Washington, DC.

Andrade, J. E. (2009). A predictive framework for liquefaction instability. *Géotechnique*, (8):673–682.

Andrade, J. E., Ramos, A. M., and Lizcano, A. (2013). Criterion for flow liquefaction instability. *Acta Geotechnica*.

Andrianopoulos, K. I., Papadimitriou, A. G., Bouckovalas, G. D., and Karamitros, D. K. (2014). Insight into the seismic response of earth dams with an emphasis on seismic coefficient estimation. *Computers and Geotechnics*, 55:195–210.

Andrianov, I. V., Danishevs, V. V., Ryzhkov, O. I., and Weichert, D. (2013). Dynamic homogenization and wave propagation in a nonlinear 1D composite material. *Wave Motion*, 50(2):271–281.

Arango, I. (1996). MAgnitude scaling factors for soil liquefaction evaluations. *Journal of Earthquake Engineering*, 122(11):929–936.

Arduino, P. and Macari, E. J. (2001). Implementation of porous media formulation for geomaterials. *Journal of engineering mechanics*, 127(February):157–166.

Aubry, D., Chouvet, D., Modaressi, A., and Modaressi, H. (1986). GEFDYN : Logiciel d'Analyse de Comportement Mécanique des Sols par Eléments Finis avec Prise en Compte du Couplage Sol-Eau-Air.

Aubry, D. and Modaressi, H. (1988). Numerical modelling of the dynamics of saturated anelastic soils. In *Seismic Hazards in Mediterranean Regions*.

Aubry, D. and Modaressi, H. (1990). Dynamic analysis of saturated non linear media. In *Numerical Methods and Constitutive Modelling in Geomechanics*, volume 311 of *International Centre for Mechanical Sciences*, pages 211–235. Springer-Verlag Wien.

Aydingun, O. and Adalier, K. (2003). Numerical analysis of seismically induced liquefaction in earth embankment foundations. part i. benchmark model. *Canadian Geotechnical Journal*, 40(4):753–765.

Baker, J. W. (2007). Quantitative Classification of Near-Fault Ground Motions Using Wavelet Analysis. *Bulletin of the Seismological Society of America*, 97(5):1486–1501.

Baker, J. W. and Cornell, C. A. (2005). A vector-valued ground motion intensity measure consisting of spectral acceleration and epsilon. *Earthquake Engineering and Structural Dynamics*, 34:1193–1217.

Baker, J. W., Lin, T., Shahi, S. K., and Jayaram, N. (2011). New Ground Motion Selection Procedures and Selected Motions for the PEER Transportation Research Program. Technical report, PEER Report 2011, Pacific Earthquake Engineering Research Center. College of Engineering. University of California, Berkeley.

Bardet, J.-P. (1997). *Experimental Soil Mechanics*. Prentice-Hall.

Bazant, Z., Belytschko, T., and Chang, T. (1985). Continuum theory for strain-softening. *Journal of Engineering Mechanics*, 110(12):1666–1692.

Bazant, Z. and Jirasek, M. (2002). Nonlocal Integral Formulations of Plasticity and Damage: Survey of Progress. *Journal of engineering mechanics*, 128(11):1119–1149.

Been, K. and Jefferies, M. (1985). A state parameter for sands. *Géotechnique*, 35(2):99–112.

Benallal, A. (2005). On localization modes in coupled thermo-hydro-mechanical problems. *Comptes Rendus Mécanique*, 333(7):557–564.

Benallal, A. and Comi, C. (2003). Perturbation growth and localization in fluid-saturated inelastic porous media under quasi-static loadings. *Journal of the Mechanics and Physics of Solids*, 51(5):851–899.

Beresnev, I. A. and Wen, K.-L. (1996). Nonlinear soil response-A reality? *Bulletin of the Seismological Society of America*, 8(6):1964–1978.

Bhattacharya, S., Hyodo, M., Goda, K., Tazoh, T., and Taylor, C. (2011). Liquefaction of soil in the Tokyo Bay area from the 2011 Tohoku (Japan) earthquake. *Soil Dynamics and Earthquake Engineering*, 31:1618–1628.

Bigoni, D. and Petryk, H. (2002). A note on divergence and flutter instabilities in elastic-plastic materials. *International Journal of Solids and Structures*, 39:911–926.

Biot, M. (1941). General theory of three-dimensional consolidation. *Journal of Applied Physics*, 12(2):155–164.

Biot, M. (1955). Theory of Elasticity and Consolidation for a Porous Anisotropic Solid. *Journal of Applied Physics*, 26(2):182–185.

Biot, M. (1956a). Theory of Deformation of a Porous Viscoelastic Anisotropic Solid. *Journal of Applied Physics*, 27(5):459–467.

Biot, M. (1956b). Theory of Propagation of Elastic Waves in a Fluid-Saturated Porous Solid. I. Low-Frequency Range. *The Journal of the Acoustical Society of America*, 28(2):168–178.

Biot, M. (1956c). Theory of Propagation of Elastic Waves in a Fluid-Saturated Porous Solid. II. Higher Frequency Range. *The Journal of the Acoustical Society of America*, 28(2):179–191.

Bishop, A. (1955). The use of the slip circle in the stability analysis of slopes. *Géotechnique*, 7(1):7–17.

Bishop, A. W. and Blight, G. (1963). Some aspects of effective stress in saturated and partly saturated soils. *Géotechnique*, 13(3):177–197.

Bolton, A., Maltman, A., and Clennell, M. (1998). The importance of overpressure timing and permeability evolution in fine-grained sediments undergoing shear. *Journal of Structural Geology*, 20(8):1013–1022.

Borja, R. I. (2002). Bifurcation of elastoplastic solids to shear band mode at finite strain. *Computer Methods in Applied Mechanics and Engineering*, 191:5287–5314.

Borja, R. I. (2006). Condition for liquefaction instability in fluid-saturated granular soils. *Acta Geotechnica*, 1:211–224.

Bouckovalas, G. D. and Papadimitriou, A. G. (2005). Numerical evaluation of slope topography effects on seismic ground motion. *Soil Dynamics and Earthquake Engineering*, 25:547–558.

Bray, J. D. and Travasarou, T. (2007). Simplified Procedure for Estimating Earthquake-Induced Deviatoric Slope Displacements. *Journal of Geotechnical and Geoenvironmental Engineering*, 133(4):381–392.

Brennan, A. and Madabhushi, S. (2002). Effectiveness of vertical drains in mitigation of liquefaction. *Soil Dynamics and Earthquake Engineering*, 22(9-12):1059–1065.

Buscarnera, G. and di Prisco, C. (2012). Discussing the definition of the second-order work for unsaturated soils. *International Journal for Numerical and Analytical Methods in Geomechanics*, 36(December 2010):36–49.

Byrne, P. M., Park, S.-s., Beaty, M., Sharp, M., Gonzalez, L., and Abdoun, T. (2004). Numerical modeling of liquefaction and comparison with centrifuge tests. *Canadian Geotechnical Journal*, 211:193–211.

Cameron, W. I. and Green, R. A. (2004). Soil Nonlinearity versus Frequency Effects. In *International Workshop on the Uncertainties in Nonlinear Soil Properties and their Impact on Modeling Dynamic Response*, Opinion Paper.

Casagrande, A. (1936). Characteristic of cohesionless soils affecting the stability of slopes and earth fills. *Journal of the Boston Society of Civil Engineers*, pages 257–276.

Castro, G. and Poulos, S. J. (1977). Factors affecting liquefaction and cyclic mobility. *Journal of the Geotechnical Engineering Division*, 103(6):501–506.

Causse, M., Laurendeau, A., Perrault, M., Douglas, J., Bonilla, L. F., and Guéguen, P. (2014a). Eurocode 8-compatible synthetic time-series as input to dynamic analysis. *Bulletin of Earthquake Engineering*, 12:755–768.

Causse, M., Laurendeau, A., Perrault, M., Douglas, J., Bonilla, L. F., and Guéguen, P. (2014b). Eurocode 8-compatible synthetic time-series as input to dynamic analysis. *Bulletin of Earthquake Engineering*, 12:755–768.

Chambon, R., Caillerie, D., and Matsuchima, T. (2001). Plastic continuum with microstructure, local second gradient theories for geomaterials: localization studies. *International Journal of Solids and Structures*, 38:8503–8527.

Chandra, J., Gueguen, P., and Bonilla, L. F. (2014). Application of pgv/vs proxy to assess nonlinear soil response: from dynamic centrifuge testing to japanese k-net and kik-net data. In *Second European Conference on Earthquake Engineering and Seismology, Istanbul Aug. 25-29, 2014*.

Charles, J., Abbiss, C., Gosschalk, E. M., and Hinks, J. (1991). An Engineering Guide to Seismic Risks to Dams in the United Kingdom. Technical report, Building Research Establishment, Garston, Watford, UK.

Chen, J.-s., Wu, C.-t., and Belytschko, T. (2000). Regularization of material instabilities by meshfree approximations with intrinsic length scales. *International journal for nuerical methods in engineering*, 47:1303–1322.

Coelho, P., Haigh, S., and Madabhushi, S. (2004). Centrifuge modelling of earthquake effects in unifrom deposits of saturated sand. In *International Conference on Case Histories in Geotechnical Engineering*, number 36.

Cornell, C. A., Jalayer, F., Hamburger, R. O., and Foutch, D. A. (2002). Probabilistic Basis for 2000 SAC Federal Emergency Management Agency Steel Moment Frame Guidelines. *Journal of Structural Engineering ASCE*, 128(4).

Costa D'Aguiar, S., Modaressi-Farahmand-Razavi, A., Dos Santos, J., and Lopez-Caballero, F. (2011). Elastoplastic constitutive modelling of soil-structure interfaces under monotonic and cyclic loading. *Computers and Geotechnics*, 38(4):430–447.

Coussy, O. (1991). *Mécanique des milieux poreux*. Technip edition.

De Boer, R., Liu, Z., and Ehlers, W. (1993). One-dimensional transient wave propagation in fluid-saturated incompressible porous media. *Archive of Applied Mechanics*, 63:59–72.

de Borst, R. and Muhlhaus, H. (1992). Gradinet-dependent plasticity: formulation and algorithmic aspects. *International journal for numerical methods in engineering*, 35:521–539.

Deb, A., Prevost, J. H., and Loret, B. (1996). Adaptive meshing for dynamic strain localization. *Computer Methods in Applied Mechanics and Engineering*, 137:285–306.

Desrues, J. and Chambon, R. (2002). Shear band analysis and shear moduli calibration. *International Journal of Solids and Structures*, 39:3757–3776.

Di, Y. and Sato, T. (2003). Liquefaction analysis of saturated soils taking into account variation in porosity and permeability with large deformation. *Computers and Geotechnics*, 30:623–635.

Di, Y. and Sato, T. (2004). A practical numerical method for large strain liquefaction analysis of saturated soils. *Soil Dynamics and Earthquake Engineering*, 24:251–260.

Dickinson, B. and Gavin, H. (2011). Parametric Statistical Generalization of Uniform-Hazard Earthquake Ground Motions. *Journal of Structural Engineering ASCE*, 137(3):410–422.

Dingreville, R. . A., Robbins, J., and Voth, T. E. (2014). Wave propagation and dispersion in elasto-plastic microstructured materials. *International Journal of Solids and Structures*, 51(11-12):2226–2237.

Duncan, J. M. and Wright, S. G. (1980). The accuracy of equilibrium methods of slope stability analysis. *Engineering Geology*, 16:5–17.

Ebeling, M. R. (1992). Introduction to the computation of response spectrum for earthquake loading. Technical report, Department of army, Washington, USA.

Ehlers, W., Graf, T., and Ammann, M. (2004). Deformation and localization analysis of partially saturated soil. *Computer Methods in Applied Mechanics and Engineering*, 193:2885–2910.

Elgamal, A., Yang, Z., and Parra, E. (2002). Computational modeling of cyclic mobility and post-liquefaction site response. *Soil Dynamics and Earthquake Engineering*, 22(4):259–271.

Elgamal, B. A.-w. M., Scott, R. F., Succarieh, M. F., and Yan, L. (1990). La villita dam response during five earthquakes including permanent deformation. *Journal of Geotechnical Engineering*, 116(10):1443–1462.

Feia, S., Sulem, J., Canou, J., Ghabezloo, S., and Clain, X. (2016). Changes in permeability of sand during triaxial loading:effect of fine particles production. *Acta Geotechnica*, 11:1–19.

Fellenius, W. (1927). *Erdstatische Berechnungen*. Ernst, Berlin.

Fernandes, R., Chavant, C., and Chambon, R. (2008). A simplified second gradient model for dilatant materials: Theory and numerical implementation. *International Journal of Solids and Structures*, 45:5289–5307.

Foerster, E. and Modaressi, H. (2007). A diagonal consistent mass matrix for earthquake site response simulations. In *4th International Conference on Earthquake Geotechnical Engineering*, number 1242, Thessaloniki, Greece.

Foucault, A. (2009). Loi de comportement cyclique de Hujeux pour les sols. *Documentation of Code_Aster [R7.01.23]*.

Foucault, A. (2010). *Modelisation du comportement cyclique des ouvrages en terre integrant des techniques de regularisation*. PhD thesis, ECP-EDF.

Foucault, A., Voldoire, F., and Modaressi, A. (2011). On the numerical implementation of a muti-mechanism cyclic plasticity model associated to a dilation second gradient model aiming strain localization mitigation. In *Advances in Bifurcation and Degradation in Geomaterials*, pages 201–208.

Gavin, H. P. and Dickinson, B. W. (2011). Generation of uniform-hazard earthquake ground motions. *Journal of Structural Engineering ASCE*, 137(3):423–432.

Germain, P. (1973). The method of virtual power in continuum mechanics. Part 2: Microstructure. *Journal of Applied Mathematics*, 25(3):556–575.

Gosschalk, E. M., Severn, R., Charles, J., and Hinks, J. (1994). An Engineering Guide to Seismic Risk to Dams in the United Kingdom, and its international relevance. *Soil Dynamics and Earthquake Engineering*, 13:163–179.

Granet, S. (2015). Modeles de comportement THHM. *Documentation of Code_Aster [R7.01.11]*.

Haigh, S., Eadington, J., and Madabhushi, S. (2012). Permeability and stiffness of sands at very low effective stresses. *Géotechnique*, 62(1):69–75.

Hamadi, K., Modaressi-Farahmand Razavi, A., and Darve, F. (2008). Bifurcation and instability modelling by a multimechanism elasto-plastic model. *International Journal for Numerical and Analytical Methods in Geomechanics*, 32:461–492.

Hill, R. (1958). A general theory of uniqueness and stability in elastic-plastic solids. *Journal of the Mechanics and Physics of Solids*, 6:236–249.

Hiraoka, N., Oya, A., Bui, H. H., Rajeev, P., and Fukagawa, R. (2013). Seismic slope failure modelling using the mesh-free SPH method. *International Journal of GEOMATE*, 5(1):660–665.

Hughes, T. (2000). *The Finite Element Method: Linear Static and DynamicFinite Element Analysis*. DOVER Publications, dover edit edition.

Hujeux, J.-C. (1985). Une loi de comportement pour le chargement cyclique des sols. *Presses ENPC*, pages 278–302.

Idriss, I. M. (2013). Nga-west2 model for estimating average horizontal values of pseudo-absolute spectral accelerations generated by crustal earthquakes. Technical Report PEER Report 2013/08, Pacific Earthquake Engineering Research Center, Headquarters, University of California, Berkeley.

Idriss, I. M. and Boulanger, R. W. (2015). 2nd ishihara lecture: Spt- and cpt-based relationships for the residual shear strength of liquefied soils. *Soil Dynamics and Earthquake Engineering*, 68:57–68.

Iervolino, I. and Cornell, C. A. (2005). Record selection for nonlinear seismic analysis of structures. *Earthquake Spectra*, 21(3):685–713.

Ishihara, K. (1993). Liquefaction and flow failure during earthquakes. *Géotechnique*, 43(3):351–415.

Ishihara, K. (2012). Liquefaction in Tokyo Bay and Kanto regions in the 2011 Great East Japan earthquake. In *Proceedings of the International Symposium on Engineering Lessons Learned from the 2011 Great East Japan Earthquake*, pages 63–81, Tokyo, Japan.

Ishikawa, H., Saito, K., Nakagawa, K., and Uzuoka, R. (2015). Liquefaction analysis of a damaged river levee during the 2011 Tohoku earthquake. In *14th International Conference of the International Association for Computer Methods and Advances in Geomechanics*, pages 673–677, Kyoto, Japan.

Jafarian, Y., Sadeghi Abdollahi, a., Vakili, R., Baziar, M., and Noorzad, a. (2011). On the efficiency and predictability of strain energy for the evaluation of liquefaction potential: A numerical study. *Computers and Geotechnics*, 38(6):800–808.

Janbu, N. (1957). Earth pressures and bearing capacity calculations by generalized procedure of slices. In *4th International Conference of Soil Mechanics Foundation Engineering*, pages 207–212, London.

Jibson, R. (1994). Predicting earthquake-induced landslide displacements using newmark's sliding block analysis.

Jibson, R. (2007). Regression models for estimating coseismic landslide displacement. *Engineering Geology*, 91:209–218.

Jirasek, M. (2015). Modeling of Localized Inelastic Deformation. Technical report, Lecture notes at the Czech Technical University in Prague.

Kavazanjian, E., Wang, J., Martin, G., Shamsabadi, A., Lam, I., Dickenson, S., and Hung, J. (2011). LRFD Seismic Analysis and Design of Transportation Geotechnical Features and Structural Foundations (FHWA-NHI-11-032). Technical Report GEC No. 3, U.S. Department of Transportation. Federal Highway Administration, Washington, DC.

Kawase, H. (2011). Strong motion characteristics and their damage impact to structures during the Off Pacific Coast of Tohoku earthquake of March 11, 2011; How extraordinary was this M9.0 earthquake? In *4th IASPEI / IAEE International Symposium: Effects of Surface Geology on Seismic Motion*, University of California Santa Barbara.

Kim, M., Lee, S., Choo, Y., and Kim, D. (2011). Seismic behaviors of earth-core and concrete-faced rock-fill dams by dynamic centrifuge tests. *Soil Dynamics and Earthquake Engineering*, 31:1579–1593.

Kontoe, S., Zdravkovic, L., and Potts, D. (2008). An assessment of time integration schemes for dynamic geotechnical problems. *Computers and Geotechnics*, pages 253–264.

Kourkoulis, R., Anastasopoulos, I., Gelagoti, F., and Gazetas, G. (2010). Interaction of foundation-structure systems with seismically precarious slopes: Numerical analysis with strain softening constitutive model. *Soil Dynamics and Earthquake Engineering*, 30:1430–1445.

Koutsourelakis, S., Prevost, J. H., and Deodatis, G. (2002). Risk assessment of an interacting structure-soil system due to liquefaction. *Earthquake Engineering & Structural Dynamics*, 31(4):851–879.

Kramer, S. and Mitchell, R. (2006). Ground motion intensity measures for liquefaction hazard evaluation. *Earthquake Spectra*, 22(2):413–438.

Kramer, S. L. (1996). *Geotechnical Earthquake Engineering*. Prentice Hall.

Kramer, S. L. and Seed, H. B. (1988). Initiation of soil liquefaction under static loading conditions. *Journal of Geotechnical Engineering*, 114(4):412–430.

Kuhl, D. and Crisfield, M. (1999). Energy-conserving and decaying algorithms in non-linear structural dynamics. *International journal for numerical methods in engineering*, 45:569–599.

Lade, P. (1994). Instability and liquefaction of granular materials. *Computers and Geotechnics*, 16:123–151.

Lakeland, D., Rechenmacher, A., and Ghanem, R. (2014). Towards a complete model of soil liquefaction: the importance of fluid flow and grain motion. *Proceedings of the Royal Society A*, 470:20130453.

Lanzo, G. and Pagliaroli, A. (2012). Seismic site effects at near-fault strong-motion stations along the aterno river valley during the mw=6.3 2009 l'aquila earthquake. *Soil Dynamics and Earthquake Engineering*, 40:1–14.

Larsson, J. and Larsson, R. (2000). Finite-element analysis of localization of deformation and fluid pressure in an elastoplastic porous medium. *International journal of solids and structures*, 37:7231–7257.

Li, S., Hao, W., and Liu, W. K. (2000). Mesh-free simulations of shear banding in large deformation. *International Journal of Solids and Structures*, 37:7185–7206.

Liel, A. and Raghunandan, M. (2011-2013). Investigation of structural collapse risk in the cascadia subduction zone. Technical Report G11AP20134, U.S. Geological Survey.

Lopez-Caballero, F., Modaressi, A., and Stamatopoulos, C. (2016). Numerical evaluation of earthquake settlements of road embankments and mitigation by preloading. *International Journal of Geomechanics*, in press.

Lopez-Caballero, F. and Modaressi-Farahmand-Razavi, A. (2013). Numerical simulation of mitigation of liquefaction seismic risk by preloading and its effects on the performance of structures. *Soil Dynamics and Earthquake Engineering*, 49:27–38.

Lopez-Caballero, F., Razavi, A. M.-F., and Modaressi, H. (2007). Nonlinear numerical method for earthquake site response analysis I-elastoplastic cyclic model and parameter identification strategy. *Bulletin of Earthquake Engineering*, 5:303–323.

Loret, B. and Prevost, J. H. (1990). Dynamic strain localization in elasto-(visco-)plastic soilds, Part 1. General formulation and one-dimensional examples. *Computer Methods in Applied Mechanics and Engineering*, 83:247–273.

Loret, B., Prevost, J. H., and Deb, A. (1995). Finite element simulation of dynamic strain-localization: A multi-scale problem. *Computer Methods in Applied Mechanics and Engineering*, 120:315–338.

Lu, C.-C., Hwang, J.-H., Juang, C. H., Ku, C.-S., and Luo, Z. (2009). Framework for assessing probability of exceeding a specified liquefaction-induced settlement at a given site in a given exposure time. *Engineering Geology*, 108:24–35.

Madeo, A., Neff, P., Ghiba, I., Placidi, L., and Rosi, G. (2015). Wave propagation in relaxed micromorphic continua: modeling metamaterials with frequency band-gaps. *Continuum Mechanics and Thermodynamics*, 27:551–570.

Maharjan, M. and Takahashi, A. (2014). Liquefaction-induced deformation of earthen embankments on non-homogeneous soil deposits under sequential ground motions. *Soil Dynamics and Earthquake Engineering*, 66:113–124.

Makdisi, F. I. and Seed, H. B. (1978). Simplified procedure for estimating dam and embankment earthquake-induced deformations. *Journal of Geotechnical Engineering*, 104(7):849–867.

Matsushima, T., Chambon, R., and Caillerie, D. (2002). Large strain finite element analysis of a local second gradient model: application to localization. *International journal for numerical methods in engineering*, 54:449–521.

Mavroeidis, G., Dong, G., and Papageorgiou, A. (2004). Near-fault ground motions and the response of elastic and inelastic single-degree-of-freedom (sdof) systems. *Earthquake Engineering and Structural Dynamics*, 33:1023–1049.

Menéndez, C., Nieto, P., Ortega, F., and Bello, A. (2010). Non-linear analysis of the consolidation of an elastic saturated soil with incompressible fluid and variable permeability by fem. *Applied Mathematics and Computation*, 216:458–476.

Meurer, T., Qu, J., and Jacobs, L. J. (2002). Wave propagation in nonlinear and hysteretic media - a numerical study. *International Journal of Solids and Structures*, 39:5585–5614.

Mindlin, R. (1965). Second gradient of strain and surface-tension in linear elasticity. *International Journal of Solids and Structures*, 1:417–438.

Mindlin, R. D. (1964). Micro-structure in Linear Elasticity. *Arch. Rational Mech. Anal.*, 16:51–78.

Misra, A. and Poorsolhjouy, P. (2016). Granular micromechanics based micromorphic model predicts frequency band gaps. *Continuum Mechanics and Thermodynamics*, 28:215–234.

Modaressi, H. (1987). *Modélisation numérique de la propagation des ondes dans les milieux poreux anélastiques*. PhD thesis, Ecole Centrale Paris.

Mohammadnejad, T. and Andrade, J. E. (2014). Flow liquefaction instability prediction using finite elements. *Acta Geotechnica*.

Montoya-Noguera, S. and Lopez-Caballero, F. (2015). Effect of coupling excess pore pressure and deformation on nonlinear seismic soil response. *Acta Geotechnica*.

NAVFAC (1982). DESIGN MANUAL 7.01: Soil Mechanics. Technical report, Naval Facilities Engineering Command, Alexandria, Virginia.

Needleman, A. (1988). Material rate dependence and mesh sensitivity in localization problems. *Computer Methods in Applied Mechanics and Engineering*, 67:69–85.

Newmark, N. M. (1965). Effects of earthquakes on dams and embankments. *Géotechnique*, 15(2):139–160.

Nguyen, T.-D. (2006). *Modélisation du comportement des matériaux granulaires. Application aux barrages en terre.* PhD thesis, Ecole Centrale Paris.

Oka, F., Adachi, T., and Yashima, A. (1995). A strain localization analysis using a viscoplastic softening model for clay. *International Journal of Plasticity*, 11(5):523–545.

Oka, F., Tsai, P., Kimoto, S., and Kato, R. (2012). Damage patterns of river embankments due to the 2011 off the Pacific Coast of Tohoku Earthquake and a numerical modeling of the deformation of river embankments with a clayey subsoil layer. *Soils and Foundations*, 52(5):890–909.

Oka, F., Yashima, A., Shibata, T., Kato, M., and Uzuoka, R. (1994). FEM-FDM Coupled Liquefaction Analysis of a Porous Soil Using an Elasto-Plastic Model. *Applied Scientific Research*, 52:209–245.

Okamura, M., Tamamura, S., and Yamamoto, R. (2013). Seismic stability of embankments subjected to pre-deformation due to foundation consolidation. *Soils and Foundations*, 53(1):11–22.

Oldecop, L., Zabala, F., and Rodari, R. (2004). Seismic security assesment of earth and rockfill dams located in epicentral regions. In *13th World Conference on Earthquake Engineering*, number 1102, Vancouver, B.C., Canada.

Ottosen, N. and Runesson, K. (1991). Properties of discontinuous bifurcation solutions in elasto-plasticity. *International Journal of Solids and Structures*, 27:401–421.

Ozutsumi, O., Sawada, S., Iai, S., Takeshima, Y., Sugiyama, W., and Shimazu, T. (2002). Effective stress analyses of liquefaction-induced deformation in river dikes. *Soil Dynamics and Earthquake Engineering*, 22:1075–1082.

Papargyri-Beskou, S., Polyzos, D., and Beskos, D. (2009). Wave dispersion in gradient elastic solids and structures: A unified treatment. *International Journal of Solids and Structures*, 46:3751–3759.

Park, D. S. and Kutter, B. L. (2012). Centrifuge Tests for Artificially Cemented Clay Slopes. In *GeoCongress 2012*, pages 2027–2036.

Pinnegar, C. R. and Mansinha, L. (2003). The S-transform with windows of arbitrary and varying shape. *Geophysics*, 68(1):381–385.

Plassart, R., Fernandes, R.and Giraud, A., Hoxha, D., and Laigle, F. . (2013). Hydromechanical modelling of an excavation in an underground research laboratory with an elastoviscoplastic behaviour law and regularization by second gradient of dilation. *International Journal of Rock Mechanics & Mining Sciences*, 58:23–33.

Polizzotto, C. (2012). A gradient elasticity theory for second-grade materials and higher order inertia. *International Journal of Solids and Structures*, 49(15-16):2121–2137.

Polizzotto, C. (2013). A second strain gradient elasticity theory with second velocity gradient inertia - Part II: Dynamic behavior. *International Journal of Solids and Structures*, 50(24):3766–3777.

Popescu, R. and Prevost, J. (1993). Centrifuge validation of a numerical model for dynamic soil liquefaction. *Soil Dynamics and Earthquake Engineering*, 12:73–90.

Porter, K. A. (2003). An overview of peer's performance-based earthquake engineering methodology. In *Ninth International Conference on Applications of Statistics and Probability in Civil Engineering (ICASP9) July 6-9, 2003, San Francisco.*

Poulos, S. J. (1971). The steady state of deformation. *ASCE Journal of the Geotechnical Engineering Division*, 107:553–562.

Prevost, J. H. (1980). Mechanics of continuous porous media. *International Journal of Engineering Science*, 18:787–800.

Pyke, R., Seed, H. B., and Chan, C. (1975). Settlements of snads under multi-directional loading. *Journal of the Geotechnical Engineering Division*, 101(4):379–398.

Rapti, I., Foucault, A., Lopez-caballero, F., and Modaressi-Farahmand Razavi, A. . (2014a). Strain localization of a road embankment founded on soil substratum due to seismic loading. In *9th International Conference on Structural Dynamics, EURODYN 2014. Porto, Portugal, 30 June - 2 July 2014*, volume 1, pages 681–688.

Rapti, I., Foucault, A., Voldoire, F., Lopez-Caballero, F., and Modaressi-Farahmand-Razavi, A. (2014b). Strain localization of a soil column due to seismic loading. In *Computer Methods and Recent Advances in Geomechanics*, pages 347–352, Kyoto, Japan.

Rapti, I., Foucault, A., Voldoire, F., Lopez-caballero, F., and Modaressi-farahmand razavi, A. (2015a). Effect of variation of permeability during earthquake-induced liquefaction. In *9ème Colloque National AFPS*, IFSTTAR, Marne-la-Vallée.

Rapti, I., Lopez-Caballero, F., Modaressi-Farahmand-Razavi, A., Foucault, A., and Voldoire, F. (2015b). Seismic evaluation of embankment-type structures with coupled hydro-mechanical model. In *5th ECCOMAS Thematic Conference on Computational Methods in Structural Dynamics and Earthquake Engineering (COMPDYN2015). Crete Island, Greece, 25-27 May 2015.*

Rathje, E., Abrahamson, N., and Bray, J. (1998). Simplified Frequency Content Estimates of Earthquake Ground Motions. *Journal of Geotechnical Engineering*, 124(2):150–159.

Raude, S., Giot, R., Foucault, A., and Fernandes, R. (2015). An identification method to calibrate higher-order parameters in local second-gradient models. *Comptes Rendus Mécanique*, 343(7-8):443–456.

Rice, J. R. (1976). The localization of plastic deformation. In Koiter, W., editor, *14th international congress on theoretical and applied mechanics*, pages 207–220, Delft.

Rudnicky, J. and Rice, J. R. (1975). Conditions for the localization of deformation in pressure-sensitive dilatant materials. *Journal of the Mechanics and Physics of Solids*, 23:371–394.

Ruiz, S. and Saragoni, G. R. (2009). Free vibration of soils during large earthquakes. *Soil Dynamics and Earthquake Engineering*, 29:1–16.

Sadeghi, H., Kimoto, S., Oka, F., and Shahbodagh, B. (2014). Dynamic analysis of river embankments during earthquakes using a finite deformation FE analysis method. In *14th International Conference of the International Association for Computer Methods and Advances in Geomechanics*, number 2011, pages 637–642, Kyoto, Japan.

Saez, E. (2009). *Dynamic nonlinear soil-structure interaction*. PhD thesis, Ecole Centrale Paris.

Sarma, S. (1975). Seismic stability of earth dams and embankments. *Géotechnique*, 25(4):743–761.

Sasaki, Y. and Tamura, K. (2007). Failure mode of embankments due to recent earthquakes in japan. In *4th International Conference on Earthquake Geotechnical Engineering*, number 1479, Thessaloniki, Greece.

Schanz, M. and Diebels, S. (2003). A comparative study of Biot's theory and the linear Theory of Porous Media for wave propagation problems. *Acta Mechanica*, 161:213–235.

Schofield, A. and Wroth, C. (1698). *Critical State Soil Mechanics*. McGraw-Hill, London.

Seed, H. B. and Idriss, I. M. (1970). Soil moduli and damping factors for dynamic response analysis. Technical report, University of California, Berkeley.

Seed, H. B. and Idriss, I. M. (1971). Simplified procedure for evaluating soil liquefaction potential. *Journal of the Soil Mechanics and Foundations Division*, 107(SM9):1249–1274.

Seed, H. B., Idriss, I. M., Lee, K. L., and Makdisi, F. I. (1975a). Dynamic analysis of the slide in the Lower San Fernando dam during the earthquake of February 9, 1971. *Journal of the geotechnical engineering division*, 101(GT9):889–911.

Seed, H. B. and Lee, K. L. (1966). Liquefaction of saturated sands under cyclic loading conditions. *Journal of the Soil Mechanics and Foundations Division*, 92(SM6):105–134.

Seed, H. B., Lee, K. L., Idriss, I. M., and Makdisi, F. I. (1973). Analysis of the slides in the San Fernando dams during the earthquake of Feb. 9, 1971. UCB/EERC-73/02. Technical report, Earthquake Engineering Reasearch Center, University of California, Berkeley.

Seed, H. B., Mori, K., and Chan, C. (1975b). Influence of seismic history on the liquefaction characteristics of sands. Technical report, Earthquake Engineering Research Center, University of California, Berkeley.

Servant, G., Darve, F., Desrues, J., and Georgopoulos, I. (2005). Diffuse modes of failures in geomaterials. In Di Benedetto, H., Doanh, T., Geoffroy, H., and Sauzéat, editors, *Deformation Characteristics of Geomaterials: Recent Investigations and Prospects*. A.A. Balkema Publishers.

Shahi, S. (2013). *A probabilistic framework to include the effects of near-fault directivity in seismic hazard assessment*. PhD thesis, Stanford University.

Shahir, H., Mohammadi-Haji, B., and Ghassemi, A. (2014). Employing a variable permeability model in numerical simulation of saturated sand behavior under earthquake loading. *Computers and Geotechnics*, 55:211–223.

Shahir, H., Pak, A., Taiebat, M., and Jeremic, B. (2012). Evaluation of variation of permeability in liquefiable soil under earthquake loading. *Computers and Geotechnics*, 40:74–88.

Sharp, M. K. and Adalier, K. (2006). Seismic response of earth dam with varying depth of liquefiable foundation layer. *Soil Dynamics and Earthquake Engineering*, 26:1028–1037.

Singh, R., Roy, D., and Jain, S. (2005). Analysis of earth dams affected by the 2001 bhuj earthquake. *Engineering Geology*, 80(3-4):282–291.

Sladen, J., D'Hollander, R., and Krahn, J. (1985). The liquefaction of sands, a collapse surface approach. *Canadian Geotechnical Journal*, 22:564–578.

Somerville, P., Smith, N., Punyamurthula, S., and Sun, J. (1997). Development of Ground Motion Time Histories for Phase 2 of the FEMA/SAC Steel Project. Technical report, SAC Joint Venture, Richmond, California.

Sorrentino, L., Kunnath, S., Monti, G., and Scalora, G. (2008). Seismically induced one-sided rocking response of unreinforced masonry facades. *Engineering Structures*, 30(8):2140–2153.

Spencer, E. (1967). A method of analysis of the stability of embankments assuming parallel inter-slice forces. *Géotechnique*, 17(1):11–26.

Stamatopoulos, C. and Aneroussis, S. (2004). Sliding-block back analyses of liquefaction-induced slides. In *13th World Conference on Earthquake Engineering, Vancouver, B.C., Canada, August 1-6, 2004*, number 3209.

Stockwell, R. G., Mansinha, L., and Lowe, R. P. (1996). Localization of the Complex Spectrum: The S-transform. *IEEE Transactions on signal processing*, 44(4):998–1001.

Sulem, J. and Ouffroukh, H. (2006). Shear banding in drained and undrained triaxial tests on a saturated sandstone: Porosity and permeability evolution. *International Journal of Rock Mechanics & Mining Sciences*, 43:292–310.

Swaisgood, J. (2003). Embankment dam deformation caused by earthquakes. In *Pacific Conference on Earthquake Engineering*.

Taiebat, M., Jeremić, B., Dafalias, Y. F., Kaynia, A. M., and Cheng, Z. (2010). Propagation of seismic waves through liquefied soils. *Soil Dynamics and Earthquake Engineering*, 30:236–257.

Taiebat, M., Shahir, H., and Pak, A. (2007). Study of pore pressure variation during liquefaction using two constitutive models for sand. *Soil Dynamics and Earthquake Engineering*, 27:60–72.

Tang, T., Roenby, J., and Hededal, O. (2012). A coupled soil-pore fluid formulation for modeling soil liquefaction and cyclic mobility in seabed using the finite volume method. In *The 2012 International Conference on Advances in Coupled Systems Mechanics*, volume m.

Terzaghi, K. and Peck, R. B. (1967). *Soil mechanics in engineering practice*. Wiley.

Tokimatsu, K. and Seed, H. (1987). Evaluation of settlements in sand due to earthquake shaking. *Journal of Geotechnical Engineering*, 113(8):861–878.

Truesdell, C. and Toupin, R. (1960). *The classical field theories. Handbuch der Physik*. Springer, Berlin.

Unjohn, S., Kaneko, M., Kataoka, S., Nagaya, K., and Matsuoka, K. (2012). Effect of earthquake ground motions on soil liquefaction. *Soils and Foundations*, 52(5):830–841.

Vaid, Y. and Chern, J. (1983). Effect of static shear on resistance to liquefaction. *Soils and Foundations*, 23(1):47–60.

Vardoulakis, I. and Aifantis, E. (1991). A gradient flow theory of plasticity for granular materials. *Acta Mechanica*, 87:197–217.

Verdugo, R. and González, J. (2015). Liquefaction-induced ground damages during the 2010 Chile earthquake. *Soil Dynamics and Earthquake Engineering*, pages 1–16.

Verdugo, R., Sitar, N., Frost, J. D., Bray, J. D., Candia, G., Eldridge, T., Hashash, Y., Olson, S. M., and Urzua, A. (2012). Seismic Performance of Earth Structures during the February 2010 Maule, Chile, Earthquake: Dams, Levees, Tailings Dams, and Retaining Walls. *Earthquake Spectra*, 28(June):75–96.

Vucetic, M. (1994). Cyclic threshold shear strains in soils. *Journal of Geotechnical Engineering*, 120(12):2208–2228.

Whitman, R. and Liao, S. (1985). Seismic design of retaining walls. Technical report, Miscellaneous Paper GL-85-1, US Army Engineer Waterways Experimental Station, Vicksburg, MS.

Xia, Z.-f., Ye, G.-l., Wang, J.-h., Ye, B., and Zhang, F. (2010). Fully coupled numerical analysis of repeated shake-consolidation process of earth embankment on liquefiable foundation. *Soil Dynamics and Earthquake Engineering*, 30(11):1309–1318.

Youd, T. and Noble, S. (1997). Magnitude scaling factors. Technical report, National Center for Earthquake Engineering Research, State University of New York at Buffalo.

Youd, T. L., Idriss, I., Andrus, R., Arango, I., Castro, G., Christian, J., Dobry, R., Finn, W., L.F., H. J., Hynes, M., Ishihara, K., Koester, J., Liao, S., W.F., M. I., Martin, G., Mitchell, J., Moriwaki, Y., Power, M., Robertson, P., Seed, R., and Stokoe II, K. (2001). Liquefaction resistance of soils: Summary report from the 1996 nceer and 1998 nceer/nsf workshops on evaluation of liquefaction resistance of soils. *Journal of Geotechnical and Geoenvironmental Engineering, ASCE*, 127(10):817–833.

Zabala, F., Rodari, R., and Oldecop, L. (2007). Seismic analysis of geotechnical structures using the material point method. In *4th International Conference on Earthquake Geotechnical Engineering*, number 1255, Thessaloniki, Greece.

Zentner, I. (2014). A procedure for simulating synthetic accelerograms compatible with correlated and conditional probabilistic response spectra. *Soil Dynamics and Earthquake Engineering*, 63:226–233.

Zentner, I. (2015). Génération de signaux sismiques. *Documentation of Code_Aster [R4.05.05]*.

Zentner, I., Allain, F., Humbert, N., and Caudron, M. . (2014). Generation ofspectrum compatibleground motion and its use in regulatory and performance-based seismicanalysis. In *9th International Conference on Structural Dynamics, EURODYN 2014*, Porto, Portugal.

Zhang, H. W., Sanavia, L., and Schrefler (2001). Numerical analysis of dynamic strain localisation in initially water saturated dense sand with a modified generalised plasticity model. *Computers and Structures*, 79:441–459.

Zienkiewicz, O. C. (1982). Basic formulation of static and dynamic behaviours of soil and other porous media. *Applied Mathematics and Mechanics*, 3(4).

Zienkiewicz, O. C., Chan, A. H. C., Pastor, M., Paul, D. K., and Shiomi, T. (1990). Static and Dynamic Behaviour of Soils: A Rational Approach to Quantitative Solutions. I. Fully Saturated Problems. In *Royal Society of London. Series A, Mathematical and Physical Sciences*, number June, pages 285–309.

Zienkiewicz, O. C. and Shiomi, T. (1984). Dynamic behaviour of saturated porous media; The generalized Biot formulation and its numerical solution. *International Journal for Numerical and Analytical Methods in Geomechanics*, 8:71–96.